THE COMPARATIVE ASSESSMENT OF CLINICAL ABLATIVE THERAPIES: EFFECTS ON PHYSIOLOGICAL AND BIOMECHANICAL PROPERTIES OF CONTRACTILE TISSUES IN RESPONSE TO THERAPEUTIC DOSES

A DISSERTATION

SUBMITTED TO THE FACULTY OF THE GRADUATE SCHOOL OF THE

UNIVERSITY OF MINNESOTA

BY

Ashish Singal

IN PARTIAL FULFILLMENT OF THE REQUIREMENTS

FOR THE DEGREE OF

DOCTOR OF PHILOSOPHY

Advisor: Paul A. Iaizzo, PhD

September 2014

Acknowledgements

The completion of this thesis would not have been possible without the unconditional support, encouragement, and guidance from several people. I would like to take this opportunity to thank those who have helped me in a myriad of ways.

First and foremost, I would like to thank my parents, Prof. Subhash Singal *(late)* and Mrs. Asha Singal, who made my education possible. Their words of inspiration and encouragement in pursuit of excellence constantly reverberate in my heart and mind. I want to thank my sister Shivika, who has constantly supported me and infused confidence in every step of the way.

I would like to express my sincere appreciation and heartfelt thanks to Prof. Paul Iaizzo. I am fortunate to have such a supportive, considerate, and outstanding advisor. His willingness to offer me so much of his time and intellect is the major reason this thesis has come to completion. Thank you Paul for giving me the opportunity to work in the Visible Heart Lab, providing constant direction and feedback on my research, but more importantly, providing an environment conducive to the best of learning. I also want to offer special thanks to my committee: Prof. Art Erdman, Prof. Will Durfee, and Prof. Bin He, from whom I have learnt so much and for the academic and research induction provided throughout the course of my research.

This large body of work would not have been possible without strong collaborations at multiple levels. I would like to thank my collaborators and

friends: Dr. Erik Cressman, Mr. Eric Rudie, Dr. John Ballard, Prof. Emad Ebinni, Prof. Dan Keefe, Dr. Peter Eckman, Dr. Farzad Azimpour, Mr. Seth Johnson, Dr. Anthony Weinhaus, Dr. Victor Barocas, Dr. Shailesh Musley, Dr. Eugenia Paulus, Dr. David Euler, Ms. Jodi Koehler, Dr. Saurav Paul, and many more for their instrumental support in designing protocols, executing studies, and analyzing data.

My words cannot measure the sincere appreciation I have for the entire lab staff. I am grateful to Monica for keeping the entire lab running smoothly, ordering supplies, but most importantly, for her tremendous efforts in preparing manuscripts. Many thanks are extended to Gary for his help with computer and technical support, all the way from data acquisition, analysis, and presentations. I am grateful to Charles who has been instrumental in helping prepare muscle bundles and seamless execution of studies, and Tinen for her ongoing support.

I have been fortunate to work with wonderful graduate students in the lab: Mike Bateman, Mark Benscoter, Mike Eggen, Salah El Haddi, Ryan Goff, Cole Holmgren, Brian Howard, Steve Howard, Lars Mattison, Steve Quallich, Jason Quill, Eric Richardson, Chris Rolfes, Megan Schmidt, Maneesh Shrivastav, Jules Spencer, and many others who I consider to be life-long friends.

I want to express my appreciation for all the dependable volunteers who helped in numerous ways. Their efforts and dedication was invaluable in helping prepare for studies, collect, and analyze data. Special thanks to Adam Beck,

Khoa Cao, Jennifer Chmura, Steve Conlon, Grant Gangeness, Chelsie GawneMark, Drew Paradis, Jake Starsiak, and Chad Thompson.

Funding for this thesis was provided, in part, by Medtronic Inc., research contract with the Visible Heart Lab.

Dedication

To family.
To medicine.

Abstract

Tissue ablation is a common medical procedure that involves manipulation of the target tissue with an aim to restore normal structure and function. Ablative treatments are performed throughout the human body for treating various carcinomas and disease conditions. Although a routine clinical procedure, in a small percentage of patients it may cause collateral damage to surrounding vital structures which can have severe clinical implications. As such, the collateral damage results in altered tissue properties those are dependent on the level of ablative energy and extent of tissue injury. Therefore, assessment of tissue properties is fundamental to advancing the understanding of underlying basic and clinical science of ablations, especially to maximize therapy efficacy and minimize procedural complications. Thus, a thorough understanding of tissue properties is critical to the successful outcome of nearly all ablation procedures.

Unique laboratory methodologies were developed that were reliably used to assess the physiological and biomechanical properties of respiratory diaphragm, esophagus, cardiac trabeculae, and vastus lateralis tissues following exposure to five different therapeutic ablative modalities: radiofrequency ablation, cryoablation, high-intensity focused ultrasound ablation, microwave ablation, and chemical ablation (with acetic acid, ethanol, hypertonic sodium chloride, and urea). The changes in physiological properties were quantified by measuring changes in peak force (strength of contractions) and baseline force (resting muscle tension) in response to ablations. The changes in biomechanical

properties were quantified by measuring the stress-strain characteristics, avulsion forces, and elastic moduli in response to ablations. Dose effect responses of each ablative modality were quantified. In addition, biomechanical properties of non-contractile tissues such as pericardium, aorta, lungs, and trachea were also measured.

To our knowledge these are the first reports of such methodological comparative assessment of tissue properties following treatment with therapeutic ablative modalities at clinically relevant doses. The understanding of tissue properties has wide applications ranging from applied research to the development of novel tools, ablation techniques, and innovative clinical treatment options. These findings may provide novel insights into the effects of ablations on various tissues which may in turn allow further improvements in ablative techniques to increase the overall safety and efficacy of ablative procedures. Knowledge gained from these studies may be used for procedure planning, modeling and dosing optimization. Furthermore, these methodologies could be utilized in a realistic framework for developing bench top testing of device-tissue interactions that can aid in novel medical device design. It is clear that the understanding of collateral damage at the cellular level, isolated tissue level, and whole organ level will be important to the future of this evolving era of ablations.

Table of Contents

List of Tables

List of Figures

1. A Review of Therapeutic Ablation Modalities and Biophysics

Preface

This review serves as an introduction to various therapeutic ablation modalities used clinically throughout the body for treatment of different diseases. Also discussed in detail is the underlying biophysics of five ablation modalities and how tissue injury results from ablative treatments. A thorough literature search was performed from multiple sources to assemble this article which is submitted to the Journal of Medical Devices in June 2014 and is currently under review. The reader can not only grasp the widespread therapeutic applications of ablative energies, but also use this information for innovation as it relates to designing new tools, techniques, and procedures for medical device design.

Ashish Singal
University of Minnesota
420 Delaware St. SE, B172 Mayo Building, MMC 195
Minneapolis, MN 55455
singa009@umn.edu

John R. Ballard
University of Minnesota
420 Delaware Street SE, G217 Mayo Building, MMC 95
Minneapolis, MN 55455
ball0250@umn.edu

Eric N. Rudie
Rudie Consulting LLC
18466 Gladstone Blvd.
Maple Grove, MN 55311
erudie@rudieconsulting.com

Erik N.K. Cressman
MD Anderson Cancer Center
Department of Interventional Radiology
FCT 14.6012 Unit 1471
1400 Pressler St.
Houston TX 77030
ECressman@mdanderson.org

Paul A. Iaizzo
University of Minnesota
420 Delaware St. SE, B172 Mayo, MMC 195
Minneapolis, MN 55455
iaizz001@umn.edu
ASME Member

Executive Summary

Understanding basic science and technical aspects is essential for scientists and engineers to develop and enhance ablative modalities, and for clinicians to effectively apply therapeutic ablative techniques. An overview of ablative modalities, anatomical locations, and indications for which ablations are performed is presented. Specifically, basic concepts and underlying biophysics of tissue injury of five currently used therapeutic ablative modalities are reviewed: radiofrequency ablation, cryoablation, microwave ablation, high-intensity focused ultrasound, and chemical ablation (ablative agents: acetic acid, ethanol, hypertonic sodium chloride, and urea). Each ablative modality could be refined for expanding applications, either independently or in combination, for future therapeutic use.

Key words: radiofrequency, cryoablation, microwave, high-intensity focused ultrasound, chemical ablation

Introduction

The fields of medical device design and applied therapies are evolving at a rapid pace. New techniques and procedures are being developed in response to the demanding challenges of increasing overall efficacy and successful outcomes of procedures. The medical community, including physicians, scientists, and engineers, is challenged by four most pressing issues: (1) reducing procedure times; (2) reducing procedure costs; (3) minimizing procedure invasiveness; and (4) increasing procedure safety and effectiveness to achieve better outcomes. Though this is applicable in every branch of medicine, we consider here the particular specialties dealing with tissue ablations.

Ablative Modalities Investigated

Ablation is a common medical procedure that involves manipulation of the target tissue with an aim to restore normal structure and function. Reports describing the clinical use of ablations date back to the late eighteenth century [1], and these therapeutic techniques have now secured a prominent place in medicine. Since then, scientists and engineers have continued to innovate and explore the electromagnetic spectrum and different sources of energy that are safe and potentially useful for various tissue ablation procedures.

To date, numerous ablative modalities are used in research and clinical medicine. The therapeutic ablative techniques reviewed in this article include: radiofrequency ablation (RFA), cryoablation (CRA), microwave ablation (MWA), high-intensity focused ultrasound (HIFU) ablation, and chemical ablation (CHA).

Importantly, ablation treatments are performed throughout the human body for various disease states, often utilizing different ablative modalities. Figure 1 illustrates a detailed list of anatomical locations where ablations are performed, along with the indications and ablative modalities that have been used. In addition, Table 1 lists some of the references for choice of ablation modality describing both for research and/or clinical practice for each anatomical location [2-91].

In general, ablative modalities can be divided into two primary categories, thermal and chemical ablation. Although procedure indications, patient selection criteria, available tools and techniques, and choice of ablative modality used vary among treatments, both categories take advantage of various physical, chemical, and biological properties of tissues to induce local cell injury, ultimately leading to cellular necrosis. The thermal ablation technique alters the focal temperature of the tissue being ablated with heating or cooling, causing direct or indirect cell death. Specifically, RFA, MWA, and HIFU ablative techniques induce heat within the target tissue to cause cell injury, whereas CRA therapy induces cooling at the target location to cause tissue destruction. In contrast, CHA agents, such as ethanol, acetic acid, hypertonic sodium chloride solution, or urea rely on focal cellular toxicity and protein denaturation to produce cellular necrosis.

Familiarity with the underlying science, biophysical mechanisms, and technical aspects of ablative techniques is essential for clinicians to effectively treat ablative cases. This article provides an overview of five currently used

ablative techniques to achieve thermal and chemical ablation of tissues. Specifically, the article addresses the basic science and principles of biophysics of ablative techniques as they relate to tissue injury.

Brain [2-5]	Tonsils [22-25]	Liver [48-50]	Cervix [76]
Occipital [6, 7]	Esophagus [26-29]	Gallbladder [51-53]	Celiac Plexus [77-78]
Dental [8-10]	Heart [30-35]	Renal [54-57]	Veins [79-81]
Ear [11, 12]	Lung [36-39]	Adrenal Gland [58-61]	Spine [82-85]
Face [13-15]	Breast [40-42]	Prostate [62-67]	Bone [86-89]
Thyroid [16, 17]	Spleen [43-44]	Bladder [68-70]	Toe [90, 91]
Parathyroid [18-21]	Pancreas [45-47]	Uterus [71-75]	

Table 1: Table of anatomical locations where ablations are performed

Figure 1: Illustration of anatomical locations where ablations are performed
List of anatomical locations where ablations are performed, disease condition, and the ablation modalities used. AF=atrial fibrillation; AVN=atrioventricular node; BPH=benign prostatic hyperplasia; Cryo=cryoablation; HCC=hepatocellular carcinoma; HIFU=high-intensity focused ultrasound; HTN=hypertension; IRE=irreversible electroporation; MWA=microwave ablation; OCD=obsessive compulsive disorder; PDT=photodynamic therapy; RFA=radiofrequency ablation; SND=sinus node dysfunction; SVT=supraventricular tachycardia; VT=ventricular tachycardia.

Region: **Brain**
Ablation: MR-guided laser-induced thermal therapy (MRgLITT), Thulium (Tm:YAP) laser ablation, MR-guided focused ultrasound (MRgFUS), Non-thermal irreversible electroporation (N-TIRE) induced ablation
Treatment: Brain tumors, OCD, Neurological Issues

Region: **Brain, PNS**
Ablation: RFA, Surgical ablation
Treatment: Occipital neuralgia, headaches, migraines

Region: **Thyroid**
Ablation: RFA, Chemical (EtOH)
Treatment: Thyroid carcinomas

Region: **Parathyroid**
Ablation: RFA, Laser, Chemical (EtOH)
Treatment: Parathyroid adenomas

Region: **Middle ear, eustachian tube**
Ablation: Laser, Electrosurgical
Treatment: Bone surface ablation of middle ear ossicles, Middle ear ventilation (otitis media)

Region: **Teeth**
Ablation: Laser
Treatment: Dental lesions and calculus

Region: **Breast**
Ablation: RFA, Cryo, MWA, Laser, HIFU
Treatment: Breast carcinomas

Region: **Lung**
Ablation: RFA, Cryo, MWA, HIFU, IRE
Treatment: Primary and metastatic tumor

Region: **Tonsils**
Ablation: RFA, Cryo, Laser
Treatment: Tonsillectomy, Tonsillar cancer

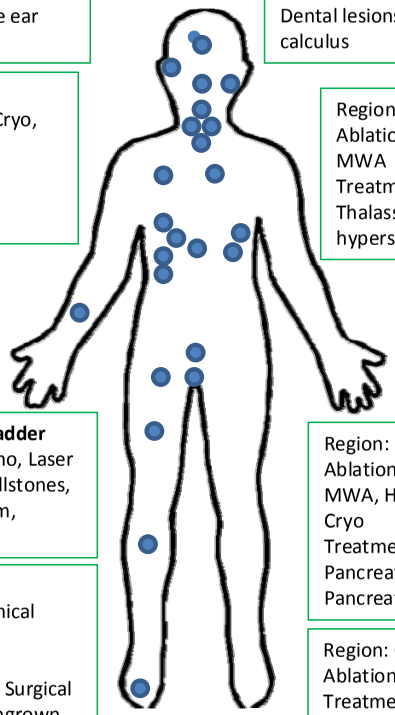

Region: **Spleen**
Ablation: RFA, MWA
Treatment: Thalassemia, hypersplenism

Region: **Face**
Ablation: Laser, RFA
Treatment: Cosmetics, burns, trigeminal neuralgia

Region: **Liver**
Ablation: RFA, Cryo, MWA, HIFU, Chemical, IRE
Treatment: HCC, Metastatic disease

Region: **Heart**
Ablation: RFA, Cryo, MWA, HIFU, Chemical (EtOH)
Treatment: AF, SND, SVT, AVN, VT

Region: **Spine**
Ablation: RFA, IRE
Treatment: Lumbar & Cervical Radiofrequency Ablation/Lesioning, Lower Back Pain, Neck Pain, Abdominal Pain, Pelvic Pain, Complex Regional Pain Syndrome, Metastatic disease

Region: **Esophagus**
Ablation: RFA, Cryo, PDT
Treatment: Barrett's esophagus, esophageal cancer

Region: **Gallbladder**
Ablation: Chemo, Laser
Treatment: Gallstones, Cholecystectom, Cholecystitis

Region: **Pancreas**
Ablation: RFA, MWA, HIFU, IRE, Cryo
Treatment: Pancreatitis, Pancreatic Cancer

Region: **Celiac Plexus**
Ablation: Chemical (EtOH)
Treatment: Chronic pain management, neurolysis

Region: **Bladder**
Ablation: Chemical, MWA, Laser
Treatment: Bladder cancer

Region: **Toes**
Ablation: Chemical (phenol)
Treatment: Matrixectomy, Surgical treatment of ingrown toenails

Region: **Cervix**
Ablation: RFA
Treatment: Cervical cancer, polyps

Region: **Prostate**
Ablation: Laser, RFA, Cryo, MWA, HIFU, Chemical
Treatment: Prostatitis, BPH, Prostate Cancer

Region: **Kidney**
Ablation: RFA, MWA, HIFU, Chemical, IRE
Treatment: Renal tumors, Refractory HTN

Region: **Adrenal Gland**
Ablation: RFA, Cryo, MWA, Chemical
Treatment: Adrenocortical carcinoma, Metastatic tumors

Region: **Bone**
Ablation: RFA, Cryo, HIFU, MWA
Treatment: Painful bone metastasis

Region: **Uterus**
Ablation: RFA, Cryo, MWA, HIFU, Chemical
Treatment: Endometrial ablation (excessive or prolonged bleeding during menses), Uterine fibroids

Region: **Veins**
Ablation: Laser, RFA, MWA, Sclerotherapy, Chemical (EtOH)
Treatment: Varicose veins, Vascular malformations (arterio-venous)

Radiofrequency Ablation

Radiofrequency catheter ablation was first introduced by Huang and colleagues in 1985 [92]. In the past three decades, it has become one of the most useful and widely employed therapies for treating various forms of diseases, and indications for its use continue to expand. RF ablative energy is a form of alternating electrical current that, when dissipated, generates a lesion in the tissue by mode of resistive (electrical) heating. Typically, alternating currents of around 500 KHz are utilized. Note that lower frequencies are more likely to stimulate surrounding tissues (muscles and nerves), however higher frequencies dissipate energy in the tissues in the form of heat. Developing an insightful understanding into the biophysics of RF energy delivery and the underlying mechanisms of tissue injury will aid in optimizing therapy and ultimately enhance its safety and efficacy.

Biophysics of Radiofrequency and Resultant Tissue Injury

The mode of tissue heating by radiofrequency energy is by resistive heating, similar to heat produced by electrical sources. As electrical current passes through a resistive medium (tissue), there is voltage drop, and heat is produced. The heat produced in the tissue is analogous to the heat produced when current flows through an incandescent light bulb. Resistive heat produced within the tissue is proportional to the RF power density at the electrode which, in turn, is proportional to the square of the current density at the electrode. Within

tissue, the current density decreases in proportion to the square of the distance from the electrode. Therefore, RF resistive heating of the tissue decreases in proportion to the fourth power as a function of distance from the RF electrode. As a result, only a narrow rim of tissue in close contact with the RF electrode is heated directly. Note that there is resultant heating of deeper layers of tissue that occurs passively through conduction, and is not considered to be harmful. In fact, depending on the therapeutic application, heating of deeper layers is often required to create a transmural lesion. The depth of both the resistive and conductive heating increases at higher power levels, which also results in an increase in the lesion volume. Numerous factors affect the quality of RF delivery and the resulting lesion size. Some of these factors are listed below:

1. **Target Selection:** If the target selection is poor, simply increasing the size and depth of lesion will not improve the chances of a successful therapeutic ablation. To optimize target location, it is necessary to understand the anatomy and pathophysiology of the target region in its entirety. The proximity of the electrode to the target where ablation needs to be performed is one of the most important factors for ablation success.
2. **Tissue Composition:** Variations in tissue composition result in different tissue thermal conductivities and electro-mechanical properties. These differences result in heterogeneous tissue responses to applied energies, which further result in different lesion sizes. For example, lesion size is

significantly impacted by formation of dense scar, and an insulating layer of fat can prevent the formation of a clinically acceptable lesion [93].

3. **Power:** In general, lesion size is proportional to the applied RF power. That is, a greater amount of RF power deposited in the tissue results in more tissue heating and a greater depth of thermal injury and lesion size as shown in Figure 3. In addition, efficiency of power delivery within the tissue plays an important role, as energy coupling can change not only with convective cooling effects, but also with scarring at the electrode-tissue interface. It should be noted that saline-irrigated RF ablation catheters have been utilized which, by design, produce a lower tip temperature (for a given RF power) but higher temperatures deeper within the tissues. This is particularly useful for cardiac ablations of ventricular myocardium since deeper transmural lesions are often required.
4. **Electrode Temperature:** In general, lesion size increases in proportion with electrode temperature until the point of tissue coagulation, which usually results in the rise in tissue impedance. This effect is confounded by the effects of convective cooling, perfusion, and relative motion between the RF electrode and target location.
5. **Peak Tissue Temperature:** This factor is the primary determinant of the ultimate RF lesion size. It should be noted that because of convective cooling effects, perfusion effects, and/or relative motion at the electrode-tissue interface, the electrode temperature (measured by a variety of

temperature sensors on RF electrodes) may often underestimate the peak tissue temperature.

6. **Electrode Contact Pressure:** A greater electrode-tissue contact pressure results in an increase in the lesion size as shown in Figure 2. This is achieved because of improved electrical coupling between the electrode-tissue interface, increased electrode contact surface area with the tissue, and reduced shunting of current in the form of convective current losses [94]. In addition, a greater contact pressure may prevent relative motion between the electrode-tissue interface resulting in more efficient RF energy coupling and delivery. However, excessive pressures may bury the electrode within the tissue resulting in an increased probability of tissue charring, thus reducing RF energy coupling and delivery.
7. **Convective Cooling:** Convective cooling occurs due to regional blood flow and perfusion at the target tissue location. In general, target locations that are highly perfused (e.g., heart) are more susceptible to convective cooling effects than target locations that are less perfused (e.g., prostate). Convective cooling results in decreased lesion size as it draws heat energy away from the target location, resulting in less heat energy available to create the lesion. Lesion size is ultimately a function of tissue heating which, in turn, is a function of magnitude of RF power that is converted into heat at the electrode-tissue interface. It should be noted that high electrode pressure (above the capillary perfusion pressure of 40

mm of Hg) could play a significant role in altering the convective cooling effects.

8. **Electrode Size:** The use of a larger electrode size will generally result in a larger lesion size as shown in Figure 3. This results from an increase in the contact surface area which allows not only efficient RF energy coupling, but also delivery of higher power without excessive current densities at the electrode-tissue interface. Moreover, coagulum formation that results in sudden rise in impedance can be avoided.
9. **Duration of Applied Energy:** Tissue temperature follows a monoexponential rise during RF energy delivery, until a steady state is achieved. Although steady state is often achieved within 8 to 15 seconds after start of RF energy delivery, the duration of energy must be titrated based on both the unique pathophysiological features of the target location and the extent of desired lesion. An illustration is shown in Figure 2.
10. **Electrode-Tissue Impedance:** According to Ohm's law, an applied voltage is equal to the product of current and impedance. Thus, for smaller impedance, greater current delivery can be achieved for a given applied voltage. Note that the relative relationship in impedance between electrode-tip and tissue-interface is complex, hence it is important to have good electrode contact with optimum pressure at the target tissue interface in an attempt to maximize energy coupling and optimize energy

delivery [95]. A greater current delivery results in greater resistive heat loss at the electrode-tissue interface, thus forming a larger lesion size.

11. **Electrode Orientation:** An orientation that results in a larger electrode-tissue contact area generally causes a larger lesion size. In many clinical situations, electrode orientation can be manipulated during therapy delivery to optimize coupling and thus, maximize energy delivery to the target area.
12. **Electrode Geometry**: In order to maximize therapy efficacy, it is best to customize electrode geometry to conform to the target location where the lesion is desired. Electrode shapes that allow greater electrode-tissue contact area generally result in higher coupling efficiency and higher power delivery, resulting in a larger lesion size.
13. **Electrode Material**: Materials with high heat transfer characteristics allow for greater current delivery at the electrode-tissue interface, thus resulting in a larger lesion size. These materials are not only effective in transferring energy at the electrode-tissue interface, but are also effectively cooled by blood perfusion.

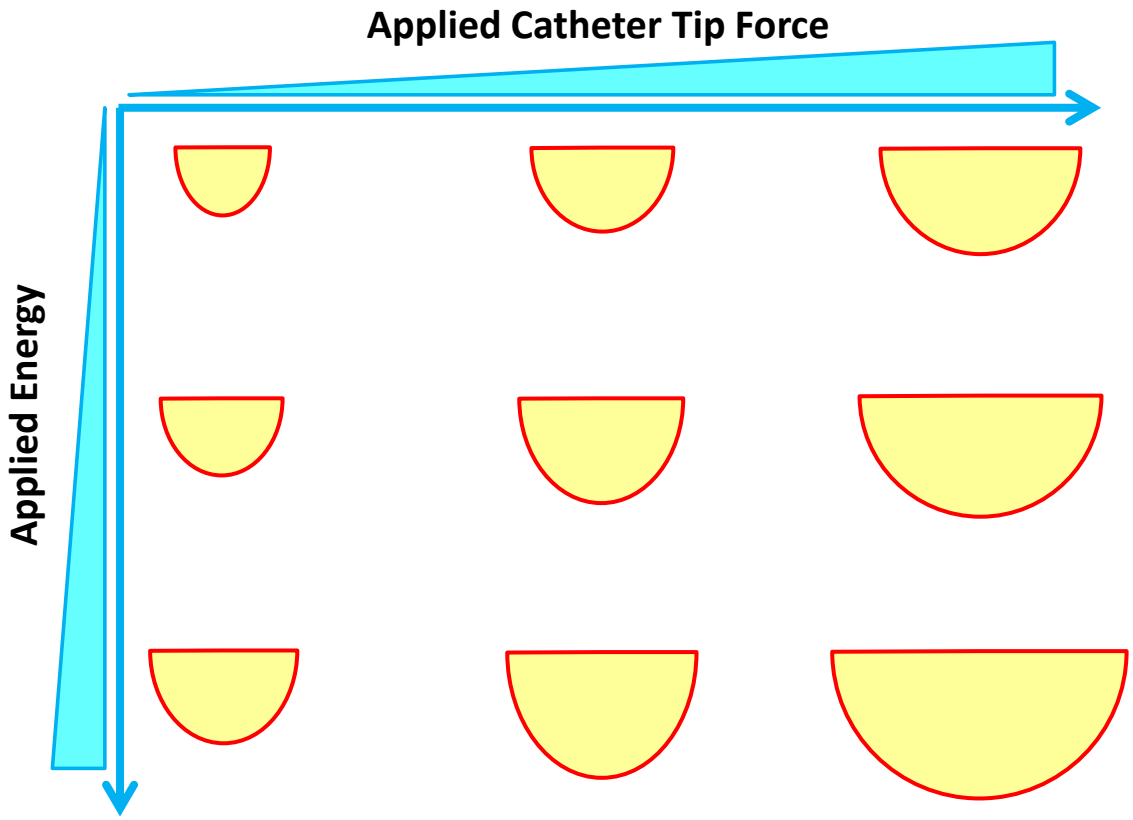

Figure 2: Effect of applied catheter tip force and energy on lesion size

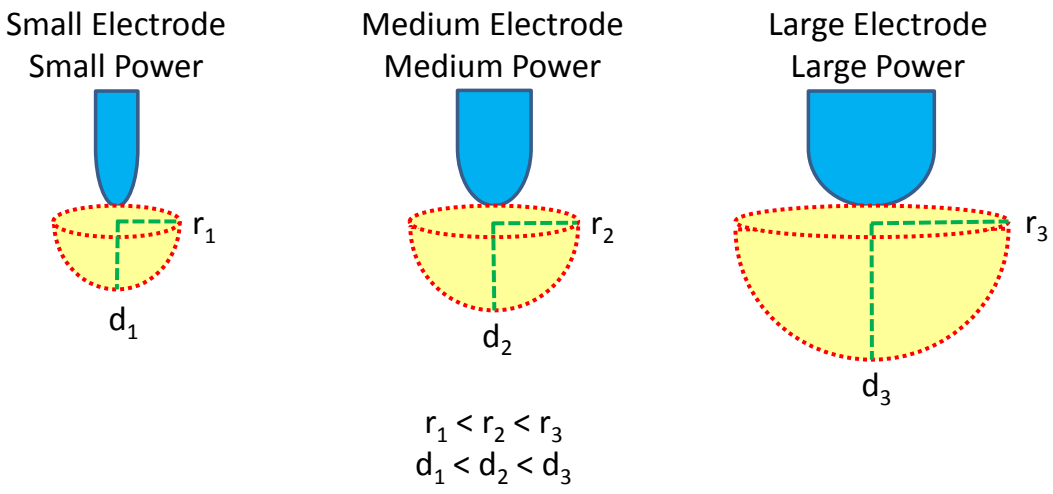

Figure 3: Effect of electrode size and applied power on lesion size

Cryoablation

Reports of using extreme hypothermia date back to 1930s, with investigations on life expectancy, recovery, and death following exposure to extreme cold [96]. Numerous cryosurgical devices were pioneered in 1960 that used liquid nitrogen as a refrigerant [97, 98]. Since then, harnessing cryoenergy has been an area of intense interest and investigation, and numerous clinical systems are now available to perform cryoablations throughout the body. For example, the safety and efficacy of cryoenergy ablation on myocardial tissue have been well recognized, where the effect of hypothermia on the conduction system was achieved using carbon dioxide [99].

Biophysics of Cryoablation and Resultant Tissue Injury

Although the exact mechanism whereby cell death is produced by hypothermia is still not clearly understood, cryoablation works by freezing tissue in a discrete and focused manner to destroy cells in a target location. It has been reported that the application of cryoenergy results in the formation of an ice-ball at the target area that causes freezing, thawing, hemorrhage, inflammation, fibrosis, and apoptosis [100]. Freezing typically extends radially into the tissue, establishing a temperature gradient. The lowest temperatures and fastest freezing rates are typically found at the cryoprobe-tissue interface, with slower freezing rates at deeper aspects of the target volume. Hypothermia causes: (1) the intracellular and extracellular environment to become cold and eventually

freeze; (2) cells to become less fluid as metabolism slows; (3) slowing in cellular functional kinetics; (4) loss of ion pump transport capabilities; and (5) intracellular pH to become more acidic [101]. The hallmark of permanent tissue injury induced by cryoablation has been considered to be ice formation. Specifically, as the targeted region is cooled, it is characterized by the formation of extra- and intracellular ice crystals [102, 103]. Formation of ice crystals causes compression and distortion which severely damages the cellular components, cellular membrane and underlying cellular machinery [103]. Ice crystal formation also results in osmolarity changes across the cell membrane, which further contributes to overall cell death and necrosis. The initial compression effects are followed by tissue destruction that occur during the ensuing thawing period that can last several hours [104, 105]. Initial rewarming causes intracellular ice crystals to enlarge and aggregate into large masses that further exacerbate cellular destruction. Hemorrhage and inflammation characterize the subsequent phase of cryoablation that involves water migration across the cells to reestablish the osmolarity equilibrium gradient that was altered by the formation of ice crystals. As a result, altered solute-solvent concentration within and outside the cell causes damage to the cell membrane, eventually leading to lysis of the cell. Furthermore, restoration of blood flow to previously frozen tissue results in edema and ischemic necrosis. Finally, cryoinjury results which triggers apoptosis, and thus a mature lesion ensues within days to weeks [106]. Numerous factors

affect the quality of cryotherapy delivery and thus the resulting lesion size. Some of these factors are listed below:

1. **Target Selection**: In general, this would be similar to what has been described in the RFA section.
2. **Tissue Composition**: In general, this would be similar to what has been described in the RFA section.
3. **Freezing Duration**: Experimental studies have demonstrated that the lesion depth is determined by the duration of freezing [107]. It is well documented that longer cryoduration results in a larger lesion size [108]. Hence, thicker tissue substrates may require much longer applications of cryotherapy to achieve transmural lesions as compared to thin areas. However, some studies have investigated improved lesion formation and size by applying double freeze cycles (i.e., freezing-thawing-freezing)[109]. That is, refreezing thick areas potentiates cell death because of repeated freeze/thaw cycle and increases lesion size.
4. **Lethal Temperatures**: Depending on the target location and relative blood perfusion, lethal temperatures are typically reached within 15 to 30 seconds of cryotherapy initiation. Although irreversible damage to cells occurs at temperatures as low as -50 to -80°C, cryomapping at temperatures close to -20°C are often utilized to evaluate the clinical effectiveness of therapy applications [110].

5. **Cryoprobe Tip Temperature**: In general, lower cryoprobe tip temperatures result in larger cryolesions. However, other variables such as rate of cooling and perfusion effects play an important role.
6. **Catheter Adhesion**: As long as there is some contact with the target tissue, the formation of an ice-ball at the tip of the catheter during cryoablation causes the catheter to adhere to the adjacent tissue being ablated (cryoadhesion). This allows for potentially sensing the electrical activity of the underlying tissue (e.g., the heart) without risk of catheter motion or dislodgement. Moreover, cryoablations can then be performed with minimal risk of dislodgement under natural movements from respiration or cardiac rhythm. Good catheter tip adhesion with the tissue results in a larger lesion size.
7. **Rate of Freezing**: A faster rate of cooling has been observed to be more lethal, contributing to faster cellular death, hence resulting in a larger lesion size [110]. At the borderline zone though, a combination of lower temperatures and reduced rate of cooling contribute to reversible cell damage. Hence, during therapy planning, rate of cooling and application duration are typically pre-determined to achieve a transmural lesion.
8. **Contact Pressure**: Increased catheter tip contact pressure results in a faster rate of freezing because of compression of tissue and decreased convection effects due to blood perfusion warming. Hence, an increased

catheter tip pressure is likely expected to result in a larger lesion size [111].

9. **Cryoprobe Size**: Cryoprobe size is an important determinant of procedural success and lesion character. Typically catheters with cryoprobe tips (4, 6, and 8 mm) and cryoballoon are available clinically. Lesion size has been shown to increase with catheter tip size [105]. A large sized catheter tip that can accommodate large diameter refrigerant channels, coupled with a larger cryoprobe-tissue contact surface area, is likely expected to result in a larger lesion size. Note, for ablation of the cardiac pulmonary-vein ostium, a cryoballoon system has been developed and utilized quite successfully [112].
10. **Blood Perfusion**: Areas having low perfusion result in larger cryolesion formation due to reduced warming convective effects from blood.
11. **Cryoprobe Orientation**: A catheter orientation that results in larger cryoprobe-tissue contact area generally results in a larger lesion size. Unlike RFA, cryoprobe orientation can only be slightly manipulated during therapy delivery due to cryoadhesion between the cryoprobe and the tissue.
12. **Cryoprobe Geometry**: In order to maximize therapy efficacy, it is best to customize cryoprobe geometry to conform to the target location where the lesion is desired. Cryoprobe shapes that allow greater cryoprobe-tissue contact area result in larger lesion size.

High-Intensity Focused Ultrasound Ablation

Ultrasound (US) consists of mechanical pressure waves with frequencies above 20 kHz (beyond human audible range of 20 Hz to 20 KHz). For medical imaging, US transducers in the frequency range of 1–20 MHz are utilized. Ultrasound requires a medium for propagation which alternates compressions and rarefactions of particles, thus advancing the pressure wave within the medium. The field of US in clinical practice is no longer limited to simple diagnostic imaging or percutaneous guidance procedures. When high intensity US waves are focused in a small region, they can be used for therapeutic purposes such as inducing deep hyperthermia and ultimately tissue ablation. Hence, HIFU systems operating in the frequency range of approximately 500 KHz–7.5 MHz are emerging as a non- or minimally invasive method for treatment of various forms of diseases.

Biophysics of High-Intensity Focused Ultrasound and Resultant Tissue Injury

The field of tissue ablation is evolving towards greater use of noninvasive or minimally invasive modalities such as HIFU. Unlike RFA or CRA, HIFU can be employed as a noninvasive or minimally invasive modality that can be used to ablate tissues lying deep within the body. In order to understand HIFU, it is important to compare the characteristic energy levels of HIFU versus diagnostic US. Most commonly used diagnostic US transducers deliver US intensities in the range of 0.1 to 300 mW/cm^2 and pressures in the range of 1KPa to 3KPa [113].

In contrast, HIFU transducers deliver US with intensities typically in the range of 100 to 10,000 W/cm^2 and pressures in the range of 10 to 30 MPa [114].

HIFU can create controlled ablative tissue lesions through two primary modes of tissue injury: thermally induced injury (from thermal energy) and mechanically induced injury (from mechanical energy). The major ablative effect of HIFU is from heat generation within tissues due to absorption of the applied acoustic energy. The amount of acoustic energy transferred from the acoustic wave to the tissue is directly proportional to the intensity of the wave and the innate absorption coefficient of that specific tissue. In continuation, the amount of heat dissipated in the tissue is dependent on numerous factors, such as: (1) frequency of incident wave; (2) thermal conductivity of the tissue; (3) tissue density; (4) and local tissue perfusion. The heat generated raises the local temperature to ablative levels causing coagulation necrosis within a few seconds. The temperature at the transducer focus can reach over 65°C within seconds, denaturing cellular proteins and resulting in coagulative necrosis [115]. Mechanical effects are representative of higher intensities, but generally not present at lower intensities [116]. Mechanical phenomena such as microcavitation as a result of oscillations and collapse of gas bubbles within the tissue can occur, and can further lead to near instantaneous boiling temperatures [117, 118]. Specifically, violent collapse and destruction of bubbles cause disruption of cell membrane, organelles, and cellular proteins from which one may anticipate mechanical damage rather than thermal damage to the cell.

It is important to note that the cells exhibit an intrinsic protective behavior when exposed to hyperthermia. When exposed to stressful heat, mammalian cells produce heat-shock proteins [119, 120]. Scientists believe that such activated proteins help to protect the cells against damage from heat. However, HIFU heats the tissues so quickly that the cells most often do not have time to transcribe these heat-shock proteins as a protective mechanism. Numerous factors affect the quality of HIFU delivery and the resulting tissue lesions. Some of these factors are listed below:

1. **Target Selection:** In general, this would be similar to what was described in the RFA section.
2. **Tissue Composition**: In general, this would be similar to what was described in the RFA section.
3. **HIFU Duration**: Although tissue injury is dependent on mechanical and thermal effects, in general, longer HIFU duration will result in a larger lesion size. HIFU energy is continuously absorbed and converted into heat within the tissue. This thermal effect can cause substantial tissue injury if the temperature elevation reaches above the threshold of injury potential and is maintained for an adequate period of time. Importantly, if not precisely controlled, this can cause collateral damage to surrounding vital structures. To minimize injury to surrounding structures, techniques such as temporal modulation have been utilized where the output of the HIFU

system is switched on and off at a predetermined rate (approximately 1 Hz) to achieve controlled conductive heat transfer [121].

4. **Incident Energy**: HIFU has the power to create controlled, localized tissue injury through both thermal (absorption of acoustic energy which is converted into heat) and mechanical (oscillation and collapse of micro-bubbles and cavitation) effects. An increase in incident energy (power and/or intensity) may cause boiling of tissue water which may lead to the formation of vapor cavities [122]. Hence, a precise control of incident energy is needed to achieve complete ablation of target tissue volumes. Techniques such as power modulation have been attempted to control induced tissue necrosis and thus minimize complications [121].
5. **Lesion Separation**: Successful HIFU treatment requires complete ablation of target tissue volume. In order to destroy the entire tissue volume, it is essential to place a contiguous array of lesions side-by-side with their lesion borders touching each other throughout the target lesion volume. In doing so, a phenomenon called lesion-to-lesion interaction has been reported [123], which occurs when the spatial separation of individual exposures are such that an existing lesion appears to affect the formation of the subsequent lesions. In some cases, this phenomenon may cause focal aberrations that may fail to cover the entire tissue volume. It has been suggested that by allowing the tissue to cool between

exposures, it may be possible to form arrays of overlapping lesions, thus successfully ablating the complete target region [124].

6. **Tissue Edema**: Although HIFU has the merit of being relatively noninvasive in nature, there is a high potential for the portion of skin and subcutaneous tissue along the pathway of focused ultrasound to be affected, thus causing tissue edema. Since large tumors require longer ablation time, the resulting cutaneous and subcutaneous tissue edema may not only reduce the targeting ability of the diagnostic ultrasound, but also negatively affect the precision of deposition of focused ultrasound onto the target lesion. Hence, large tumors may need “planned” repeated HIFU treatments, or at least subsequent treatment, once a residual lesion has been detected by US imaging.
7. **Blood Flow**: Areas having low perfusion result in larger lesion formation due to reduced convective cooling effects from blood [125].

Microwave Ablation

Microwaves (MW) are high frequency electromagnetic radiations occupying the 300 MHz to 300 GHz frequency range of the electromagnetic spectrum. The Federal Communications Commission (FCC) permits several unrestricted bands for medical use; some of the most common frequencies used for microwave ablation are 915 MHz, 2.45 GHz, and broadband frequencies between the range of 1 GHz and 10 GHz [126]. The earliest use of microwaves

for ablative therapy date back to the early 1990s, when Langberg et al [127] used microwaves to ablate the cardiac atrioventricular junction using a helical microwave antenna. Since then, numerous advances in this field have prompted clinicians to develop newer antenna designs and therapeutic ablation techniques. Unlike RFA, the application of microwaves causes dielectric heating of tissues and the underlying biophysics are discussed below.

Biophysics of Microwave Ablation and Resultant Tissue Injury

MWA is one of the more recent techniques in the field of clinical ablation therapies that relies on dielectric heating of tissue rather than electrical resistive heating as with RFA. At such high frequencies, dielectric heating of tissue occurs when electromagnetic radiation stimulates oscillations of dipole molecules such as water within the cellular and extracellular medium, which converts the electromagnetic energy into oscillating kinetic energy. This energy is dissipated as heat at the target location which results in thermal injury. These electromagnetic waves can propagate in free space and in conductive mediums like the human body, thus allowing for a greater amount of heat deposited in deeper structures. With regard to biological tissues, there are inherent differences in tissue properties related to thermal conductivity and dielectric constant. Moreover, tissue properties along with tissue electrical conductivity and relative permittivity vary as a function of frequency. These differences are significant among different types of tissues in the human body which makes them

respond differently to these high frequency microwaves. Along their propagation path within the body, MWs are extracted and absorbed in various tissues. Tissues with higher water concentration (e.g., muscle, blood) absorb more waves which results in higher heating due to dielectric dissipation of energy converted into kinetic energy, as compared to tissues with lower water concentration (e.g., bone). However, tissues with lower water concentration absorb less MWs, thus allowing deeper penetration of waves. Some of the considered advantages of MWA are: (1) MW antennas radiate electromagnetic waves in the surrounding medium [127]; (2) wave propagation in conductive medium allows for deeper heating [128]; (3) unlike RFA, a return/dispersive electrode on patient skin is not required [126]; and (4) MWA does not require tissue contact for energy delivery and ablation [126]. In regards to the propagation of MWs in biological medium and their ability to cause hyperthermia injury, the important factors for consideration are listed below:

1. **Target Selection:** In general, this would be similar to what was described in the RFA section.
2. **Operating Frequency**: MW penetration and rate of hyperthermia in tissue are highly dependent on operating MWA frequency. Typically, lower frequency waves provide a deeper field penetration inducing deeper heating, as observed with 915 MHz waves compared to 2.45 GHz [129]. Lower frequencies (915 MHz) have been utilized to achieve deeper ablations, for example of hepatic tumors [130]. On the other hand, higher

frequencies (2.45 GHz) have been utilized to induce shallow ablations, for example of endometrial lining of the uterus [74, 131].

3. **Therapy Duration**: Longer ablation duration results in a larger lesion size [132]. For example, for a linear antenna, a prolonged energy application will result in significantly larger width and depth of lesion as compared to the length of lesion.
4. **Antenna Size**: The lesion created by MWA is highly dependent on the antenna size which includes its geometry, shape, and dimensions. Typically a large sized antenna will result in a larger lesion. The shape of the antenna governs the energy density of the generated electromagnetic field around the antenna which, in turn, governs the resultant shape and size of the lesion.
5. **Tissue Composition**: The propagation of MWs in biological tissue is regulated by tissue composition and dielectric permittivity. Biological tissues not only differ in water content [133], but also in their respective conductivities and dielectric constants as a function of frequency [134, 135]. These differences are significant in affecting MWs as they propagate within the body. As the MW field propagates in the tissue medium, energy is extracted from the MW field and absorbed in the tissue medium (i.e., converted into heat). This absorption of the MW field results in progressive reduction in MW power and intensity along its propagation path. Tissues with high water content extract the MW energy more efficiently by

stimulating oscillations of water-dipoles and converting the electromagnetic energy into kinetic energy (heat). Hence, MWs propagate through low-water content tissue relatively easily to deliver energy to deeper seated tissues.

6. **Catheter Temperature**: Higher catheter temperatures generally result in larger lesion size for catheters that are not cooled at the MW antenna. However, as the MW antenna need not be in electrical contact with the tissue, application of MW energy is often combined with simultaneous cooling of the antenna that results in an even larger lesion size with cooler catheter temperatures [136]. Antenna cooling may allow creation of a lesion at a distance from the MW antenna while preventing thermal injury to the tissue in close proximity to the catheter [137]. For example, in one application, nerves adjacent an artery may be ablated by a cooled MW antenna catheter placed within the artery, without thermal injury or collateral damage to the artery itself.
7. **Blood Perfusion**: Areas having low circulatory blood perfusion result in larger MW lesion formation due to reduced convective cooling effects.

Chemical Ablation

Chemical ablation is a non-surgical technique that uses homogeneous or heterogeneous chemical agents at lethal concentrations that are directly injected into the target lesion site. CHA works by denaturing proteins, creating focal tissue

damage and tissue lesion, ultimately leading to tissue necrosis in the location of injection [138].

Biophysics of Chemical Ablation and Resultant Tissue Injury

The structural organization of proteins determines their biological function. Disruption of protein structure often results in loss of cellular function. Loss of protein structure from denaturation may be temporary or permanent, and varies depending on the mode of interaction of the denaturing/ablative agent with the active protein. It should be noted that the use of many other chemical agents have been described in the literature, for example, silver nitrate-dextran paste [139], benzalkonium chloride [140], and doxorubicin [141], to name a few. However, this review will not cover all such agents, but will focus on only four. Listed below are biological interactions of four chemicals that have been used as ablative agents: acetic acid, ethanol, hypertonic sodium chloride, and urea. The resultant lesion size as a result of chemical ablation depends on the factors listed below:

1. **Target Selection**: In general, this would be similar to what was described in the RFA section with an understanding of injecting chemical agents in target locations.
2. **Agent Concentration**: The concentration of a given ablative agent must be selected based on the target site and extent of desired lesion. As concentration of the agent increases, so does the resulting lesion size, the

scale of induced injury, and lethal damage. Higher concentrations minimize the volume required for chemical ablation [138].

3. **Agent Volume**: This factor is selected based on the target location and surrounding blood flow. Therefore, a precise control over administered volume is needed to localize the agent at the target location, thus preventing or minimizing collateral damage and systemic toxicity. Often, a fraction (10% to 50%) of the target volume is selected as total dose during any one session. However, if a larger volume is needed, the dose is often divided and administered in multiple sessions [142]. Doing so ensures localization of agent in the target lesion volume, thus minimizing collateral damage and maximizing therapy efficacy.
4. **Blood Flow**: An increased blood flow at the target site not only washes out the agent from the administered location, but also dilutes the agent's concentration at an enhanced rate, thus minimizing lesion size and tissue necrosis.
5. **Rate of Administration**: An increase in the rate of administration of an ablative agent will typically result in a larger volume of agent, hence increased lesion size.
6. **Type of Agent**: To date, each of the commonly utilized ablative agents have a specific toxicological profile and a therapeutic index that makes them unique in terms of interactions with the target tissue and underlying cellular components. In general, every chemical agent has unique

therapeutic properties that can be used to not only to select the appropriate agent for administration, but also to tailor the ablation therapy for specific use.

Urea

Urea is an endogenous agent capable of being filtered by the kidneys, and is believed to have a high therapeutic index. Urea solution is known to denature proteins through a combination of processes. One process involves direct interaction with the proteins whereby urea forms hydrogen bonds with hydrogen atoms linked to oxygen or nitrogen, such as those found on peptide groups. This mutual influence weakens the intermolecular bonds and interactions that stabilize the structural organization of the protein, thus weakening its overall secondary and tertiary structure. This results in gradual unfolding of the protein, permitting water and urea to access the hydrophobic inner core of the protein, thus speeding up the overall denaturation process. The other indirect process by which urea denatures proteins is by affecting the attributes of the solvent in which the proteins are immersed. By changing the structure and hydrodynamics of the solvent, similar to putting a non-polar solute into the mix, urea further encourages the destabilization of internal bonds. In other words, it appears that the direct interaction of urea with proteins through hydrogen bonding is the likely beginning of protein unraveling, which is assisted by the indirect solvent and solute interactions that result in protein denaturation and thereby chemical ablation.

Ethanol

Ethanol at elevated concentrations has toxic effects at the cellular level. It diffuses into cells, producing rapid dehydration, membrane lysis, and protein denaturation, which in turn is followed by fibrosis, microvascular occlusion/thrombosis, and subsequent regional ischemia [138, 143]. The combination of these factors leads to an overall coagulation necrosis. Further, ethanol can disrupt the intra-molecular hydrogen bonding by forming new hydrogen bonds between the protein chain and the alcohol molecule, thus destroying the three-dimensional structure of the protein, denaturing it, hence resulting in tissue ablation.

Acetic Acid

Acetic acid has been shown to have a strong ability to penetrate cells and dissolve lipids, collagen, and proteins [144]. The lethal effect increases with concentration, however, and the use of concentrations of approximately 50% have been reported [145, 146]. Even at these concentrations, the effects of acetic acid are much greater than similar volumes of ethanol, urea, or sodium chloride. Importantly, tissue injections of acetic acid result in low focal pH in surrounding areas that induces swelling of collagen fibers. This process facilitates dissociation of intermolecular cross-links leading to protein denaturation and deamidation [147]. The effects of acetic acid on protein structure could be the consequence of one or all three repercussions arising from

the addition of the acid. First, the addition of an acid to a medium would likely result in an increase in the concentration of hydrogen ions which could then protonate the carboxyl and amino groups, as well as other ionizable groups in the side chains of the constituent amino acids. This would alter the interactions and affect the overall conformations of proteins. Second, as the pH of the environment decreases, most proteins (which at physiological pH are above their isoelectric points and have a net negative charge) will approach their isoelectric pH and tend to get precipitated, since charge repulsion will be minimal or zero. Below the isoelectric point, the affected proteins will likely contain more positive charges, which may cause them to repel each other, and the intra-molecular repulsion may be great enough to cause permanent unfolding of these molecules. Third, the presence of the ionized carboxyl group of acetic acid could compete with the acidic functional groups of a given protein for its positively charged side-chain moieties. This would disrupt existing salt bridges that hold the structure of the protein in its biologically active form. Hence, a combination of these mechanisms would result in protein denaturation resulting in chemical ablation.

Sodium Chloride

Hypertonic saline creates a marked osmotic imbalance across the cell membrane that can then result in intracellular dehydration and eventual cell death [138]. It is observed that an increase in salinity does not affect the pH as

much as it denatures proteins, because the ions from the salt bind to ionic "R" side-chain groups. The positive and negative ions in the salt exhibit a replacement reaction with similarly charged groups, thus interfering with dipolar interactions, and in turn disrupt the ionic salt bridges that stabilize tertiary and quaternary protein structures. An increase in focal salt concentrations also alters the protein-solvent interactions and changes the dielectric constant, providing a destabilizing influence on the structure of the protein resulting in chemical ablation.

Conclusion

The ablative modalities discussed in this review are currently in use worldwide. The tissue response to any given ablation modality is unique. A better understanding of the biophysics of ablation allows one to gain insights into the mechanisms of action and predictive tissue injury both at the cellular and subcellular level that will result from utilization of these ablative techniques. Each therapeutic approach, although similar in purpose, has specific and optimal indications. The information presented in this review can help inform the clinician when faced with practical technical options. Importantly, in those cases where patients are unable to undergo invasive surgical procedures due to advanced tumor state, severity of organ dysfunction, and/or poor clinical status, less invasive techniques such as percutaneous ablation techniques have been employed for treatment and management of various disease states. Such therapies being non- or minimally invasive are a genuine clinical need that has promoted the continued development and refinement of current procedures and techniques, and has also fueled innovations in the field of medical device design. In the future, introduction of advanced ablative techniques will hopefully lead to curative treatments with high safety and efficacy.

Acknowledgements

We gratefully acknowledge the assistance of Monica Mahre, Dave Euler, Eugenia Paulus, and Shailesh Musley for reviewing the manuscript and for discussions related to this review.

2. The Comparative Assessment of Clinically Applied Ablative Therapies: Part I. Methodologies for determining the physiological and biomechanical properties of contractile tissues in response to varied therapeutic dosages

Preface

This paper discusses the detailed methodologies that were developed to assess the physiological and biomechanical properties of tissues in response to ablations. This paper was submitted to the International Journal of Hyperthermia in July 2014 and is currently under review.

Ashish Singal
University of Minnesota
singa009@umn.edu

Charles L. Soule
University of Minnesota
soule005@umn.edu

John R. Ballard
University of Minnesota
ball0250@umn.edu

Eric N. Rudie
Rudie Consulting, LLC
erudie@rudieconsulting.com

Erik N.K. Cressman
MD Anderson Cancer Center
Department of Interventional Radiology
ECressman@mdanderson.org

Paul A. Iaizzo (Corresponding Author)
University of Minnesota
420 Delaware St. SE
B172 Mayo, MMC 195
Minneapolis, MN 55455
T: 612-624-7912; F: 612-624-2002
iaizz001@umn.edu

Running Title: Comparative assessment of ablative therapies

Key Words: Radiofrequency ablation; cryoablation; microwave ablation; high-intensity focused ultrasound ablation; chemical ablation

Executive Summary

Purpose: Although tissue ablation is a routine clinical procedure, it may cause collateral damage to surrounding vital structures in a small percentage of patients, which can have severe clinical implications. As such, the collateral damage results in altered tissue properties that are, in turn, dependent on the extent of tissue injury. Therefore, assessment of tissue properties is fundamental to advancing the understanding of underlying basic and clinical science of ablation, especially to maximize therapy efficacy and minimize procedural complications. There is a need to develop laboratory methodologies that can be reliably used to assess the physiological and biomechanical properties of tissues following exposure to various ablative modalities.

Materials and Methods: Unique experimental methodologies were developed to comparatively assess changes in tissue properties in response to five different therapeutic ablation modalities: (1) radiofrequency ablation, (2) cryoablation, (3) microwave ablation, (4) high-intensity focused ultrasound ablation, and (5) chemical ablation (using acetic acid, ethanol, hypertonic sodium chloride, and urea). In particular, physiological assessment included measurement of change in peak force (strength of contractions) as well as baseline force (resting muscle tension); and biomechanical assessment included measurement of uniaxial stress-strain characteristics of tissue samples in response to ablation. Tissue bath studies were performed to measure physiological responses relative to

applied therapies, and uniaxial stress tests were performed to assess resultant biomechanical responses.

Conclusion: Results from these studies may enable comparative assessment of ablation modalities, and also allow further improvements in ablative techniques to increase the overall safety and efficacy of ablative procedures.

Introduction

Reports of the therapeutic use of ablation in the field of medicine date back to as early as the late eighteenth century [1]. Today, ablations are commonly performed worldwide, in numerous anatomical locations throughout the human body as a means to treat a plethora of disorders. Specifically, tissue ablation is defined as a medical procedure which involves the skillful, focused destruction of the target tissue so as to restore normal structure and function. However, in a small percentage of cases, it can cause collateral damage of surrounding vital organs which can have severe clinical implications.

In one clinical example, complications resulting from ablations in the liver for treatment of hepatocellular carcinoma (HCC) include: (1) collateral damage to the respiratory diaphragm [2]; (2) hemoperitoneum, intraperitoneal hemorrhage, hepatic infarction, hepatic perforation, diaphragmatic necrosis, visceral organ perforation and gastric perforation [3-5]; (3) pneumothorax [6]; (4) pleural effusion [7]; and/or (5) cardiac tamponade [8]. In an effort to improve on therapies, numerous ablative modalities have been used for the treatment of HCC, some of which include: radiofrequency ablation (RFA), microwave ablation (MWA), cryoablation (CRA), chemical ablation (CHA) using percutaneous ethanol injection, high-intensity focused ultrasound ablation (HIFU), transarterial chemoembolization, radioembolization, radiation therapy, stereotactic radiotherapy, systemic chemotherapy, irreversible electroporation, and molecularly targeted therapies [9-10]. Ultimately, the management of HCC is

based on tumor size, number, location, stage, extra-hepatic spread, clinical status of the patient, and underlying liver function.

Similarly, injuries to the phrenic nerve, chest wall, and diaphragm have been reported as a result of ablations in the lung for treatment of lung cancer [11-13]. Numerous ablation modalities have been used for treatment of lung cancer, including: RFA, CRA, MWA, CHA, and HIFU [14].

In an additional example, in the heart, ablations are routinely performed in the left and right atria to isolate the pulmonary veins for treatment and management of atrial fibrillation (AF)[15, 16]. These ablative procedures are associated with high risk of esophageal thermal injury because of the close proximity of the esophagus to the left atrial posterior wall that renders it susceptible to unintended collateral damage. Esophageal injury can range from superficial ulceration and gastroparesis, to the rare but catastrophic atrioesophageal (AE) fistula [17]. AE fistulas are a known complication resulting in collateral damage from ablative procedures performed in the left atrium with variable incidences as high as 1%, and a high rate of mortality [18]. Additionally, AE fistulas have been shown to result from application of many different forms of ablative energies that include: (1) RFA [19-20]; (2) CRA [21-22]; and (3) HIFU ablation [23]. Ablations are also performed in the cardiac chambers (atria or ventricles) for management and treatment of arrhythmogenic substrates such as supraventricular tachycardia, idiopathic ventricular tachycardia, and ventricular ectopic beats [24-27] that could be associated with collateral injury of

surrounding structures.

Ablative procedures performed for pulmonary vein isolation are also associated with a significant incidence of phrenic nerve injury (PNI)[28-30]. The close proximity of the phrenic nerves to the pulmonary veins makes them susceptible to injury from ablative energies. Since the phrenic nerves supply motor and sensory information to the diaphragm, PNI can cause significant diaphragmatic dysfunction and paralysis [31-33].

In view of the complications discussed above, in our laboratory we have been able to study isolated contractile samples of the respiratory diaphragm, esophagus, and cardiac trabeculae for both physiological and biomechanical assessment. We hope to provide comparative assessment of ablation modalities that can eventually be used to better understand ablation procedures and develop insights into minimizing these complications. The ablation modalities investigated in these studies include: RFA, CRA, MWA, HIFU ablation, and CHA. In this paper, we provide detailed methodologies that can be utilized for unique reproducible comparative assessment of these tissue properties.

Materials and Methods

Tissue Preparation

These studies were approved by the University of Minnesota Institutional Animal Care and Use Committee. Fresh tissue biopsies were obtained from healthy castrated male Yorkshire-cross swine (n=85, mean weight of approximately 70 kg) which were euthanized as part of another unrelated protocol. Whenever possible, fresh human tissue biopsies (n=24) were obtained through research collaboration with LifeSource (St. Paul, MN, USA). Experimental samples included respiratory diaphragm, esophagus, and cardiac trabeculae, with multiple individually prepared samples used from each biopsy. In these investigations, these three tissues were used since they are susceptible to collateral damage from clinical ablation procedures of interest in our laboratory. However, it should be noted that any contractile tissue can be used utilizing these unique methodologies.

Following resection, each biopsy was pinned in a dissection dish and dissected in oxygenated, temperature-controlled normal or modified cardiac muscle Krebs-Ringer solution. The normal Krebs-Ringer solution contained (mM) 118.1 NaCl, 3.4 KCl, 1.2 KH_2PO_4, 1.0 $MgSO_4.7H_2O$, 11.0 D-Glucose $C_6H_{12}O_6$, 25.0 $NaHCO_3$, and 2.5 $CaCl_2.2H_2O$ (pH = 7.4, 37 °C); and the modified cardiac Krebs-Ringer solution contained (mM) 118.0 NaCl, 16.0 D-Mannitol, 11.5 D-Glucose, $C_6H_{12}O_6$, 20.0 $NaHCO_3$, 0.32 2Na-EDTA.$2H_2O$, 4.5 KCl, 1.46 $MgCl_2.6H_2O$, 1.2 $NaH_2PO_4.H_2O$, 1.81 $CaCl_2.2H_2O$, and 10U/L Insulin (pH = 7.4,

37 °C). The muscle bundle preparation involved cleaning up the biopsy by removing excess fat and surrounding connective tissue so that well defined muscle bundles could be prepared. The diaphragm and trabeculae muscle bundles were dissected in an identifiable cylindrical shape having lengths of 15 to 25 mm and diameters of 2 to 4 mm. In the case of esophageal tissue, the esophagus is composed of many cellular layers. As one traverses from inside to outside the esophagus, those layers are: (1) mucosa (composed of stratified squamous non-keratinized epithelium, lamina propria, and muscularis mucosa), (2) submucosa (composed of mucus glands, ducts lined with stratified cuboidal epithelium), and (3) muscularis externa (composed of inner layer of circular muscle cells and outer layer of longitudinal muscle cells). In preparing esophageal muscle bundles, the external muscularis and internal squamous epithelium layers were first separated, and then muscle bundles of the muscularis layer were prepared along the circular layer of muscle fibers in an identifiable cuboidal shape having lengths of 15 to 25 mm, widths of 3 to 5 mm, and thickness of 1.5 to 3 mm. The dissected muscle bundles were then tied on both ends with 2-0 silk sutures with a free loop on either end so that they could be mounted in either the tissue baths for physiological studies or on the uniaxial pull machine for biomechanical studies. In all cases, control muscle bundles were prepared for physiological testing, biomechanical testing, and control experiments where no ablations were performed.

Physiological Testing in Tissue Baths

The tissue bath system used in these investigations (Figure 4) is an adaptation of one that was previously described [34, 35]. Tissue bath studies were performed to investigate changes in physiological properties of tissues in response to different ablative modalities. Muscle bundles were mounted in 16 parallel, 50 ml tissue baths containing Krebs–Ringer buffer at 37°C and gassed with 95% O_2 and 5% CO_2 to maintain tissue viability. Each tissue bath was water jacketed and connected to a heater pump (Haake Model DC1, Germany) that maintained a temperature of 37°C throughout the duration of the experiment. The lower end of the muscle bundle was secured to a fixed hook, and the upper end was attached to a force transducer (Model FT03 with peak capacity of 50 grams, Natus Neurology, Warwick, RI, USA). The acquired data was amplified, digitized (data acquisition card: PCI-MIO-16E-4, National Instruments, Austin, TX, USA), and saved on a computer using custom built data acquisition software (LabView, Ver 6.1, Austin, TX, USA). Each force transducer was calibrated at 0 gram weight, by hanging a 10 gram weight prior to each study.

On any given study day, physiological data from the same tissue type were collected from all 16 tissue baths simultaneously. Following mounting, the muscle bundles were allowed to acclimate for approximately one hour, during which time the stimulation voltage and length-tension relationship were determined and optimized for each muscle bundle before starting an ablation study protocol [35]. The muscle bundle length resulting in maximal peak force (twitch force) was

used for the remainder of the study. The muscle bundle samples were randomly assigned to the ablation group or the control group. Each muscle bundle was tested just once for any given treatment. Peak forces (strength of contractions) as well as baseline forces (resting muscle tensions) were measured pre- and post-ablation for every muscle bundle. Following a given ablative treatment, tissues were allowed to recover for a period of at least 3 hours, to assess tissue damage (necrosis) and recovery as a result of exposure to different ablative modalities of varying doses.

Stimulation Protocol

The muscle bundles in each tissue bath were electrically stimulated by field stimulation simultaneously with a pair of bilateral platinum electrodes (length: 50.0 mm, width: 10.0 mm, thickness: 0.3 mm) immersed within the tissue bath, positioned near to but not touching the muscle bundle sample (Figure 4). The diaphragm and trabeculae muscle bundles were stimulated once every 10 seconds with a square-wave pulse width of 1.0 ms, whereas the esophageal muscle bundles were stimulated once every 30 seconds with a train of 8 square-wave pulses of 1.0 ms duration and a pulse interval of 30 ms. The electrical field stimulation elicited an electro-mechanical twitch response that was digitally recorded using a force transducer at a sampling rate of 250 Hz. If reproducible mechanical twitches could not be elicited with stimulation, or the peak force was <1 gram, the muscle bundle was discarded.

Calculation of Percent Change in Peak Force and Baseline Force

Although peak force and baseline force data were acquired continuously for the entire duration of the experiment, data were analyzed at 14 unique time points: pre-ablation *(2 minutes of data averaged just before ablation)*, post-ablation *(2 minutes of data averaged right after ablation)*, and 12 additional time points at 15-minute intervals post-ablation *(2 minute data averaged)* for a period of 3 hours. Data were used to calculate the percent change in peak force and baseline force for all muscle bundles using the following formulas (at any given time t):

$$\% \text{ Change in Peak Force} = [\ (PF_t - PF_{\text{pre-ablation}}) / (PF_{\text{pre-ablation}})\ ] \times 100\%$$

$$\% \text{ Change in Baseline Force} = [\ (BF_t - BF_{\text{pre-ablation}}) / (BF_{\text{pre-ablation}})\ ] \times 100\%$$

All tissue bath data was analyzed as percent change in peak force and baseline force with respect to the pre-ablation time point; thus, every graph has 13 bars within each ablation dose, where the leftmost bar represents the percent change right after ablation and every subsequent bar represents percent change at 15-minute intervals. Data were analyzed by grouping all the samples exposed to the same ablation dose, and performing statistical analyses by calculating the mean and standard deviation of the percent change in peak force and baseline force for every ablation modality.

Ablative Modalities Investigated

In general, ablation modalities can be divided into two categories, thermal and chemical ablation. Thermal ablation modalities employed were RFA, CRA, MWA, and HIFU ablation. Four CHA agents were employed, which included: 97% glacial acetic acid, 200 proof ethanol, 30% hypertonic sodium chloride solution, and 8 M urea. Clinically available RFA and CRA systems along with respective catheters manufactured by Medtronic Inc. were used as thermal ablative modalities. A custom-designed HIFU system operating at 2.5 MHz with 80% duty cycle was used as the ultrasonic ablative system. A custom-built MWA system operating at 1.3 GHz was used to perform MWA. For performing CHA, chemical agents were directly injected into a given muscle bundle.

Cryoablation

CRA equipment from CryoCath (Medtronic Inc., Minneapolis, MN, USA) was used to perform CRA. This system uses a refrigerant (liquefied nitrous oxide, N_2O) to remove heat from a specific area in the tissue to freeze the tissue at temperatures close to -75°C and destroy it. The Freezor MAX CRA catheter (tip length: 8 mm, catheter diameter: 9 Fr) was used for these studies. A thermocouple integrated into the tip of the catheter allowed real-time temperature monitoring during the ablation procedure. The CRA system was operated in the clinical mode, and dose effects were typically studied by selecting up to 4 different durations of exposure (15 sec, 30 sec, 60 sec, and 120 sec). A special

acrylic fixture was built to mount the CRA catheter to the uniaxial machine's force transducer, to apply a constant force of 0.1 N (10 grams) on the muscle bundle. Thus, all CRAs were performed under constant catheter force as shown in Figure 5.

To perform CRA, the muscle bundle was unmounted from the tissue bath, pinned in the ablation dish, and stretched to the same length as in the tissue bath (same baseline force). CRA was performed near the center of the muscle bundle. Following completion of ablation, the thaw time for ice-ball melt was measured. The total time the muscle bundle was in the ablation dish was typically <3 min. The muscle bundle was then removed from the ablation dish, mounted back on the tissue bath, and data were collected for a period of at least 3 hours to study recovery and post-ablation effects on muscle physiology.

RF Ablation

A RF Atakr II system (Medtronic Inc.) was used to perform RFA. This system generates a sinusoidal waveform at a frequency of 484 KHz with a maximum power output of 100 W. At such high frequencies, there was no tissue capture or unintended stimulation; instead the energy was dissipated as heat in the tissue. A RF Contactr catheter (electrode length: 8mm, catheter diameter: 7 Fr) was used for these studies. The Atakr II RF generator provides high power output with the integral safety of closed-loop temperature control using the embedded thermocouple in the ablation catheter. All ablations were performed in

temperature mode in which the system adjusted the power applied to achieve the user-set temperature and maintained it for the duration of ablation. The system power was set at 50 W, ablation duration at 60 seconds, and typically up to 5 different doses were investigated by altering the set-point temperature from 50°C to 70°C in steps of 5°C. A laptop computer connected to the Atakr II RF generator via the serial communication port enabled digital recording of ablation parameters during RFA. For each sample, average and maximum power, temperature, voltage, current, and impedance were recorded. A special acrylic fixture was built to mount the RFA catheter to the uniaxial machine's force transducer to apply a constant force of 0.1 N (10 grams) on the muscle bundle. Thus, all RFAs were performed under constant catheter force as shown in Figure 6.

To perform RFA, the muscle bundle was unmounted from the tissue bath, pinned in the ablation dish, and stretched to the same length as in tissue bath (same baseline force). RFA was performed near the center of the muscle bundle. The total time the muscle bundle was in the ablation dish was typically <2 min. Following ablation, the muscle bundle was removed from the ablation dish, mounted back on the tissue bath, and data were collected for a period of at least 3 hours.

HIFU Ablation

The HIFU ablation system was custom built in the lab as shown in Figure 7.

The HIFU transducer was a high-efficiency, broad bandwidth single element transducer (Model: H-108, Sonic Concepts, Bothell, WA, USA) that was excited with a 2.5 MHz sinusoidal waveform. The signal was amplified and focused ultrasound wave acoustic energy was used to perform ablations. The transducer was completely immersed (for acoustic coupling) in an ablation chamber that contained approximately 4 liters of temperature-controlled oxygenated Krebs-Ringer buffer. A given muscle bundle was placed in front of the transducer's focal point for HIFU ablations. After gaining experience from pilot studies, system settings were set at 80% duty cycle with system forward-power of 50-60 W and durations of 2-10 sec. Typically up to 6 different doses were investigated by adjusting the HIFU forward-power and ablation duration.

To perform HIFU ablations, the muscle bundle was unmounted from the tissue bath, stretched and pinned on a vertical rubber pad (acoustic material) to the same length as in the tissue bath (same baseline tension). A micro-positioner and transducer-focusing aid were used to position the muscle bundle at the focal point of the acoustic energy delivered by the HIFU transducer. HIFU ablation was performed near the center of the muscle bundle as shown in Figure 8. The total time the muscle bundle was in the ablation chamber was typically <1 min. Following ablation, the muscle bundle was removed from the ablation chamber, mounted back on the tissue bath, and data were collected for a period of at least 3 hours.

Microwave Ablation

The MWA system was custom built in the lab as shown in Figure 9. The MWA generator (Prostatron, 100 W maximum power) produced microwaves at 1.3 GHz which were used for ablations. A stub-tuner was placed between the MWA generator and microwave antenna to ensure impedance matching for optimizing microwave energy delivery. Dose effects were studied by selecting the microwave incident power between 10 and 20 W, and exposure duration between 60 and 240 sec. Typically up to 6 different doses were investigated by adjusting the microwave incident power and ablation duration. During the ablation, incident power and reflected power were recorded, and average power was used to calculate the MWA energy. A special acrylic fixture was built to mount the MWA antenna to the uniaxial machine's force transducer to apply a constant force of 0.1 N (10 grams) on the muscle bundle. Thus, all MWA were performed under constant catheter force (Figure 10).

To perform MWA, muscle bundle was unmounted from the tissue bath, pinned in the ablation dish, and stretched to the same length as in the tissue bath (same baseline force). A thin sheet of plastic film was placed between the microwave antenna and the tissue to ensure ablation from electric field dielectric heating, and not from electrical conduction between the tissue and conductive Krebs-Ringer solution. MWA was performed near the center of the muscle bundle. The total time the muscle bundle was in the ablation dish was typically <5 min. Following completion of ablation, the muscle bundle was removed from the

ablation dish, mounted back on the tissue bath, then data were collected for a period of at least 3 hours.

Chemical Ablation

Four different chemical ablative agents were employed in these investigations. The chemical agents included: 97% glacial acetic acid (Item 320099-500ml, molecular formula: $C_2H_4O_2$, molecular weight: 60.05 gms/mol, Sigma-Aldrich, St. Louis, MO, USA); 200 proof ethanol (Item 2716, molecular formula: C_2H_5OH, molecular weight: 46.07 gms/mol, Decon Labs, PA, USA); 30% hypertonic sodium chloride (Item 7581-06, molecular formula: NaCl, molecular weight: 58.44 gms/mol, Macron Fine Chemicals, PA, USA); and 8 M urea (Item U4883-6x25ml, molecular formula: CH_4N_2O, molecular weight: 60.06 gms/mol, Sigma-Aldrich). A special syringe with an ultra-fine short needle and resolution of 5 µL was used for injections (Item 328438, 31 G x 5/16 in., 3/10 mL Lo-Dose™ Ultra-Fine™ short needle with permanently attached needle, BD Syringes, NJ, USA). Typically up to 6 different agent volumes between 10 and 100 µL were investigated depending on the desired dose and/or tissue type.

To perform chemical ablations, the tissue bath was lowered without altering the muscle bundle in any way, and the chemical ablative agent was injected near the center of the muscle bundle (Figure 11). Extreme care was exercised during injections, especially to localize the entire volume of the ablative agent within the muscle bundle (prevent agent from oozing out) to maximize ablation efficiency

and repeatability. The rate of injection was approximately 5 μL per second, and all injections were typically completed within 30 seconds. Following completion of ablation, the tissue bath was raised and data were collected for a period of at least 3 hours.

Control Samples

There were three sets of controls. The first set of controls included muscle bundles that were left in the tissue bath throughout the duration of the physiological testing protocol. The second set of controls was for the thermal ablation modalities. These muscle bundles were unmounted from the tissue bath and subjected to the same thermal ablation conditions, except that they were not ablated. The third set of controls was for the chemical ablation modalities. These muscle bundles were injected with Krebs-Ringer buffer solution instead of the chemical ablative agents.

Biomechanical Characterization under Uniaxial Stress

The biomechanical properties of any tissue describe how that tissue will react to internal and/or external physical forces. Biomechanical properties can be determined through a series of standardized mechanical tests, one of which is the uniaxial stress test. After completion of the physiological testing protocol, the muscle bundles were subjected to avulsion (tearing apart) uniaxial stress tests for assessment of changes in biomechanical properties as a result of ablative

treatments. Since avulsion is a destructive test, biomechanical characterization was the last step done in the overall study protocol. Uniaxial pull tests (tensile strength measurements) were performed using a digital uniaxial force measurement system (Chatillon TCD 110 Series, Largo, FL, USA). This system was equipped with two force transducers (load cells), one that could measure a maximum force of 10 N (accuracy: 0.01 N, resolution: 0.001 N) and the other a maximum force of 100 N (accuracy: 0.1 N, resolution: 0.01 N). Therefore, it was essential to choose the right force transducer for each tissue type, as exceeding the maximum transducer rating could not only damage the transducer resulting in erroneous readings, but also limit the utilization of maximum dynamic range available for recordings. The pull protocol was designed after conducting an extensive literature search and gaining experience from many pilot studies on different tissue types.

Results from pilot studies were not only helpful in selection of the proper force transducer, but were also essential in developing the overall study protocol. Since the tissues under investigation exhibit the features of hysteresis, relaxation, and creep, they have been modeled as viscoelastic materials. The biomechanical properties of the tissues do not change as quickly as the physiological properties. Therefore, the criterion for tissue viability was relaxed so that tissues could be used after the completion of physiological testing. Tissue pull testing was performed at room temperature ($22.5 \pm 2°C$). The uniqueness of this protocol was that it allowed for a slow, controlled pull of samples until

avulsion occurred. However, it should be noted that there appeared to be an optimal rate of pull that was determined in preliminary experiments. After careful assessment, the pull protocol was selected to have a constant speed (rate of pull) of 10 mm per min (velocity: 0.167 mm/s, and strain rate of approximately 8.33×10^{-3} s^{-1}) over the avulsion stretch distance. Sample alignment has been considered to be less of a concern with soft biological tissues than with harder materials, but the problems of firmly gripping the tissue on the test machine are much more severe. The gripping solution is often specific to the characteristics of the specimen, dimension, material, and the conditions of the test. More importantly, the gripping technique must be capable of securely holding soft tissue without causing damage to the tissue itself.

Taking these factors into consideration, a novel method of securing the tissue sample was devised that would not only minimize tissue slippage, but also prevent tissue damage. This was achieved by tying the sutures on either end of the muscle bundle and dissecting in a unique way so as to impart a dog-bone shape to the muscle bundle. This shape has been shown to be especially important while performing pull testing of any material that calls for firm grip on either end to prevent slippage [36]. In conjunction with the dog-bone shape, liquid super glue (Loctite Liquid, Henkel Corp., Rocky Hill, CT, USA) was applied on either end of the muscle bundle at the suture-tissue interface. This allowed for added support, enhanced grip, and increased bonding strength at an otherwise vulnerable location (tissue-suture interface) due to increased stress caused by a

reduction in cross-sectional area from tying suture knots. Care was taken to localize application of super glue only at the muscle bundle ends to strengthen the suture-tissue interface.

Force-displacement Measurements

Once the super glue dried (<2 min), tissue samples were mounted on the uniaxial pull machine via custom-designed hooks of stainless steel material (made from needle of polypropylene sutures, Ethicon, Somerville, NJ, USA). The bottom suture loop was secured to the lower immobile hook mounted on the vice and the top suture loop was fixed to the uniaxial pull machine's force transducer (Figure 12). During execution of pilot studies we observed that tissue fiber orientation strongly influenced the tensile strength measurements, so all tissue samples were stretched along the longitudinal axis of the sample until avulsion occurred. During execution, the system console displayed 3 quantities [load (N), stretch distance (mm), and speed (10 mm/min)]. The load and stretch were continuously acquired at a sampling rate of 100 Hz and saved to the hard drive for post-processing. Before starting the pull test, the initial tissue sample dimensions (length and diameter for cylindrical samples and length, width, and thickness for cuboidal samples) were recorded for each tissue sample to allow determination of elastic modulus for each sample. Three readings of diameter, or width and thickness, towards the top, middle, and bottom of the muscle bundle, and three readings of the length of each muscle bundle were obtained, and the

averages recorded in the data sheet. A force-displacement graph was generated and recorded for each sample.

Determination of Avulsion Location

There are numerous factors to consider that determine where a given muscle bundle would avulse along its longitudinal axis. For example, the muscle bundle could avulse at or near the center, or at the sutures. Some of the factors that determine where the muscle bundle avulses include: (1) the quality of dissection; (2) strength of suture knots placed at the ends of the muscle bundle, suture material, and/or style of suture knots; (3) type and drying time of various super glue formulations; (4) type of ablation, location of ablation, and ablation dose; (5) tissue type, species, dimensions of tissue, tissue health, fiber orientation, and/or shape of tissue sample (dog-bone versus straight cylinder); (6) the applied uniaxial pull parameters including velocity of pull, rate of strain, preconditioning the tissue, tissue securing mechanism, relative degree of tissue damage following securing; and (7) skill level of the operator.

Although the goal was to have every tissue sample avulse in the center, this was not always the case due to the confounding factors discussed above. Thus, a systematic assessment was performed to determine the exact location of avulsion for each muscle bundle. A guideline was established to mark the avulsion location of each muscle bundle as shown in Figure 13. Five different locations were determined and a number assigned to every sample based on the

avulsion location as described in Table 2.

Stress-Strain Characteristics

Stress-strain curves for each sample were calculated using the obtained force-displacement data. A representative example of a force-displacement graph of a muscle bundle with six biomechanical parameters that were calculated is shown in Figure 14. Nominal stress-strain characteristics were determined for all samples. The tissue samples were assumed to be incompressible so the volume of the samples was assumed to be conserved during the stretch. It was observed that the reduction in cross-sectional area was significant as the muscle bundle was stretched along its longitudinal axis. Assuming a constant volume model, the reduction in cross-sectional area was calculated, which was further used to calculate the “true stress-strain” relationship for each sample (Cauchy stress). The Cauchy stress relationship (load/deformed area) accounts for reduced cross-sectional area as the muscle bundle is stretched [37].

A custom designed software program was used to calculate the elastic modulus of each sample and the statistics for the entire treatment group. As shown in Figure 15, the program allowed the placement of two free-form points (x1, y1, x2, and y2) on the linear region of the force-displacement graph. The elastic modulus of each sample was derived by calculating the slope of the initial linear region (before avulsion) using the following equation:

Elastic Modulus (EM) = Stress / Strain (N/m^2)

Stress = Force / Area = F / A (N/m^2), where Area, $A = \pi r^2 = \pi d^2/4$

Strain = Change in length / Original length = $\Delta l / L$

Therefore, $EM = (F/A) / (\Delta l/L) = (F/\Delta l) \times (L/A)$ (N/m^2)

The force data (F) and change in length (Δl) were obtained from the uniaxial pull machine. The original length (L) and cross-sectional area (A) were measured before the pull test started. Therefore, using these quantities, the elastic modulus for any given sample could be calculated, and data were further used to calculate the statistics of the entire treatment group.

Muscle Bundle Mass

After completion of the uniaxial tests, the sutures on both ends of each of the muscle bundle were cut and discarded. The wet mass of each muscle bundle was measured using a weighing scale with a resolution of 10 mg.

Statistical Analyses

Data analysis was performed using Excel (office 2010) and Matlab (Ver. R2012b). Data were presented as the mean $\pm$ STD, and $p<0.05$ was considered statistically significant. Peak forces and baseline forces (at each ablation dose and at each time point), and biomechanical avulsion parameters (at each ablation dose) were analyzed using analysis of variance (ANOVA analysis). The Tukey test was used post-hoc to compare different levels of each fixed factor

(Minitab, ver.17) for every ablation modality investigated. A separate ANOVA model was created for each ablation modality and for both peak force and baseline force. The variables entered into the ANOVA model for thermal ablation modalities were sample, time, and dose, where sample was treated as a random factor. The variables entered into the ANOVA model for the chemical ablation modality were sample, time, dose, and agent (chemical agent or Krebs), where sample was treated as a random factor.

Discussion

We have developed experimental methodologies that can be reliably used to assess the physiological and biomechanical properties of a wide range of contractile tissues following exposure to various ablation modalities. To our knowledge, similar studies performed in a methodological comparative style have not been reported to date in the literature. Importantly, we propose that the understanding of tissue properties has wide applications ranging from applied research to the development of novel tools, ablation techniques, and/or novel clinical treatment options. Furthermore, results from such investigations may enable comparative assessment of ablation modalities as a means to better determine their effects on various tissues post-ablation, including healthy or disease specimens. The stress-strain relationships evaluated in our described investigation can not only be used to measure native intra- and inter-tissue variability in mechanical behavior, but they also provide critical insights in the therapeutic mechanisms by which ablations effect the mechanical behavior of affected tissues. In other words, the critical assessment and interpretation of obtained experimental results can be further used to reduce complication rates, understand mechanisms of disease recurrence, and increase overall effectiveness and efficacy of ablative procedures. Moreover, increasing knowledge in this area is fueling the demand to introduce new procedures, modify current ones, and reduce procedural times, all of which positively impact development of novel treatments.

It is important to note that our experimental approach not only allows one to determine the relative viability of a given sample before and after a chosen ablative therapy, but it also provides knowledge as to the viability of the sample relative to assessment of its biomechanical characteristics. We were also able to apply these methodologies to a variety of contractile tissue types from both swine and human samples, hence allowing for translational insights. Furthermore, not all obtained human samples are healthy specimens, thus allowing one to gain insights into physiological and biomechanical changes of a given tissue type relative to different disease states. It is important to note that our described methodologies are mature and highly reproducible. This has been possible after executing many pilot trials and a given degree of skill in sample preparation.

Conclusion

In summary, we describe here a novel experimental approach that may allow for important comparative understanding of both physiological and biomechanical tissue properties associated with the current applications of ablative therapies. These methodologies were developed with the important perspective that they could be utilized in a realistic framework for developing bench top testing of device-tissue interactions that can aid in novel medical device design.

Acknowledgements

We gratefully acknowledge the assistance of Monica Mahre, Dave Euler, and Shailesh Musley for reviewing the manuscript. The authors wish to thank Seth Johnson and Daniel Keefe for their assistance with implementing the elastic modulus calculation program. This research was supported, in part, by Medtronic, Inc.

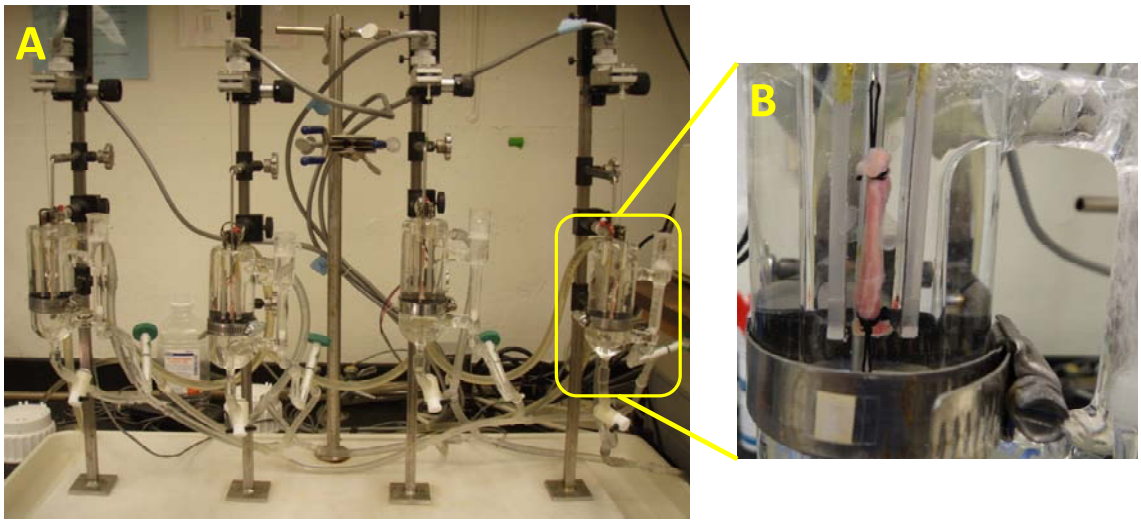

Figure 4: Tissue bath system setup for performing physiological studies
A) Data from sixteen muscle bundles (4 shown) were acquired simultaneously. B) One tissue bath showing the muscle bundle.

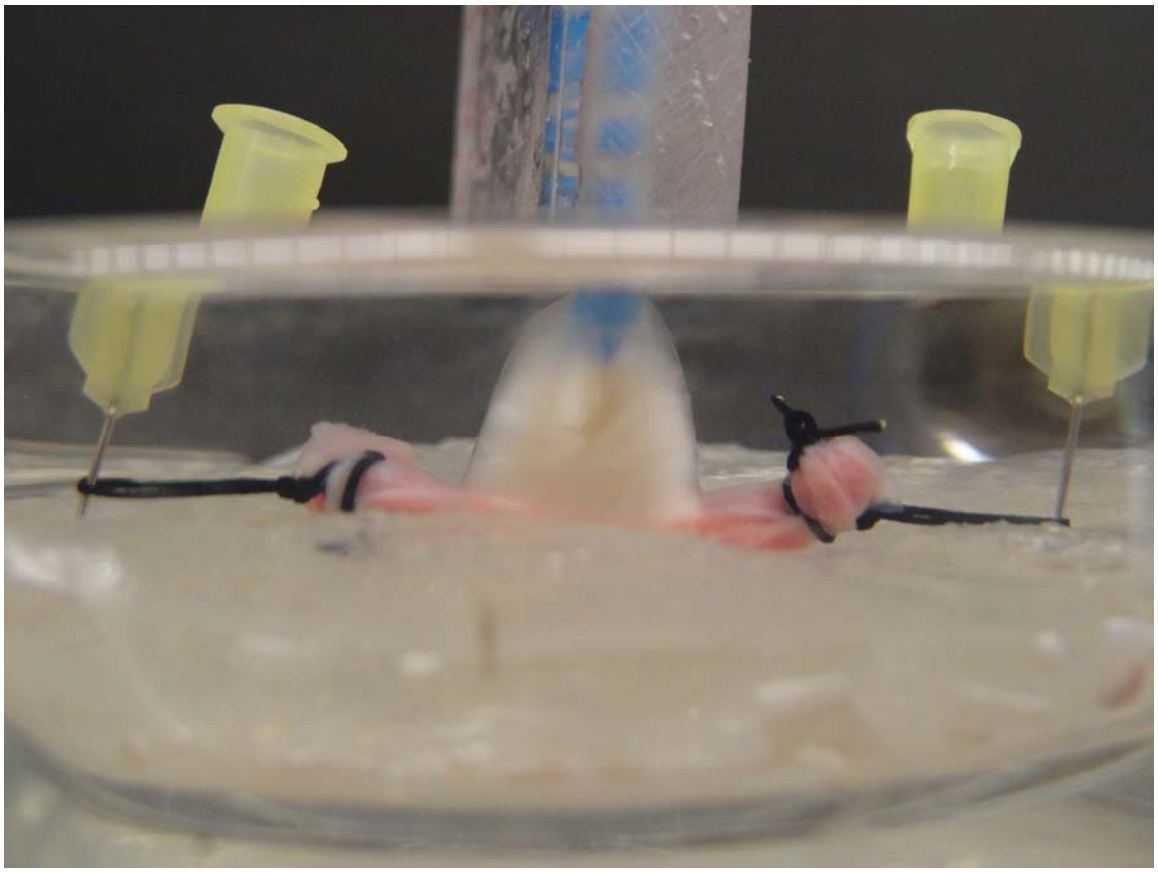

Figure 5: Muscle bundle undergoing cryoablation near its center in the ablation dish with the catheter imparting 0.1 N (10 grams) of force

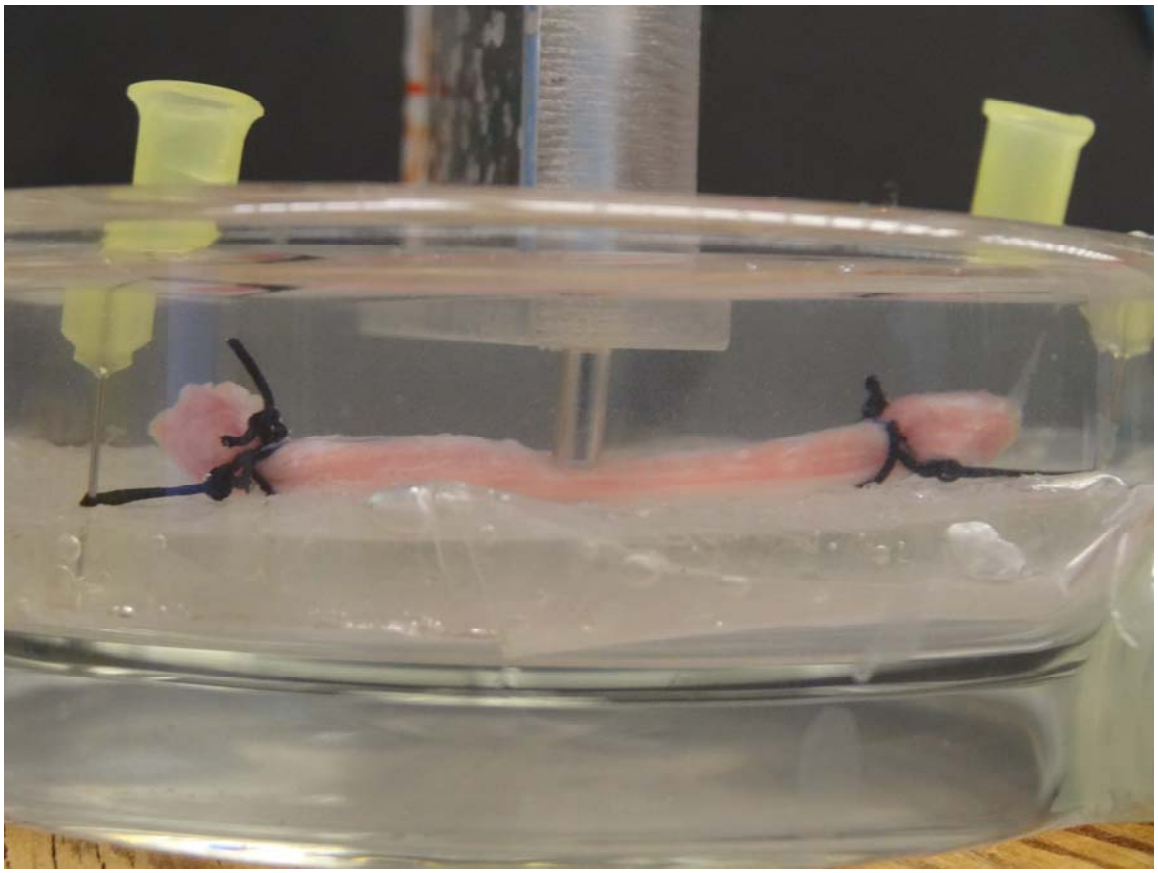

Figure 6: Muscle bundle undergoing RF ablation near its center in the ablation dish with catheter imparting 0.1 N (10 grams) force

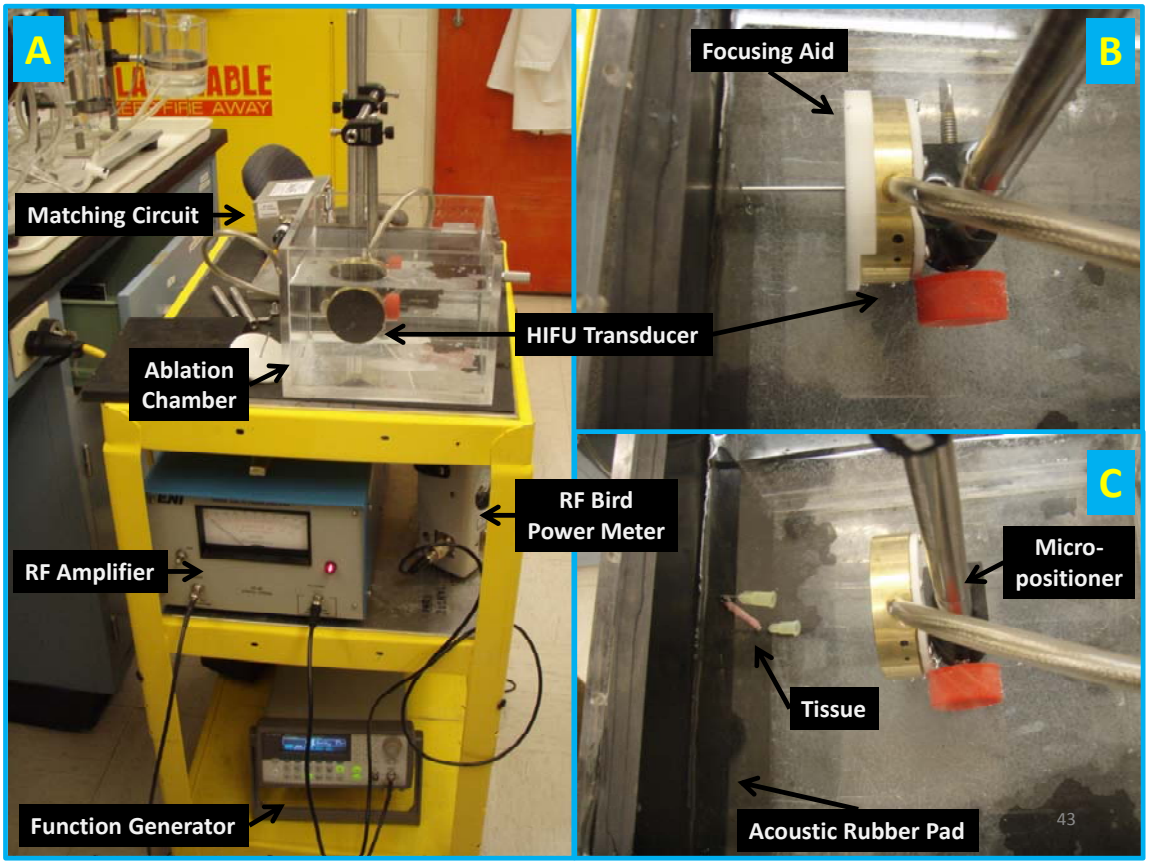

Figure 7: Custom designed HIFU ablation setup

A) Custom designed system setup for performing high-intensity focused ultrasound (HIFU) ablations. The function generator generated a sinusoidal waveform of 2.5 MHz frequency with 80% duty cycle that was fed to the RF amplifier for amplification. The amplified signal was routed to the RF bird power meter which indicated the forward HIFU power. The signal was further routed to the matching circuit and finally to the acoustic HIFU transducer. The HIFU transducer was completely immersed in the HIFU ablation tank containing temperature-controlled oxygenated Krebs-Ringer solution. B) Illustration of HIFU transducer along with its focusing aid. The stem of the focusing aid was calibrated for the HIFU transducer, such that it allowed the transducer to be positioned exactly in front of the muscle bundle being ablated, so that acoustic energy could be focused at the center of the muscle bundle. C) Illustration of a muscle bundle sample mounted on a rubber pad acoustic material, and positioned at the focal point of the HIFU transducer undergoing HIFU ablation.

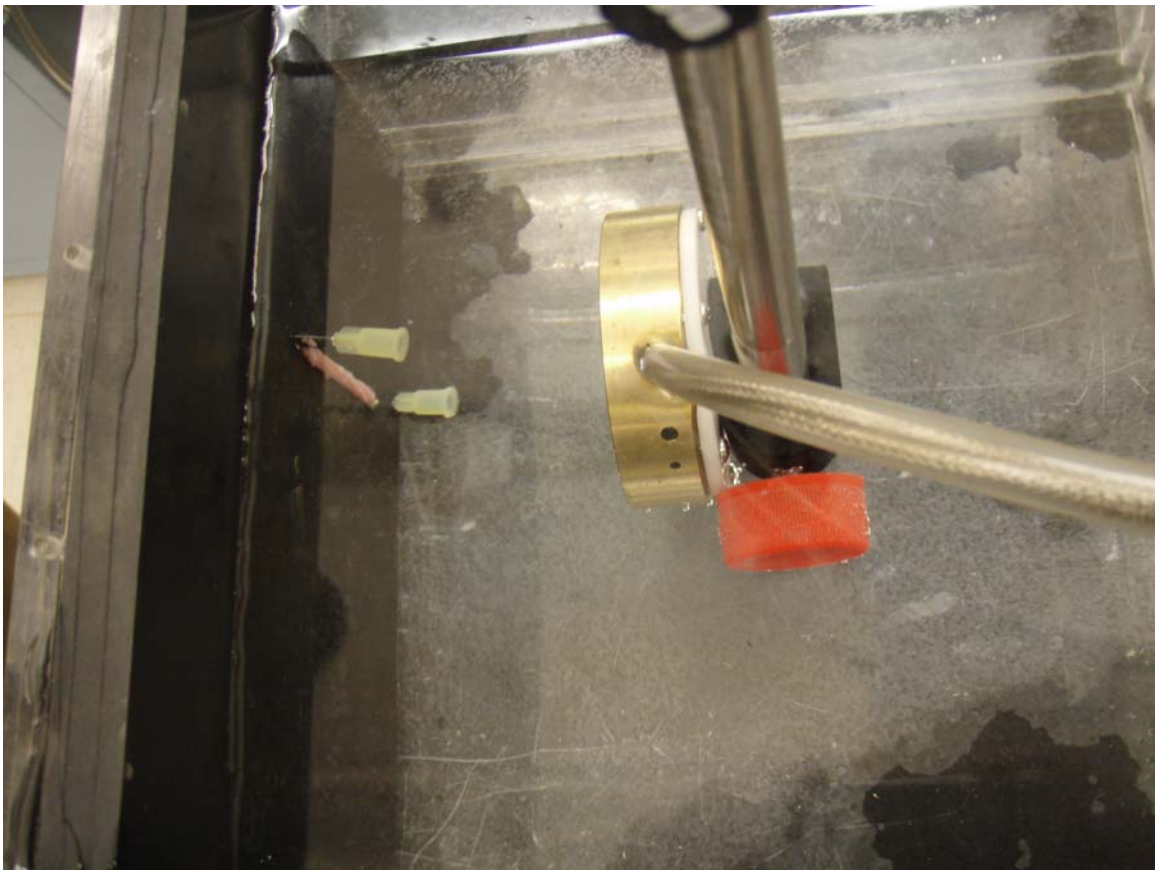

Figure 8: Muscle bundle undergoing HIFU ablation

Muscle bundle in the high-intensity focused ultrasound (HIFU) ablation chamber pinned on a rubber pad and positioned at the focal spot of the HIFU transducer undergoing HIFU ablation near the center of the muscle bundle.

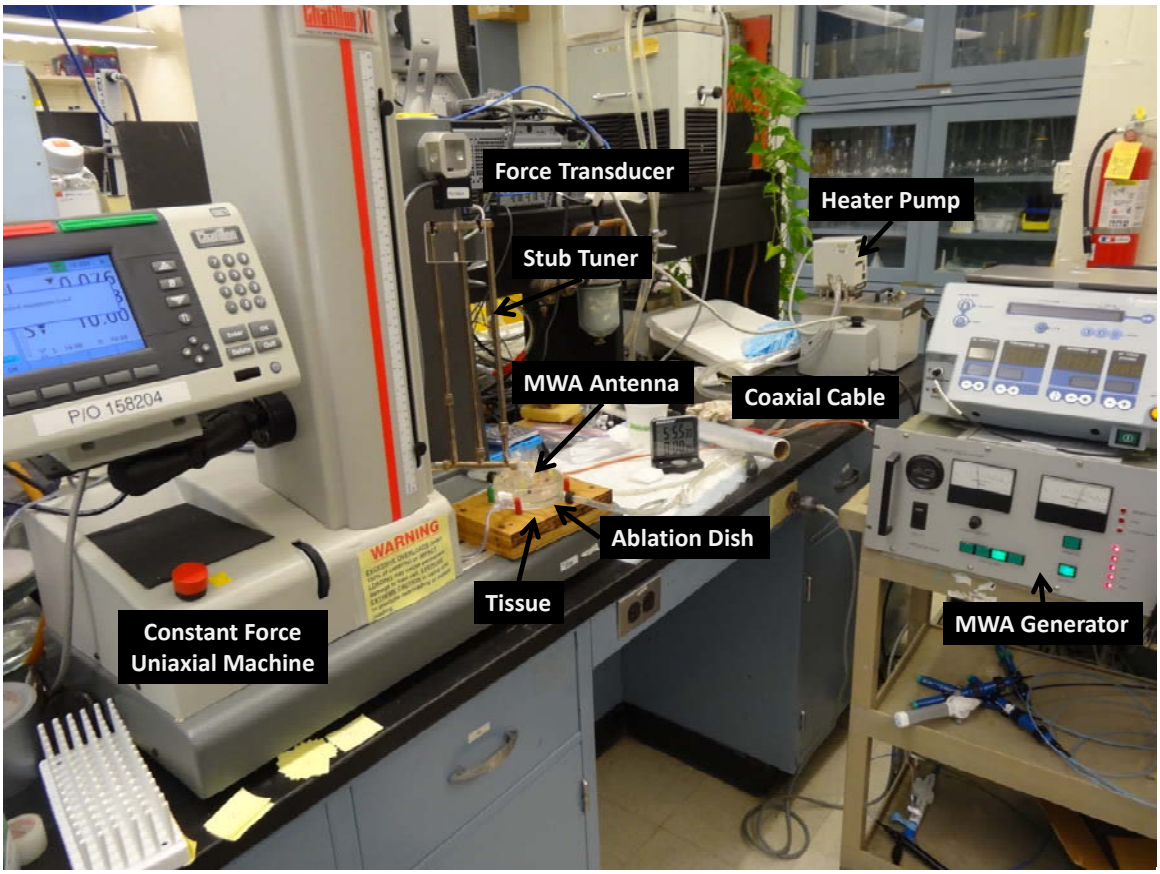

Figure 9: Custom designed microwave ablation setup

Custom designed system setup for performing microwave ablations (MWA). The MW generator generated a sinusoidal waveform of 1.3 GHz frequency that was fed to the stub tuner via a coaxial cable. The rungs on the stub tuner were calibrated to achieve optimum impedance match at 1.3 GHz ablation frequency. The signal was ultimately routed to the MW antenna for performing MWAs.

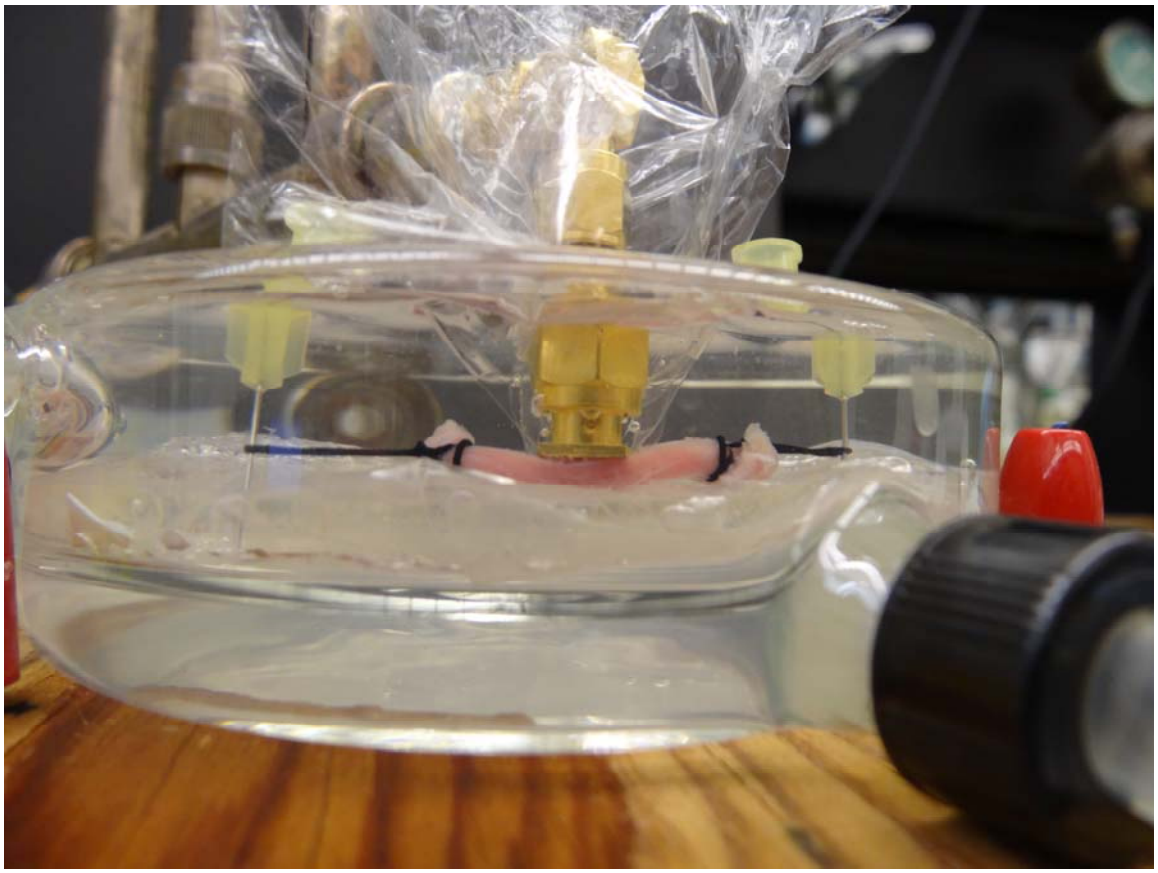

Figure 10: Muscle bundle undergoing microwave ablation

Muscle bundle undergoing microwave ablation near its center in the ablation dish with microwave antenna imparting 0.1 N (10 grams) force. A thin sheet of plastic film was placed between the microwave antenna and the muscle bundle to ensure ablation from electric field dielectric heating, and not from electrical conduction between the tissue and conductive Krebs-Ringer solution.

Figure 11: Muscle bundle undergoing chemical ablation
Illustration of injection of a chemical ablation agent near the center of a muscle bundle. The muscle bundle is mounted on the tissue bath apparatus

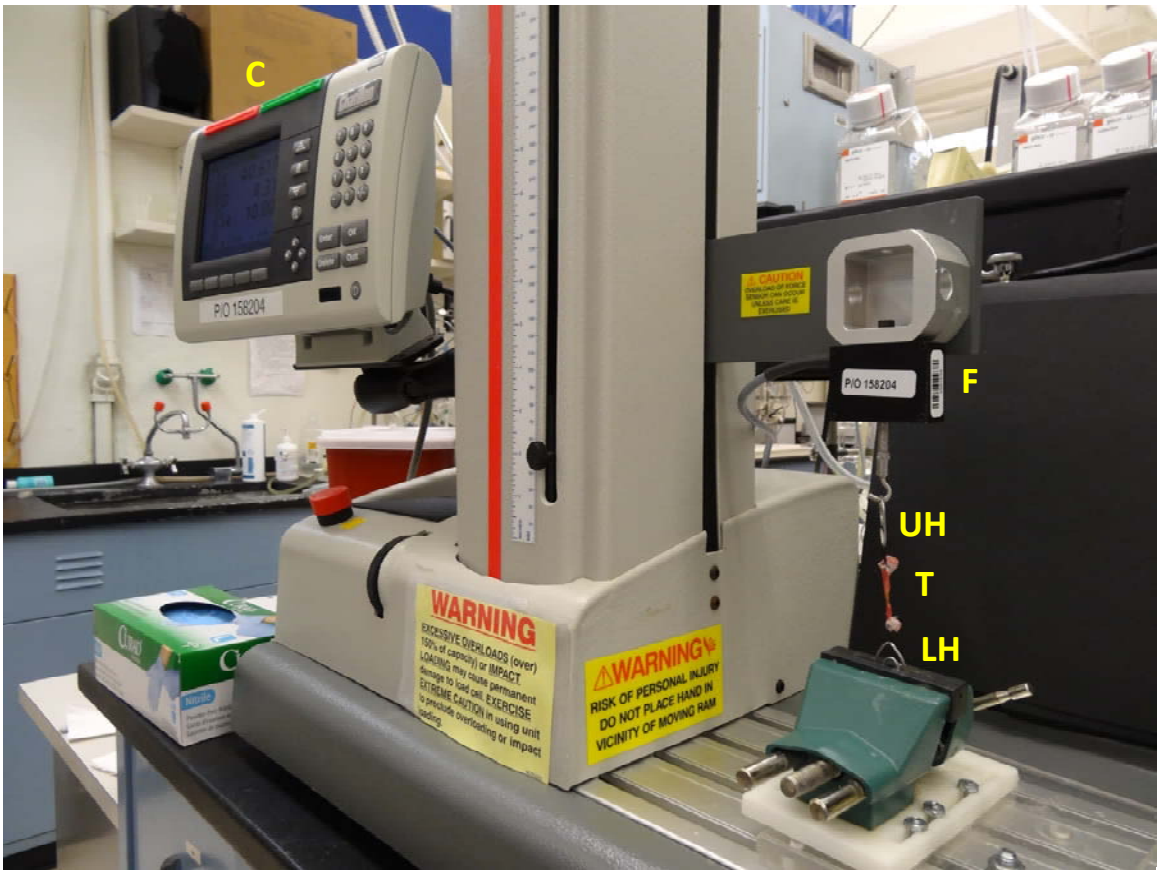

Figure 12: Uniaxial force measurement system

Uniaxial force measurement system for performing uniaxial biomechanical testing of various tissues. C: system console to control the operation of uniaxial system; T: muscle bundle undergoing tensile strength test; F: force transducer (load cell) connected to the movable arm of the uniaxial machine; UH and LH: custom designed upper and lower tissue holder hooks, respectively. The upper hook is connected to the force transducer and lower hook is held firmly to the vice as the muscle sample is pulled to measure tensile strength.

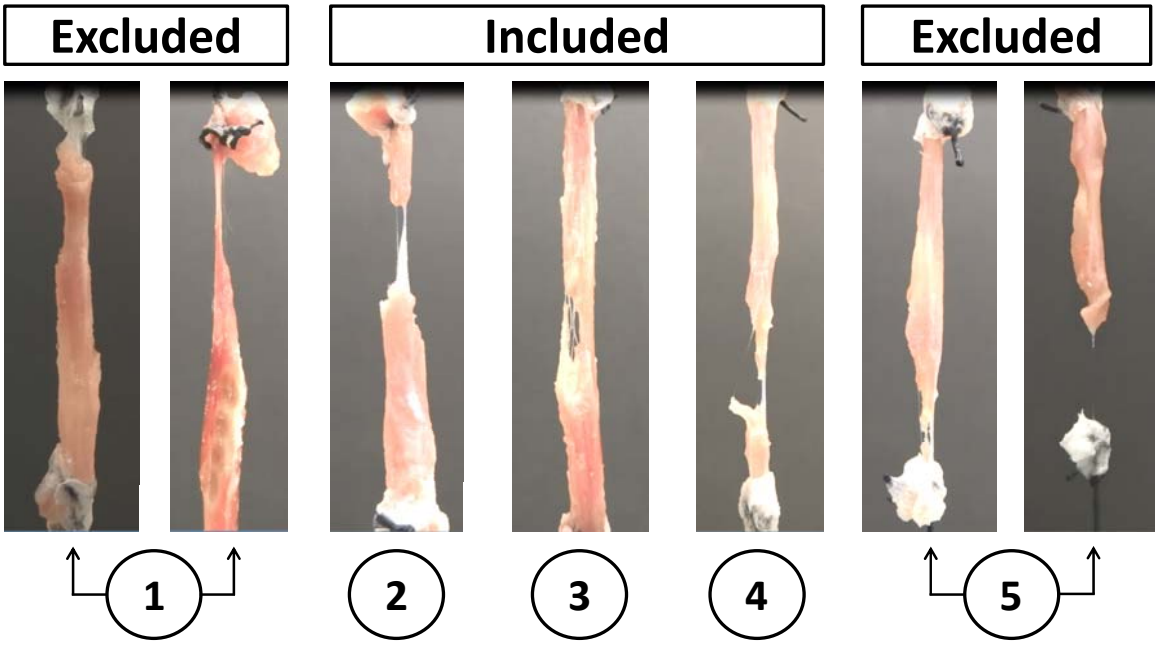

Figure 13: Illustration showing representative examples of avulsion location of muscle bundles

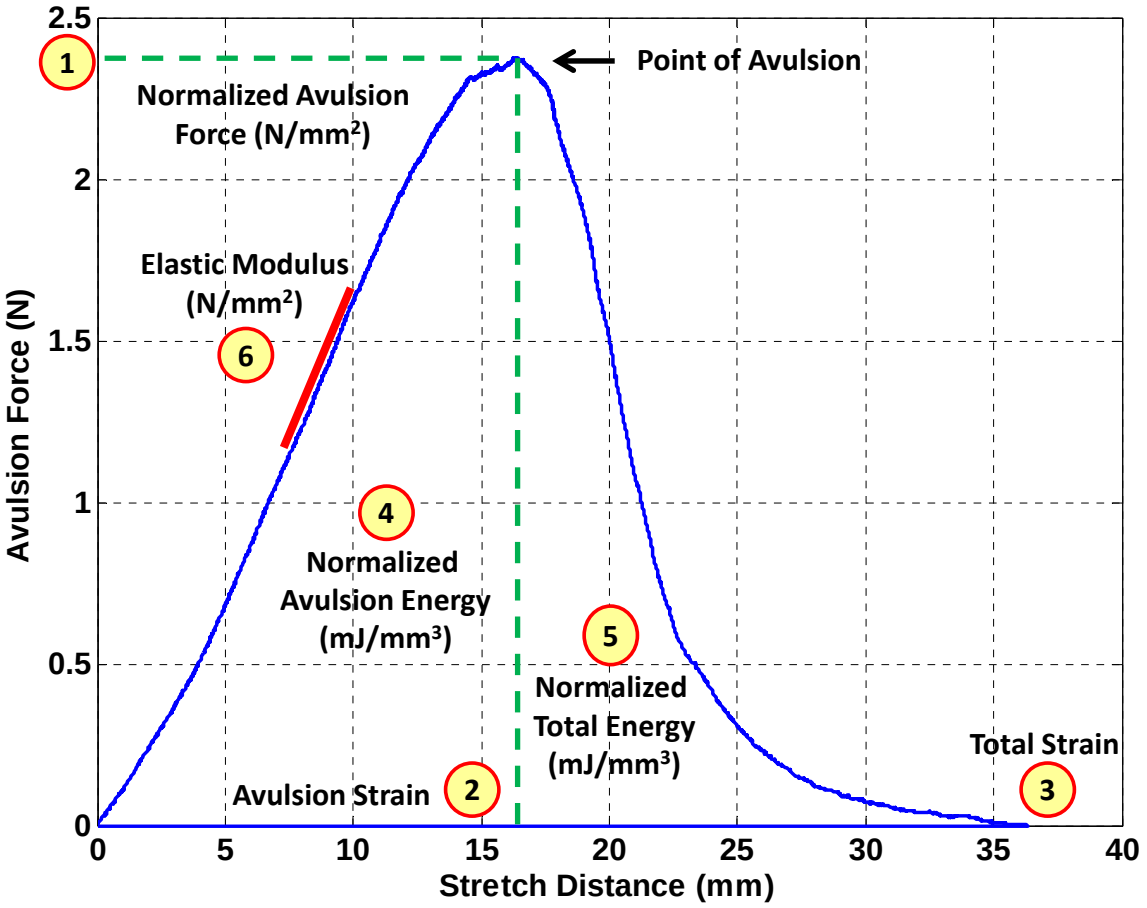

Figure 14: Force-displacement graph of a muscle bundle

Example of force-displacement graph of a muscle bundle illustrating the six biomechanical parameters that were calculated for each sample from the obtained force-displacement data. The initial sample dimensions were measured for each sample so that normalized data could be calculated.

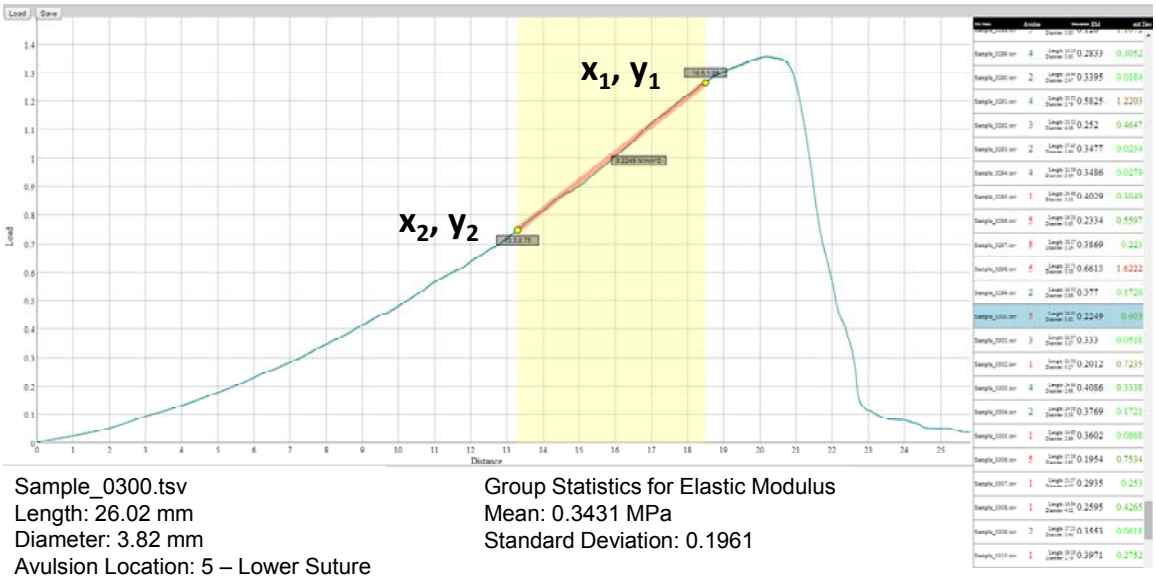

Sample_0300.tsv
Length: 26.02 mm
Diameter: 3.82 mm
Avulsion Location: 5 – Lower Suture

Group Statistics for Elastic Modulus
Mean: 0.3431 MPa
Standard Deviation: 0.1961

Figure 15: Calculation of elastic moduli

Example of force-displacement graph of a given muscle bundle illustrating the selection of two free-form points on the linear region of the graph to calculate the elastic modulus. The text below shows the dimensions and avulsion characteristics of the given muscle bundle, along with the mean and standard deviation of the entire population. The panel on right shows the elastic modulus of all samples in the treatment group.

Determination	Avulsion Location	Sample Data Included in Analysis?
1	Sample slipped out of the top suture; Sample avulsed at or near top suture	No
2	Sample avulsed in between the center and top region of the muscle bundle	Yes
3	Sample avulsed in the center	Yes
4	Sample avulsed in between the center and bottom region of the muscle bundle	Yes
5	Sample slipped out of the bottom suture; Sample avulsed at or near the bottom suture	No

Table 2: Criteria for determination of avulsion location of any given muscle bundle

3. The Comparative Assessment of Clinically Applied Ablative Therapies: Part II. The assessment of physiological and biomechanical properties of isolated respiratory diaphragm in response to varied therapeutic dosages

Preface

This paper discusses the detailed methodologies that were developed to assess the physiological and biomechanical properties of tissues in response to ablations. This paper was submitted to the International Journal of Hyperthermia in July 2014 and is currently under review.

Ashish Singal
University of Minnesota
singa009@umn.edu

Charles L. Soule
University of Minnesota
soule005@umn.edu

John R. Ballard
University of Minnesota
ball0250@umn.edu

Eric N. Rudie
Rudie Consulting, LLC
erudie@rudieconsulting.com

Erik N.K. Cressman
MD Anderson Cancer Center
Department of Interventional Radiology
ECressman@mdanderson.org

Paul A. Iaizzo (Corresponding Author)
University of Minnesota
420 Delaware St. SE, B172 Mayo, MMC 195
Minneapolis, MN 55455
iaizz001@umn.edu

Running Title: Comparative assessment of ablative therapies. Part II

Key Words: Radiofrequency ablation; cryoablation; microwave ablation; high-intensity focused ultrasound ablation; chemical ablation

Executive Summary

Purpose: Ablation is a common medical procedure used worldwide for the treatment of cardiac arrhythmias, lung cancers, hepatocellular carcinomas, and other conditions. In some cases, ablative treatment can cause collateral injury to the respiratory diaphragm, which can have important clinical implications. Collateral damage may result in altered diaphragmatic properties and/or respiratory dysfunction. It is important to understand the physiological and biomechanical properties of the diaphragm that may be potentially affected by various modes of ablative therapies. Such knowledge may help maximize the efficacy of ablative procedures and minimize procedural complications.

Materials and Methods: We characterized physiological and biomechanical properties of swine diaphragm muscle bundles when exposed to five therapeutic ablation modalities (radiofrequency ablation, cryoablation, high-intensity focused ultrasound ablation, microwave ablation, and chemical ablation using acetic acid, ethanol, hypertonic sodium chloride, and urea). Physiological properties were assessed by performing in-vitro tissue bath studies to measure changes in peak forces (strength of contractions) as well as baseline forces (resting muscle tension). Biomechanical properties were assessed by performing uniaxial stress tests to measure force-displacement responses, stress-strain characteristics, and alterations of avulsion forces, strains, energies, and elastic moduli.

Results: We observed dose-dependent sustained reductions in peak forces and transient increases in baseline forces following treatment with all ablative modalities. Yet, no dose-dependent responses were consistently observed relative to the biomechanical responses following ablations.

Conclusions: These data may provide novel insights into the effects of ablation on the diaphragm which may enable further improvements in ablative techniques to increase safety and efficacy of ablative procedures.

Introduction

The respiratory diaphragm is a dome-shaped internal skeletal muscle separating the thoracic and abdominal cavity that plays an important function in respiration [1]. Any form of injury to the diaphragm or its innervation can significantly alter its function, which may compromise respiration. Although injury to the diaphragm can occur in many ways, this article focuses on diaphragmatic injury especially in the form of collateral damage from ablative therapies used for treating various diseases, such as: hepatocellular carcinoma (HCC), atrial fibrillation (AF), lung carcinoma, and continuous mechanical ventilation resulting in ventilator-induced diaphragmatic dysfunction (VIDD). Because of the diaphragm's susceptibility to collateral damage, we consider that it is essential to understand both the physiological and biomechanical properties of diaphragmatic tissue under various therapeutic ablative treatments. This will not only allow us to understand the interactions of diaphragmatic tissue in response to ablation, but it will also help in developing tools and techniques, and refining procedures to minimize or prevent collateral damage. The ablative modalities employed in this investigation were: radiofrequency ablation (RFA), cryoablation (CRA), high-intensity focused ultrasound ablation (HIFU), microwave ablation (MWA), and chemical ablation (CHA). Four chemical agents were used: 99.97% glacial acetic acid, 200 proof ethanol, 30% hypertonic sodium chloride solution, and 8M urea. The in vitro physiological assessments included alterations in peak forces (strength of contractions) as well as changes in baseline forces (resting muscle

tension) of isolated diaphragmatic muscle bundles stimulated within tissue baths [2, 3]. Biomechanical assessment included measurement of uniaxial stress-strain characteristics of the same tissue samples employing a uniaxial testing machine.

Diaphragm Dysfunction from Continuous Mechanical Ventilation

Although mechanical ventilation is a life-saving intervention, it is often associated with numerous complications of diaphragmatic dysfunction. A large body of evidence suggests that there is a decrease in diaphragmatic strength with an increased duration of mechanical ventilation [4]. This may result in an early-onset and progressive decrease in diaphragmatic force-generating capacity leading to VIDD. The mechanisms of VIDD are not fully elucidated, but have been reported to include muscle atrophy [5], oxidative stress [6, 7], structural injury [8], muscle fiber remodeling [9], and/or mitochondrial dysfunction [10]. The experimental methodologies described in this investigation may help provide insights into the pathophysiology of VIDD by comparative assessment of normal versus diseased samples, thereby reducing associated complications.

Diaphragm Injury during Treatment of Lung Cancer

Diaphragm has been shown to be susceptible to damage from RFA therapeutic applications in the lungs, during treatments for cancer [11, 12]. Although common complications such as pneumothorax, pleural effusion, and parenchymal hemorrhage can be treated conservatively, fatal complications such

as massive hemorrhage, pulmonary artery pseudoaneurysms, and diaphragmatic injury may require extensive medical management. For example, a case of intestinal obstruction due to left diaphragmatic hernia was reported to have developed following RFA treatment of pulmonary metastasis [13]. In another study, the diaphragm suffered collateral damage following the therapeutic application of RFA of the laterobasal segment of the lower lobe of the right lung, which was performed to treat lung metastasis from uterine cervical cancer [14].

Diaphragm Injury during Treatment of Cardiac Arrhythmias

It has been noted that the diaphragm is highly susceptible to secondary damage leading to diaphragmatic paralysis after traumatic phrenic nerve injury (PNI) following endocardial ablations of the heart. PNI can occur following cardiac ablations performed with different energy sources including radiofrequency, cryoablation, ultrasound, and laser [15]. For example, right hemi-diaphragmatic paralysis developed after cardiac RFA [16] and cryoballoon ablation [17] of pulmonary veins for the management of AF. In another case, permanent right diaphragm paralysis was reported following PNI from RFA cardiac procedures [18]. Similarly, left PNI after cryoballoon ablation of the pulmonary veins has also been reported [19]. It is hypothesized that local focused thermal energy at the time of ablation may cause direct neuronal damage to the phrenic nerve by axonal coagulation necrosis (from hyperthermic injury), or by cooling and freezing the axonal tissue thus interrupting nerve

conduction (from hypothermic injury). Intracardiac echocardiography has been utilized for continuous diaphragmatic visualization during cryoballoon ablation of the pulmonary veins [20]. This technique allows monitoring of phrenic nerve function during ablation preventing the need of fluoroscopy, thus significantly minimizing radiation to both the patient and the operator. It should be noted that the diaphragm itself may suffer collateral injury from ablations performed in the ventricles to treat ventricular arrhythmias.

Diaphragm Injury during Treatment for HCC

Although surgical resection remains the first line curative treatment for hepatocellular carcinoma (HCC), most patients are unable to undergo this invasive procedure because of advanced disease stage, severe liver dysfunction, poor clinical status, and/or other comorbidities. Therefore, less invasive techniques such as image-guided percutaneous tumor ablation have been adopted for the treatment of unresectable HCC [21]. Thermal ablations located close to vital structures such as diaphragm are technically challenging because of the risk of unintended collateral damage. Hence, it is essential to select a proper method for ablation therapy of liver tumors, especially treating ones located near vital structures and those that are difficult to visualize and approach by percutaneous techniques.

There have been many instances where the diaphragm has suffered injury from ablation procedures involving treatment of HCC. In one study, 5 out of 29 (17%) patients who underwent percutaneous RFA of hepatic tumors adjacent to the diaphragm suffered injury which was clinically apparent with right shoulder pain [22]. Furthermore, there have been reports of pneumothorax induced by RFA for HCC treatment beneath the diaphragm under real-time computed tomography-fluoroscopic guidance [23-26].

Numerous techniques have been attempted to prevent thermal injury to the diaphragm and abutting structures to and near the liver during ablations of the liver. Artificial ascites (formulated with 5% dextrose in water solution) around the liver is considered as a simple and safe technique for the treatment of hepatic dome tumors abutting the diaphragm [27]. In order to minimize diaphragmatic injury, percutaneous RFA in conjunction with artificial ascites has been successfully attempted [28-31]. An improvement in the therapeutic window has been shown by separating the RFA zone from the diaphragm by downward displacement of the liver with the use of this simple and inexpensive technique [32]. Alternatively, there are reports in which artificial ascites has not shown a heat-sink effect on the volume of the ablation zone after percutaneous RFA for the treatment of a hepatic tumor abutting the diaphragm [33]. Thoracoscopic RFA, allowing visualization of therapy, has also been suggested to be a feasible technique [34, 35]. RFA in combination with artificial pleural effusion has also been demonstrated to be a safe and beneficial treatment option that offers

excellent local control through visualization of HCC under the diaphragm [36-38]. When performed under ultrasound guidance with strict temperature monitoring [39] or under thoracoscopic visualization with ultrasonography [40], percutaneous MWA of liver tumors adjacent to the diaphragm has been shown to be a safe and highly effective treatment.

The primary objectives of the present study were to gain new insights to the changes in both physiological and biomechanical properties of the diaphragm muscle in response to applied ablative therapies. To do so, we performed in vitro analyses on isolated swine diaphragm muscle bundles using methods detailed in Part 1 of our paired reports (Chapter 2).

Materials and Methods

Tissue Preparation

These investigations were approved by the University of Minnesota Institutional Animal Care and Use Committee. Fresh respiratory diaphragm tissue biopsies were obtained from healthy castrated male Yorkshire-cross swine (n=56, mean weight of approximately 70 kg) that were euthanized as part of another unrelated protocol. Briefly, following resection, the diaphragm tissue was pinned in a dissection dish, dissected in oxygenated, temperature-controlled skeletal muscle Krebs-Ringer solution, and muscle bundles were prepared. The physiological testing was performed using tissue baths, and biomechanical testing was performed using a uniaxial testing machine as described in detail in

Chapter 2. The diaphragmatic tissue response to the following five different ablation modalities was investigated:

- *Radiofrequency ablation*: RFA (484 KHz sinusoidal waveform) at five different ablation doses was studied: 50°C, 55°C, 60°C, 65°C, and 70°C (corresponding to 348 J, 580 J, 812 J, 1043 J, and 1275 J energy levels, respectively).
- *Cryoablation*: Cryoablation exposure (operated in the clinical mode, approximately -75°C) at four different ablation doses was studied: 15 sec, 30 sec, 60 sec, and 120 sec.
- *Microwave ablation*: MWA (1.3 GHz continuous sinusoidal waveform) with ablation duration between 60 sec and 240 sec at six different ablation doses was studied: 168 J, 289 J, 410 J, 821 J, 1231 J, and 1642 J.
- *HIFU ablation*: HIFU ablation (2.5 MHz sinusoidal waveform, 80% duty cycle) at six different ablation doses was studied: 98 J, 116 J, 132 J, 232 J, 464 J, and 696 J.
- *Chemical ablation*: Chemical ablations with all four agents (acetic acid, ethanol, hypertonic sodium chloride, and urea) were performed independently by injecting the chemical ablative agent individually at six different ablation doses: 10 µl, 25 µl, 40 µl, 50 µl, 75 µl, and 100 µl.

Data Analyses

Statistical analyses were performed using ANOVA and the Tukey test to identify differences in peak force and baseline force for all ablation modalities where a $p<0.05$ is considered statistically significant. All data are presented as mean $\pm$ standard deviation.

Results

Results of Physiological Assessment

A total number of 212 muscle bundles were studied for physiological assessment in tissue baths as shown in Table 3. The table summarizes muscle bundle characteristics and allocations to different ablative modalities. As seen in this table, the parameters length, diameter, mass, initial peak force, and baseline force of muscle bundles were similar across the different groups.

The percent change in peak force and baseline force in response to all ablation modalities were calculated for the diaphragm tissue as shown in Figure 16 to Figure 33. There was a dose-dependent sustained reduction in peak force and a transient increase in baseline force following treatment with all ablative modalities. With some ablative modalities (e.g., RFA, hypertonic sodium chloride), the peak force reduced initially, but showed some improvement over the 3-hour recovery period. This phenomenon of partial improvement in peak force was more pronounced at lower ablation doses. Although there was a dose-dependent transient increase in baseline force for all ablation modalities, the

baseline force recovered consistently below the pre-ablation level at the 3-hour recovery period (except for acetic acid). An interesting finding was observed with 100 µl dose of hypertonic sodium chloride where the baseline force did not exhibit the dose-dependent response. Typically, the transient elevation in baseline force was maintained for a period of approximately one hour post-ablation; later it decreased below the pre-ablation levels. This phenomenon was not observed for the following therapies: (1) acetic acid where the baseline force remained at elevated levels, and (2) in cases of hypertonic sodium chloride and urea, where the baseline force reduced to pre-ablation levels within approximately 15 minutes. The percent reduction in peak forces for all chemical ablation modalities, except acetic acid, was similar at every ablation dose. Among all the chemical ablative agents utilized for performing ablations, acetic acid was the most potent agent as it caused the maximum reduction in peak force at every ablation dose. The post-ablation percent change in baseline force for ethanol was consistently the highest at every ablation dose, and that of hypertonic sodium chloride was consistently the lowest. For control and control-remove muscle bundles, similar changes in peak force and baseline force were observed (as shown in Figure 34 and Figure 35), suggesting that unmounting the muscle bundles from the tissue baths for ablations had minimal impact on subsequent muscle physiological response. The peak force and baseline force of muscle bundles injected with Krebs-Ringer solution were similar for every injected dose and no significant dose-effects were observed (as shown in Figure

32 and Figure 33). Moreover, the fact that peak forces and baseline forces for muscle bundles injected with Krebs-Ringer solution were very similar to those of control and control-remove muscle bundles suggests minimal (if any) mechanical damage resulted from injection of chemical agents or the Krebs-Ringer solution.

For all thermal ablation modalities (RFA, CRA, MWA, and HIFU), statistically significant differences ($p<0.05$) were observed for both dose and time variables, as calculated using the Tukey test. For all chemical ablation agents, statistically significant differences ($p<0.05$) were observed for dose, time, and agent (Krebs-Ringer solution versus chemical ablative agent) variables, calculated using the Tukey test.

Results of Biomechanical Assessment

A total number of 733 muscle bundles were studied for biomechanical assessment which included the 212 muscle bundles which were also used in the physiological assessment described above. All muscle bundles were subjected to a uniaxial pull test, and force versus stretch data were obtained for all the samples. At the completion of the uniaxial pull test, an assessment was made where each muscle bundle avulsed; this is summarized in Table 4 as a percentage of avulsion location of muscle bundles for each treatment along with the number of samples in each case. Figure 40 shows the graphical distribution of avulsion locations for all muscle bundles. For biomechanical assessment, only the muscle bundles that avulsed at or near the center of the muscle bundle were

included in the analysis. Based on these data, the key biomechanical parameters of all samples in each treatment group were calculated as shown in Table 5. As seen in the table, the initial cross-sectional area and volume of the muscle bundles were similar across different groups. The avulsion force was defined as the value of the maximum force that was required to cause tissue avulsion. Since the force required to avulse the tissue was dependent on cross-sectional area of the muscle bundle, the avulsion force was normalized to the cross-sectional area and is reported in units of N/mm^2. The avulsion strain was defined as the ratio of stretch to the point of avulsion and the original length of the muscle bundle; the total strain was defined as the ratio of stretch to the point where force returned to zero following avulsion and the original length of the muscle bundle. The avulsion energy was defined as the integral of area under the force-displacement curve until the point of avulsion; the total energy was defined as the integral of area under the entire force-displacement curve. Since energy required to avulse the tissue was dependent on avulsion force and stretch distance, energy was normalized to the volume of the tissue and is reported in units of mJ/mm^3. Cross-sectional area normalization of avulsion force and volume normalization of energy allowed comparative assessment between different treatment groups. The elastic modulus, avulsion and total strain, and avulsion and total energy of samples were also calculated, allowing assessment of relative stiffness of the samples between each group. As an example, an average model of stress-strain characteristics of non-ablated (control) swine diaphragm muscle bundles was

developed by averaging all samples (n=187) as shown in Figure 41. The “true stress-strain” relationship (Cauchy’s stress) was also calculated by taking into account the reduction in cross-sectional area of the samples during the stretch. The average avulsion stress and Cauchy’s avulsion stress were calculated to be 0.11 MPa and 0.24 MPa, respectively, and the avulsion strain was calculated to be 1.35. Note that Cauchy’s stress was found to be 2.18 times higher than the conventional stress. In a similar manner, the stress-strain characteristics of all muscle bundles in every treatment group were calculated (graphs not shown); the key biomechanical parameters are summarized in Table 5.

The percent change in each of the six biomechanical parameters in each treatment group were calculated with respect to control samples (n=187, non-ablated) as shown in Table 6. A positive value indicates an increase and a negative value a decrease with respect to controls. Percent change in avulsion force, elastic modulus, strain, and energy are shown along with individual statistical significance ($p<0.05$, marked in bold). The avulsion force increased for every ablative treatment except RFA and MWA. There was a 31% increase in avulsion force following treatment with acetic acid and a reduction of 38% following treatment with MWA. The elastic modulus increased following treatment with every ablative modality except RFA and MWA. There was a 90% increase in elastic modulus following treatment with CRA and a 58% reduction following treatment with MWA. The avulsion and total strain decreased following treatment with every ablation modality except MWA. A significant reduction in avulsion and

total energy was observed following application of CRA. Dose effects of each of the six biomechanical parameters for all ablation modalities were analyzed using ANOVA. Unlike physiological results, statistically significant dose effects were not observed in biomechanical properties following the application of any ablation modality, as shown in Figure 42 to Figure 50.

Discussion

This study demonstrates that both physiological and biomechanical properties of swine respiratory diaphragm are altered when subjected to various ablation therapies. Although the mechanisms of action of every ablation modality are unique and complex, they are discussed briefly to highlight the mechanisms of tissue injury that result in reduction on peak force post-ablation. RFA energy is a form of alternating electrical current that dissipates within the tissue and generates a lesion by mode of resistive (electrical) heating [41, Chapter 2]; this results in protein denaturation and coagulation necrosis. CRA works by freezing tissue in a discrete and focused manner to destroy cells in a target location. It has been reported that the application of cryoenergy results in the formation of an ice -ball at the target area that causes freezing, thawing, hemorrhage, inflammation, fibrosis, and apoptosis [42]. In the case of HIFU, high-intensity US waves are focused in a small region of the target tissue that induce deep hyperthermia and ultimately tissue ablation through two primary modes of tissue injury: thermally-induced injury (from thermal energy/effects) and mechanically-

induced injury (from mechanical energy/effects). The temperature at the transducer focus can reach over 65°C within seconds, denaturing cellular proteins and resulting in coagulative necrosis [43]. MWA therapy results in dielectric heating of tissue when high frequency electromagnetic radiation stimulates oscillations of dipole molecules such as water within the cellular and extracellular medium, which converts the electromagnetic energy into oscillating kinetic energy. This energy is dissipated as heat at the target location which ultimately results in thermal injury [44]. CHA, on the other hand, uses chemical agents at lethal concentrations that work by denaturing proteins and creating focal tissue damage and lesion, ultimately leading to tissue necrosis in the location of injection [45].

A dose-dependent sustained reduction in peak force was observed for each ablation modality investigated. At the cellular level, the protein structure dictates its specificity, and the three-dimensional (tertiary) structure is particularly important for its overall function. When this specific three-dimensional structure is disrupted as a result of exposure to extreme temperatures during ablation, the protein loses its functionality and undergoes denaturation [46]. Typically, the application of hyperthermic temperatures during ablative procedures cause cell membrane collapse, protein denaturation, and cessation in enzymatic function, as well as mitochondrial dysfunction further leading to coagulation necrosis [47]. Similarly, it is considered that achieving hypothermic temperatures during cryoablation procedures induces direct cellular injury from ice crystal formation,

vascular ischemia, and apoptosis [48, 49]. In contrast, dehydration, membrane lysis, disruption of structural organization of proteins, and protein denaturation are the hallmarks following chemical ablation [45]. These cascaded events are considered to lead to disruption of the protein structure and function, which include the contractile myofilaments, intrinsic, and extrinsic proteins of the cell [42]. When viewed at the muscle level, the ability of the diaphragmatic muscle to elicit an electromechanical response resulting in contraction is dependent on the viability of the muscle fibers. Since ablation results in immediate tissue injury leading to cell death, tissue viability is compromised [47] and results in reduction of peak force. Moreover, as expected, a higher level of ablative dose is expected to cause an increased level of cellular injury. This is consistent with a trend in reduction in peak force with increasing levels of ablative dose that was observed in this study. Yet, in some cases, especially at lower doses, the peak force reduced initially, but showed some recovery over the 3-hour measurement period. This could be explained by the effects of skeletal muscle stunning that have been reported following ischemic injury [50]. One way to further interpret these force reductions is by considering the underlying cellular functions associated with ischemic injury which are induced by ablative procedures. For example, contractile dysfunction has been reported to occur rapidly during ablation, as a consequence of many factors, one of which includes ischemic injury [51]. One of the proposed mechanisms involves the generation of inorganic phosphate, largely attributed to the breakdown of creatine phosphate reserves

shortly after ischemic injury. Accumulation of inorganic phosphate inhibits the contractile proteins and may be the earliest factor responsible for the loss of contractility during ablations [52]. A second factor is the rapid fall of intracellular pH which inhibits Ca^{2+} binding to contractile proteins and thus further reduces contractility. It is generally considered that the initial decrease in contractility during ablation is fully reversible if the ablative dose is well below the threshold that causes tissue injury. However, if the ablative dose exceeds the threshold window, then contractile function does not return to baseline levels, even if there is no cell death associated with the ablative exposure. This failure of recovery of contractile function is termed "stunning," and is slowly reversible over a period of time until a plateau is reached. There appear to be two mechanisms, possibly interrelated, that are responsible for the stunning effect. The first is the generation of reactive oxygen species and the second is the selective proteolysis of proteins that is thought to be due to activation of proteases by the rise in cytosolic calcium [52].

In our study, a dose-dependent transient increase in baseline force as a function of increasing ablative dose was observed. This response may also be considered to occur due to the stunning effect. As discussed above, as a result of ablation exposure, muscle cells generally become incapable of eliciting an electromechanical response (i.e., either contracting or relaxing). This condition is called physiologic contracture, which is caused by the lack of ATP within the muscle fibers [53]. It has been reported that at very low ATP levels, active

transport of Ca^{2+} ions into the sarcoplasmic reticulum slows (due to impaired SERCA function), thus Ca^{2+} ions accumulate within the sarcoplasm, and ATP is unavailable to bind to the myosin molecules that have formed cross-bridges with the actin myofilaments [54, 55]. As a consequence, the previously formed cross-bridges cannot release, resulting in physiologic contracture. These effects not only result in elevated baseline forces following ablations, but the toxic Ca^{2+} overload causes a variety of pathological changes including necrosis and apoptosis [56]. In general, it has been observed that a reversible increase in tonic resting muscle tension is observed at temperatures between 45°C and 50°C. Typically, above 50°C *(isotherm of irreversible tissue injury)*, the muscle elicits evidence of irreversible contracture [57]. It is deemed that the induced hyperthermia and hypothermia causes Ca^{2+} accumulation in the diaphragm muscle cells which ultimately leads to Ca^{2+} overload [58, 59]. Furthermore, these observations have been confirmed with calcium-sensitive Fluo-3 AM fluorescent dye studies, where hyperthermic increases in muscle tension as a result of increased intracellular Ca^{2+} concentration correlated well with increased Fluo-3 AM fluorescence [60]. It can be concluded that exposure to extreme temperatures results in significant increases in intracellular Ca^{2+}, probably as a result of nonspecific transmembrane transit through thermally induced sarcolemmal pores [57]. With increased intracellular Ca^{2+} entry, impaired ability of the sarcoplasmic reticulum to sequester Ca^{2+} and dysfunctional ion pump kinetics (due to lack of ATP, Ca^{2+} overload within the cytosol) ensue. In this case,

cell contracture and death occur at lower temperatures than expected. In our study we had an interesting observation with all muscle bundles that were ablated with acetic acid. After approximately 30 min of ablation, microbubble droplets were observed on the ablated region of the muscle bundles caused by excessive dehydration as shown in Figure 51. The mechanisms of chemical ablation with acetic acid, and other chemical agents used in this investigation, are based on the induction of intracellular dehydration, intracellular protein damage, and thrombo-ischemic effects on the muscle cells [61]. This eventually resulted in: (1) contracture which caused an increase in baseline force, (2) cellular injury which caused reduction in peak force, and (3) protein denaturation and dehydration which caused stiffness and an increase in avulsion force.

In this investigation, the main objective was to perform the tissue bath study (for physiological assessment) and then follow up with the uniaxial pulls (for biomechanical assessment). No dose-dependent response was consistently observed in any of the six biomechanical parameters as a result of treatment with all ablation modalities. In part, this was due to many confounding factors, some of which are alluded to in “Part 1” of the article (Chapter 2). One possible explanation for these observations is that the ablation doses used for physiological assessment did not cause a significant change in biomechanical properties of the diaphragmatic tissue. This hypothesis was tested by ablating a separate set of diaphragm muscle bundles at much higher ablative doses, typically a combination of longer durations or multiple exposures, and then

performing the biomechanical uniaxial pulls (data not shown). It was observed that when these muscle bundles were mounted in tissue baths, no peak forces could be registered. This was, in part, due to much higher levels of cellular injury which resulted in significant compromise of the contractile protein network, hence complete loss of contractility. However, when these muscle bundles were subjected to uniaxial pulls, significant changes in biomechanical properties were noted. For example, with respect to controls, the average avulsion forces typically: (1) increased by 12% when muscle bundles were exposed to three RFA of 1-min duration each, (2) increased by 25% when muscle bundles were exposed to four MWA of 4-min duration each, and (3) decreased by 45% when muscle bundles were exposed to two CRA of 4-min duration each. All these ablations were performed sequentially, side-by-side, near the center of the muscle bundle. As noted before, when these muscle bundles were mounted in tissue baths after ablations, no contractions could be elicited even at supra-maximal stimulation levels suggesting severe cellular injury. Since no contractions could be elicited, physiological assessment protocol could not be performed on these muscle bundles, and at these ablative doses. Thus, ablation doses were selected that were not only clinically relevant, but also with a view of an acceptable model, so that both tissue bath studies and uniaxial pull studies could be performed on the same muscle bundles. These observations suggest that the sensitivity of both techniques (tissue baths and uniaxial pulls) may be quite different. In other words, significantly higher ablative energies are required

before any appreciable change in biomechanical properties of the diaphragmatic tissue can be observed. Moreover, due to variability introduced from multiple sources, the uniaxial pull measurements may not be sensitive enough to discriminate small differences in biomechanical properties resulting from the ablation dose levels selected in this study. Clinically, an increase in avulsion force means that it would require a higher force to cause tissue avulsion. This may be due to many factors of which the primary ones are denaturation of proteins, elastin and collagen. Collagen is the most abundant structural protein in mammals [62], making up 25% to 35% of the whole-body protein content. Moreover, collagen within the extracellular matrix is the primary structural protein providing a mechanical scaffold for cells within tissues [63]. Ablations cause coagulation necrosis of the tissue during which collagen undergoes post-translational changes that alter its organization, which in turn is thought to contribute to tissue stiffness [64]. Hence, an increase in avulsion force was observed in a majority of the ablation modalities investigated. It should be noted that the ablations typically resulted in a localized tissue injury which either caused a biomechanical “weakness” or “strengthening” near the ablated region. It was observed that post-ablation, the muscle bundles typically avulsed at the ablated region or at the healthy-ablated tissue interface.

We consider that this series of experiments offers a unique ability to collect both physiological and biomechanical data, with a high level of consistency and repeatability. This enabled us to closely explore highly relevant ablative doses,

those that might be encountered clinically. It is understood that there are three potential differences as far as tissue response is concerned between the intact whole diaphragm and muscle bundles. One, the intact diaphragm is susceptible to secondary collateral injury from ablative procedures performed in a different organ. The extent of collateral injury depends on the type of ablative energy used, duration, and proximity to the diaphragm. Moreover, these injuries generally tend to be localized to a region of the diaphragm. Our set of experiments mimics the collateral injury by directly ablating the diaphragmatic muscle bundles in localized regions with various ablative treatments. Although the way diaphragm incurs damage may be different between the secondary collateral injuries versus direct injury, the end result is the same—cellular injury leading to diaphragmatic dysfunction. In view of this, future investigations could more closely mimic the collateral damage by including a biopsy of the primary target organ between the ablative source and the diaphragmatic muscle bundle.

Second, there will be small stimulation and electro-mechanical differences between the intact diaphragm versus diaphragmatic muscle bundles; muscle bundles are bathed in Krebs solution in tissue baths, whereas intact diaphragm is perfused with normal blood within the body. However, stimulation within a muscle bundle requires similar voltage gradients and transmembrane potentials to elicit a contraction as stimulation with the intact diaphragm; we feel that it is likely to show similar responses and trends in action potential initiation and propagation.

Lastly, the biomechanical parameters of the intact diaphragm within its

native environment will be different than those of isolated muscle bundles. We believe this is not only because of the bulk muscle volume, but also because of its adhesion to surrounding structures and relation to surrounding organs. In order to perform a fair and consistent comparison between muscle bundles exposed to various treatments, all biomechanical data were normalized either to the muscle bundle cross-sectional area or volume based on the quantity measured. Nevertheless, it is these responses and trends that we feel are important to guide further research.

In this investigation, we employed four thermal ablative modalities and four chemical ablative agents. Each ablative technique, although similar in purpose, has specific and optimal indications. Choice of the most appropriate ablative modality is vital to the success of any ablative procedure. The type of tissue to be ablated, regional blood flow, and the size of desired lesion are three important factors in this decision. Each ablation modality has its unique advantages. For example, the noninvasive, high-precision nature of HIFU makes it attractive in stationary or superficial regions. Among all ablation modalities, RFA has been in practice for the longest time which makes it an attractive modality of choice. One of the advantages of a CRA probe is that it adheres to the target location by forming an ice-ball. Therefore, CRA works well in areas where catheter instability is high due to relative motion between the probe and the target location. MWA is one of the newer ablation techniques offering noncontact therapy application by electric field radiation and dielectric heating. Although it may be applicable to a

broader spectrum of tissues, its long-term effectiveness still needs to be evaluated. Compared to any thermal ablation modality, CHA is the most cost-effective option as it does not require any capital equipment for performing ablations. Although relatively inexpensive, it is restricted to use in target areas with low blood perfusion rates to minimize dilution and wash out, and prevent systemic side effects by localizing the action of injected ablative agent.

Since no similar studies have been performed in this area previously, it was not possible to compare these results with literature. It is important to note that our study approach can be considered to have a few limitations. For example, only a selected number of ablation settings were used in this study, cumulative effects of ablations were not studied, and only uniaxial pulls were done. Moreover, we did not test RFA using irrigated catheters, cryoballoon ablation catheters, phased-array HIFU transducers, different MWA antenna designs, and different chemical ablative agents, all of which may have resulted in different findings. Furthermore, this model can only investigate acute effects of ablation, i.e., within hours after ablation. Nevertheless, we hope to make this work translational by utilizing human tissue when it becomes available. The results from this investigation can be used to better understand device-tissue interaction, and to aid in novel medical device design.

Conclusion

In this investigation we utilized novel in vitro methodologies to assess how physiological and biomechanical properties of diaphragmatic tissue change as a result of exposure to various ablative modalities. The results show that these methodologies are applicable for analyzing a spectrum of ablation modalities, ones used in this investigation as well as future options, for example, laser ablation and irreversible electroporation.

To our knowledge, these are first reports of comparing the effects of ablation modalities and dosages on both the physiological and biomechanical properties of isolated functional diaphragm muscle bundles. We observed unique dose responses for each ablation modality investigated as well as therapeutic differences regarding their effects on the muscle parameters studies. The understanding of diaphragmatic tissue properties has wide applications ranging from basic research to novel medical device design. This unique data set could provide important insights to both clinicians and medical device designers. Results from these studies could enable head-to-head comparison of ablative modalities to determine their effects on tissue response. Interpretation of these results can further be used to reduce complication rates, as well as increase effectiveness and overall efficacy of therapies. Moreover, increasing knowledge in this area is fueling the demand for introducing new procedures, modifying current ones, and reducing procedural time to positively impact the efficiency and efficacy of treatment delivered.

Acknowledgements

We gratefully acknowledge the assistance of Monica Mahre and Dave Euler for reviewing the manuscript.

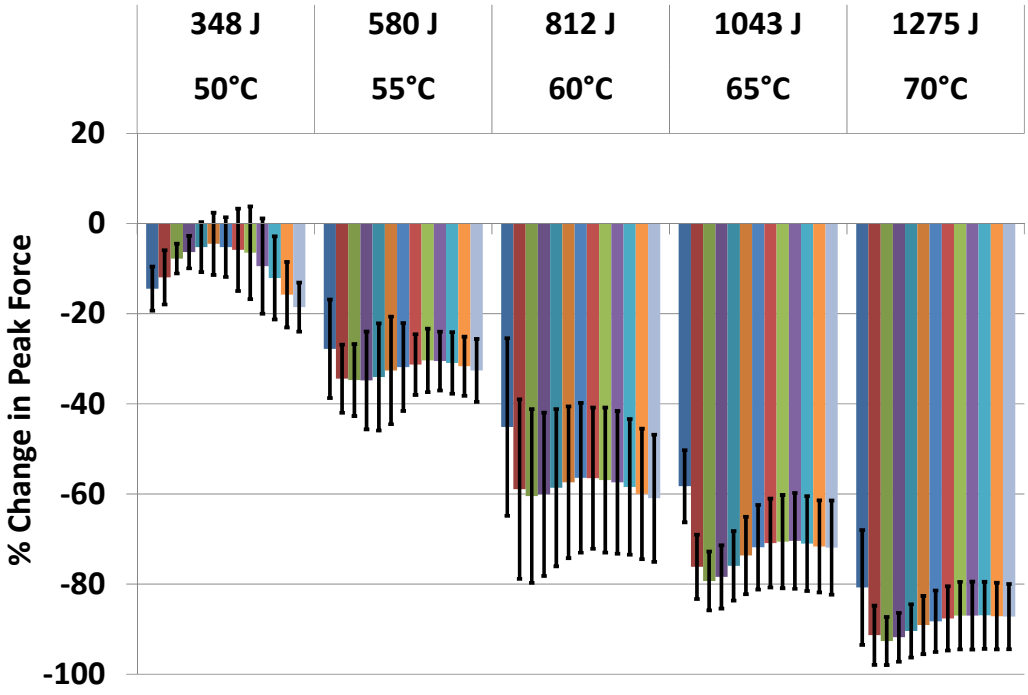

Figure 16: Dose effects of percent change in peak force of swine diaphragm post radiofrequency ablation (RFA)

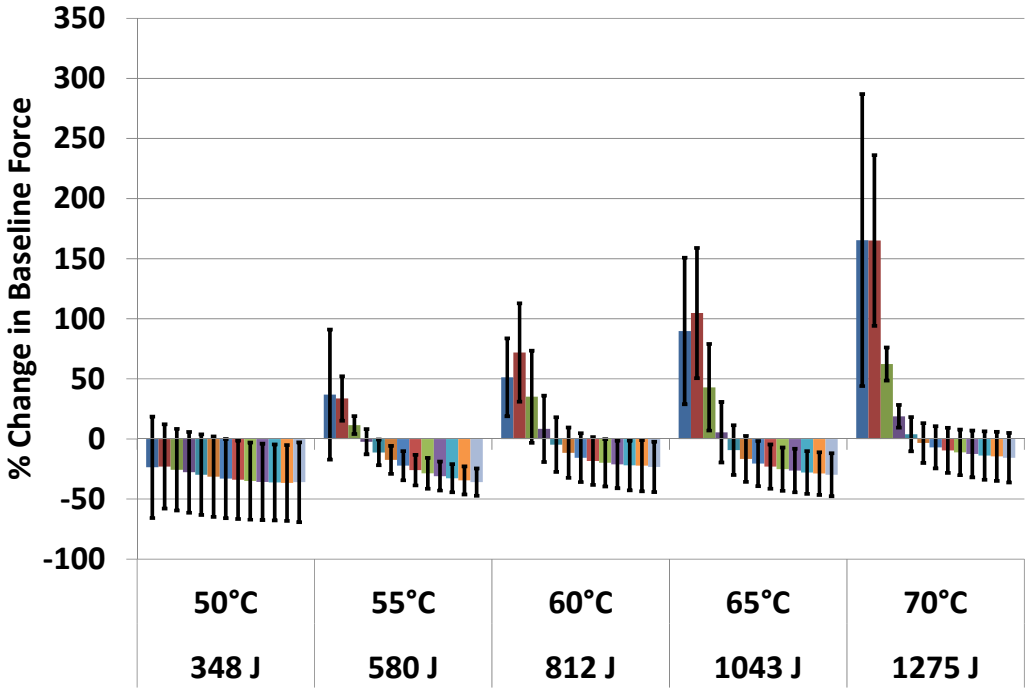

Figure 17: Dose effects of percent change in baseline force of swine diaphragm post radiofrequency ablation (RFA)

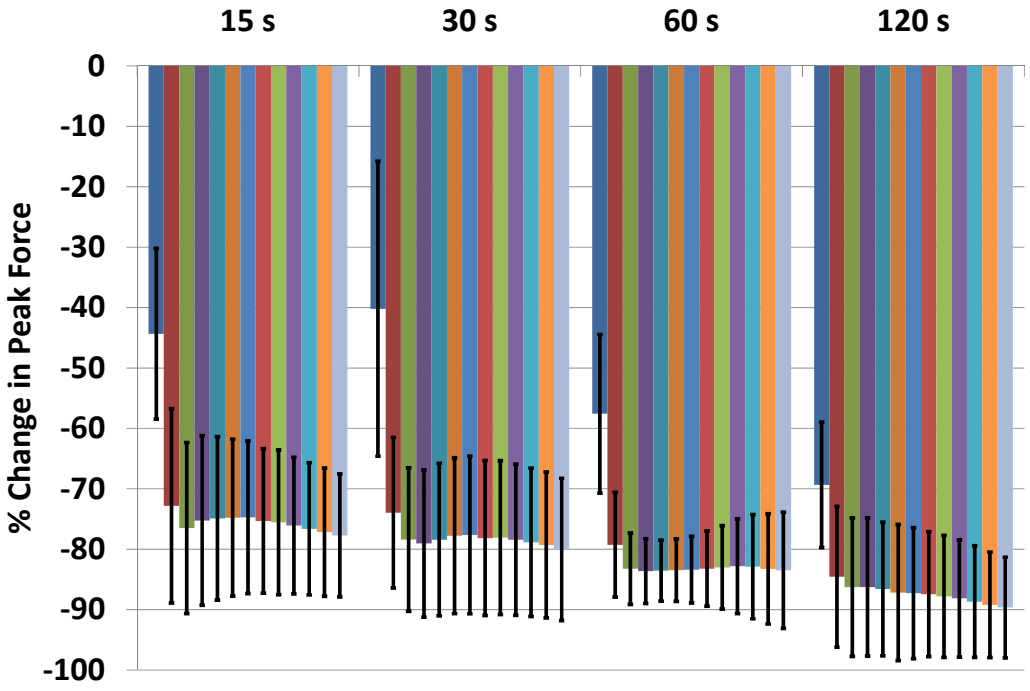

Figure 18: Dose effects of percent change in peak force of swine diaphragm post cryoablation (CRA)

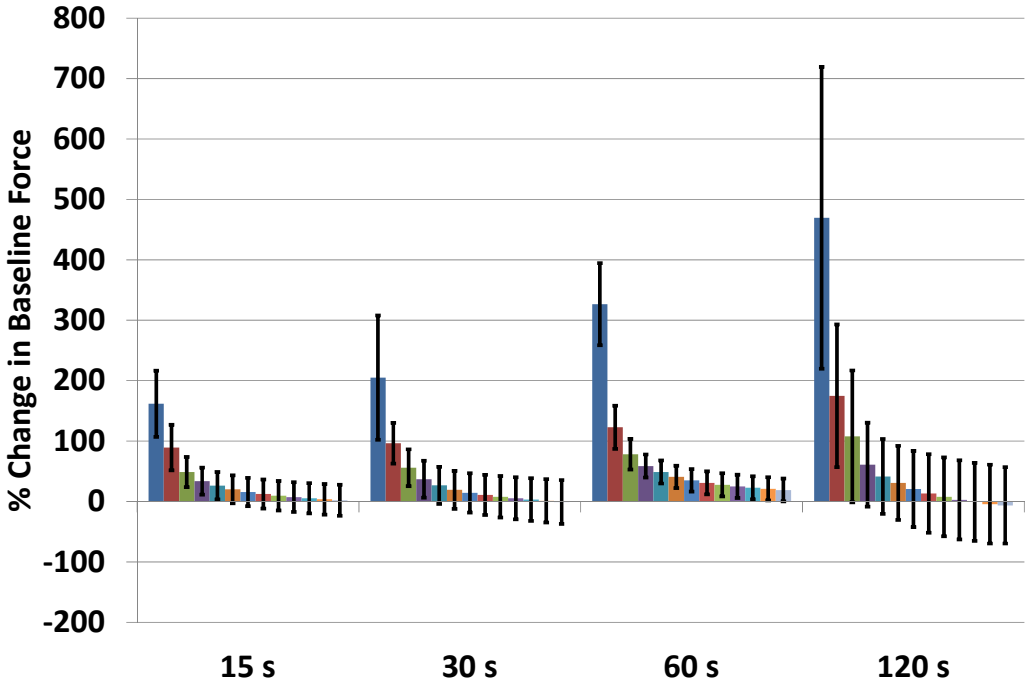

Figure 19: Dose effects of percent change in baseline force of swine diaphragm post cryoablation (CRA)

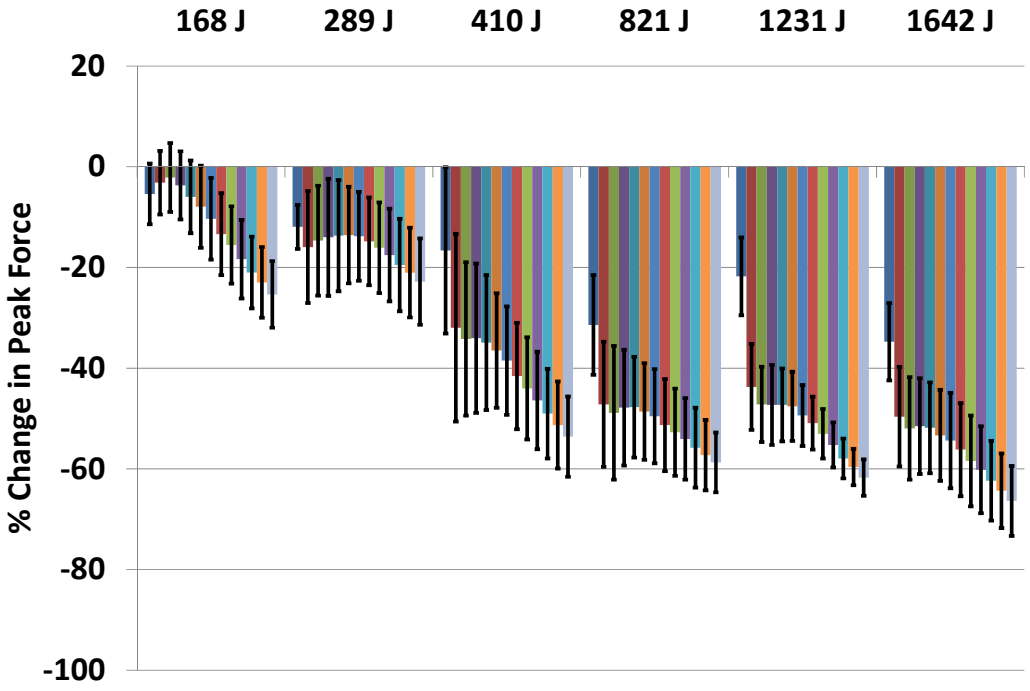

Figure 20: Dose effects of percent change in peak force of swine diaphragm post microwave ablation (MWA)

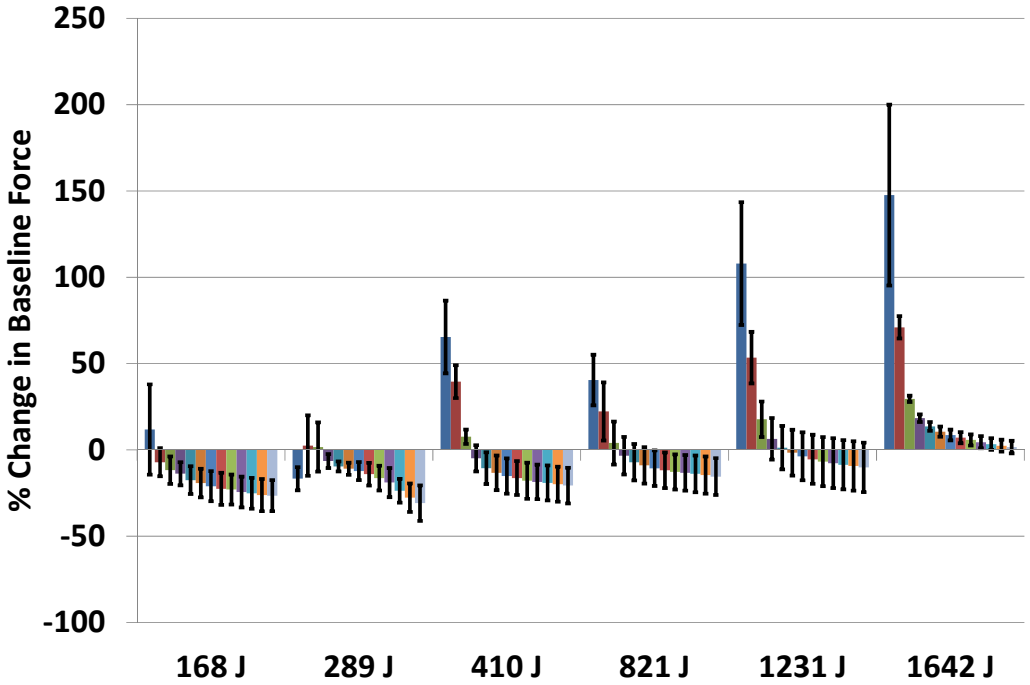

Figure 21: Dose effects of percent change in baseline force of swine diaphragm post microwave ablation (MWA)

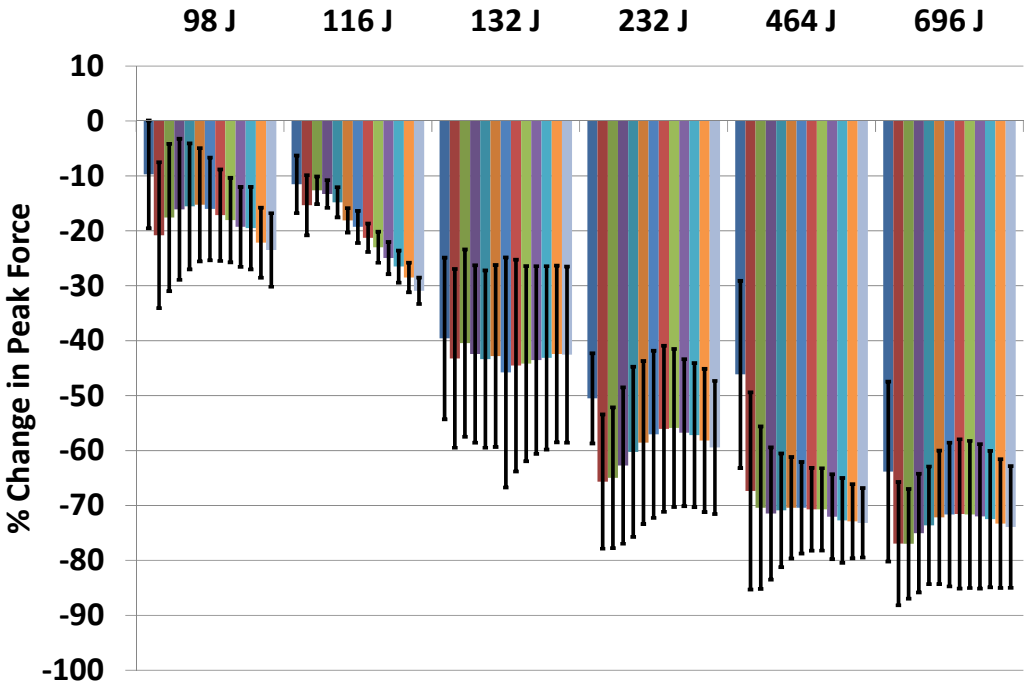

Figure 22: Dose effects of percent change in peak force of swine diaphragm post HIFU (high-intensity focused ultrasound) ablation

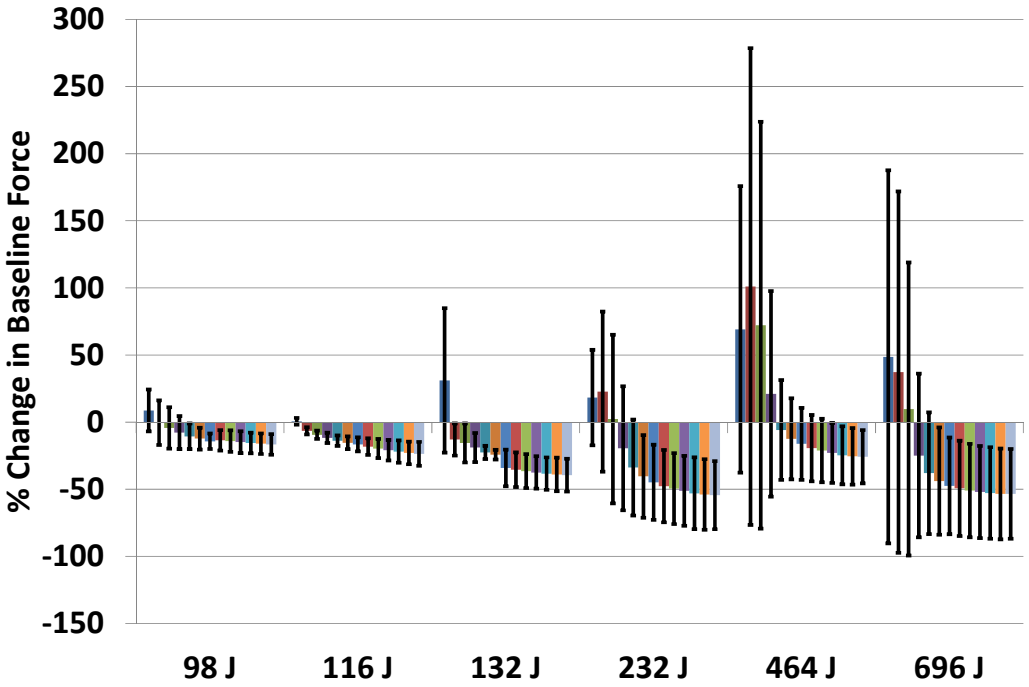

Figure 23: Dose effects of percent change in baseline force of swine diaphragm post HIFU (high-intensity focused ultrasound) ablation

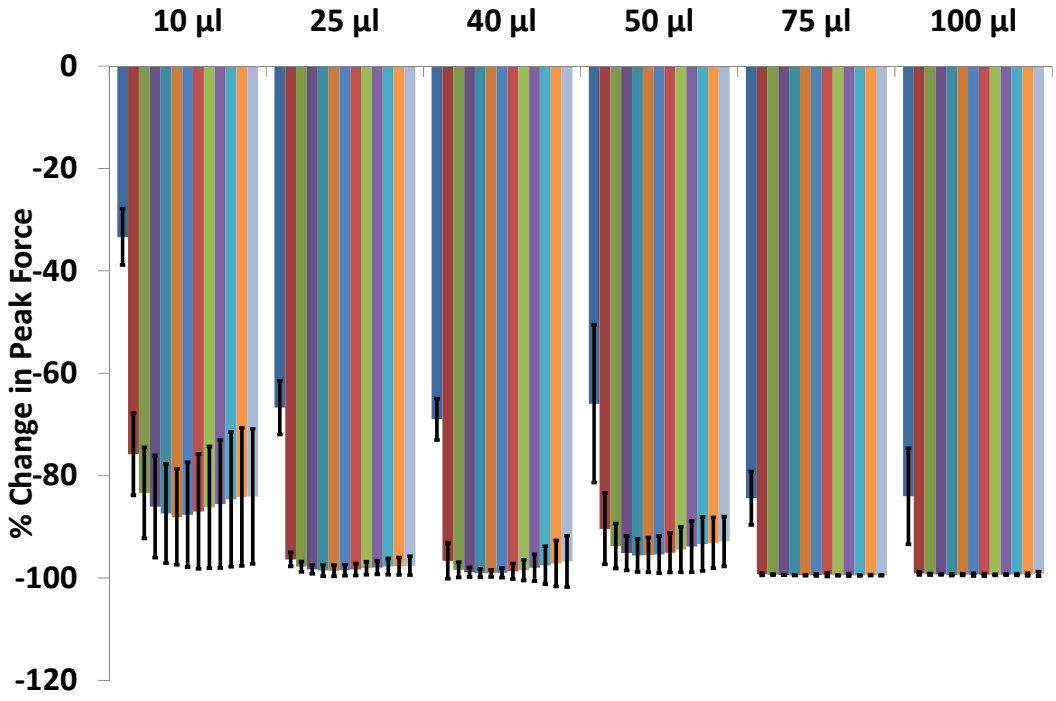

Figure 24: Dose effects of percent change in peak force of swine diaphragm post acetic acid ablation

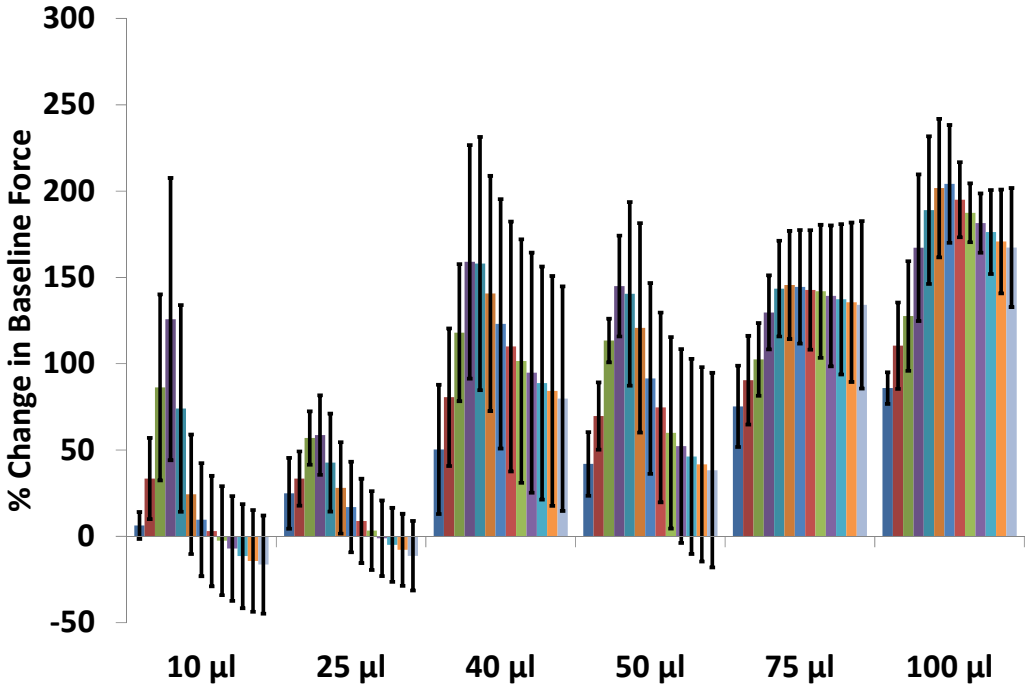

Figure 25: Dose effects of percent change in baseline force of swine diaphragm post acetic acid ablation

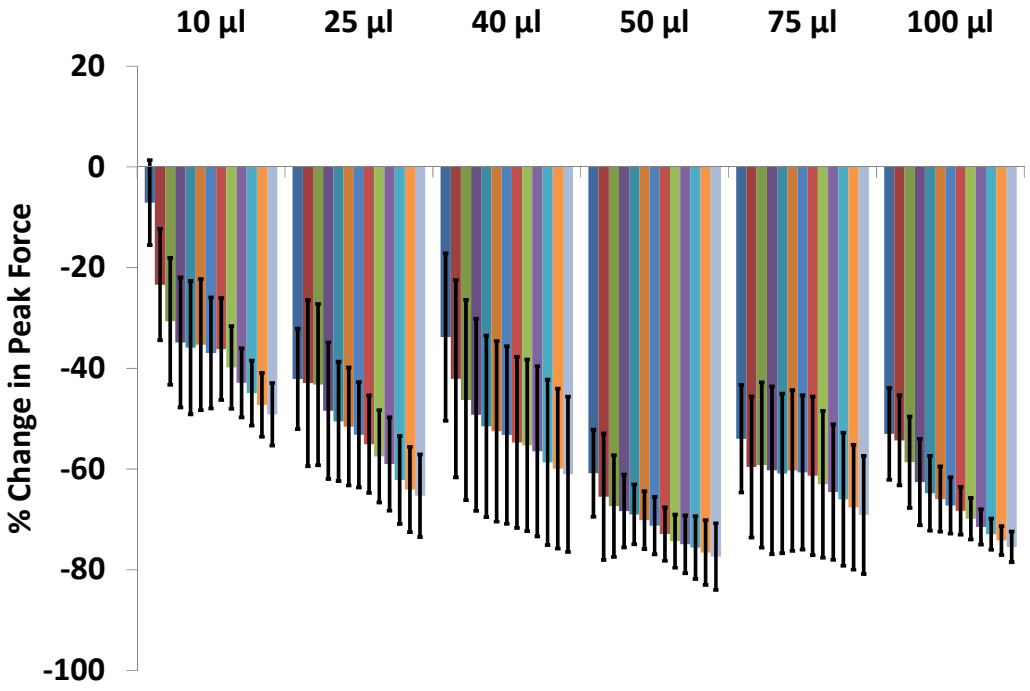

Figure 26: Dose effects of percent change in peak force of swine diaphragm post ethyl alcohol ablation

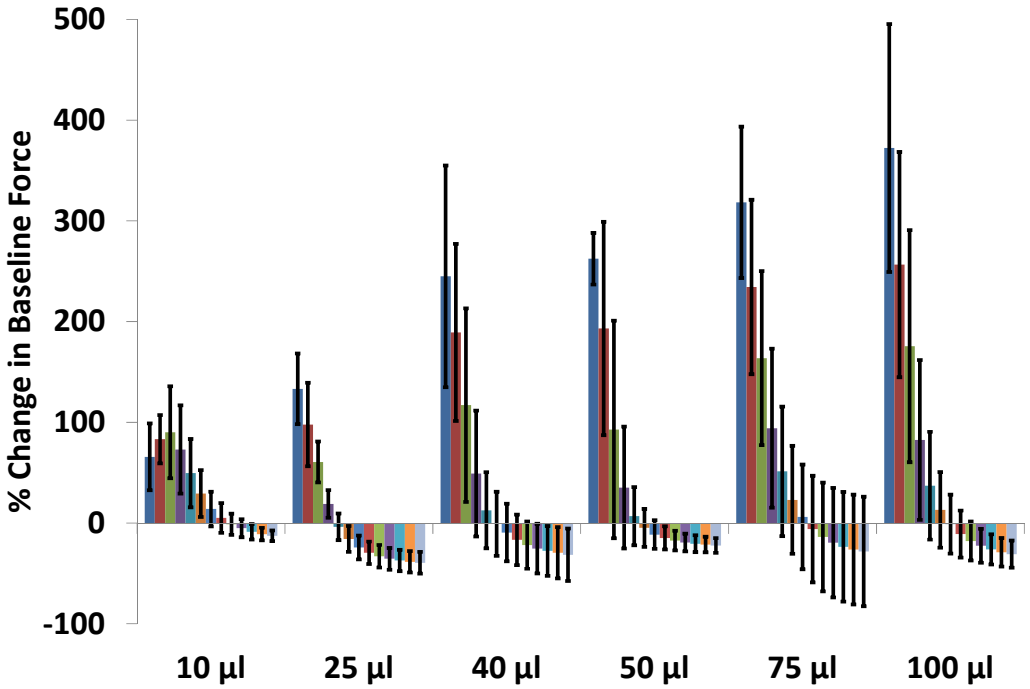

Figure 27: Dose effects of percent change in baseline force of swine diaphragm post ethyl alcohol ablation

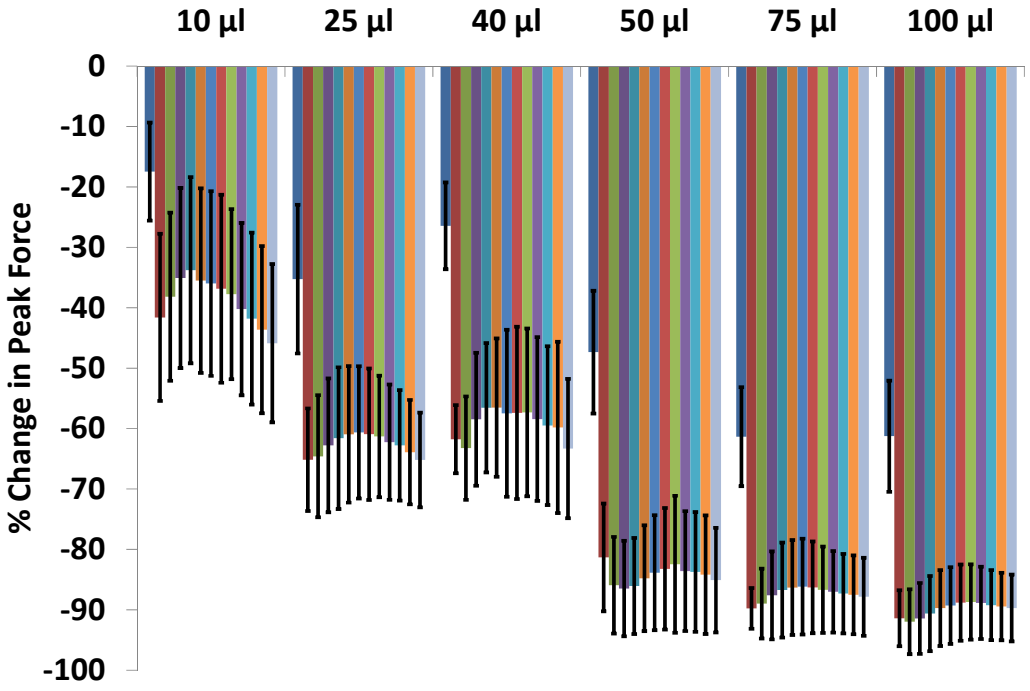

Figure 28: Dose effects of percent change in peak force of swine diaphragm post NaCl ablation

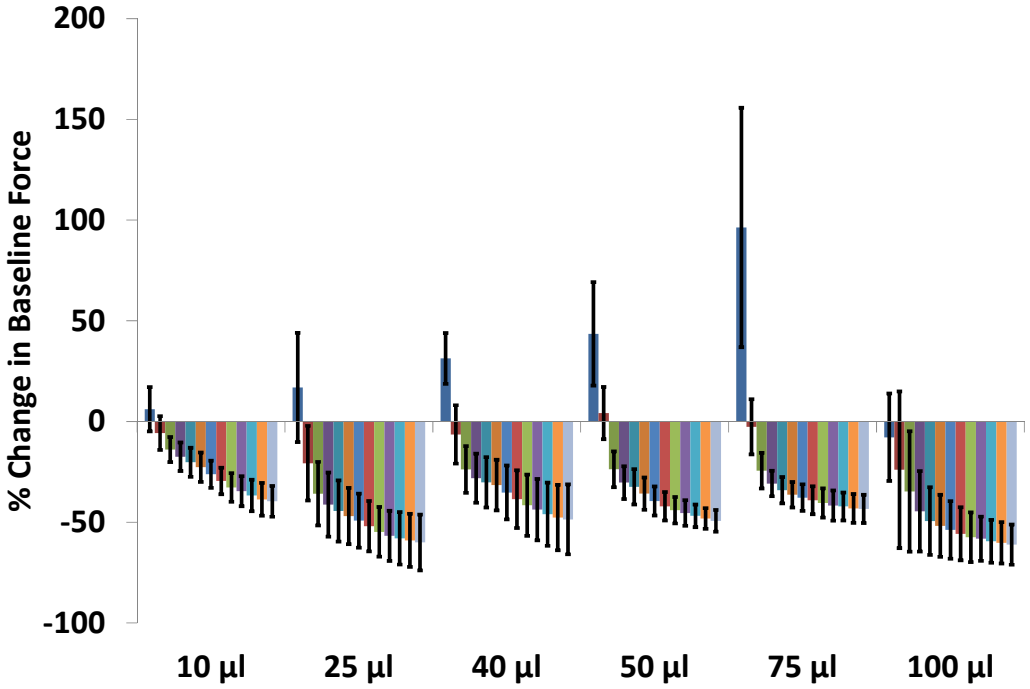

Figure 29: Dose effects of percent change in baseline force of swine diaphragm post NaCl ablation

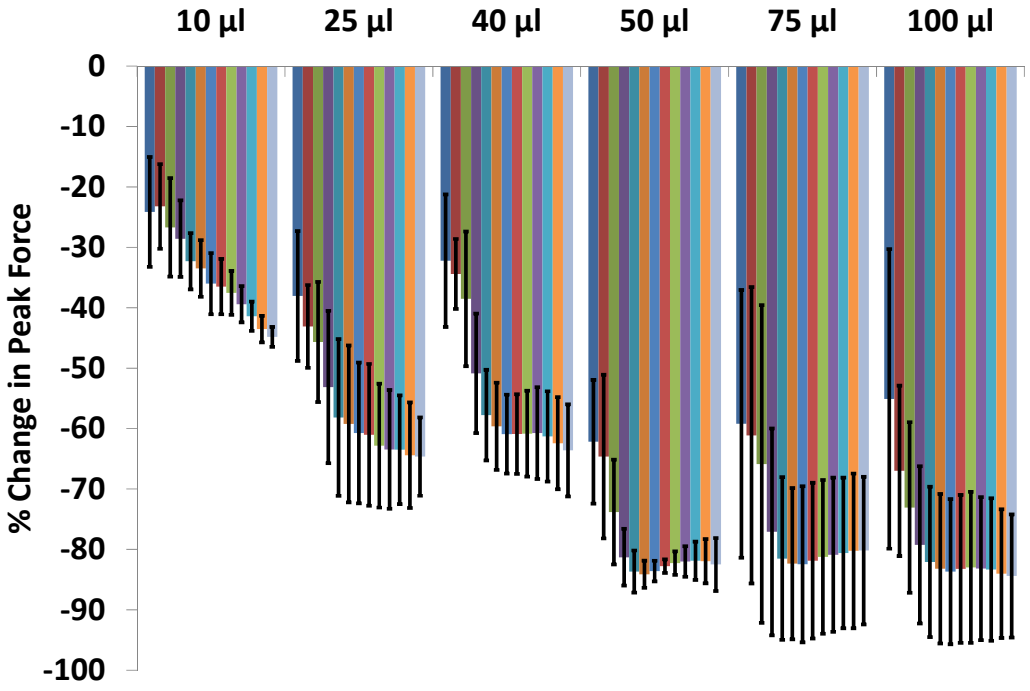

Figure 30: Dose effects of percent change in peak force of swine diaphragm post urea ablation

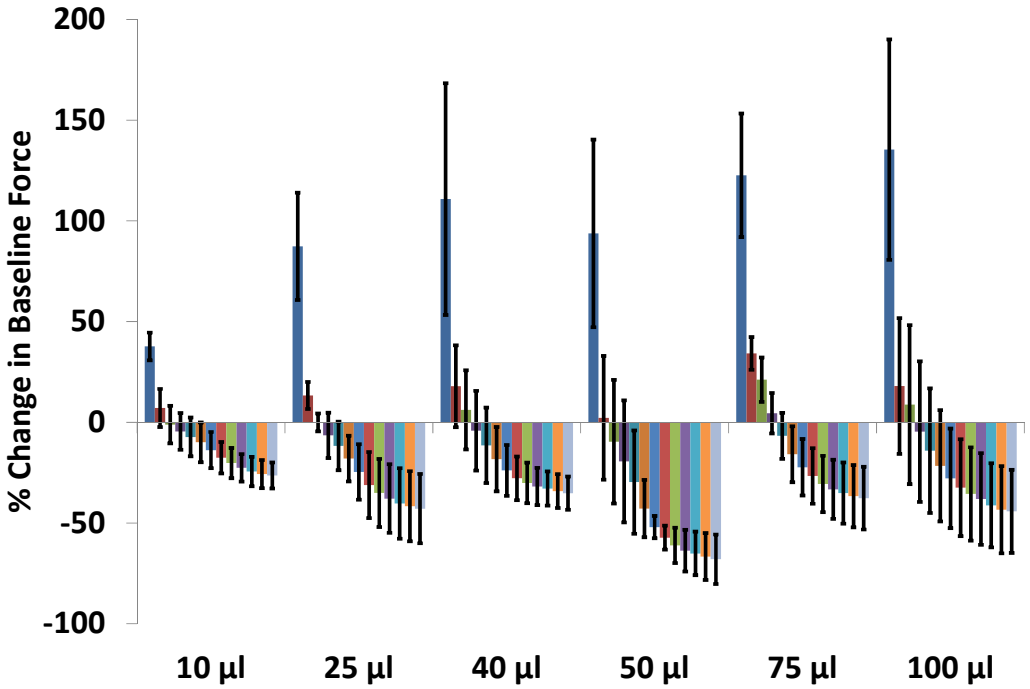

Figure 31: Dose effects of percent change in baseline force of swine diaphragm post urea ablation

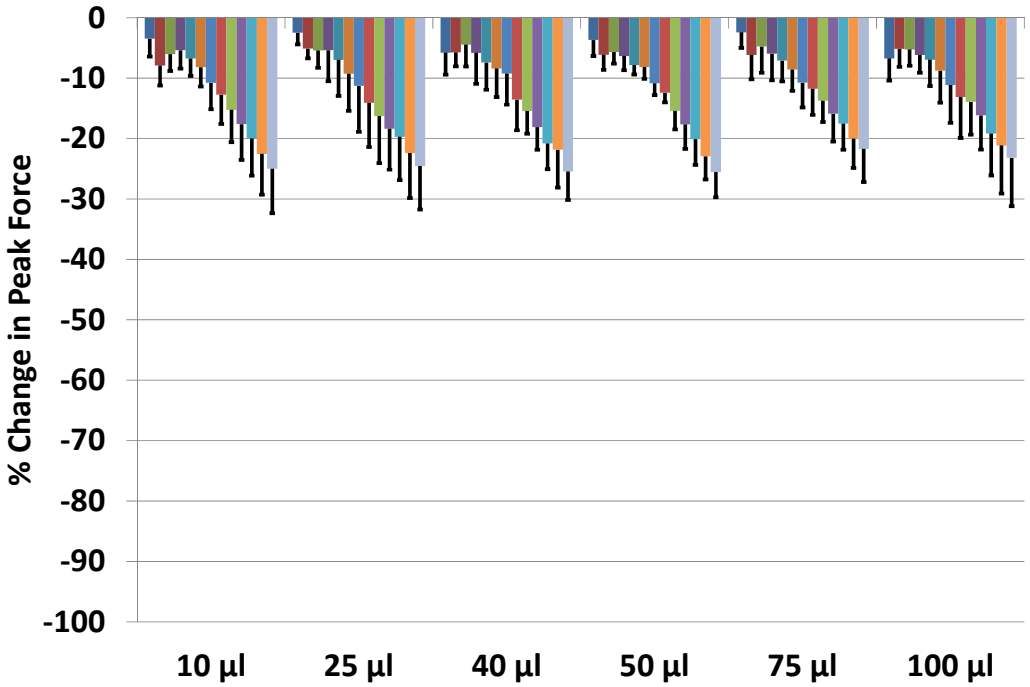

Figure 32: Dose effects of percent change in peak force of swine diaphragm post injection of Krebs-buffer solution

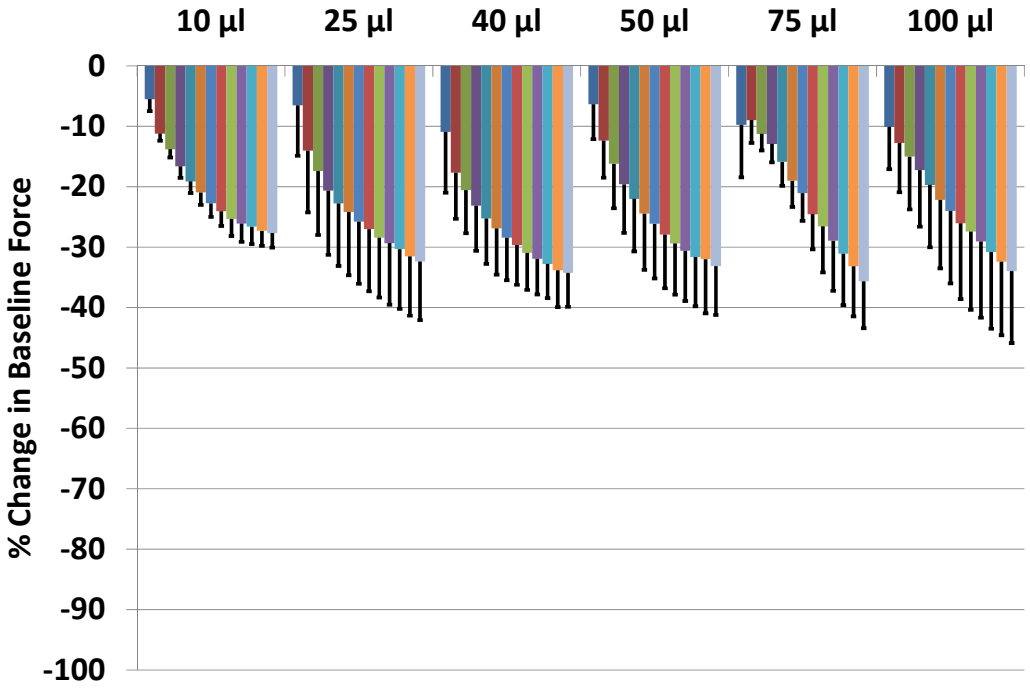

Figure 33: Dose effects of percent change in baseline force of swine diaphragm post injection of Krebs-buffer solution

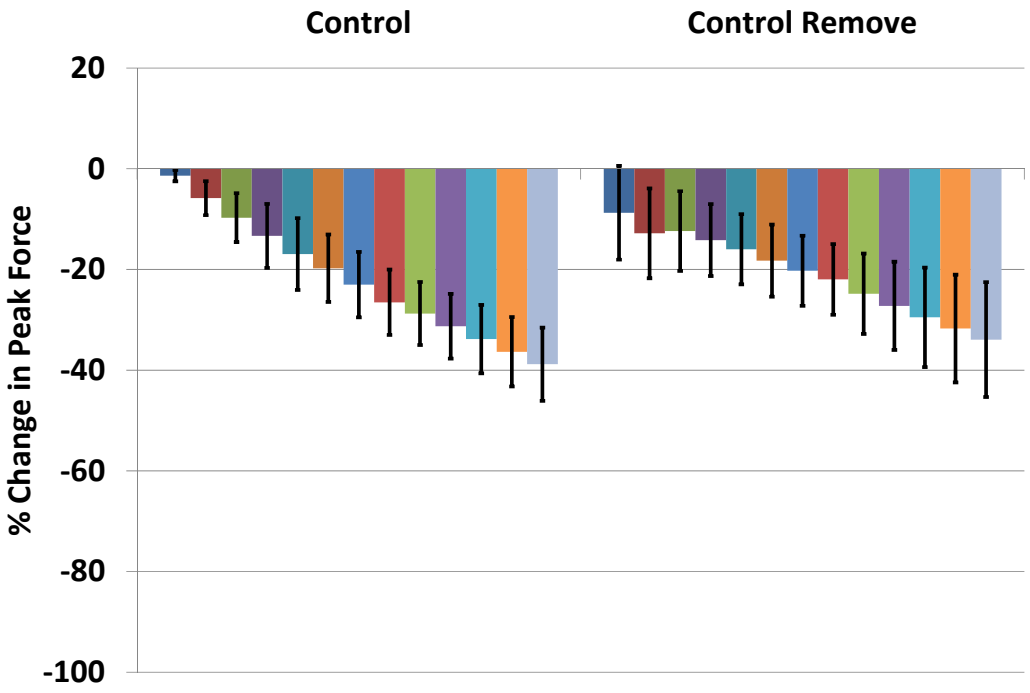

Figure 34: Percent change in peak force of control and control-remove swine diaphragm muscle bundles

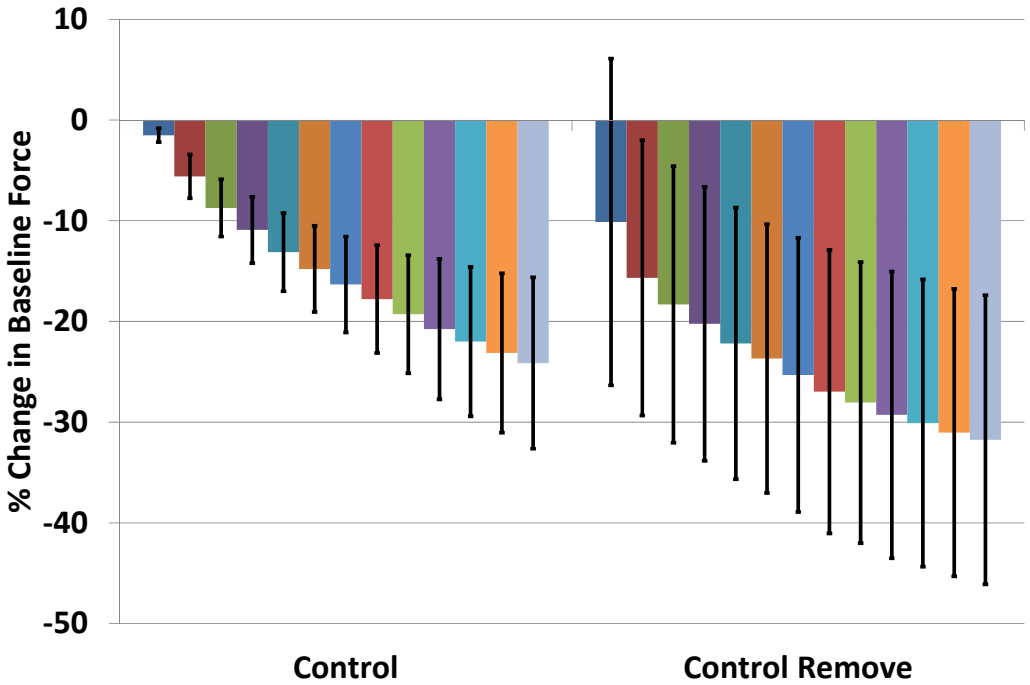

Figure 35: Percent change in baseline force of control and control-remove swine diaphragm muscle bundles

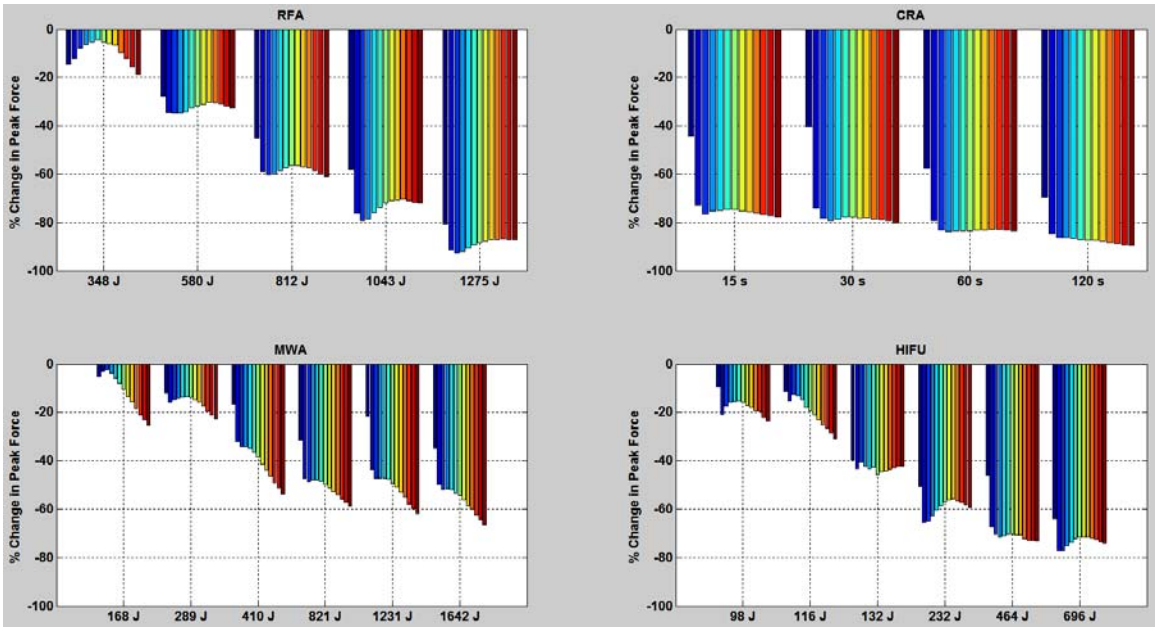

Figure 36: Dose effects on peak force of swine diaphragm for all thermal ablative modalities

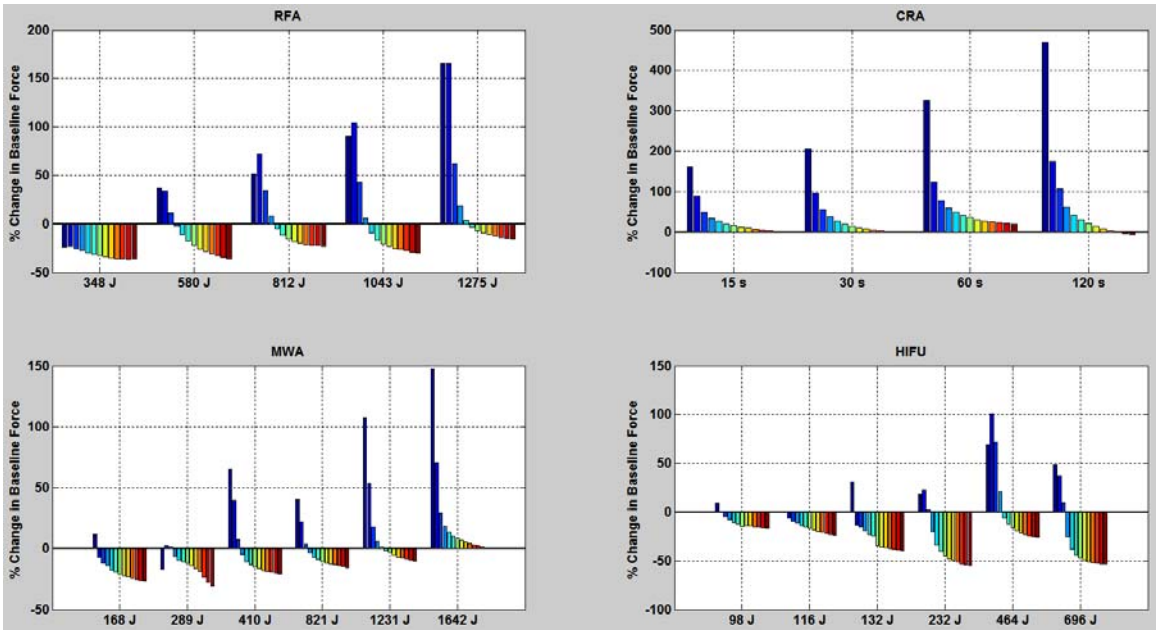

Figure 37: Dose effects on baseline force of swine diaphragm for all thermal ablative modalities

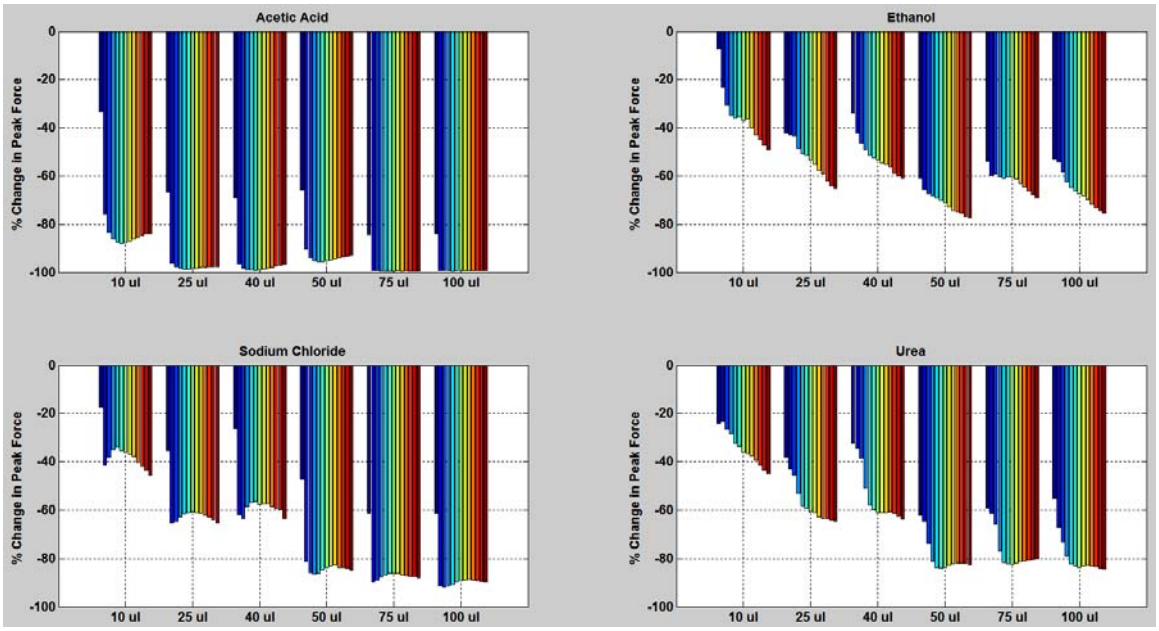

Figure 38: Dose effects on peak force of swine diaphragm for all chemical ablative modalities

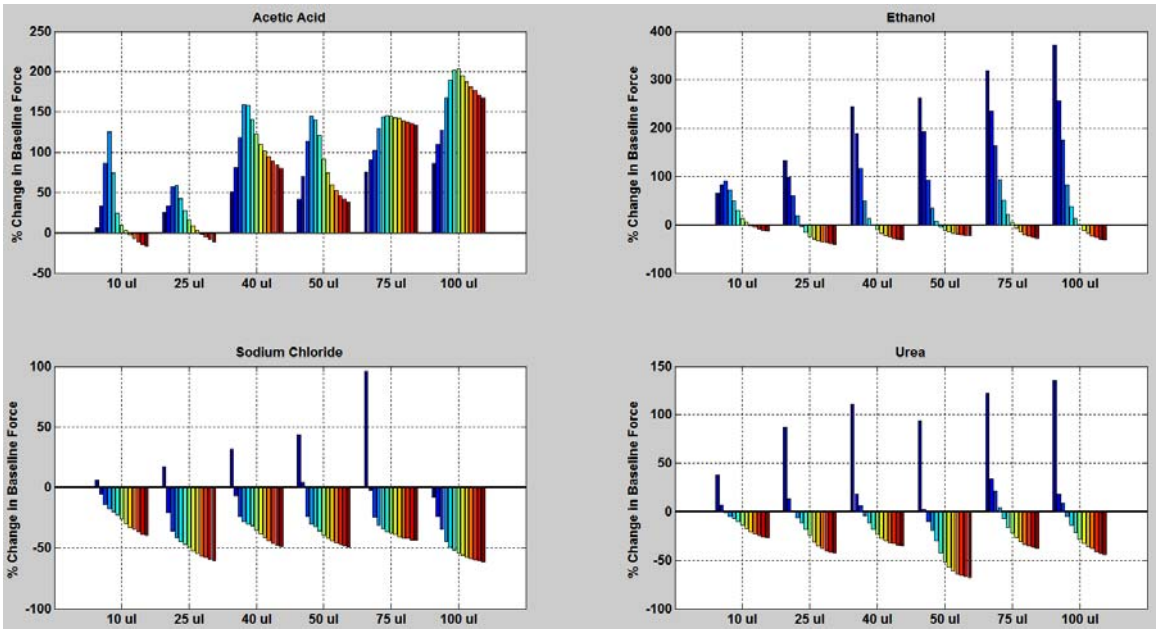

Figure 39: Dose effects on baseline force of swine diaphragm for all chemical ablative modalities

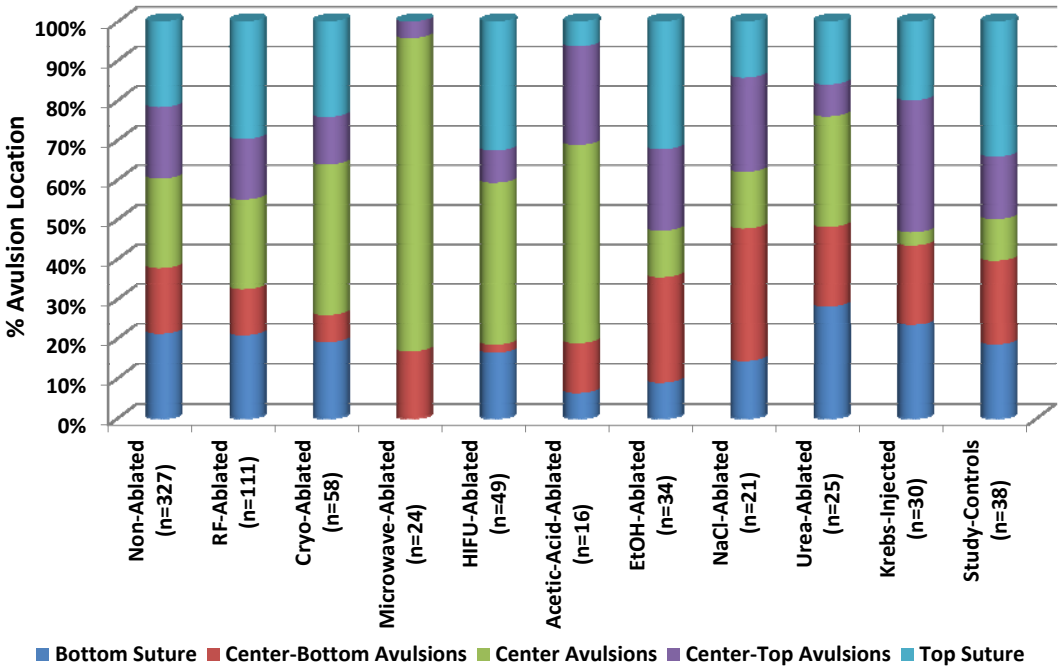

Figure 40: Avulsion location for each treatment displayed as percentage for all muscle bundles tested in this investigation

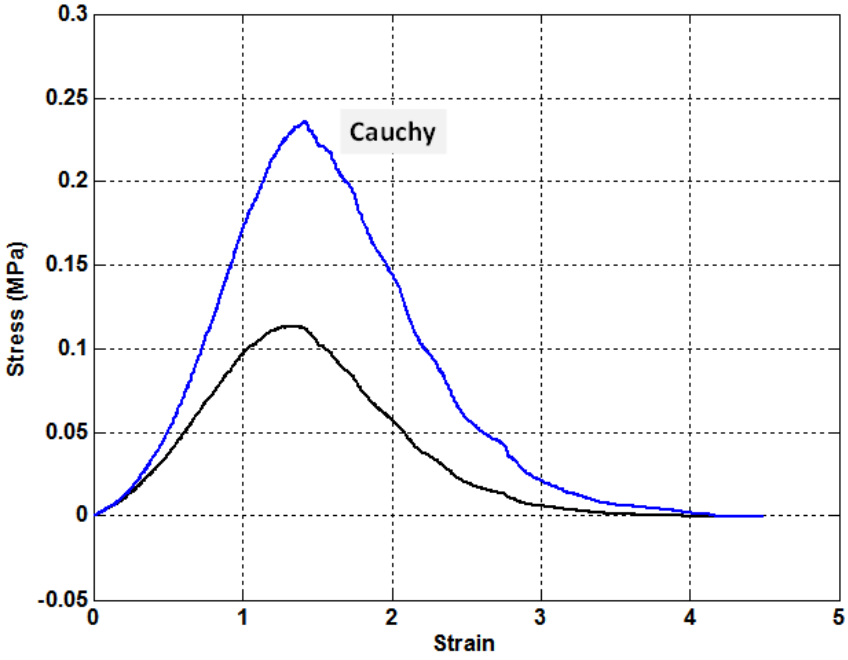

Figure 41: Average model of stress-strain characteristics of non-ablated "control" swine diaphragm muscle bundles (n=187)

The maximum stress was 0.11 MPa and maximum Cauchy-stress was 0.24 MPa. The avulsion strain was 1.35.

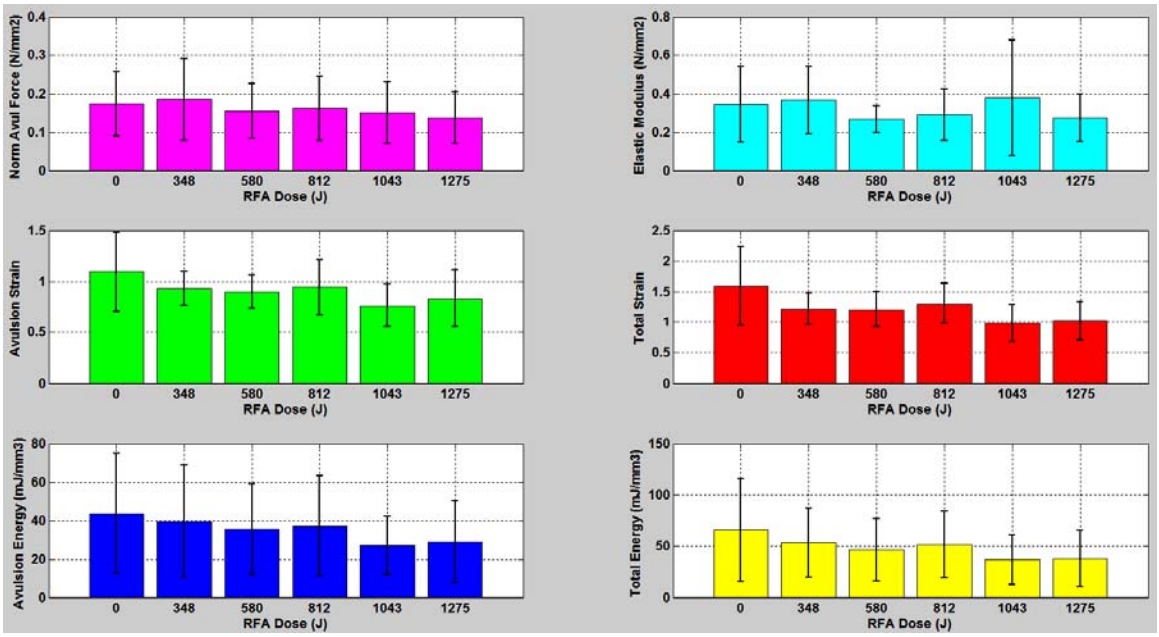

Figure 42: Dose effects of radiofrequency ablation (RFA) on biomechanical properties of swine diaphragm muscle bundles

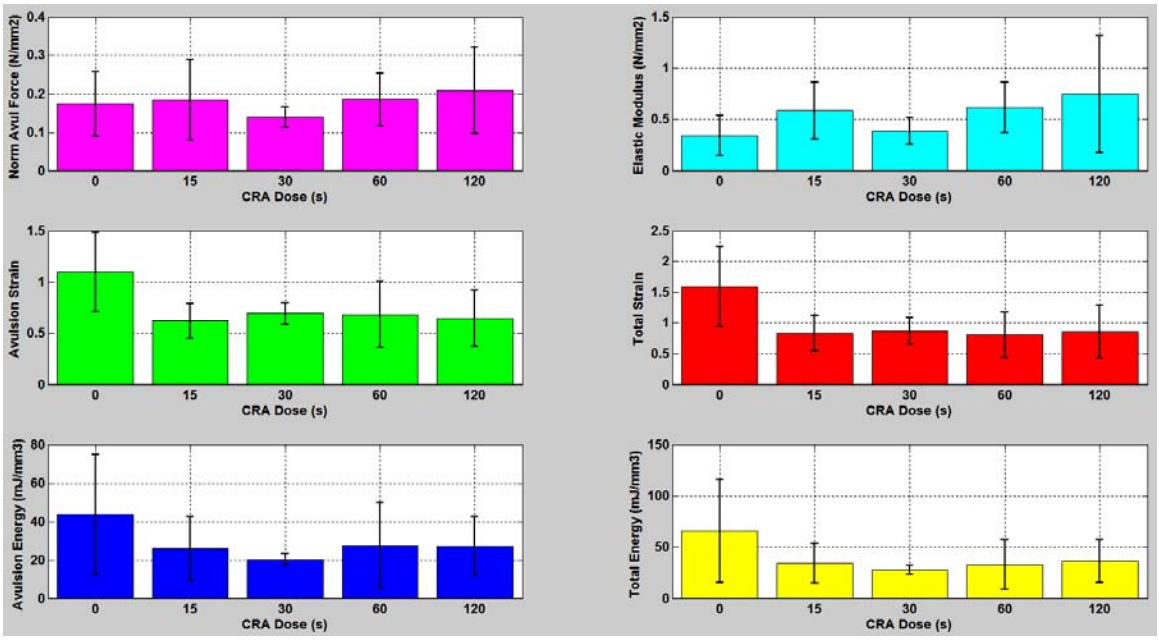

Figure 43: Dose effects of cryoablation (CRA) on biomechanical properties of swine diaphragm muscle bundles

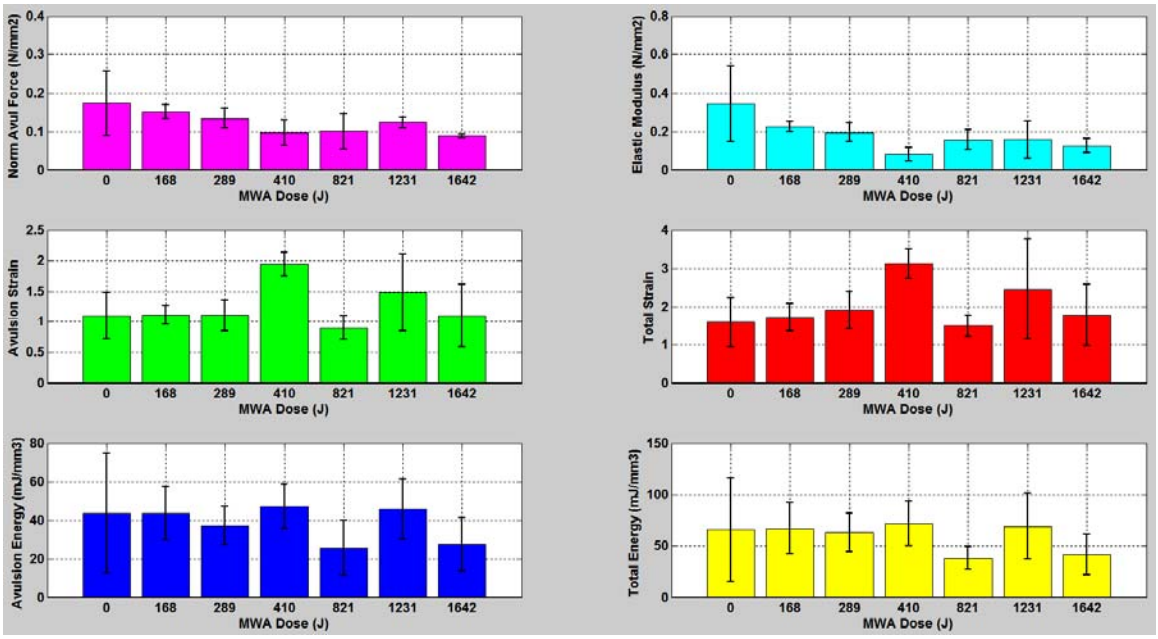

Figure 44: Dose effects of microwave ablation (MWA) on biomechanical properties of swine diaphragm muscle bundles

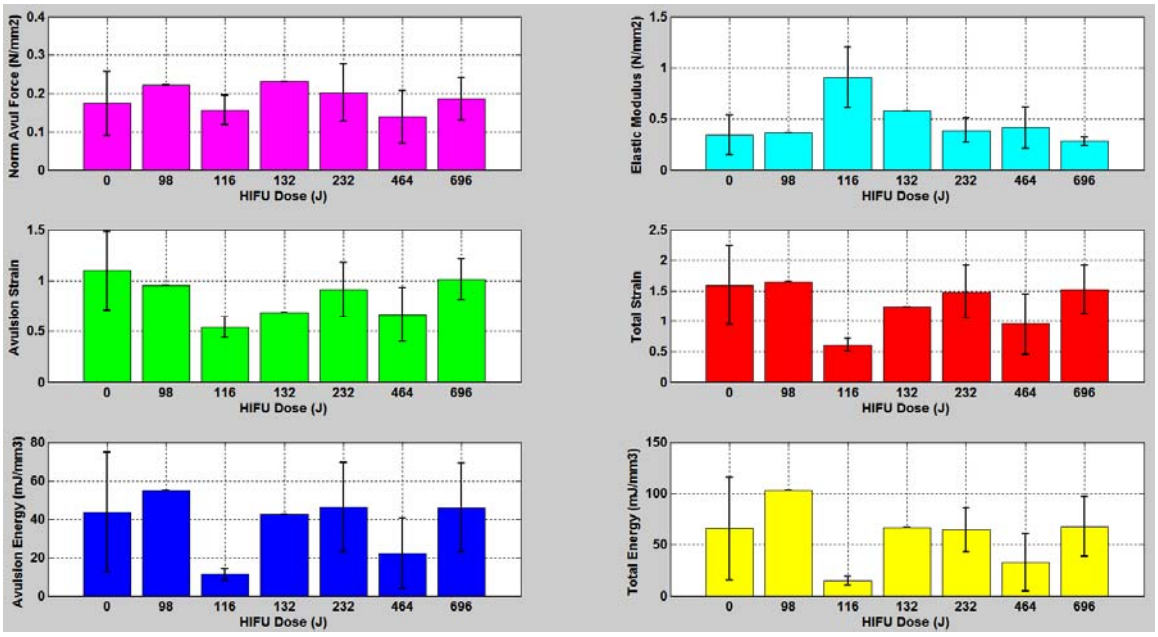

Figure 45: Dose effects of high-intensity focused ultrasound (HIFU) ablations on biomechanical properties of swine diaphragm muscle bundles

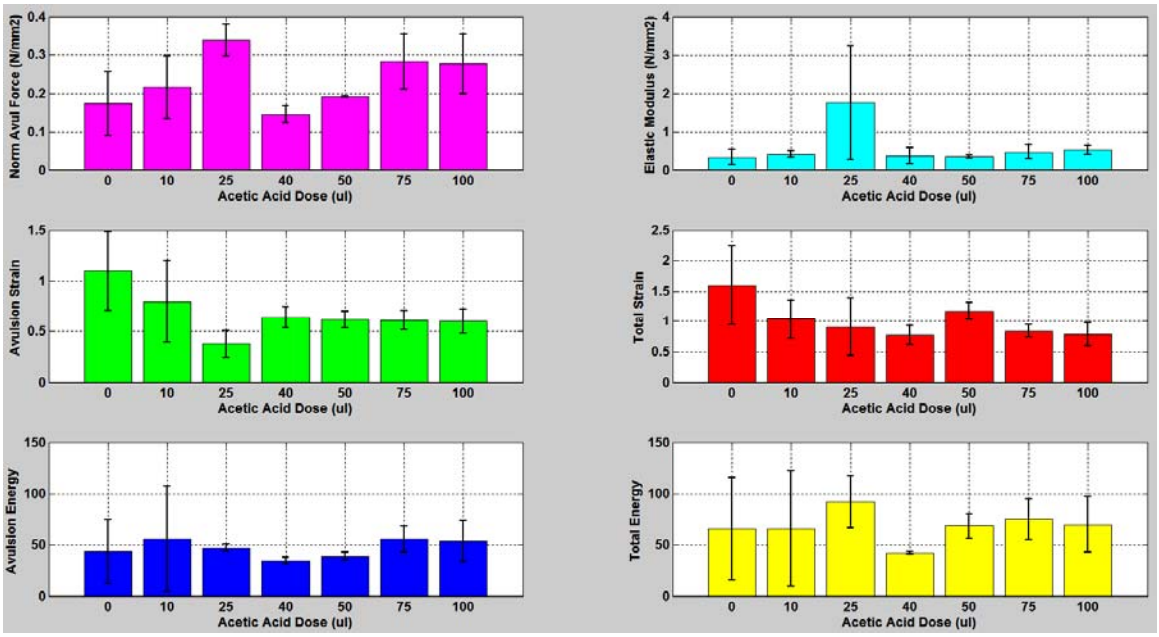

Figure 46: Dose effects of chemical ablation with acetic-acid on biomechanical properties of swine diaphragm muscle bundles

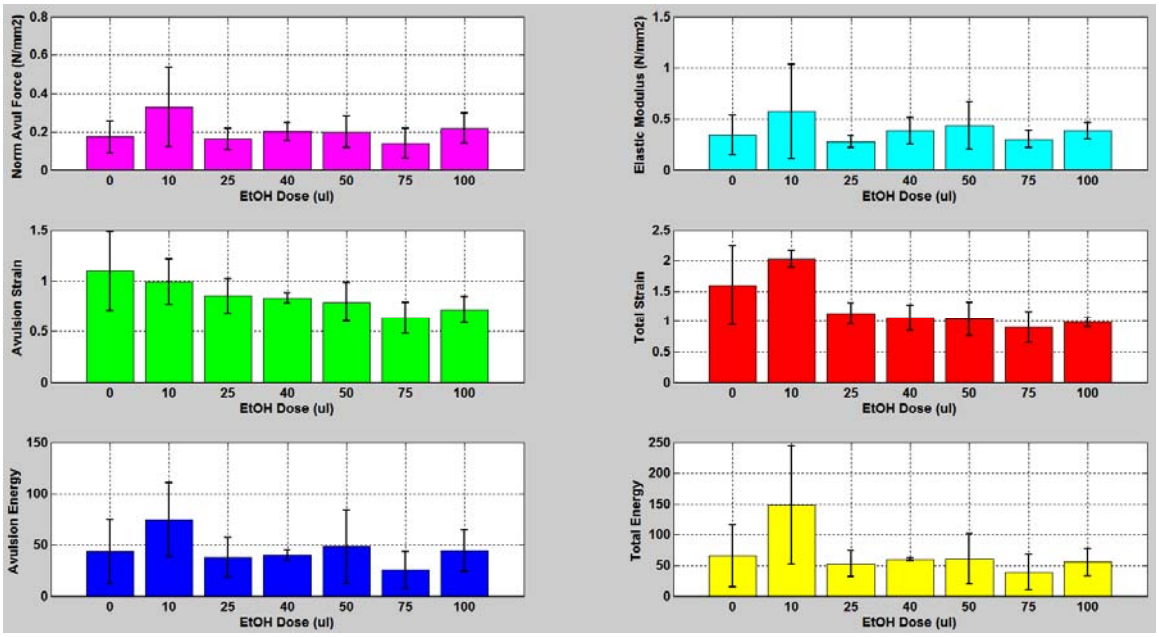

Figure 47: Dose effects of chemical ablation with ethanol on biomechanical properties of swine diaphragm muscle bundles

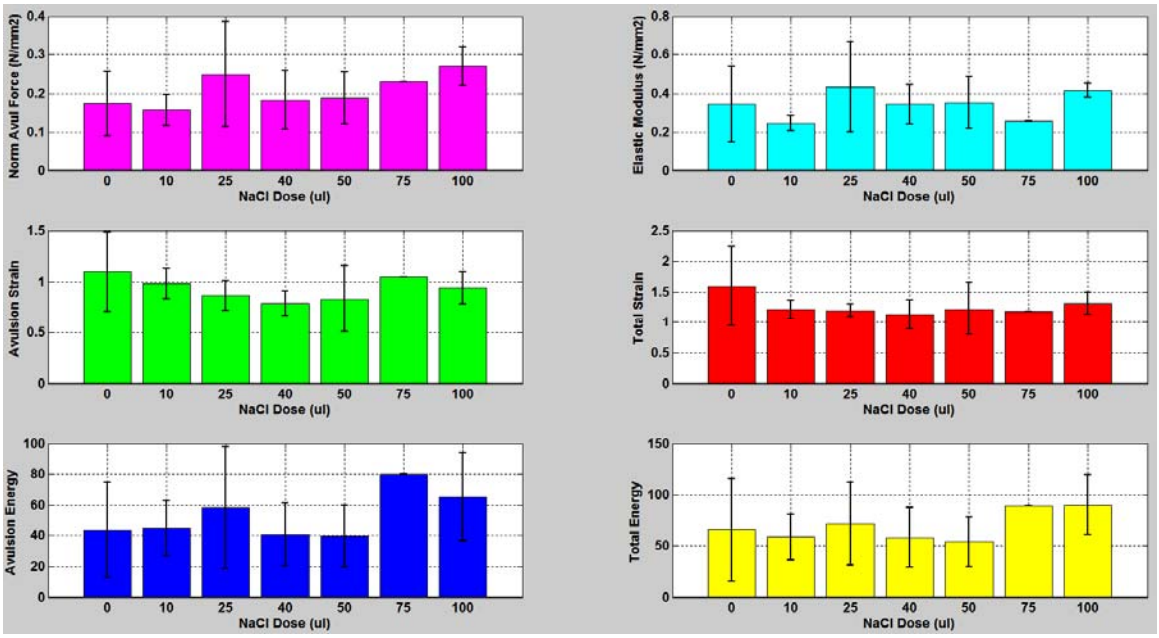

Figure 48: Dose effects of chemical ablation with hypertonic sodium chloride on biomechanical properties of swine diaphragm muscle bundles

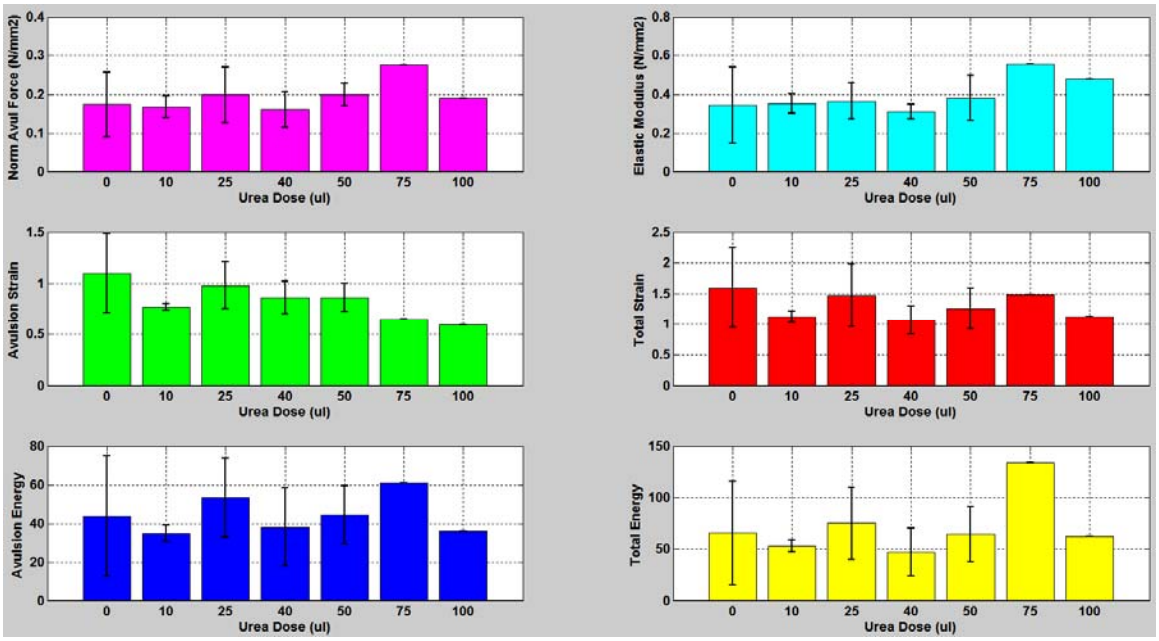

Figure 49: Dose effects of chemical ablation with urea on biomechanical properties of swine diaphragm muscle bundles

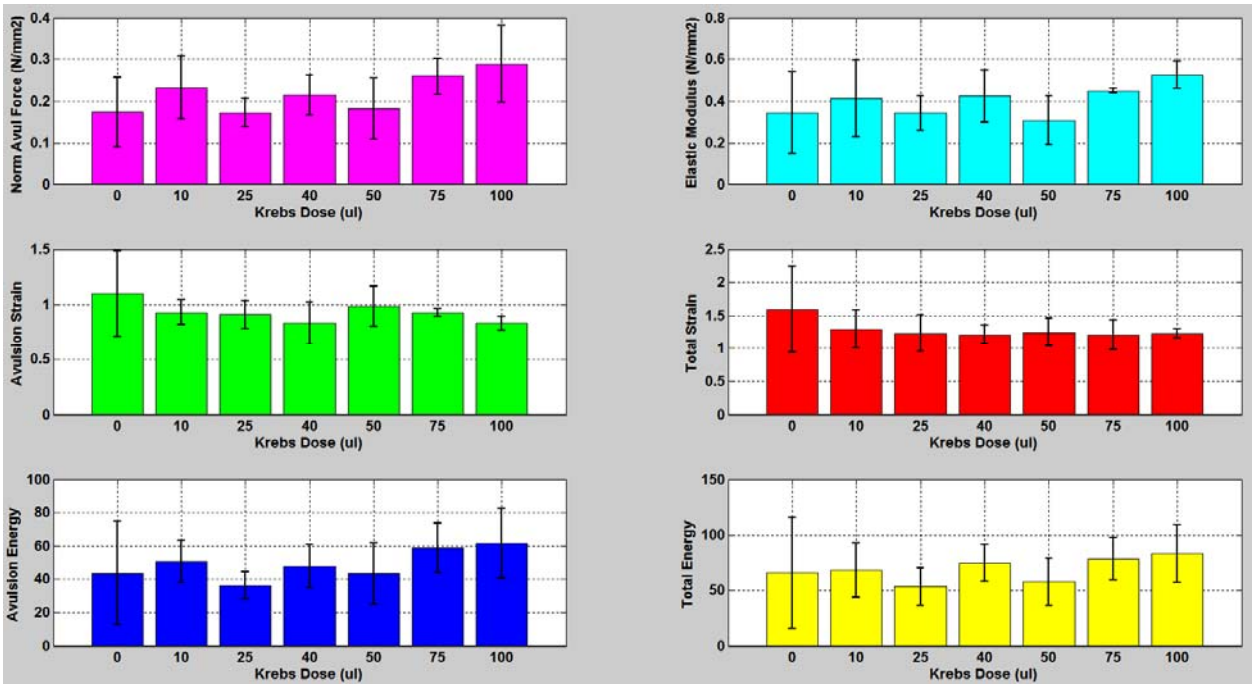

Figure 50: Dose effects of Krebs injections on biomechanical properties of swine diaphragm muscle bundles

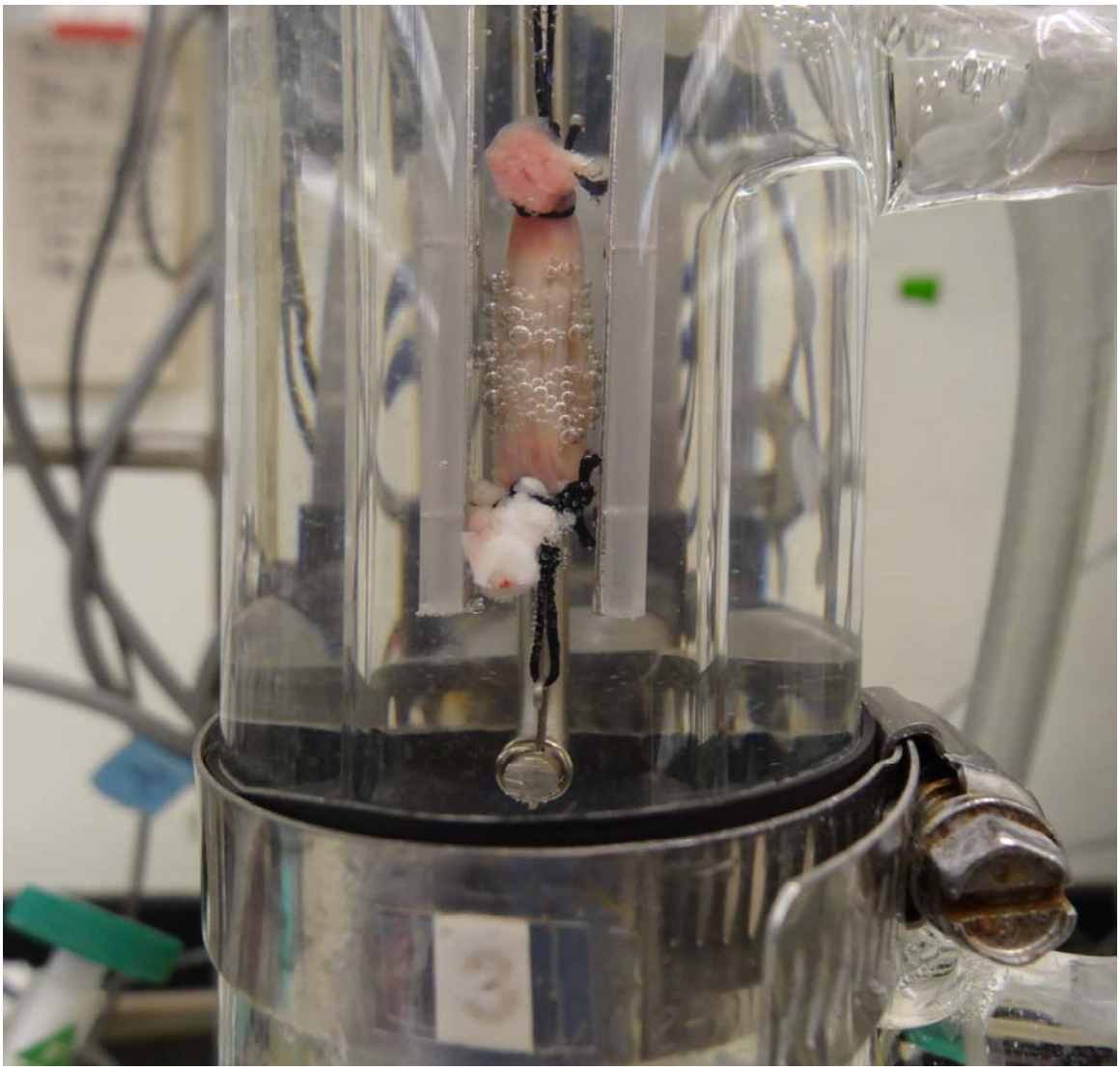

Figure 51: A swine diaphragm muscle ablated with 50 µl of acetic acid
Microbubbles on the ablated region of the muscle bundle are caused by excessive dehydration, which further leads to tissue necrosis.

Ablation Modality	# of Doses	# of Muscle Bundles	Length (mm)	Diameter (mm)	Mass (mg)	Pre-Ablation Peak Force (grams)	Pre-Ablation Baseline Force (grams)
RFA	5	20	23.17 ± 3.10	3.42 ± 0.55	277.00 ± 48.46	2.95 ± 1.21	2.08 ± 0.29
CRA	4	16	36.28 ± 5.71	3.26 ± 0.70	332.50 ± 137.86	3.37 ± 1.37	2.19 ± 0.47
MWA	6	24	36.61 ± 4.93	2.81 ± 0.37	235.83 ± 52.91	5.76 ± 2.15	2.47 ± 0.17
HIFU	6	24	27.25 ± 8.09	3.13 ± 0.52	264.00 ± 68.84	4.27 ± 2.64	2.22 ± 0.76
Acetic Acid	6	24	27.93 ± 4.56	2.93 ± 0.46	242.71 ± 55.48	4.37 ± 1.20	2.26 ± 0.24
EtOH	6	24	26.75 ± 5.46	2.92 ± 0.51	260.46 ± 85.78	4.11 ± 1.97	2.04 ± 0.23
NaCl	6	24	26.58 ± 3.68	2.94 ± 0.42	283.75 ± 60.14	4.03 ± 1.59	2.20 ± 0.19
Urea	6	24	26.91 ± 6.41	2.85 ± 0.59	296.21 ± 129.89	3.45 ± 1.63	2.15 ± 0.19
Krebs	6	24	31.21 ± 4.04	3.12 ± 0.43	302.75 ± 50.48	4.67 ± 1.49	2.63 ± 0.19
Study Controls	N/A	8	39.08 ± 3.71	3.21 ± 0.47	451.25 ± 105.35	3.24 ± 1.16	1.89 ± 0.30

Table 3: Mean ± SD characteristics of swine diaphragm muscle bundles that underwent physiological testing in tissue baths (n=212)
A set of 4 muscle bundles were exposed to every ablation dose

Avulsion Location (%)	% Bottom Suture Breakage	% Center-Bottom Avulsions	% Center Avulsions	% Center-Top Avulsions	% Top Suture Breakage
Non-Ablated (Biomechanical) (n=327)	21.10% (n=69)	16.51% (n=54)	22.64% (n=74)	18.04% (n=59)	21.71% (n=71)
RFA (n=111)	20.72% (n=23)	11.71% (n=13)	22.52% (n=25)	15.32% (n=17)	29.73% (n=33)
CRA (n=58)	18.96% (n=11)	6.90% (n=4)	37.93% (n=22)	12.07% (n=7)	24.14% (n=14)
MWA (n=24)	0.00% (n=0)	16.67% (n=4)	79.17% (n=19)	4.16% (n=1)	0.00% (n=0)
HIFU (n=49)	16.33% (n=8)	2.04% (n=1)	40.82% (n=20)	8.16% (n=4)	32.65% (n=16)
Acetic-Acid (n=16)	6.25% (n=1)	12.50% (n=2)	50.00% (n=8)	25.00% (n=4)	6.25% (n=1)
EtOH (n=34)	8.83% (n=3)	26.47% (n=9)	11.76% (n=4)	20.59% (n=7)	32.35% (n=11)
NaCl (n=21)	14.29% (n=3)	33.33% (n=7)	14.29% (n=3)	23.81% (n=5)	14.28% (n=3)
Urea (n=25)	28.00% (n=7)	20.00% (n=5)	28.00% (n=7)	8.00% (n=2)	16.00% (n=4)
Krebs Injected (n=30)	23.34% (n=7)	20.00% (n=6)	3.33% (n=1)	33.33% (n=10)	20.00% (n=6)
Study Controls (n=38)	18.42% (n=7)	21.05% (n=8)	10.53% (n=4)	15.79% (n=6)	34.21% (n=13)

Table 4: Tabulation of the avulsion location of swine diaphragm muscle bundles (n=733) as a percentage for each ablative modality

	Initial Cross-sectional Area (mm^2)	Initial Volume (mm^3)	Avulsion Force (N/mm^2)	Elastic Modulus (N/mm^2)	Avulsion Strain ($\Delta l/L$)	Total Strain ($\Delta l/L$)	Avulsion Energy (mJ/mm^3)	Total Energy (mJ/mm^3)
Biomech (n=187)	8.85±3.07	170.21±60.31	0.19±0.08	0.36±0.17	1.14±0.41	1.74±0.71	48.12±32.84	74.72±55.96
RFA (n=55)	8.90±2.56	195.12±68.71	0.18±0.07	0.34±0.19	0.96±0.26	1.37±0.39	42.00±18.94	58.89±27.44
CRA (n=33)	7.48±3.13	216.35±81.23	0.20±0.09	0.68±0.47	0.68±0.27	0.89±0.38	27.42±15.87	36.02±17.55
MWA (n=24)	10.57±3.66	201.59±48.88	0.12±0.03	0.16±0.07	1.27±0.48	2.08±0.84	37.82±14.64	58.58±24.09
HIFU (n=25)	7.62±2.47	212.28±123.97	0.19±0.08	0.44±0.24	0.86±0.25	1.37±0.46	39.18±23.31	59.10±30.45
Acetic Acid (n=14)	7.31±1.86	190.89±43.36	0.24±0.08	0.47±0.15	0.62±0.16	0.92±0.23	49.08±20.13	69.85±27.61
EtOH (n=20)	7.39±2.60	182.70±65.82	0.21±0.09	0.41±0.18	0.75±0.22	1.10±0.40	45.95±26.99	66.05±45.13
NaCl (n=15)	9.36±2.36	241.07±89.45	0.22±0.08	0.39±0.14	0.88±0.23	1.24±0.31	52.98±25.50	70.91±32.19
Urea (n=14)	6.86±1.94	149.27±47.19	0.20±0.05	0.40±0.12	0.85±0.20	1.36±0.36	49.63±15.25	73.36±29.51
Krebs Injected (n=17)	8.08±1.83	202.42±57.14	0.22±0.07	0.41±0.14	0.89±0.16	1.25±0.21	48.25±14.16	68.20±18.92
Study Controls (n=18)	7.74±3.86	249.13±138.73	0.22±0.10	0.69±0.47	0.77±0.38	1.05±0.58	36.85±25.60	51.05±38.43

Table 5: Mean ± SD dimensional characteristics and biomechanical parameters of swine diaphragm muscle bundles that avulsed at or near the center of the muscle bundle

	% Diff Avulsion Force	% Diff Elastic Modulus	% Diff Avulsion Strain	% Diff Total Strain	% Diff Avulsion Energy	% Diff Total Energy
RFA (n=55)	-2.31 p=0.8058	-8.43 p=0.5237	**-15.03 p=0.0024**	**-20.91 p<0.05**	-12.25 p=0.1884	**-20.78 p=0.0440**
CRA (n=33)	+6.29 p=0.4539	**+90.00 p<0.05**	**-40.18 p<0.05**	**-48.74 p<0.05**	**-43.02 p<0.05**	**-51.80 p<0.05**
MWA (n=24)	**-37.85 p<0.05**	**-57.74 p<0.05**	+11.75 p=0.1412	**+19.36 p=0.0339**	-21.41 p=0.1313	-21.59 p=0.1650
HIFU (n=25)	+2.05 p=0.8259	+24.79 p=0.0196	**-24.80 p<0.05**	**-21.34 p=0.0120**	-18.58 p=0.1895	-20.91 p=0.1732
Acetic Acid (n=14)	**+30.88 p=0.0123**	+32.38 p=0.0126	**-45.39 p<0.05**	**-47.00 p<0.05**	+2.00 p=0.9143	-6.52 p=0.7478
EtOH (n=20)	+13.17 p=0.2099	+16.48 p=0.1388	**-33.81 p<0.05**	**-37.06 p<0.05**	-4.51 p=0.7758	-11.60 p=0.5040
NaCl (n=15)	+16.73 p=0.1597	+8.74 p=0.4808	**-22.50 p=0.0177**	**-29.05 p=0.0071**	+10.09 p=0.5771	-5.10 p=0.7952
Urea (n=14)	+7.45 p=0.5360	+13.22 p=0.2995	**-25.84 p=0.0084**	**-22.20 p=0.0462**	+3.12 p=0.8655	-1.81 p=0.9289
Krebs Injected (n=17)	+18.18 p=0.1014	+16.23 p=0.1666	**-22.02 p=0.0130**	**-28.01 p=0.0055**	+0.26 p=0.9875	-8.16 p=0.6563
Study Controls (n=18)	+19.23 p=0.0857	**+93.41 p<0.05**	**-32.32 p<0.05**	**-39.78 p<0.05**	-23.43 p=0.1588	-31.68 p=0.0811

Table 6: Percent change in biomechanical properties of swine diaphragm muscle bundles post ablation with different ablative modalities

All values are with respect to controls (n=187, non-ablated) muscle bundles. A positive value indicates an increase and a negative value a decrease with respect to controls. Percent change in avulsion force, elastic modulus, strain, and energy are shown along with individual statistical significance ($p<0.05$, marked in bold).

4. The Assessment of Physiological and Biomechanical Properties of Isolated Swine Esophagus in Response to Clinically Applied Ablative Therapies

Preface

We plan to submit this paper to the Journal of Cardiothoracic Surgery (2014).

Ashish Singal
University of Minnesota
420 Delaware St. SE, B172 Mayo Building, MMC 195
Minneapolis, MN 55455
singa009@umn.edu

Charles L. Soule
University of Minnesota
420 Delaware St. SE, B172 Mayo Building, MMC 195
Minneapolis, MN 55455
soule005@umn.edu

Paul A. Iaizzo
University of Minnesota
420 Delaware St. SE, B172 Mayo, MMC 195
Minneapolis, MN 55455
iaizz001@umn.edu

Executive Summary

Atrial fibrillation is one of the most common sustained cardiac arrhythmia, whose prevalence is increasing with age and incidence with time. Catheter ablation is a common medical procedure performed worldwide for the treatment of atrial fibrillation. Although believed to be a generally safe procedure, in small percentage of cases, it can cause collateral injury to the surrounding structures including the esophagus, which can have important clinical implications. Such collateral injury of the esophagus may result in altered structural and/or physiological changes that are dependent on both the level of ablative energy applied and the extent of tissue injury produced. Thus, it is important to understand the physiological and biomechanical properties of the esophagus that may be potentially affected by various modes of ablative therapies. Such knowledge may not only help maximize the efficacy of ablative procedures, but also aid in minimizing procedural complications. In this investigation, we have characterized specific physiological and biomechanical properties of the esophageal muscle bundles when exposed to five different therapeutic ablation modalities (radiofrequency ablation, cryoablation, high-intensity focused ultrasound ablation, microwave ablation, and chemical ablation using acetic acid, ethanol, hypertonic sodium chloride, and urea). The physiological properties were assessed by performing in-vitro tissue bath studies to measure changes in peak forces (strength of contractions) as well as baseline forces (resting muscle tension) in response to ablation. The biomechanical properties were assessed

by performing uniaxial stress tests to measure the force-displacement responses, stress-strain characteristics, and calculations of avulsion forces and elastic moduli in response to ablative therapies. In general, we observed dose-dependent sustained reduction in peak force and a transient increase in baseline force following treatment with all ablative modalities. Yet, no dose-dependent responses were consistently observed relative to the biomechanical responses following ablations. The data presented here may provide novel insights into the effects of ablations on the esophagus which may in turn allow further improvements in ablative techniques to increase the overall safety and efficacy of cardiac and esophageal ablative procedures.

Introduction

The esophagus is a hollow, muscular, tubular organ connecting the pharynx to the stomach that plays an important role in digestion by conveying boluses of food from the pharynx to the stomach [1]. Any form of injury to the esophagus or its innervation can significantly alter its function [2], which may compromise the gastro-intestinal system. Although injury to the esophagus can occur in many ways, this article focuses on esophageal injury especially in the form of collateral damage from ablative treatments for atrial fibrillation (AF).

AF is the most common sustained cardiac arrhythmia whose prevalence is increasing with age, and incidence with time [3]. The median age for patients with AF is 66.8 years for men, and 74.6 years for women [4]. Approximately 2.5

million people are living with AF and as many as 12 million people are expected to have the condition by 2050 [4]. Although the first line of management of AF is primarily done through medication, depending on the disease state, AF duration, and circulatory instability, electrophysiological studies are performed in the heart that allow electrical mapping of myocardium to isolate areas responsible for irregular rhythm. These studies are often performed along with catheter ablation of abnormal electrical pathways causing disturbance in normal heart rhythm [5]. Since its inception in the early 1980's [6,7], catheter ablation has become one of the most useful and widely employed therapeutic modalities for treating medically refractory, intractable, and disabling AF. With over 50,000 and 60,000 cardiac ablation procedures performed each year in the USA and Europe, respectively, indications for its use continue to expand. Along with known benefits, there are significant complications associated with the ablative procedures that can be as high as 5% [8]. Some of the potential complications include: (1) vascular access bleeding, (2) vascular injury resulting from catheter manipulations, (3) cardioembolic events, and (4) collateral injury from delivery of ablative energies within the heart [9,10]. Specifically, the most frequent complications are vascular related, followed by esophageal injury, phrenic nerve injury, pericardial effusion/tamponade, neurologic events (stroke and transient ischemic attacks), and injury to lungs [8]. One of the complications of particular importance to interventional cardiologists and electro-physiologists is the creation of atrioesophageal fistulas (AEF) which often have fatal consequences [11,12].

Catheter ablations are routinely performed in the left and right atrium (LA and RA) to isolate the pulmonary veins (PVs) for treatment and management of AF [13,14]. In general, the goal of ablations is to create a series of transmural lesions in the LA, however, in most of the ablation modalities (like radiofrequency ablation and cryoablation), only the temperature and duration of the energy delivered can be controlled [15]. Since there is no accurate way to control the depth of the lesion created, it is possible to create a lesion that is too deep, consequently causing injury to adjacent vital structures. More importantly, it has been observed that heat generated from ablative energy that is dissipated within the LA by the ablation probe can result in esophageal injury without the probe coming into direct contact with the esophagus [11]. Hence, it has been well documented that these ablative procedures are associated with high risk of esophageal thermal injury because of the close proximity of the esophagus to the LA posterior wall that renders it susceptible to unintended collateral damage [16]. Esophageal injury can range from superficial ulceration and gastroparesis, to the rare but catastrophic AEF [17]. AEF are a known complication resulting from collateral damage from ablative procedures performed in the LA with variable incidences that could be as high as 1%, and having a high rate of mortality [18]. The etiology of esophageal injury is multifactorial, and AEF have been shown to result from application of many different forms of ablative energies that include: (1) radiofrequency ablation [19,20]; (2) cryoballoon ablation [21,22]; and (3) high-intensity focused ultrasound ablation [23]. Ablations are also performed in the

cardiac chambers (atria or ventricles) for management and treatment of arrhythmogenic substrates such as supraventricular tachycardia, idiopathic ventricular tachycardia, and ventricular ectopic beats [24,25,26,27] that could also be associated with collateral injury of surrounding structures including the esophagus.

Numerous studies have been performed to establish a relationship between the esophagus and the posterior LA wall as it relates to the relevance for performing ablations in the LA and PVs [16,28,29,30]. In summary, the following observations were reported: (1) the left-sided PVs are closer than the right-sided PVs, (2) typically, presence and thickness of pericardial fat pads are more prominent near the superior PVs than inferior PVs, (3) the length of contact between esophagus and posterior LA wall was longer in the AF patients than normal subjects, and (4) patients with AF had less fat-pad around the inferior PVs than normal subjects. In addition, in a cadaveric study, although the proximity of the esophageal wall to the endocardial surface of the LA was found to be variable, the distance was <5 mm. Moreover, it is conceivable that enlargement and thinning of the atrial wall in patients with AF could make this distance even shorter. Thus, in view of these important observations, a great precaution must be exercised while performing ablations around left-sided PVs. In addition, it is believed that the presence of fat-pads may have an insulating effect, however, whether it actually provides protection against fistula formation is not clear and needs to be investigated.

Because esophagus is susceptible to collateral damage, it is essential to understand the physiological and biomechanical properties of esophageal tissue under various therapeutic ablative treatments. This will not only allow us to understand the interactions of esophageal tissue in response to ablation, but also help in developing tools, techniques, and refining procedures to minimize and prevent collateral damage. The ablative modalities employed in this investigation were: radiofrequency ablation (RFA), cryoablation (CRA), high-intensity focus ultrasound ablation (HIFU), microwave ablation (MWA), and chemical ablation (CHA). Four chemical agents were used: 99.97% glacial acetic acid, 200 proof ethanol, 30% hypertonic sodium chloride solution, and 8M urea. The physiological assessment included measurement of changes in peak force (strength of contractions) as well as baseline force (resting muscle tension) in tissue baths [31,32]; and biomechanical assessment included measurement of uniaxial stress-strain characteristics of tissue samples in an uniaxial testing machine (Chapter 2).

The primary objectives of the present study were to gain new insights as to the changes in both physiological and biomechanical properties of the esophagus in response to applied ablative therapies. To do so, we performed in vitro analyses on isolated swine esophageal muscle bundles using methodologies developed by our laboratory (Chapter 2).

Methods

Tissue Preparation

The study was approved by the University of Minnesota Institutional Animal Care and Use Committee. Fresh esophagus tissue biopsies were obtained from healthy castrated male Yorkshire-cross swine (n=24, mean weight of approximately 70 kg), which were euthanized as part of another unrelated protocol. Following resection, the esophagus tissue was pinned in a dissection dish, dissected in oxygenated, temperature-controlled Krebs-Ringer solution. The muscle bundle preparation involved initially cleaning up the biopsy by removing excess fat and surrounding connective tissue so that well defined muscle bundles could be prepared. The external muscularis and internal squamous epithelium layers were first separated and then tissue bundles of both the muscularis layer and squamous epithelium layer were prepared. Muscle bundles of muscularis layer were prepared along the internal circular layer of muscle fibers of muscularis externa in an identifiable cuboidal shape having lengths of 15 to 25 mm, widths of 3 to 5 mm, and thickness of 1.5 to 3 mm. Tissue bundles of squamous epithelial layer were prepared in an identifiable cylindrical shape having lengths of 15 to 25 mm and diameters of 1.5 to 3mm. The physiological testing was performed using tissue baths and biomechanical testing was performed using a uniaxial testing machine as previously described in detail (Chapter 2, submitted for publication). Note that the squamous epithelium is a non-contractile tissue; hence, only biomechanical tests were

performed on these tissue bundles. However, both physiological and biomechanical tests were performed on the muscularis muscle bundles.The esophageal tissue responses to the following five different ablation modalities were investigated:

Radiofrequency Ablation: RFA (484 KHz sinusoidal waveform) at five different ablation doses were studied: 50 °C, 55 °C, 60 °C, 65 °C, and 70 °C (corresponding to 440 J, 740 J, 840 J, 1060 J, and 1200 J energy levels, respectively).

Cryoablation: Cryoablation exposure (operated in the clinical mode, approximately -75 °C) at four different ablation doses were studied: 15 sec, 30 sec, 60 sec, and 120 sec.

Microwave Ablation: MWA (1.3 GHz continuous sinusoidal waveform) with ablation duration between 60 sec and 240 sec at six different ablation doses were studied: 226 J, 318 J, 526 J, 1052 J, 1579 J, and 2105 J.

HIFU Ablations: HIFU ablations (2.5 MHz sinusoidal waveform, 80% duty cycle) at five different ablation doses were studied: 228 J, 342 J, 456 J, 570 J, and 684 J.

Chemical Ablations: Chemical ablations with all four agents (acetic acid, ethanol, hypertonic sodium chloride, and urea) were performed independently by injecting the chemical ablative agent individually at four different ablation doses: 10 µl, 25 µl, 50 µl, and 100 µl.

Data Analyses

Statistical analyses were performed using ANOVA and Tukey tests to identify differences in peak forces and baseline forces for all ablation modalities, where a $p<0.05$ was considered statistically significant. All data were presented as means $\pm$ standard deviations.

Results

Results of Physiological Assessment

A total number of 168 muscle bundles were studied for physiological assessment in tissue baths as shown in Table 7. The table summarizes the muscle bundle characteristics and allocations to different ablative modalities. As can be observed in this table, the lengths, widths, thicknesses, masses, initial peak forces, and baseline forces of muscle bundles were similar for each group investigated.

The percent change in peak force and baseline force in response to all ablation modalities were calculated for the esophagus tissue as shown in Figure 52 through Figure 67. There were dose-dependent sustained reductions in peak force and a transient increase in baseline force following treatment with each ablative modality. With some ablative modalities (eg: RFA, MWA, sodium chloride), the peak force reduced initially, but showed some improvement over the 3-hour in vitro recovery period. This phenomenon was more pronounced at low therapy doses relative to the high ones. Although there were dose-

dependent transient increases in baseline forces for all ablation modalities, the baseline forces were observed to recover consistently below the pre-ablation level at the 3-hour recovery period (except for acetic acid). Typically, the transient elevations in baseline forces were maintained for a period of approximately one hour post-ablation following which they reduced below pre-ablation levels. This phenomenon was not observed in following therapies: (1) acetic acid where the baseline force remained at elevated levels, and (2) sodium chloride, where the baseline force reduced to pre-ablation levels within approximately 15 minutes. Among all the chemical ablative agents utilized for performing ablations, acetic acid was the most potent agent as it caused the maximum reduction in peak force at every ablation dose. Similar changes in peak force and baseline force were observed for control and control-remove muscle bundles (as shown in Figure 70 and Figure 71) suggesting that unmounting the muscle bundles from the tissue baths for performing ablations had minimal impact on subsequent physiological response. The peak force and baseline force of muscle bundles injected with Krebs-Ringer solution were similar for every injected dose, thus no significant dose-effects were observed (as shown in Figure 68 and Figure 69). Moreover, the fact that peak forces and baseline forces for muscle bundles injected with Krebs-Ringer solution were very similar to that of control and control-remove muscle bundles, suggests minimal (if any) mechanical damage resulting from injection of chemical agents or the Krebs-Ringer solution.

For all thermal ablation modalities (RFA, CRA, MWA, and HIFU), statistically significant differences ($p<0.05$) were observed for both dose and time variables calculated using the Tukey test. For all chemical ablation agents, statistically significant differences ($p<0.05$) were observed for dose, time, and agent (Krebs-Ringer solution versus chemical ablative agent) variables calculated using the Tukey test.

Results of Biomechanical Assessment

A total number of 563 muscle bundles were studied for biomechanical assessment which included the 168 muscle bundles studied for physiological assessment as described above. All muscle bundles were subjected to uniaxial pull test and thus, force versus stretch data was obtained for each sample. At the completion of each uniaxial pull test, an assessment was made where the given muscle bundle avulsed; which is summarized in Table 8 as a percentage of avulsion location of muscle bundles for each treatment group along with the number of samples in each case. Figure 76 provides a graphical distribution of avulsion locations for all muscle bundles investigated. Importantly, for subsequent biomechanical assessments, only the muscle bundles that avulsed at or near the center of the muscle bundle were included in the analysis. Based on these data, the key biomechanical parameters of all samples in each treatment group were calculated as shown in Table 9. As can be observed from this table, the initial cross-sectional area and volume of the muscle bundles were similar across the different therapeutic groups. The avulsion force was defined as the value of the maximum force that was required to cause tissue avulsion. Since force required to avulse the tissue was dependent on cross-sectional area of the muscle bundle, the avulsion force was normalized to the cross-sectional area and is reported in the units of N/mm^2. The avulsion strain was defined as the ratio of stretch to the point of avulsion and the original length of the muscle bundle; whereas the total strain was defined as the ratio of stretch to the point

where force returned to zero following avulsion and the original length of the muscle bundle. The avulsion energy was defined as the integral of area under the force-displacement curve until the point of avulsion; whereas the total energy was defined as the integral of area under the entire force-displacement curve. Since energy required to avulse the tissue was dependent on avulsion force and stretch distance, energy was normalized to the volume of the tissue and is reported in the units of mJ/mm^3. Cross-sectional area normalization of avulsion force and volume normalization of energies allowed comparative assessment of these quantities between different treatment groups. The elastic modulus, avulsion and total strain, and avulsion and total energy of samples were also calculated that allowed assessment of relative stiffness of samples between each group. As an example, an average model of stress-strain characteristics of non-ablated (control) swine esophagus muscle bundles was developed by averaging all samples (n=297) as shown in Figure 77. The "true stress-strain" relationship (Cauchy's stress) was also calculated by taking into account the reduction in cross-sectional area of each sample during the stretch. The average avulsion stress and Cauchy's avulsion stress were calculated to be 0.33 MPa and 0.72 MPa, respectively, and the avulsion strain was calculated to be 1.35. The Cauchy's stress was found to be 2.18 times higher than conventional stress. In a similar manner, the stress-strain characteristics of all muscle bundles in every treatment group were also calculated (graphs not shown); however, the key biomechanical parameters are summarized in Table 9.

The percent change in each of the six biomechanical parameters in each treatment group were calculated with respect to control samples (n=297, non-ablated) as shown in Table 10. As can be observed in this table, a positive value indicates an increase and a negative value a decrease with respect to controls. Percent change in avulsion force, elastic modulus, strain, and energy are shown along with individual statistical significance ($p<0.05$, marked in bold). Statistically significant increase in avulsion forces (range: 17.25% to 43.81%) were observed for each ablative treatment except CRA and sodium chloride, where an increase was observed, but the response was not statistically significant. Similarly, an increase in elastic moduli (range: 12.55% to 45.35%) were observed for each ablative treatment except CRA and sodium chloride, where a minor reduction was observed. In general, reductions in the avulsion and total strains were observed; and increases in the avulsion and total energies were observed for every ablative modality investigated. Dose effects for each of the six biomechanical parameters for each ablation modality were analyzed using ANOVA. Unlike physiological results, statistically significant dose effects were not observed in biomechanical properties for any ablation modality as shown in Figure 78 through Figure 86.

The formation of an AEF is characterized by an abnormal connection between the esophagus and the atria. Thus, in order for the fistula to form, it must affect both the muscularis and squamous epithelial layers. We separately tested the previously dissected squamous epithelium to assess its biomechanical

properties (n=26). As compared to the muscularis layer, all biomechanical parameters of squamous epithelium layer were consistently higher, which were calculated to be: (1) avulsion force = 0.78 N/mm^2 (66.4% higher), (2) elastic modulus = 0.75 N/mm^2 (7.5% higher), (3) avulsion strain = 1.54 (15.5% higher), (4) total strain = 1.93 (10.5% higher), (5) avulsion energy = 339.9 mJ/mm^3 (145.2% higher), and (6) total energy = 407.7 mJ/mm^3 (128.2% higher). In other words, the squamous epithelium possessed greater stiffness as compared to the muscle layer.

Discussions

This study demonstrates that both physiological and biomechanical properties of swine esophagus are altered when subjected to various ablative therapies. The mechanisms of action of every ablation modality are unique and complex; they are discussed in detail in Chapter 3. The cellular mechanisms of injury, protein denaturation, membrane collapse, cessation of enzymatic function, mitochondrial dysfunction, Ca^{2+} overload, further leading to coagulation necrosis and apoptosis are also discussed in detail in Chapter 3, hence not repeated here. Like the diaphragmatic tissue, we had an interesting observation with the esophageal tissue as well. After approximately 30 min of ablation, microbubble droplets were observed on the ablated region of the muscle bundles caused by excessive dehydration as shown in Figure 87. The mechanisms of chemical ablation with acetic acid, and other chemical agents used in this investigation are

based on the induction of intracellular dehydration, intracellular protein damage, and thrombo-ischemic effects on the muscle cells. This eventually resulted in: (1) contracture which caused an increase in baseline force, (2) cellular injury which caused reduction in peak force, and (3) protein denaturation and dehydration which caused stiffness and an increase in avulsion force.

In this investigation, the main objective was to perform the tissue bath study (for physiological assessment) and then follow up with the uniaxial pulls (for biomechanical assessment). No dose-dependent response was consistently observed in any of the six biomechanical parameters as a result of treatment with all ablation modalities. This was in part, due to many confounding factors, some of which are alluded to in “part 1” of the article. One possible explanation for these observations is that the ablation doses used for physiological assessment did not cause a significant change in biomechanical properties of the esophageal tissue. This hypothesis was tested by ablating a separate set of esophagus muscle bundles at much higher ablative doses, typically a combination of longer durations or multiple exposures, and then performing the biomechanical uniaxial pulls (data not shown). It was observed that when these muscle bundles were mounted in tissue baths, no peak forces could be registered. This was in part due to much higher levels of cellular injury which resulted in significant compromise of the contractile protein network, hence complete loss of contractility. However, when these muscle bundles were subjected to uniaxial pulls, significant changes in biomechanical properties were noted. For example,

with respect to controls, the average avulsion forces typically: (1) increased by 25% when esophageal muscle bundles were exposed to three RFA of 1 min duration each, (2) increased by 9% when esophageal muscle bundles were exposed to two CRA of 4 min duration each. Alternatively, with respect to controls, the average elastic modulus typically: (1) decreased by 33% after RFA, and (2) decreased by 24% after CRA. All these ablations were performed sequentially, side-by-side, near the center of the muscle bundle. As noted before, when these muscle bundles were mounted in tissue baths after ablations, no contractions could be elicited even at supra-maximal stimulation levels suggesting severe cellular injury. Since no contractions could be elicited, physiological assessment protocol could not be performed on these muscle bundles, and at these ablative doses. Thus, ablation doses were selected that were not only clinically relevant, but also with a view of an acceptable model so that both tissue bath studies and uniaxial pull studies could be performed on the same muscle bundles. These observations suggest that the sensitivity of both techniques (tissue baths and uniaxial pulls) may be quite different. In other words, significantly higher ablative energies are required before any appreciable change in biomechanical properties of the esophageal tissue can be observed. Moreover, due to variability introduced from multiple sources, the uniaxial pull measurements may not be sensitive enough to discriminate small differences in biomechanical properties resulting from the ablation dose levels selected in this study. Clinically, an increase in avulsion force means that it would require a

higher force to cause tissue avulsion. This may be due to many factors of which the primary ones are denaturation of proteins, elastin and collagen.

It is considered here that our series of experiments offered a unique ability to collect both physiological and biomechanical data, with high level of consistency and repeatability. This enabled us to closely explore highly relevant ablative doses, those that might be encountered clinically. It is understood that there are three potential differences as far as tissue response is concerned between the intact whole esophagus and esophageal muscle bundles. One, the intact esophagus is susceptible to secondary collateral injury from ablative procedures performed in a different organ. The extent of collateral injury depends on the type of ablative energy used, duration, and proximity to the esophagus. Moreover, these injuries generally tend to be localized to a region of the esophagus. Our set of experiments mimics the collateral injury by directly ablating the esophageal muscle bundles in localized regions with various ablative treatments. Although the way esophagus incurs damage may be different between the secondary collateral injuries versus direct injury, the end result is the same; that is cellular injury leading to esophageal dysfunction. In view of this, future investigations could more closely mimic the collateral damage by including a biopsy of primary target organ between the ablative source and the esophageal muscle bundle. Second, there will be small stimulation and electro-mechanical differences between the intact esophagus versus esophageal muscle bundles; as muscle bundles are bathed in Krebs solution in tissue baths, whereas intact

esophagus is perfused with normal blood within the body. However, stimulation within a muscle bundle requires similar voltage gradients and transmembrane potentials to elicit a contraction as stimulation with the intact esophagus; and we feel that it is likely to show similar responses and trends in action potential initiation and propagation. Lastly, the biomechanical parameters of the intact esophagus within its native environment will be different than those of isolated esophageal muscle bundles. We believe this is not only because of the bulk muscle volume, but also because of its adhesion to surrounding structures and relation to surrounding organs. In order to perform a fair and consistent comparison between muscle bundles exposed to various treatments, all biomechanical data was normalized either to the muscle bundle cross-sectional area or volume based on the quantity measured. Nevertheless, it is these responses and trends that we feel are important to guide further research.

In this investigation, we employed four thermal ablative modalities and four chemical ablative agents. Each ablative technique, although similar in purpose, has specific and optimal indications. Choice of the most appropriate ablative modality is vital to the success of any ablative procedure. The type of tissue to be ablated, regional blood flow, and the size of desired lesion are three important factors in this decision. Each ablation modality has its unique advantages. For example, the non-invasive, high-precision nature of HIFU makes it attractive in stationary or superficial regions. Among all ablation modalities, RFA has been in practice for the longest time which makes it an attractive modality of choice. One

of the advantages of a CRA probe is that it adheres to the target location by forming an ice-ball. Therefore, CRA works well in areas where catheter instability is high due to relative motion between the probe and the target location. MWA is one of the newer ablation techniques offering non-contact therapy application by electric field radiation and dielectric heating. Although it may be applicable to a broader spectrum of tissues, its long-term effectiveness still needs to be evaluated. Compared to any thermal ablation modality, CHA is the most cost-effective options as it does not require any capital equipment for performing ablations. Although cheap, it is restricted to use in target areas with low blood perfusion rates to minimize dilution and wash out, and prevent systemic side effects by localizing the action of injected ablative agent.

Since no similar studies have been performed in this area previously, it was not possible to compare these results with literature. It is important to note that our study approach can be considered to have a few limitations. For example, only a selected number of ablation settings were used in this study, cumulative effects of ablations were not studied, and only uniaxial pulls were done. Moreover, we did not test RFA using irrigated catheters, cryoballoon ablation catheters, phased-array HIFU transducers, different MWA antenna designs, and different chemical ablative agents, all of which may have resulted in different findings. Furthermore, this model can only investigate acute effects of ablation, i.e. within hours after ablation. Nevertheless, we hope to make this work translational by utilizing human tissue when it becomes available. The results

from this investigation can not only be used in understanding device-tissue interaction, but also aid in novel medical device design.

Conclusions

In this investigation we utilized novel in vitro methodologies to assess the potential for esophageal injury following the therapeutic delivery of clinically applied ablative therapies. Specifically, how physiological and biomechanical properties of esophageal tissue change as a result of exposure to various ablative modalities were assessed. These results demonstrate that these methodologies are applicable for analyzing a spectrum of ablation modalities; ones that are used in this investigation and others that could be used in the future, for example, laser ablation and irreversible electroporation.

To our knowledge this is the first study of its kind to compare the effects of ablation modalities and dosages on both the physiological and biomechanical properties of isolated functional esophagus muscle bundles. We observed unique dose responses for each ablation modality investigated as well as therapeutic differences as to their effects on the muscle parameters studies. The understanding of esophageal tissue properties has wide applications ranging from basic research to novel medical device design. This unique data set could provide important insights to both clinician as well as medical device designers developing clinical applied procedures. Results from these studies could enable head-to-head comparison of employed ablative modalities to determine their

effects on tissue response. Interpretation of these results can further be used to reduce complication rates, as well as increase effectiveness and overall efficacy of therapies. Moreover, increasing knowledge in this area is fueling the demand of introducing new procedures, modifying current ones, and reducing procedural time to positively impact the efficiency and efficacy of treatment delivered.

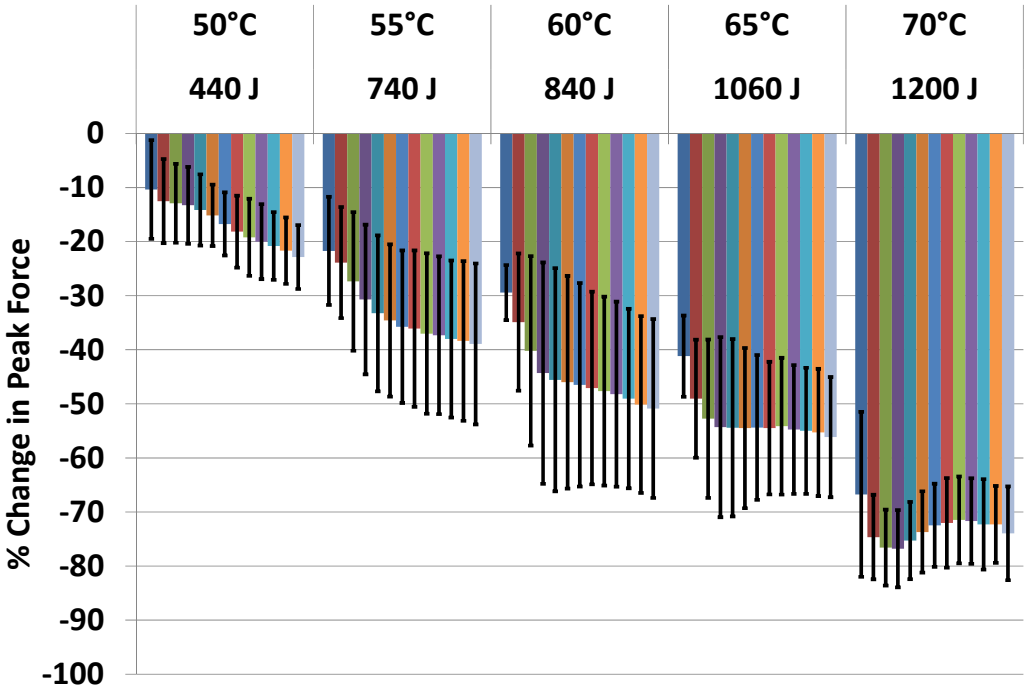

Figure 52: Dose effects of percent change in peak force of swine esophagus post radiofrequency ablation (RFA)

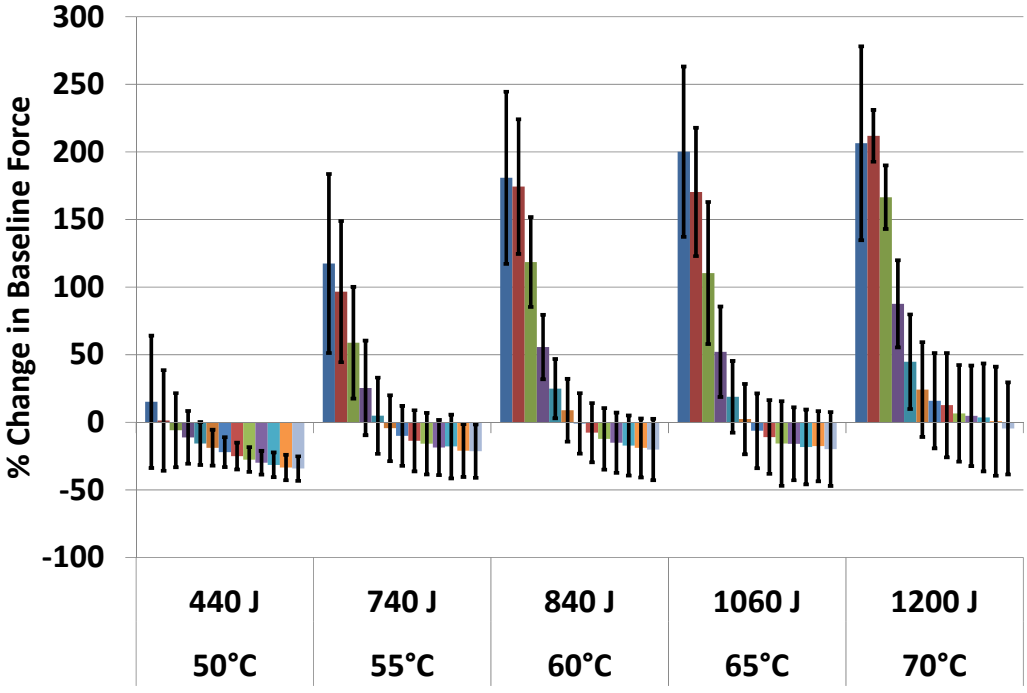

Figure 53: Dose effects of percent change in baseline force of swine esophagus post radiofrequency ablation (RFA)

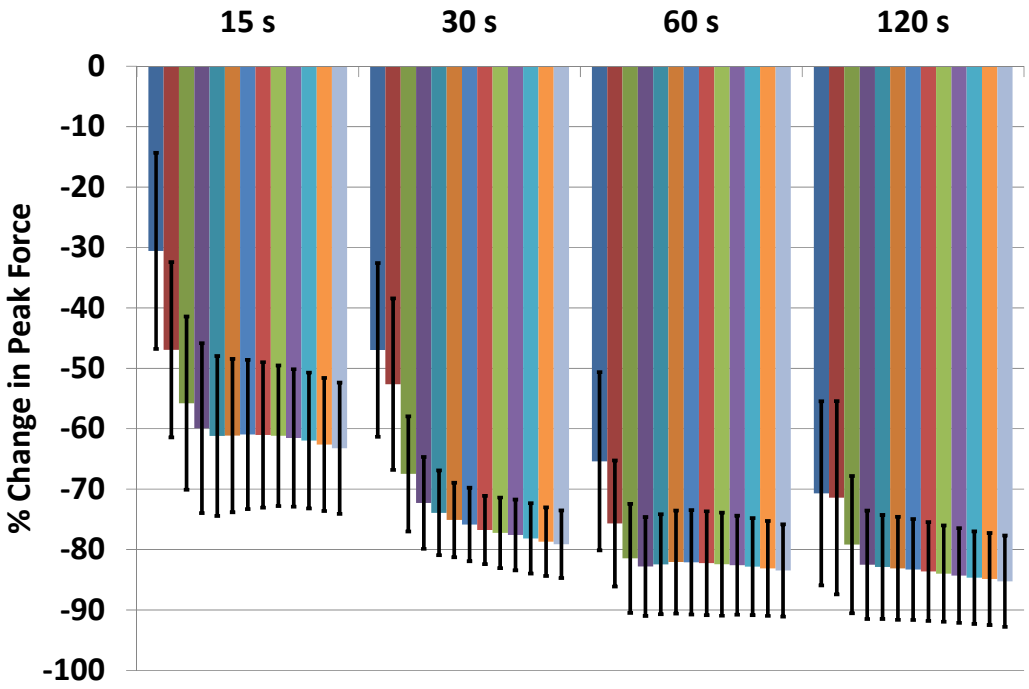

Figure 54: Dose effects of percent change in peak force of swine esophagus post cryoablation (CRA)

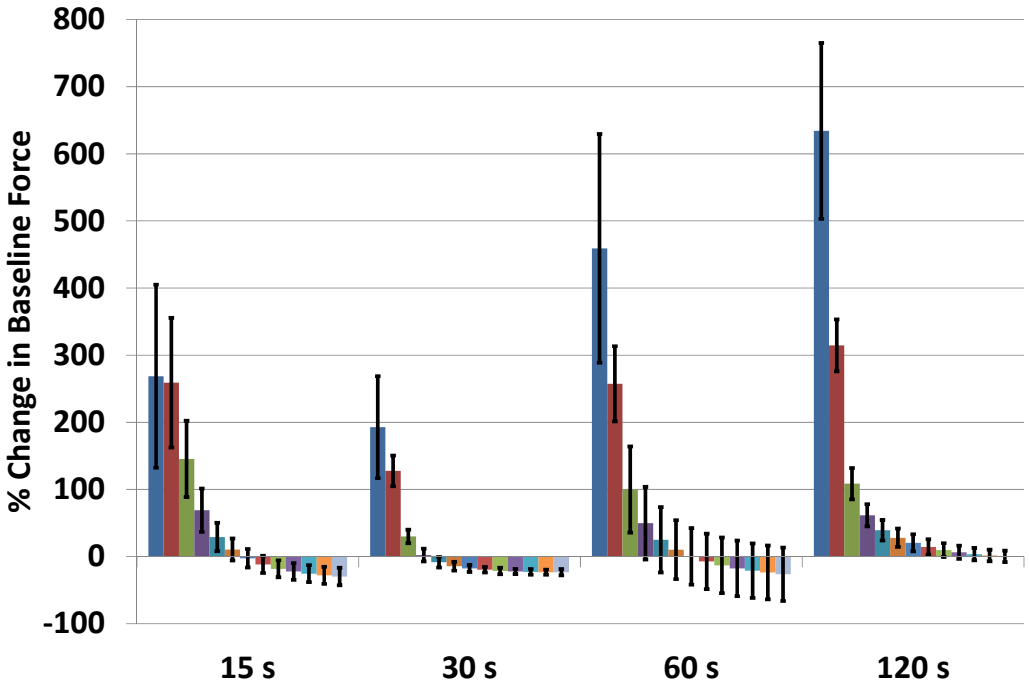

Figure 55: Dose effects of percent change in baseline force of swine esophagus post cryoablation (CRA)

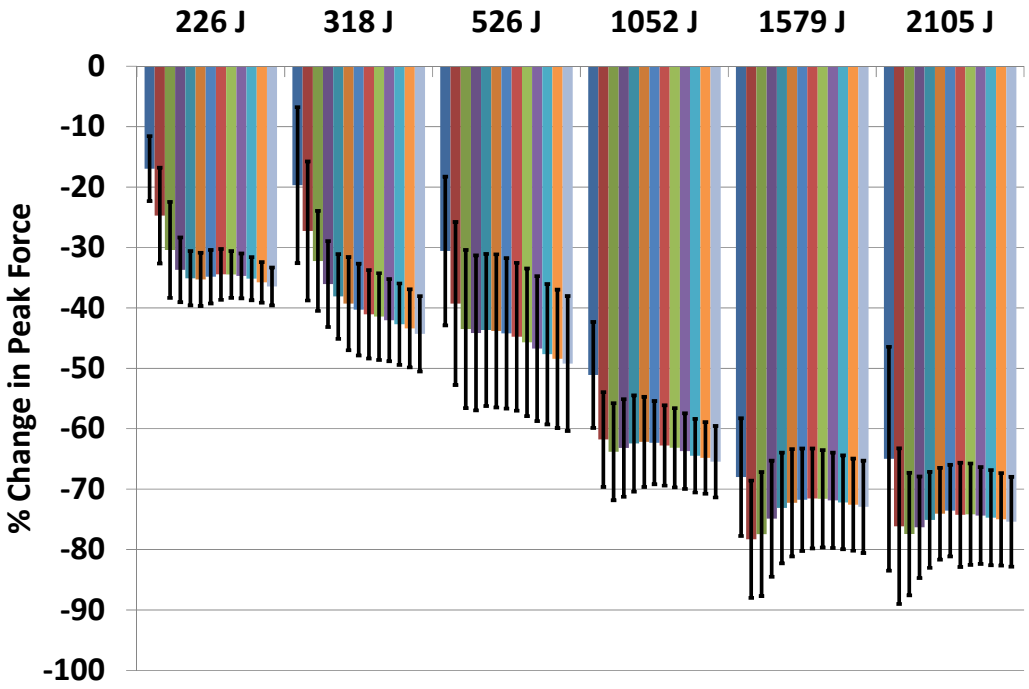

Figure 56: Dose effects of percent change in peak force of swine esophagus post microwave ablation (MWA)

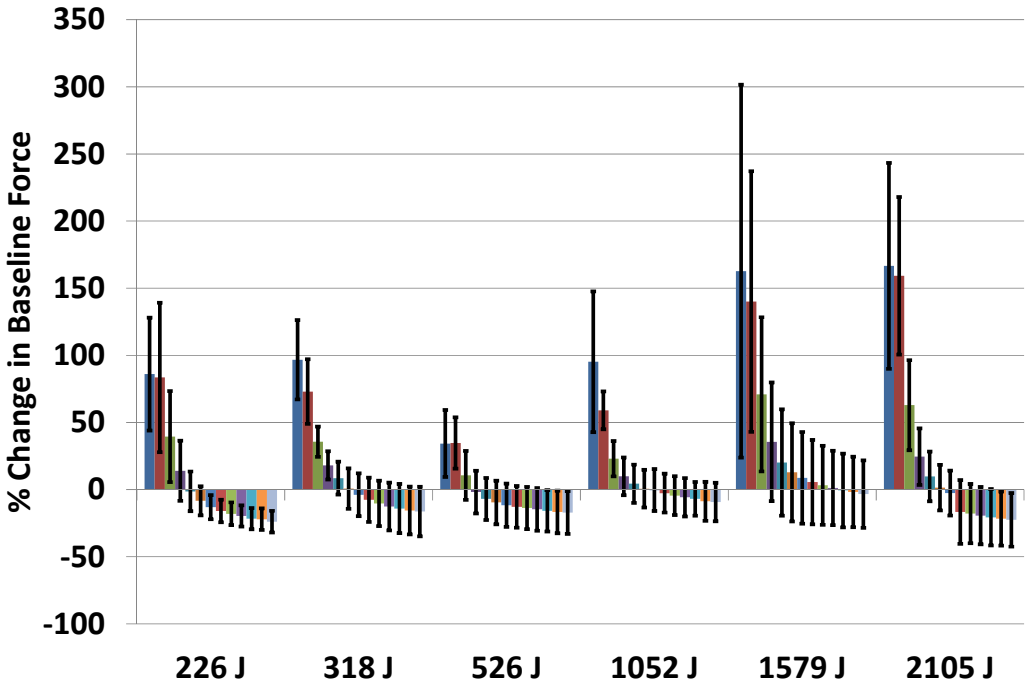

Figure 57: Dose effects of percent change in baseline force of swine esophagus post microwave ablation (MWA)

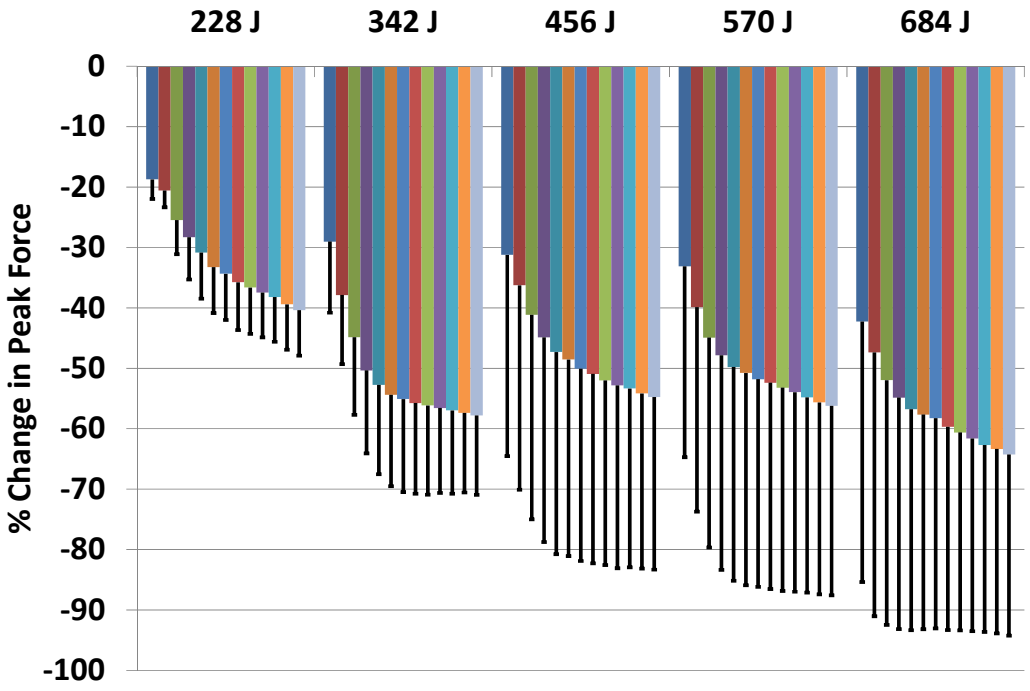

Figure 58: Dose effects of percent change in peak force of swine esophagus post high-intensity focused ultrasound ablation (HIFU)

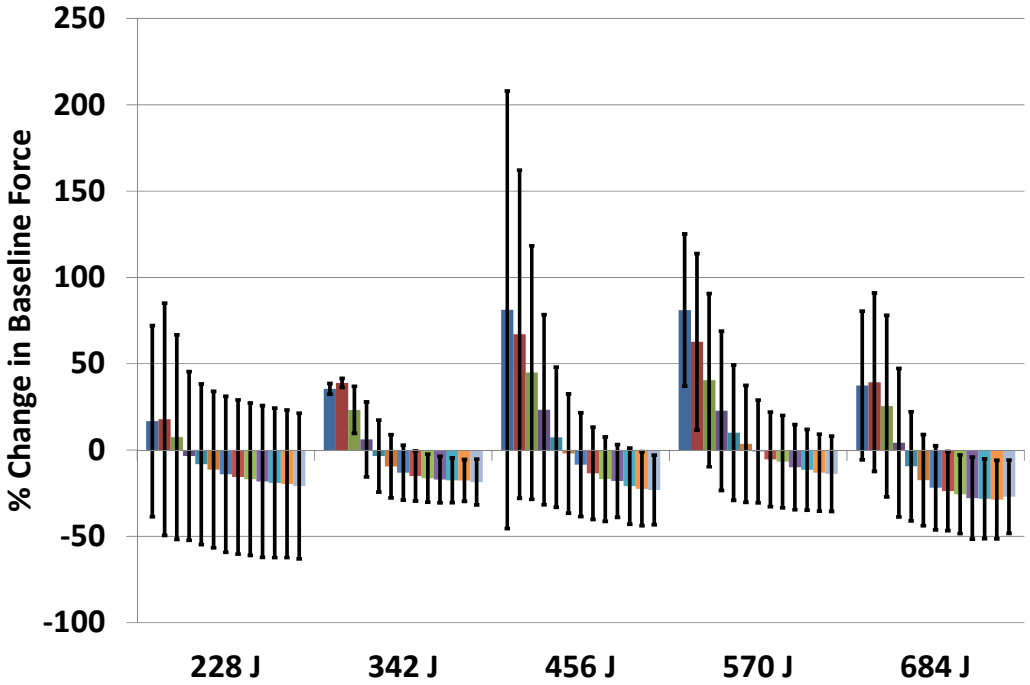

Figure 59: Dose effects of percent change in baseline force of swine esophagus post high-intensity focused ultrasound ablation (HIFU)

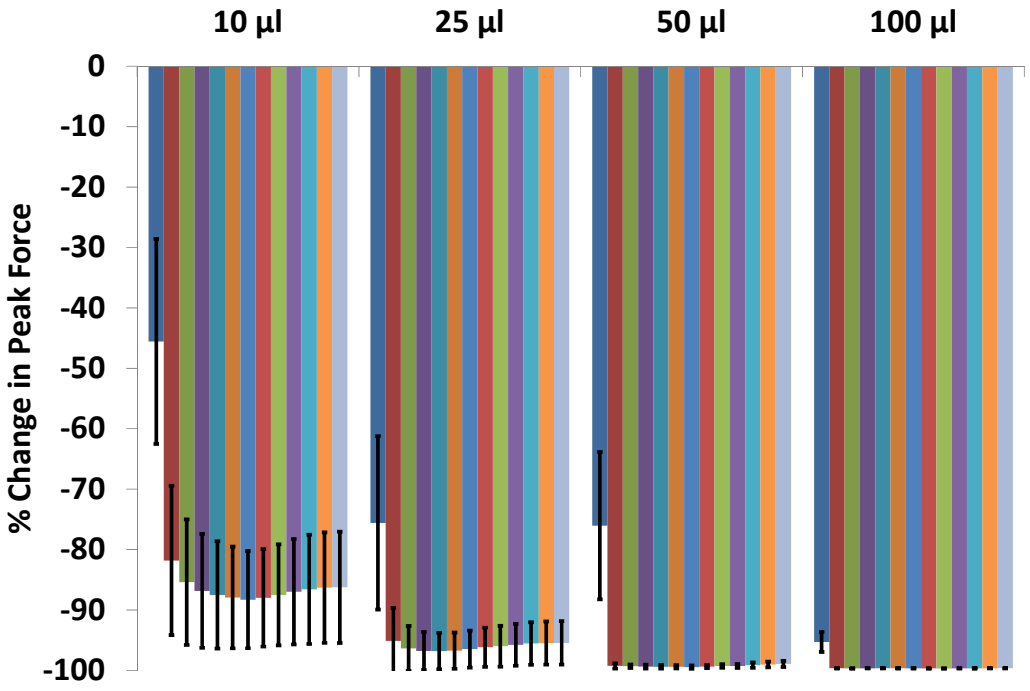

Figure 60: Dose effects of percent change in peak force of swine esophagus post chemical ablation with acetic acid

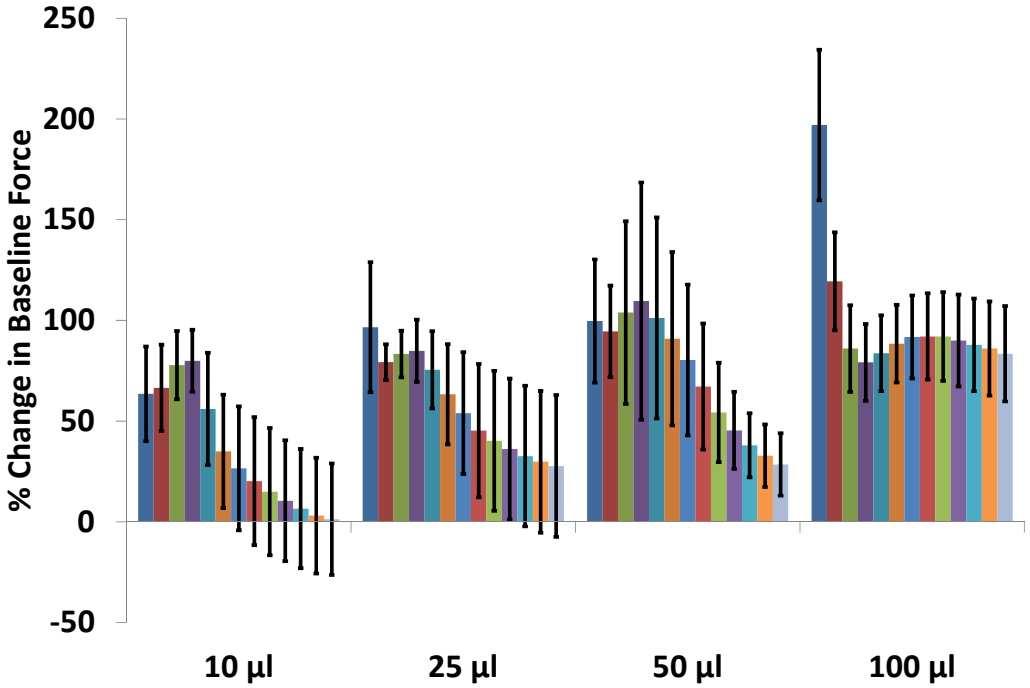

Figure 61: Dose effects of percent change in baseline force of swine esophagus post chemical ablation with acetic acid

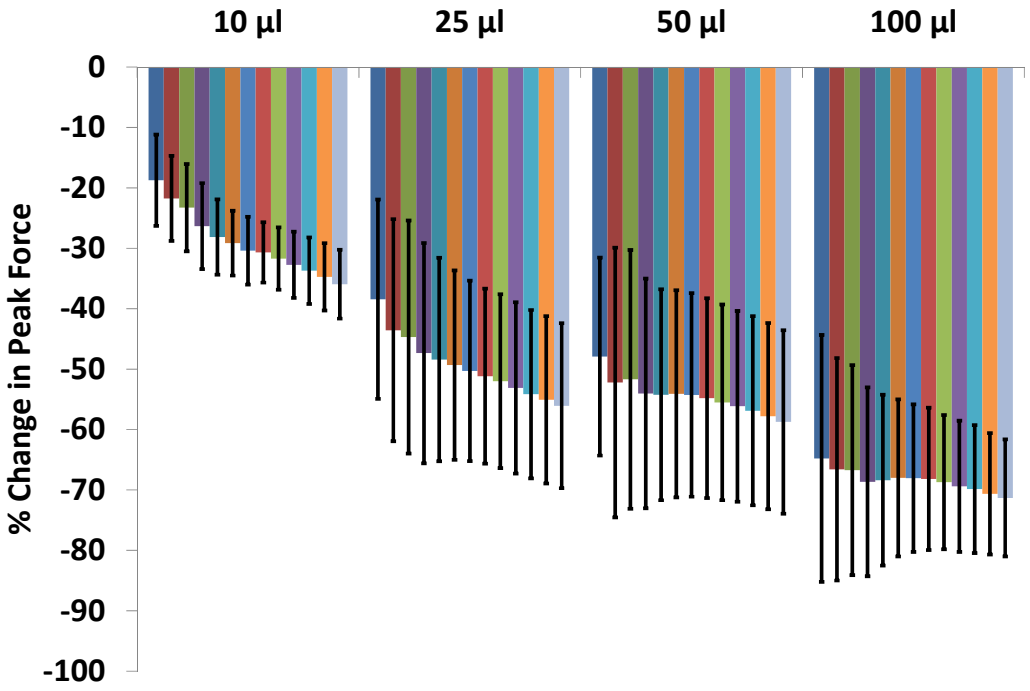

Figure 62: Dose effects of percent change in peak force of swine esophagus post chemical ablation with ethanol

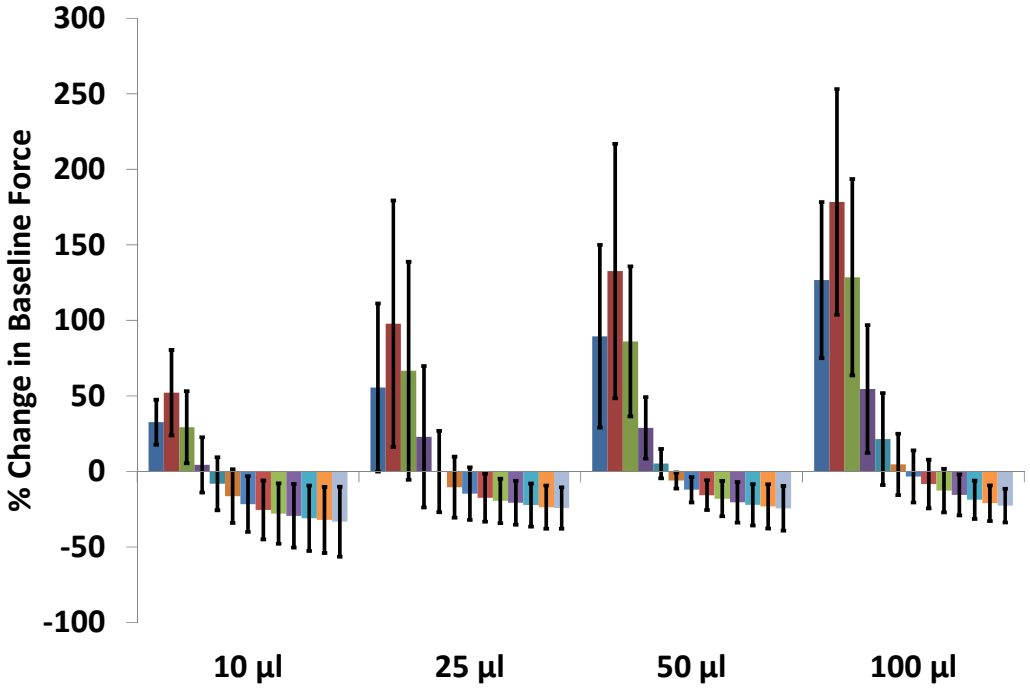

Figure 63: Dose effects of percent change in baseline force of swine esophagus post chemical ablation with ethanol

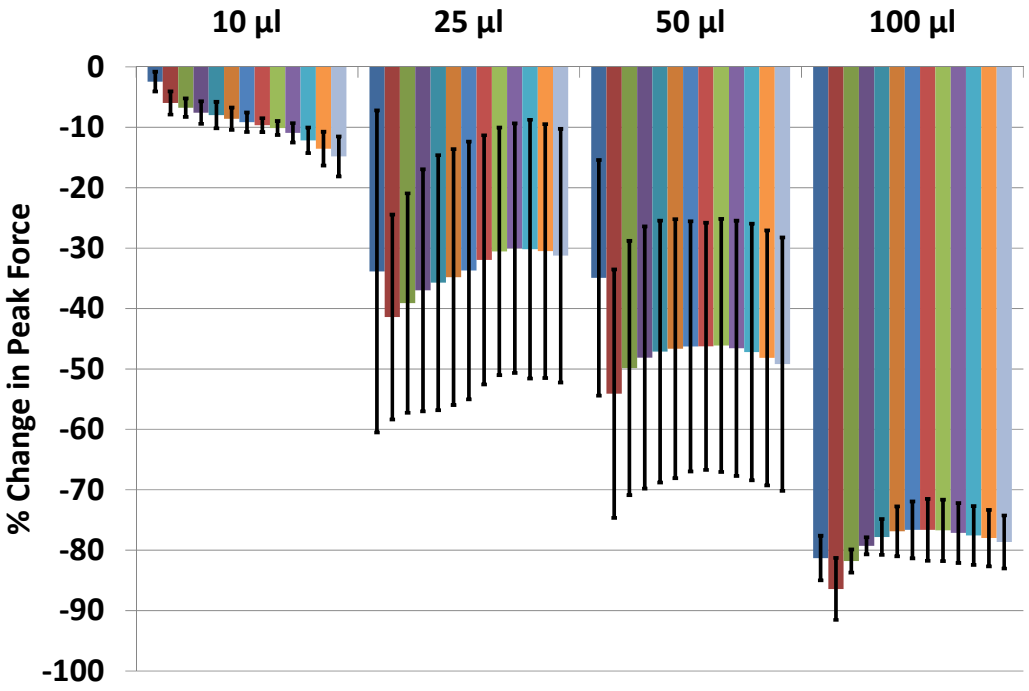

Figure 64: Dose effects of percent change in peak force of swine esophagus post chemical ablation with sodium chloride

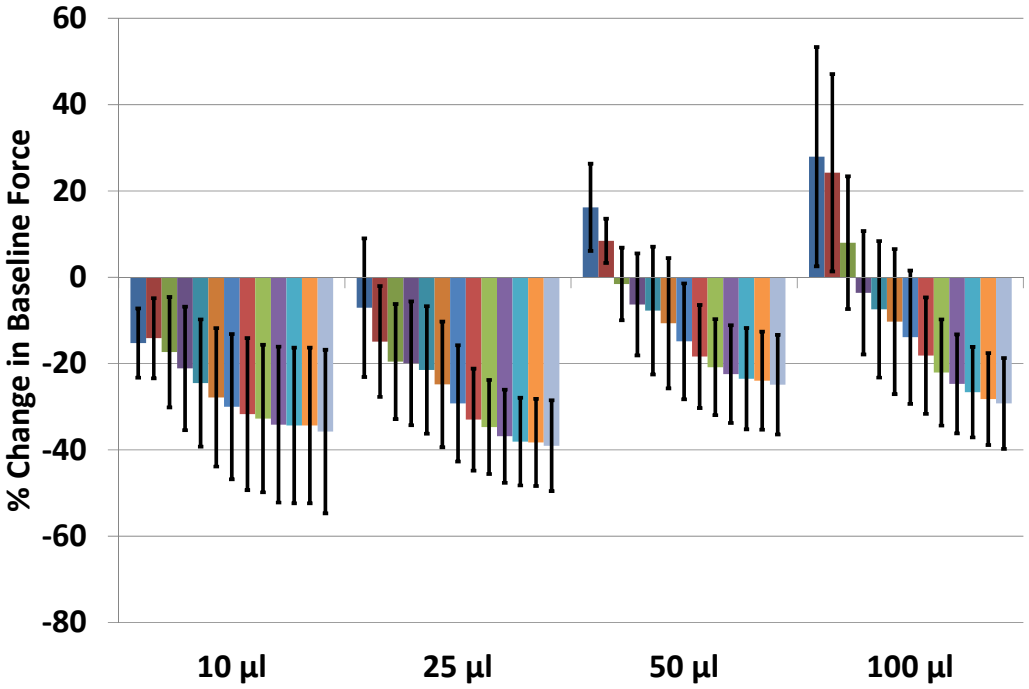

Figure 65: Dose effects of percent change in baseline force of swine esophagus post chemical ablation with sodium chloride

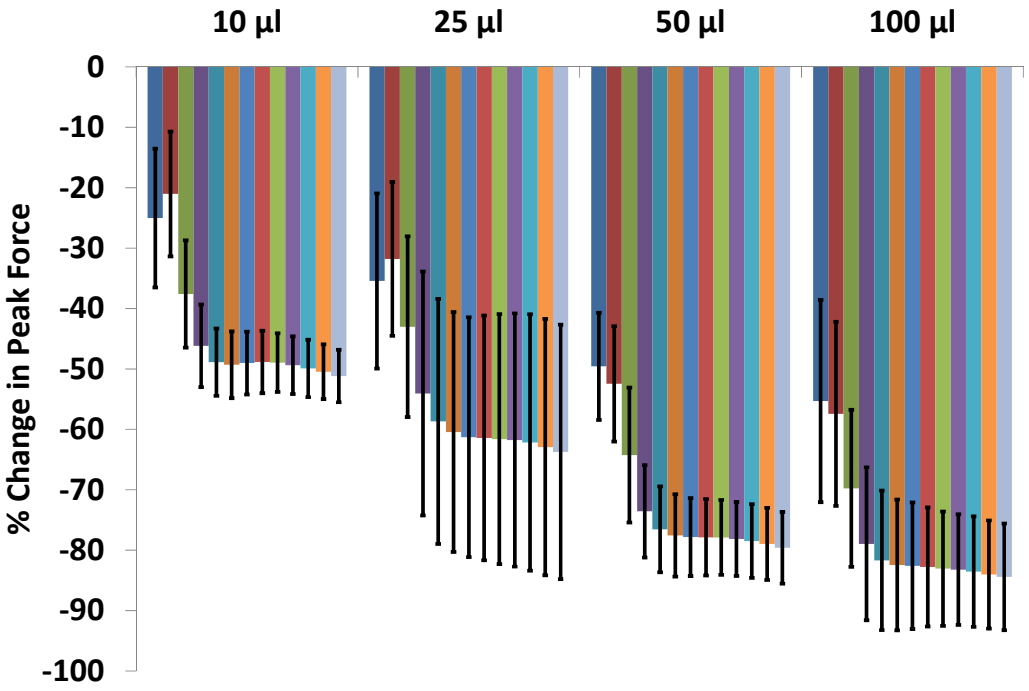

Figure 66: Dose effects of percent change in peak force of swine esophagus post chemical ablation with urea

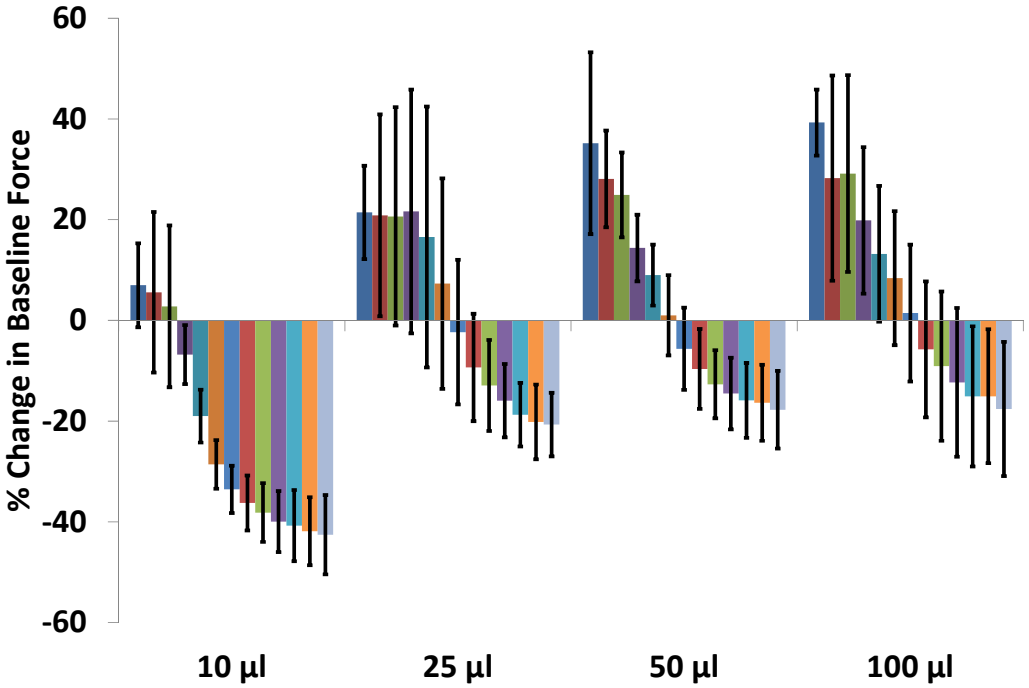

Figure 67: Dose effects of percent change in baseline force of swine esophagus post chemical ablation with urea

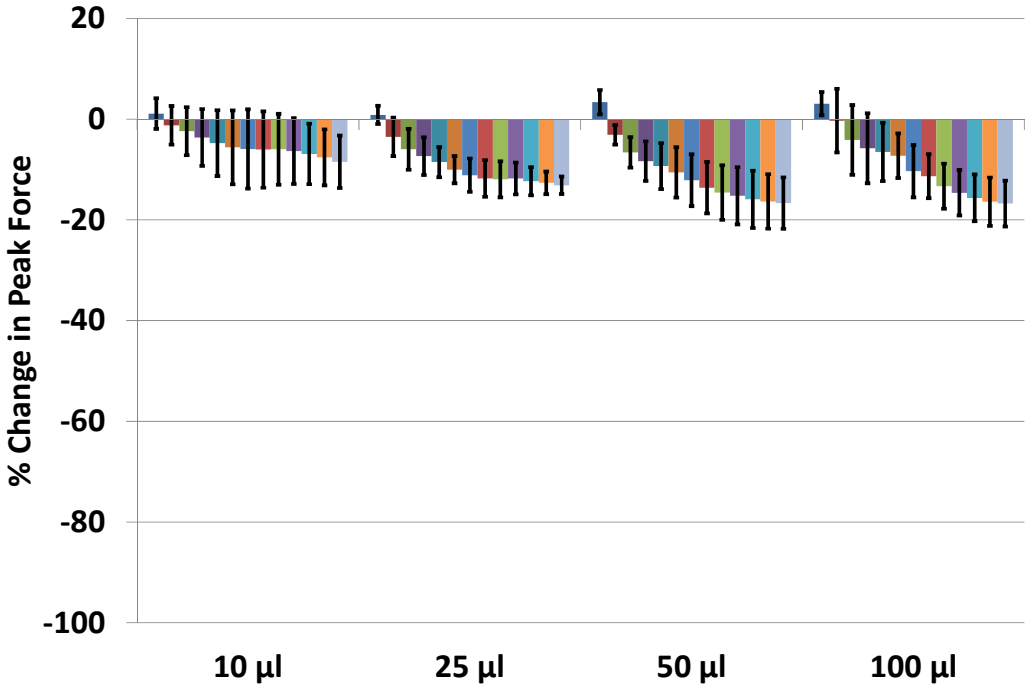

Figure 68: Dose effects of percent change in peak force of swine esophagus post injection with Krebs-buffer solution

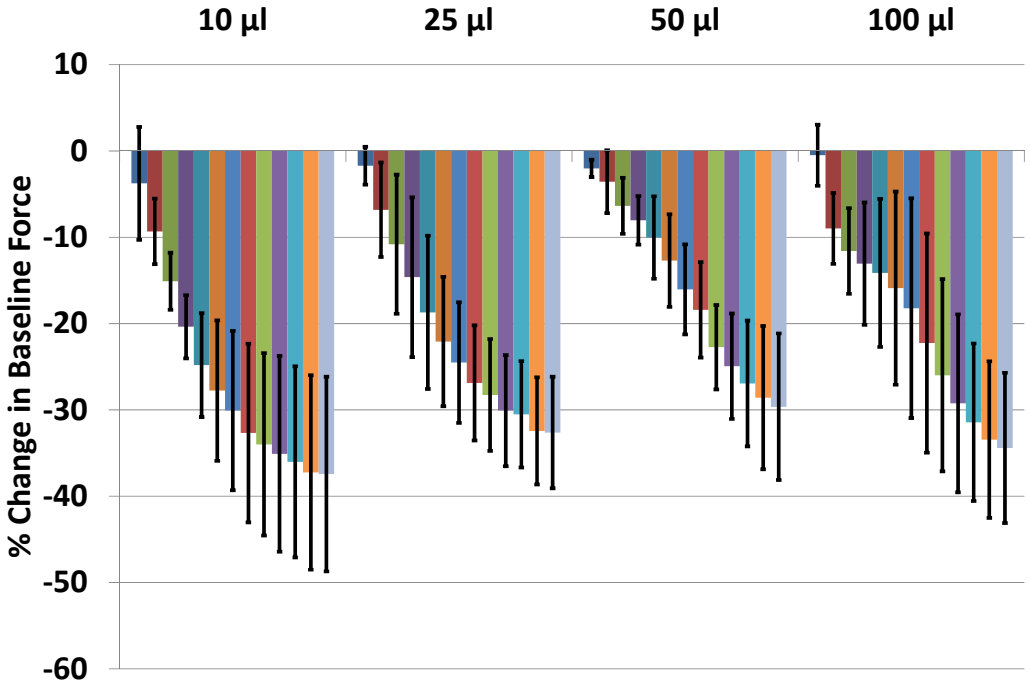

Figure 69: Dose effects of percent change in baseline force of swine esophagus post injection with Krebs-buffer solution

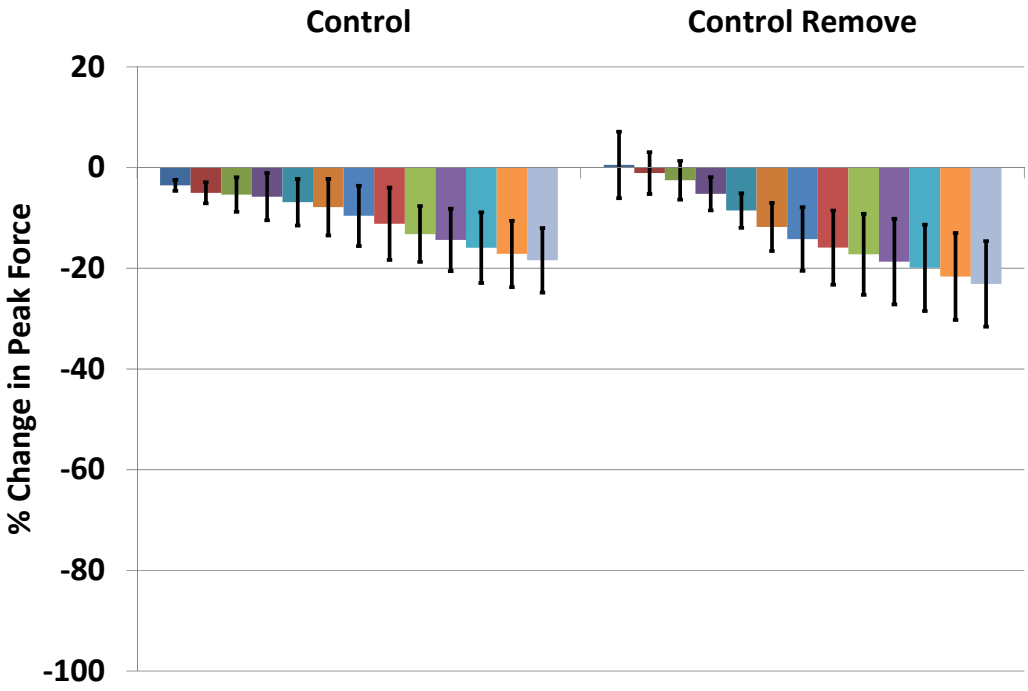

Figure 70: Percent change in peak force of swine esophagus for control and control-remove muscle bundles

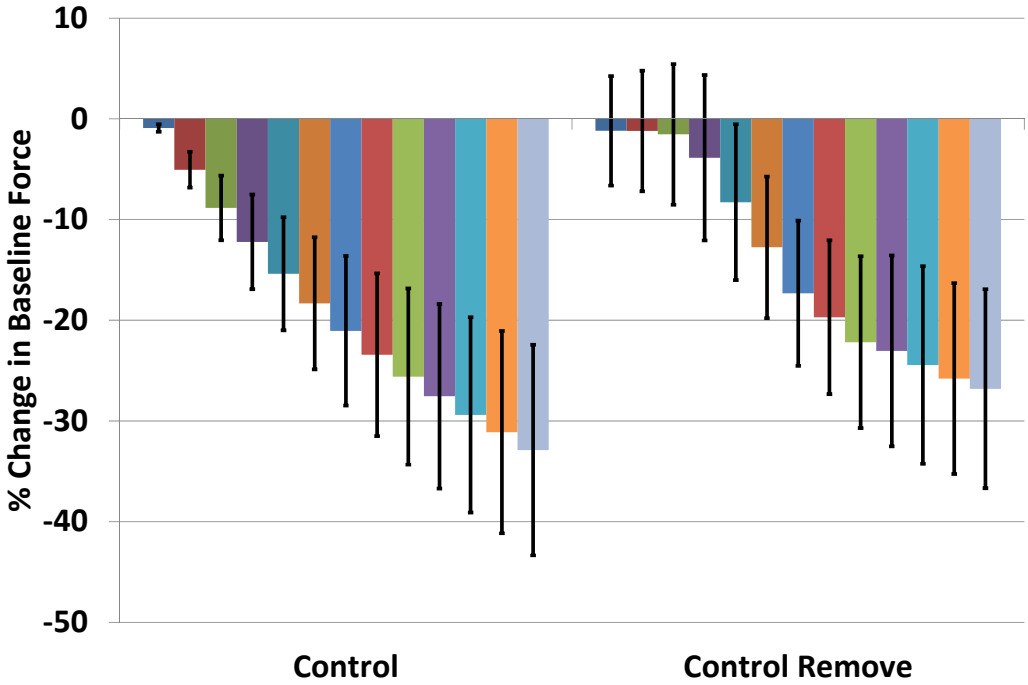

Figure 71: Percent change in baseline force of swine esophagus for control and control-remove muscle bundles

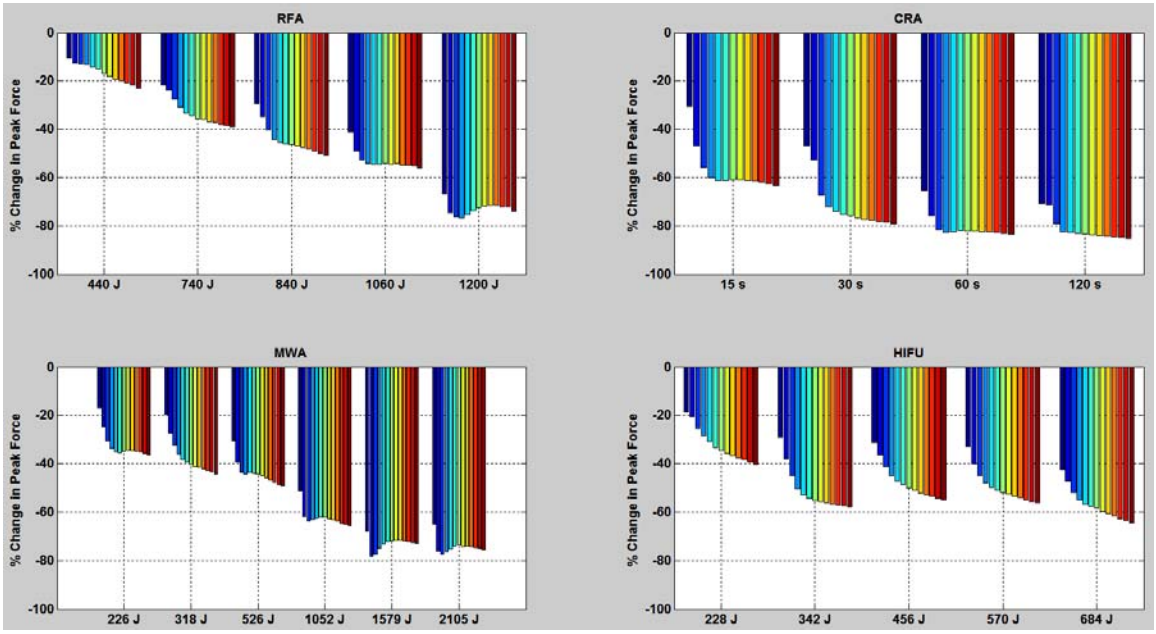

Figure 72: Dose effects on peak force of swine esophagus for all thermal ablative modalities

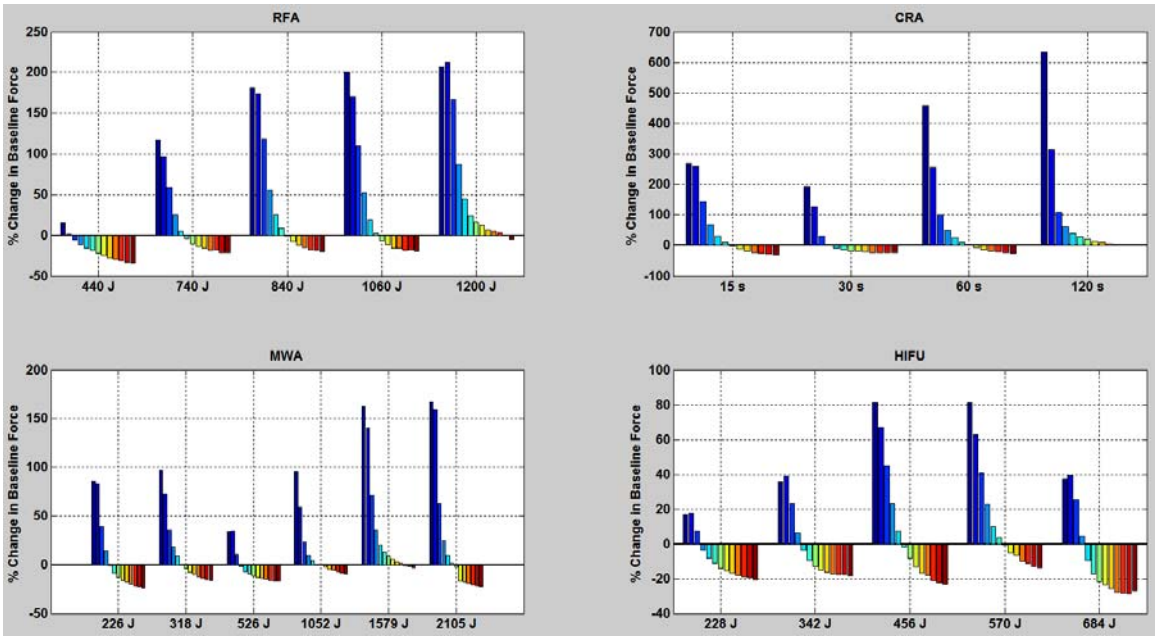

Figure 73: Dose effects on baseline force of swine esophagus for all thermal ablative modalities

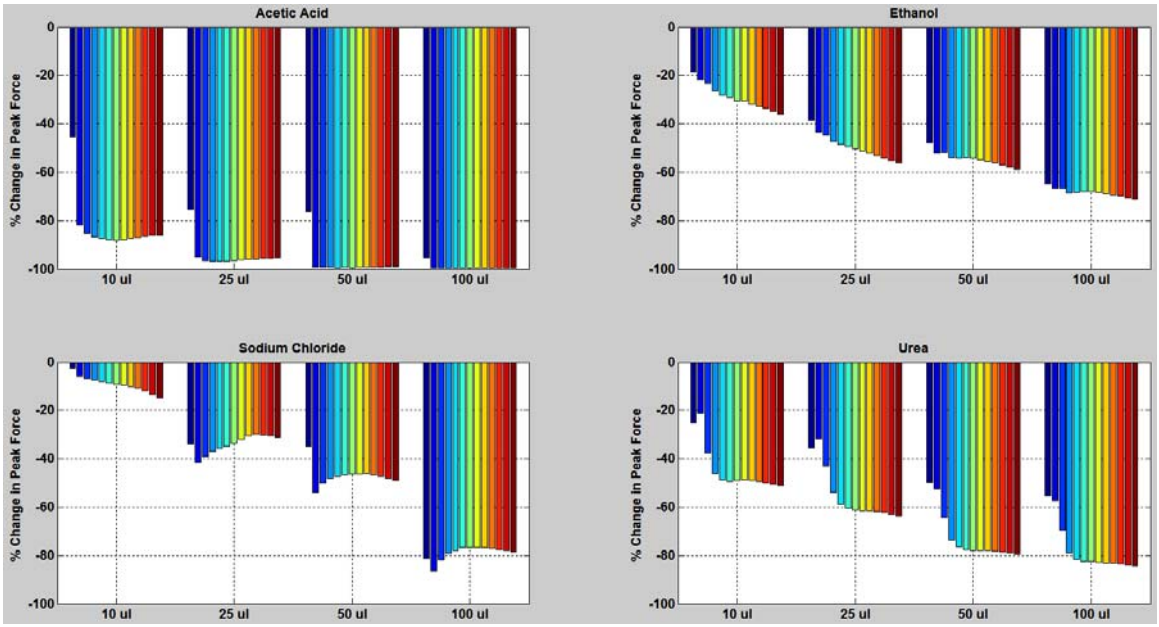

Figure 74: Dose effects on peak force of swine esophagus for all chemical ablative modalities

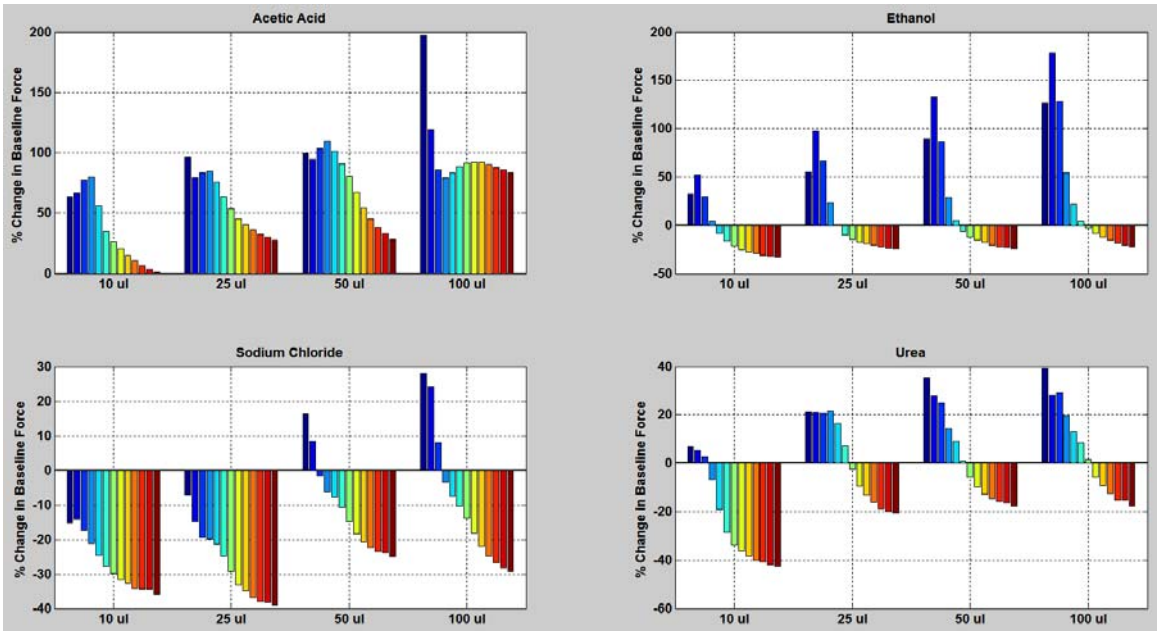

Figure 75: Dose effects on baseline force of swine esophagus for all chemical ablative modalities

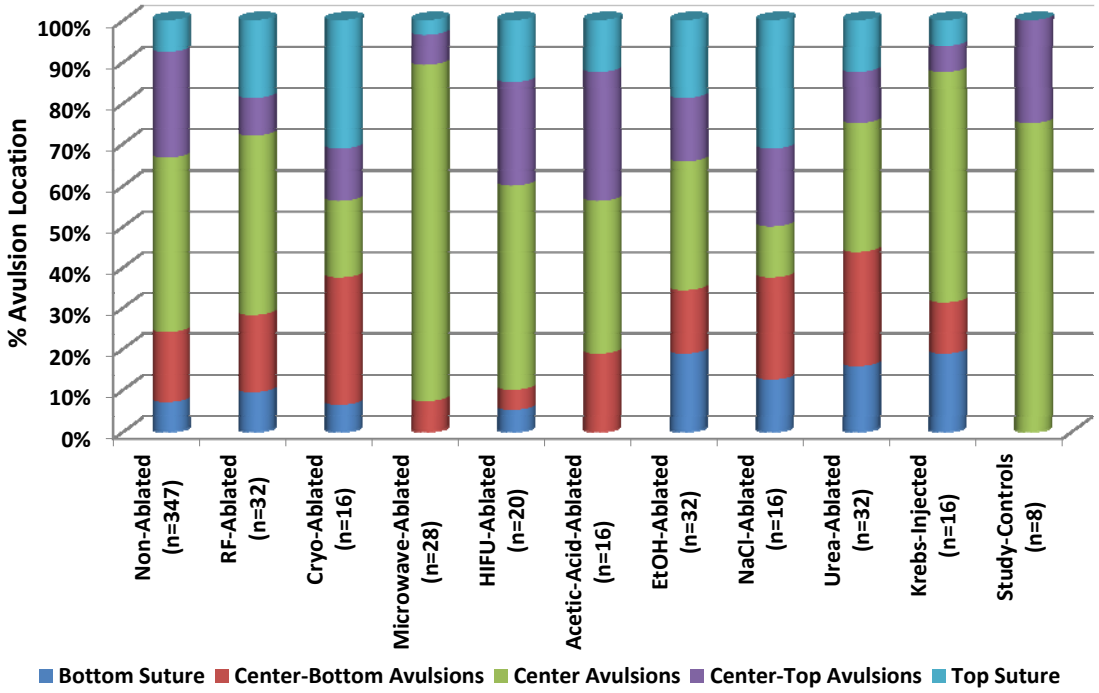

Figure 76: Avulsion location for each treatment displayed as percentage for all swine esophagus muscle bundles tested for biomechanical assessment

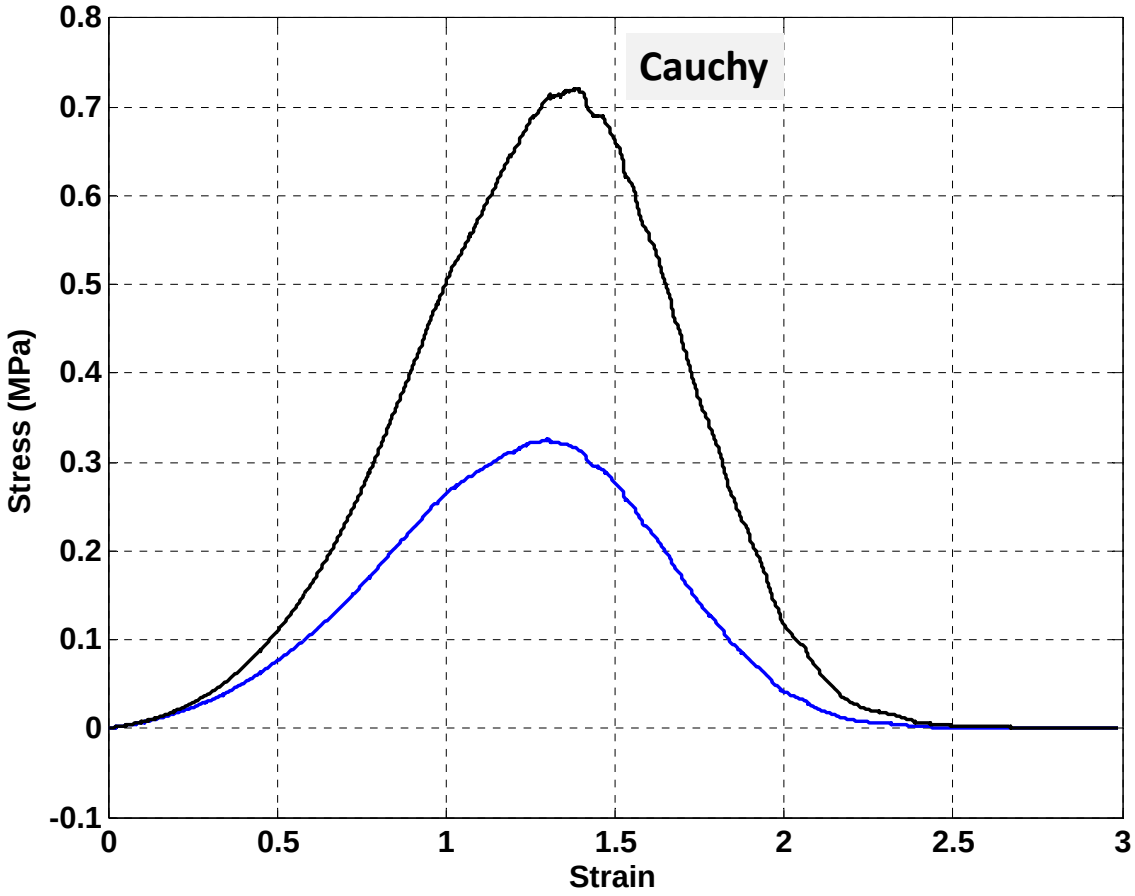

Figure 77: Average model of stress-strain characteristics of swine esophagus

Average model of stress-strain characteristics of non-ablated "control" swine esophagus muscle bundles (n=297). The maximum stress was 0.33 MPa and maximum Cauchy-stress was 0.72 MPa. The avulsion strain was 1.35.

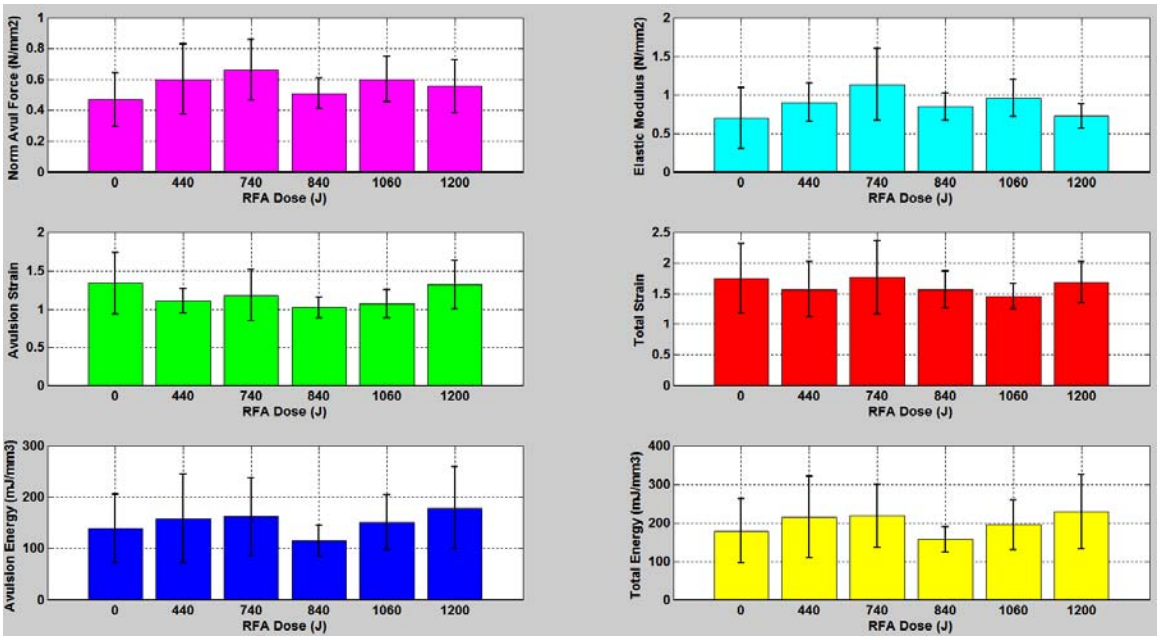

Figure 78: Dose effects of radiofrequency ablation (RFA) on biomechanical properties of swine esophagus muscle bundles

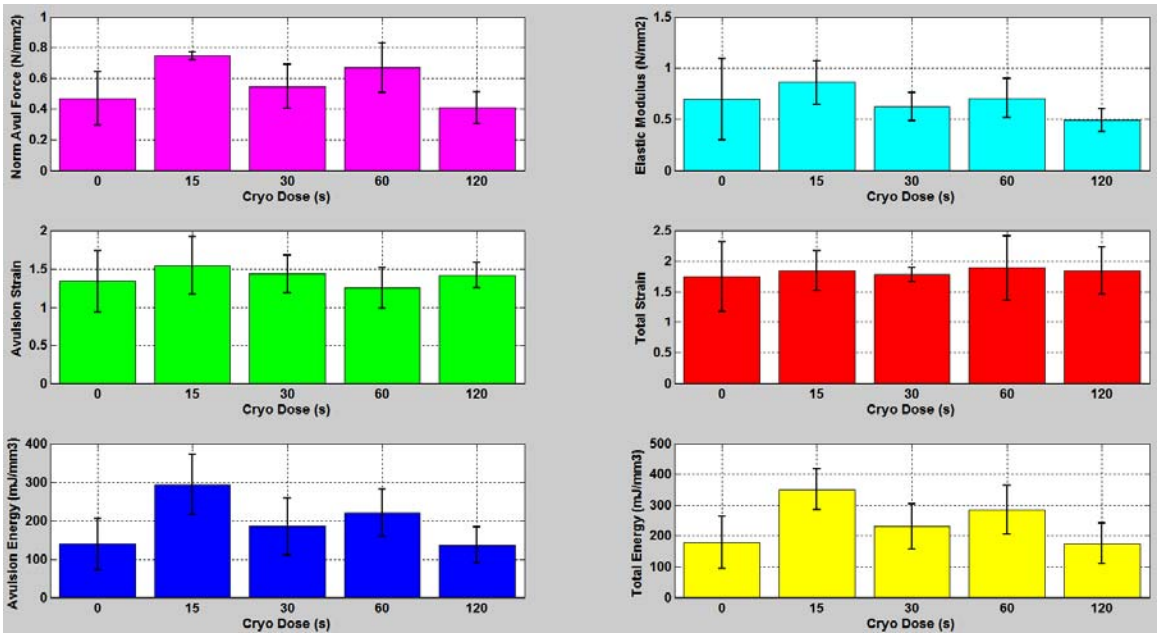

Figure 79: Dose effects of cryoablation (CRA) on biomechanical properties of swine esophagus muscle bundles

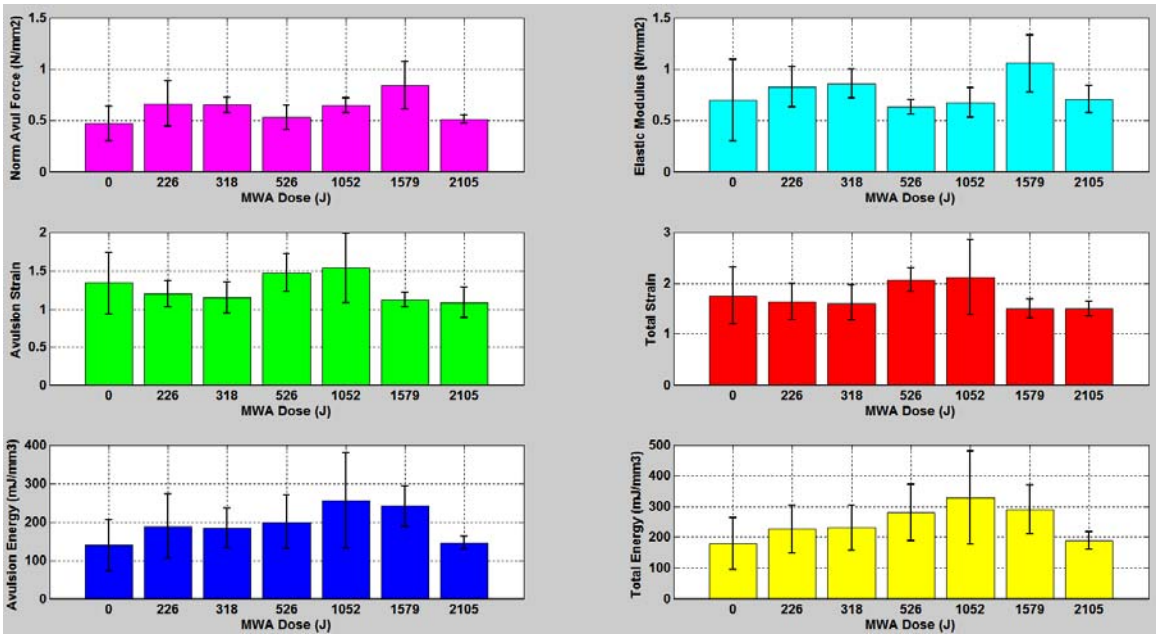

Figure 80: Dose effects of microwave ablation (MWA) on biomechanical properties of swine esophagus muscle bundles

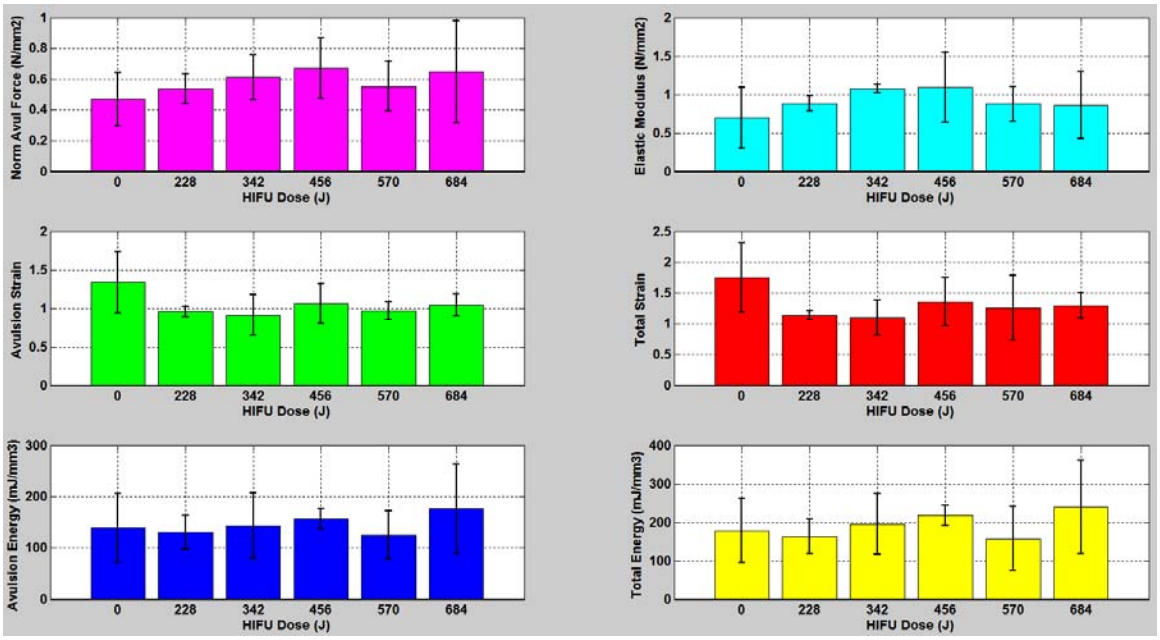

Figure 81: Dose effects of high-intensity focused ultrasound ablation (HIFU) on biomechanical properties of swine esophagus muscle bundles

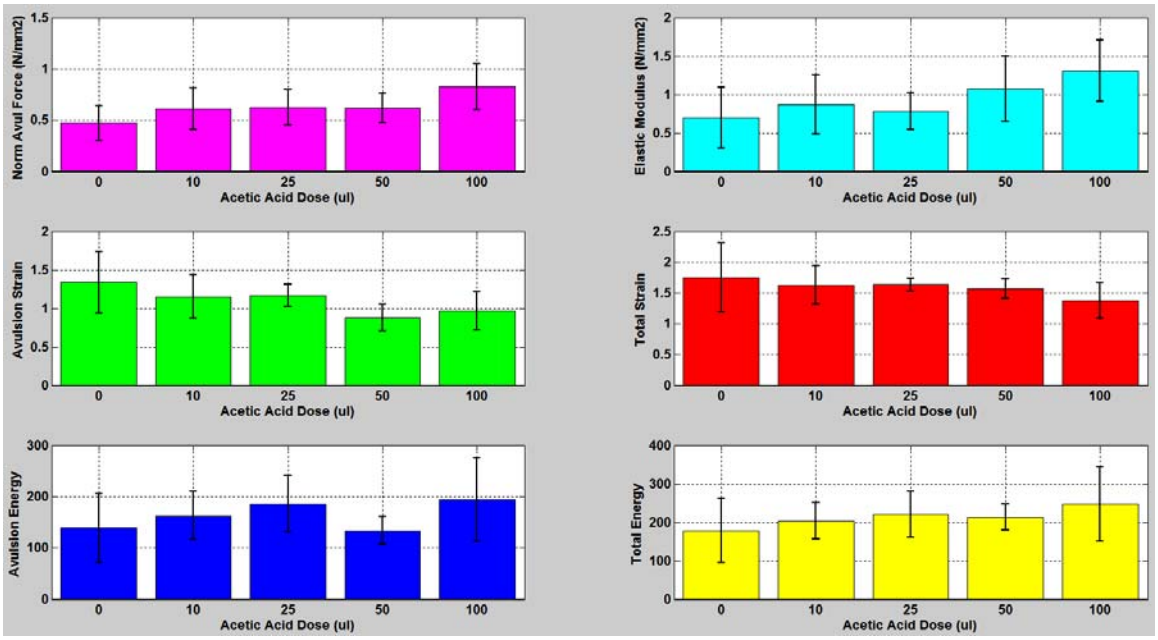

Figure 82: Dose effects of chemical ablation with acetic-acid on biomechanical properties of swine esophagus muscle bundles

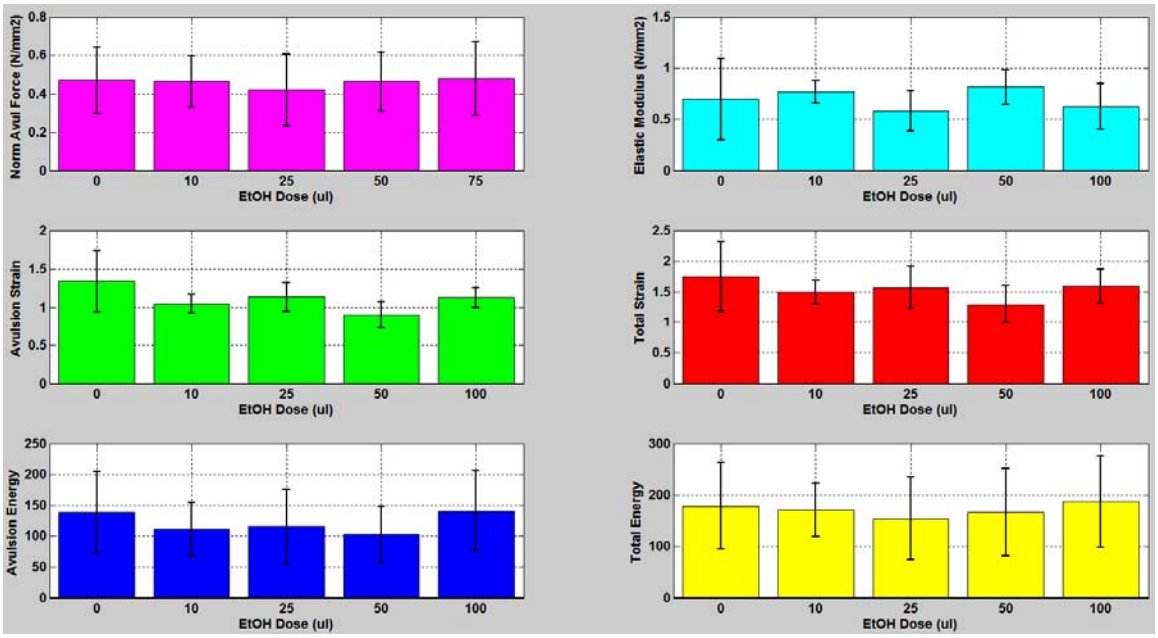

Figure 83: Dose effects of chemical ablation with ethanol on biomechanical properties of swine esophagus muscle bundles

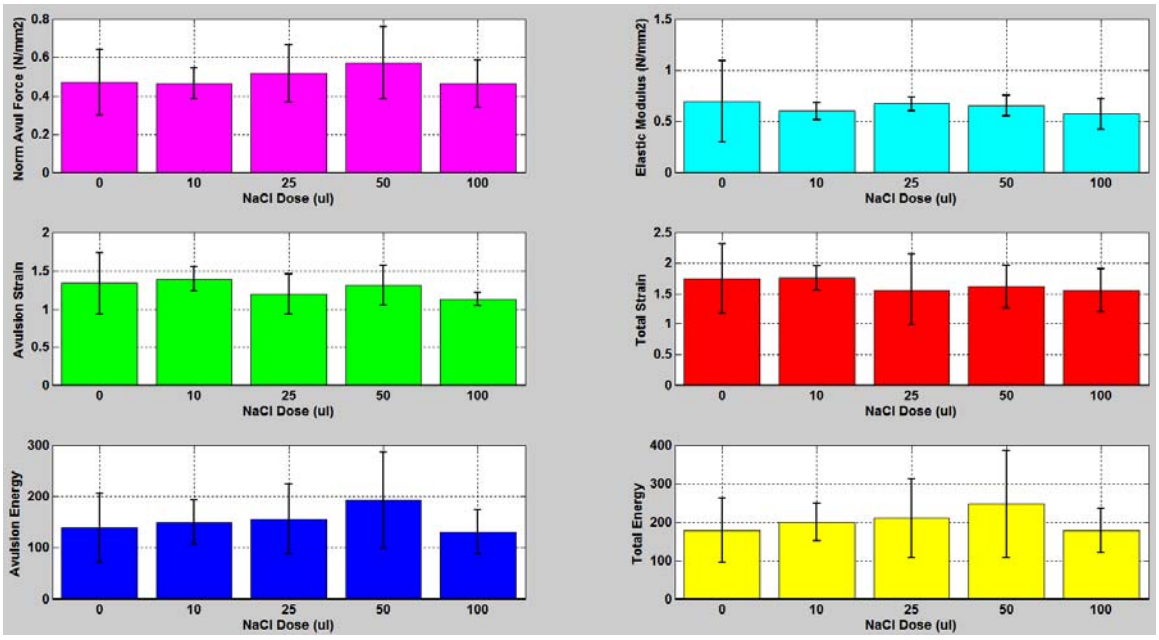

Figure 84: Dose effects of chemical ablation with sodium chloride on biomechanical properties of swine esophagus muscle bundles

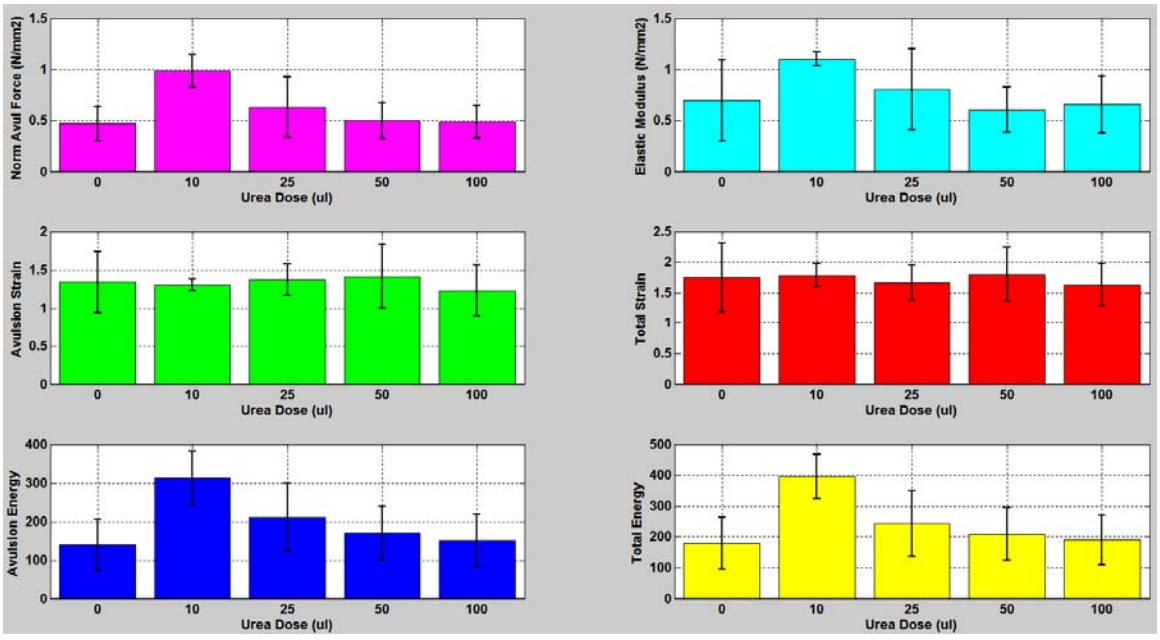

Figure 85: Dose effects of chemical ablation with urea on biomechanical properties of swine esophagus muscle bundles

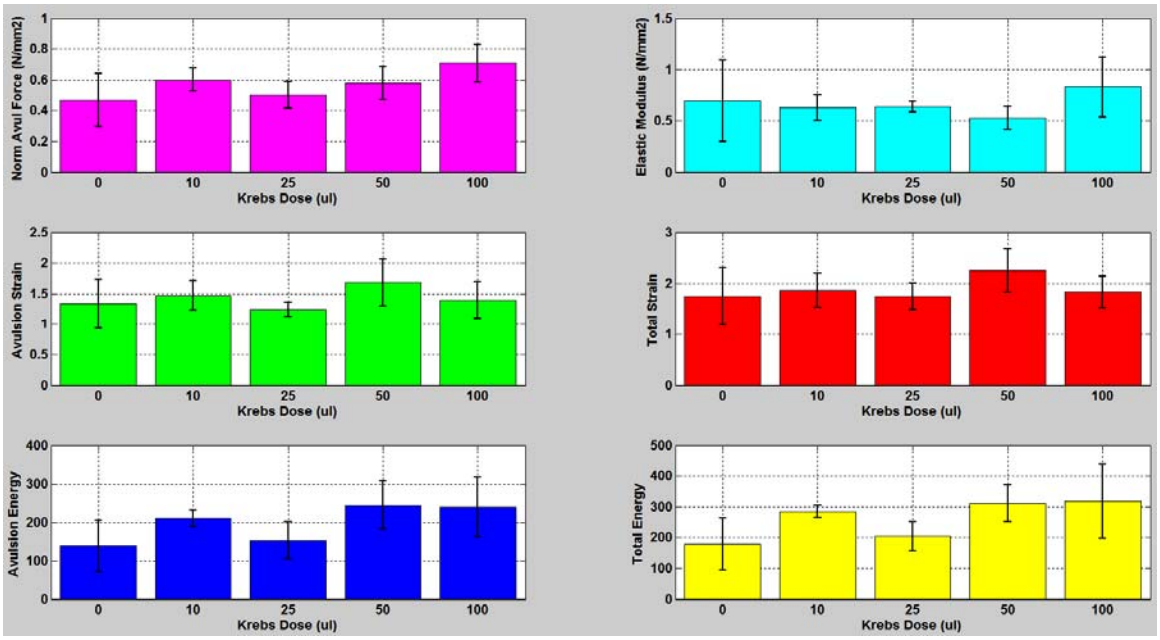

Figure 86: Dose effects of Krebs injections on biomechanical properties of swine esophagus muscle bundles

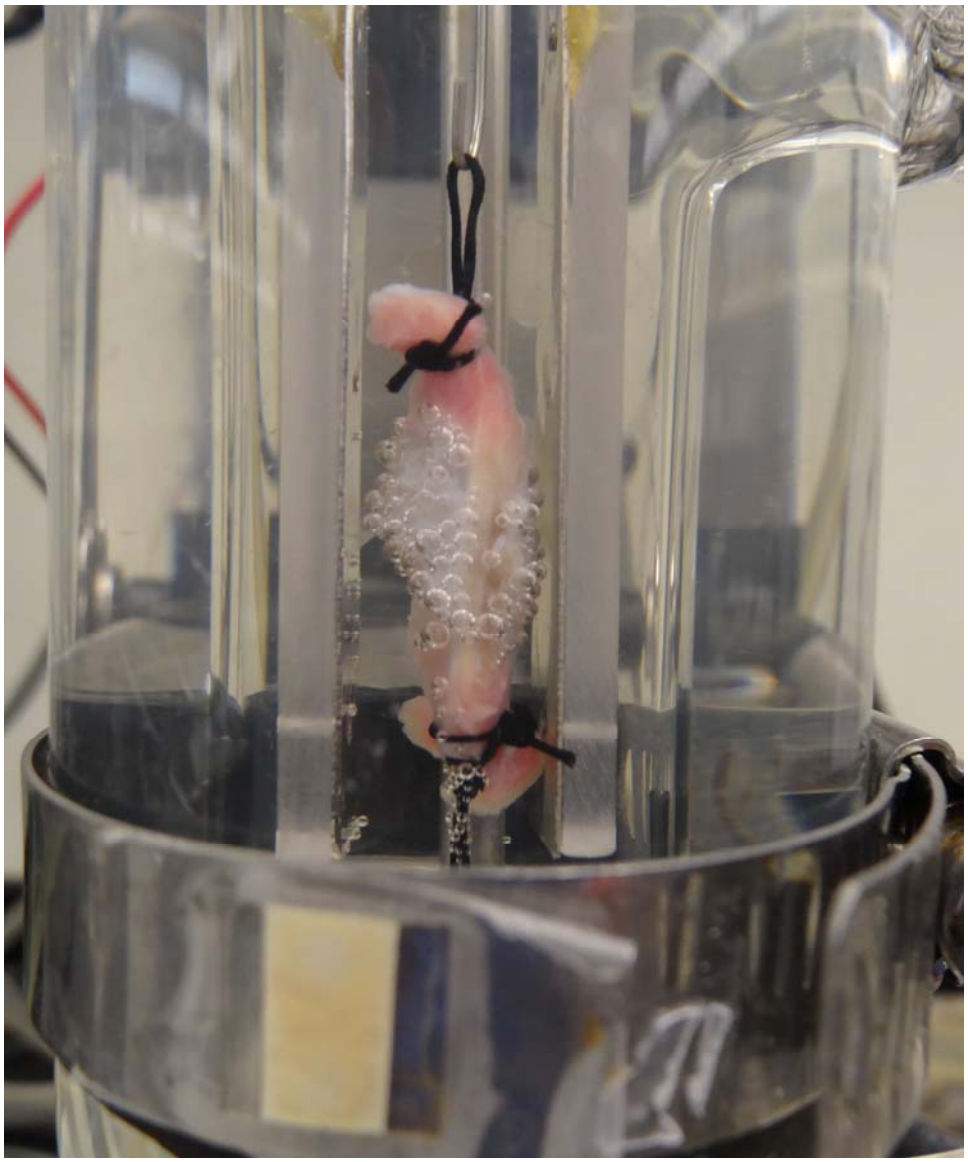

Figure 87: A swine esophagus muscle ablated with 50 µl of acetic acid
Microbubbles on the ablated region of the muscle bundle are caused by excessive dehydration, which further leads to tissue necrosis

Ablation Modality	# of Doses	# of Muscle Bundles	Length (mm)	Width (mm)	Thickness (mm)	Mass (mg)	Pre-Ablation Peak Force (grams)	Pre-Ablation Baseline Force (grams)
RFA	5	20	22.09 ± 2.16	3.87 ± 0.41	2.21 ± 0.31	196.21 ± 37.21	23.17 ± 11.55	2.38 ± 0.27
CRA	4	16	19.17 ± 2.49	4.05 ± 0.56	1.98 ± 0.24	214.38 ± 40.98	23.93 ± 6.46	2.54 ± 0.23
MWA	6	24	19.72 ± 2.96	3.84 ± 0.36	2.06 ± 0.18	180.00 ± 39.23	24.04 ± 7.33	2.34 ± 0.19
HIFU	5	20	21.46 ± 2.78	3.88 ± 0.60	2.08 ± 0.25	248.00 ± 46.29	28.24 ± 7.38	2.34 ± 0.32
Ac Acid	4	16	21.27 ± 2.22	3.80 ± 0.47	2.38 ± 0.31	198.13 ± 33.51	27.64 ± 6.29	2.43 ± 0.20
EtOH	4	16	18.94 ± 2.65	4.08 ± 0.40	2.21 ± 0.37	165.00 ± 23.09	26.80 ± 7.55	2.39 ± 0.12
NaCl	4	16	18.87 ± 2.50	4.64 ± 0.58	2.36 ± 0.39	242.50 ± 61.16	26.34 ± 5.19	2.51 ± 0.15
Urea	4	16	20.93 ± 3.56	3.82 ± 0.67	2.05 ± 0.22	183.13 ± 31.35	23.66 ± 5.41	2.50 ± 0.15
Krebs	4	16	19.14 ± 2.54	4.22 ± 0.54	2.29 ± 0.29	213.75 ± 47.03	21.84 ± 7.01	2.56 ± 0.10
Study Controls	N/A	8	22.76 ± 3.06	3.49 ± 0.47	2.05 ± 0.21	201.25 ± 40.16	28.41 ± 4.92	2.40 ± 0.22

Table 7: Mean ± SD characteristics of swine esophageal muscle bundles that underwent physiological testing in tissue baths (n=168)
A set of 4 muscle bundles were exposed to every ablation dose

Avulsion Location (%)	% Bottom Suture Breakage	% Center-Bottom Avulsions	% Center Avulsions	% Center-Top Avulsions	% Top Suture Breakage
Non-Ablated (Biomechanical) (n=347)	6.92% (n=24)	17.00% (n=59)	42.65% (n=148)	25.94% (n=90)	7.49% (n=26)
RFA (n=32)	9.38% (n=3)	18.75% (n=6)	43.74% (n=14)	9.38% (n=3)	18.75% (n=6)
CRA (n=16)	6.25% (n=1)	31.25% (n=5)	18.75% (n=3)	12.50% (n=2)	31.25% (n=5)
MWA (n=28)	0.00% (n=0)	7.14% (n=2)	82.15% (n=23)	7.14% (n=2)	3.57% (n=1)
HIFU (n=20)	5.00% (n=1)	5.00% (n=1)	50.00% (n=10)	25.00% (n=5)	15.00% (n=3)
Ac Acid (n=16)	0.00% (n=0)	18.75% (n=3)	37.50% (n=6)	31.25% (n=5)	12.50% (n=2)
EtOH (n=32)	18.75% (n=6)	15.63% (n=5)	31.25% (n=10)	15.63% (n=5)	18.74% (n=6)
NaCl (n=16)	12.50% (n=2)	25.00% (n=4)	12.50% (n=2)	18.75% (n=3)	31.25% (n=5)
Urea (n=32)	15.62% (n=5)	28.13% (n=9)	31.25% (n=10)	12.50% (n=4)	12.50% (n=4)
Krebs-Injected (n=16)	18.75% (n=3)	12.50% (n=2)	56.25% (n=9)	6.25% (n=1)	6.25% (n=1)
Study-Controls (n=8)	0.00% (n=0)	0.00% (n=0)	75.00% (n=6)	25.00% (n=2)	0.00% (n=0)

Table 8: Tabulation of the avulsion location of swine esophagus muscle bundles (n=563) as a percentage for each ablative modality

	Initial Cross-sectional Area (mm^2)	Initial Volume (mm^3)	Avulsion Force (N/mm^2)	Elastic Modulus (N/mm^2)	Avulsion Strain ($\Delta l/L$)	Total Strain ($\Delta l/L$)	Avulsion Energy (mJ/mm^3)	Total Energy (mJ/mm^3)
Biomech (n=297)	9.99±2.95	177.67±55.58	0.47±0.17	0.70±0.40	1.35±0.40	1.78±0.57	138.89±62.85	179.31±79.33
RF (n=23)	9.65±2.40	188.35±49.06	0.59±0.17	0.91±0.32	1.13±0.21	1.65±0.37	156.81±63.12	207.25±69.96
CRA (n=10)	9.19±2.00	158.53±37.55	0.57±0.13	0.67±0.22	1.35±0.26	1.86±0.37	189.57±50.10	244.86±61.45
MWA (n=27)	8.29±1.64	143.66±37.32	0.64±0.17	0.80±0.21	1.25±0.28	1.75±0.41	201.24±76.25	255.88±92.19
HIFU (n=12)	9.76±2.33	213.48±52.18	0.61±0.20	0.93±0.30	1.03±0.15	1.27±0.30	152.59±53.04	198.82±76.09
Ac Acid (n=14)	8.57±2.21	171.98±42.22	0.68±0.18	1.01±0.33	1.02±0.20	1.52±0.20	172.67±58.80	220.96±61.84
EtOH (n=20)	8.84±2.17	162.33±38.82	0.55±0.16	0.78±0.22	1.07±0.17	1.55±0.26	147.97±52.88	208.00±64.00
NaCl (n=9)	10.13±1.69	171.61±38.93	0.58±0.12	0.66±0.08	1.33±0.20	1.76±0.37	191.12±59.11	248.93±92.18
Urea (n=23)	9.83±1.93	188.32±38.62	0.63±0.22	0.80±0.27	1.30±0.33	1.71±0.36	201.57±80.04	251.28±95.91
Krebs-Injected (n=12)	10.54±1.16	188.47±25.02	0.59±0.13	0.67±0.22	1.43±0.32	1.90±0.38	201.89±59.08	263.04±65.46
Study-Controls (n=7)	8.77±1.83	170.42±33.70	0.57±0.10	0.80±0.23	1.15±0.29	1.54±0.33	152.06±44.97	201.90±41.99

Table 9: Mean ± SD dimensional characteristics and biomechanical parameters of swine esophagus muscle bundles that avulsed at or near the center of the muscle bundle

	% Diff Avulsion Force	% Diff Elastic Modulus	% Diff Avulsion Strain	% Diff Total Strain	% Diff Avulsion Energy	% Diff Total Energy
RF (n=23)	**+25.83% p=0.0010**	**+30.52% p=0.0124**	**-16.36% p=0.0088**	-6.98% p=0.3032	+12.90% p=0.1888	+15.58% p=0.1020
CRA (n=10)	+21.71% p=0.0597	-3.74% p=0.8360	-0.35% p=0.9701	+4.47% p=0.6605	**+36.49% p=0.0122**	**+36.56% p=0.0102**
MWA (n=27)	**+36.31% p<0.05**	+15.39% p=0.1654	-7.39% p=0.2027	-1.79% p=0.7758	**+44.89% p<0.05**	**+42.70% p<0.05**
HIFU (n=12)	**+29.53% p=0.0059**	**+33.98% p=0.0414**	**-24.24% p=0.0048**	**-28.52% p=0.0023**	+9.86% p=0.4574	+10.88% p=0.4036
Ac Acid (n=14)	**+43.81% p<0.05**	**+45.35% p=0.0035**	**-24.45% p=0.0022**	-14.78% p=0.0854	**+24.32% p=0.0497**	+23.23% p=0.0538
EtOH (n=20)	**+17.25% p=0.0376**	+12.55% p=0.3292	**-20.82% p=0.0018**	-13.06% p=0.0705	+6.54% p=0.5283	+16.00% p=0.1146
NaCl (n=9)	+22.66% p=0.0615	-4.56% p=0.8103	-1.44% p=0.8840	-1.16% p=0.9139	**+37.61% p=0.0145**	**+38.83% p=0.0103**
Urea (n=23)	**+33.84% p<0.05**	+14.26% p=0.2381	-4.01% p=0.5249	-3.84% p=0.5704	**+45.13% p<0.05**	**+40.14% p<0.05**
Krebs-Injected (n=12)	**+25.36% p=0.0163**	-3.45% p=0.8346	+5.31% p=0.5379	+6.57% p=0.4807	**+45.37% p<0.05**	**+46.70% p<0.05**
Study-Controls (n=7)	+19.85% p=0.1470	+14.39% p=0.5051	-14.82% p=0.1865	-13.31% p=0.2729	+9.49% p=0.5821	+12.60% p=0.4537

Table 10: Percent change in biomechanical properties of swine esophagus muscle bundles post ablation with different ablative modalities

All values are with respect to controls (n=297, non-ablated) muscle bundles. A positive value indicates an increase and a negative value a decrease with respect to controls. Percent change in avulsion force, elastic modulus, strain, and energy are shown along with individual statistical significance ($p<0.05$, marked in bold).

5. Comparative Assessment of Physiological and Biomechanical Properties of Human Esophagus in Response to Therapeutic Ablative Treatments

Preface

We plan to submit this paper to the Journal of Cardiothoracic Surgery (2014).

Ashish Singal
University of Minnesota
singa009@umn.edu

Charles L. Soule
University of Minnesota
soule005@umn.edu

Paul A. Iaizzo (Corresponding Author)
University of Minnesota
420 Delaware St. SE
B172 Mayo, MMC 195
Minneapolis, MN 55455
T: 612-624-7912; F: 612-624-2002
iaizz001@umn.edu

Introduction

Our lab has unique research collaboration with LifeSource (St. Paul, MN). LifeSource is an organization with a mission of saving lives by transplanting donated organs and tissues in patients needing a transplant. This collaboration allowed us to perform research on fresh human tissue (obtained within few hours of death) that was deemed non-transplantable. We utilized this unique opportunity by performing research on human esophagus that was received along with the heart-lung bloc. Collateral injury to the esophagus is a known complication of catheter ablations performed in the left atrium and left pulmonary veins. In order to better understand the esophageal response to ablative therapies, it is essential to understand its physiological and biomechanical properties. Thus, in this paper, we detail the physiological and biomechanical results obtained after ablating the human esophagus with 3 different ablative modalities (RFA, CRA, and HIFU). We also utilized the squamous epithelium dissected from human esophagi to compare the biomechanical properties of both the muscularis and squamous epithelium layers. Once the techniques and methodologies were perfected, experiments were performed to study the tissue response to above mentioned ablative modalities.

Methods

Tissue Preparation

Fresh human tissue biopsies of esophagus (n=7) were obtained through research collaboration with LifeSource (St. Paul, MN). Following dissectional separation from the heart-lung bloc, the esophagus tissue was pinned in a dissection dish, dissected in oxygenated, temperature-controlled Krebs-Ringer solution. The muscle bundle preparation involved initially cleaning up the biopsy by removing excess fat and surrounding connective tissue so that well defined muscle bundles could be prepared. The external muscularis and internal squamous epithelium layers were first separated and then tissue bundles of both the muscularis layer and squamous epithelial layer were prepared. Muscle bundles of muscularis layer were prepared along the internal circular layer of muscle fibers of muscularis externa in an identifiable cuboidal shape having lengths of 15 to 25 mm, widths of 3 to 5 mm, and thickness of 1.5 to 3 mm. Tissue bundles of squamous epithelial layer were prepared in an identifiable cylindrical shape having lengths of 15 to 25 mm and diameters of 1.5 to 3 mm. The physiological testing was performed using tissue baths and biomechanical testing was performed using a uniaxial testing machine as described in detail in Chapter 2 (submitted for publication). Note that the squamous epithelium is a non-contractile tissue; hence, only biomechanical tests were performed on these tissue bundles. However, both physiological and biomechanical tests were

performed on the muscularis muscle bundles. The esophageal tissue response to the following three different ablation modalities was investigated:

Radiofrequency Ablation: RFA (484 KHz sinusoidal waveform) at four different ablation doses were studied: 55 °C, 60 °C, 65 °C, and 70 °C (corresponding to 534 J, 750 J, 972 J, and 1188 J energy levels, respectively).

Cryoablation: Cryoablation exposure (operated in the clinical mode, approximately -75 °C) at four different ablation doses were studied: 15 sec, 30 sec, 60 sec, and 120 sec.

HIFU Ablations: HIFU ablations (2.5 MHz sinusoidal waveform, 80% duty cycle) at four different ablation doses were studied: 272 J, 352 J, 448 J, and 480 J.

Data Analyses

Statistical analyses were performed using ANOVA and the Tukey test to identify differences in peak forces and baseline forces for all ablation modalities where a $p<0.05$ is considered statistically significant. All data are presented as mean $\pm$ standard deviation.

Results

Figure 88 shows a representative example of human esophageal muscularis muscle bundle contraction elicited by electro-mechanical stimulation. Also shown in the figure is a value of typical resting muscle tension and peak force that was generated from muscle bundles mounted in tissue baths. Figure 89 shows a comparison between the swine and human esophageal electro-mechanical response. The contraction duration was approximately 0.7 sec for swine esophagus samples and approximately 7 sec for human esophagus samples. Contrasting differences were observed in the electro-mechanical response of human and swine esophagus muscle bundles. Depending on which section of the human esophagus (superior, middle, or inferior) the muscle bundles were prepared, different response was observed, representative examples are shown in Figure 90. These differences may be attributed to the gradual transition and spatial distribution of the skeletal, smooth, and mixed muscle fibers, and also due to the differences in motor innervation of neural supply along the entire length of the human esophagus [1,2,3]. Figure 91 and Figure 93 show the comparison of stress-strain characteristics of esophageal muscularis layer and squamous epithelial layer, respectively, between the two species. A comparison of biomechanical parameters of both species, and for both layers was also done which is shown in Figure 92 and Figure 94. In general, biomechanical properties of swine were always higher than that of human tissue.

A total number of 48 muscle bundles were studied for physiological assessment in tissue baths as shown in Table 11. The table summarizes the muscle bundle characteristics and allocations to different ablative modalities. As can be seen in this table, the dimensional characteristics of all muscle bundles were similar across different treatment groups. However, a large variation was observed in the peak forces which were attributed to tissue viability. The esophagus along with the heart-lung bloc was received in an ice package. It is conceivable that the longer the tissue sat in the package, the longer the tissue sustained injury due to cell death. Hence, this could have contributed to the high variability in initial peak forces and baseline forces of muscle bundles observed with human samples.

Discussions

It was observed that the avulsion force and elastic modulus increased for both the muscularis and squamous epithelium layers as a result of RFA, but decreased as a result of CRA. Moreover, the avulsion energy (which is a combination of peak force and avulsion stretch) increased following exposure to RFA and decreased following exposure to CRA. These results could have important implications in terms of perforations during cardiac ablation procedures. A reduction in avulsion force and energy required to cause avulsions means that the tissue would be susceptible to tearing/perforations with forces smaller than when ablations were initiated.

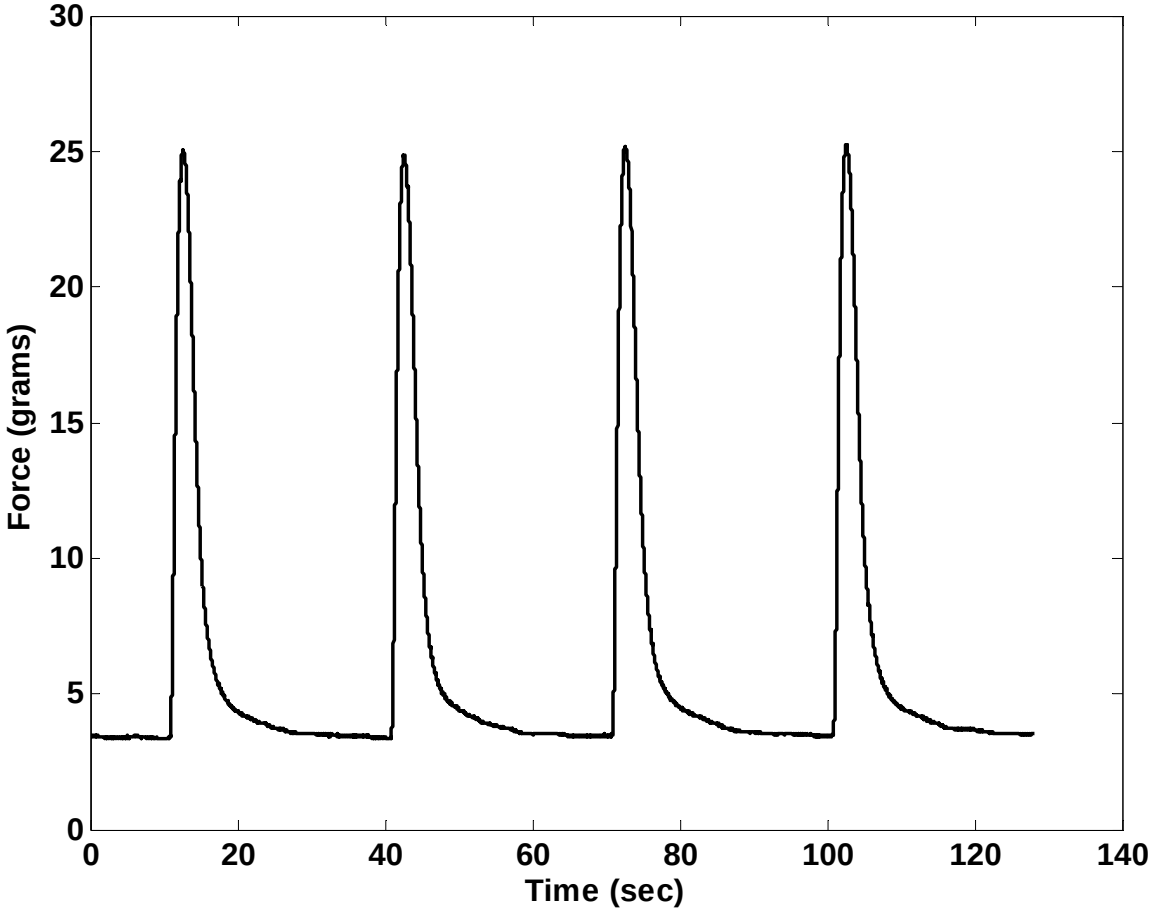

Figure 88: Human esophagus electro-mechanical response

A representative example of human esophageal muscularis muscle bundle contraction elicited by electro-mechanical stimulation. This muscle bundle has a resting muscle tension of approximately 3.5 grams and is generating a peak force of approximately 21.5 grams. The contraction duration is approximately 10 sec.

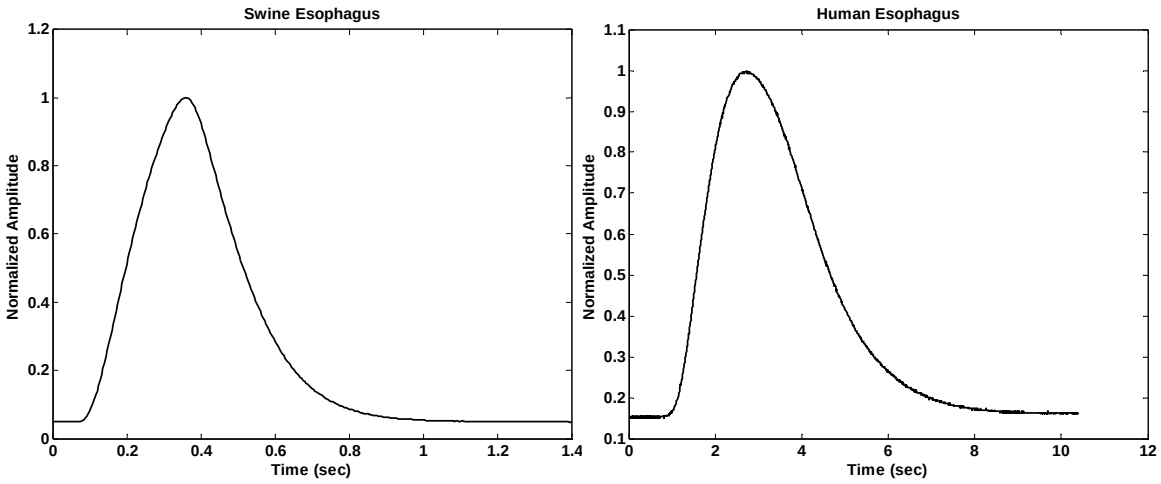

Figure 89: Comparison of electro-mechanical response of swine and human esophageal muscle bundles

The data is normalized to the peak force of individual muscle bundle samples. Both the swine and human esophageal muscle bundles were stimulated once every 30 seconds with a train of 8 square-wave pulses of 1.0 ms duration and a pulse interval of 30 ms. The approximately contraction duration of swine esophagus was 0.7 sec, whereas, the approximate contraction duration of human esophagus was 7 seconds.

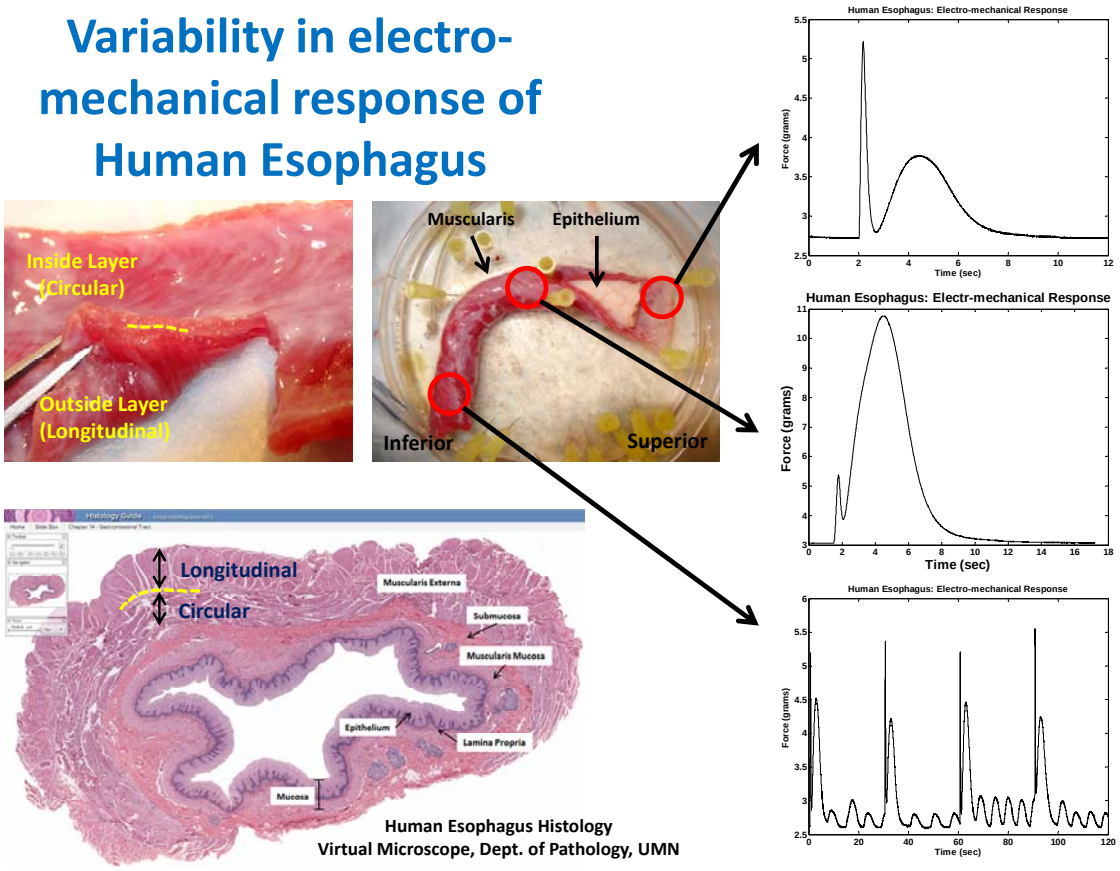

Figure 90: Variability in electro-mechanical response of human esophagus

Variability in the electro-mechanical response of human esophagus was observed while performing tissue bath studies. This variability could be attributed to a number of reasons, for example, (1) the spatial distribution (gradual transition) of skeletal, smooth, and mixed muscle fibers along the entire length of the human esophagus, (2) differences in motor neural supply to the esophagus (striated muscles of the human esophagus are innervated by the lower motor neurons in the brain stem, whereas, smooth muscle are innervated by the nerve fibers that originate in the dorsal motor nucleus of the vagus). Nevertheless, a thorough understanding of this anatomic and electrical variability is crucial to assessing differences in species, designing medical devices, and measuring esophageal response to ablative therapies.

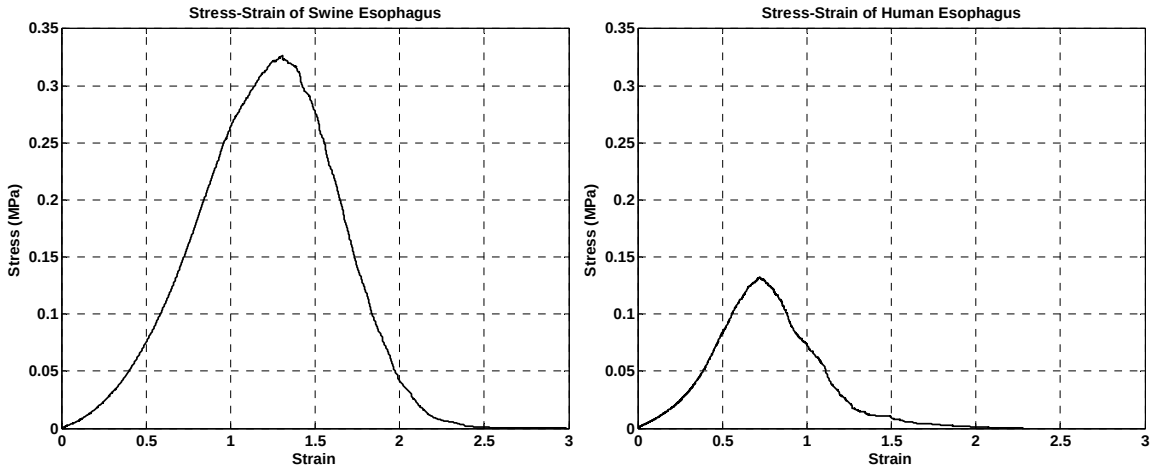

Figure 91: Stress-Strain response of swine and human esophagus muscularis layer

Average stress-strain model of non-ablated samples from both species was created. Characteristic differences between the two species were observed, where stress-strain behavior of swine was consistently higher than human samples.

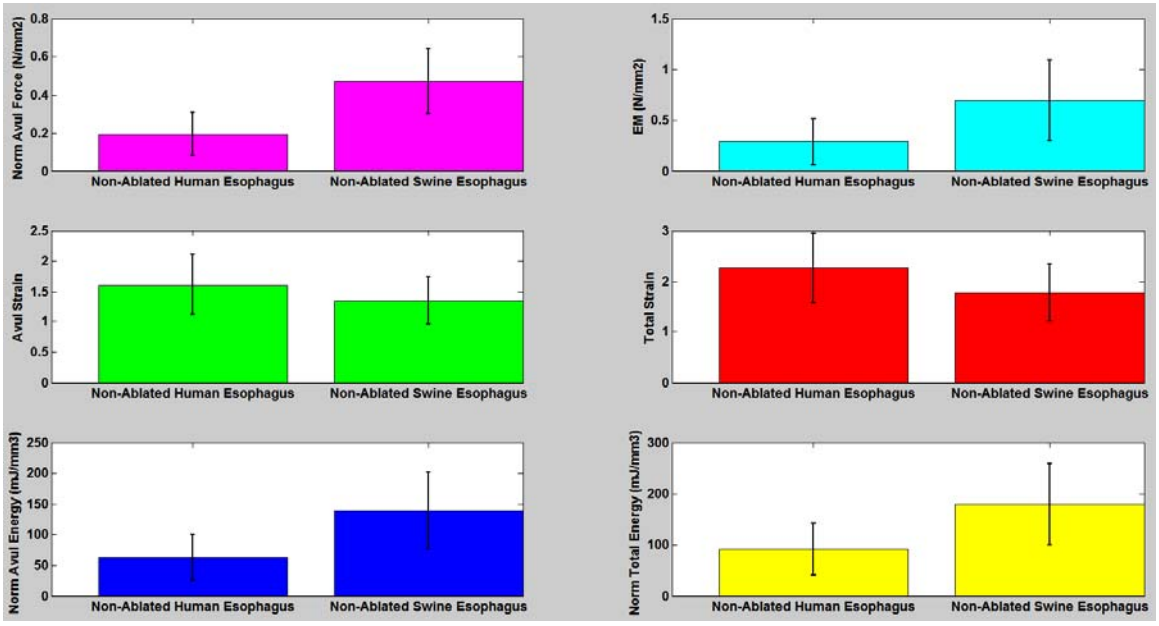

Figure 92: Comparative assessment of human and swine esophagus biomechanical properties of muscularis layer

With respect to the human values, the percent change in swine values were: (1) avulsion force (+141.50%), (2) elastic modulus (+140.81%), (3) avulsion strain (-15.77%), (4) total strain (-21.44%), (5) avulsion energy (+119.95%), (6) total energy (+95.54%). All values were statistically significant.

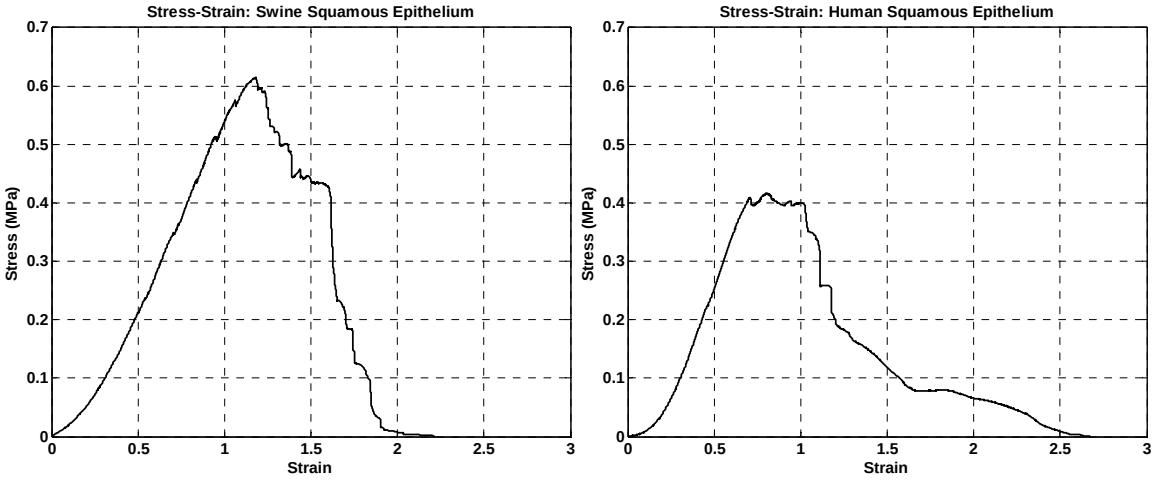

Figure 93: Stress-Strain response of swine and human esophagus squamous epithelium layer

Average stress-strain model of non-ablated samples from both species was created. Characteristic differences between the two species were observed, where stress-strain behavior of swine was consistently higher than human samples.

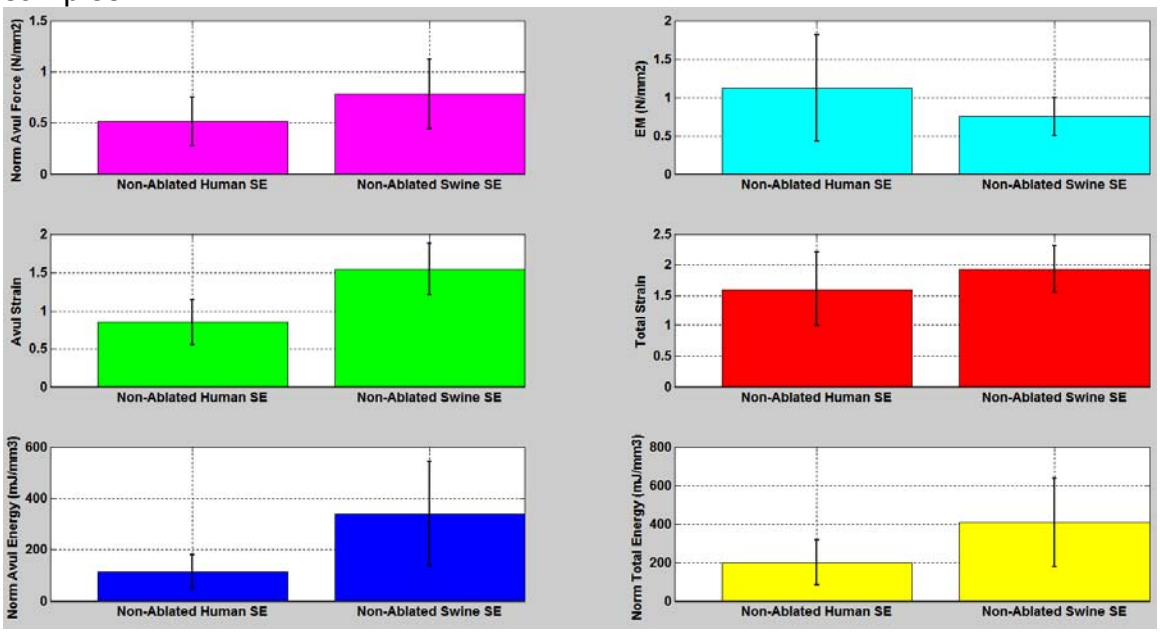

Figure 94: Comparative assessment of human and swine esophagus biomechanical properties of squamous epithelium layer

With respect to the human values, the percent change in swine values were: (1) avulsion force (+51.50%), (2) elastic modulus (-32.88%), (3) avulsion strain (+84.02%), (4) total strain (+21.31%), (5) avulsion energy (+198.23%), (6) total energy (+104.56%). All values were statistically significant.

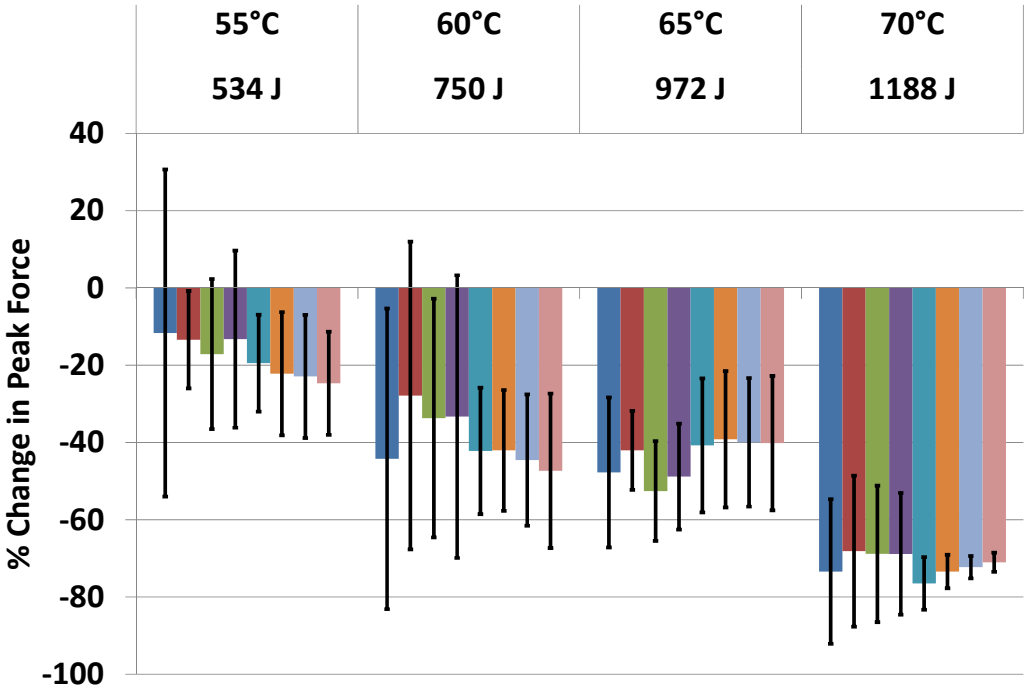

Figure 95: Dose effects of percent change in peak force of human esophagus post RFA

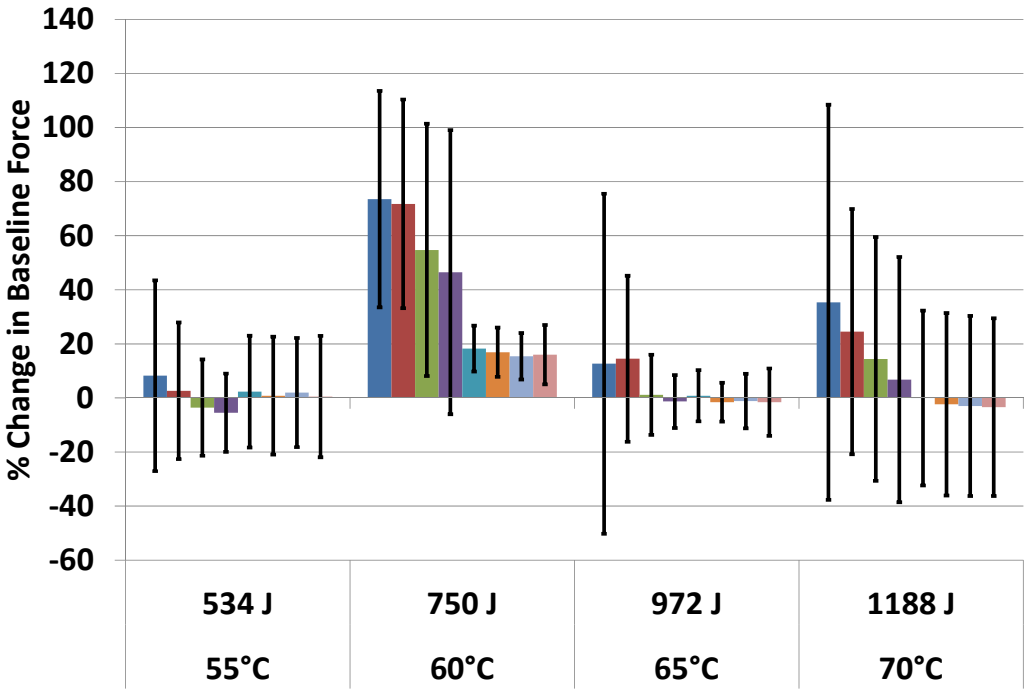

Figure 96: Dose effects of percent change in baseline force of human esophagus post RFA

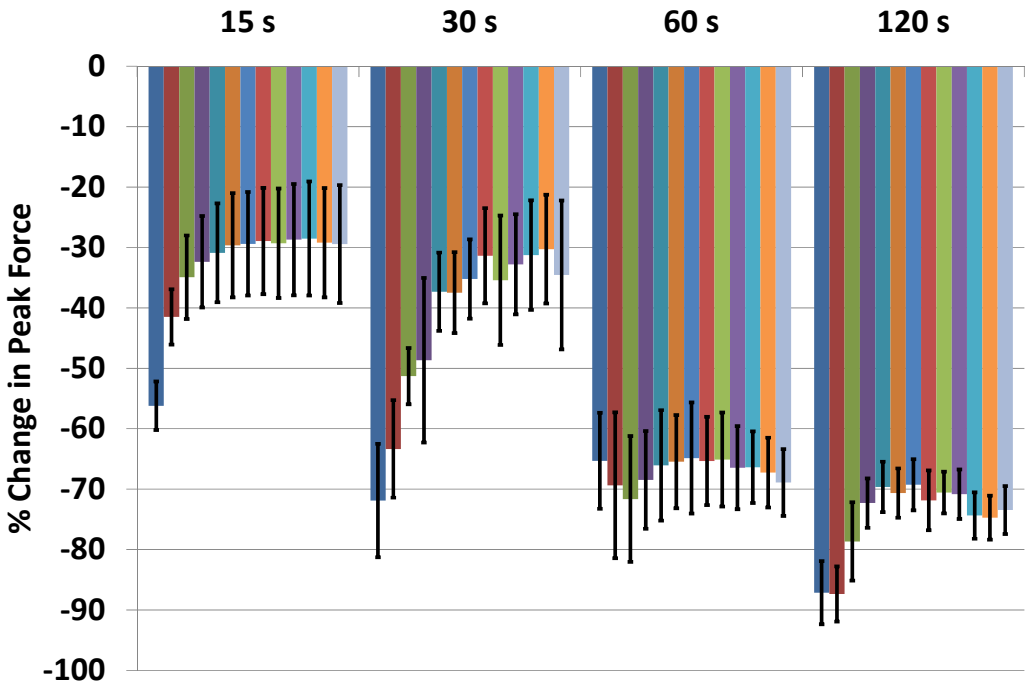

Figure 97: Dose effects of percent change in peak force of human esophagus post CRA

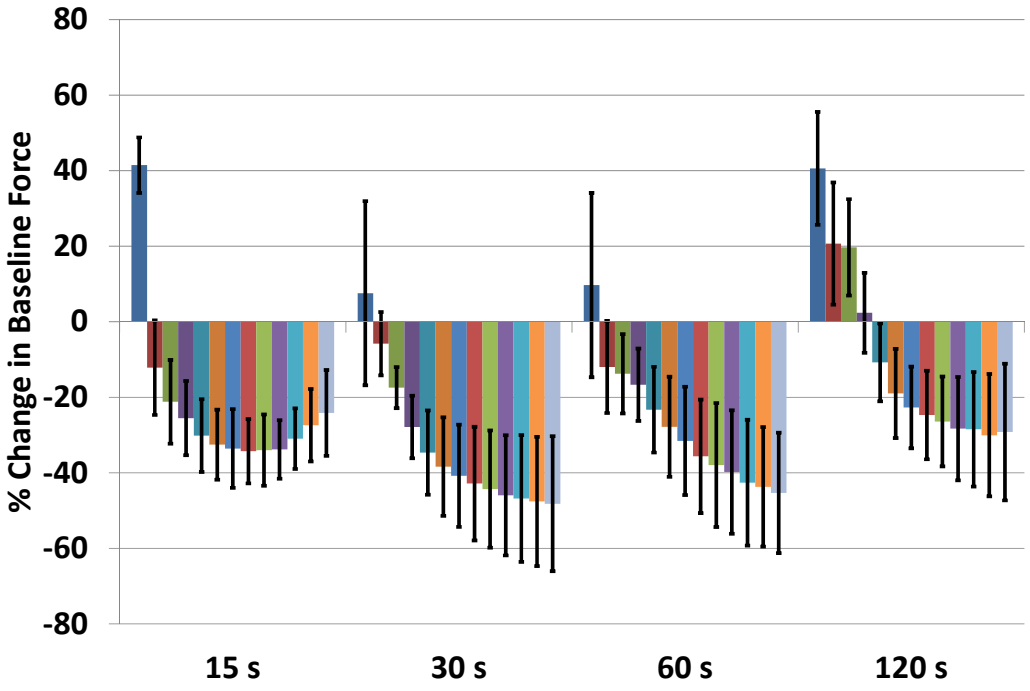

Figure 98: Dose effects of percent change in baseline force of human esophagus post CRA

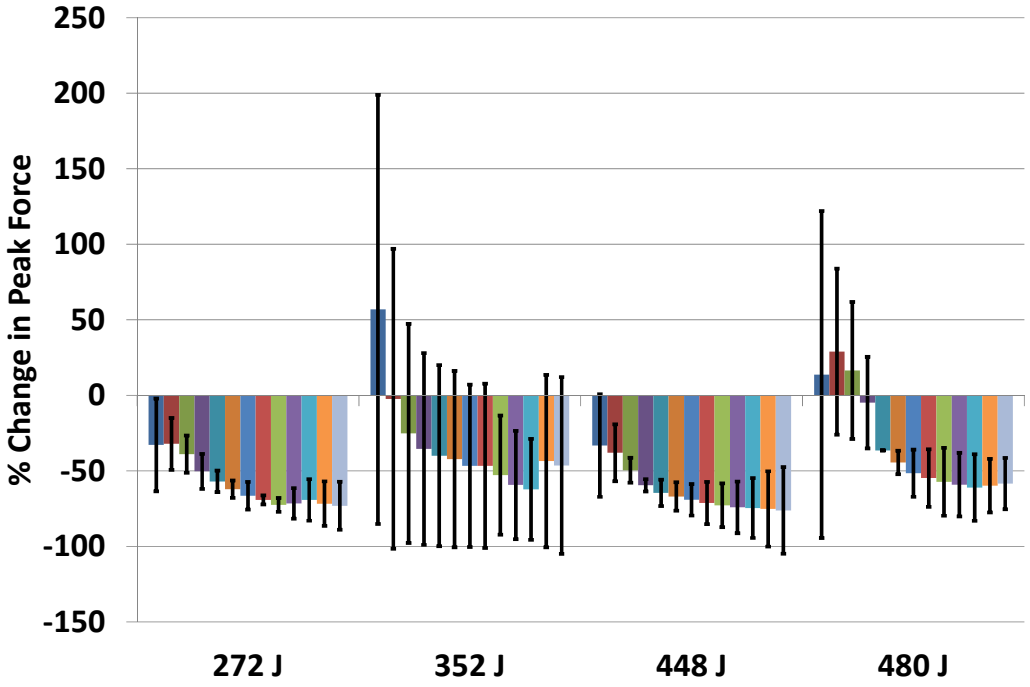

Figure 99: Dose effects of percent change in peak force of human esophagus post HIFU ablation

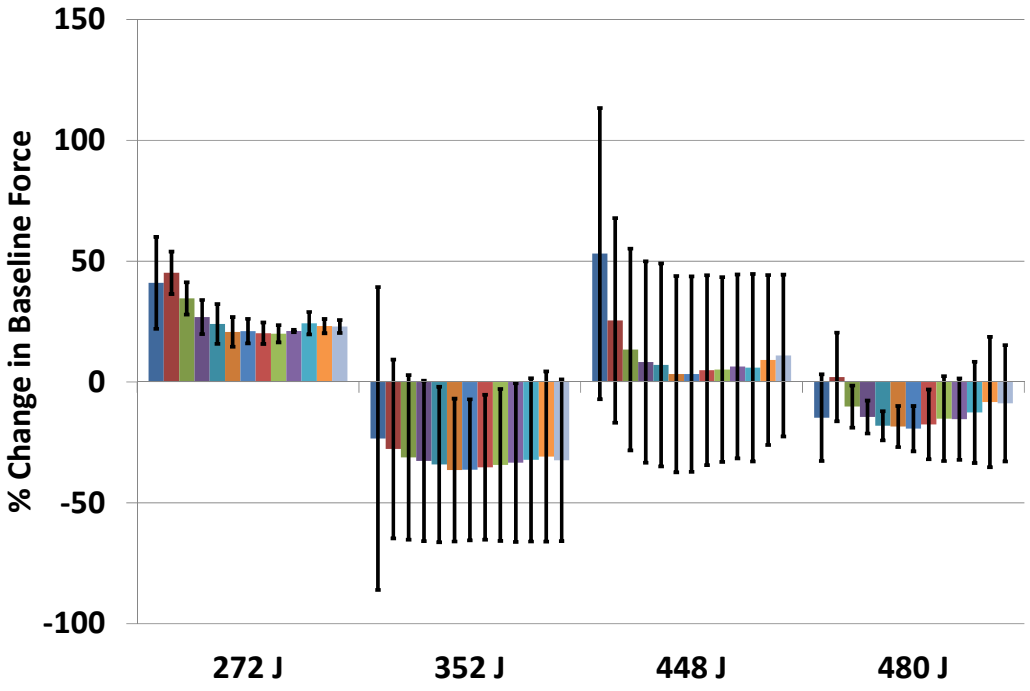

Figure 100: Dose effects of percent change in baseline force of human esophagus post HIFU ablation

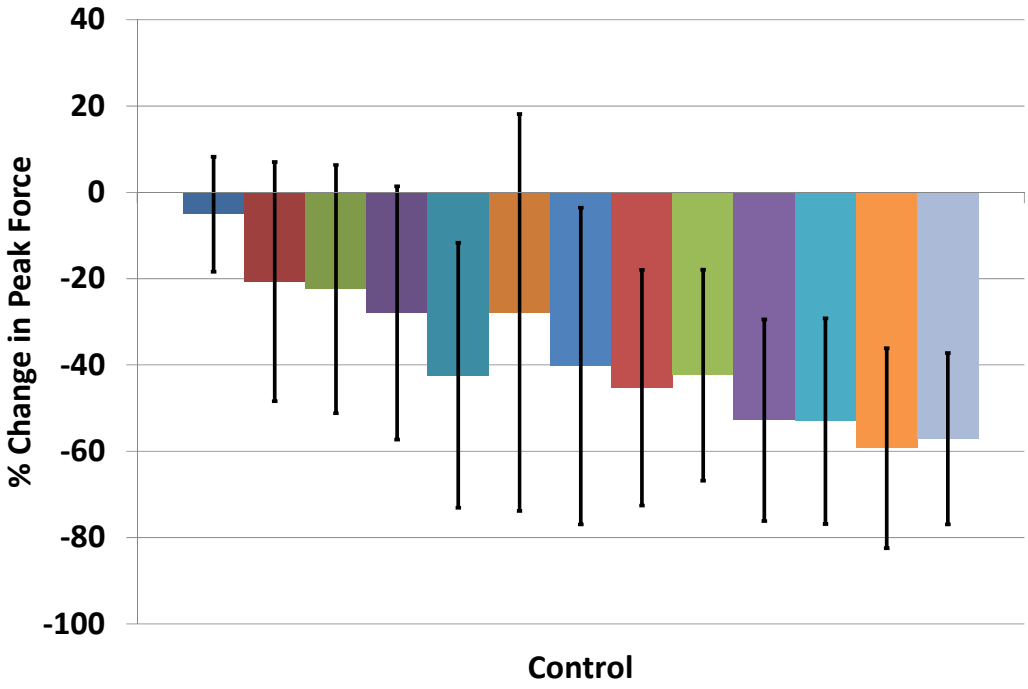

Figure 101: Percent change in peak force of "control" human esophagus muscle bundles

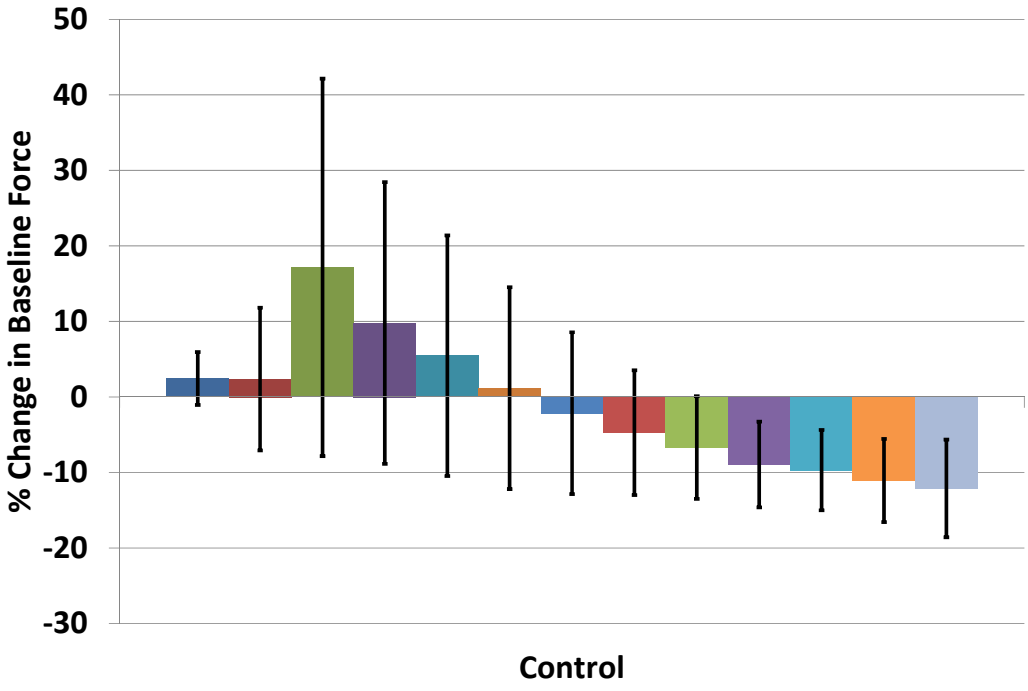

Figure 102: Percent change in baseline force of "control" human esophagus muscle bundles

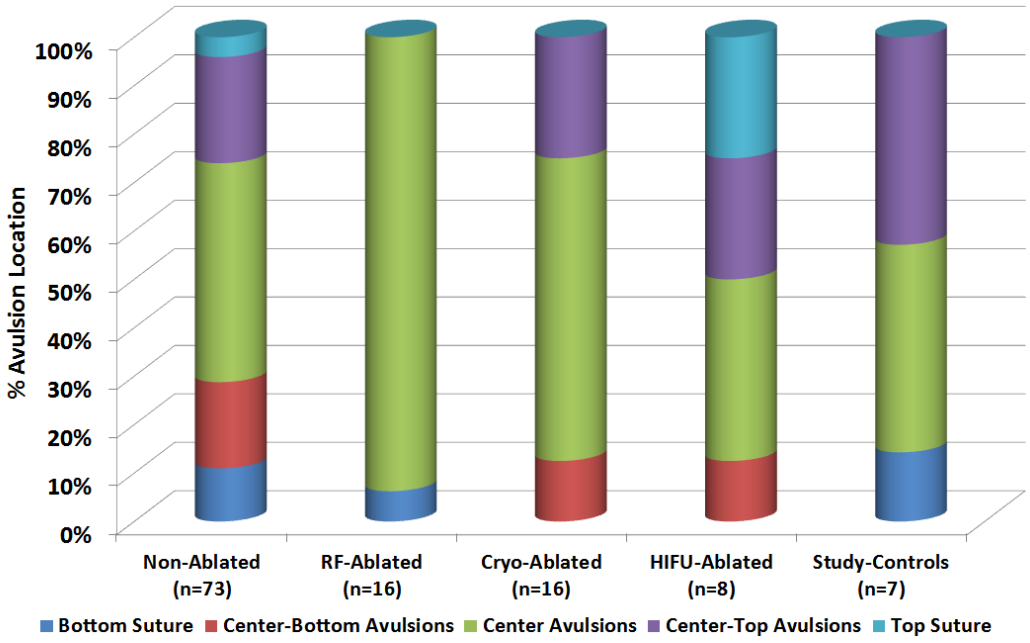

Figure 103: Avulsion location for each treatment displayed as percentage for all human esophagus muscle bundles tested for biomechanical assessment

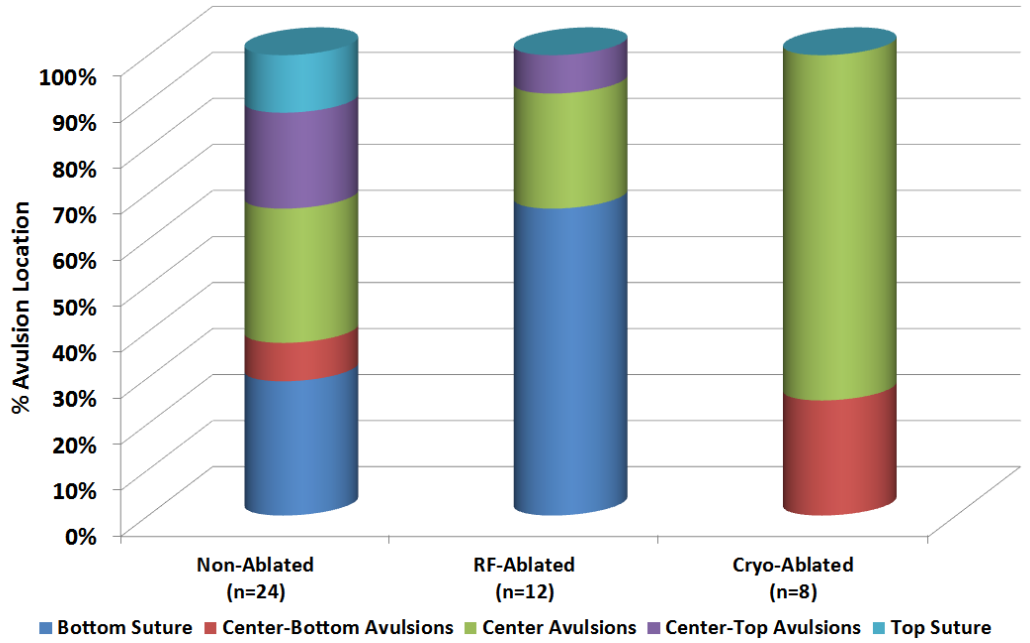

Figure 104: Avulsion location for each treatment displayed as percentage for all human esophageal squamous epithelium tissue bundles tested for biomechanical assessment

Ablation Modality	# of Doses	# of Muscle Bundles	Length (mm)	Width (mm)	Thickness (mm)	Mass (mg)	Pre-Ablation Peak Force (grams)	Pre-Ablation Baseline Force (grams)
RFA	4	16	16.18 ± 2.79	3.88 ± 0.52	2.01 ± 0.31	191.07 ± 53.36	6.97 ± 5.39	1.88 ± 0.65
CRA	4	16	28.15 ± 5.11	4.68 ± 0.51	2.61 ± 0.39	426.88 ± 99.51	12.40 ± 5.47	2.70 ± 0.82
HIFU	4	8	19.21 ± 4.45	4.70 ± 0.80	2.49 ± 0.38	278.10 ± 107.56	2.50 ± 1.71	1.98 ± 0.34
Study Controls	N/A	8	14.57 ± 6.80	4.49 ± 0.78	2.65 ± 0.17	254.50 ± 146.20	1.76 ± 1.80	2.31 ± 0.98

Table 11: Mean ± SD characteristics of human esophageal muscle bundles that underwent physiological testing in tissue baths (n=48)

A set of 4 muscle bundles were exposed to RFA and CRA ablation modalities and a set of 2 muscle bundles were exposed to the HIFU ablation modality.

Avulsion Location (%)	% Bottom Suture Breakage	% Center-Bottom Avulsions	% Center Avulsions	% Center-Top Avulsions	% Top Suture Breakage
Muscularis Layer Muscle Bundles					
Non-Ablated (Biomechanical) (n=73)	10.96% (n=8)	17.81% (n=13)	45.21% (n=33)	21.92% (n=16)	4.10% (n=3)
RFA (n=16)	6.25% (n=1)	0.00% (n=0)	93.75% (n=15)	0.00% (n=0)	0.00% (n=0)
CRA (n=16)	0.00% (n=0)	12.50% (n=2)	62.50% (n=10)	25.00% (n=4)	0.00% (n=0)
HIFU (n=8)	0.00% (n=0)	12.50% (n=1)	37.50% (n=3)	25.00% (n=2)	25.00% (n=2)
Study-Controls (n=7)	14.28% (n=1)	0.00% (n=0)	42.86% (n=3)	42.86% (n=3)	0.00% (n=0)
Squamous Epithelium Layer Tissue Bundles					
Non-Ablated (Biomechanical) (n=24)	29.17% (n=7)	8.33% (n=2)	29.17% (n=7)	20.83% (n=5)	12.50% (n=3)
RFA (n=12)	66.67% (n=8)	0.00% (n=0)	25.00% (n=3)	8.33% (n=1)	0.00% (n=0)
CRA (n=8)	0.00% (n=0)	25.00% (n=2)	75.00% (n=6)	0.00% (n=0)	0.00% (n=0)

Table 12: Tabulation of the avulsion location of human esophagus muscularis layer muscle bundles (n=120) and squamous epithelium layer tissue bundles (n=44) as a percentage for each ablative modality

	Initial Cross-sectional Area (mm^2)	Initial Volume (mm^3)	Avulsion Force (N/mm^2)	Elastic Modulus (N/mm^2)	Avulsion Strain ($\Delta l/L$)	Total Strain ($\Delta l/L$)	Avulsion Energy (mJ/mm^3)	Total Energy (mJ/mm^3)
Muscularis Layer Muscle Bundles								
Biomech (n=62)	12.42±4.43	218.77±109.19	0.20±0.11	0.29±0.22	1.61±0.50	2.26±0.69	63.14±37.23	91.70±50.90
RF (n=15)	11.95±2.91	202.36±54.40	0.50±0.19	0.61±0.24	1.48±0.28	2.02±0.53	165.71±71.75	208.60±79.57
CRA (n=10)	11.31±3.34	316.46±77.45	0.20±0.06	0.39±0.22	1.08±0.30	1.66±0.53	46.14±11.14	70.18±21.01
HIFU (n=6)	11.37±2.44	262.56±111.16	0.27±0.07	0.52±0.10	0.99±0.29	1.67±0.52	65.24±34.57	115.76±49.71
Study-Controls (n=7)	12.90±2.25	260.44±147.16	0.29±0.07	0.48±0.07	1.00±0.19	1.80±0.36	73.26±28.21	115.07±44.59
Squamous Epithelium Layer Tissue Bundles								
Non-Ablated (Biomechanical) (n=14)	7.84±2.41	218.06±81.33	0.56±0.26	1.34±0.79	0.78±0.34	1.68±0.65	115.11±76.32	222.46±135.93
RFA (n=4)	2.95±1.40	46.36±31.57	1.27±0.92	1.45±0.51	1.17±0.27	1.84±0.22	573.72±619.75	691.45±582.04
CRA (n=8)	9.90±3.62	377.09±145.59	0.38±0.22	0.98±0.45	0.77±0.20	1.65±0.34	69.36±43.30	141.40±60.99

Table 13: Mean ± SD dimensional characteristics and biomechanical parameters of human esophagus muscularis layer muscle bundles and squamous epithelium layer tissue bundles that avulsed at or near the center of the bundle

	% Diff Avulsion Force	% Diff Elastic Modulus	% Diff Avulsion Strain	% Diff Total Strain	% Diff Avulsion Energy	% Diff Total Energy
Muscularis Layer Muscle Bundles						
RF (n=15)	**+157.70% p<0.05**	**+111.29% p<0.05**	-8.10% p=0.3334	-10.79% p=0.2021	**+162.43% p<0.05**	**+127.49% p<0.05**
CRA (n=10)	+1.88% p=0.9014	+36.38% p=0.0979	**-33.10% p<0.05**	**-26.55% p=0.0017**	-26.93% p=0.0761	-23.46% p=0.1034
HIFU (n=6)	+39.39% p=0.1095	**+78.77% p=0.0170**	**-38.41% p=0.0041**	**-26.22% p=0.0434**	+3.31% p=0.8953	+26.24% p=0.2720
Study-Controls (n=7)	+47.52% p=0.0539	**+65.22% p=0.0461**	**-38.09% p=0.0041**	-20.50% p=0.1079	+16.02% p=0.5206	+25.48% p=0.2826
Squamous Epithelium Layer Tissue Bundles						
RFA (n=4)	**+126.58 p=0.0159**	+8.72 p=0.7871	+50.40 p=0.0502	+9.14 p=0.6555	**+398.40 p=0.0100**	**+210.82 p=0.0094**
CRA (n=8)	-32.33 p=0.1161	-26.75 p=0.2574	-1.12 p=0.9483	-1.93 p=0.8980	-39.74 p=0.1371	-36.44 p=0.1286

Table 14: Percent change in biomechanical properties of human esophagus muscularis layer muscle bundles and squamous epithelium layer tissue bundles post ablation with different ablative modalities

All values are with respect to respective controls. A positive value indicates an increase and a negative value a decrease with respect to controls. Percent change in avulsion force, elastic modulus, strain, and energy are shown along with individual statistical significance ($p<0.05$, marked in bold).

6. Assessment of Physiological and Biomechanical Properties of Human Vastus Lateralis in Response to Therapeutic Ablative Treatments

Ashish Singal, Charles L. Soule, Paul A. Iaizzo

Preface

Our lab is one of the diagnostic centers for an autosomal dominant disorder called malignant hyperthermia (MH). We often receive a biopsy of a human skeletal muscle (usually vastus lateralis) for clinical assessment of MH. Whenever possible, the waste human tissue left following the MH studies was utilized for assessment of physiological and biomechanical properties of the vastus lateralis skeletal muscle. Although there are vast similarities in different muscles of the body, there may be unique differences in each muscle type, in terms of how the muscle responds to ablative therapies and their biomechanical properties. Hence, the methodologies described in this investigation were used to quantify the effects of ablation on the physiological and biomechanical properties of the vastus lateralis muscle obtained from humans.

Introduction

The role of thermal ablative therapies continues to expand. Treating cardiac arrhythmias as well as ablative treatment of soft tissue hepatic and renal tumors has become common [1,2]. Musculoskeletal therapies of radiofrequency ablation of osteoid osteoma are performed with good outcomes [3]. While rare, skeletal muscle metastases of primary tumors have been reported, RFA has been indicated for treatment of these metastases [4,5,6,7,8]. Furthermore, RFA treatment of varicose veins and chronic venous ulcers has been utilized successfully [9,10].

In general there is a low but significant occurrence of complications using thermal ablative therapies [11]. Among those seen during atrial and pulmonary vein isolation treatments are esophageal injury, phrenic nerve injury, pericardial effusion/tamponade, and injury to lungs [11]. Furthermore, there have been reports of pneumothorax induced by RFA for hepatocellular carcinoma treatment beneath the diaphragm under real-time computed tomography-fluoroscopic guidance [12,13,14,15]. As applications of musculoskeletal thermo ablative modalities increase, it is likely to see similar trends in collateral damage. Further complicating potential musculoskeletal ablative therapies is presentation of compromised surrounding tissues. For instance osteoblastomas and osteiod osteomas can present with skeletal muscle atrophy [16,17]. To better understand how thermal ablative therapies might affect nearby skeletal muscle, it

is essential to study both their physiological and biomechanical properties in response to various therapeutically used ablative modalities.

In our lab, we have developed methodologies (Chapter 2, in press) that systematically allowed assessment of both physiological and biomechanical properties of human vastus lateralis muscle in response to radiofrequency ablation (RFA), cryoablation (CRA), and microwave ablation (MWA).

Methods

These studies were approved by the Institutional Review Board at the University of Minnesota. The human vastus lateralis muscle used in this study was tissue considered as waste tissue following completion of a clinical diagnostic contracture test for MH. Muscle fiber segments approximately 40 mm in length and 15 mm in width were dissected under local anesthesia or with anesthetics not considered to trigger MH [18]. These fiber segments were immediately placed in oxygenated Krebs buffer solution and transported to the lab (within 5 minutes) where it was pinned in a dissection dish and further dissected in oxygenated Krebs buffer solution to make smaller muscle bundles of approximately 25 mm in length and 2 mm in diameter in an identifiable cylindrical shape for physiological contracture testing [19,20].

Following completion of the MH contracture testing, waste tissue muscle bundles including bundles not required for contracture testing and those bundles exposed to 10 minutes of 3% halothane (not less than 90 minutes after halothane

exposure was stopped) were included in this study. These muscle bundles were used for physiological and biomechanical assessment as described previously [Singal et al, 2014]. The muscle bundles were exposed to the following ablation modalities and doses, which were used in this investigation:

Radiofrequency Ablation: RFA at three different ablation doses were studied: 50 °C, 60 °C, and 70 °C (corresponding to 312 J, n=4; 739 J, n=5; and 1169 J, n=5, respectively).

Cryoablation: CRA at three different ablation doses were studied: 15 sec (n=3), 30 sec (n=3), and 60 sec (n=3).

Microwave Ablation: MWA at three different ablation doses were studied: 410 J (n=3), 821 J (n=4), and 1231 J (n=3).

Controls: Both control (n=10) and control-remove (n=8) muscle bundles were evaluated. Control muscle bundles were those that were left in the tissue baths; and control-remove muscle bundles were those that that were exposed to the same conditions as the experimental group, except no ablations were performed.

Results

A total of 87 muscle bundles were prepared from biopsies obtained from 9 patients for physiological and biomechanical assessment. RFA, CRA, and MWA modalities were used for performing ablations. The RF ablation parameters were recorded during RFA, and the plot of average power as a function of average temperature is shown in Figure 105. A best, linear fit model was used to

calculate the average power at respective ablation doses, which was further used to calculate the ablation energy at the RF catheter. Figure 106 shows representative examples of muscle bundles that were ablated with the above mentioned ablation modalities. Figure 107 through Figure 112 show the dose effects of percent change in peak force and baseline force for all three ablation modalities. A dose dependent sustained reduction in peak force and a transient increase in baseline force were observed in each treatment case. The baseline force consistently returned near or below the pre-ablation level for every ablation modality investigated. Similar changes in peak force and baseline force of control and control-remove muscle bundles were observed (Figure 113 and Figure 114). This suggests that there were minimal changes in muscle physiology when muscle bundles were removed from tissue baths for performing ablations. Table 15 shows the biomechanical parameters of muscle bundles tested in each treatment group. As can be seen in Table 16, in general, there was a reduction in every biomechanical parameter in every treatment group with respect to controls, except in the MWA group. A statistically significant increase in the elastic modulus and a non-significant increase in the avulsion force were observed as a result of MWA. Table 17 shows the percent avulsion location for every ablation modality which is graphically shown in Figure 115.

Discussion

Avulsion forces were consistently higher than physiologically induced forces. With our stimulation protocol, twitch forces on top of the normal baseline force was generally much less than half of avulsion forces seen in either control group. Interestingly though, during contracture testing for MH the additive doses of caffeine especially can bring physiological forces much closer to avulsion. In fact, at 32 mM caffeine concentration, the dose used to identify the validity of the contracture testing with maximal sustained contracture, the total physiological forces can reach as high as 75% of these avulsion forces (data not shown). With such a low margin of error in avulsion forces these data reinforce the importance of not only maintaining good technique in dissection of the tissue bundles, but also in tying suture loops to the ends of cut tissue like the vastus lateralis. Whereas intact tendon to tendon muscle bundles allow the additional strength of connective tissue at the suture tissue interface, these cut bundles are tied directly to the muscle fibers creating a compression of tissue near the suture. This compression has already been shown to cause a zone of depolarization at the suture underpinning the physiological changes that these sutures cause [18]. For biomechanical assessment, superglue was applied on both ends of the muscle bundle to strengthen the suture-tissue interface so that higher percentage of avulsions could be obtained near the center of the muscle bundle.

In general for both RFA and MWA treatments, physiological response to ablations was more sensitive to the ablations while CRA had a similar response

compared to swine diaphragm tissue (Chapter 3, in press). These changes could be related to either tissue type or species differences. If these differences are related to tissue type though it suggests that physiologically collateral damage by heating thermal therapies could be greater in treating musculoskeletal disorders. In patients such as those presenting with muscle atrophy, collateral damage could be more problematic.

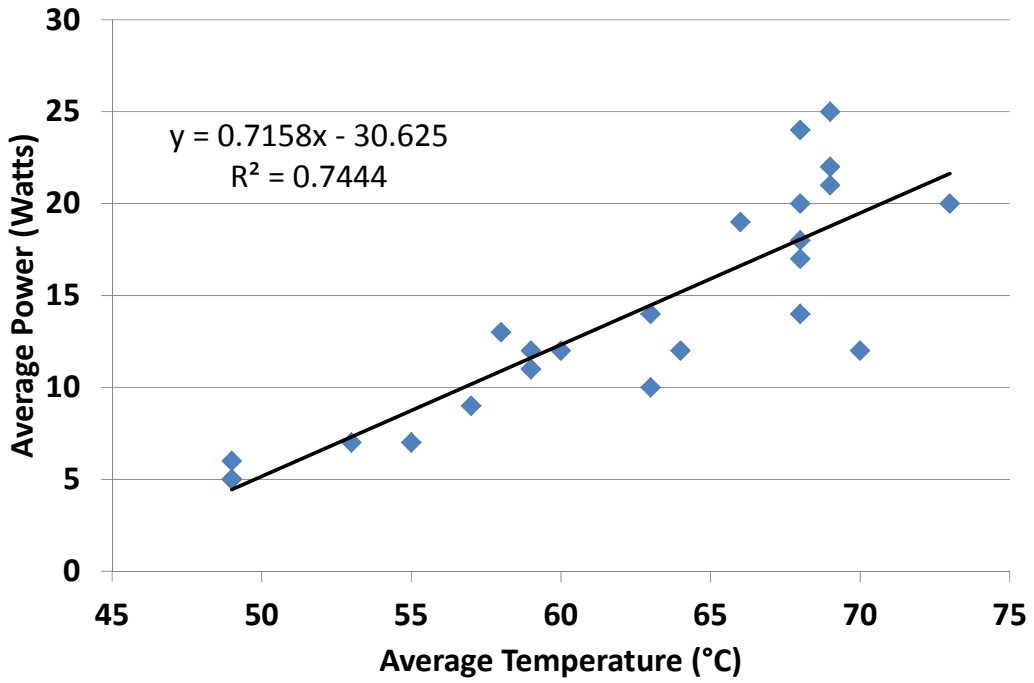

Figure 105: Average power versus catheter tip temperature for human vastus lateralis

Plot of average RF power as a function of average temperature (n=25) at the RF catheter tip measured during the ablation. The samples were exposed to varying levels of RF dose (increasing temperature), out of which 3 different doses were selected to study the dose effects (50 °C, 60 °C, and 70 °C). A linear curve was fitted through the data to obtain the best fit equation what was used to calculate the average power at respective ablation temperatures.

Figure 106: Representative examples of human vastus lateralis samples ablated with MWA (A), B (CRA), C (RFA). Control samples (non-ablated) are shown in D

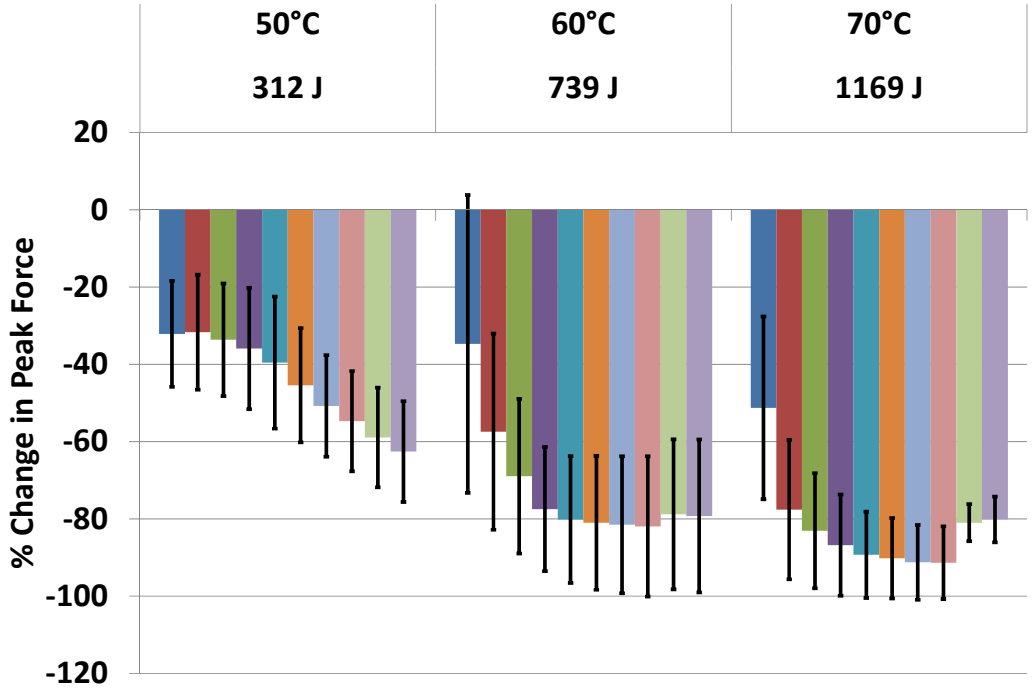

Figure 107: Dose effects of percent change in peak force of human vastus lateralis post RFA

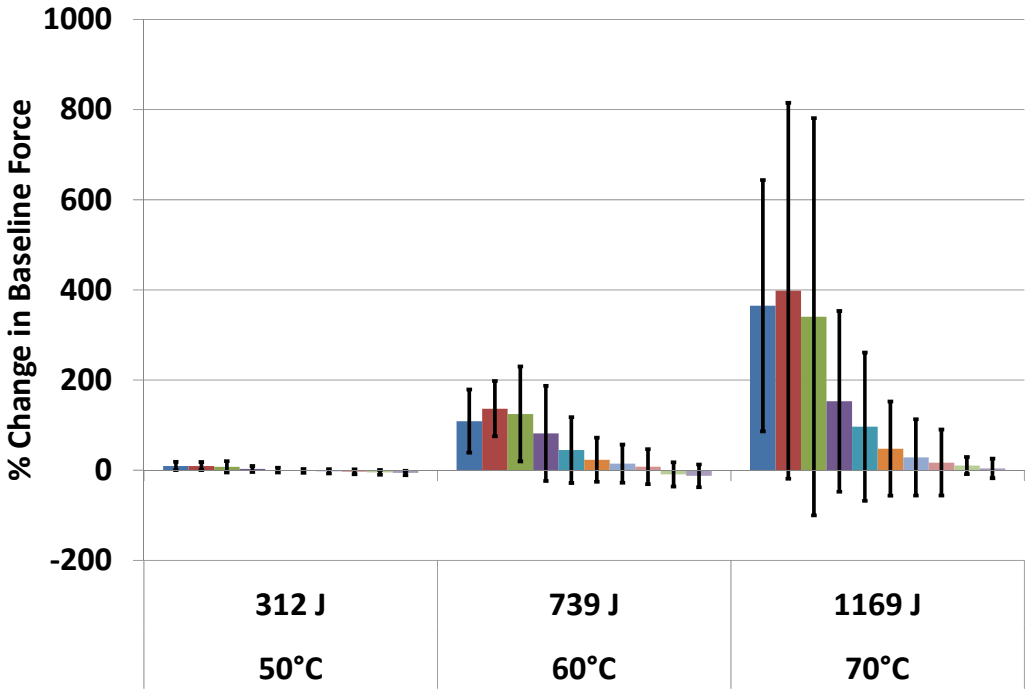

Figure 108: Dose effects of percent change in baseline force of human vastus lateralis post RFA

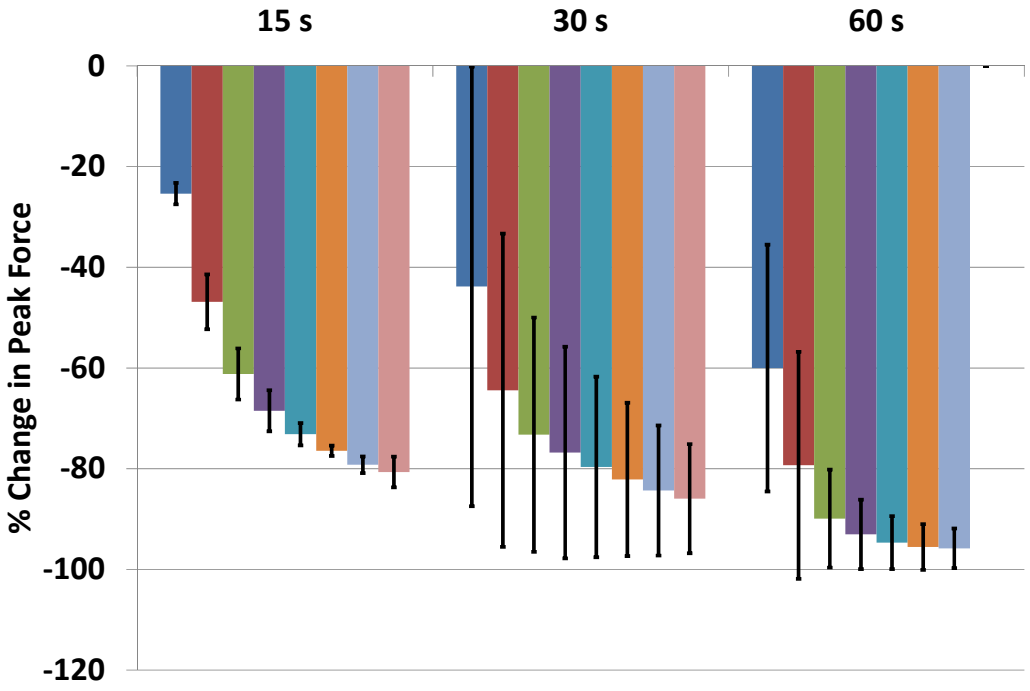

Figure 109: Dose effects of percent change in peak force of human vastus lateralis post CRA

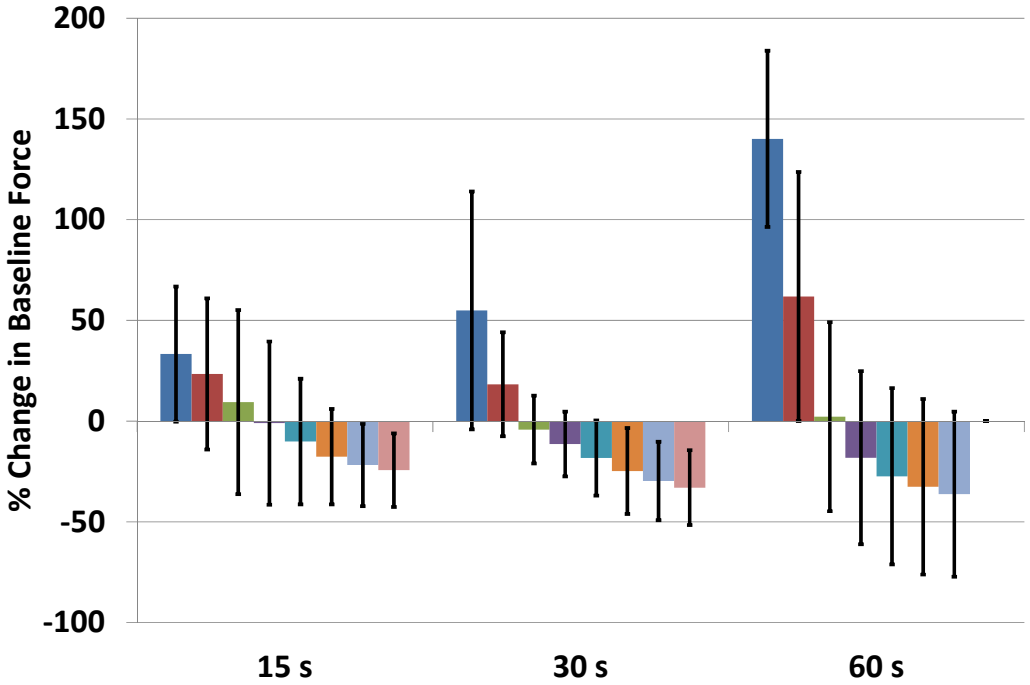

Figure 110: Dose effects of percent change in baseline force of human vastus lateralis post CRA

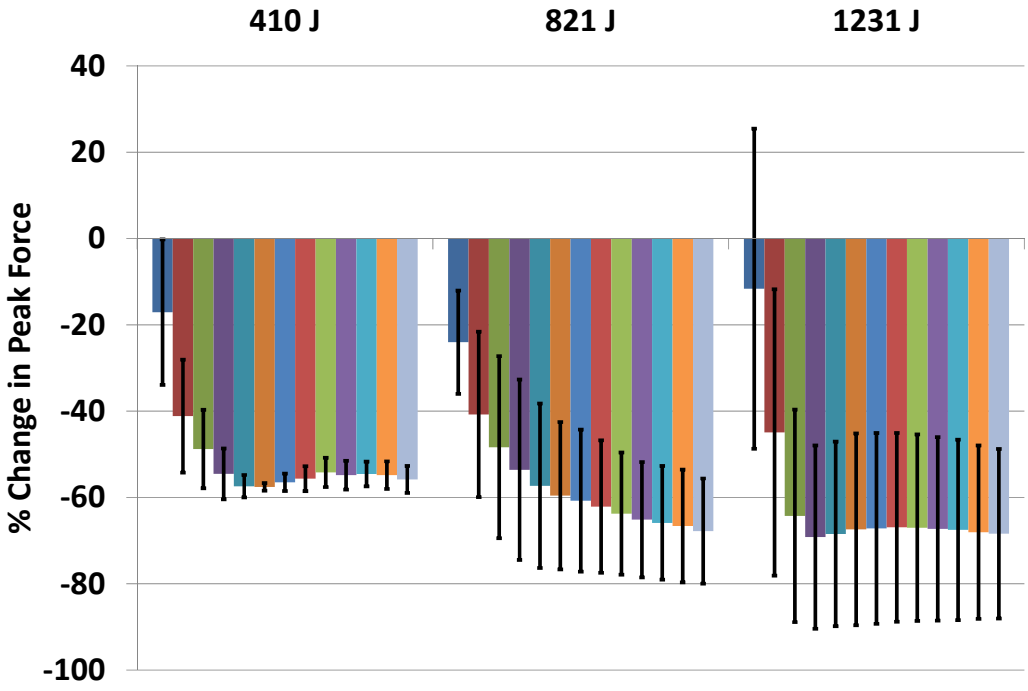

Figure 111: Dose effects of percent change in peak force of human vastus lateralis post MWA

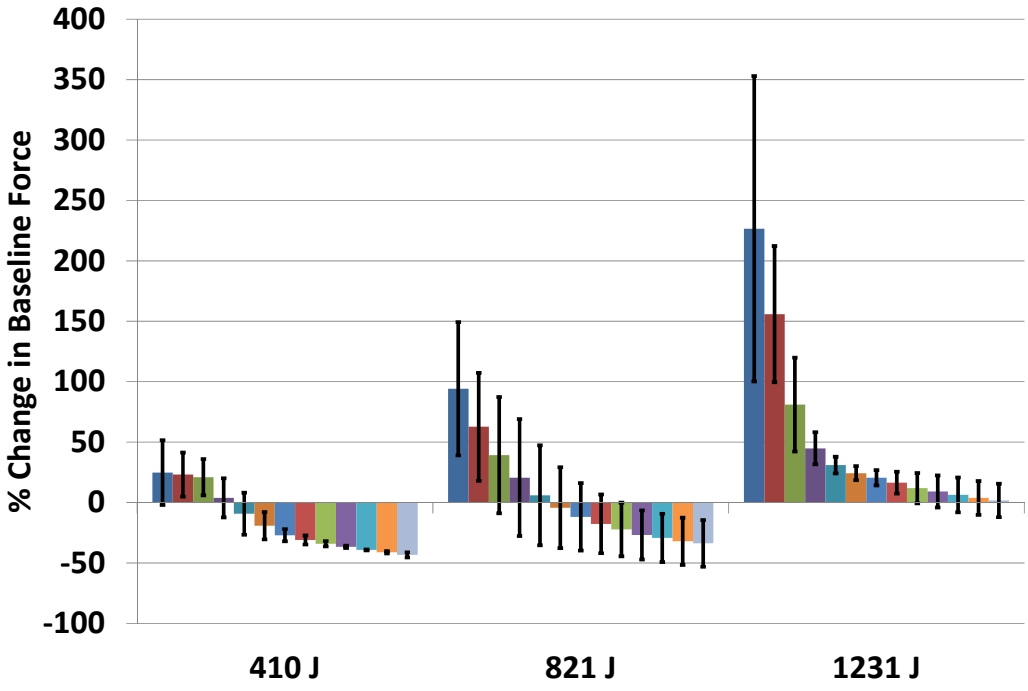

Figure 112: Dose effects of percent change in baseline force of human vastus lateralis post MWA

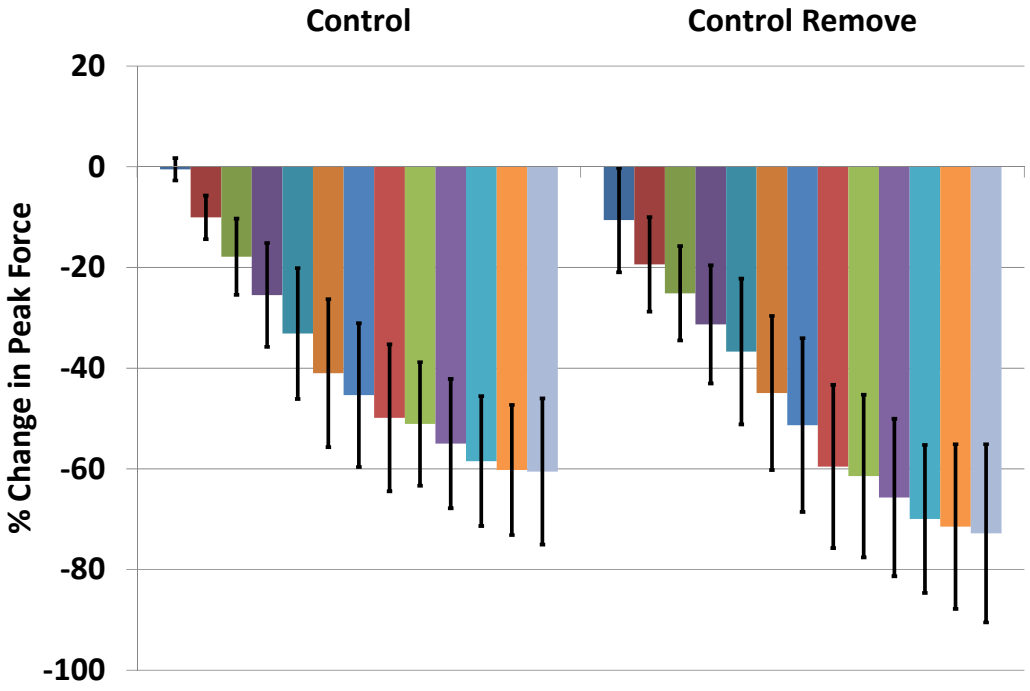

Figure 113: Percent change in peak force of control and control-remove human vastus lateralis muscle bundles

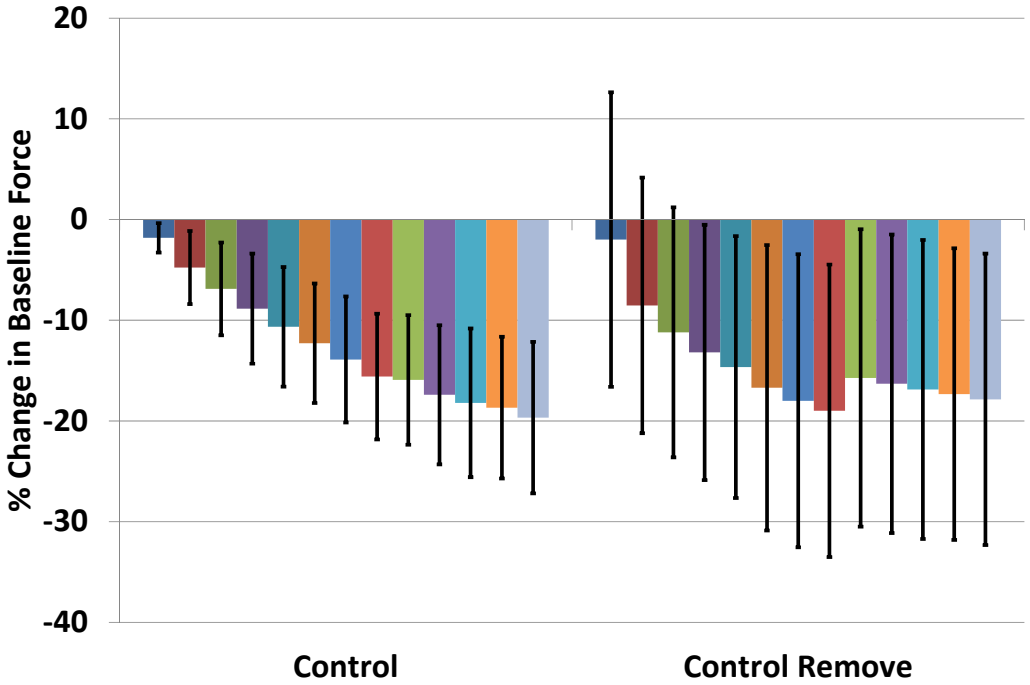

Figure 114: Percent change in baseline force of control and control-remove human vastus lateralis muscle bundles

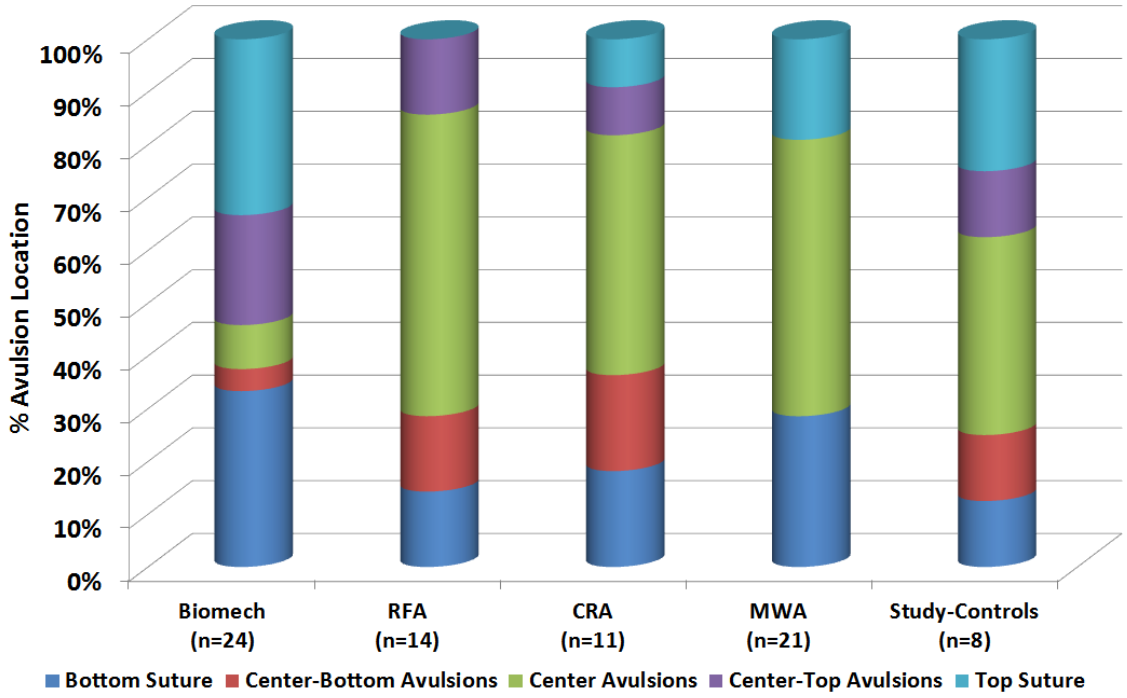

Figure 115: Avulsion location for each treatment displayed as percentage for all human vastus lateralis muscle bundles tested in this investigation

	Initial Cross-sectional Area (mm^2)	Initial Volume (mm^3)	Avulsion Force (N/mm^2)	Elastic Modulus (N/mm^2)	Avulsion Strain ($\Delta l/L$)	Total Strain ($\Delta l/L$)	Avulsion Energy (mJ/mm^3)	Total Energy (mJ/mm^3)
Biomech (n=8)	7.15±5.40	143.46±127.10	0.11±0.10	0.21±0.12	0.87±0.48	1.41±0.99	28.83±30.39	55.97±69.29
RFA (n=12)	6.86±4.58	198.12±149.15	0.07±0.04	0.18±0.12	0.64±0.32	0.94±0.41	12.83±8.44	18.78±12.99
CRA (n=8)	10.71±4.04	360.54±189.38	0.07±0.05	0.15±0.11	1.05±0.63	1.33±0.68	19.42±20.39	24.34±25.22
MWA (n=11)	4.64±2.73	194.36±130.25	0.13±0.04	0.50±0.24	0.57±0.24	0.74±0.32	20.21±11.63	27.55±14.93
Study Controls (n=5)	2.66±1.48	92.47±60.19	0.09±0.05	0.41±0.28	0.45±0.32	0.65±0.35	9.39±5.67	13.79±7.59

Table 15: Mean ± SD dimensional characteristics and biomechanical parameters of human vastus lateralis muscle bundles that avulsed at or near the center of the muscle bundle

	% Diff Avulsion Force	% Diff Elastic Modulus	% Diff Avulsion Strain	% Diff Total Strain	% Diff Avulsion Energy	% Diff Total Energy
RFA (n=12)	-38.39 p=0.2163	-10.11 p=0.7020	-27.01 p=0.2035	-32.92 p=0.1643	-55.48 p=0.0978	-66.45 p=0.0830
CRA (n=8)	-34.98 p=0.3660	-26.63 p=0.3436	+20.30 p=0.5371	-5.55 p=0.8576	-32.64 p=0.4791	-56.52 p=0.2451
MWA (n=11)	+25.57 p=0.4165	**+142.54 p=0.0056**	-34.24 p=0.0915	-47.16 p=0.0525	-29.89 p=0.3992	-50.77 p=0.2004
Study Controls (n=5)	-18.86 p=0.6867	+98.62 p=0.0949	-48.57 p=0.1093	-53.56 p=0.1360	-67.42 p=0.1913	-75.36 p=0.2092

Table 16: Percent change in biomechanical properties of human vastus lateralis muscle bundles post ablation with different ablative modalities.
All values are with respect to controls (n=8, non-ablated) muscle bundles. A positive value indicates an increase and a negative value a decrease with respect to controls. Percent change in avulsion force, elastic modulus, strain, and energy are shown along with individual statistical significance ($p<0.05$, marked in bold).

Avulsion Location (%)	% Bottom Suture Breakage	% Center-Bottom Avulsions	% Center Avulsions	% Center-Top Avulsions	% Top Suture Breakage
Non-Ablated (Biomechanical) (n=24)	33.33% (n=8)	4.17% (n=1)	8.34% (n=2)	20.83% (n=5)	33.33% (n=8)
RFA (n=14)	14.29% (n=2)	14.29% (n=2)	57.14% (n=8)	14.28% (n=2)	0.00% (n=0)
CRA (n=11)	18.18% (n=2)	18.18% (n=2)	45.46% (n=5)	9.09% (n=1)	9.09% (n=1)
MWA (n=21)	28.57% (n=6)	0.00% (n=0)	52.38% (n=11)	0.00% (n=0)	19.05% (n=4)
Study-Controls (n=8)	12.50% (n=1)	12.50% (n=1)	37.50% (n=3)	12.50% (n=1)	25.00% (n=2)

Table 17: Tabulation of the avulsion location of human vastus lateralis muscle bundles (n=78) as a percentage for each ablative modality

7. The Assessment of Physiological and Biomechanical Properties of Isolated Swine and Human Trabeculae in Response to Clinically Applied Ablative Therapies

Ashish Singal, Charles L. Soule, Paul A. Iaizzo

Preface

Our plan is to submit this article as a research paper in the Journal of Medical Devices 2015.

Introduction

Catheter ablations are often performed in the heart to treat drug refractory, idiopathic, and intractable arrhythmias. Specifically, ablations are performed in the left and right atrium (LA and RA), pulmonary veins (PVs), and the ventricles for treatments of atrial fibrillation (AF) [1] or ventricular arrhythmias [2]. In general, the goal of ablations is to create a series of transmural lesions to selectively ablate (and kill) the arrhythmogenic substrate responsible for irregular rhythm. In most of the ablative modalities used clinically today (like radiofrequency ablation and cryoablation), only the temperature and duration of the energy delivered can be controlled [3]. Since there is no accurate way to control the radial extent and depth of the lesion created, it is possible to create a

lesion that is too wide or too deep, consequently causing injury to healthy endocardium or even adjacent vital structures. Nevertheless, delivery of ablative energy results in alterations of physiological and biomechanical properties of myocardium. In this investigation, we sought out to investigate how the physiological and biomechanical properties of human and swine trabecular muscle bundles are affected by two ablation modalities: radiofrequency ablation (RFA) and high-intensity focused ultrasound (HIFU).

Methods

The study was approved by the University of Minnesota Institutional Animal Care and Use Committee. Fresh ventricular biopsies were obtained from healthy castrated male Yorkshire-cross swine (n=3, mean weight of approximately 70 kg). Fresh biopsies from human hearts (n=3) were obtained through research collaboration with LifeSource (St. Paul, MN). The heart biopsies were dissected in oxygenated cardiac Krebs solution to prepare isolated muscle bundles from endocardial trabeculations. Muscle bundles were prepared in an identifiable cylindrical shape having lengths of 10 to 15 mm and diameters of 2 to 4 mm. The physiological testing was performed using tissue baths and biomechanical testing was performed using a uniaxial testing machine as described in detail in Chapter 2. The tissue response to following two ablation modalities was investigated:

Radiofrequency Ablation: RFA was performed using the RF generator operating at 484 KHz sinusoidal waveform. Human and swine trabeculae muscle bundles were studied at five different ablation doses ranging between: 50 °C, 55 °C, 60 °C, 65 °C, and 70 °C. A total of 16 human and 8 swine trabecular muscle bundles were utilized for RFA testing. All RFA were performed under a constant catheter-tip force of 10 grams (0.1 N) under the uniaxial machine.

HIFU Ablations: HIFU ablations (2.5 MHz sinusoidal waveform, 80% duty cycle) at two different ablation doses were studied for human trabeculae muscle bundles only at the following doses: 286 J and 715 J. A total of 6 human trabeculae muscle bundles were utilized for HIFU ablation testing.

Controls: There were two sets of control muscle bundles. One, that were left in the tissue bath for the entire experiment; and two, that were removed from the tissue baths and exposed to the same set of ablation conditions as the experimental muscle bundles, except they were not ablated. A total of 2 human trabeculae muscle bundles were used, and 6 swine trabeculae muscle bundles were used as control muscle bundles.

A separate group of swine trabeculae muscle bundles (n=23) were ablated with 200 proof ethanol. These muscle bundles were only tested for uniaxial pulls following ablations with ethanol.

Data Analyses

Statistical analyses were performed using ANOVA and the Tukey test to identify differences in peak forces and baseline forces for both ablation modalities (RFA and HIFU) where a $p<0.05$ is considered statistically significant. All data are presented as mean $\pm$ standard deviation.

Results

Figure 116 show comparison of normalized electro-mechanical response of swine and human trabeculae muscle bundles, which were observed to be very similar. These twitch responses were measured in the tissue baths with 1 ms electrical field stimulation from platinum electrodes adjacent to the muscle bundles. Figure 117 and Figure 118 show the percent change in peak force and baseline force of human trabeculae muscle bundles, respectively, in response to RFA. In this case, data was acquired for duration of 75 min post-RFA. Although some dose-effect trends can be observed in peak force, but no consistent trends are observed in baseline force. As can be observed, the percent reduction in peak force is related to the ablative dose, where a larger reduction is observed at higher doses. Moreover, the results have high variability which can be attributed to a small sample size of muscle bundles tested. Figure 119 and Figure 120 show the percent change in peak force and baseline force of human trabeculae muscle bundles, respectively, in response to HIFU ablations. In this case, data was acquired for duration of 135 min post HIFU ablations. Although only 2 ablation doses were used, no dose effects were evident in ether the peak forces

or baseline forces. Figure 123 and Figure 124 illustrate the percent change in peak force and baseline force, respectively, of swine trabeculae muscle bundles in response to RFA. Once again, no dose effects were evident in either peak force or baseline force in response to RFA. The transient increase in peak force at 70 °C suggests that the given muscle bundle may not have completely recovered and stabilized following mounting in the tissue bath. The respective control and control-remove characteristics are also shown for both species in Figure 121, Figure 122, Figure 125, and Figure 126.

Figure 127 shows the stress-strain characteristics of swine and human trabeculae muscle bundles. As can be observed in this figure, the highest stresses were measured from the moderator bands that are found in the right ventricle of the heart; which typically extend from the inter-ventricular septum to the base of the anterior papillary muscle. The moderator bands naturally possess a cylindrical shape and are far more uniform in shape than the rest of the trabecular muscle bundles that were dissected. Because of their uniform cylindrical shape, the cardiac muscle fiber bundles are densely packed in a longitudinal fashion, which not only impart mechanical strength to the lateral and medial wall of the right ventricle, but also efficiently transmit action potentials. Thus, the moderator bands registered the maximum forces as they were longitudinally stretched resulting in highest stress-strain characteristics. However, because of their native cylindrical shape, a dog-bone shape could not be imparted to the moderator band muscle bundles. Due to this, during the

uniaxial pull, the suture often slipped from either the top or bottom end of the muscle bundle. Figure 128 shows the average stress-strain model derived by averaging the individual stress-strain response of each of the swine and human trabeculae muscle bundles. Table 18 shows the dimensional characteristics and biomechanical parameters of swine and human trabeculae muscle bundles that were tested in this investigation. As can be observed in this table, with respect to controls, for the human trabeculae muscle bundles, the average avulsion force and elastic modulus increased by 69.6% and 163.6%, respectively, following treatment with HIFU ablation. Alternatively, the average avulsion force and elastic modulus decreased by 17.4% and 12.1%, respectively, following treatment with RFA. In case of swine trabeculae muscle bundles, the avulsion force and elastic modulus increased by 60.9% and 33.3%, respectively, following treatment with RFA. Alternatively, the average avulsion force and elastic modulus decreased by 17.4% and 25%, respectively, following treatment with ethanol. No significant changes were observed in the biomechanical properties of study-control muscle bundles in both species. On an average, the avulsion force and elastic modulus between the two species was found to be similar, that is, 0.23 N/mm^2 and approximately 0.35 N/mm^2, respectively. However, the avulsion strain and total strain for both species was found to be different with swine being lower than human. Hence, the energies required for avulsion and total energy were lower for the swine species as well.

Discussions

Our laboratory has developed unique methodologies to assess the physiological and biomechanical properties of tissues. In this investigation we tested the response of isolated trabeculae muscle bundles of swine and human to different ablative modalities. We report that the tissue properties of both species tested change, and that they respond differently to ablative modalities, which can be measured using the methodologies detailed previously (Chapter 2). To our knowledge no literature exists exploring the comparative changes in tissue properties as a result of application of different therapeutic ablative modalities, but work is ongoing in our laboratory to study these investigations.

The variability observed in these results is large which is due to multifactorial reasons. One of the major reasons for variability is the viability of the tissue before the experiment is started. Specifically, the duration from time of death of the donor to the time when isolated muscle bundles are prepared and mounted in tissue baths for study is quite variable. Our experience has shown that longer duration affects the viability of the cardiac tissue due to hypoxia, ischemia, and cellular injury. It has been shown that myocardium is a metabolically demanding active organ relying on a constant source of oxygen, which is highly susceptible to ischemic and hypoxic injury [4]. Moreover, we have consistently observed that the isolated trabeculae muscle bundles from either species do not generally generate large forces. Often the peak forces measured in tissue baths are <1 gram after mounting, and typically the baseline

forces would rise for approximately 1 hour until they stabilize. The rise in baseline forces (rising baseline tension) is often correlated with contracture or some form of cellular injury. It should be noted that the muscle bundles rely on passive diffusion for nutrients and oxygen to diffuse into the core of the muscle bundle. Hence, the viability of muscle fibers is in a way related to the diameter of the muscle bundle, where a thicker diameter muscle bundle may suffer a far greater hypoxic injury as compared to a thinner diameter muscle bundle. Ultimately, the small peak forces limit the number of muscle bundles that can be utilized for experimental studies. Another source of variability is because of the small/limited sample size. We believe that increasing the sample size would reduce variability and increase in the confidence level of results.

All RFA on trabeculae muscle bundles in both species were performed under a constant catheter-tip force of 10 grams (0.1 N) under the uniaxial machine. The muscle bundle were stretched and pinned longitudinally in the ablation dish. The catheter had a hemispherical round tip that approached the muscle bundle perpendicularly to apply a constant force on the muscle bundle. Because of the cylindrical shape of the muscle bundle and round shape of the catheter-tip, the catheter would slip lying next to the muscle bundle and not imparting the constant force as planned. Unlike other muscle bundles tested (like, diaphragm and esophagus), this issue was specific to the trabecular muscle bundles because of their morphology and shape. The differences observed in

dose-effects as a result of RFA could be possible explained by catheter-tissue interaction behavior.

It is hoped that as more data are collected on swine and human tissue samples, the questions regarding species differences and differences between healthy and diseased state can be answered.

Conclusions

Here we employed a novel in vitro methodological approach to begin to understand how ablative modalities may influence properties of cardiac trabeculae from swine and human species. Despite current clinical use, questions regarding dosing, thermal injury, choice of modality, and device-tissue interactions remain unanswered.

Our data shows that ablations performed at clinically relevant doses influences the properties of trabeculae of both species. Higher ablative energies result in higher levels of cellular injury in both species causing larger reductions in peak forces. However, due to high variability in baseline force (resting muscle tension), no firm conclusions could be made. Though, higher baseline forces result in contracture, which is considered as a surrogate of cellular injury.

The peak stress to avulsion for swine trabeculae was found to be approximately 50% higher than human samples; however, the avulsion-strain was approximately 40% lower. These results could have important clinical implications, especially for interventional catheter design for procedures where

cardiac interventions are required. Nevertheless, further work is needed to determine if these differences are due to species differences or from healthy versus diseased myocardium.

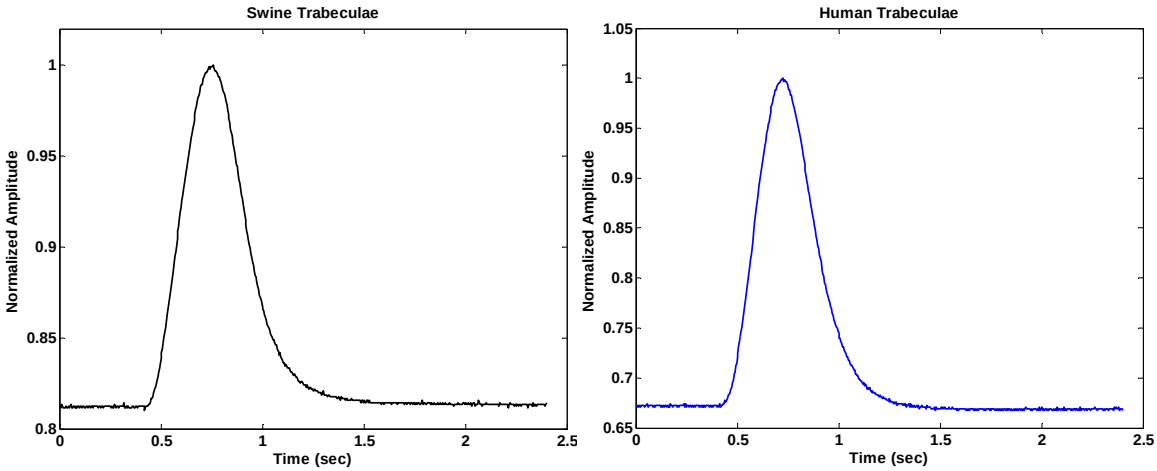

Figure 116: Comparative electro-mechanical response of swine and human trabeculae

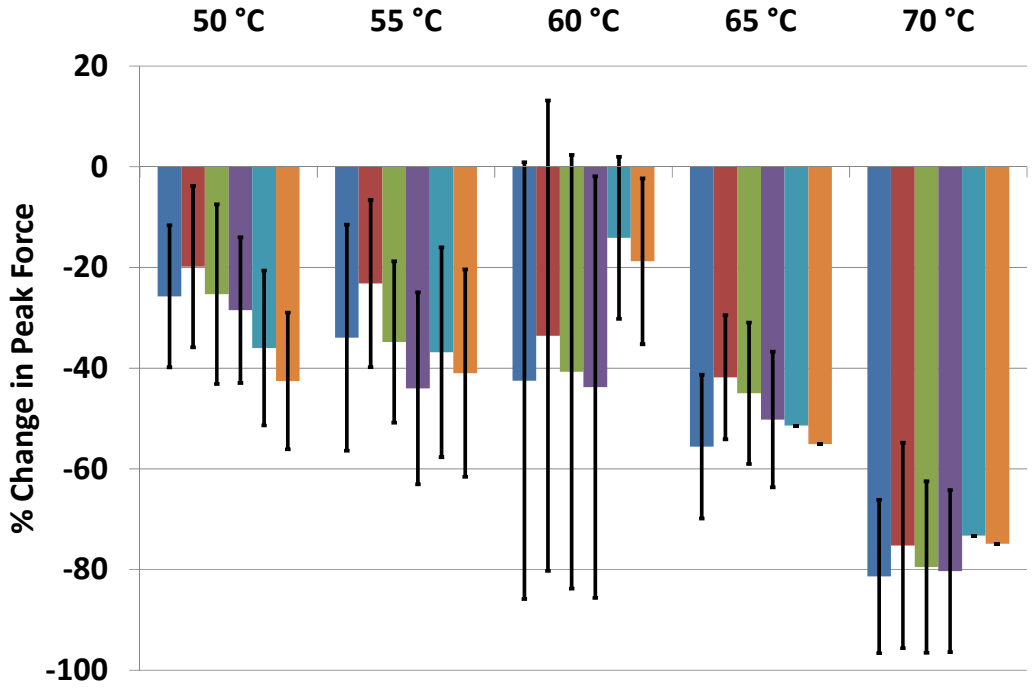

Figure 117: Percent change in peak force of human trabeculae muscle bundles post RFA

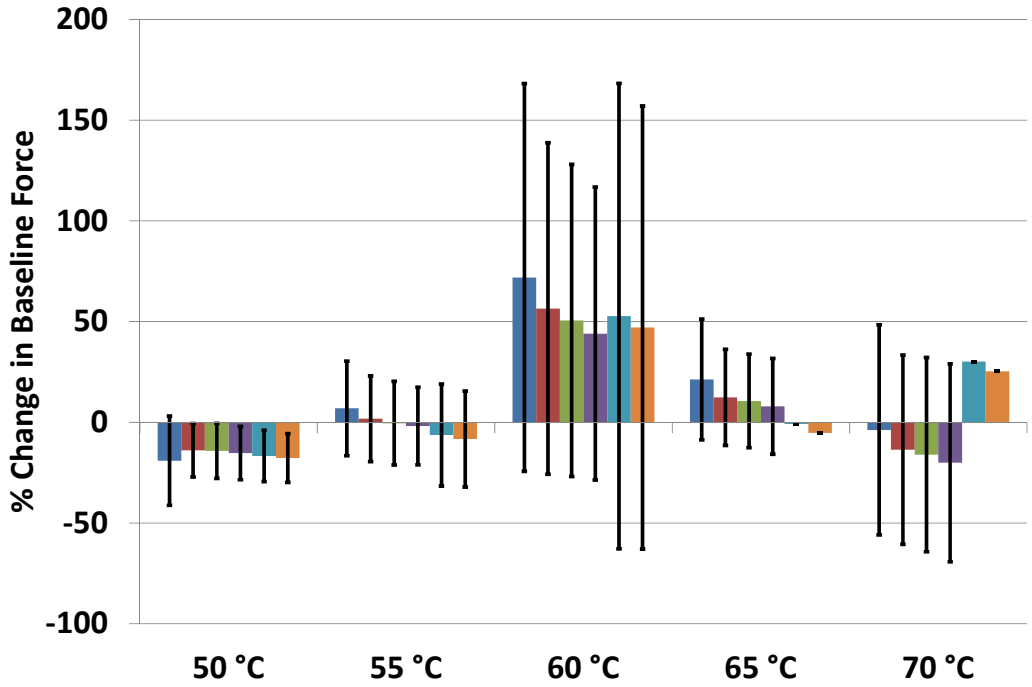

Figure 118: Percent change in baseline force of human trabeculae muscle bundles post RFA

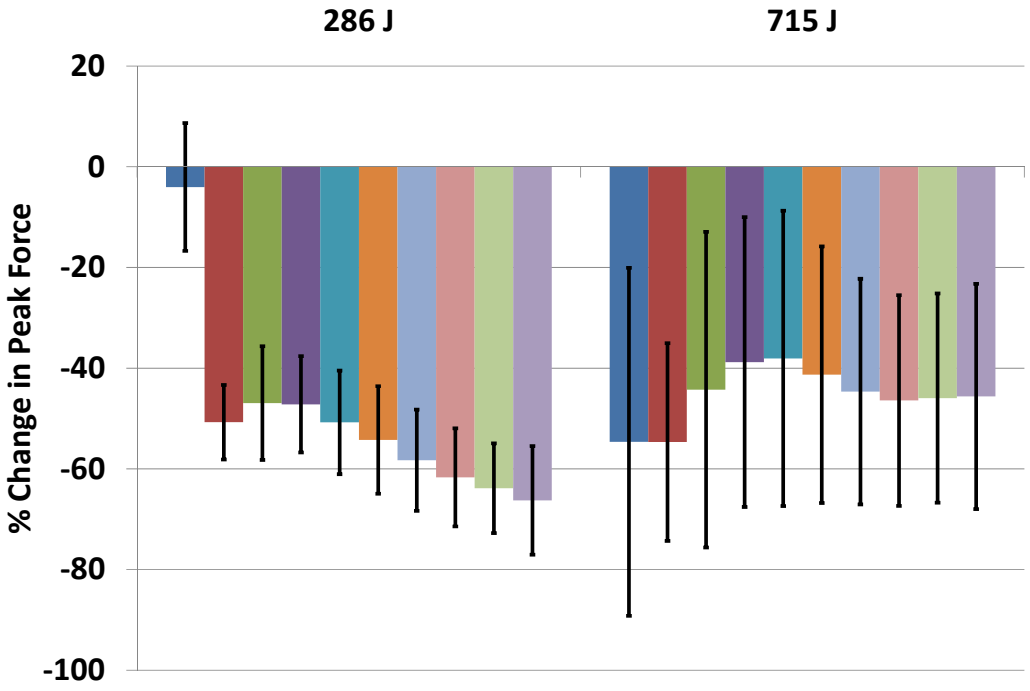

Figure 119: Percent change in peak force of human trabeculae muscle bundles post HIFU ablation

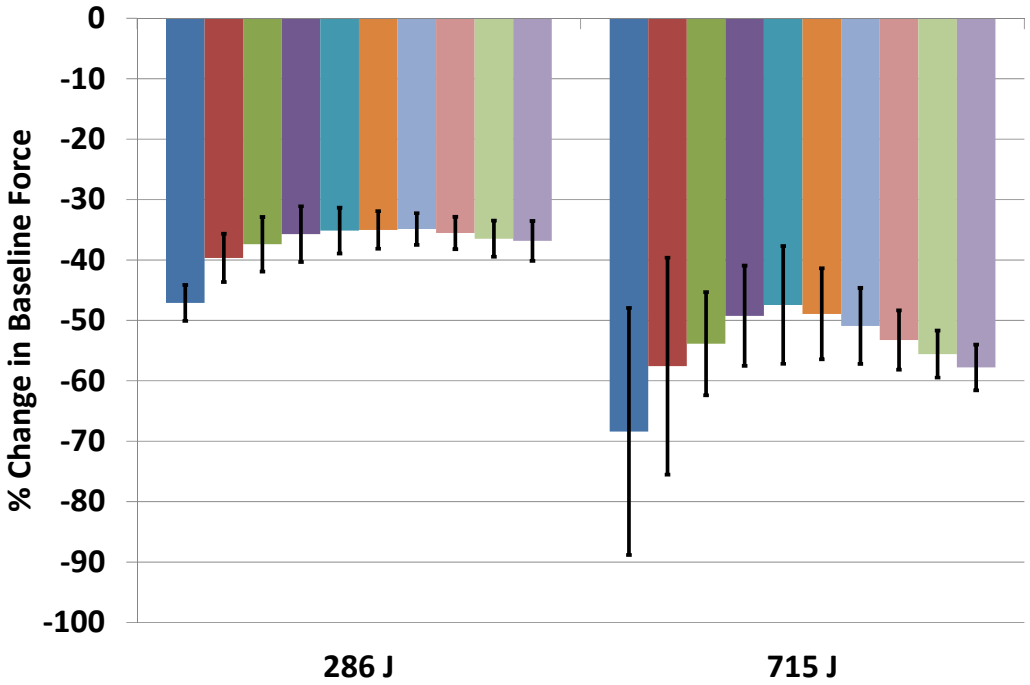

Figure 120: Percent change in baseline force of human trabeculae muscle bundles post HIFU ablation

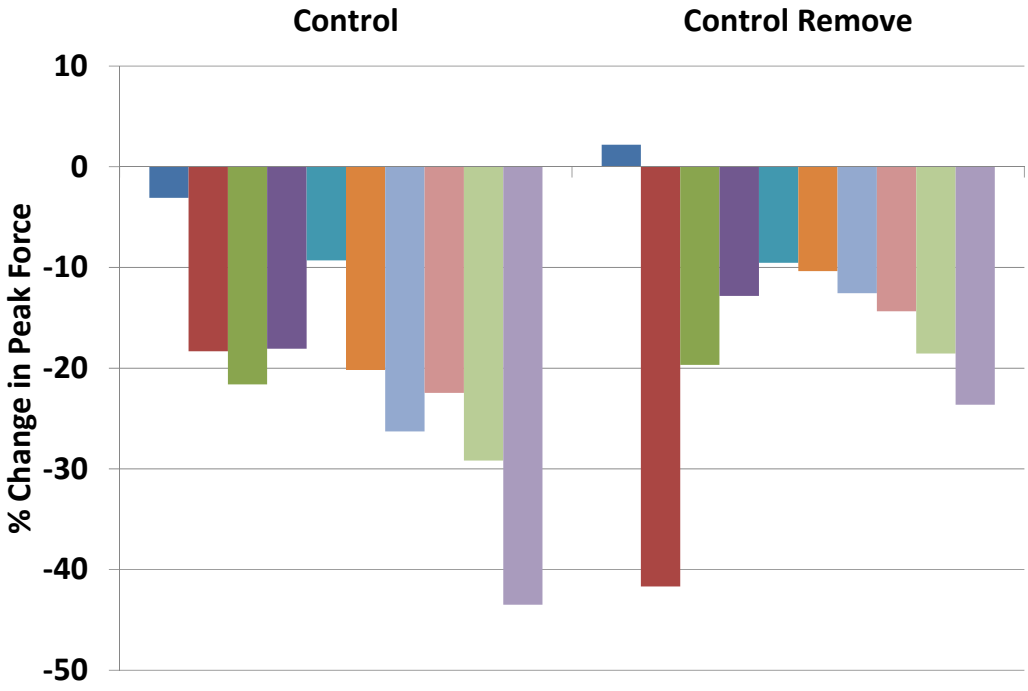

Figure 121: Percent change in peak force of control and control remove muscle bundles of human trabeculae

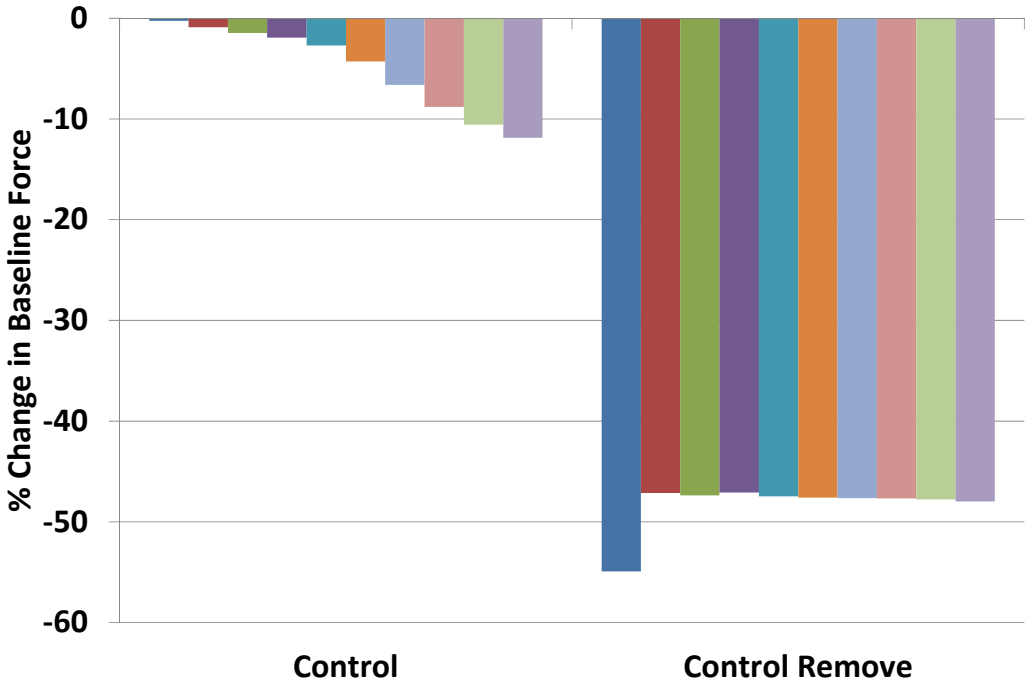

Figure 122: Percent change in baseline force of control and control remove muscle bundles of human trabeculae

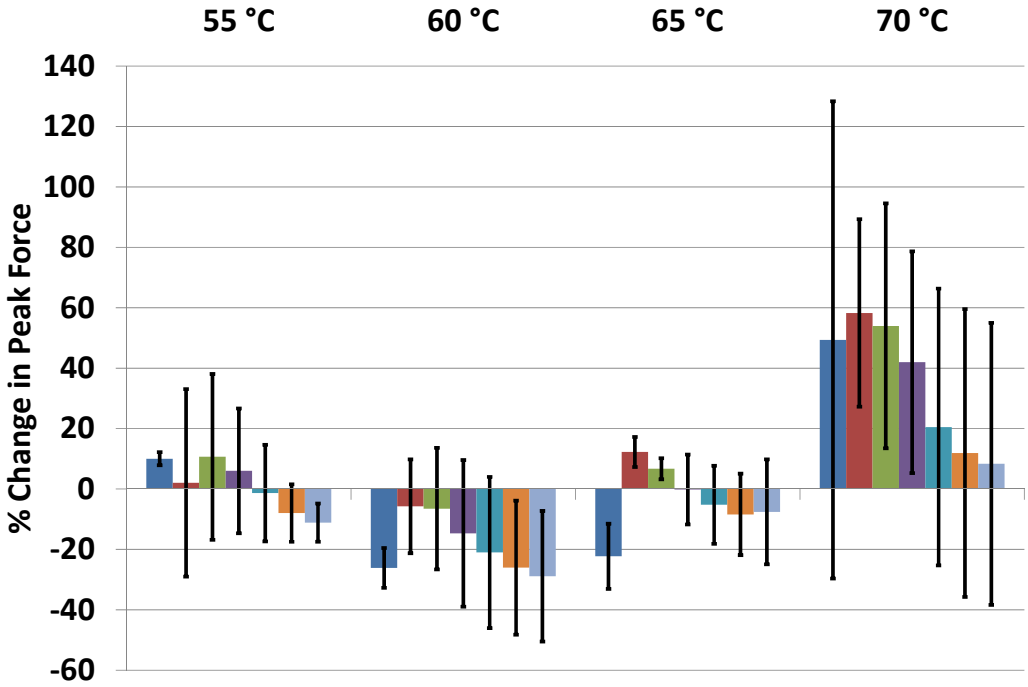

Figure 123: Percent change in peak force of swine trabeculae muscle bundles post RFA

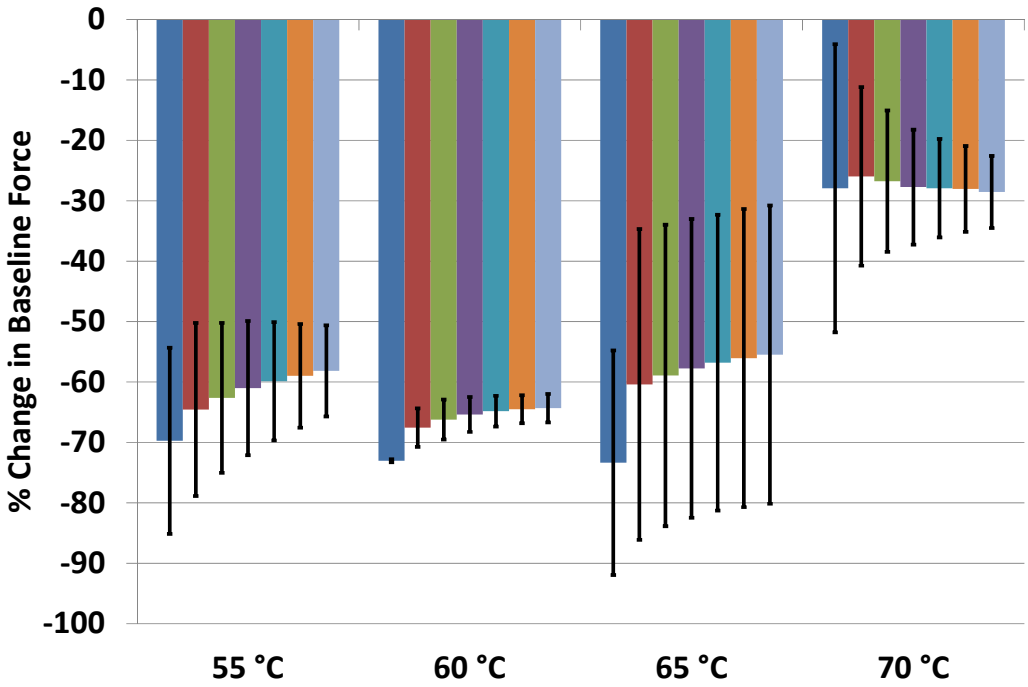

Figure 124: Percent change in baseline force of swine trabeculae muscle bundles post RFA

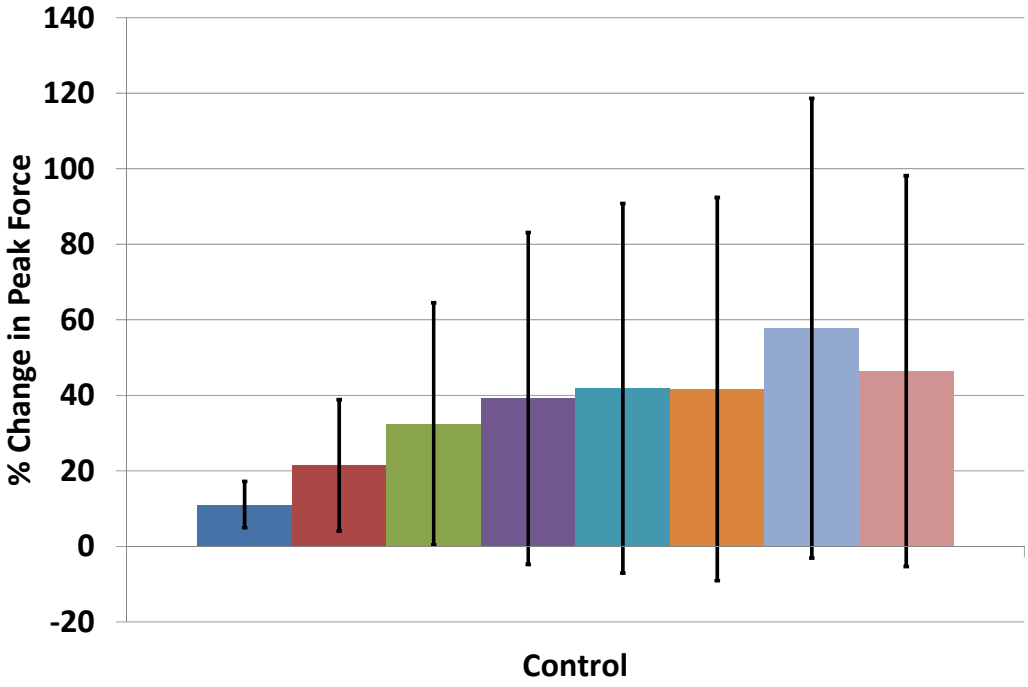

Figure 125: Percent change in peak force of control muscle bundles of swine trabeculae

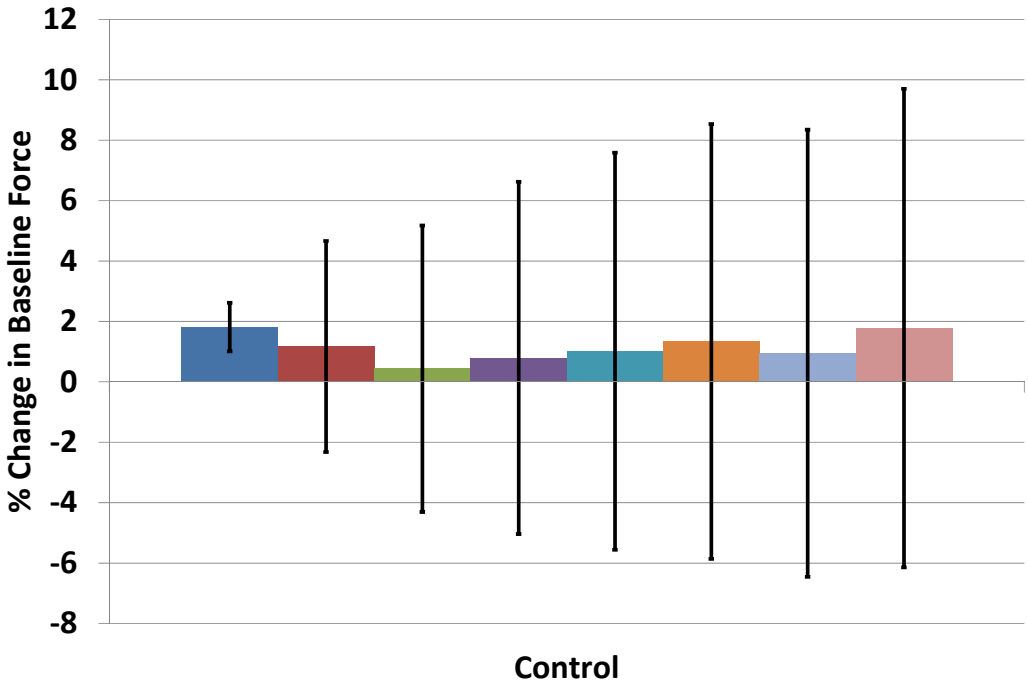

Figure 126: Percent change in baseline force of control muscle bundles of swine trabeculae

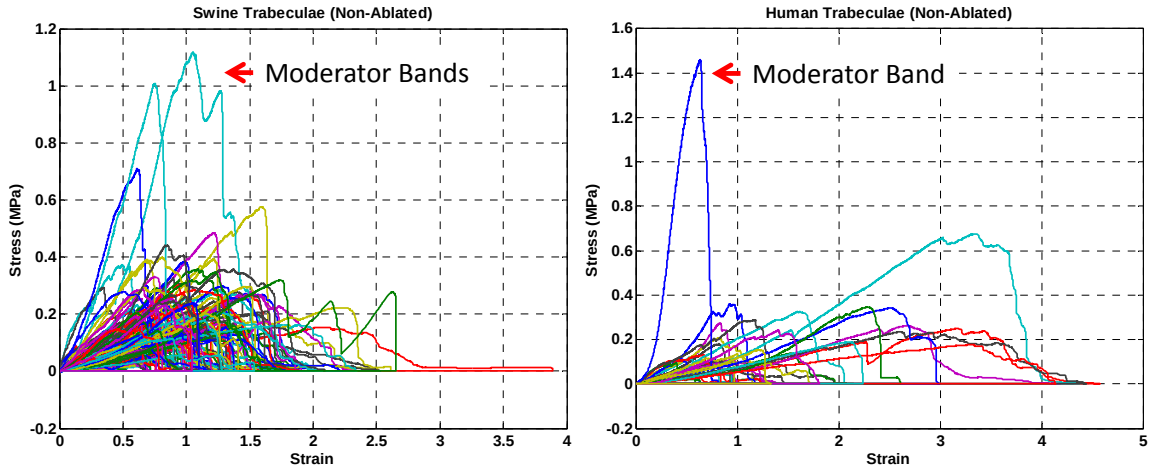

Figure 127: Stress-strain characteristics of swine and human trabeculae muscle bundles

Stress-strain characteristics of swine trabeculae (left, n=117) and human trabeculae (right, n=34) muscle bundles. The moderator bands naturally possess a cylindrical shape and are far more uniform in shape than the rest of the trabecular muscle bundles that were dissected. They registered maximum forces during the uniaxial pulls.

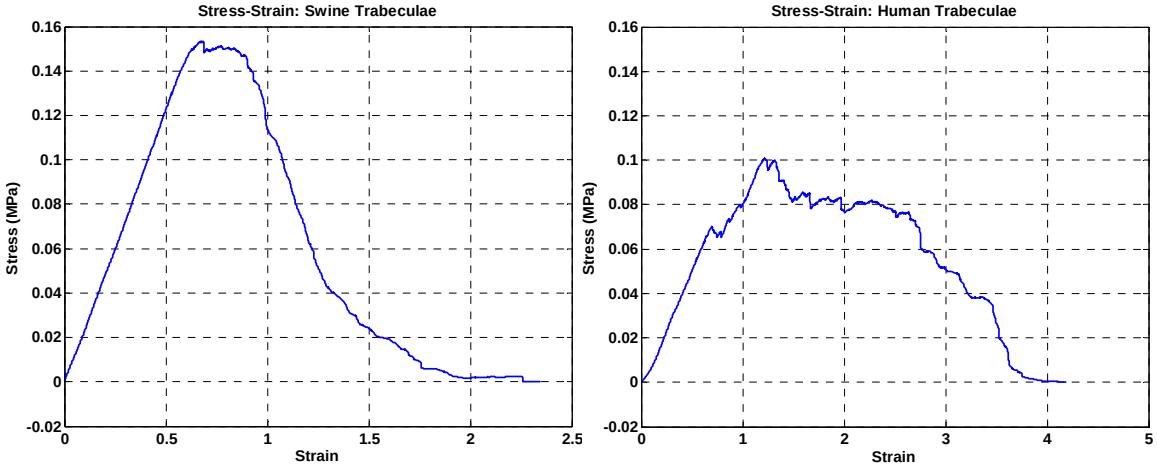

Figure 128: Average model of stress-strain characteristic of swine (left) and human (right) trabeculae

	Initial Cross-sectional Area (mm^2)	Initial Volume (mm^3)	Avulsion Force (N/mm^2)	Elastic Modulus (N/mm^2)	Avulsion Strain ($\Delta l/L$)	Total Strain ($\Delta l/L$)	Avulsion Energy (mJ/mm^3)	Total Energy (mJ/mm^3)
Human Trabeculae Muscle Bundles								
Biomech (n=34)	17.33±8.73	121.21±120.23	0.23±0.25	0.33±0.58	1.32±0.88	1.81±1.20	92.10±116.52	123.63±150.82
RF (n=16)	11.56±3.47	122.24±43.87	0.19±0.12	0.29±0.17	1.04±0.37	1.36±0.65	54.63±42.97	73.48±65.08
HIFU (n=6)	7.88±2.65	100.07±38.62	0.39±0.11	0.87±0.56	0.83±0.28	1.22±0.30	86.60±28.46	116.26±37.56
Study-Controls (n=2)	9.92±1.34	94.25±14.27	0.19±0.02	0.34±0.08	0.59±0.02	1.68±0.88	37.93±5.75	72.16±20.20
Swine Trabeculae Muscle Bundles								
Biomech (n=117)	13.19±4.88	201.20±97.18	0.23±0.15	0.36±0.28	1.02±0.36	1.41±0.54	67.08±46.30	91.90±64.92
RF (n=7)	9.78±2.97	131.09±54.52	0.37±0.14	0.48±0.32	1.18±0.28	1.53±0.49	129.22±55.22	165.76±63.55
EtOH (n=23)	16.66±8.38	250.67±114.91	0.19±0.09	0.27±0.13	1.01±0.34	1.28±0.39	64.84±46.51	82.59±55.22
Study-Controls (n=10)	14.61±8.02	219.45±131.63	0.30±0.13	0.35±0.14	1.22±0.41	1.58±0.45	109.34±72.14	141.78±87.70

Table 18: Mean ± SD dimensional characteristics and biomechanical parameters of human and swine trabeculae muscle bundles

Thesis Summary

Ablation is a routine medical procedure that is used worldwide. As with any medical procedure, a thorough understanding of the procedural details, underlying biophysics, and device-tissue interactions is essential. For the clinician, this understanding is paramount to deliver safe and efficacious therapy. For the medical device engineer, this knowledge is fundamental to design and develop medical devices. Since ablative energy directly affects the target tissue, it is necessary to assess the changes in tissue properties as a result of ablations. Moreover, there are a plethora of ablative modalities used clinically, which makes the problem not only complex, but also challenging. In view of this, the question still remains: What is the impact of ablative modalities on tissues?

As part of these research investigations, there were several learnings. These learnings provided a platform for development of study protocols, execution of ablative studies, analysis of data, and drawing conclusions. These conclusions helped answer some questions, but opened up a whole new spectrum of areas worth investigation in future. Highlighted below are learnings, conclusions, and future outlook.

Learnings:

- Ablations are performed throughout the human body in numerous anatomical locations for treating various carcinomas and disease conditions

- In general, ablative modalities are characterized in two categories: thermal and chemical
- Although there are numerous ablative modalities that are used clinically, for my studies, I used 4 thermal ablation modalities (radiofrequency ablation, cryoablation, microwave ablation, and high-intensity focused ultrasound ablations), and 4 chemical ablative agents (acetic acid, ethanol, hypertonic sodium chloride, and urea)
- Some of the other ablative modalities include: laser ablation, irreversible electroporation, photodynamic therapy, electrosurgical, and ablations using nanoparticles
- Typically, the location and size of tumor dictates the choice of ablation modality, however, therapy choices and applications continue to expand
- Although considered to be relatively safe procedures, ablative treatments can result in significant collateral injury to adjacent structures that might have severe clinical implications
- Examples of collateral injury include damage to the diaphragm while performing ablations in the liver for treatment of liver carcinoma, and damage to the esophagus while performing ablations in the heart for treatment of atrial fibrillation
- The incidence and prevalence of collateral injury due to various ablative modalities is variable

- Several techniques and procedures have been implemented to reduce the incidence of collateral injury, but it still remains an unsolved medical need
- Ablations directly affect the target tissue properties
- In order to assess the quality and efficacy of applied ablative therapy, and minimize collateral injury, it is essential to understand how tissues respond to ablations
- In an attempt to gain this understanding, changes in physiological and biomechanical properties of ablated tissues in response to ablative energies were quantified
- However, the question still remains: What is the impact of ablative modalities on tissues?

Conclusions:

- We developed unique methodologies to study the physiological and biomechanical properties of tissues in response to various ablative modalities
- These methodologies are applicable for analyzing a spectrum of ablation modalities; ones that were used in this investigation and others that could be used in the future, for example, laser ablation, irreversible electroporation, photodynamic therapy, and electro-surgery.

- Designed and conducted over 125 experiments and executed approximately 2500 isolated muscle bundle studies from 19 different tissues (8 human and 11 swine)
- To our knowledge this is the first study of its kind to compare the effects of ablation modalities and dosages on both the physiological and biomechanical properties of isolated functional muscle bundles.
- Physiological and biomechanical properties of different tissues that are susceptible to collateral injury during ablative treatments were characterized.
- Our results demonstrated noteworthy dose responses in physiological properties for each tissue type and each ablation modality investigated.
- Specifically, a given tissue responds to different ablative modalities differently, and a given ablative modality affects different tissues differently
- We are now capable of selecting ablative doses at appropriate clinical settings to perform ablations, as well as studying dosing requirements to achieve a given level of tissue injury.
- Each ablative technique, although similar in purpose, has specific and optimal indications.
- Choice of the most appropriate ablative modality is vital to the success of any ablative procedure. The type of tissue to be ablated, regional blood

flow, and the size of desired lesion are three important factors in this decision.

- Each ablation modality has its unique advantages. For example, the non-invasive, high-precision nature of HIFU makes it attractive in stationary or superficial regions. Among all ablation modalities, RFA has been in practice for the longest time which makes it an attractive modality of choice. One of the advantages of a CRA probe is that it adheres to the target location by forming an ice-ball. Therefore, CRA works well in areas where catheter instability is high due to relative motion between the probe and the target location. MWA is one of the newer ablation techniques offering non-contact therapy application by electric field radiation and dielectric heating. Although it may be applicable to a broader spectrum of tissues, its long-term effectiveness still needs to be evaluated. Compared to any thermal ablation modality, CHA is the most cost-effective options as it does not require any capital equipment for performing ablations. Although cheap, it is restricted to use in target areas with low blood perfusion rates to minimize dilution and wash out, and prevent systemic side effects by localizing the action of injected ablative agent.
- Unique methodologies were developed to test the mechanical strength of tissues under the uniaxial pull machine
- Sophisticated algorithms along with automated data analysis routines were implemented to translate raw data into tangible, meaningful results

- Our results did not demonstrate dose responses in biomechanical properties for any tissue investigated, due to multifactorial reasons
- Significant changes in biomechanical properties were observed as a result of ablative treatments in terms of altered avulsion forces, elastic moduli, strains, and energies
- Conventional and true (Cauchy) stress-strain characteristics of each tissue type were derived
- Nevertheless, in spite of all the advances in the field, ablations are still considered a combination of art and science

Future:

- The translational component of this work could span a broad spectrum, such as: (1) provide novel insights into precise ablation techniques, (2) provide data for procedural modeling and dosing optimization, (3) assessment of post-ablation differences between healthy and diseased tissues, (4) increasing the safety and efficacy of ablative procedures.
- The knowledge gained from these investigations can help the medical community by making an impact in the following areas: (1) reducing procedure times, (2) reducing procedure costs, (3) minimizing procedure invasiveness, and (4) increasing procedure safety and effectiveness to achieve better outcomes.

- The innovative component of this work could serve as a platform for developing new tools and medical devices, such as novel catheters, that can assess the electrical and biomechanical properties of ablated tissue in real-time that further helps to increase the safety and efficacy of ablative procedures.
- Combined knowledge of tissue properties can aid in better understanding of the device-tissue interactions to minimize collateral injury to surrounding structures while performing ablations.
- The methodologies developed herein can allow experimentation with other ablative modalities to include, laser, irreversible electroporation, photodynamic therapy, and electro-surgery.
- Assessment of physiological and biomechanical properties can potentially increase the efficacy and effectiveness of ablation procedures performed.
- Although there were 19 different tissue types assessed in this investigation, this methodology can be applied to investigate any tissue
- Assessment of catheter-tip contact force measurements as that plays a key role in catheter based ablation therapies
- It is clear that understanding of collateral damage at the cellular level, isolated tissue level, and whole heart level will be important to the future of this evolving era of ablations.

To conclude, the work included in this thesis was highly collaborative and novel pursuits. These are innovative methodologies that have been developed in the Visible Heart Lab and can be applied to make a positive impact in the field of ablations.

References

References for Chapter 1

[1] Little, W. J., 1876, “Ablation of the Cuboid Bone in Congenital Varus,” Br. Med. J., **1**(802), p. 594.

[2] Liao, H., Fujiwara, K., Ando, T., Maruyama, T., Kobayashi, E., Muragaki, Y., Iseki, H., and Sakuma, I., 2013, “Automatic Laser Scanning Ablation System for High-precision Treatment of Brain Tumors,” Lasers Med. Sci., **28**(3), pp. 891-900. DOI: 10.1007/s10103-012-1164-6

[3] Lipsman, N., Schwartz, M. L., Huang, Y., Lee, L., Sankar, T., Chapman, M., Hynynen, K., and Lozano, A. M., 2013, “MR-guided Focused Ultrasound Thalamotomy for Essential Tremor: A Proof-of-Concept Study,” Lancet Neurol., **12**(5), pp. 462-468. DOI: 10.1016/S1474-4422(13)70048-6

[4] Tierney, T. S., Abd-El-Barr, M. M., Stanford, A. D., Foote, K. D., and Okun, M. S., 2014, “Deep Brain Stimulation and Ablation for Obsessive Compulsive Disorder: Evolution of Contemporary Indications, Targets and Techniques,” Int. J. Neurosci., **124**(6), pp. 394-402. DOI: 10.3109/00207454.2013.852086

[5] Tovar-Spinoza, Z., Carter, D., Ferrone, D., Eksioglu, Y., and Huckins, S., 2013, “The Use of MRI-guided Laser-induced Thermal Ablation for Epilepsy,” Childs Nerv. Syst., **29**(11), pp. 2089-2094. DOI: 10.1007/s00381-013-2169-6

[6] Gazelka, H. M., Knievel, S., Mauck, W. D., Moeschler, S. M., Pingree, M. J., Rho, R. H., and Lamer, T. J., 2014, “Incidence of Neuropathic Pain after Radiofrequency Denervation of the Third Occipital Nerve,” J. Pain Res., **7**, pp. 195-198. DOI: 10.2147/JPR.S60925

[7] Vu, T., and Chhatre, A., 2014, “Cooled Radiofrequency Ablation for Bilateral Greater Occipital Neuralgia,” Case Rep. Neurol. Med., 2014, Abstract 257373. DOI 10.1155/2014/257373

[8] Assa, S., Meyer, S., and Fried, D., 2008, “Ablation of Dental Hard Tissues with a Microsecond Pulsed Carbon Dioxide Laser Operating at 9.3-μm with an Integrated Scanner,” Proc. Soc. Photo Opt. Instrum. Eng., 6843, Abstract 684308.

[9] Harris, D. M., White, J. M., Goodis, H., Arcoria, C. J., Simon, J., Carpenter, W. M., Fried, D., Burkart, J., Yessik, M., and Myers, T., 2002, “Selective Ablation of Surface Enamel Caries with a Pulsed Nd: YAG Dental Laser,” Lasers Surg. Med., **30**(5), pp. 342-350.

[10] Lamantia, N. R., Tom, H., Chan, K. H., Simon, J. C., Darling, C. L., and Fried, D., 2014, “High Contrast Optical Imaging Methods for Image Guided Laser Ablation of Dental Caries Lesions,” Proc. Soc. Photo Opt. Instrum. Eng., Feb 18, 8929. DOI: 10.1117/12.2045683

[11] Ilgner, J., Wehner, M., Lorenzen, J., Bovi, M., and Westhofen, M., 2006, “Morphological Effects of Nanosecond- and Femtosecond-pulsed Laser Ablation on Human Middle Ear Ossicles,” J. Biomed. Opt., **11**(1), 014004.

[12] Sedlmaier, B., Pomorzev, A., Haisch, A., Halleck, P., Scherer, H., and Göktas, O., 2009, “The Improvement of Middle Ear Ventilation by Laser Ablation of the Epipharyngeal Eustachian Tube: A Prospective Study,” Lasers Med. Sci., **24**(5), pp. 793-800. DOI: 10.1007/s10103-009-0646-7

[13] Barret, J. P., 2014, “From Partial to Full-face Transplantation: Total Ablation and Restoration, A Change in the Reconstructive Paradigm,” Int. J. Surg., **12**(2), pp. 109-112. DOI: 10.1016/j.ijsu.2013.11.016

[14] Field, L. M., 1981, “Ablation of a Persistent Angiomatous Condition on the Face in Stages by a Variety of Flap Techniques and Selective Dermabrasion,” J. Dermatol. Surg. Oncol., **7**(3), pp. 266-269.

[15] Tanenbaum, M., Karas, S., and McCord, C. D. Jr., 1988, “Laser Ablation of Blepharopigmentation,” Ophthal. Plast. Reconstr. Surg., **4**(1), pp. 49-56.

[16] Fuller, C. W., Nguyen, S. A., Lohia, S., and Gillespie, M. B., 2014, “Radiofrequency Ablation for Treatment of Benign Thyroid Nodules: Systematic Review,” Laryngoscope, **124**(1), pp. 346-353. DOI: 10.1002/lary.24406

[17] Wong, K. P., and Lang, B. H., 2013, “Use of Radiofrequency Ablation in Benign Thyroid Nodules: A Literature Review and Updates,” Int. J. Endocrinol., 2013, 428363.

[18] Andrioli, M., Riganti, F., Pacella, C. M., and Valcavi, R., 2012, “Long-term Effectiveness of Ultrasound-guided Laser Ablation of Hyperfunctioning Parathyroid Adenomas: Present and Future Perspectives,” AJR Am. J. Roentgenol., **199**(5), pp. 1164-1168. DOI: 10.2214/AJR.11.8442

[19] Chen, H. H., Lin, C. J., Wu, C. J., Lai, C. T., Lin, J., Cheng, S. P., and Yang, T. L., 2011, “Chemical Ablation of Recurrent and Persistent Secondary Hyperparathyroidism after Subtotal Parathyroidectomy,” Ann. Surg., **253**(4), pp. 786-790. DOI: 10.1097/SLA.0b013e318211ccc2

[20] Sung, J. Y., Baek, J. H., Kim, K. S., Lee, D., Ha, E. J., and Lee, J. H., 2013, “Symptomatic Nonfunctioning Parathyroid Cysts: Role of Simple Aspiration and Ethanol Ablation,” Eur. J. Radiol., **82**(2), pp. 316-320. DOI: 10.1016/j.ejrad.2012.10.009

[21] Xu, S. Y., Wang, Y., Xie, Q., and Wu, H..Y, 2013, “Percutaneous Sonography-guided Radiofrequency Ablation in the Management of Parathyroid Adenoma,” Singapore Med. J., **54**(7), pp. e137-140.

[22] Friedman, M., LoSavio, P., Ibrahim, H., and Ramakrishnan, V., 2003, “Radiofrequency Tonsil Reduction: Safety, Morbidity, and Efficacy,” Laryngoscope, **113**(5), pp. 882-887.

[23] Krespi, Y. P., and Kizhner, V., 2013, “Laser Tonsil Cryptolysis: In-office 500 Cases Review,” Am. J. Otolaryngol., **34**(5), pp. 420-424. DOI: 10.1016/j.amjoto.2013.03.006

[24] Plant, R. L., 2002, “Radiofrequency Treatment of Tonsillar Hypertrophy,” Laryngoscope, **112**(8 Pt 2 Suppl 100), pp. 20-22.

[25] Zbyshko, Ia. B., 2007, “A Comparative Analysis of Tonsillectomy and Ablation of the Palatine Tonsils with CO2 Laser,” Vestn. Otorinolaringol., (4), pp. 15-17.

[26] Akiyama, J., Roorda, A., and Triadafilopoulos, G., 2013, “Managing Barrett's Esophagus with Radiofrequency Ablation,” Gastroenterol. Rep., **1**(2), pp. 95-104. DOI: 10.1093/gastro/got009

[27] Ertan, A., Zaheer, I., Correa, A. M., Thosani, N., and Blackmon, S. H., 2013, “Photodynamic Therapy vs Radiofrequency Ablation for Barrett's Dysplasia: Efficacy, Safety and Cost-comparison,” World J. Gastroenterol., **19**(41), pp. 106-113. DOI: 10.3748/wjg.v19.i41.7106

[28] Gosain, S., Mercer, K., Twaddell, W. S., Uradomo, L., and Greenwald, B. D., 2013, “Liquid Nitrogen Spray Cryotherapy in Barrett's Esophagus with High-grade Dysplasia: Long-term Results,” Gastrointest. Endosc., **78**(2), pp. 260-265. DOI: 10.1016/j.gie.2013.03.002

[29] Kawasaki, R., Gauri, A., Elmouchi, D., Duggal, M., and Bhan, A., 2014, “Atrioesophageal Fistula Complicating Cryoballoon Pulmonary Vein Isolation for Paroxysmal Atrial Fibrillation,” J. Cardiovasc. Electrophysiol. Apr 4 2014 [Epub ahead of print]. DOI: 10.1111/jce.12426

[30] Borchert, B., Lawrenz, T., Hansky, B., and Stellbrink, C., 2008, “Lethal Atrioesophageal Fistula after Pulmonary Vein Isolation using High-intensity Focused Ultrasound (HIFU),” Heart Rhythm, **5**(1), pp. 145-148.

[31] Challa, P. K., and Mansour, M., 2011, “Atrial Fibrillation: Update on Ablation Strategies and Technology,” Curr. Cardiol. Rep., **13**(5), pp. 394-398. DOI: 10.1007/s11886-011-0205-2

[32] Chiu, H. M., Mohan, A. S., Weily, A. R., Guy, D. J., and Ross, D. L., 2003, “Analysis of a Novel Expanded Tip Wire (ETW) Antenna for Microwave Ablation of Cardiac Arrhythmias,” IEEE Trans. Biomed. Eng., **50**(7), pp. 890-899.

[33] D'Avila, A., and Dukkipati, S., 2009, “Esophageal Damage during Catheter Ablation of Atrial Fibrillation: Is Cryo Safer than RF?,” Pacing Clin. Electrophysiol., **32**(6), pp. 709-710. DOI: 10.1111/j.1540-8159.2009.02355.x

[34] Nellens, P., Gürsoy, S., Andries, E., and Brugada, P., 1992, “Transcoronary Chemical Ablation of Arrhythmias,” Pacing Clin. Electrophysiol., **15**(9), pp. 1368-1373.

[35] Piccini, J. P., and Daubert, J. P., 2011, “Cryoablation of Atrial Fibrillation,” J. Interv. Card. Electrophysiol., **32**(3), pp. 233-242. DOI: 10.1007/s10840-011-9603-z

[36] Alexander, E. S., and Dupuy, D. E., 2013, “Lung Cancer Ablation: Technologies and Techniques,” Semin. Intervent. Radiol., **30**(2), pp. 141-150.

[37] Colak, E., Tatlı, S., Shyn, P. B., Tuncalı, K., and Silverman, S. G., 2014, “CT-guided Percutaneous Cryoablation of Central Lung Tumors,” Diagn. Interv. Radiol., April 30 214 [Epub ahead of print]. DOI: 10.5152/dir.2014.13440

[38] Robert Sheu, Y., and Hong, K., 2013, “Percutaneous Lung Tumor Ablation,” Tech. Vasc. Interv. Radiol., **16**(4), pp. 239-252. DOI: 10.1053/j.tvir.2013.09.001

[39] Vaezy, S., Zderic, V., Karmy-Jones, R., Jurkovich, G. J., Cornejo, C., and Martin, R. W., 2007, “Hemostasis and Sealing of Air Leaks in the Lung using High-intensity Focused Ultrasound,” J. Trauma, **62**(6), pp. 1390-1395.

[40] Bland, K. L., Gass, J., and Klimberg, V. S., 2007, “Radiofrequency, Cryoablation, and Other Modalities for Breast Cancer Ablation,” Surg. Clin. North Am., **87**(2), pp. 539-550, xii.

[41] Brenin, D. R., 2011, “Focused Ultrasound Ablation for the Treatment of Breast Cancer,” Ann. Surg. Oncol., **18**(11), pp. 3088-3094. DOI: 10.1245/s10434-011-2011-x

[42] Phasukkit, P., Sanpanich, A., Tungjitkusolmun, S., and Hamamoto, K., 2013, “Effect of Phase Difference in Multi-antenna Microwave Thermal Ablation for Breast Cancer Treatment,” Conf. Proc. IEEE Eng. Med. Biol. Soc., 2013, pp. 3718-3721. DOI: 10.1109/EMBC.2013.6610351

[43] Hashemieh, M., Akhlaghpoor, S., Azarkeivan, A., Azizahari, A., Shirkavand, A., and Sheibani, K., 2012, “Partial Radiofrequency Ablation of the Spleen in Thalassemia,” Diagn. Interv. Radiol., **18**(4), pp. 397-402. DOI: 10.4261/1305-3825.DIR.4537-11.1

[44] Liang, P., Gao, Y., Zhang, H., Yu, X., Wang, Y., Duan, Y., and Shi, W., 2011, “Microwave Ablation in the Spleen for Treatment of Secondary Hypersplenism: A Preliminary Study,” AJR Am. J. Roentgenol., **196**(3), pp. 692-696. DOI: 10.2214/AJR.10.4193

[45] Chen, X. L., Ma, Y., Wan, Y., and Duan, L. G., 2010, “Experimental Study of the Safety of Pancreas Cryosurgery: The Comparison of 2 Different Techniques of Cryosurgery,” Pancreas, **39**(1), pp. 92-96. DOI: 10.1097/MPA.0b013e3181bdd41a

[46] Date, R. S., and Siriwardena, A. K., 2005, “Radiofrequency Ablation of the Pancreas. II: Intra-operative Ablation of Non-resectable Pancreatic Cancer. A Description of Technique and Initial Outcome,” JOP, **6**(6), pp. 588-592.

[47] Miura, T., Haida, K., Haida, S., and Wada, T., 1982, “Intraarterial Infusion Chemotherapy in Combination with 2450-MHz Microwave Hyperthermia for Cancer of the Head of the Pancreas,” Prog. Clin. Biol. Res., **107**, pp. 767-774.

[48] Clark, T. W., and Soulen, M. C., 2002, “Chemical Ablation of Hepatocellular Carcinoma,” J. Vasc. Interv. Radiol., **13**(9 Pt 2), pp. S245-252.

[49] Dunne, R. M., Shyn, P. B., Sung, J. C., Tatli, S., Morrison, P. R., Catalano, P. J., and Silverman, S. G., 2014, “Percutaneous Treatment of Hepatocellular Carcinoma in Patients with Cirrhosis: A Comparison of the Safety of Cryoablation and Radiofrequency Ablation,” Eur. J. Radiol., **83**(4), pp. 632-638. DOI: 10.1016/j.ejrad.2014.01.007

[50] Hoang, N. H., Murad, H. Y., Ratnayaka, S. H., Chen, C., and Khismatullin, D. B., 2014, “Synergistic Ablation of Liver Tissue and Liver Cancer Cells with High-

Intensity Focused Ultrasound and Ethanol," Ultrasound Med. Biol., **40**(8), pp. 1869-1881. DOI: 10.1016/j.ultrasmedbio.2014.02.026

[51] Becker, C. D., and Burhenne, H. J., 1990, "Ablation of the Cystic Duct and the Gallbladder. Experimental Basis and Initial Clinical Observations," Radiol. Clin. North Am., **28**(6), pp. 1277-1287.

[52] Coleman, C. C., Vennes, J. A., Posalaky, I. P., and Amplatz, K., 1991, "Thermal Ablation of the Gallbladder," Radiology, **180**(2), pp. 363-366.

[53] Majeed, A. W., Reed, M. W., Stephenson, T. J., and Johnson, A. G., 1997, "Chemical Ablation of the Gallbladder," Br. J. Surg., **84**(5), pp. 638-641.

[54] Klatte, T., Kroeger, N., Zimmermann, U., Burchardt, M., Belldegrun, A. S., and Pantuck, A. J., 2014, "The Contemporary Role of Ablative Treatment Approaches in the Management of Renal Cell Carcinoma (RCC): Focus on Radiofrequency Ablation (RFA), High-intensity Focused Ultrasound (HIFU), and Cryoablation," World J. Urol., **32**(3), pp. 597-605. DOI: 10.1007/s00345-014-1284-7

[55] Lee, Y. R., and Lee, K. B., 2003, "Ablation of Symptomatic Cysts using Absolute Ethanol in 11 Patients with Autosomal-dominant Polycystic Kidney Disease," Korean J. Radiol., **4**(4), pp. 239-242.

[56] Lin, Y., Liang, P., Yu, X. L., Yu, J., Cheng, Z. G., Han, Z. Y., and Liu, F. Y., 2014, "Percutaneous Microwave Ablation of Renal Cell Carcinoma is Safe in Patients with a Solitary Kidney," Urology, **83**(2), pp. 357-363. DOI: 10.1016/j.urology.2013.05.071

[57] Olweny, E. O., and Cadeddu, J. A., 2012, "Novel Methods for Renal Tissue Ablation," Curr. Opin. Urol., **22**(5), pp. 379-384. DOI: 10.1097/MOU.0b013e328355ecf5

[58] Kigure, T., Harada, T., Satoh, Y., Fujieda, N., and Wakayama, Y., 1996, "Microwave Ablation of the Adrenal Gland: Experimental Study and Clinical Application," Br. J. Urol., **77**(2), pp. 215-220.

[59] Moll, R., Gassel, H. J., Timmermann, W., and Schindler, G., 2004, "Radiofrequency Ablation as Minimal Invasive Procedure in the Treatment of Adrenal Gland Tumor," Dtsch. Med. Wochenschr., **129**(19), pp. 1071-1074.

[60] Welch, B. T., Atwell, T. D., Nichols, D. A., Wass, C. T., Callstrom, M. R., Leibovich, B. C., Carpenter, P. C., Mandrekar, J. N., and Charboneau, J. W., 2011, "Percutaneous Image-guided Adrenal Cryoablation: Procedural

Considerations and Technical Success," Radiology, **258**(1), pp. 301-307. DOI: 10.1148/radiol.10100631

[61] Xiao, Y. Y., Tian, J. L., Li, J. K., Yang, L., and Zhang, J. S., 2008, "CT-guided Percutaneous Chemical Ablation of Adrenal Neoplasms," AJR Am. J. Roentgenol., **190**(1), pp. 105-110.

[62] Chen, J. C., Moriarty, J. A., Derbyshire, J. A., Peters, R. D., Trachtenberg, J., Bell, S. D., Doyle, J., Arrelano, R., Wright, G. A., Henkelman, R. M., Hinks, R. S., Lok, S. Y., Toi, A., and Kucharczyk, W., 2000, "Prostate Cancer: MR Imaging and Thermometry during Microwave Thermal Ablation-Initial Experience, Radiology, **214**(1), pp. 290-297.

[63] Chen, L., Meng, S., Wang, H., Bali, P., Bai, W., Li, B., Atadja, P., Bhalla, K. N., and Wu, J., 2005, "Chemical Ablation of Androgen Receptor in Prostate Cancer Cells by the Histone Deacetylase Inhibitor LAQ824," Mol. Cancer Ther., **4**(9), pp. 1311-1319.

[64] Crouzet, S., Rouviere, O., Martin, X., and Gelet, A., 2014, "High-intensity Focused Ultrasound as Focal Therapy of Prostate Cancer," Curr. Opin. Urol., **24**(3), pp. 225-230. DOI: 10.1097/MOU.0000000000000053

[65] Durand, M., Barret, E., Galiano, M., Rozet, F., Sanchez-Salas, R., Ahallal, Y., Macek, P., Gaya, J. M., Cerruti, J., Devilliers, H., Loeffler, J., Amiel, J., Vallancien, G., and Cathelineau, X., 2014, "Focal Cryoablation: A Treatment Option for Unilateral Low-risk Prostate Cancer," BJU Int., **113**(1), pp. 56-64. DOI: 10.1111/bju.12370

[66] Jindal, G., Friedman, M., Locklin, J., and Wood, B. J., 2006, "Palliative Radiofrequency Ablation for Recurrent Prostate Cancer," Cardiovasc. Intervent. Radiol., **29**(3), pp. 482-485.

[67] Wenger, H., Yousuf, A., Oto, A., and Eggener, S., 2014, "Laser Ablation as Focal Therapy for Prostate Cancer," Curr. Opin. Urol., **24**(3), pp. 236-240. DOI: 10.1097/MOU.0000000000000044

[68] Damyanov, C., 1996, "Ethanol Sclerotherapy in Superficial Bladder Tumors," Ann. Urol., **30**(5), pp. 244-246.

[69] Fenner, A., 2013, "Bladder Cancer: Outpatient Laser Ablation is an Option for Localized Bladder Cancer Treatment," Nat. Rev. Urol., **10**(7), p. 368. DOI: 10.1038/nrurol.2013.120

[70] Sun, Y., Xu, C., Qian, S., Qu, C., Zhao, J., and Ma, Y., 2001, “Transurethral Microwave Needle Ablation for Bladder Cancer,” Chin. Med. J., **114**(5), pp. 546-547.

[71] Berman, J. M., Guido, R. S., and Chudnoff, S. G., 2014, “Radiofrequency Volumetric Thermal Ablation of Fibroids: Analysis of 3-year Outcomes,” Obstet. Gynecol., **123(**Suppl 1), pp. 121S-122S. DOI: 10.1097/01.AOG.0000447078.42115.f4

[72] Kucukozkan, T., Kadioglu, B. G., Uygur, D., Moroy, P., Mollamahmutoglu, L., and Besli, M., 2004, “Chemical Ablation of Endometrium with Trichloroacetic Acid,” Int. J. Gynaecol. Obstet., **84**(1), pp. 41-46.

[73] Kumar, S., Suneetha, P. V., Dadhwal, V., and Mittal, S., 2002, “Endometrial Cryoablation in the Treatment of Dysfunctional Uterine Bleeding,” Int. J. Gynaecol. Obstet., **76**(2), pp. 189-190.

[74] Nakayama, K., Ishibashi, T., Ishikawa, M., Katagiri, A., Katagiri, H., Iida, K., Nakayama, N., and Miyazaki, K., 2014, “Microwave Endometrial Ablation at a Frequency of 2.45 GHz for Menorrhagia: Analysis of Treatment Results at a Single Facility,” J. Obstet. Gynaecol. Res., **40**(1). pp. 224-229. DOI: 10.1111/jog.12163

[75] Park, M. J., Kim, Y. S., Rhim, H., and Lim, H. K., 2014, “Safety and Therapeutic Efficacy of Complete or Near-complete Ablation of Symptomatic Uterine Fibroid Tumors by MR Imaging-guided High-intensity Focused US Therapy,” J. Vasc. Interv. Radiol., **25**(2), pp. 231-239. DOI: 10.1016/j.jvir.2013.11.011

[76] Marincaş, M., Prunoiu, V., Ionescu, S., and Brătucu, E., 2014, “The Place of Radiofrequency Ablation in the Multimodal Treatment of Cervical Cancer. Our experience,” Chirurgia (Bucur). **109**(2), pp. 168-173.

[77] Nitschke, A. M., and Ray, CE Jr., 2013, “Percutaneous Neurolytic Celiac Plexus Block,” Semin. Intervent. Radiol., **30**(3), pp. 318-321.

[78] Walsh, N., and Sarria, J. E., 2012, “Management of Chronic Pain in a Patient with Autosomal Dominant Polycystic Kidney Disease by Sequential Celiac Plexus Blockade, Radiofrequency Ablation, and Spinal Cord Stimulation,” Am. J. Kidney Dis., **59**(6), pp. 858-861. DOI: 10.1053/j.ajkd.2011.12.018

[79] Avery, J., Kumar, K., Thakur, V., and Thakur, A., 2014, “Radiofrequency Ablation as First-line Treatment of Varicose Veins,” Am. Surg., **80**(3), pp. 231-235.

[80] Mao, J., Zhang, C., Wang, Z., Gan, S., and Li, K., 2012, “A Retrospective Study Comparing Endovenous Laser Ablation and Microwave Ablation for Great Saphenous Varicose Veins,” Eur. Rev. Med. Pharmacol. Sci., **16**(7), pp. 873-877.

[81] Lorenz, M. B., Gkogkolou, P., and Görge, T., 2014, “Sclerotherapy of Varicose Veins in Dermatology,” J. Dtsch. Dermatol. Ges., **12**(5), pp. 391-393. DOI: 10.1111/ddg.12333

[82] Chua, N. H., Vissers, K. C., and Sluijter, M. E., 2011, “Pulsed Radiofrequency Treatment in Interventional Pain Management: Mechanisms and Potential Indications-A Review,” Acta Neurochir. (Wien), **153**(4), pp. 763-771. DOI: 10.1007/s00701-010-0881-5

[83] Mukai, A., and Kancherla, V., 2011, “Interventional Procedures for Cervical Pain,” Phys. Med. Rehabil. Clin. N. Am., **22**(3), pp. 539-549, x. DOI: 10.1016/j.pmr.2011.02.008

[84] Nagda, J. V., Davis, C. W., Bajwa, Z. H., and Simopoulos, T. T., 2011, “Retrospective Review of the Efficacy and Safety of Repeated Pulsed and Continuous Radiofrequency Lesioning of the Dorsal Root Ganglion/Segmental Nerve for Lumbar Radicular Pain,” Pain Physician, **14**(4), pp. 371-376.

[85] Straube, S., Derry, S., Moore, R. A., and Cole, P., 2013, “Cervico-thoracic or Lumbar Sympathectomy for Neuropathic Pain and Complex Regional Pain Syndrome,” Cochrane Database Syst. Rev., **9**, CD002918. DOI: 10.1002/14651858.CD002918

[86] Callstrom, M. R., and Charboneau, J. W., 2005, “Percutaneous Ablation: Safe, Effective Treatment of Bone Tumors,” Oncology (Williston Park), **19**(11 Suppl 4), pp. 22-26.

[87] Chen, W., Wang, Z., Wu, F., Zhu, H., Zou, J., Bai, J., Li, K., and Xie, F., 2002, “High Intensity Focused Ultrasound in the Treatment of Primary Malignant Bone Tumor,” Zhonghua Zhong Liu Za Zhi, **24**(6), pp. 612-615.

[88] Fan, Q., Ma, B., Zhou, Y., Zhang, M., and Hao, X., 2003, “Bone Tumors of the Extremities or Pelvis Treated by Microwave-induced Hyperthermia,” Clin. Orthop. Relat. Res., **406**, pp. 165-175.

[89] Simon, C. J., and Dupuy, D. E., 2006, “Percutaneous Minimally Invasive Therapies in the Treatment of Bone Tumors: Thermal Ablation,” Semin. Musculoskelet. Radiol., **10**(2), pp. 137-144.

[90] Becerro de Bengoa Vallejo, R., Losa Iglesias, M. E., Sanchez Gomez, R., and Jules, K. T., 2008, "Gauze Application of Phenol for Matrixectomy," J. Am. Podiatr. Med. Assoc., **98**(5), pp. 418-421.

[91] Záborszky, Z., Fekete, L., Tauzin, F., and Orgován, G., 1997, "Treatment of Ingrowing Toenail with Segmental Chemical Ablation," Acta Chir. Hung., **36**(1-4), pp. 398-400.

[92] Huang, S. K., Jordan, N., Graham, A., Bharati, S., Lampe, L., Odell, R., and Marcus, F. I., 1985, "Closed Chest Catheter Desiccation of the Atrioventricular Junction using Radiofrequency Energy: A New Method of Catheter Ablation [Abstract #1556]," Circulation, **72**, III-389.

[93] Hong, K. N., Russo, M. J., Liberman, E. A., Trzebucki, A., Oz, M. C., Argenziano, M., and Williams, M. R., 2007, "Effect of Epicardial Fat on Ablation Performance: A Three-energy Source Comparison," J. Card. Surg., **22**(6), pp. 521-524.

[94] Yokoyama, K., Nakagawa, H., Shah, D. C., Lambert, H., Leo, G., Aeby, N., Ikeda, A., Pitha, J. V., Sharma, T., Lazzara, R., and Jackman, W. M., 2008, "Novel Contact Force Sensor Incorporated in Irrigated Radiofrequency Ablation Catheter Predicts Lesion Size and Incidence of Steam Pop and Thrombus," Circ. Arrhythm. Electrophysiol., **1**(5), pp. 354-362. DOI: 10.1161/CIRCEP.108.803650

[95] Haines, D. E., and Verow, A. F., 1990, "Observations on Electrode-tissue Interface Temperature and Effect on Electrical Impedance during Radiofrequency Ablation of Ventricular Myocardium," Circulation, **82**(3), pp. 1034-1038.

[96] Britton, S. W., 1930, "Extreme Hypothermia in Various Animals and in Man: With Notes on the Detection of Life and the Possibility of Recovery in Cases of Apparent Death from Exposure to Cold," Can. Med. Assoc. J., **22**(2), pp. 257-261.

[97] Cooper, I. S., 1962, "A Cryogenic Method for Physiologic Inhibition and Production of Lesions in the Brain," J. Neurosurg., **19**, pp. 853-858.

[98] Hass, G. M., and Taylor, C. B., 1947, "A Quantitative Hypothermal Method for Production of Local Injury to Tissue," Fed. Proc., **6**(1), p. 393.

[99] Lister, J. W., Hoffman, B. F., and Kavaler, F., 1964, "Reversible Cold Block of the Specialized Cardiac Tissues of the Unanaesthetized Dog," Science, **145**(3633), pp. 723-725.

[100] Lustgarten, D. L., Keane, D., and Ruskin, J., 1999, “Cryothermal Ablation: Mechanism of Tissue Injury and Current Experience in the Treatment of Tachyarrhythmias,” Prog. Cardiovasc. Dis., **41**(6), pp. 481-498.

[101] Baust, J., Gage, A. A., Ma, H., and Zhang, C. M., 1997, “Minimally Invasive Cryosurgery--Technological Advances,” Cryobiology, **34**(4), pp. 373-384.

[102] Gage, A. A., Baust, J. M., and Baust, J. G., 2009, “Experimental Cryosurgery Investigations In Vivo,” Cryobiology, **59**(3), pp. 229-243. DOI: 10.1016/j.cryobiol.2009.10.001

[103] Whittaker, D. K., 1984, “Mechanisms of Tissue Destruction following Cryosurgery,” Ann. R. Coll. Surg. Engl., **66**(5), pp. 313-318.

[104] Budman, H., Shitzer, A., and Dayan, J., 1995, “Analysis of the Inverse Problem of Freezing and Thawing of a Binary Solution during Cryosurgical Processes,” J. Biomech. Eng., **117**(2), pp. 193-202.

[105] Mikat, E. M., Hackel, D. B., Harrison, L., Gallagher, J. J., and Wallace, A. G., 1977, “Reaction of the Myocardium and Coronary Arteries to Cryosurgery,” Lab Invest., **37**(6), pp. 632-641.

[106] Mazur, P., 1970, “Cryobiology: The Freezing of Biological Systems,” Science, **168**(3934), pp. 939-949.

[107] Holman, W. L., Kirklin, J. K., Anderson, P. G., and Pacifico, A. D., 1992, “Variation in Cryolesion Penetration due to Probe Size and Tissue Thermal Conductivity,” Ann. Thorac. Surg., **53**(1), pp. 123–126.

[108] Hashimoto, K., Watanabe, I., Okumura, Y., Ohkubo, K., Ashino, S., Kofune, M., Nakai, T., Kunimoto, S., Kasamaki, Y., and Hirayama, A., 2009, “Comparison of Endocardial and Epicardial Lesion Size Following Large-tip and Extra-large-tip Transcatheter Cryoablation,” Circ. J., **73**(9), pp. 1619-1626.

[109] Stewart, G., Preketes, A., Horton, M., Ross, W., and Morris, D., 1995, “Hepatic Cryotherapy: Double-freeze Cycles Achieve Greater Hepatocellular Injury in Man,” Cryobiology, **32**(3), pp. 215–219.

[110] Schwagten, B., Van Belle, Y., and Jordaens, L., 2010, “Cryoablation: How to Improve Results in Atrioventricular Nodal Reentrant Tachycardia Ablation?,” Europace, **12**(11), pp. 522-525. DOI: 10.1093/europace/euq294.

[111] Ikeda, A., Nakagawa, H., Pitha, J. V., Swank, S., Barold, H. S., Sharma, T., and Jackman, W. M., 2008, "Increasing Contact Force Increases Lesion Size during Cryo-ablation," Circulation, **118**, pp. S829-S830.

[112] Avitall, B., Urboniene, D., Rozmus, G., Lafontaine, D., Helms, R., and Urbonas, A., 2003, "New Cryotechnology for Electrical Isolation of the Pulmonary Veins," J. Cardiovasc. Electrophysiol., **14**(3), pp. 281-286.

[113] Wilkens, V., and Reimann, H. P., 2004, "Output Intensity Measurement on a Diagnostic Ultrasound Machine using a Calibrated Thermoacoustic Sensor," J. Phys. Conf. Ser., **1**, pp. 140-145.

[114] Dubinsky, T. J., Cuevas, C., Dighe, M. K., Kolokythas, O., and Hwang, J. H., 2008, "High-intensity Focused Ultrasound: Current Potential and Oncologic Applications," AJR Am. J. Roentgenol., **190**(1), pp. 191-199.

[115] Zhou, Y., 2013, "Generation of Uniform Lesions in High Intensity Focused Ultrasound Ablation," Ultrasonics, **53**(2), pp. 495-505. DOI: 10.1016/j.ultras.2012.09.001

[116] Roberts, W. W., Hall, T. L., Ives, K., Wolf, J. S. Jr, Fowlkes, J. B., and Cain, C. A., 2006, "Pulsed Cavitational Ultrasound: A Noninvasive Technology for Controlled Tissue Ablation (Histotripsy) in the Rabbit Kidney," J. Urol., **175**(2), pp. 734-738.

[117] Khokhlova, V. A., Bailey, M. R., Reed, J. A., Cunitz, B. W., Kaczkowski, P. J., and Crum, L. A., 2006, "Effects of Nonlinear Propagation, Cavitation, and Boiling in Lesion Formation by High Intensity Focused Ultrasound in a Gel Phantom," J. Acoust. Soc. Am., **119**(3), pp. 1834-1848.

[118] Wang, Y. N., Khokhlova, T., Bailey, M., Hwang, J. H., and Khokhlova, V., 2013, "Histological and Biochemical Analysis of Mechanical and Thermal Bioeffects in Boiling Histotripsy Lesions Induced by High Intensity Focused Ultrasound," Ultrasound Med. Biol., **39**(3), pp. 424-438. DOI: 10.1016/j.ultrasmedbio.2012.10.012.

[119] Anderson, R. L., Herman, T. S., van Kersen, I., and Hahn, G. M., 1988, "Thermotolerance and Heat Shock Protein Induction by Slow Rates of Heating," Int. J. Radiat. Oncol. Biol. Phys., **15**(3), pp. 717-725.

[120] Repasky, E., and Issels, R., 2002, "Physiological Consequences of Hyperthermia: Heat, Heat Shock Proteins and the Immune Response," Int. J. Hyperthermia, **18**(6), pp. 486-489.

[121] Neven, K., Schmidt, B., Metzner, A., Otomo, K., Nuyens, D., De Potter, T., Chun, K. R., Ouyang, F., and Kuck, K. H., 2010, “Fatal End of a Safety Algorithm for Pulmonary Vein Isolation with Use of High-Intensity Focused Ultrasound,” Circ. Arrhythm. Electrophysiol., **3**(3), pp. 260-265. DOI: 10.1161/CIRCEP.109.922930

[122] Malcolm, A. L., and ter Haar, G. R., 1996, “Ablation of Tissue Volumes using High Intensity Focused Ultrasound,” Ultrasound Med. Biol., **22**(5), pp. 659-669.

[123] Chen, L., ter Haar, G., and Hill, C. R., 1997, “Influence of Ablated Tissue on the Formation of High-intensity Focused Ultrasound Lesions,” Ultrasound Med. Biol., **23**(6), pp. 921-931.

[124] Häcker, A., Peters, K., Knoll, T., Marlinghaus, E., Alken, P., Jenne, J. W., and Michel, M. S., 2006, “Ablation of Clinically Relevant Kidney Tissue Volumes by High-intensity Focused Ultrasound: Preliminary Results of Standardized Ex-vivo Investigations,” J. Endourol., **20**(11), pp. 930-938.

[125] Payne, A., Vyas, U., Blankespoor, A., Christensen, D., and Roemer, R., 2010, “Minimisation of HIFU Pulse Heating and Interpulse Cooling Times,” Int. J. Hyperthermia, **26**(2), pp. 198-208. DOI: 10.3109/02656730903436459

[126] Brace, C. L., 2010, “Microwave Tissue Ablation: Biophysics, Technology, and Applications,” Crit. Rev. Biomed. Eng., **38**(1), pp. 65-78.

[127] Langberg, J. J., Wonnell, T., Chin, M, C., Finkbeiner, W., Scheinman, M., and Stauffer, P., 1991, “Catheter Ablation of the Atrioventricular Junction using a Helical Microwave Antenna: A Novel Means of Coupling Energy to the Endocardium,” Pacing Clin. Electrophysiol., **14**(12), pp. 2105-2113.

[128] Rappaport, C., 2004, “Cardiac Tissue Ablation with Catheter-based Microwave Heating,” Int. J. Hyperthermia, **20**(7), pp. 69-80.

[129] Sun, Y., Wang, Y., Ni, X., Gao, Y., Shao, Q., Liu, L., and Liang, P., 2009, “Comparison of Ablation Zone between 915- and 2,450-MHz Cooled-shaft Microwave Antenna: Results in In Vivo Porcine Livers,” AJR Am. J. Roentgenol., **192**(2), pp. 511-514. DOI: 10.2214/AJR.07.3828

[130] Liu, F. Y., Yu, X. L., Liang, P., Wang, Y., Zhou, P., and Yu, J., 2010, “Comparison of Percutaneous 915 MHz Microwave Ablation and 2450 MHz Microwave Ablation in Large Hepatocellular Carcinoma,” Int. J. Hyperthermia, **26**(5), pp. 448-455. DOI: 10.3109/02656731003717574

[131] Kanaoka, Y., Hirai, K., Ishiko, O., and Ogita, S., 2001, “Microwave Endometrial Ablation at a Frequency of 2.45 GHz. A Pilot Study,” J. Reprod. Med., **46**(6), pp. 559-563.

[132] Tse, H. F., Liao, S., Siu, C. W., Yuan, L., Nicholls, J., Leungm G,, Ormsbym T., Feld, G. K., and Lau, C. P., 2009, “Determinants of Lesion Dimensions during Transcatheter Microwave Ablation,” Pacing Clin. Electrophysiol., **32**(2), pp. 201-208. DOI: 10.1111/j.1540-8159.2008.02203.x

[133] Zhou, W., Liang, M., Pan, H., Liu, X., Jiang, Y., Wang, Y., Ling, L., Ding, Q., and Wang, S., 2013, “Comparison of Ablation Zones among Different Tissues using 2450-MHz Cooled-shaft Microwave Antenna: Results in Ex Vivo Porcine Models,” PLoS One, **8**(8), p. e71873. DOI: 10.1371/journal.pone.0071873

[134] Schepps, J. L., Foster, K. R., 1980, “The UHF and Microwave Dielectric Properties of Normal and Tumour Tissues: Variation in Dielectric Properties with Tissue Water Content,” Phys. Med. Biol., **25**(6), pp. 1149-1159.

[135] Pethig, R., 1987, “Dielectric Properties of Body Tissues,” Clin. Phys. Physiol. Meas., **8**(Suppl A), pp. 5-12.

[136] Zhang, X., Chen, B., Hu, S., Wang, L., Wang, K., Wachtel, M. S., and Frezza, E. E., 2008, “Microwave Ablation with Cooled-tip Electrode for Liver Cancer: An Analysis of 160 Cases,” Hepatogastroenterology, **55**(88), pp. 2184-2187.

[137] Kuang, M., Lu, M. D., Xie, X. Y., Xu, H. X., Mo, L. Q., Liu, G. J., Xu, Z. F., Zheng, Y. L., and Liang, J. Y., 2007, “Liver Cancer: Increased Microwave Delivery to Ablation Zone with Cooled-shaft Antenna--Experimental and Clinical Studies,” Radiology, **242**(3), pp. 914-924.

[138] Rehman, J., Landman, J., Sundaram, C., and Clayman, R. V., 2003, “Tissue Chemoablation,” J. Endourol., **17**(8), pp. 647-657.

[139] Neuwirth, R.S., and Singer, A., 2013, “Evaluation of a Silver Nitrate Endometrial Ablation Fluid Delivery System as a Chemical Treatment for Menorrhagia,” J. Minim. Invasive Gynecol., **20**(5), pp. 627-630. DOI: 10.1016/j.jmig.2013.04.003

[140] Holle, G. E., and Forth, W., 1990, “Myoelectric Activity of Small Intestine after Chemical Ablation of Myenteric Neurons,” Am. J. Physiol., **258**(4 Pt 1), pp. G519-526.

[141] Hong, C. W., Libutti, S. K., and Wood, B. J., 2013, “Liposomal Doxorubicin Plus Radiofrequency Ablation for Complete Necrosis of a Hepatocellular Carcinoma,” Curr. Oncol., **20**(3), pp. e274-277. DOI: 10.3747/co.20.1266

[142] Ditrolio, J., Patel, P., Watson, R. A., and Irwin, R. J., 2002, “Chemo-ablation of the Prostate with Dehydrated Alcohol for the Treatment of Prostatic Obstruction,” J. Urol., **167**(5), pp. 2100-2103, discussion 2103-2104.

[143] Burgener, F. A., and Steinmetz, S. D., 1987, “Treatment of Experimental Adenocarcinomas by Percutaneous Intratumoral Injection of Absolute Ethanol,” Invest. Radiol., **22**(6), pp. 472–478.

[144] Ohnishi, K., Ohyama, N., Ito, S., and Fujiwara, K., 1994, “Small Hepatocellular Carcinoma: Treatment with US-guided Intratumoral Injection of Acetic Acid,” Radiology, **193**(3), pp. 747-752.

[145] Lubienski, A., Düx, M., Lubienski, K., Grenacher, L., and Kauffmann, G., 2005, “Radiofrequency Thermal Ablation: Increase in Lesion Diameter with Continuous Acetic Acid Infusion,” Cardiovasc. Intervent. Radiol., **28**(6), pp. 789-794.

[146] Shah, S. S., Jacobs, D. L., Krasinkas, A. M., Furth, E. E., Itkin, M., and Clark, T. W., 2004, “Percutaneous Ablation of VX2 Carcinoma-induced Liver Tumors with Use of Ethanol versus Acetic Acid: Pilot Study in a Rabbit Model,” J. Vasc. Interv. Radiol., **15**(1 Pt 1), pp. 63-67.

[147] Liao, L., Zhao, M., Ren, J., Zhao, H., Cui, C., and Hu, X., 2010, “Effect of Acetic Acid Deamidation-induced Modification on Functional and Nutritional Properties and Conformation of Wheat Gluten,” J. Sci. Food Agric., **90**(3), pp. 409-417. DOI: 10.1002/jsfa.3830

References for Chapter 2

[1] Little WJ, Ablation of the cuboid bone in congenital varus. Br Med J 1876;1:594.

[2] Head HW, Dodd GD 3rd, Dalrymple NC, Prasad SR, El-Merhi FM, Freckleton MW, et al. Percutaneous radiofrequency ablation of hepatic tumors against the diaphragm: frequency of diaphragmatic injury. Radiology 2007;243:877-84.

[3] Eisele RM, Schumacher G, Jonas S, Neuhaus P. Radiofrequency ablation prior to liver transplantation: Focus on complications and on a rare but severe case. Clin Transplant 2008;22:20-8.

[4] Kanso F, Nahon P, Blaison D, Trinchet JC, Beaugrand M, Seror O, et al. Diaphragmatic necrosis after radiofrequency ablation of hepatocellular carcinoma: A successful surgical repair. Clin Res Hepatol Gastroenterol 2013;37:e59-63.

[5] Zhou M, He H, Cai H, Chen H, Hu Y, Shu Z, et al. Diaphragmatic perforation with colonic herniation due to hepatic radiofrequency ablation: A case report and review of the literature. Oncol Lett 2013;6:1719-22.

[6] Miura H, Yamagami T, Terayama K, Yoshimatsu R, Matsumoto T, Nishimura T. Pneumothorax induced by radiofrequency ablation for hepatocellular carcinoma beneath the diaphragm under real-time computed tomography-fluoroscopic guidance. Acta Radiol 2010;51:613-8.

[7] Soon JL, Jeyaraj PR, Agasthian T. Thoracic complications of radiofrequency ablation of recurrent hepatoma. Ann Acad Med Singapore 2008;37:75-6.

[8] Moumouh A, Hannequin J, Chagneau C, Rayeh F, Jeanny A, Weber-Holtzscherer A, et al. A tamponade leading to death after radiofrequency ablation of hepatocellular carcinoma. Eur Radiol 2005;15:234-7.

[9] Crissien AM, Frenette C. Current management of hepatocellular carcinoma. Gastroenterol Hepatol (NY) 2014;10:153-61.

[10] Reataza M, Imagawa DK. Advances in managing hepatocellular carcinoma. Front Med 2014;8:175-89.

[11] Alberti N, Ferretti G, Buy X, Desjardin M, Al Ammari S, Cazzato RL, et al. Diaphragmatic hernia after lung percutaneous radiofrequency ablation: Incidence and risk factors. Cardiovasc Intervent Radiol 2014 Feb 12; [Epub ahead of print].

[12] Matsui Y, Hiraki T, Gobara H, Uka M, Masaoka Y, Tada A, et al. Phrenic nerve injury after radiofrequency ablation of lung tumors: retrospective evaluation of the incidence and risk factors. J Vasc Interv Radiol 2012;23:780-5.

[13] Hiraki T, Gobara H, Fujiwara H, Ishii H, Tomita K, Uka M, et al. Lung cancer ablation: Complications. Semin Intervent Radiol 2013;30:169-75.

[14] Alexander ES, Dupuy DE. Lung cancer ablation: technologies and techniques. Semin Intervent Radiol 2013;30:141-50.

[15] Dong J, Calkins H. Technology insight: Catheter ablation of the pulmonary veins in the treatment of atrial fibrillation. Nat Clin Pract Cardiovasc Med 2005; 2:159-66.

[16] Hayward RM, Upadhyay GA, Mela T, Ellinor PT, Barrett CD, Heist EK, et al. Pulmonary vein isolation with complex fractionated atrial electrogram ablation for paroxysmal and nonparoxysmal atrial fibrillation: A meta-analysis. Heart Rhythm 2011;8:994-1000.

[17] Koruth JS, Reddy VY, Miller MA, Patel KK, Coffey JO, Fischer A, et al. Mechanical esophageal displacement during catheter ablation for atrial fibrillation. J Cardiovasc Electrophysiol 2012;23:147-54.

[18] Preis O, Digumarthy SR, Wright CD, Shepard JA. Atrioesophageal fistula after catheter pulmonary venous ablation for atrial fibrillation: imaging features. J Thorac Imaging 2007;22:283-5.

[19] Ghia KK, Chugh A, Good E, Pelosi F, Jongnarangsin K, Bogun F, et al. A nationwide survey on the prevalence of atrioesophageal fistula after left atrial radiofrequency catheter ablation. J Interv Card Electrophysiol 2009;24:33-6.

[20] Gilcrease GW, Stein JB. A delayed case of fatal atrioesophageal fistula following radiofrequency ablation for atrial fibrillation. J Cardiovasc Electrophysiol 2010;21:708-11.

[21] Stöckigt F, Schrickel JW, Andrié R, Lickfett L. Atrioesophageal fistula after cryoballoon pulmonary vein isolation. J Cardiovasc Electrophysiol 2012;23:1254-7.

[22] Kawasaki R, Gauri A, Elmouchi D, Duggal M, Bhan A. Atrioesophageal fistula complicating cryoballoon pulmonary vein isolation for paroxysmal atrial fibrillation. J Cardiovasc Electrophysiol 2014 Apr 4; doi: 10.1111/jce.12426 [Epub ahead of print].

[23] Borchert B, Lawrenz T, Hansky B, Stellbrink C. Lethal atrioesophageal fistula after pulmonary vein isolation using high-intensity focused ultrasound (HIFU). Heart Rhythm 2008;5:145-8.

[24] Aizawa Y, Chinushi M, Naitoh N, Kusano Y, Kitazawa H, Takahashi K, et al. A catheter ablation with radiofrequency current of ventricular tachycardia originating from the right ventricle. Am Heart J 1993;125:1269-75.

[25] Suh WM, Fowler SJ, Yeh T, Krishnan SC. Successful catheter ablation of focal ventricular fibrillation originating from the right ventricle. J Interv Card Electrophysiol 2009;26:139-42.

[26] Senderek T, Lelakowski J, Majewski J, Bednarek J, Pudło J. Effectiveness of RF ablation of ventricular ectopic beats from the right and (or) left ventricle. Pol Merkur Lekarski 2012;33:133-7.

[27] Wu JT, Dong JZ. Unusual perforation of the left ventricle during radiofrequency catheter ablation for ventricular tachycardia. Cardiovasc J Afr 2014;25:e1-4.

[28] Dib C, Kapa S, Powell BD, Packer DL, Asirvatham SJ. Successful use of "cryo-mapping" to avoid phrenic nerve damage during ostial superior vena caval ablation despite nerve proximity. J Interv Card Electrophysiol 2008;22:23-30.

[29] Lakhani M, Saiful F, Bekheit S, Kowalski M. Use of intracardiac echocardiography for early detection of phrenic nerve injury during cryoballoon pulmonary vein isolation. J Cardiovasc Electrophysiol 2012;23:874-6.

[30] Hermida JS, Traullé S, Kubala M. Left phrenic nerve injury after cryoballoon ablation of the pulmonary veins. Europace 2013;15:514.

[31] Swallow EB, Dayer MJ, Oldfield WL, Moxham J, Polkey MI. Right hemi-diaphragm paralysis following cardiac radiofrequency ablation. Respir Med 2006;100:1657-9.

[32] Franceschi F, Dubuc M, Guerra PG, Delisle S, Romeo P, Landry E, et al. Diaphragmatic electromyography during cryoballoon ablation: a novel concept in the prevention of phrenic nerve palsy. Heart Rhythm 2011;8:885-91.

[33] Lambiris I, Mehta J, Helguera M. Shortness of breath after AV ablation: Case of left phrenic nerve palsy. J Community Hosp Intern Med Perspect 2013;3:doi: 10.3402/jchimp.v3i1.19123.

[34] Iaizzo PA, Lehmann-Horn F. The in vitro determination of susceptibility to malignant hyperthermia. Muscle Nerve 1989;12:184-90.

[35] Iaizzo PA, Wedel DJ, Gallagher WJ. In vitro contracture testing for determination of susceptibility to malignant hyperthermia: A methodologic update. Mayo Clin Proc 1991;66:998-1004.

[36] Kemper AR, Santago AC, Stitzel JD, Sparks JL, Duma SM. Biomechanical response of human liver in tensile loading. Ann Adv Automot Med 2010;54:15-26.

[37] Chow MJ, Zhang Y. Changes in the mechanical and biochemical properties of aortic tissue due to cold storage. J Surg Res 2011;171:434-42.

References for Chapter 3

[1] Downey R. Anatomy of the normal diaphragm. Thorac Surg Clin 2011;21:273-9.

[2] Iaizzo PA, Lehmann-Horn F. The in vitro determination of susceptibility to malignant hyperthermia. Muscle Nerve 1989;12:184-90.

[3] Iaizzo PA, Wedel DJ, Gallagher WJ. In vitro contracture testing for determination of susceptibility to malignant hyperthermia: a methodologic update. Mayo Clin Proc 1991;66:998-1004.

[4] Powers SK, Shanely RA, Coombes JS, Koesterer TJ, McKenzie M, Van Gammeren D, Cicale M, et al. Mechanical ventilation results in progressive contractile dysfunction in the diaphragm. J Appl Physiol 2002;92:1851-8.

[5] Grosu HB, Lee YI, Lee J, Eden E, Eikermann M, Rose KM. Diaphragm muscle thinning in patients who are mechanically ventilated. Chest. 2012;142:1455-60.

[6] Hussain SN, Mofarrahi M, Sigala I, Kim HC, Vassilakopoulos T, Maltais F, et al. Mechanical ventilation-induced diaphragm disuse in humans triggers autophagy. Am J Respir Crit Care Med 2010;182:1377-86

[7] Lawler JM, Cline CC, Hu Z, Coast JR. Effect of oxidative stress and acidosis on diaphragm contractile function. Am J Physiol 1997;273:R630-6.

[8] Jubran A. Critical illness and mechanical ventilation: effects on the diaphragm. Respir Care 2006;51:1054-61.

[9] Vassilakopoulos T, Petrof BJ. Ventilator-induced diaphragmatic dysfunction. Am J Respir Crit Care Med 2004;169:336-41.

[10] Gayan-Ramirez G, Decramer M. Effects of mechanical ventilation on diaphragm function and biology. Eur Respir J 2002;20:1579-86.

[11] Hiraki T, Gobara H, Fujiwara H, Ishii H, Tomita K, Uka M, et al. Lung cancer ablation: complications. Semin Intervent Radiol 2013;30:169-75.

[12] Kashima M, Yamakado K, Takaki H, Kodama H, Yamada T, Uraki J, et al. Complications after 1000 lung radiofrequency ablation sessions in 420 patients: a single center's experiences. AJR Am J Roentgenol 2011;197:W576-80.

[13] Schwartz A, Desolneux G, Desjardin M, Evrard S, Bechade D. Symptomatic diaphragmatic hernia after pulmonary radiofrequency ablation. J Visc Surg 2013;150:157-8.

[14] Mori T, Kawanaka K, Ohba Y, Shiraishi K, Iwatani K, Yoshimoto K, et al. Diaphragm perforation after radio-frequency ablation for metastatic lung cancer. Ann Thorac Cardiovasc Surg 2010;16:426-8.

[15] Bai R, Patel D, Di Biase L, Fahmy TS, Kozeluhova M, Prasad S, et al. Phrenic nerve injury after catheter ablation: should we worry about this complication? J Cardiovasc Electrophysiol 2006;17:944-8.

[16] Swallow EB, Dayer MJ, Oldfield WL, Moxham J, Polkey MI. Right hemi-diaphragm paralysis following cardiac radiofrequency ablation. Respir Med 2006;100:1657-9.

[17] Linhart M, Nielson A, Andrié RP, Mittmann-Braun EL, Stöckigt F, Kreuz J, et al. Fluoroscopy of spontaneous breathing is more sensitive than phrenic nerve stimulation for detection of right phrenic nerve injury during cryoballoon ablation of atrial fibrillation. J Cardiovasc Electrophysiol 2014 (Apr 11);doi: 10.1111/jce.12431.

[18] Durante-Mangoni E, Del Vecchio D, Ruggiero G. Right diaphragm paralysis following cardiac radiofrequency catheter ablation for inappropriate sinus tachycardia. Pacing Clin Electrophysiol 2003;26:783-4.

[19] Hermida JS, Traullé S, Kubala M. Left phrenic nerve injury after cryoballoon ablation of the pulmonary veins. Europace 2013;15:514.

[20] Lakhani M, Saiful F, Bekheit S, Kowalski M. Use of intracardiac echocardiography for early detection of phrenic nerve injury during cryoballoon pulmonary vein isolation. J Cardiovasc Electrophysiol 2012;23:874-6.

[21] Wood TF, Rose DM, Chung M, Allegra DP, Foshag LJ, Bilchik AJ. Radiofrequency ablation of 231 unresectable hepatic tumors: indications, limitations, and complications. Ann Surg Oncol 2000;7:593-600.

[22] Head HW, Dodd GD 3rd, Dalrymple NC, Prasad SR, El-Merhi FM, Freckleton MW, et al. Percutaneous radiofrequency ablation of hepatic tumors

against the diaphragm: frequency of diaphragmatic injury. Radiology 2007;243:877-84.

[23] Iguchi T, Inoue D, Yabushita K, Sakaguchi K, Tatsukawa M, Sasaki H, et al. Effect of CT fluoroscopy-guided transpulmonary radiofrequency ablation of liver tumours on the lung. Br J Radiol 2012;85:e373-7.

[24] Kato T, Yamagami T, Hirota T, Matsumoto T, Yoshimatsu R, Nishimura T. Transpulmonary radiofrequency ablation for hepatocellular carcinoma under real-time computed tomography-fluoroscopic guidance. Hepatogastroenterology 2008;55:1450-3.

[25] Miura H, Yamagami T, Terayama K, Yoshimatsu R, Matsumoto T, Nishimura T. Pneumothorax induced by radiofrequency ablation for hepatocellular carcinoma beneath the diaphragm under real-time computed tomography-fluoroscopic guidance. Acta Radiol 2010;51:613-8.

[26] Toyoda M, Kakizaki S, Horiuchi K, Katakai K, Sohara N, Sato K, et al. Computed tomography-guided transpulmonary radiofrequency ablation for hepatocellular carcinoma located in hepatic dome. World J Gastroenterol 2006;12:608-11.

[27] Chen EA, Neeman Z, Lee FT, Kam A, Wood B. Thermal protection with 5% dextrose solution blanket during radiofrequency ablation. Cardiovasc Intervent Radiol 2006;29:1093-6.

[28] Adán Merino L, Olveira Martín A, Pérez Robledo JP, Prieto I, Gea Rodriguez F, Castillo Grau P, et al. Percutaneous radiofrequency ablation with artificial ascites for hepatocellular carcinoma adjacent to the diaphragm. Gastroenterol Hepatol 2010;33:709-15.

[29] Kang TW, Rhim H, Lee MW, Kim YS, Choi D, Lee WJ, Lim HK. Radiofrequency ablation for hepatocellular carcinoma abutting the diaphragm: comparison of effects of thermal protection and therapeutic efficacy. AJR Am J Roentgenol 2011;196:907-13.

[30] Rhim H, Lim HK, Kim YS, Choi D. Percutaneous radiofrequency ablation with artificial ascites for hepatocellular carcinoma in the hepatic dome: initial experience. AJR Am J Roentgenol 2008;190:91-8.

[31] Song I, Rhim H, Lim HK, Kim YS, Choi D. Percutaneous radiofrequency ablation of hepatocellular carcinoma abutting the diaphragm and gastrointestinal tracts with the use of artificial ascites: safety and technical efficacy in 143 patients. Eur Radiol 2009;19:2630-40.

[32] Rhim H, Lim HK. Radiofrequency ablation for hepatocellular carcinoma abutting the diaphragm: the value of artificial ascites. Abdom Imaging 2009;34:371-80.

[33] Nam SY, Rhim H, Kang TW, Lee MW, Kim YS, Choi D, et al. Percutaneous radiofrequency ablation for hepatic tumors abutting the diaphragm: clinical assessment of the heat-sink effect of artificial ascites. AJR Am J Roentgenol 2010;194:W227-31.

[34] Ishiko T, Beppu T, Mizumoto T, Hosaka S, Nakahara O, Okabe H, et al. Thoracoscopic radio-frequency ablation therapy for liver surface tumor located under the diaphragm. Gan To Kagaku Ryoho 2006;33:1857-9.

[35] Kang CM, Lee KH, Kim KM, Baik SH. "Dual-scopic" intraoperative radiofrequency ablation for the treatment of a hepatic metastatic tumor located beneath the diaphragm. Surg Laparosc Endosc Percutan Tech 2008;18:202-6.

[36] Koda M, Ueki M, Maeda Y, Mimura K, Okamoto K, Matsunaga Y, et al. Percutaneous sonographically guided radiofrequency ablation with artificial pleural effusion for hepatocellular carcinoma located under the diaphragm. AJR Am J Roentgenol 2004;183:583-8.

[37] Liu LN, Xu HX, Lu MD, Xie XY. Percutaneous ultrasound-guided thermal ablation for liver tumor with artificial pleural effusion or ascites. Chin J Cancer 2010;29:830-5.

[38] Uehara T, Hirooka M, Ishida K, Hiraoka A, Kumagi T, Kisaka Y, et al. Percutaneous ultrasound-guided radiofrequency ablation of hepatocellular carcinoma with artificially induced pleural effusion and ascites. J Gastroenterol 2007;42:306-11.

[39] Li M, Yu XL, Liang P, Liu F, Dong B, Zhou P. Percutaneous microwave ablation for liver cancer adjacent to the diaphragm. Int J Hyperthermia 2012;28:218-26.

[40] Ishikawa T, Kohno T, Shibayama T, Fukushima Y, Obi S, Teratani T, et al. Thoracoscopic thermal ablation therapy for hepatocellular carcinoma located beneath the diaphragm. Endoscopy 2001;33:697-702.

[41] Haemmerich D. Biophysics of radiofrequency ablation. Crit Rev Biomed Eng 2010;38:53-63.

[42] Lustgarten DL, Keane D, Ruskin J. Cryothermal ablation: mechanism of tissue injury and current experience in the treatment of tachyarrhythmias. Prog Cardiovasc Dis 1999;41:481-98.

[43] Zhou Y. Generation of uniform lesions in high intensity focused ultrasound ablation. Ultrasonics 2013;53:495-505.

[44] Brace CL. Microwave tissue ablation: biophysics, technology, and applications. Crit Rev Biomed Eng 2010;38:65-78.

[45] Rehman J, Landman J, Sundaram C, Clayman RV. Tissue chemoablation. J Endourol 2003;17: 647-57.

[46] Bischof JC, He X. Thermal stability of proteins. Ann N Y Acad Sci 2005;1066:12-33.

[47] Chu KF, Dupuy DE. Thermal ablation of tumours: biological mechanisms and advances in therapy. Nat Rev Cancer 2014;14:199-208.

[48] Whittaker DK. Mechanisms of tissue destruction following cryosurgery. Ann R Coll Surg Engl 1984;66:313-8.

[49] Gage AA, Baust JM, Baust JG. Experimental cryosurgery investigations in vivo. Cryobiology 2009;59:229-43.

[50] Keller MW. Arteriolar constriction in skeletal muscle during vascular stunning: role of mast cells. Am J Physiol 1997;272:H2154-63.

[51] Kandarian SC, White TP. Force deficit during the onset of muscle hypertrophy. J Appl Physiol 1989;67:2600-7.

[52] Steenbergen C, Frangogiannis NG. Ischemic heart disease. In: Hill J, Olson E, eds. Muscle: Fundamental Biology and Mechanisms of Disease. Boston: Elsevier, 2012, p. 497.

[53] Sink JD, Pellom GL, Currie WD, Chitwood WR Jr, Hill RC, Wechsler AS. Protection of mitochondrial function during ischemia by potassium cardioplegia: correlation with ischemic contracture. Circulation 1979;60:158-63.

[54] Endo M. Calcium-induced calcium release in skeletal muscle. Physiol Rev 2009;89:1153-76.

[55] Fuchs F, Gertz EW, Briggs FN. The effect of quinidine on calcium accumulation by isolated sarcoplasmic reticulum of skeletal and cardiac muscle. J Gen Physiol 1968;52:955-68.

[56] Berchtold MW, Brinkmeier H, Müntener M. Calcium ion in skeletal muscle: its crucial role for muscle function, plasticity, and disease. Physiol Rev 2000;80:1215-65.

[57] Haines DE. Biophysics of radiofrequency lesion formation. In: Huang SKS, Wood MA, eds. Catheter Ablation of Cardiac Arrhythmias. 2nd edition. Philadelphia: Saunders (Elsevier), 2011, p. 3.

[58] Boutilier RG. Mechanisms of cell survival in hypoxia and hypothermia. J Exp Biol 2001;204:3171-81.

[59] Zhao X, Min CK, Ko JK, Parness J, Kim do H, Weisleder N, et al. Increased store-operated Ca2+ entry in skeletal muscle with reduced calsequestrin-1 expression. Biophys J 2010;99:1556-64.

[60] Everett TH 4th, Nath S, Lynch C 3rd, Beach JM, Whayne JG, Haines DE. Role of calcium in acute hyperthermic myocardial injury. J Cardiovasc Electrophysiol 2001;12:563-9.

[61] Ahmed M, Goldberg SN. Image-guided tumor ablation: basic science. In: van Sonnenberg E, McMullen W, Solbiati L, eds. Tumor Ablation: Principles and Practice. New York: Springer Science + Business Media, Inc., 2005, p. 24.

[62] Di Lullo GA, Sweeney SM, Korkko J, Ala-Kokko L, San Antonio JD. Mapping the ligand-binding sites and disease-associated mutations on the most abundant protein in the human, type I collagen. J Biol Chem 2002;277:4223-31.

[63] Smith LR, Barton ER. Collagen content does not alter the passive mechanical properties of fibrotic skeletal muscle in mdx mice. Am J Physiol Cell Physiol 2014;306:C889-98.

[64] Kjaer M. Role of extracellular matrix in adaptation of tendon and skeletal muscle to mechanical loading. Physiol Rev 2004;84:649-98.

References for Chapter 4

[1] Yazaki E, Sifrim D. Anatomy and physiology of the esophageal body. Dis Esophagus. 2012 May;25(4):292-8.

[2] Neville AL, Crookes P, Velmahos GC, Vlahos A, Theodorou D, Lucas CE. Esophageal dysfunction in cervical spinal cord injury: a potentially important mechanism of aspiration. J Trauma. 2005 Oct;59(4):905-11.

[3] Fuster V, Ryden LE, Cannom DS, Crijns HJ, Curtis AB, Ellenbogen KA, et al. ACC/AHA/ESC 2006 Guidelines for the Management of Patients with Atrial Fibrillation: A Report of the American College of Cardiology/American Heart Association Task Force on Practice Guidelines and the European Society of Cardiology Committee for Practice Guidelines. Circulation. 2006;114(7):e257–354.

[4] Lloyd-Jones D, Adams RJ, Brown TM, Carnethon M, Dai S, De Simone G, Ferguson TB, Ford E, Furie K, Gillespie C, Go A, Greenlund K, Haase N, Hailpern S, Ho PM, Howard V, Kissela B, Kittner S, Lackland D, Lisabeth L, Marelli A, McDermott MM, Meigs J, Mozaffarian D, Mussolino M, Nichol G, Roger VL, Rosamond W, Sacco R, Sorlie P, Stafford R, Thom T, Wasserthiel-Smoller S, Wong ND, Wylie-Rosett J; American Heart Association Statistics Committee and Stroke Statistics Subcommittee. Executive summary: Heart disease and stroke statistics - 2010 update: A report from the American Heart Association. Circulation 2010; 121:948-954.

[5] Healey JS, Israel CW, Connolly SJ, Hohnloser SH, Nair GM, Divakaramenon S, Capucci A, Van Gelder IC, Lau CP, Gold MR, Carlson M, Themeles E, Morillo CA. Relevance of electrical remodeling in human atrial fibrillation: results of the Asymptomatic Atrial Fibrillation and Stroke Evaluation in Pacemaker Patients and the Atrial Fibrillation Reduction Atrial Pacing Trial mechanisms of atrial fibrillation study. Circ Arrhythm Electrophysiol. 2012 Aug 1;5(4):626-31.

[6] Sealy WC, Gallagher JJ, Kasell J. His bundle interruption for control of inappropriate ventricular responses to atrial arrhythmias. Ann Thorac Surg. 1981 Nov;32(5):429-38.

[7] Huang, S. K., Jordan, N., Graham, A., Bharati, S., Lampe, L., Odell, R., and Marcus, F. I., 1985, “Closed Chest Catheter Desiccation of the Atrioventricular Junction using Radiofrequency Energy: A New Method of Catheter Ablation [Abstract #1556],” Circulation, 72, III-389.

[8] Hoyt H, Bhonsale A, Chilukuri K, Alhumaid F, Needleman M, Edwards D, Govil A, Nazarian S, Cheng A, Henrikson CA, Sinha S, Marine JE, Berger R, Calkins H, Spragg DD. Complications arising from catheter ablation of atrial fibrillation: temporal trends and predictors. Heart Rhythm. 2011 Dec;8(12):1869-74.

[9] Aldhoon B, Wichterle D, Peichl P, Čihák R, Kautzner J. Complications of catheter ablation for atrial fibrillation in a high-volume centre with the use of intracardiac echocardiography. Europace. 2013 Jan;15(1):24-32.

[10] Dhruvakumar S, Gerstenfeld EP. Complications associated with catheter ablation of atrial fibrillation. Minerva Cardioangiol. 2007 Jun;55(3):353-68.

[11] Doll N, Borger MA, Fabricius A, Stephan S, Gummert J, Mohr FW, Hauss J, Kottkamp H, Hindricks G. Esophageal perforation during left atrial radiofrequency ablation: Is the risk too high? J Thorac Cardiovasc Surg. 2003 Apr;125(4):836-42.

[12] Scanavacca M, Hachul D, Sosa E. Atrioesophageal fistula--a dangerous complication of catheter ablation for atrial fibrillation. Nat Clin Pract Cardiovasc Med. 2007 Nov;4(11):578-9.

[13] Dong J, Calkins H. Technology insight: catheter ablation of the pulmonary veins in the treatment of atrial fibrillation. Nat Clin Pract Cardiovasc Med. 2005 Mar;2(3):159-66.

[14] Hayward RM, Upadhyay GA, Mela T, Ellinor PT, Barrett CD, Heist EK, Verma A, Choudhry NK, Singh JP. Pulmonary vein isolation with complex fractionated atrial electrogram ablation for paroxysmal and nonparoxysmal atrial fibrillation: A meta-analysis. Heart Rhythm. 2011 Jul;8(7):994-1000.

[15] Gillinov AM, Pettersson G, Rice TW. Esophageal injury during radiofrequency ablation for atrial fibrillation. J Thorac Cardiovasc Surg. 2001 Dec;122(6):1239-40.

[16] Lemola K, Sneider M, Desjardins B, Case I, Han J, Good E, Tamirisa K, Tsemo A, Chugh A, Bogun F, Pelosi F Jr, Kazerooni E, Morady F, Oral H. Computed tomographic analysis of the anatomy of the left atrium and the esophagus: implications for left atrial catheter ablation. Circulation. 2004 Dec 14;110(24):3655-60.

[17] Koruth JS, Reddy VY, Miller MA, Patel KK, Coffey JO, Fischer A, Gomes JA, Dukkipati S, D'Avila A, Mittnacht A. Mechanical esophageal displacement during catheter ablation for atrial fibrillation. J Cardiovasc Electrophysiol. 2012 Feb;23(2):147-54.

[18] Preis O, Digumarthy SR, Wright CD, Shepard JA. Atrioesophageal fistula after catheter pulmonary venous ablation for atrial fibrillation: imaging features. J Thorac Imaging. 2007 Aug;22(3):283-5.

[19] Ghia KK, Chugh A, Good E, Pelosi F, Jongnarangsin K, Bogun F, Morady F, Oral H. A nationwide survey on the prevalence of atrioesophageal fistula after left atrial radiofrequency catheter ablation. J Interv Card Electrophysiol. 2009 Jan;24(1):33-6.

[20] Gilcrease GW, Stein JB. A delayed case of fatal atrioesophageal fistula following radiofrequency ablation for atrial fibrillation. J Cardiovasc Electrophysiol. 2010 Jun 1;21(6):708-11.

[21] Stöckigt F, Schrickel JW, Andrié R, Lickfett L. Atrioesophageal fistula after cryoballoon pulmonary vein isolation. J Cardiovasc Electrophysiol. 2012 Nov;23(11):1254-7.

[22] Kawasaki R, Gauri A, Elmouchi D, Duggal M, Bhan A. Atrioesophageal Fistula Complicating Cryoballoon Pulmonary Vein Isolation for Paroxysmal Atrial Fibrillation. J Cardiovasc Electrophysiol. 2014 Apr 4.

[23] Borchert B, Lawrenz T, Hansky B, Stellbrink C. Lethal atrioesophageal fistula after pulmonary vein isolation using high-intensity focused ultrasound (HIFU). Heart Rhythm. 2008 Jan;5(1):145-8.

[24] Aizawa Y, Chinushi M, Naitoh N, Kusano Y, Kitazawa H, Takahashi K, Uchiyama H, Shibata A. Catheter ablation with radiofrequency current of ventricular tachycardia originating from the right ventricle. Am Heart J. 1993 May;125(5 Pt 1):1269-75.

[25] Suh WM, Fowler SJ, Yeh T, Krishnan SC. Successful catheter ablation of focal ventricular fibrillation originating from the right ventricle. J Interv Card Electrophysiol. 2009 Nov;26(2):139-42.

[26] Senderek T, Lelakowski J, Majewski J, Bednarek J, Pudło J. Effectiveness of RF ablation of ventricular ectopic beats from the right and (or) left ventricle. Pol Merkur Lekarski. 2012 Sep;33(195):133-7.

[27] Wu JT, Dong JZ. Unusual perforation of the left ventricle during radiofrequency catheter ablation for ventricular tachycardia. Cardiovasc J Afr. 2014 Apr 23;25(2):e1-4.

[28] Sánchez-Quintana D, Cabrera JA, Climent V, Farré J, Mendonça MC, Ho SY. Anatomic relations between the esophagus and left atrium and relevance for ablation of atrial fibrillation. Circulation. 2005 Sep 6;112(10):1400-5.

[29] Wang SL, Ooi CG, Siu CW, Yiu MW, Pang C, Lau CP, Tse HF. Endocardial visualization of esophageal-left atrial anatomic relationship by three-dimensional

multidetector computed tomography "navigator imaging". Pacing Clin Electrophysiol. 2006 May;29(5):502-8.

[30] Jang SW, Kwon BJ, Choi MS, Kim DB, Shin WS, Cho EJ, Kim JH, Oh YS, Lee MY, Rho TH, Kim JH, Lee BY, Kim HL, Jung JI, Song KS. Computed tomographic analysis of the esophagus, left atrium, and pulmonary veins: implications for catheter ablation of atrial fibrillation. J Interv Card Electrophysiol. 2011 Oct;32(1):1-6.

[31] Iaizzo PA, Lehmann-Horn F. The in vitro determination of susceptibility to malignant hyperthermia. Muscle Nerve 1989;12:184-90.

[32] Iaizzo PA, Wedel DJ, Gallagher WJ. In vitro contracture testing for determination of susceptibility to malignant hyperthermia: A methodologic update. Mayo Clin Proc 1991;66:998-1004.

References for Chapter 5

[1] Monro AK. The Anatomy, Physiology and Surgical Consideration of the Oesophagus. Postgrad Med J. 1944 Oct;20(227):273-7.

[2] Meyer GW, Austin RM, Brady CE 3rd, Castell DO. Muscle anatomy of the human esophagus. J Clin Gastroenterol. 1986 Apr;8(2):131-4.

[3] Yazaki E1, Sifrim D. Anatomy and physiology of the esophageal body. Dis Esophagus. 2012 May;25(4):292-8.

References for Chapter 6

[1] McCarley JR, Soulen MC. Percutaneous ablation of hepatic tumors. Semin Intervent Radiol. 2010 Sep;27(3):255-60.

[2] De Filippo M, Bozzetti F, Martora R, Zagaria R, Ferretti S, Macarini L, Brunese L, Rotondo A, Rossi C. Radiofrequency thermal ablation of renal tumors. Radiol Med. 2014 Jul;119(7):499-511.

[3] Earhart J, Wellman D, Donaldson J, Chesterton J, King E, Janicki JA. Radiofrequency ablation in the treatment of osteoid osteoma: results and complications. Pediatr Radiol. 2013 Jul;43(7):814-9.

[4] Güngör T, Akbay S, Aksüt H, Yılmaz B. Rectus abdominalis muscle metastasis from uterine leiomyosarcoma: An unusual case and review of the literature. J Turk Ger Gynecol Assoc. 2014 Jun 1;15(2):122-4.

[5] Suzuki K, Yasuda T, Nagao K, Hori T, Watanabe K, Kanamori M, Kimura T. Metastasis of gastrointestinal stromal tumor to skeletal muscle: a case report. J Med Case Rep. 2014 Jul 18;8(1):256.

[6] Kwas HH, Zendah I, Ghedira H. Skeletal muscle metastases from lung cancer. Asian Cardiovasc Thorac Ann. 2013 Dec;21(6):741-3.

[7] Yamada K, Yatabe Y, Sugiura H. Osteosarcoma with skeletal muscle metastasis. Arch Orthop Trauma Surg. 2008 Jul;128(7):695-9.

[8] Ward E, Munk PL, Rashid F, Torreggiani WC. Musculoskeletal interventional radiology: radiofrequency ablation. Radiol Clin North Am. 2008 May;46 (3):599-610, vi-vii.

[9] Ravi R, Rodriguez-Lopez JA, Trayler EA, Barrett DA, Ramaiah V, Diethrich EB. Endovenous ablation of incompetent saphenous veins: a large single-center experience. J Endovasc Ther. 2006 Apr;13(2):244-8.

[10] Sufian S, Lakhanpal S, Marquez J. Superficial vein ablation for the treatment of primary chronic venous ulcers. Phlebology. 2011 Oct;26(7):301-6.

[11] Hoyt H, Bhonsale A, Chilukuri K, Alhumaid F, Needleman M, Edwards D, Govil A, Nazarian S, Cheng A, Henrikson CA, Sinha S, Marine JE, Berger R, Calkins H, Spragg DD. Complications arising from catheter ablation of atrial fibrillation: temporal trends and predictors. Heart Rhythm. 2011 Dec;8(12):1869-74.

[12] Iguchi T, Inoue D, Yabushita K, Sakaguchi K, Tatsukawa M, Sasaki H, Kanazawa S. Effect of CT fluoroscopy-guided transpulmonary radiofrequency ablation of liver tumours on the lung. Br J Radiol. 2012 Aug;85(1016):e373-7.

[13] Kato T, Yamagami T, Hirota T, Matsumoto T, Yoshimatsu R, Nishimura T. Transpulmonary radiofrequency ablation for hepatocellular carcinoma under real-time computed tomography-fluoroscopic guidance. Hepatogastroenterology. 2008 Jul-Aug;55(85):1450-3.

[14] Miura H, Yamagami T, Terayama K, Yoshimatsu R, Matsumoto T, Nishimura T. Pneumothorax induced by radiofrequency ablation for hepatocellular carcinoma beneath the diaphragm under real-time computed tomography-fluoroscopic guidance. Acta Radiol. 2010 Jul;51(6):613-8.

[15] Toyoda M, Kakizaki S, Horiuchi K, Katakai K, Sohara N, Sato K, Takagi H, Mori M, Nakajima T. Computed tomography-guided transpulmonary radiofrequency ablation for hepatocellular carcinoma located in hepatic dome. World J Gastroenterol. 2006 Jan 28;12(4):608-11.

[16] Kroon HM, Schurmans J. Osteoblastoma: clinical and radiologic findings in 98 new cases. Radiology. 1990 Jun;175(3):783-90.

[17] Akgül S, Uzümcügil A, Bozkurt MF, Topçu M. Osteoid osteoma in a 16-year-old boy presenting with atrophy of the left thigh: diagnostic difficulties. Turk J Pediatr. 2008 Jul-Aug;50(4):373-6.

[18] Lehmann-Horn F, Iaizzo PA. Resealed fiber segments for the study of the pathophysiology of human skeletal muscle. Muscle Nerve. 1990 Mar;13(3):222-31.

[19] Iaizzo PA, Lehmann-Horn F. The in vitro determination of susceptibility to malignant hyperthermia. Muscle Nerve. 1989 Mar;12(3):184-90.

[20] Iaizzo PA, Wedel DJ, Gallagher WJ. In vitro contracture testing for determination of susceptibility to malignant hyperthermia: a methodologic update. Mayo Clin Proc. 1991 Oct;66(10):998-1004.

References for Chapter 7

[1] Al-Khatib SM, Allen LaPointe NM, Chatterjee R, Crowley MJ, Dupre ME, Kong DF, Lopes RD, Povsic TJ, Raju SS, Shah B, Kosinski AS, McBroom AJ, Sanders GD. Rate- and rhythm-control therapies in patients with atrial fibrillation: a systematic review. Ann Intern Med. 2014 Jun 3;160(11):760-73.

[2] Mallidi J, Nadkarni GN, Berger RD, Calkins H, Nazarian S. Meta-analysis of catheter ablation as an adjunct to medical therapy for treatment of ventricular tachycardia in patients with structural heart disease. Heart Rhythm. 2011 Apr;8(4):503-10.

[3] Gillinov AM, Pettersson G, Rice TW. Esophageal injury during radiofrequency ablation for atrial fibrillation. J Thorac Cardiovasc Surg. 2001 Dec;122(6):1239-40.

[4] Weber KT, Janicki JS. The metabolic demand and oxygen supply of the heart: physiologic and clinical considerations. Am J Cardiol. 1979 Oct;44(4):722-9.

Appendix 1: Assessment of Physiological Properties of Respiratory Diaphragm: Preliminary Ablation Studies Performed in Tissue Baths

Introduction: A series of studies were performed to develop the methodologies for assessing physiological properties of various tissues in response of ablative treatments. Initial studies were performed to investigate if ablations could be performed within the tissue baths itself, so that removal of the muscle bundles from the tissue baths to perform ablations could be avoided. The experience gained from executing these studies helped mature the overall experimental protocol; and results from these studies helped mature the physiological assessment methodologies.

Methods: The same RFA and CRA ablation systems/equipment as described in the "Methods" chapter was used in these investigations. After the pre-ablation data was acquired, RFA and CRA catheters were introduced inside the tissue baths as shown in Figure 129 to perform ablations on muscle bundles within the tissue baths itself. Ablation catheters were stabilized by hand and by mounting on a stand during ablations. RFA was performed at 6 different doses: 50 °C (n=5), 55 °C (n=3), 60 °C (n=5), 65 °C (n=3), 70 °C (n=5), and 80 °C (n=2). The RFA system settings were set to 50 W of RF power and 1 min ablation duration.

CRA was performed at 6 different doses: 15 sec (n=4), 30 sec (n=4), 60 sec (n=11), 120 sec (n=11), 180 sec (n=12), and 240 sec (n=7). The CRA system was operated in clinical mode with CRA temperatures of approximately -75 °C.

Results: Figure 132 and Figure 133 illustrate the dose effects of percent change in peak force and baseline force, respectively, for swine diaphragm muscle bundles in response to RFA. Although a sustained reduction in peak force and a transient increase in baseline force with increasing levels of RF dose were observed, they were not consistent, especially at higher doses. Moreover, the variability in peak force and baseline data was very high which could have been from the lack of effective coupling between the RFA catheter and the muscle bundle. Figure 134 and Figure 135 illustrate the dose effects of percent change in peak force and baseline force, respectively, for swine diaphragm muscle bundles in response to CRA. As can be seen, no dose dependent responses were observed in either peak force or baseline force, and variability in results was very high.

Discussions: This study investigated whether ablations could be performed within the tissue baths and whether this would be an acceptable methodological model for further studies. Catheter stability in relation to the muscle bundle and application of a constant force during ablations were found to be major factors influencing the quality of ablations. This investigation showed that although

ablations can be performed within the tissue bath, there are inherent challenges that need to be overcome.

In case of RFA, significant slippage between the RFA catheter and the muscle bundle was observed. It was hard to keep the RFA catheter steady while performing RFA ablations which made the ablations very subjective. The catheter slippage (or unintended movement with respect to the muscle bundle) was primarily due to the inherent tension in the catheter and tremors from the subject's hands that were easily transmitted to the muscle bundle via the catheter. This prevented consistent and steady contact between the catheter and the muscle bundle, which compromised optimum RF energy delivery to the tissue. Another important observation was the delivery of RF energy significantly affecting the operation of tissue bath amplifiers which caused high-frequency interference (484 kHz) and disruption in acquired signal quality. An example of corruption in peak force and baseline force data is shown in Figure 130 and Figure 131. In fact, there was a concern that the tissue bath system amplifiers could suffer unintentional damage if RF energy within the tissue baths was not properly grounded.

In case of CRA, once the ice-ball formed, there was a firm contact between the CRA catheter and the muscle bundle. However, because of the inherent tension in the catheter and tremors from subject's hands, there was relative movement and slippage between the catheter and the muscle bundle. This subjected the muscle bundle to unintended stresses and strains that affected the

baseline force of the muscle bundle. Moreover, during CRA, due to initial slippage of the catheter, the user could not precisely control the exact location of ablation on the muscle bundle. This was because as soon as the CRA machine was turned on, the ice-ball started to form and based on where the catheter tip-electrode was, that's where the catheter got adhered to the muscle bundle, and that's where the ablation resulted.

Conclusion: Although RFA and CRA could be performed within the tissue baths, due to the challenges discussed above, this was not an acceptable methodological model for performing physiological studies in response to ablative treatments. The methods were refined to achieve consistency, repeatability and reproducibility in application and delivery of ablative energies. These methods were used for further studies and are discussed in detail in Chapter 2. Moreover, due to the nature of HIFU and MWA setup, these ablative treatments could not be performed within the tissue baths unless significant modifications to the tissue baths or the system setup were done. Since this was outside the scope of this thesis, this idea was not pursued further. Though, this could be one of the future expansions of this work.

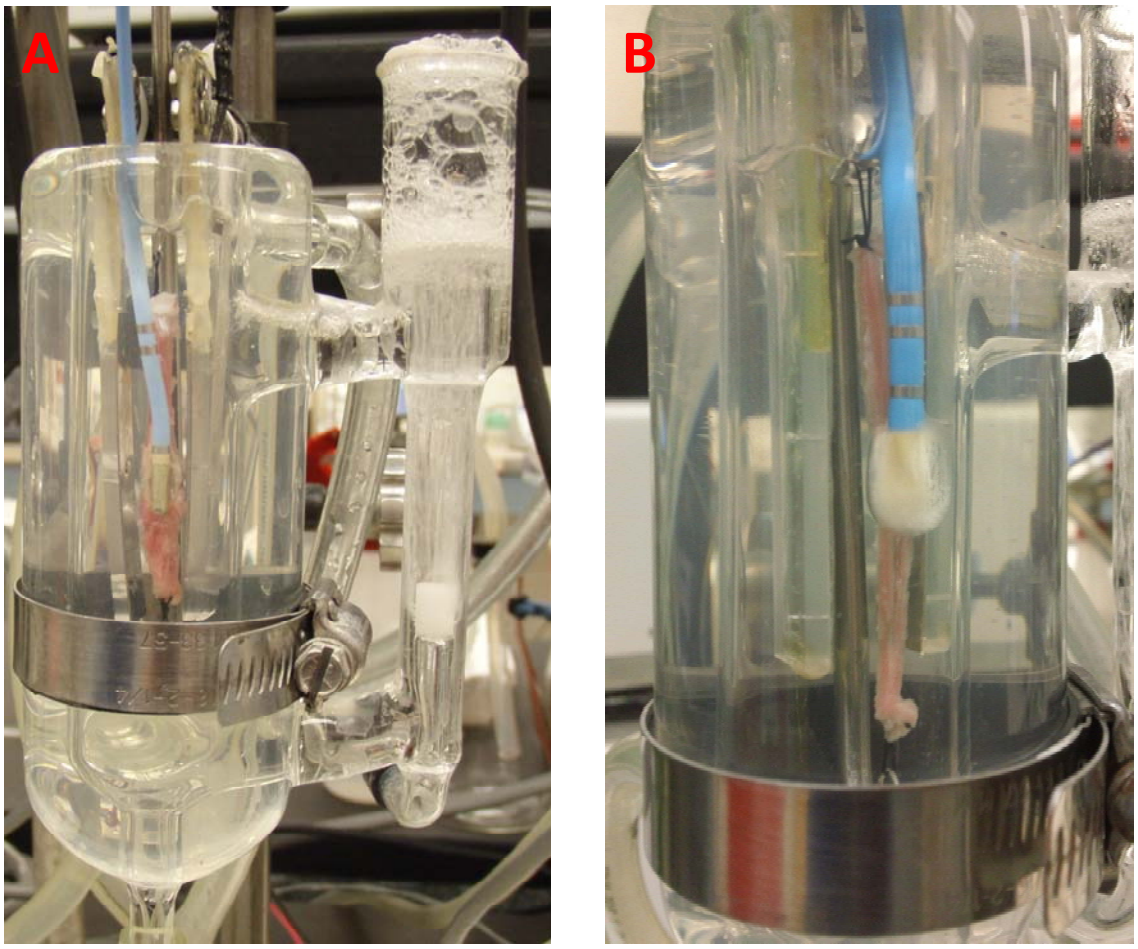

Figure 129: RFA and CRA performed in tissue baths

Illustration of RFA (A) and CRA (B) being performed on a swine diaphragm muscle bundle inside the tissue bath. The return electrode for RFA is placed inside the tissue bath behind the muscle bundle (not visible in inset). The ablation catheters are held as stationary as possible by hand in both treatments. The RFA and CRA catheters apply a lateral force (value unknown) on the respective muscle bundles during ablations causing the muscle bundles to bend/bulge, which in turn affects the baseline tension.

- Ablations performed in one bath causes interference in other baths
- Severity of data corruption depends on the level and duration of interference
- Severity of interference is unpredictable
- An example is illustrated here – Peak Force (this slide) and Baseline Force (next slide)

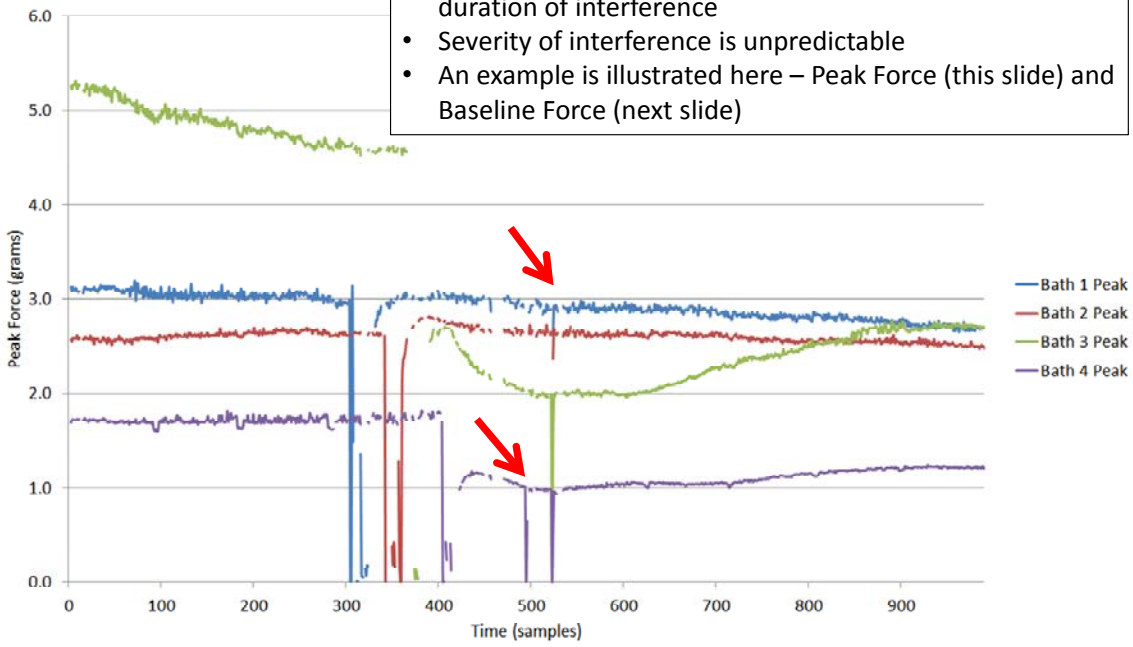

Figure 130: RF interference in tissue bath during peak force analysis

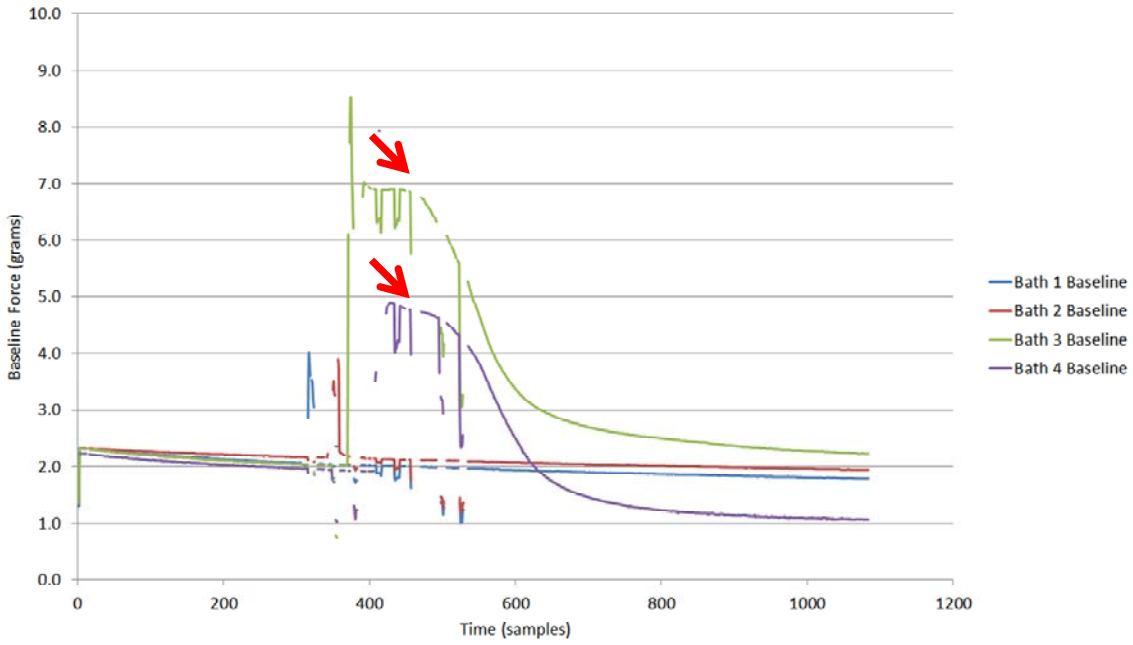

Figure 131: RF interference in tissue bath during baseline force analysis

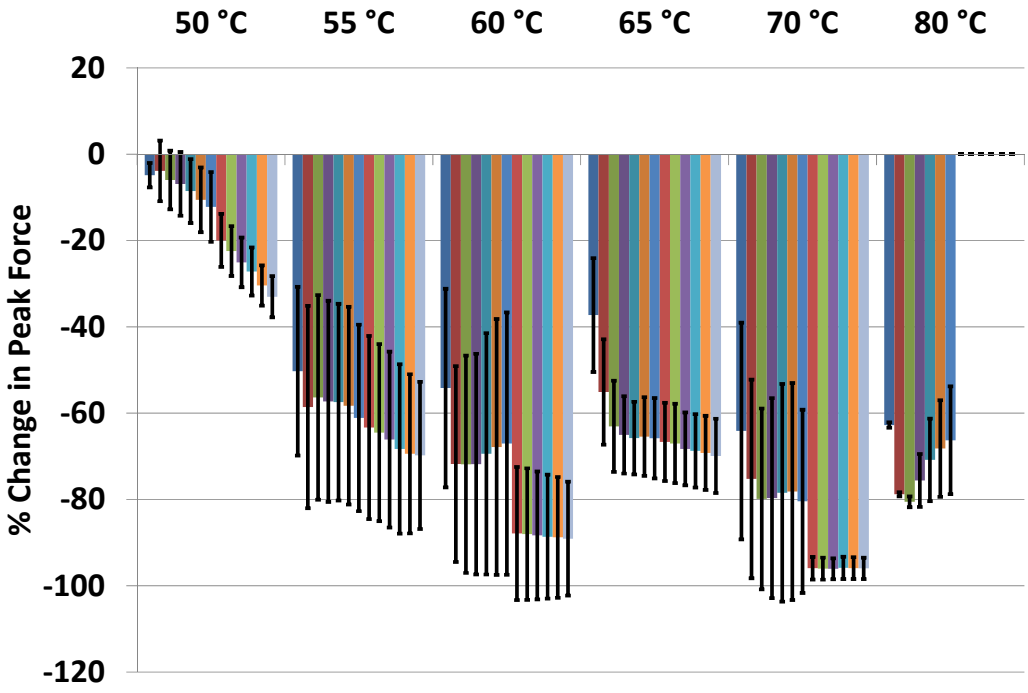

Figure 132: Dose effects of percent change in peak force of swine diaphragm post RFA in tissue bath

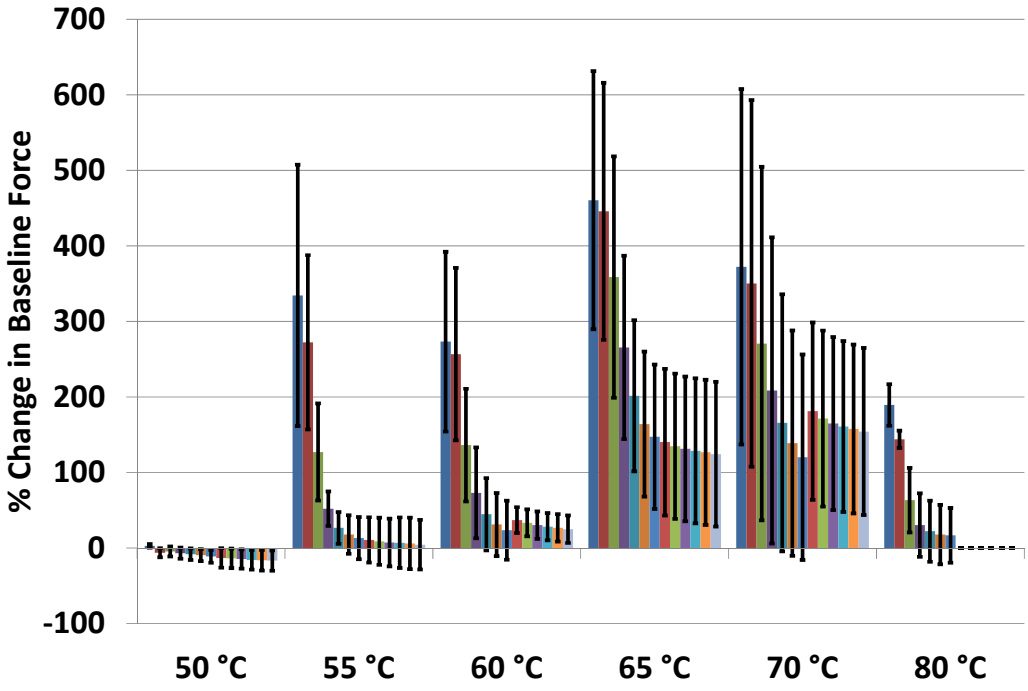

Figure 133: Dose effects of percent change in baseline force of swine diaphragm post RFA in tissue bath

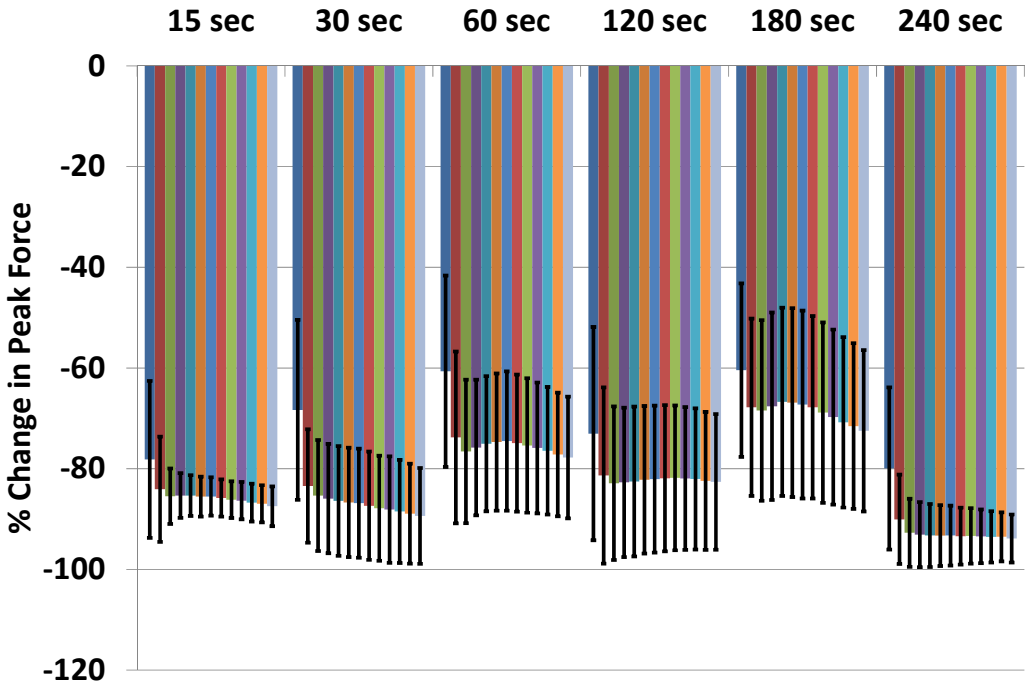

Figure 134: Dose effects of percent change in peak force of swine diaphragm post CRA in tissue bath

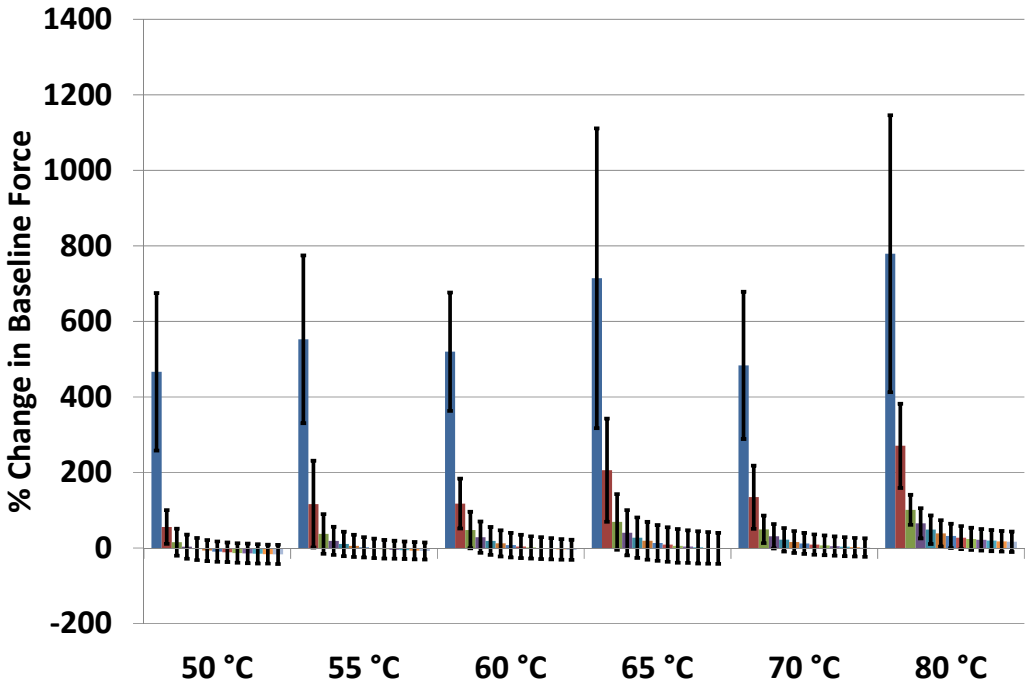

Figure 135: Dose effects of percent change in baseline force of swine diaphragm post CRA in tissue bath

Appendix 2: Study Data Management

Introduction: Large amounts of physiological data were acquired using tissue baths and biomechanical data using uniaxial machine. Briefly, the goal of this appendix is to highlight the key steps and custom software programs utilized in data acquisition and analysis as illustrated in Figure 136. The additional figures in this appendix illustrate the key steps involved with physiological and biomechanical data collection.

Tissue Bath Studies: Tissue bath data was acquired using custom built LabView software at a sampling rate of 250 Hz. On a typical experiment day, for a 5 hour experiment, approximately 72 million data points were acquired simultaneously from 16 tissue baths.

Uniaxial Pull Studies: Biomechanical data was acquired using a custom pull program on the uniaxial machine at a sampling rate of 100 Hz. On a typical experiment day, for approximately 32 samples (16 experimental and 16 control), approximately 1 million data points were acquired.

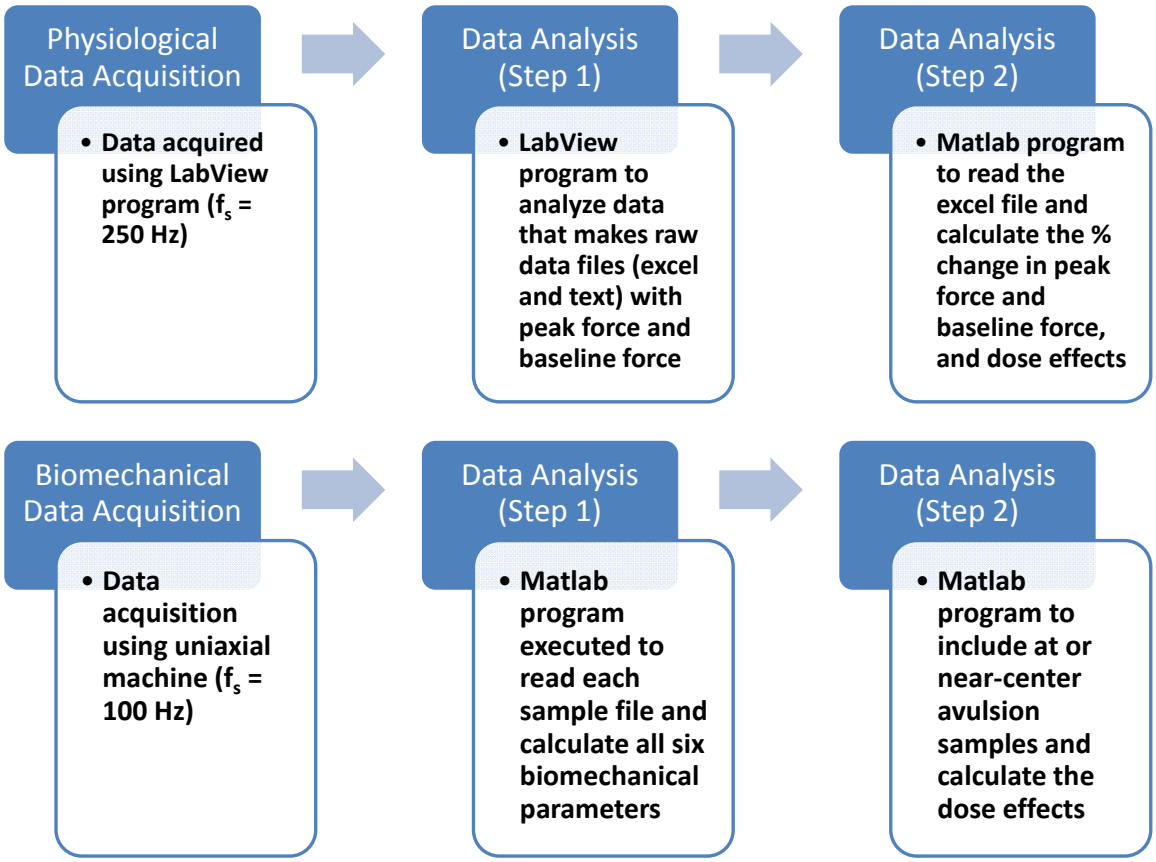

Figure 136: Steps highlighting data acquisition and analysis for physiological and biomechanical studies

Methods: Physiological Assessment

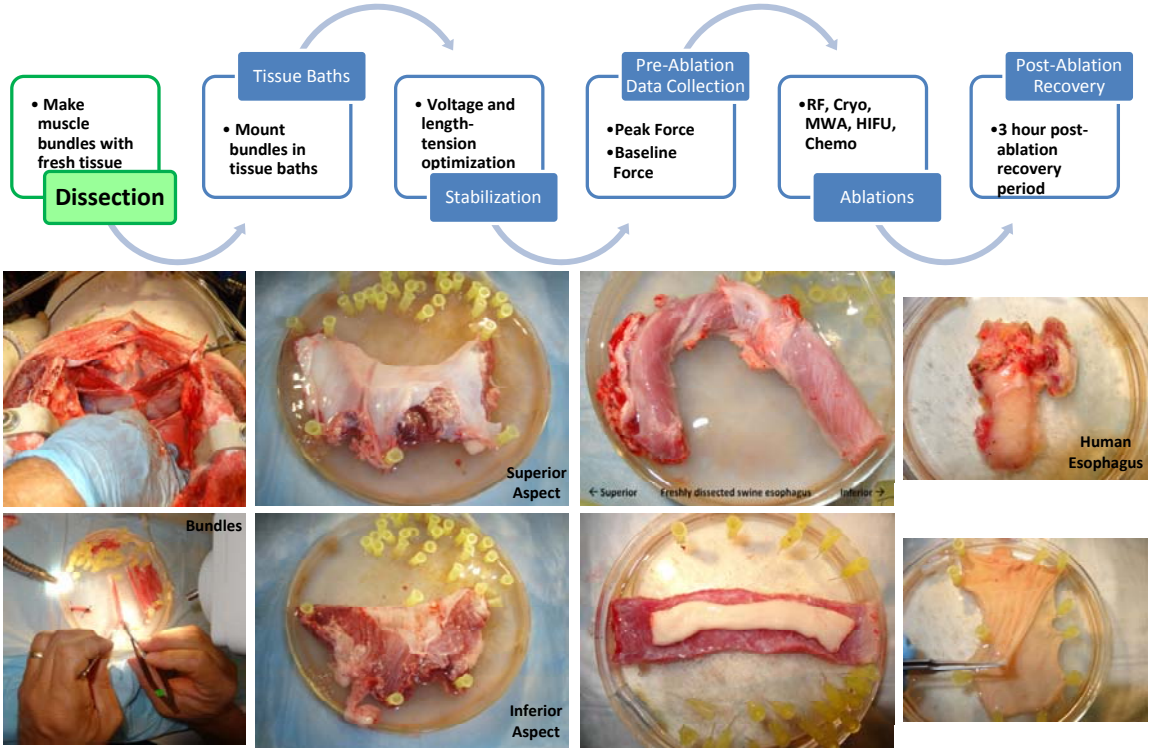

Figure 137: Methods for Physiological Assessment: Dissection

The first step involved the dissection of the tissue. Shown are the freshly obtained swine diaphragm and esophagus tissues. Also shown is the human esophagus on the right panel. In case of esophageal tissue, the muscularis and squamous epithelium layers were first separated. Each tissue was cleaned, connective tissue removed, and muscle bundles were prepared.

Methods: Physiological Assessment

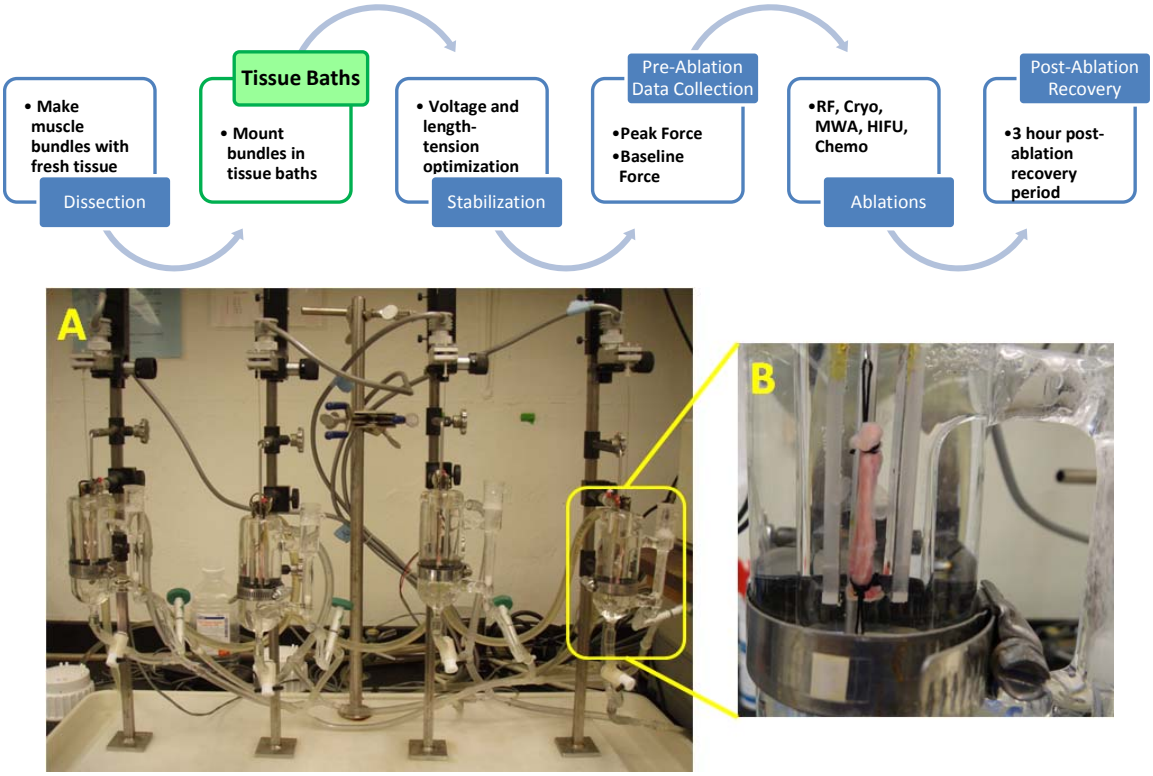

Figure 138: Methods for Physiological Assessment: Tissue Baths

The muscle bundles were mounted in 16 parallel tissue baths (4 shown). A zoomed-in version of the tissue bath is shown in the panel on the right. The bottom suture of the tissue was mounted on an immobile hook and the top suture was connected to a force transducer. Two platinum electrodes were positioned on either side of the muscle bundle to provide electrical stimulation. The approximately volume of each tissue bath was 50 ml which was filled with Krebs buffer. Each tissue bath was water jacketed to maintain a constant temperature of 37 °C and oxygenated to keep the tissue viable.

Methods: Physiological Assessment

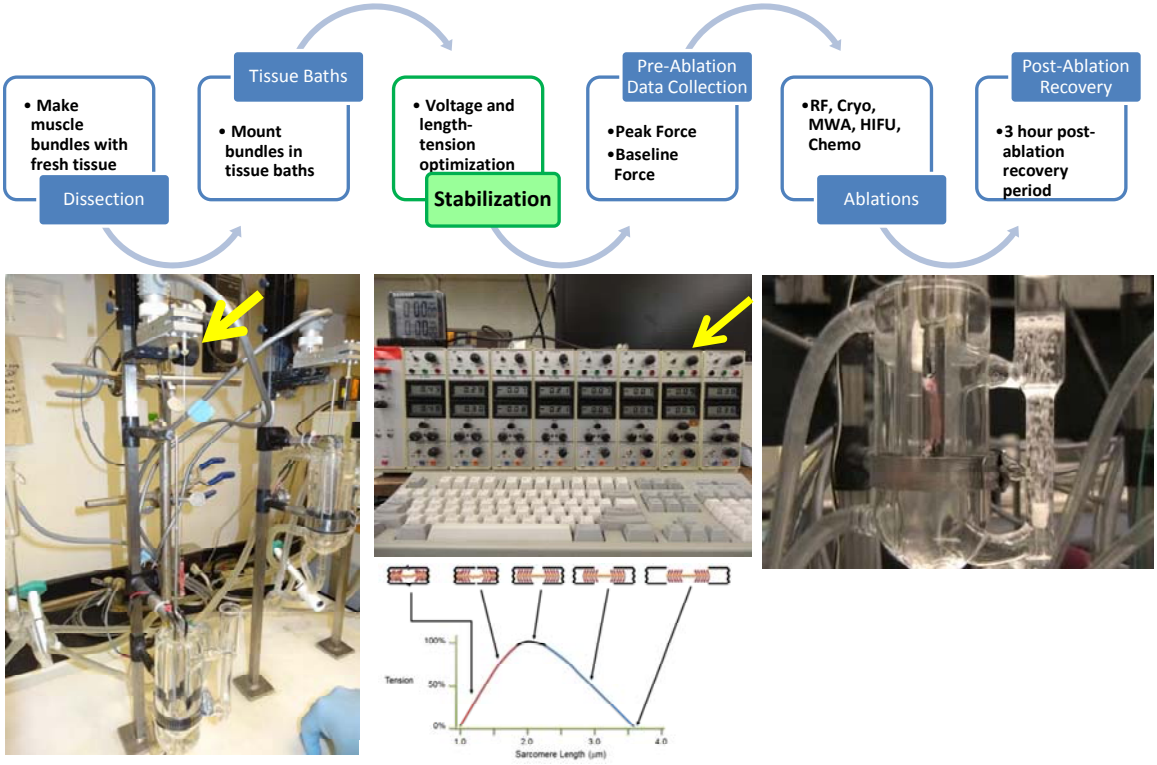

Figure 139: Methods for Physiological Assessment: Stabilization

Following mounting in tissue baths, each muscle bundle was allowed to stabilize and accommodate to the new in-vitro environment. Voltage stabilization was performed by adjusting the stimulating voltage to achieve the maximal twitch response (peak force). Length-tension optimization was performed by adjusting the baseline force (resting muscle tension) by stretching the muscle bundle to an optimum length that resulted in maximal twitch force response. The classic length-tension curve is shown that further illustrates the length-tension optimization.

Methods: Physiological Assessment

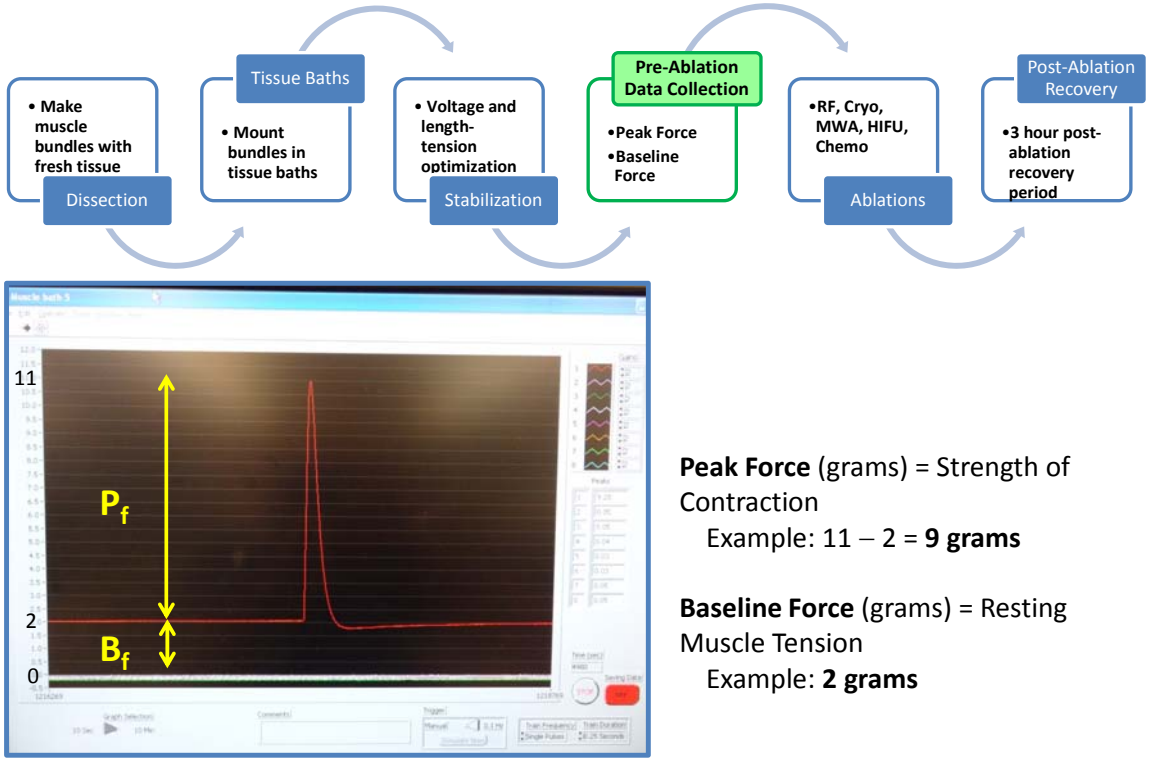

Figure 140: Methods for Physiological Assessment: Pre-Ablation Data Collection

The plateauing of the amplitude of twitch force (peak force) marked the completion of stabilization period for each muscle bundle. Following which the pre-ablation data was collected. Peak force and baseline force for each muscle bundle was digitally recorded. As a representative example, the peak force and baseline force of a given muscle bundle is shown, which is 9 grams and 2 grams of force, respectively.

Methods: Physiological Assessment

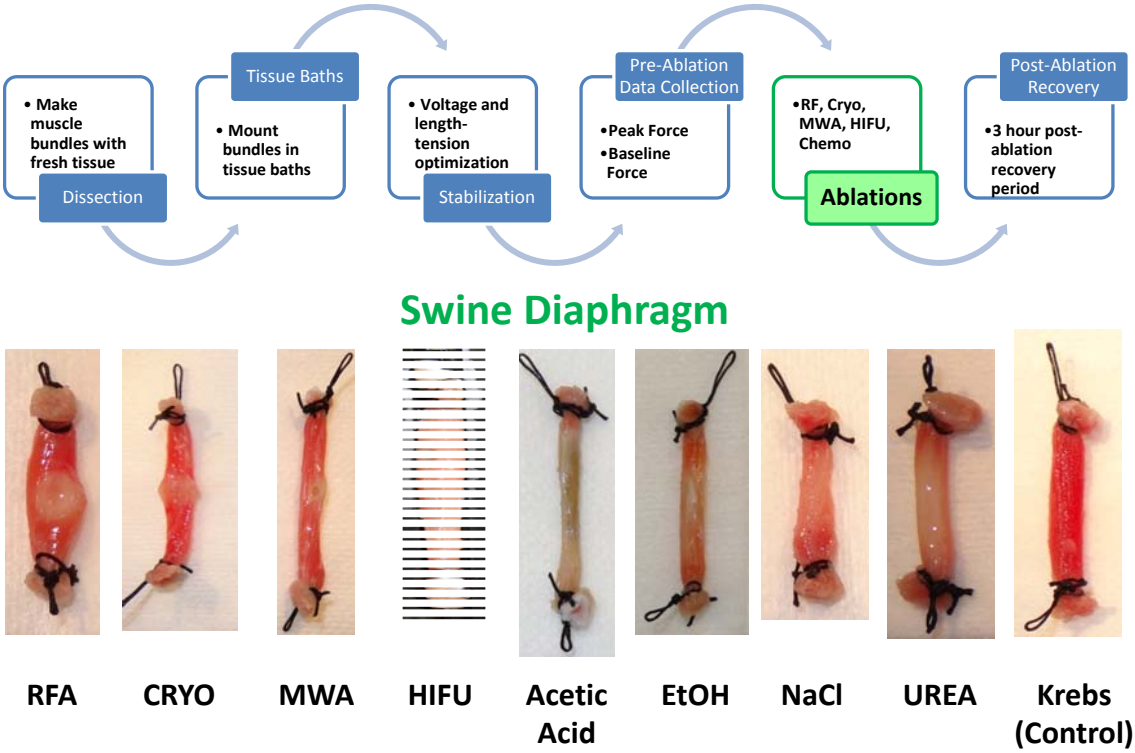

Figure 141: Methods for Physiological Assessment: Ablations (Swine Diaphragm)

A representative example of the swine diaphragm muscle bundles is shown following exposure to every single ablation modality investigated. Shown in far right is a control muscle bundle that can be compared to all the ablated muscle bundles. Notice that the chemical ablative modalities have a wider spread in tissue ablation/necrosis as compared to the thermal ablative modalities. MWA and HIFU have a focused ablative effect as compared to RFA and Cryo. Local hemorrhage and inflammation can be observed in the case of Cryo.

Methods: Physiological Assessment

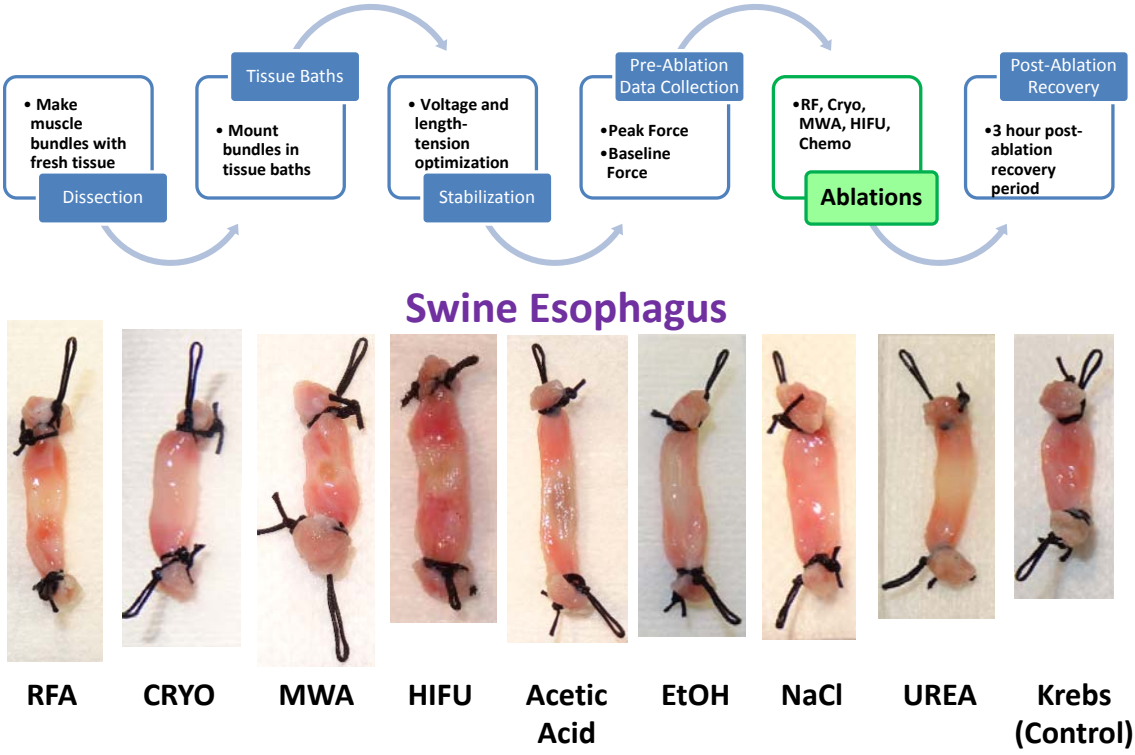

Figure 142: Methods for Physiological Assessment: Ablations (Swine Esophagus)

A representative example of the swine esophagus muscle bundles is shown following exposure to every single ablation modality investigated. The muscle bundle on the far right is a control muscle bundle that can be compared to all the ablated muscle bundles.

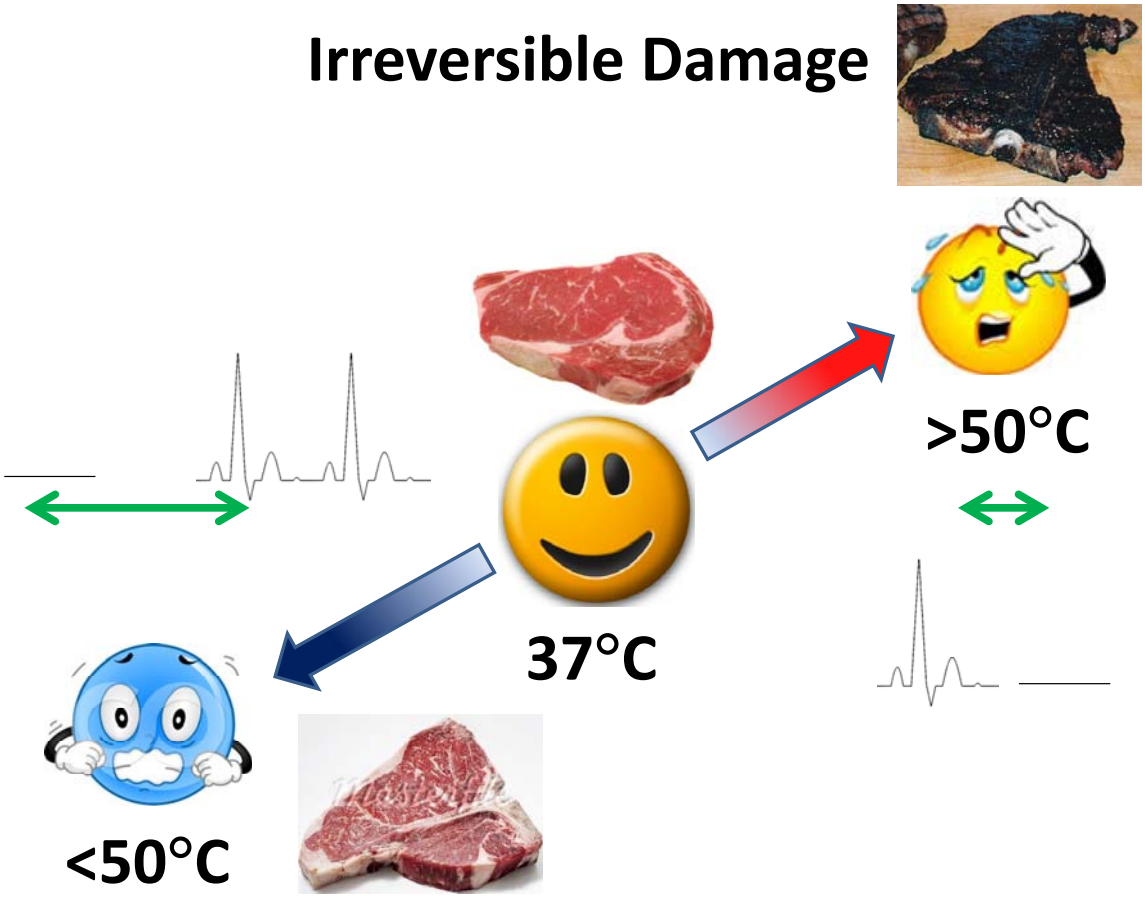

Figure 143: Hyperthermic and hypothermic tissue damage

A pictorial representation showing morphologic changes the tissue undergoes when it is subjected to hyperthermic and hypothermic temperatures. Notice that the physiological effects of application of hyperthermic temperatures are typically irreversible. On the other hand, unlike hyperthermia, effects of application of hypothermic temperatures are typically reversible within a given range of application. In clinical medicine these effects are exploited by performing cryomapping which allows the physician to test the region where cryoablation is being performed to assess whether permanent ablation would terminate the arrhythmia.

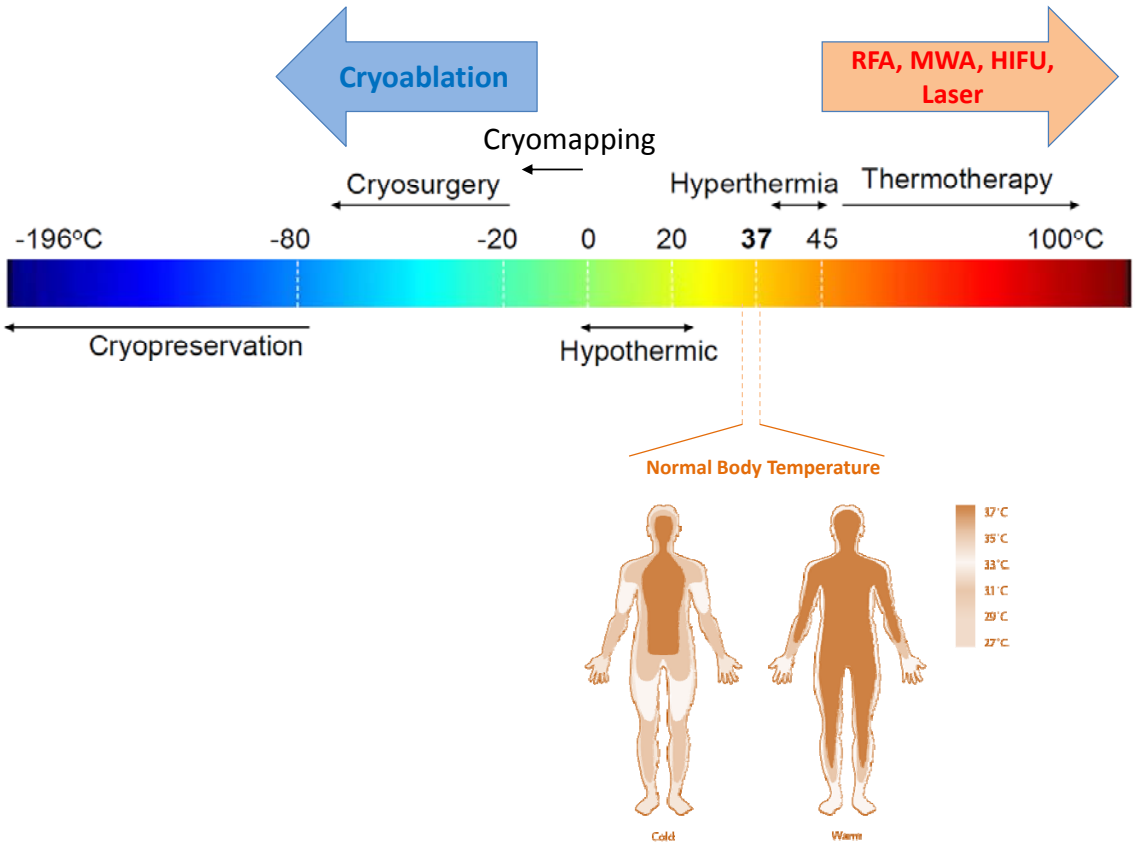

Figure 144: Hyperthermic and hypothermic thermal spectrum

Chemical Agent Injection: Incompressible Muscle Bundle

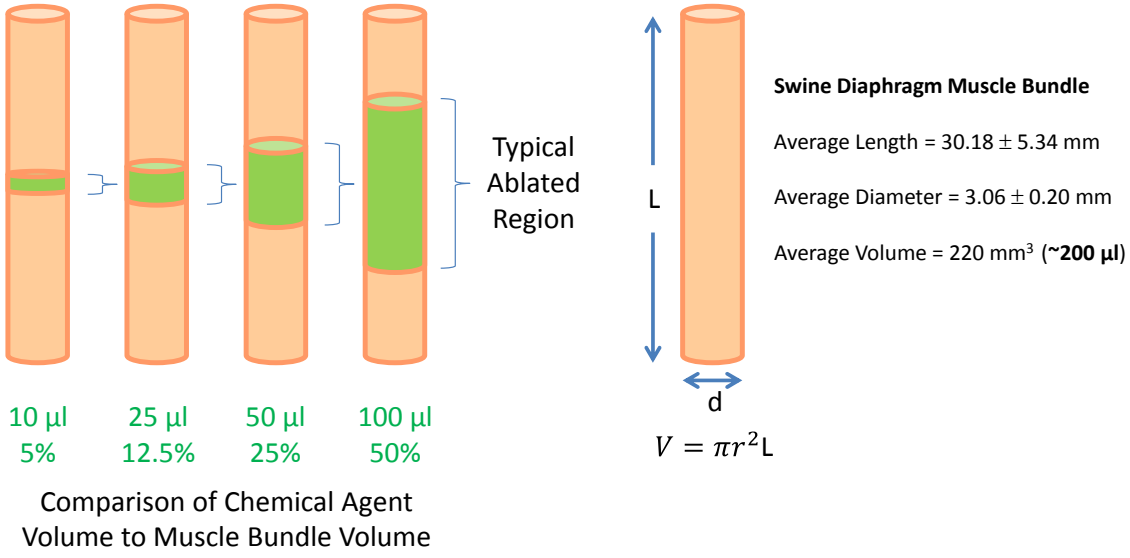

Figure 145: Volume analysis of chemical agents

A pictorial representation of amount of chemical ablative agent injected into a muscle bundle that is considered an incompressible material. A typical swine diaphragm muscle bundle has a volume of approximately 200 µl. Chemical agent volumes varying between 10 µl and 100 µl were injected into the muscle bundle. As can be seen, it was relatively easier to internalize a smaller volume of chemical agent within the muscle bundle as compared to a larger volume. Moreover, the ablative effect of chemical agents has a much wider spread as compared to thermal ablative modalities.

Methods: Physiological Assessment

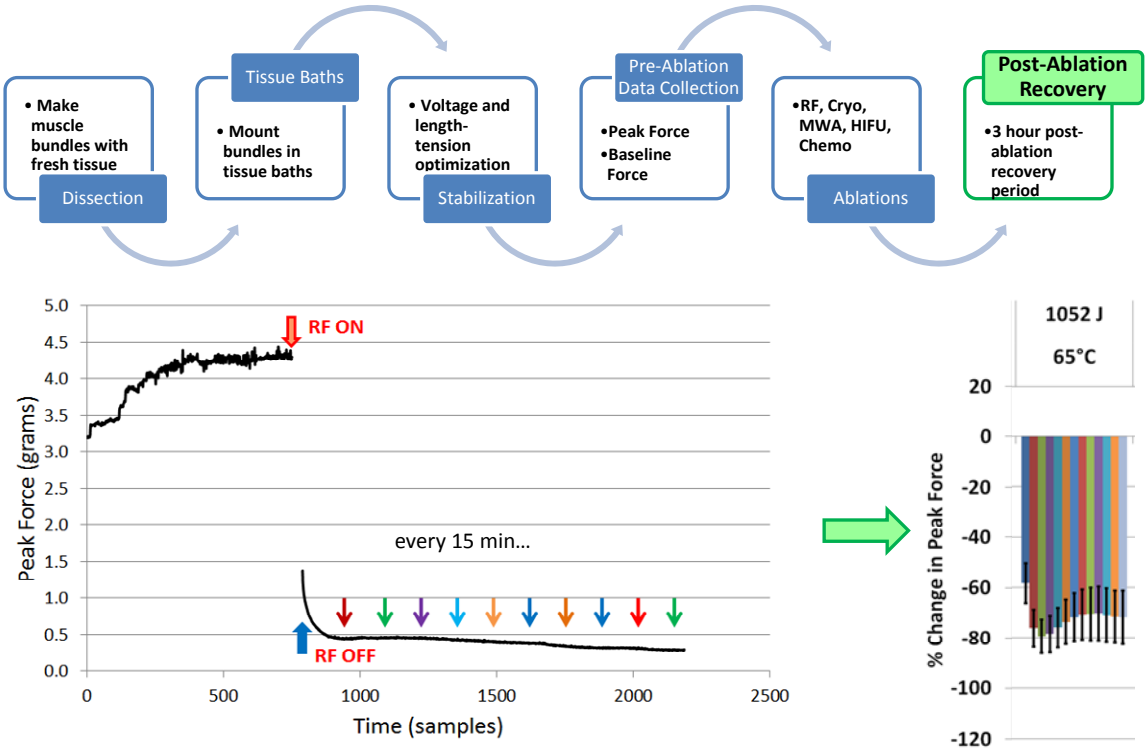

Figure 146: Methods for Physiological Assessment: Post-Ablations Recovery

Following ablations, each muscle bundle was allowed to recover for a period of at least 3 hours. A representative example of data collection from a given muscle bundle is shown. The peak force versus time graph illustrates the mounting of muscle bundle in the tissue bath, the stabilization period, the pre-ablation data collection, the application of ablation (RF-ON and RF-OFF), and the post-ablation recovery period. As can be seen, data was continuously collected throughout the duration of the experiment. However, for display and analysis purposes, data was samples every 15 minutes which is shown as colored arrows corresponding to the colored bars in the bar graph.

Methods: Biomechanical Assessment

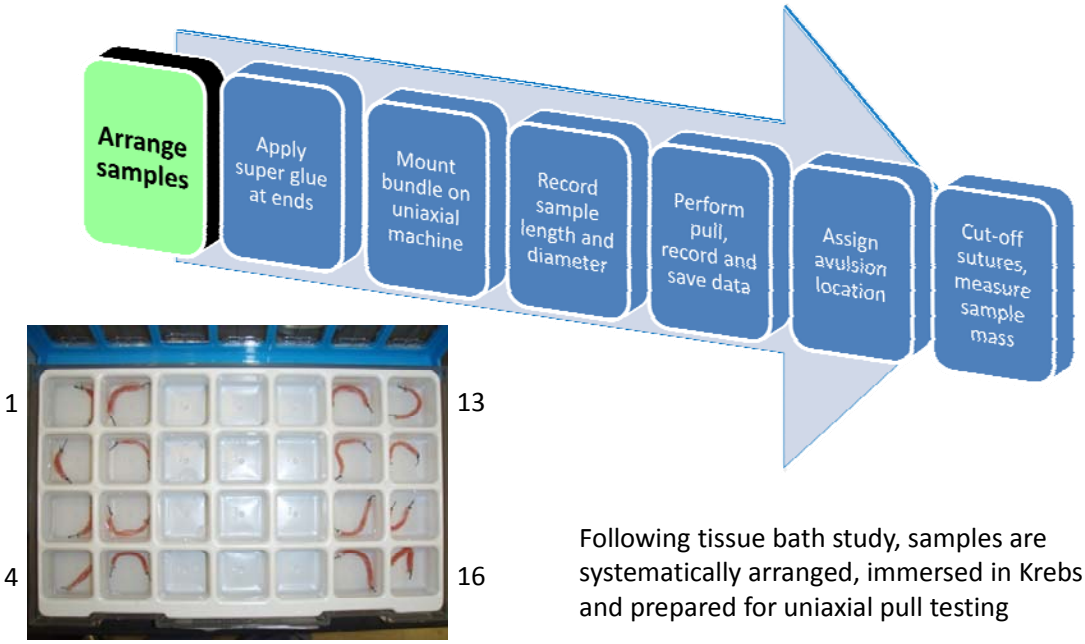

Figure 147: Methods for Biomechanical Assessment: Arrange Samples

Following completion of the physiological assessment protocol, the samples were arranged systematically based on treatment and ablative dose to perform the biomechanical assessment as shown in the inset.

Methods: Biomechanical Assessment

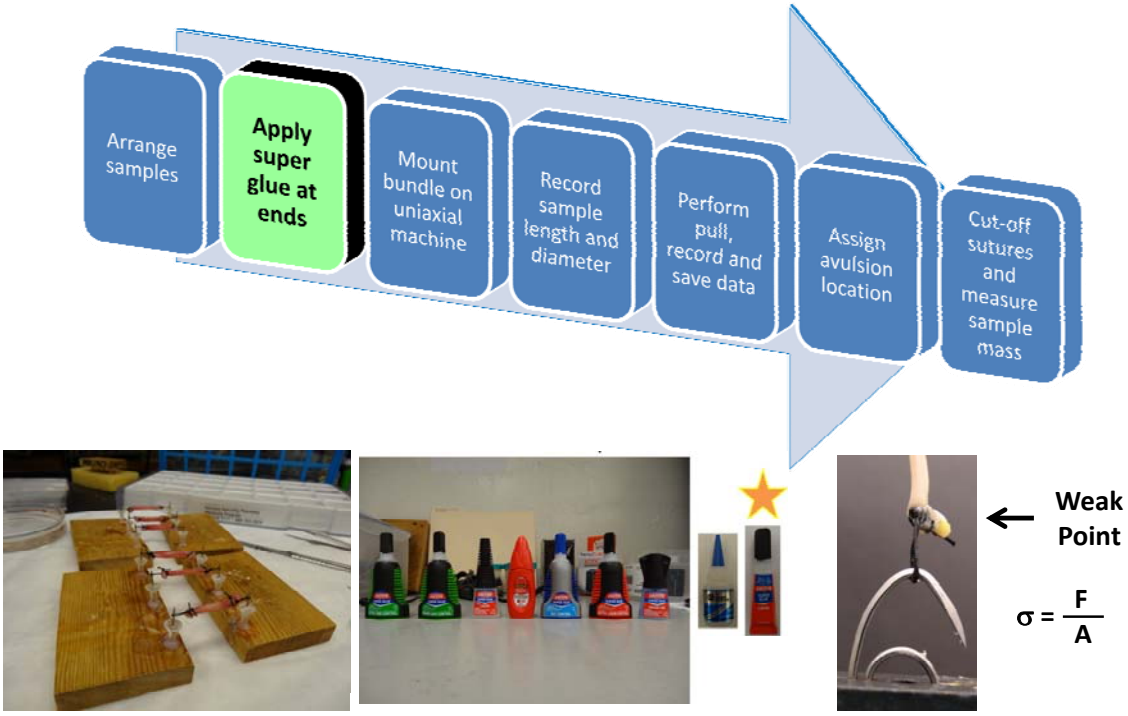

Figure 148: Methods for Biomechanical Assessment: Application of Super Glue

Tying sutures on either ends of the muscle bundle reduces the cross-sectional area at that point. As a result, the stresses at the suture-tissue interface go up which makes the muscle bundle vulnerable to breakage at that point. In order to strengthen the muscle bundle at the suture-tissue interface and avoid breakage at the sutures, a small application (1 or 2 drops) of super glue was applied. A lot of pilot studies were performed during which various super glues were tried/tested before finalizing a liquid-based super glue that cured within a few seconds and provided a strong suture-tissue interface.

Methods: Biomechanical Assessment

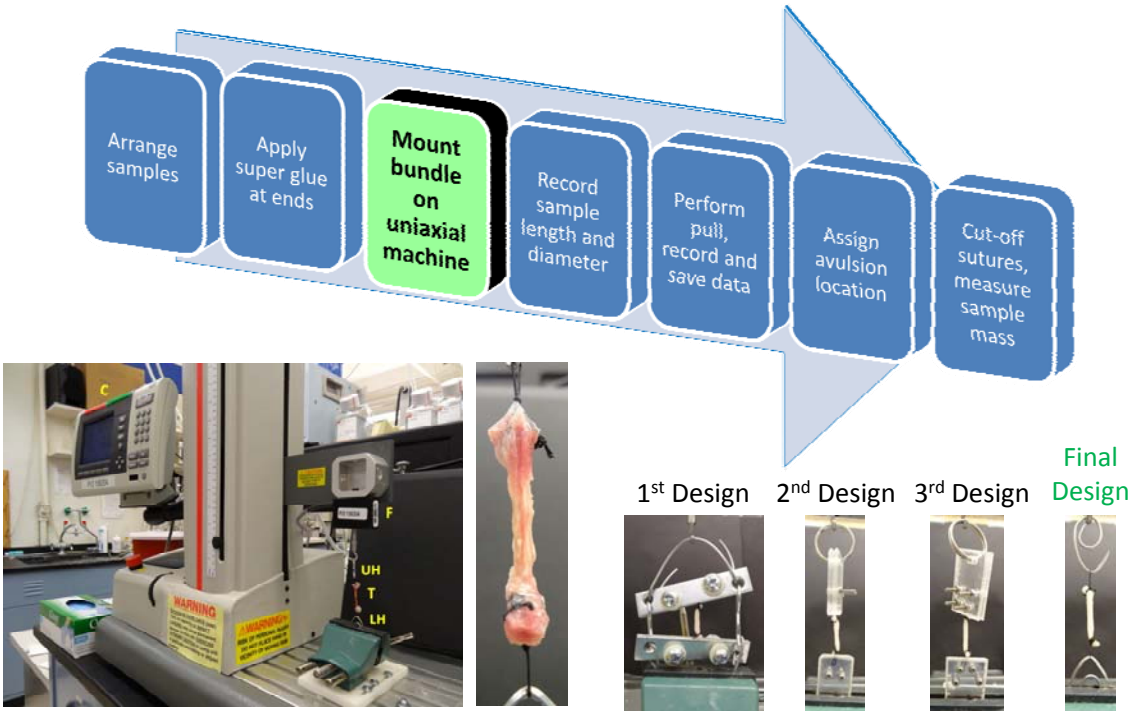

Figure 149: Methods for Biomechanical Assessment: Mounting on Uniaxial Machine

Each muscle bundle was mounted on the uniaxial pull machine to perform the pull. The fixtures required to mount the muscle bundle was not trivial. Numerous pilot studies were performed with various designs of fixtures as shown in the illustration. The main challenges were tissue slippage from the fixture, inappropriate bundle breakage, excessive time required to screw and unscrew the fixture. The final design was made up of stainless-steel hooks, which was elegant, simple to use and allowed easy mounting and unmounting of the muscle bundle. It also had a high success rate of pulls with no issue of tissue slippage.

Methods: Biomechanical Assessment

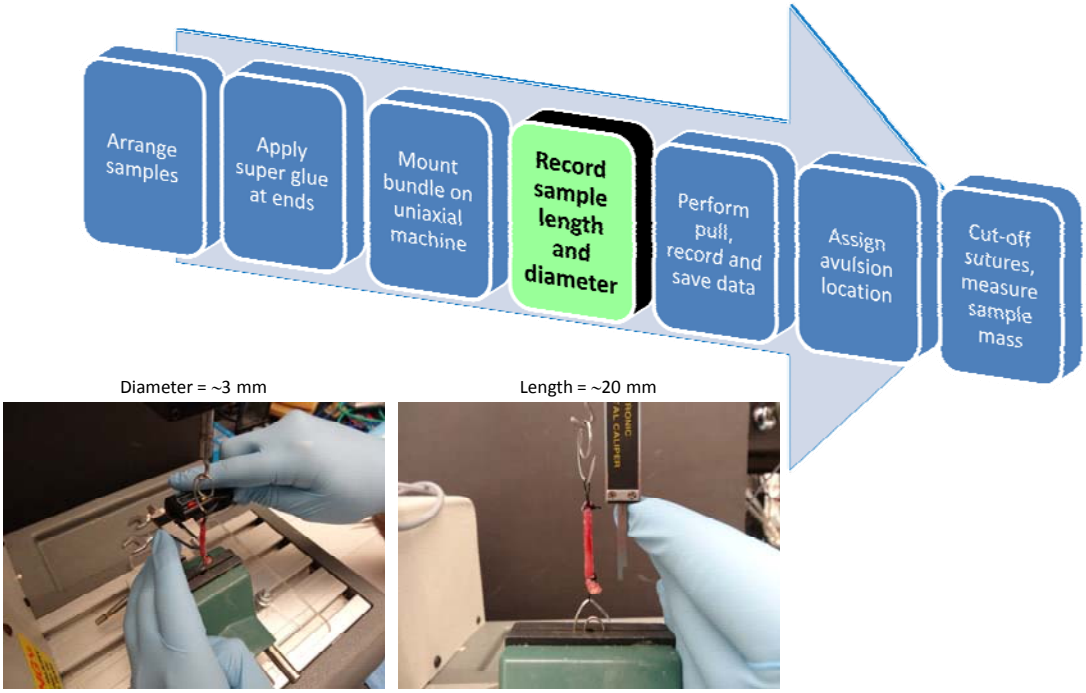

Figure 150: Methods for Biomechanical Assessment: Recording Sample Dimensions

Once the muscle bundle was mounted on the uniaxial machine, the muscle bundle was stretched just enough so that the sample hangs freely under the influence of gravity and registers minimal load on the monitor. This was considered the starting/initial length of the sample. Initial length and diameter of each sample was measured before the pull started so that biomechanical parameters could be calculated.

Methods: Biomechanical Assessment

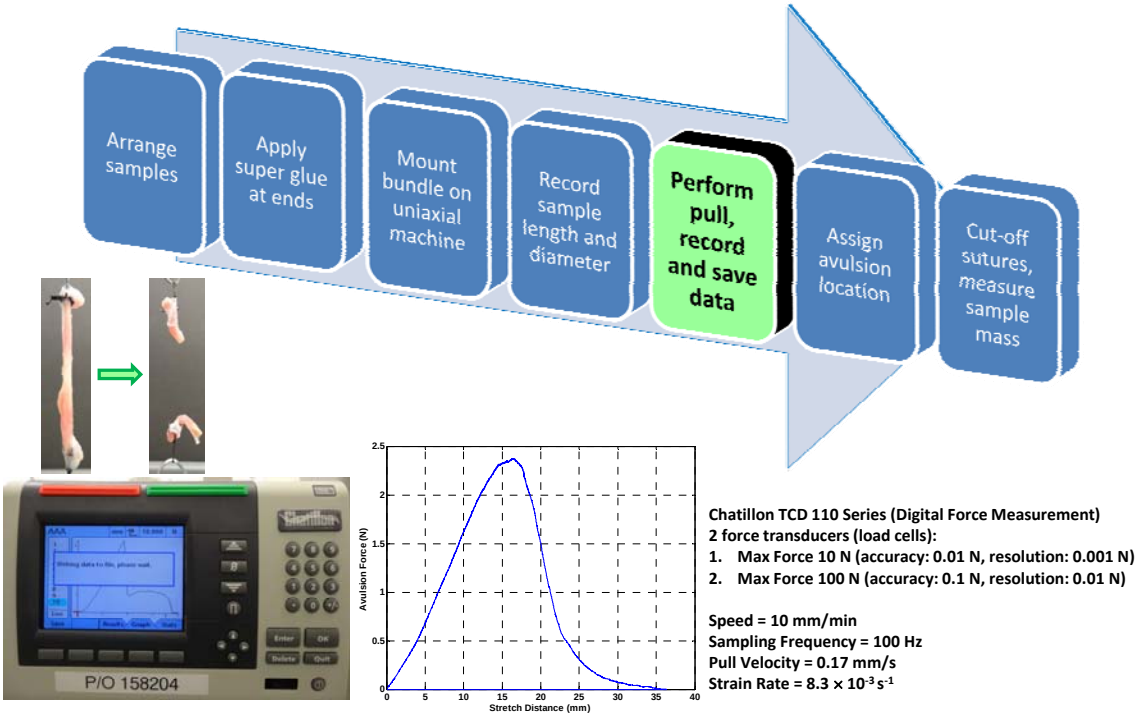

Figure 151: Methods for Biomechanical Assessment: Perform Pull

Uniaxial pull was performed for each sample. A representative example of load versus stretch graph is shown for a given sample until the sample avulsed as shown in the inset. The stretch characteristics, force transducer rating, and technical details are also mentioned.

Methods: Biomechanical Assessment

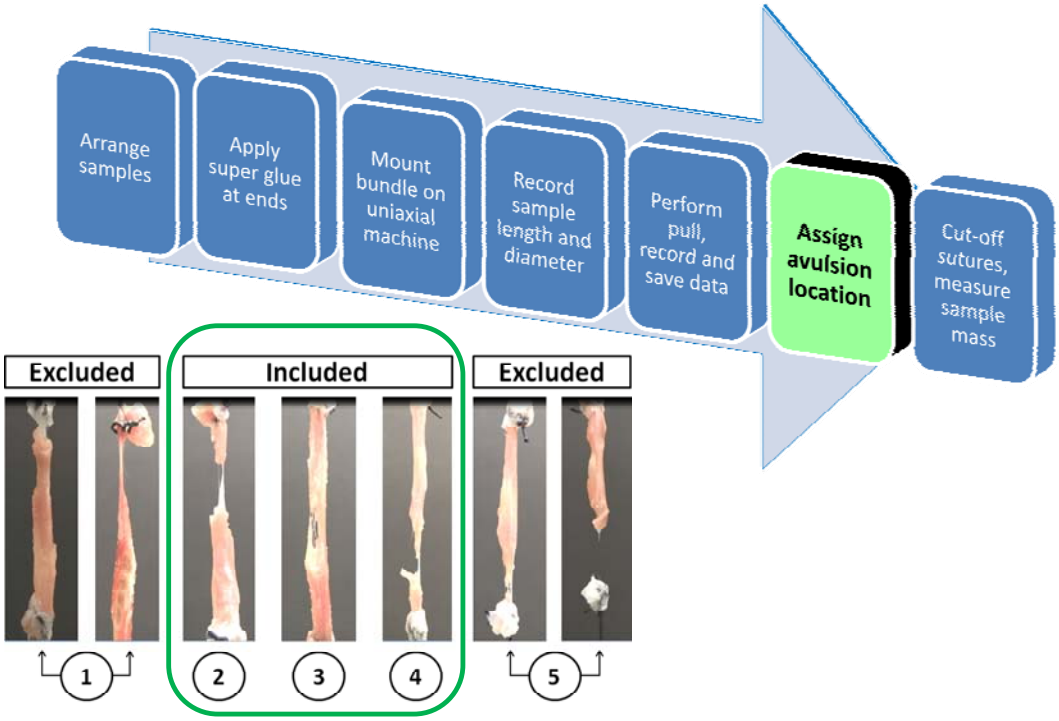

Figure 152: Methods for Biomechanical Assessment: Assign Avulsion Location

The figure illustrates sample avulsions at various locations along the length/longitudinal axis of the muscle bundle. Five different locations were determined. Any samples that avulsed at the suture or slipped out of the suture (top or bottom) were excluded from analysis. Any samples that avulsed at or near the center of the muscle bundle were included in the analysis.

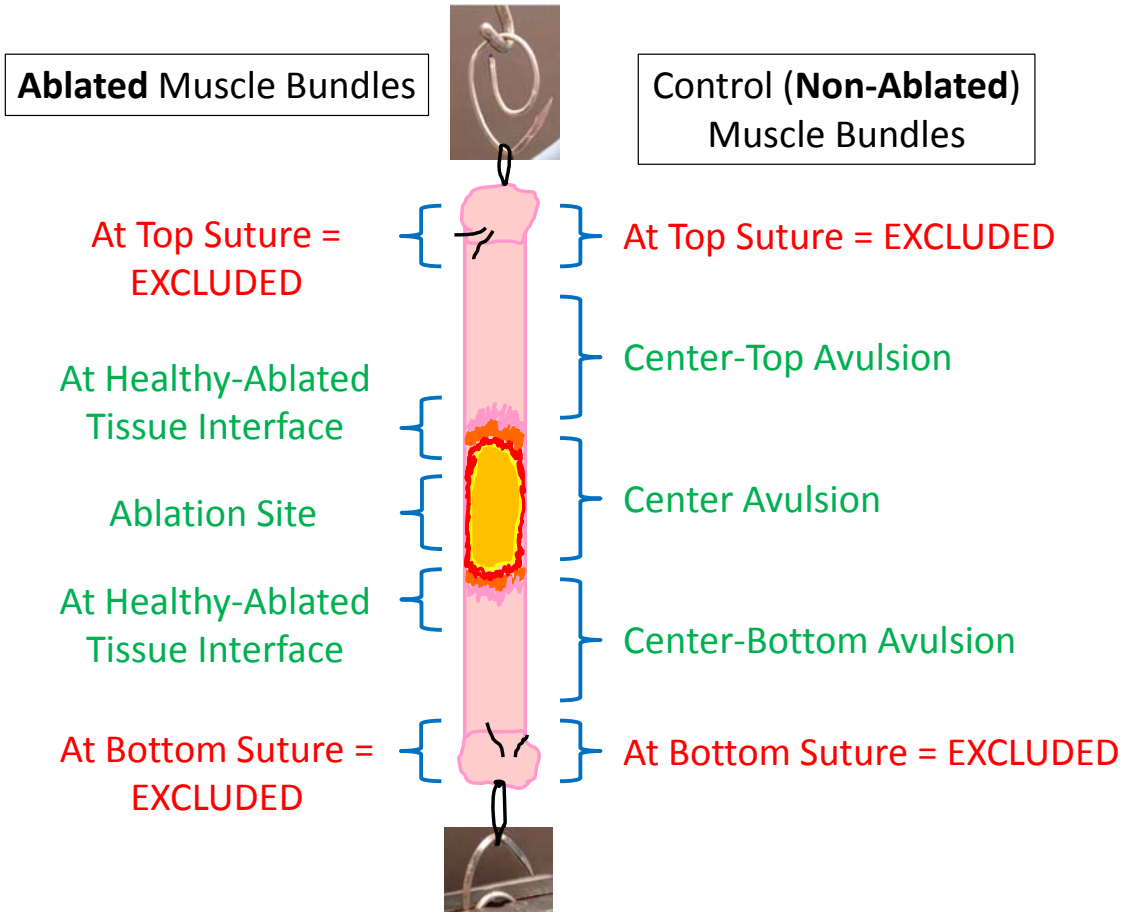

Figure 153: Pictorial representation of Avulsion

A pictorial representation of avulsion location is shown. Any sample avulsing/breaking at the sutures or slipping out of the sutures (top or bottom) were excluded; and center and near center avulsions were included in the overall statistical analysis. As shown, following ablation, the muscle bundle could avulse at the center, or in the zone of the healthy-ablated tissue interface.

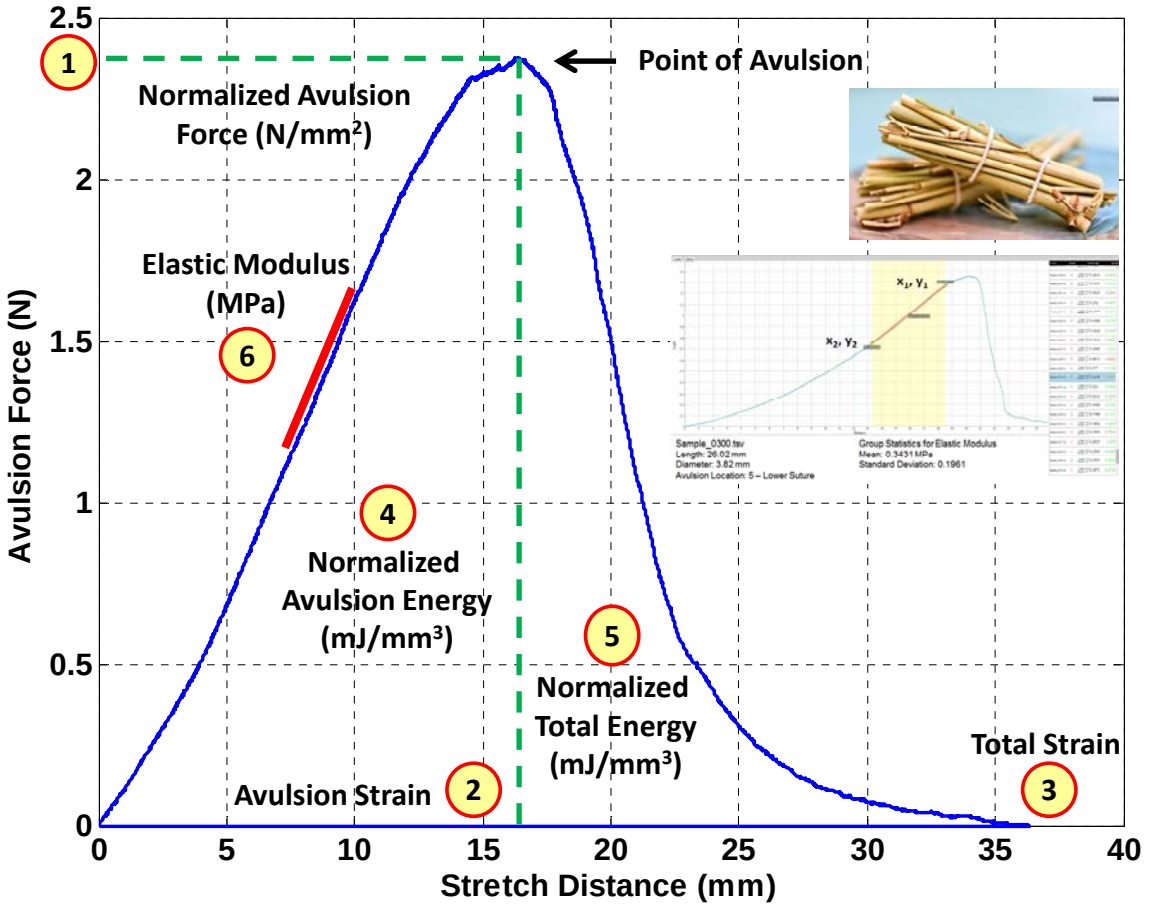

Figure 154: A representative example of force-stretch graph

A representative example of force-stretch graph of a given sample is shown. Also shown are the 6 biomechanical parameters that were calculated for each sample. In order to perform a fair comparison between samples of the same tissues, different tissues, and different species, all forces were normalized to the cross-sectional area of the sample, and all energies were normalized to the volume of the sample. A sophisticated program was developed that allowed calculation of the initial linear region of the force-stretch graph to calculate the elastic modulus of each sample.

Methods: Biomechanical Assessment

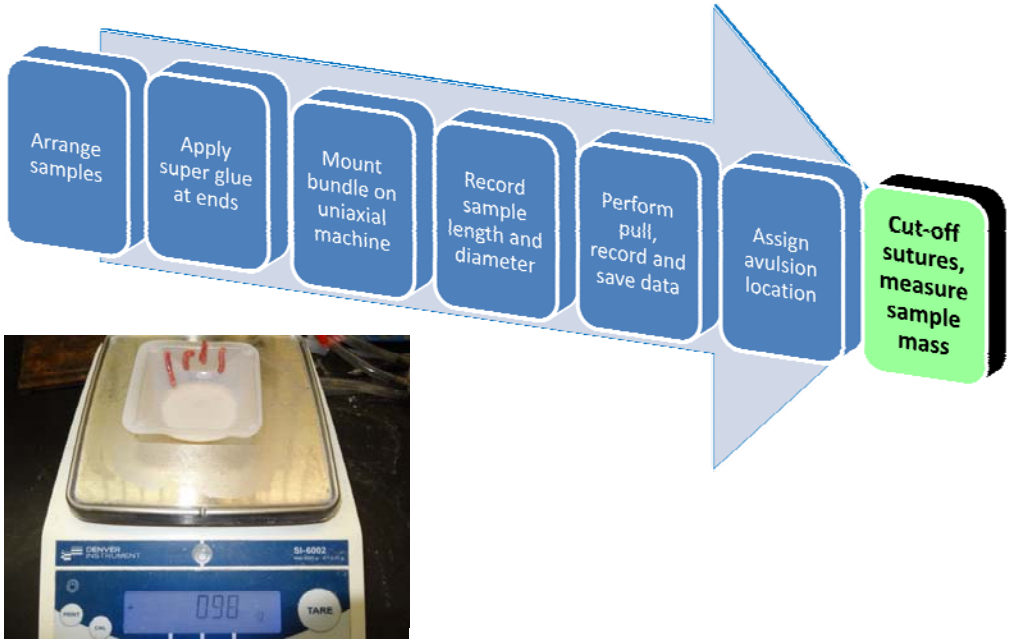

Figure 155: Methods for Biomechanical Assessment: Measure Mass

The last step in the biomechanical assessment involved measuring the mass of each sample.

Appendix 3: Statistical Results of Swine Diaphragm

Introduction: The following graphs/figures/tables/illustrations are supplementary information for swine diaphragm muscle bundles that was not included in the individual chapters. Hence, this information is included in this appendix to allow better understanding of the results and for completeness.

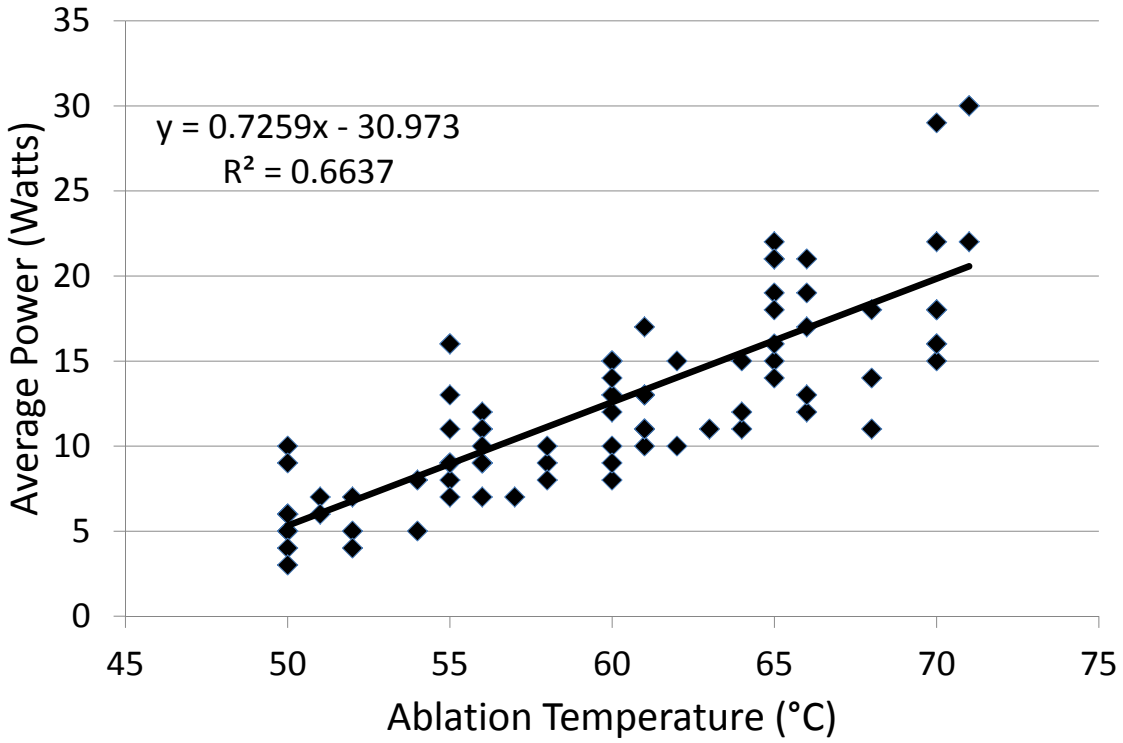

Figure 156: Plot of average power and catheter tip ablation temperature for swine diaphragm

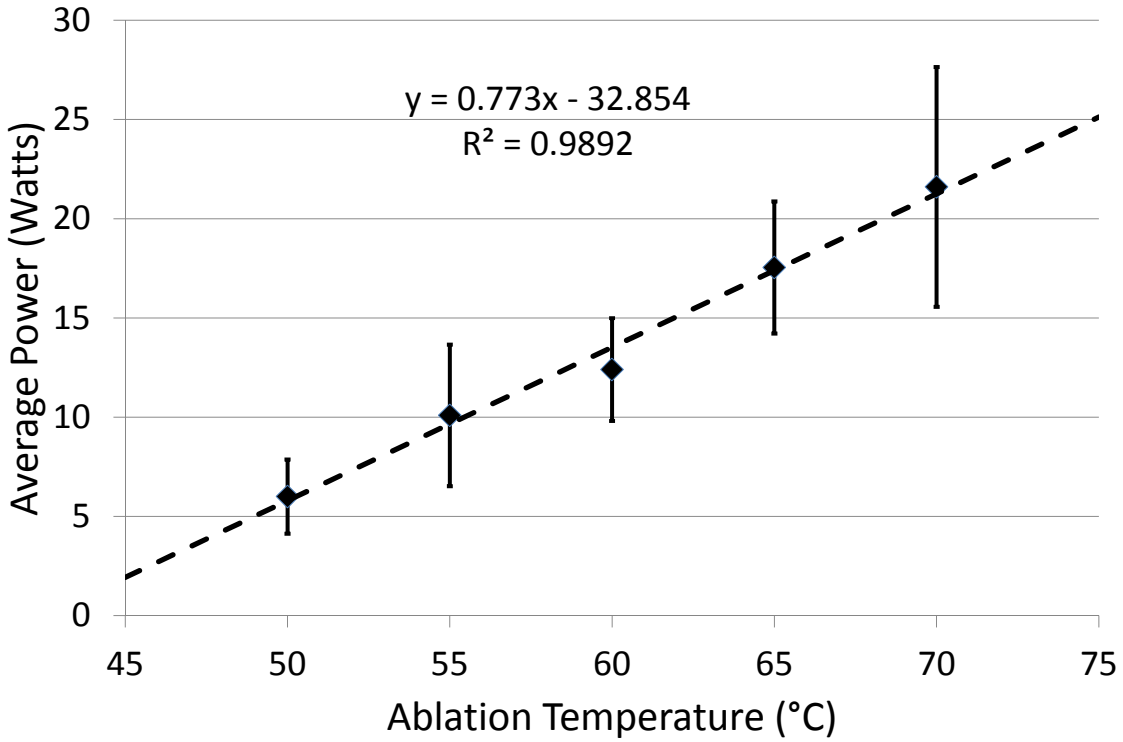

Figure 157: Plot of average power and catheter tip ablation temperature for swine diaphragm

Ablation Temperature (°C)	Average Power (W, μ±σ)	Ablation Duration (s)	Energy, E = W.s (J, μ±σ)
50	6.0 ± 1.87	60	360 ± 112
55	10.09 ± 3.56	60	605 ± 214
60	12.40 ± 2.59	60	744 ± 155
65	17.54 ± 3.33	60	1052 ± 200
70	21.60 ± 6.04	60	1296 ± 362

Table 19: Dose table for RFA, showing the catheter tip ablation temperature, average power, ablation duration, and energy during RFA of swine diaphragm

Average Power (W)	Ablation Duration (s)	Energy (J)
2.80	60	168
4.82	60	289
6.84	60	410
6.84	120	821
6.84	180	1231
6.84	240	1642

Table 20: Dose table for MWA of swine diaphragm, showing average power, duration and energy

Average Power (W)	Ablation Duration (s)	Energy (J)
49	2	98
58	2	116
66	2	132
58	4	232
58	8	464
58	12	696

Table 21: Dose table for HIFU ablations of swine diaphragm, showing average power, duration, and energy

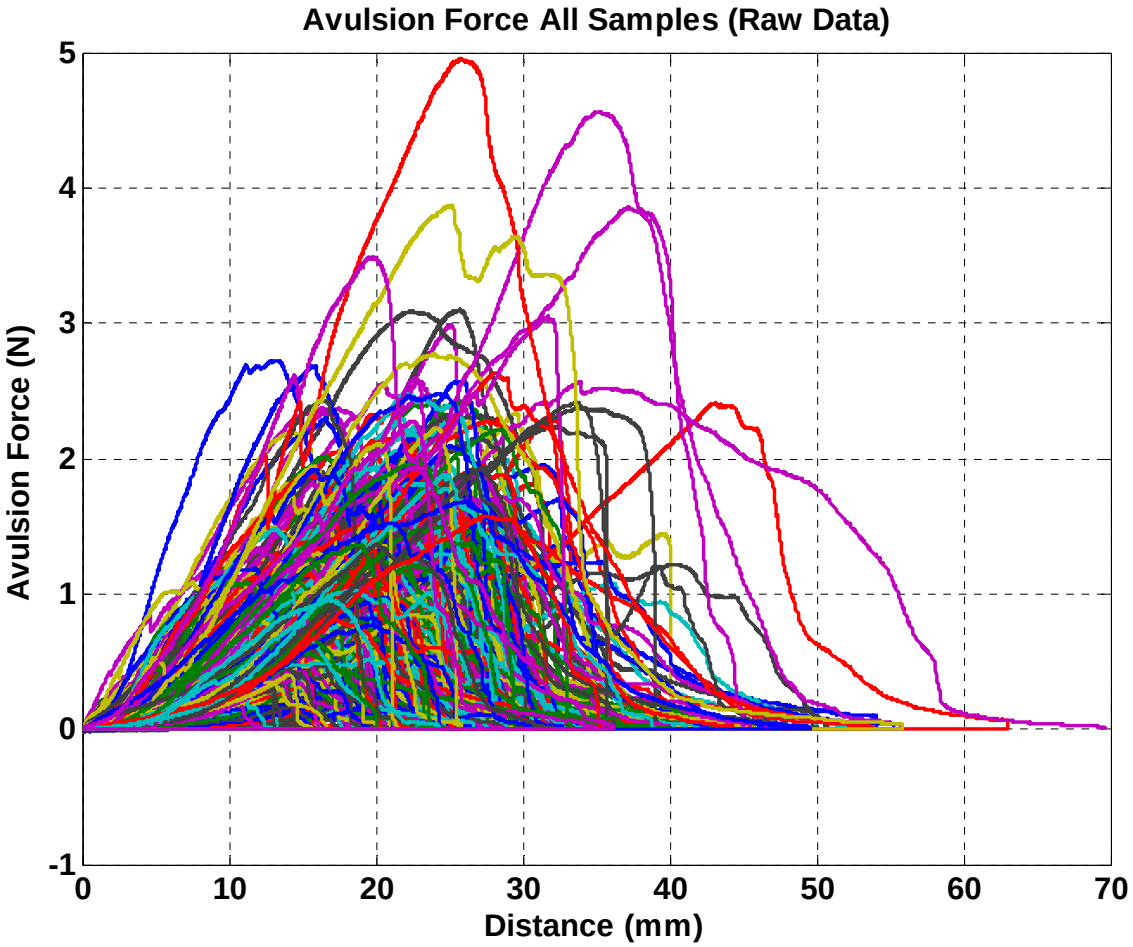

Figure 158: Raw data of force versus stretch data of swine diaphragm control muscle bundles

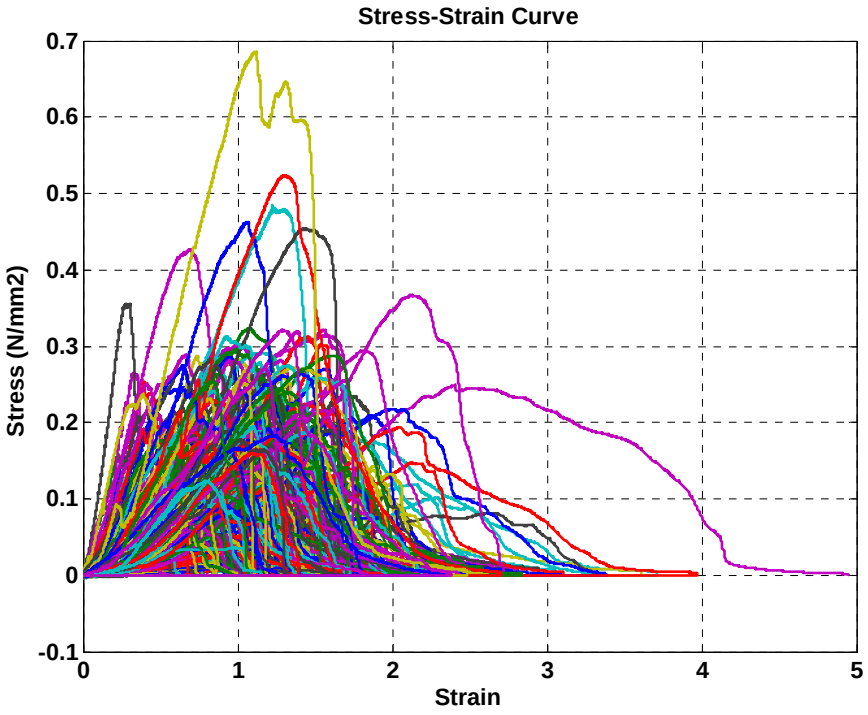

Figure 159: Stress-strain curve of swine diaphragm control muscle bundles

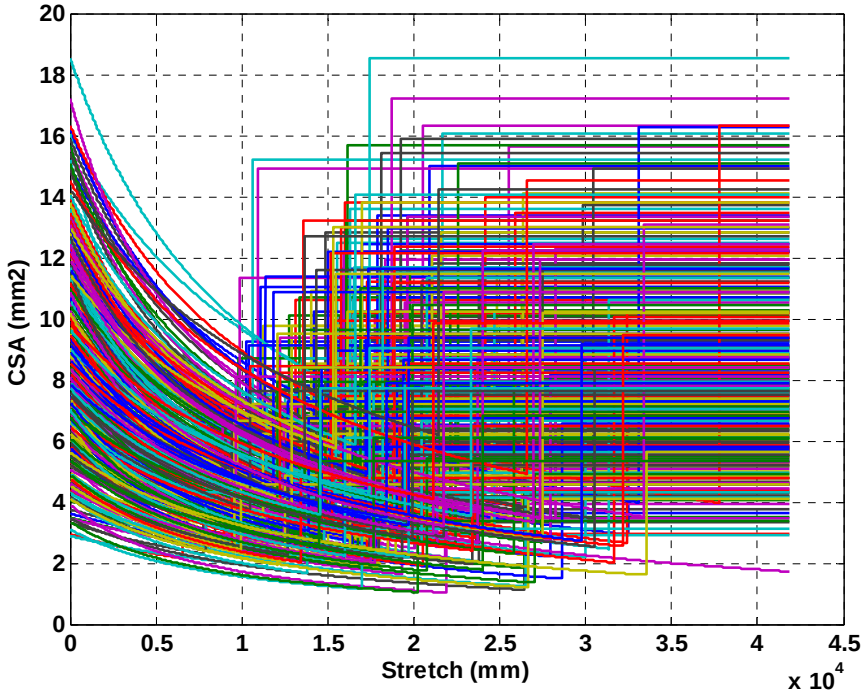

Figure 160: Change in cross-sectional area of muscle bundles as a function of stretch

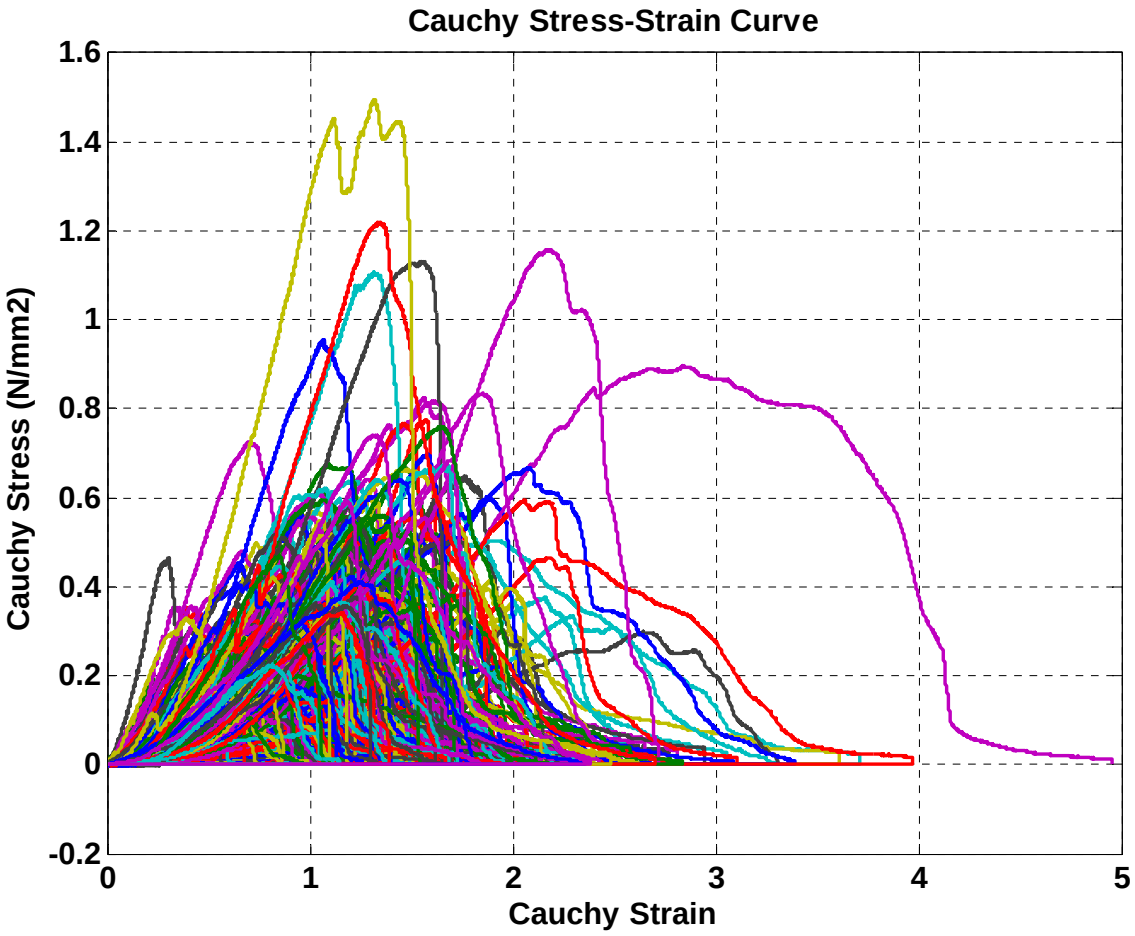

Figure 161: Cauchy's stress-strain curve of swine diaphragm control muscle bundles

All Samples	Avulsion Force (N/mm^2)	Elastic Modulus (N/mm^2)	Avulsion Strain ($\Delta l/L$)	Total Strain ($\Delta l/L$)	Avulsion Energy (mJ/mm^3)	Total Energy (mJ/mm^3)
Controls (n=327)	0.17 ± 0.08	0.34 ± 0.20	1.10 ± 0.39	1.59 ± 0.65	43.60 ± 31.06	65.75 ± 50.23
RF (n=111)	0.16 ± 0.08	0.33 ± 0.21	0.90 ± 0.30	1.20 ± 0.42	35.06 ± 22.20	47.76 ± 29.87
Cryo (n=58)	0.19 ± 0.08	0.66 ± 0.39	0.63 ± 0.25	0.80 ± 0.34	24.11 ± 15.08	31.59 ± 17.80
MWA (n=24)	0.12 ± 0.03	0.16 ± 0.07	1.27 ± 0.48	2.08 ± 0.84	37.82 ± 14.64	58.58 ± 24.09
HIFU (n=49)	0.17 ± 0.07	0.49 ± 0.29	0.78 ± 0.28	1.12 ± 0.50	32.86 ± 25.83	46.98 ± 33.94
AAcid (n=16)	0.25 ± 0.08	0.47 ± 0.15	0.61 ± 0.17	0.89 ± 0.23	49.34 ± 18.89	69.86 ± 25.75
EtOH (n=34)	0.18 ± 0.08	0.39 ± 0.16	0.71 ± 0.21	1.01 ± 0.36	38.80 ± 24.11	55.64 ± 39.48
NaCl (n=21)	0.21 ± 0.07	0.37 ± 0.13	0.88 ± 0.20	1.20 ± 0.28	50.77 ± 23.83	67.11 ± 29.75
Urea (n=25)	0.19 ± 0.05	0.38 ± 0.11	0.85 ± 0.18	1.28 ± 0.34	46.64 ± 14.86	67.51 ± 25.97
Krebs (n=30)	0.22 ± 0.07	0.41 ± 0.15	0.89 ± 0.18	1.23 ± 0.24	47.14 ± 17.78	67.87 ± 29.03

Table 22: Biomechanical parameters of all swine diaphragm muscle bundles

All Samples	% Diff Avulsion Force	% Diff Elastic Modulus	% Diff Avulsion Strain	% Diff Total Strain	% Diff Avulsion Energy	% Diff Total Energy
RF (n=111)	-7.78 p=0.1359	-4.18 p=0.5124	-17.84 p<0.005	-24.31 p<0.005	-19.59 p=0.0078	-27.37 p<0.005
Cryo (n=58)	+7.27 p=0.2873	+93.17 p<0.005	-42.57 p<0.005	-49.54 p<0.005	-44.71 p<0.005	-51.95 p<0.005
MWA (n=24)	-33.09 p<0.005	-54.10 p<0.005	+16.06 p=0.0352	+30.89 p<0.005	-13.26 p=0.3669	-10.90 p=0.4891
HIFU (n=49)	-0.23 p=0.9749	+41.59 p<0.005	-29.06 p<0.005	-29.50 p<0.005	-24.64 p=0.0218	-28.54 p=0.0119
AAcid (n=16)	+45.29 p<0.005	+79.02 p<0.005	-44.68 p<0.005	-43.80 p<0.005	+13.16 p=0.4650	+6.26 p=0.7453
EtOH (n=34)	+5.46 p=0.5272	+12.23 p=0.2279	-35.42 p<0.005	-36.64 p<0.005	-11.01 p=0.3829	-15.38 p=0.2561
NaCl (n=21)	+21.66 p=0.0441	+8.27 p=0.5138	-19.77 p=0.0114	-24.73 p=0.0061	+16.43 p=0.3005	+2.07 p=0.9023
Urea (n=25)	+12.38 p=0.2039	+11.89 p=0.3044	-22.21 p=0.0020	-19.42 p=0.0192	+6.96 p=0.6288	+2.67 p=0.8627
Krebs (n=30)	+24.21 p=0.0080	+18.68 p=0.0820	-18.51 p=0.0047	-22.88 p=0.0025	+8.11 p=0.5395	+3.23 p=0.8198

Table 23: Percent change in biomechanical properties of swine diaphragm muscle bundles post ablation with different ablative modalities

Values of avulsion force, elastic moduli, strain, and energy are shown along with statistical significance (marked by blue color). A positive value indicates an increase, and negative value a decrease with respect to control swine diaphragm muscle bundles (n=327).

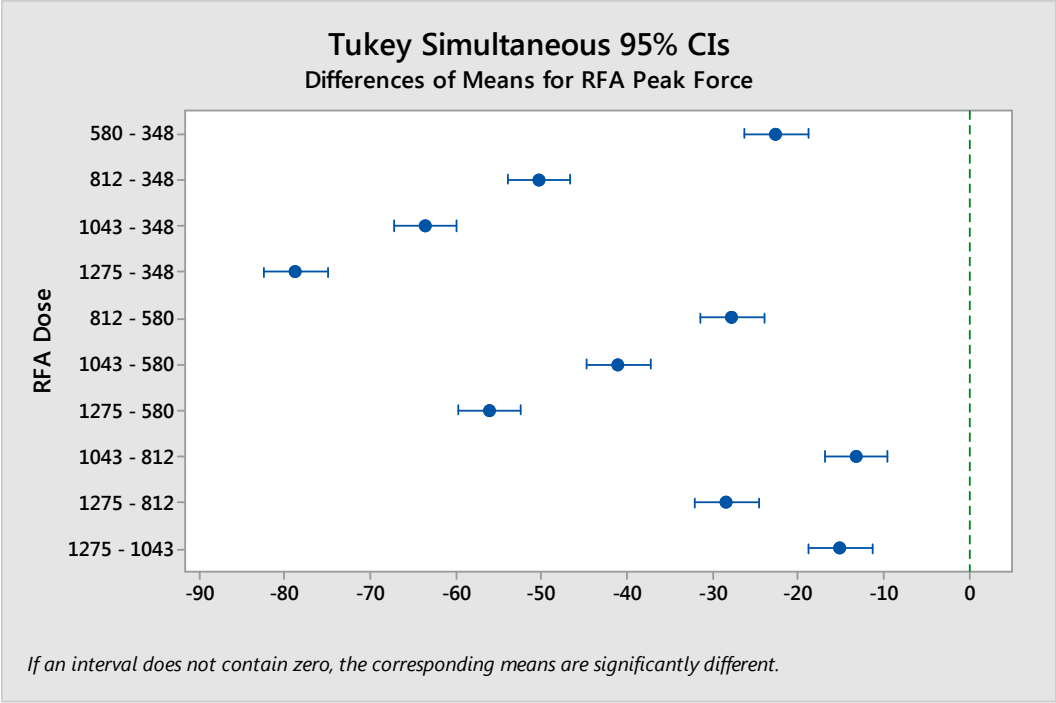

Figure 162: Statistical analysis for swine diaphragm RFA peak force

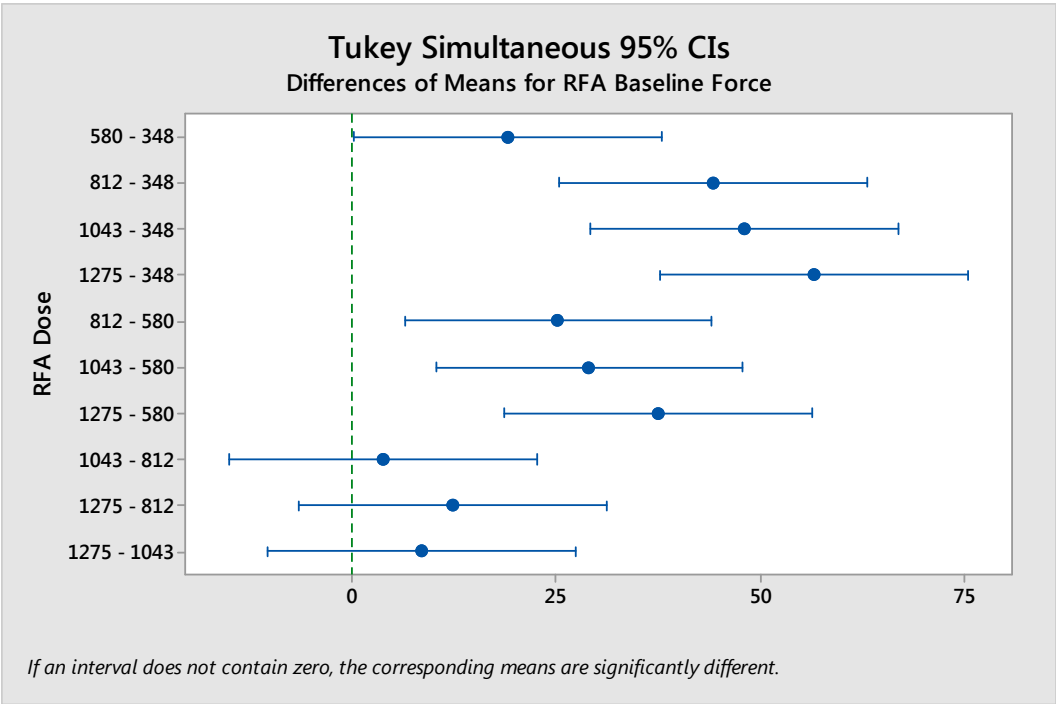

Figure 163: Statistical analysis for swine diaphragm RFA baseline force

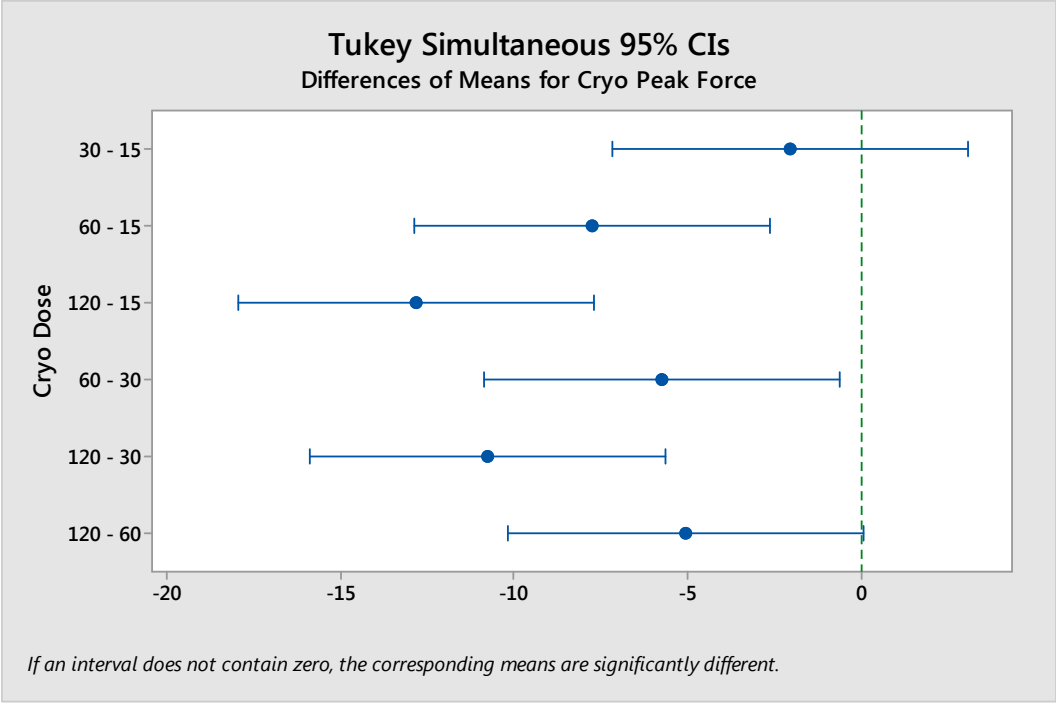

Figure 164: Statistical analysis for swine diaphragm CRA peak force

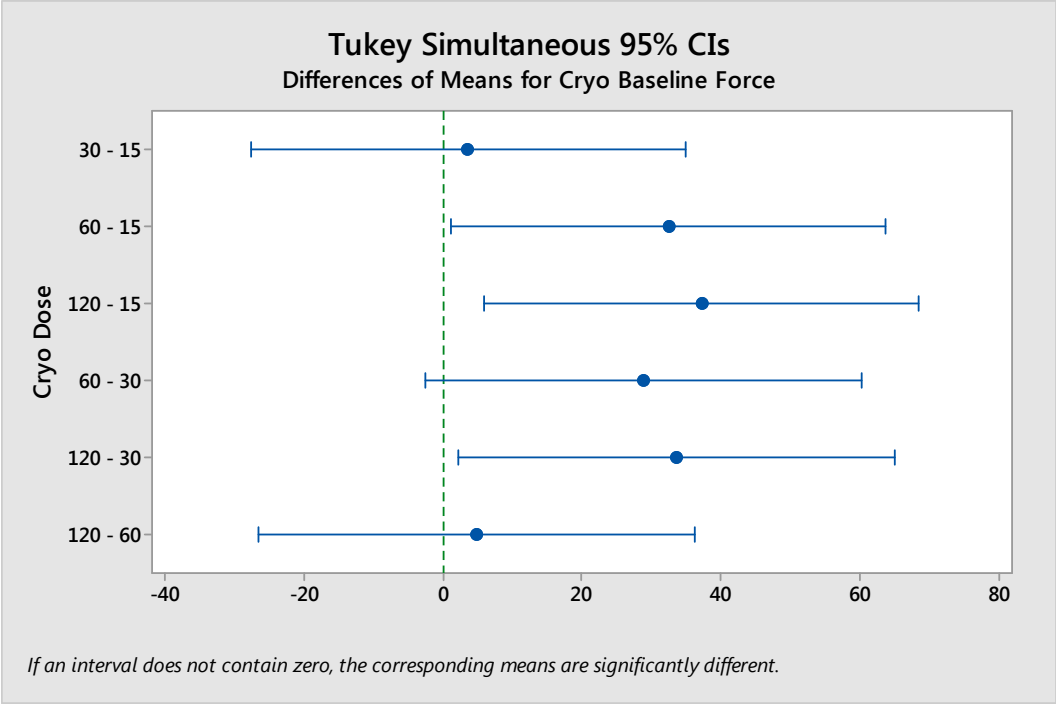

Figure 165: Statistical analysis for swine diaphragm CRA baseline force

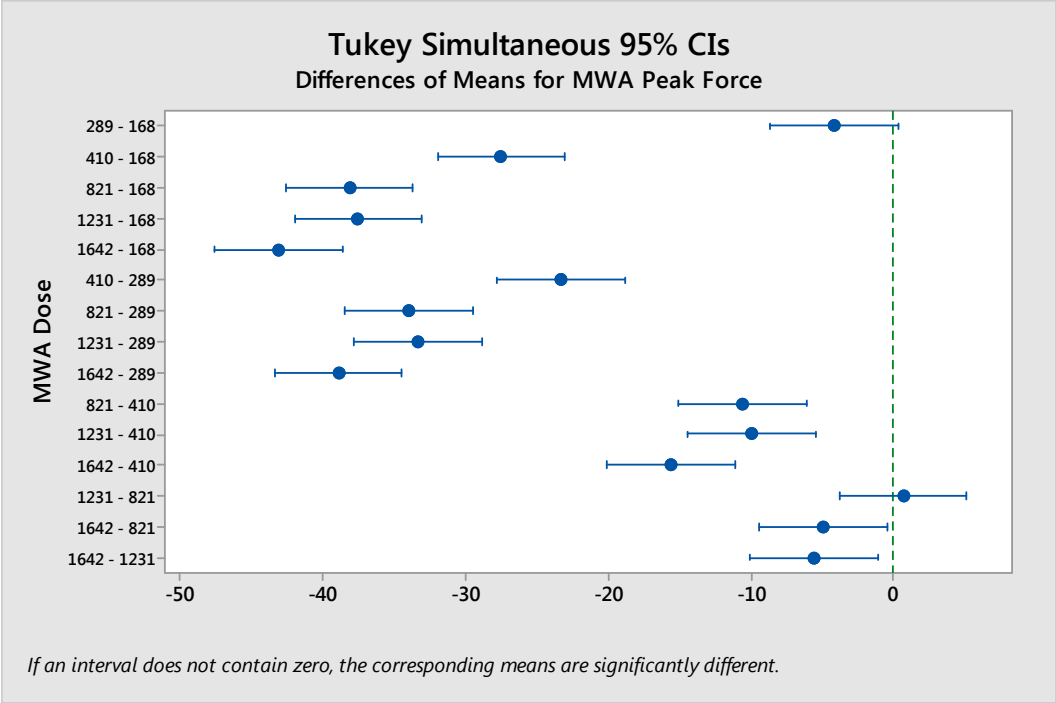

Figure 166: Statistical analysis for swine diaphragm MWA peak force

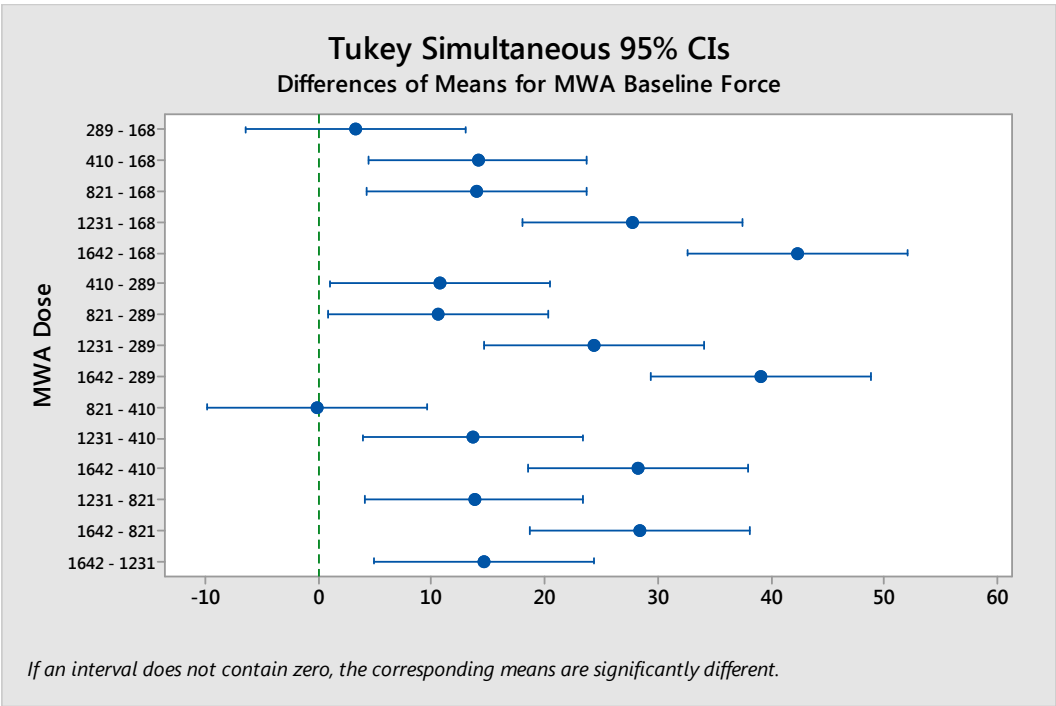

Figure 167: Statistical analysis for swine diaphragm MWA baseline force

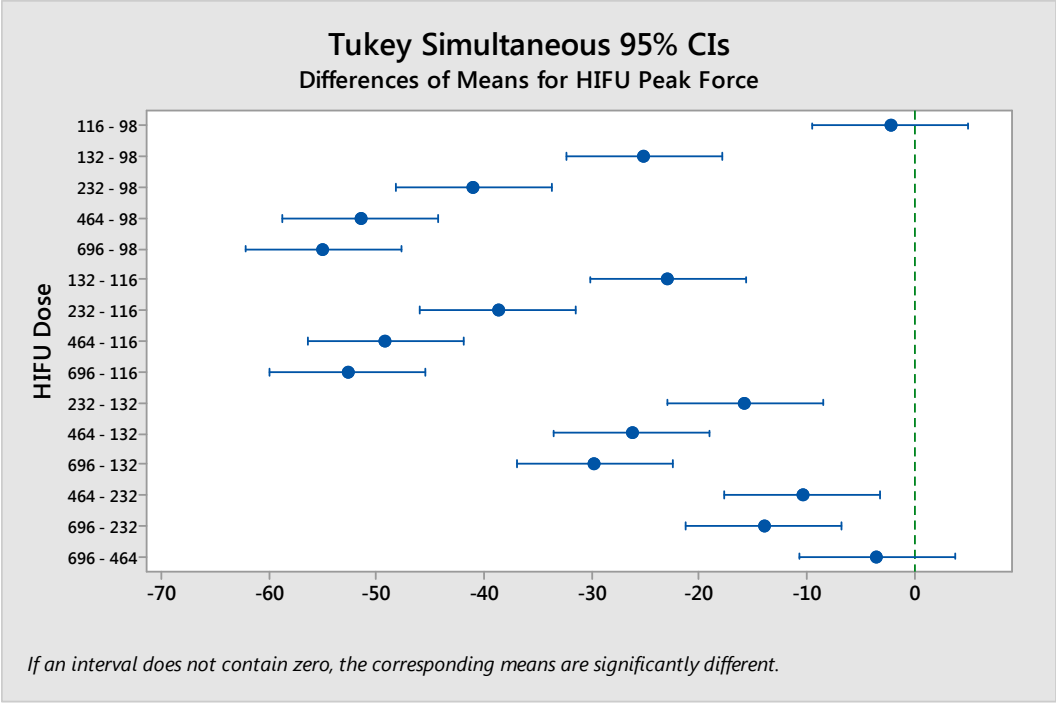

Figure 168: Statistical analysis for swine diaphragm HIFU peak force

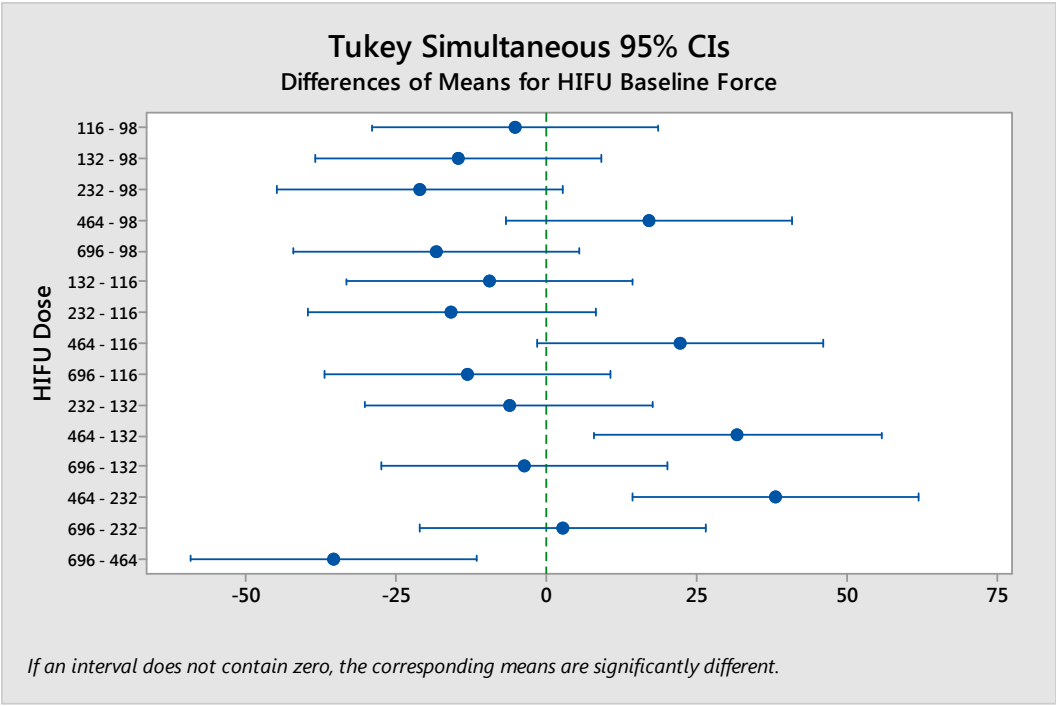

Figure 169: Statistical analysis for swine diaphragm HIFU baseline force

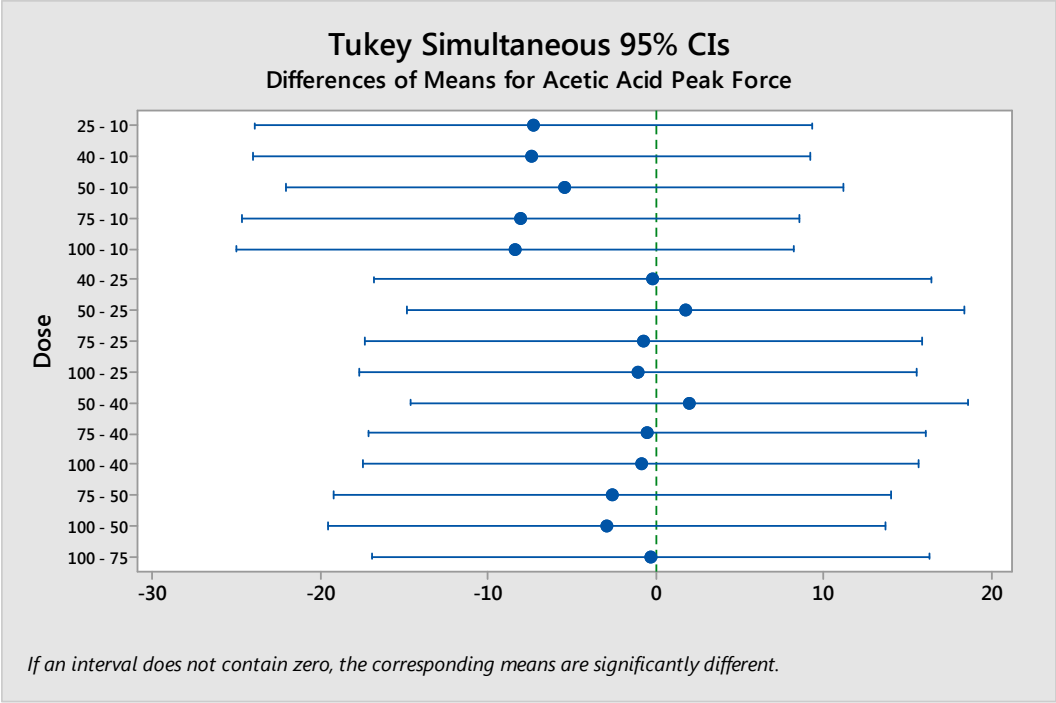

Figure 170: Statistical analysis for swine diaphragm acetic acid peak force

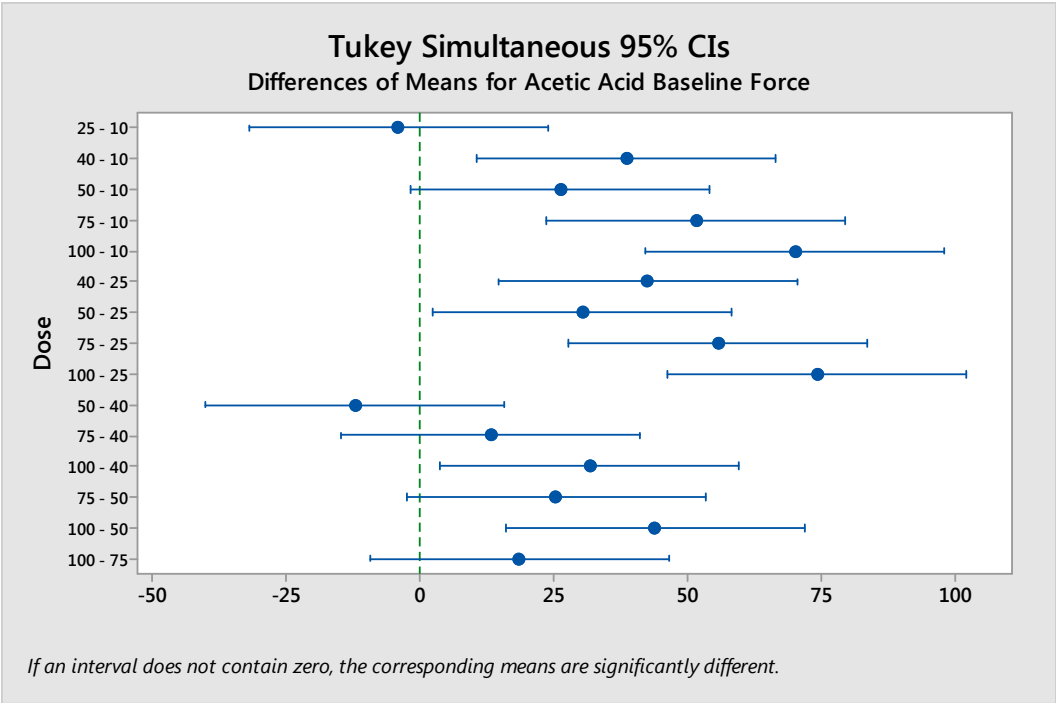

Figure 171: Statistical analysis for swine diaphragm acetic acid baseline force

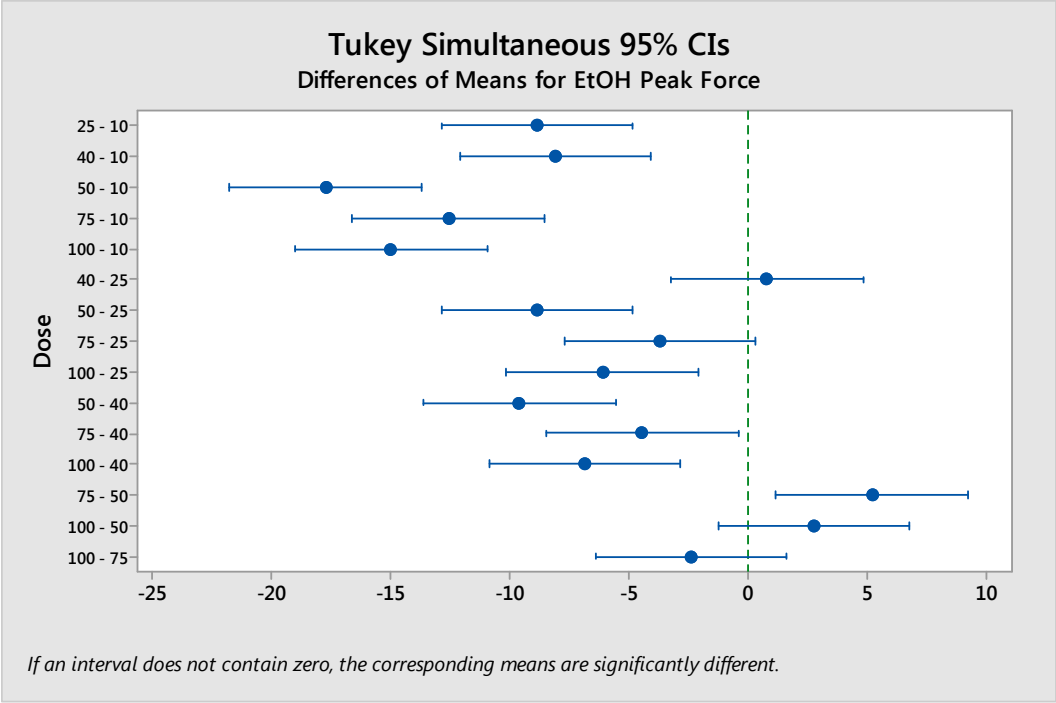

Figure 172: Statistical analysis for swine diaphragm ethanol peak force

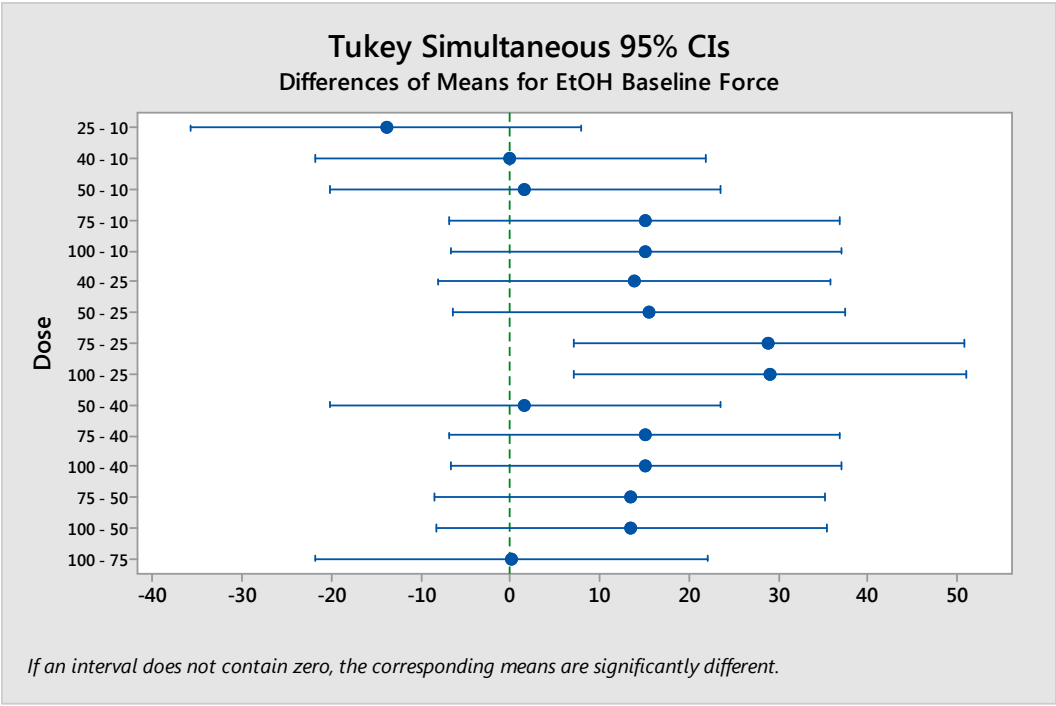

Figure 173: Statistical analysis for swine diaphragm ethanol baseline force

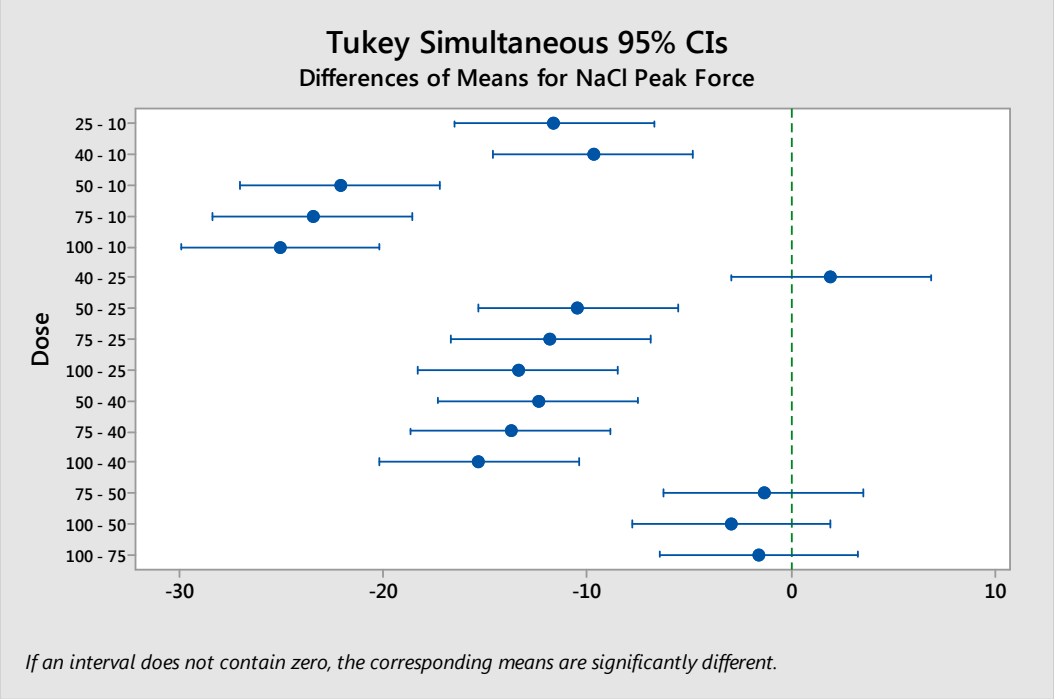

Figure 174: Statistical analysis for swine diaphragm hypertonic sodium chloride peak force

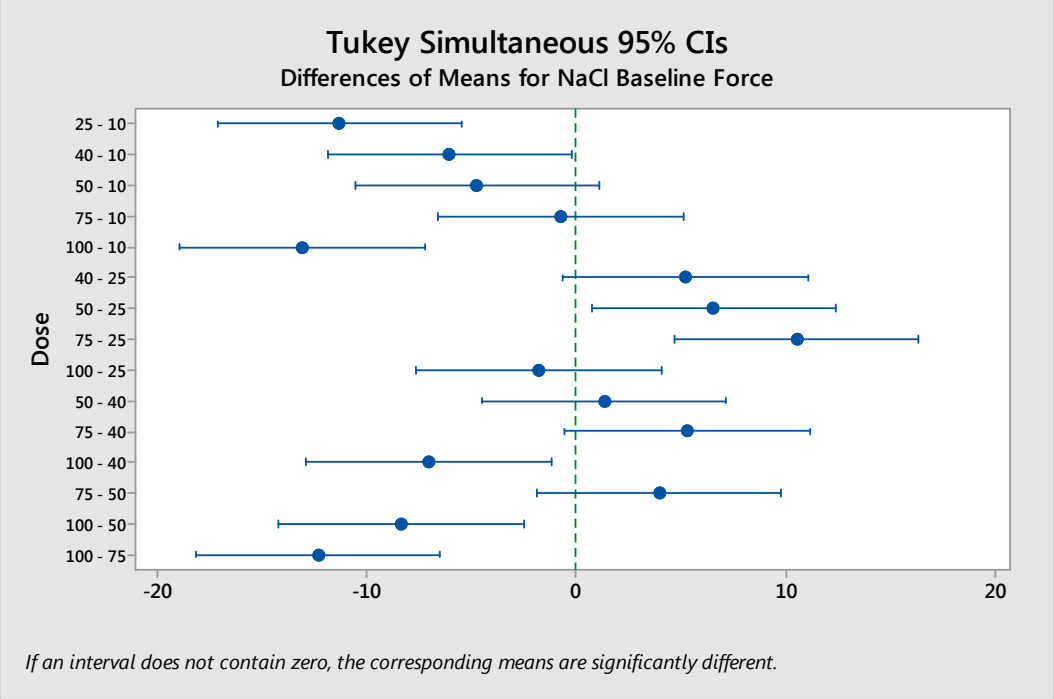

Figure 175: Statistical analysis for swine diaphragm hypertonic sodium chloride baseline force

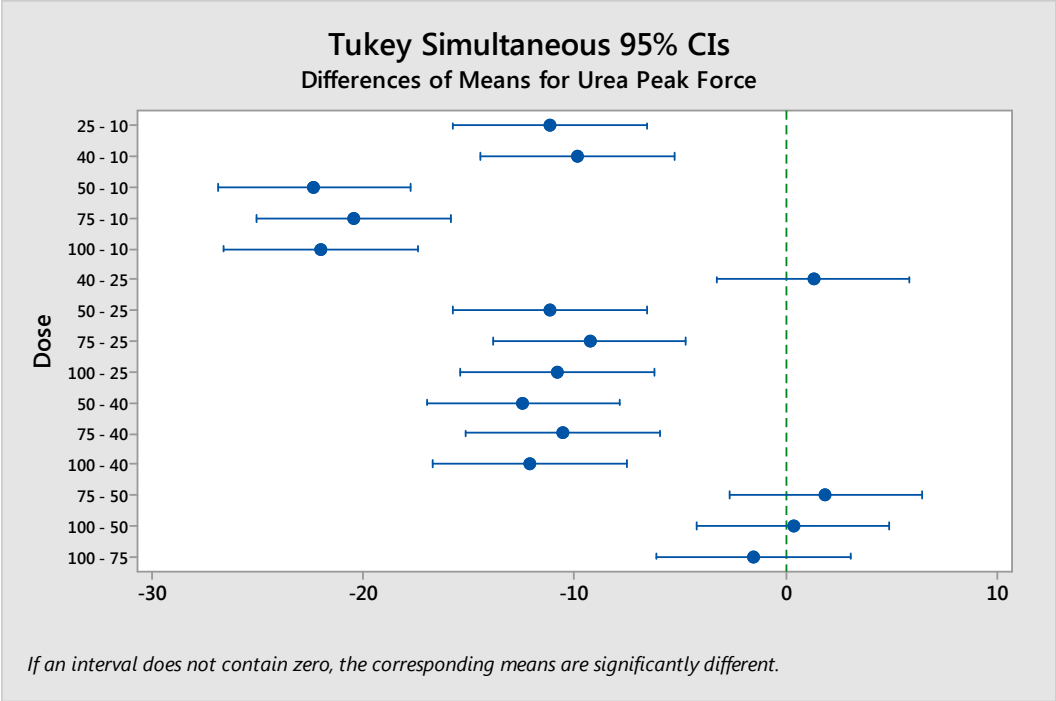

Figure 176: Statistical analysis for swine diaphragm urea peak force

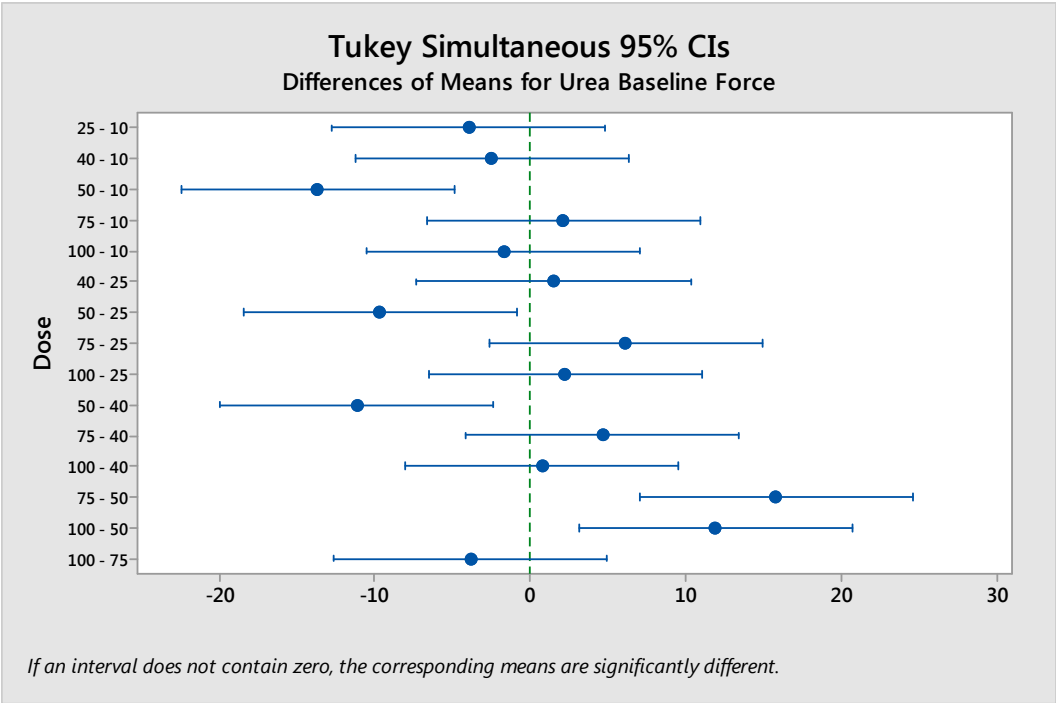

Figure 177: Statistical analysis for swine diaphragm urea baseline force

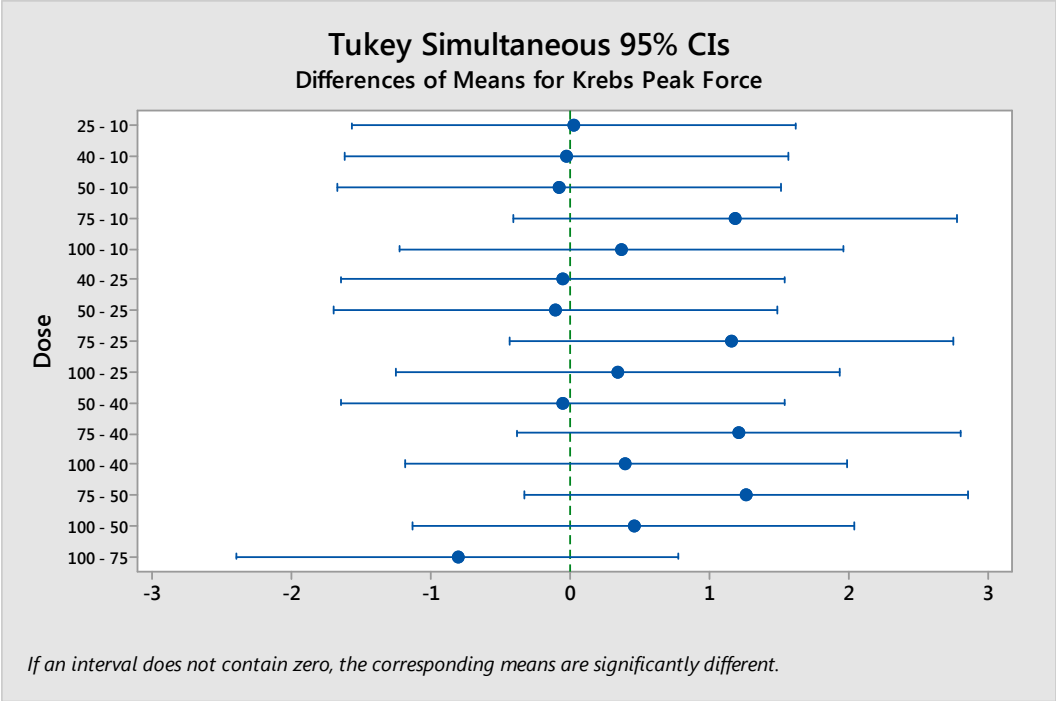

Figure 178: Statistical analysis for swine diaphragm Krebs injection peak force

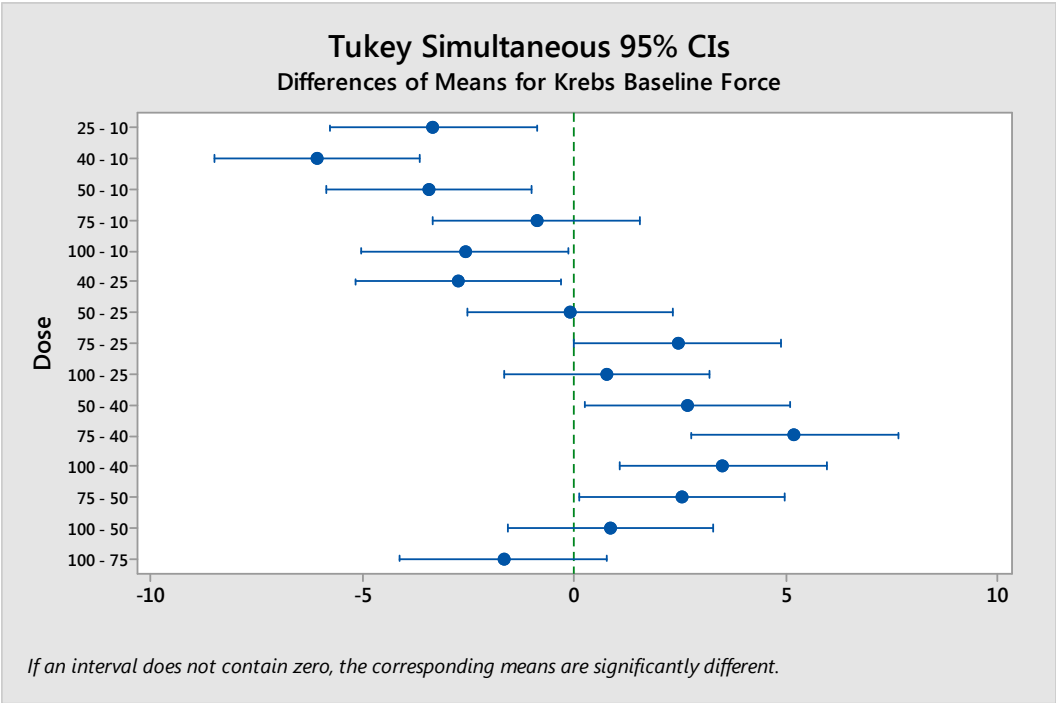

Figure 179: Statistical analysis for swine diaphragm Krebs injection baseline force

Appendix 4: Statistical Results of Swine Esophagus

Introduction: The following graphs/figures/tables/illustrations are supplementary information for swine esophagus muscle bundles that was not included in the individual chapters. Hence, this information is included in this appendix to allow better understanding of the results and for completeness.

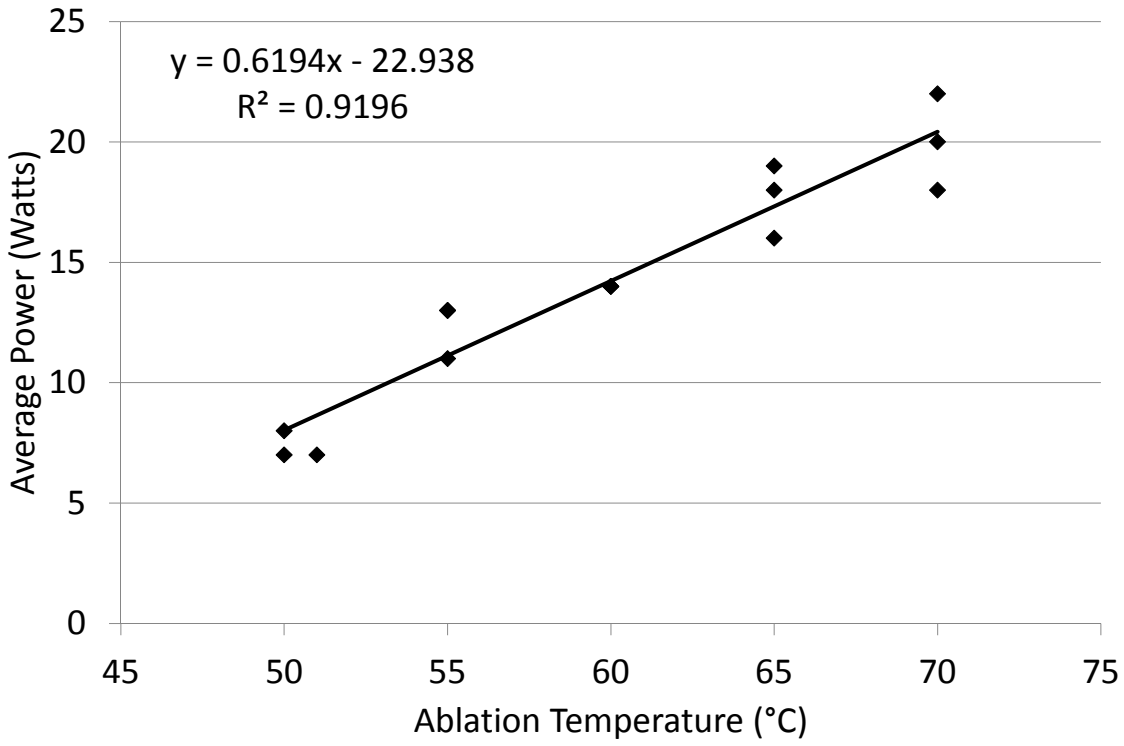

Figure 180: Relationship between average power and catheter tip ablation temperature for all experimental runs of RF ablation on swine esophagus

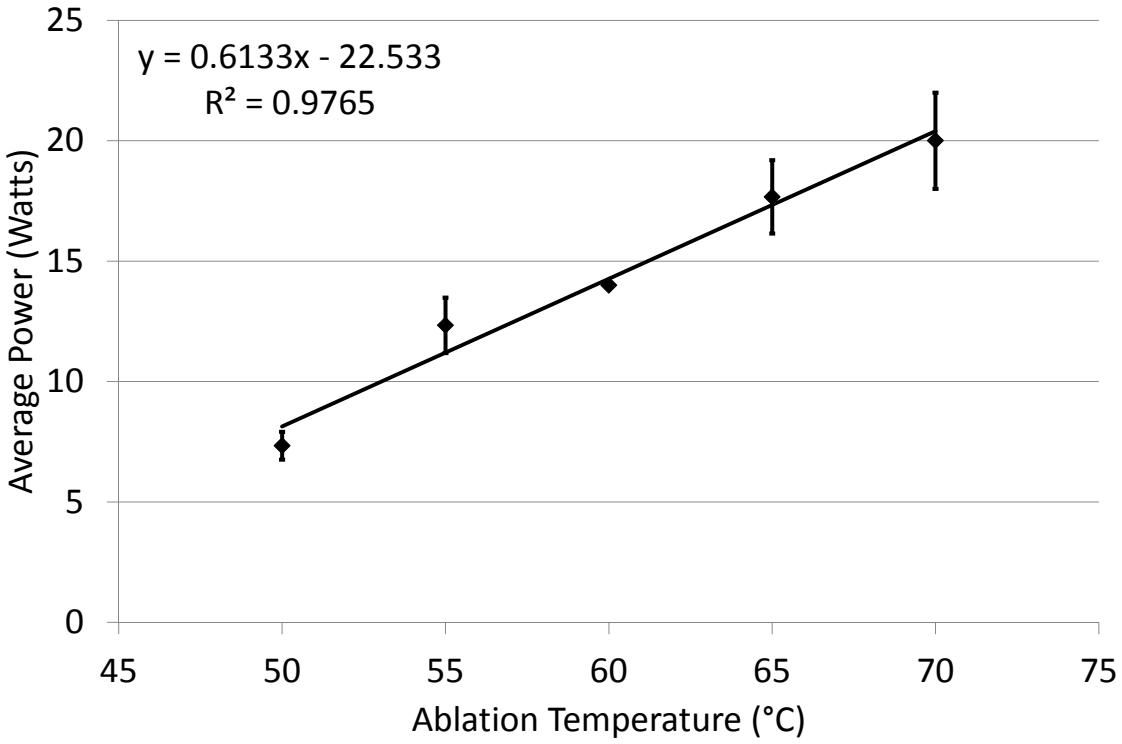

Figure 181: Relationship between average power and catheter tip ablation temperature for all experimental runs of RF ablation on swine esophagus

Ablation Temperature (°C)	Average Power (W, μ±σ)	Ablation Duration (s)	Energy, E = W×s (J, μ±σ)
50	7.33 ± 0.58	60	440 ± 35
55	12.33 ± 1.15	60	740 ± 69
60	14.00 ± 0.00	60	840 ± 0
65	17.67 ± 1.53	60	1060 ± 92
70	20.00 ± 2.00	60	1200 ± 120

Table 24: Dose table for RFA, showing the catheter tip ablation temperature, average power, ablation duration, and energy during RFA of swine esophagus

Average Power (W)	Ablation Duration (s)	Energy (J)
3.76	60	226
5.30	60	318
8.77	60	526
8.77	120	1052
8.77	180	1579
8.77	240	2105

Table 25: Dose table for MWA of swine esophagus, showing average power, duration, and energy

Average Power (W)	Ablation Duration (s)	Energy (J)
57	4	228
57	6	342
57	8	456
57	10	570
57	12	684

Table 26: Dose table for HIFU ablations of swine esophagus, showing average power, duration, and energy

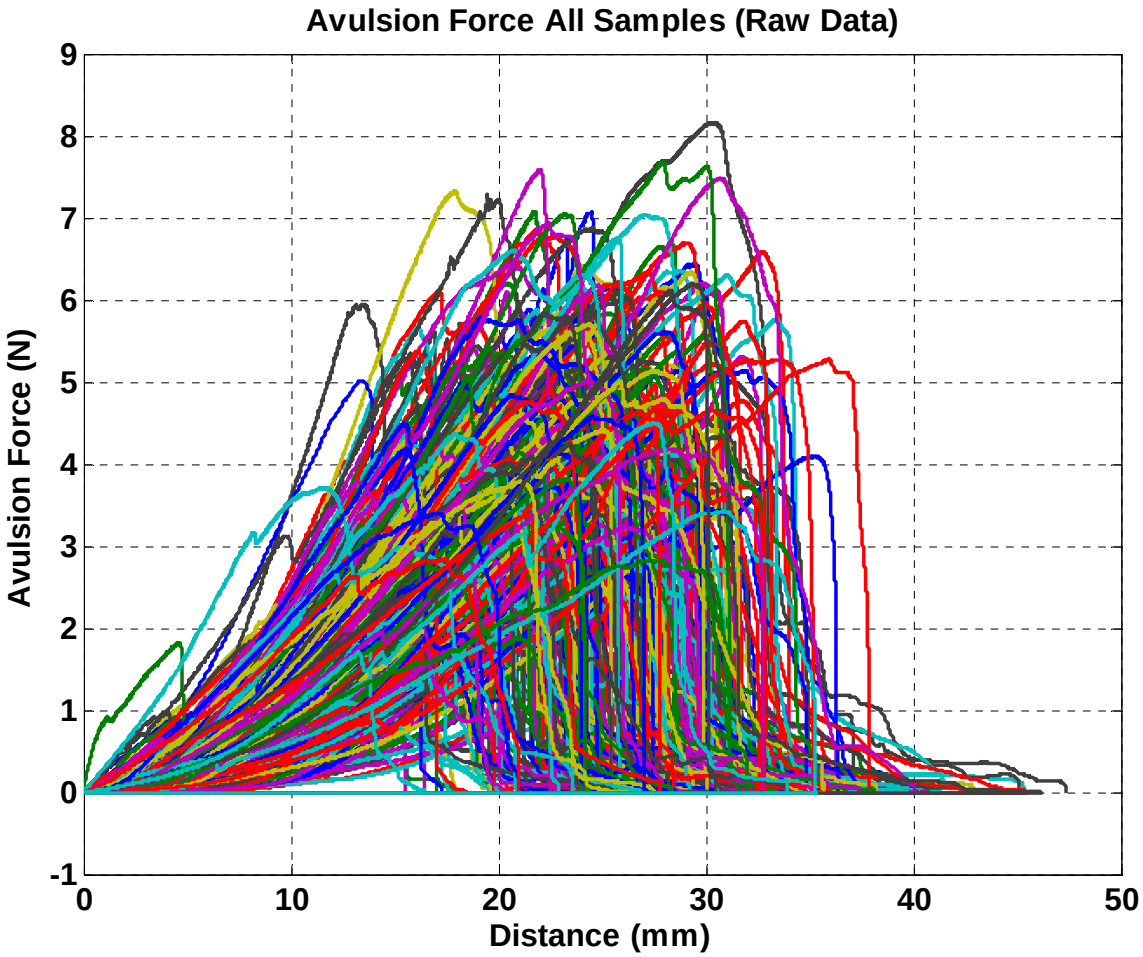

Figure 182: Raw data of force versus stretch of swine esophagus control muscle bundles

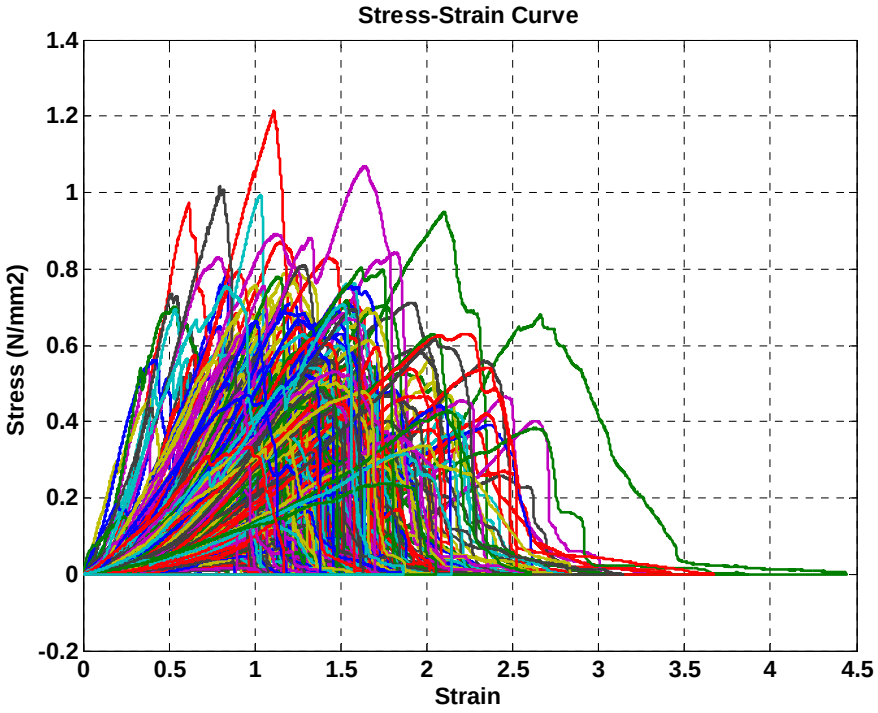

Figure 183: Stress-strain curve of swine esophagus control muscle bundles

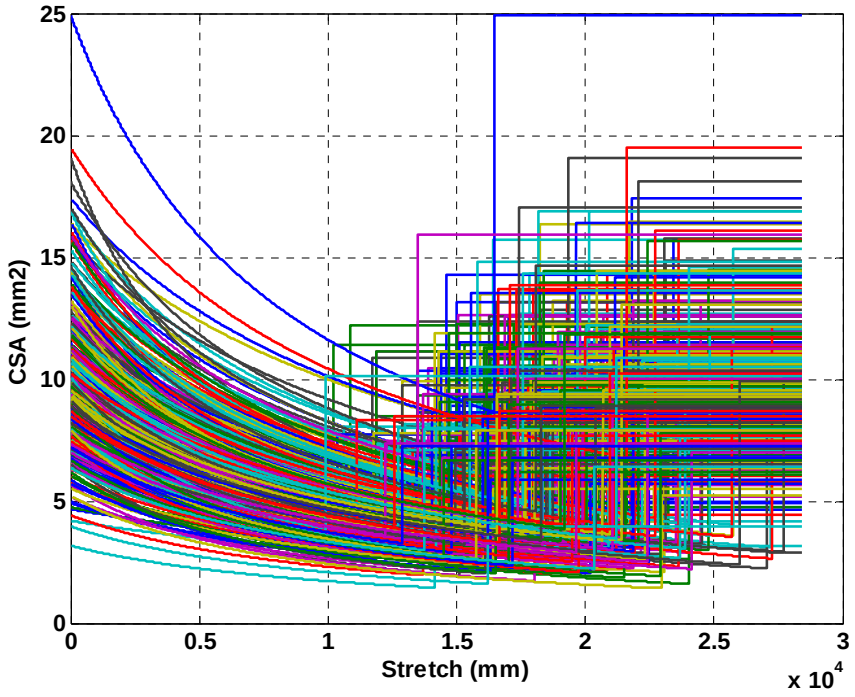

Figure 184: Change in CSA of muscle bundles as a function of stretch

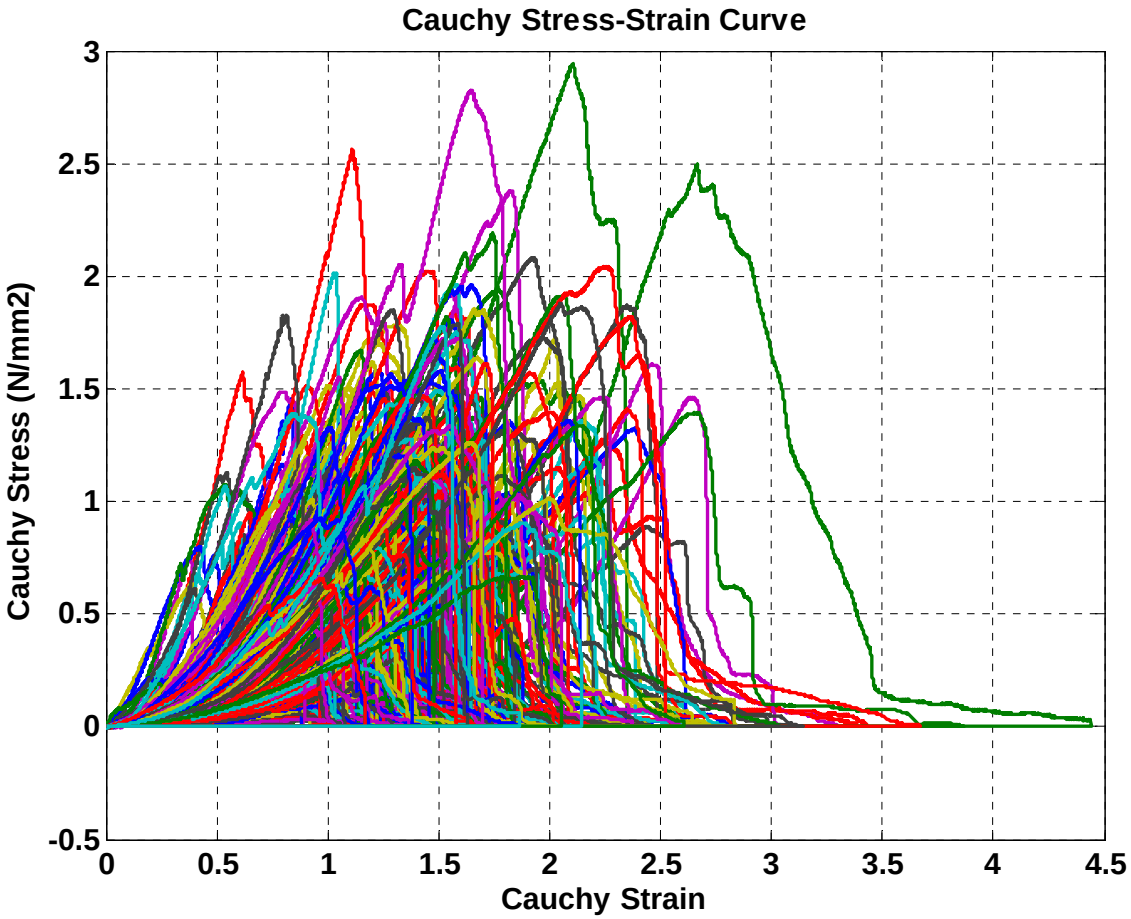

Figure 185: Cauchy's stress-strain curve for swine esophagus muscle bundles

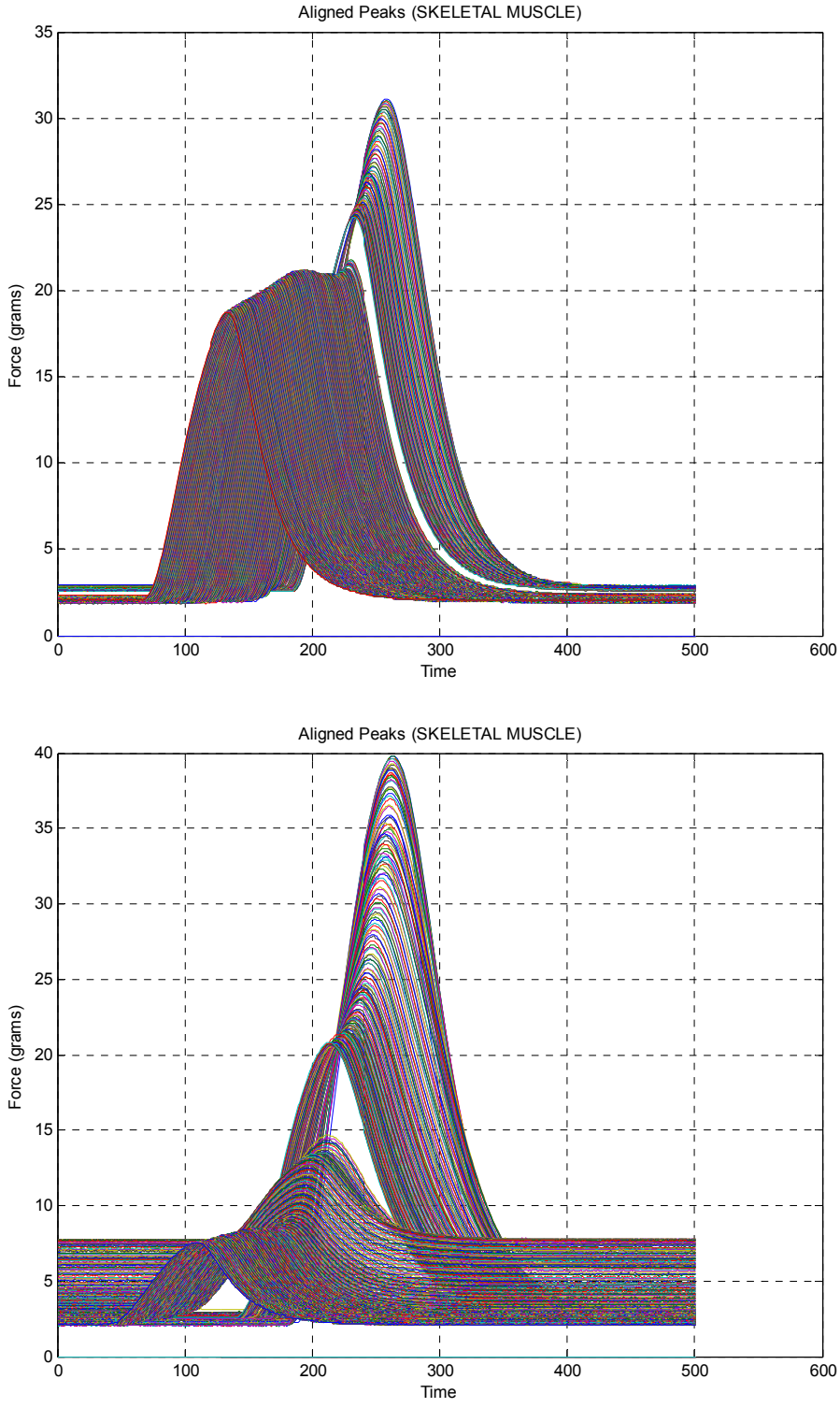

Figure 186: Swine esophagus change in peak force profile after RF ablation
A representative example showing change in peak force profile following low RF dose (55 °C, top graph) and high RF dose (65 °C, bottom graph).

All Samples	Avulsion Force (N/mm^2)	Elastic Modulus (N/mm^2)	Avulsion Strain ($\Delta l/L$)	Total Strain ($\Delta l/L$)	Avulsion Energy (mJ/mm^3)	Total Energy (mJ/mm^3)
Controls (n=347)	0.47 ± 0.17	0.70 ± 0.40	1.34 ± 0.40	1.75 ± 0.57	138.64 ± 66.75	178.70 ± 84.37
RF (n=32)	0.58 ± 0.17	0.89 ± 0.29	1.15 ± 0.24	1.60 ± 0.38	152.43 ± 65.35	200.59 ± 77.05
Cryo (n=16)	0.59 ± 0.17	0.67 ± 0.20	1.41 ± 0.27	1.84 ± 0.33	208.80 ± 83.93	260.15 ± 92.35
MWA (n=28)	0.64 ± 0.17	0.80 ± 0.21	1.25 ± 0.28	1.72 ± 0.42	200.03 ± 75.10	253.34 ± 91.46
HIFU (n=16)	0.60 ± 0.18	0.96 ± 0.28	0.99 ± 0.17	1.23 ± 0.30	146.28 ± 50.84	194.71 ± 73.65
AAcid (n=16)	0.67 ± 0.19	1.01 ± 0.39	1.04 ± 0.23	1.55 ± 0.23	169.17 ± 55.62	221.11 ± 59.23
EtOH (n=32)	0.48 ± 0.19	0.71 ± 0.24	1.05 ± 0.18	1.48 ± 0.29	128.45 ± 62.77	177.08 ± 81.59
NaCl (n=16)	0.50 ± 0.13	0.62 ± 0.10	1.26 ± 0.21	1.62 ± 0.36	156.72 ± 63.02	208.47 ± 88.32
Urea (n=32)	0.57 ± 0.26	0.71 ± 0.31	1.31 ± 0.29	1.69 ± 0.32	182.20 ± 89.00	224.28 ± 108.58
Krebs (n=16)	0.60 ± 0.12	0.66 ± 0.19	1.45 ± 0.30	1.93 ± 0.36	211.46 ± 62.86	279.51 ± 79.39

Table 27: Biomechanical parameters of swine esophagus muscle bundles.

All Samples	% Diff Avulsion Force	% Diff Elastic Modulus	% Diff Avulsion Strain	% Diff Total Strain	% Diff Avulsion Energy	% Diff Total Energy
RF (n=32)	+23.48 p<0.005	+28.02 p=0.0067	-14.26 p=0.0087	-8.56 p=0.1428	+9.95 p=0.2631	+12.25 p=0.1582
Cryo (n=16)	+26.30 p=0.0052	-4.07 p=0.7756	+5.49 p=0.4701	+5.18 p=0.5248	+50.61 p<0.005	+45.58 p<0.005
MWA (n=28)	+36.82 p<0.005	+14.40 p=0.1847	-6.76 p=0.2436	-1.42 p=0.8198	+44.29 p<0.005	+41.77 p<0.005
HIFU (n=15)	+28.54 p=0.0034	+37.18 p=0.0125	-26.16 p<0.005	-29.85 p<0.005	+5.51 p=0.6617	+8.96 p=0.4704
AAcid (n=16)	+42.29 p<0.005	+44.49 p=0.0023	-22.15 p=0.0037	-11.26 p=0.1659	+22.02 p=0.0726	+23.73 p=0.0477
EtOH (n=32)	+2.79 p=0.6826	+2.13 p=0.8344	-21.37 p<0.005	-15.22 p=0.0088	-7.34 p=0.4073	-0.91 p=0.9166
NaCl (n=16)	+7.21 p=0.4381	-10.51 p=0.4602	-5.95 p=0.4327	-7.28 p=0.3728	+13.05 p=0.2889	+16.66 p=0.1694
Urea (n=32)	+20.54 p=0.0041	+1.12 p=0.9135	-1.74 p=0.7491	-3.21 p=0.5806	+31.42 p<0.005	+25.50 p=0.0046
Krebs (n=16)	+27.21 p=0.0035	-5.89 p=0.6797	+8.28 p=0.2774	+10.16 p=0.2135	+52.53 p<0.005	+56.41 p<0.005
Study Control (n=7)	+20.58 p=0.1395	+14.07 p=0.5138	-13.76 p=0.2294	-11.87 p=0.3335	+9.69 p=0.5969	+12.98 p=0.4690

Table 28: Percent change in biomechanical properties of swine esophagus muscle bundles

Analysis performed on all samples post ablation with different ablative modalities. Values of avulsion force, elastic moduli, strain, and energy are shown along with statistical significance (marked by blue color). A positive value indicates an increase, and negative value a decrease with respect to control swine esophagus muscle bundles (n=347).

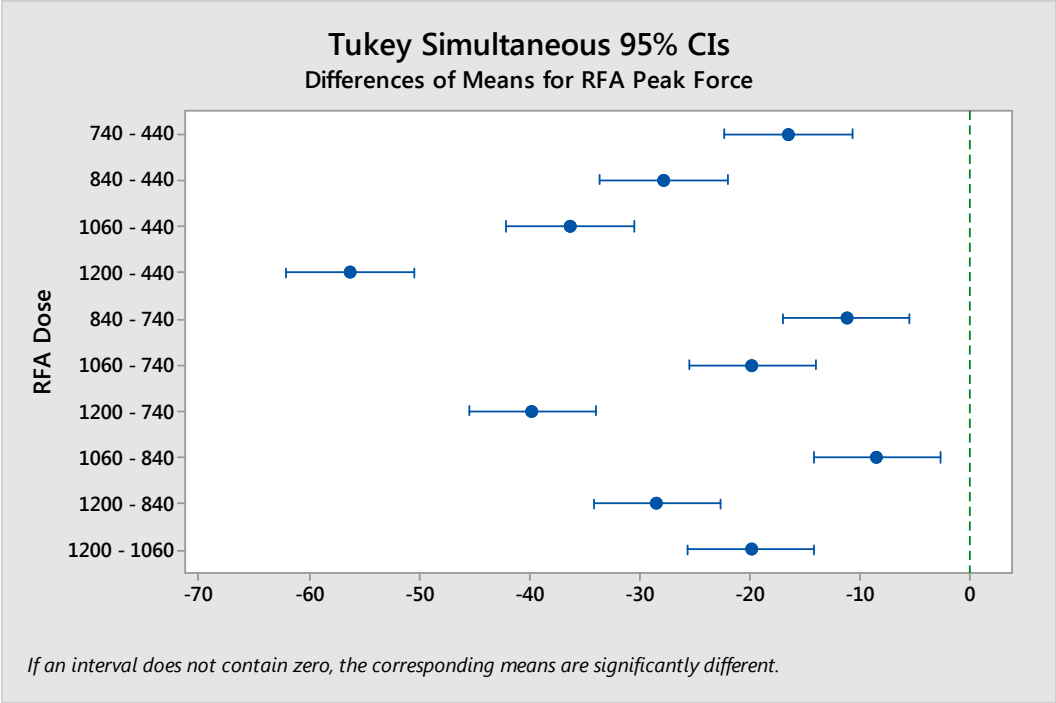

Figure 187: Statistical analysis for swine esophagus RFA peak force

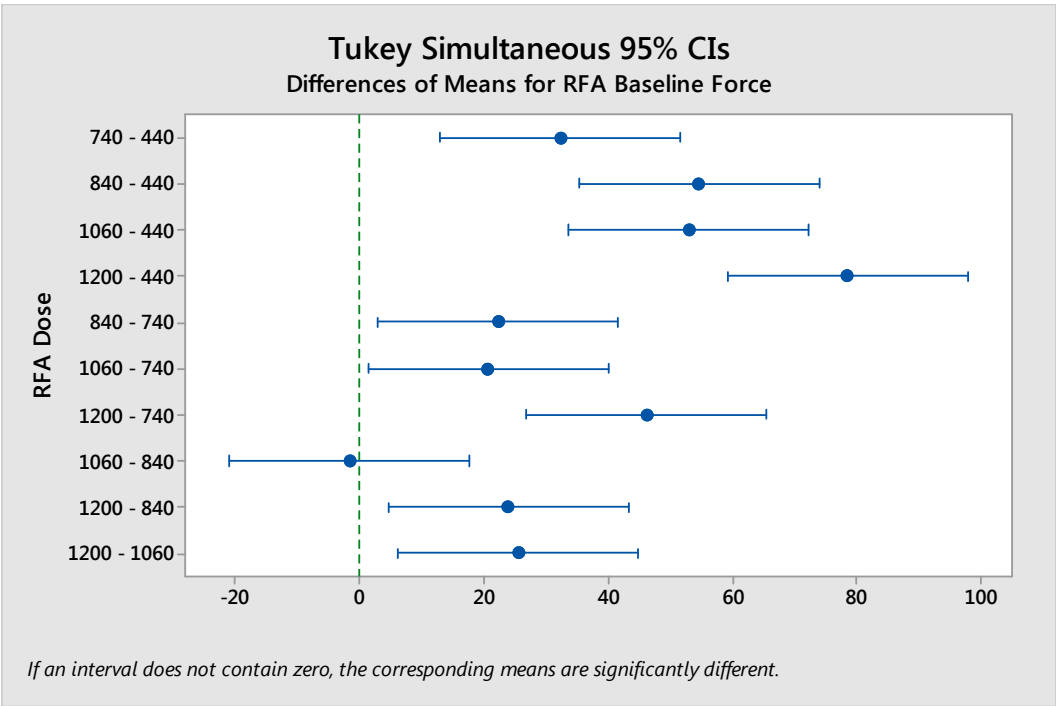

Figure 188: Statistical analysis for swine esophagus RFA baseline force

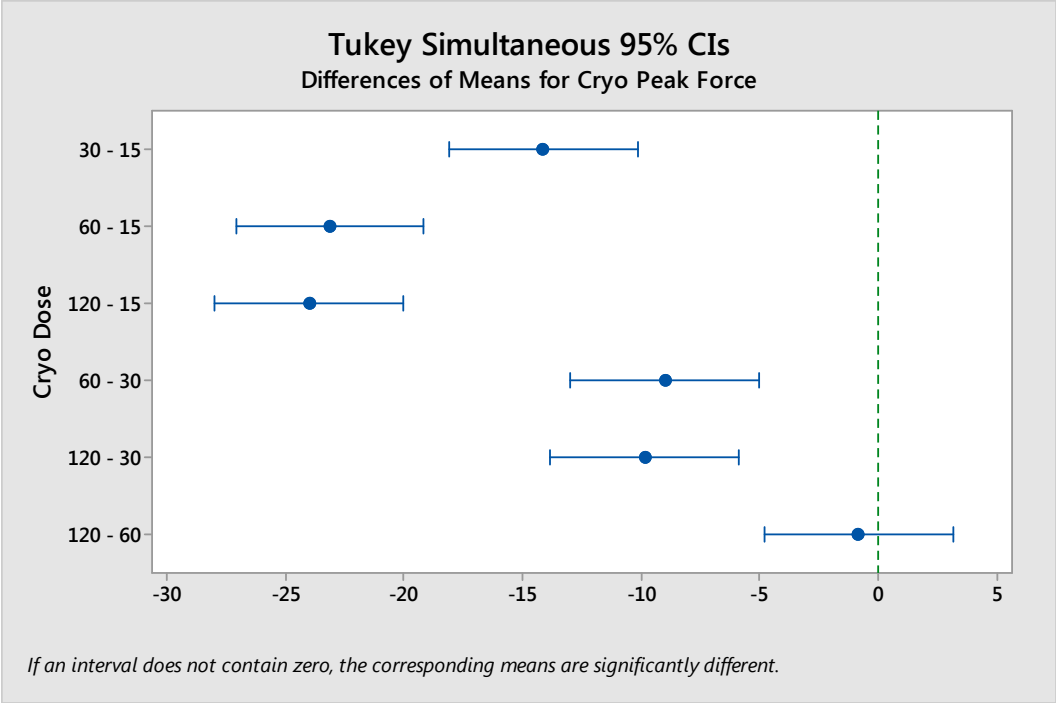

Figure 189: Statistical analysis for swine esophagus CRA peak force

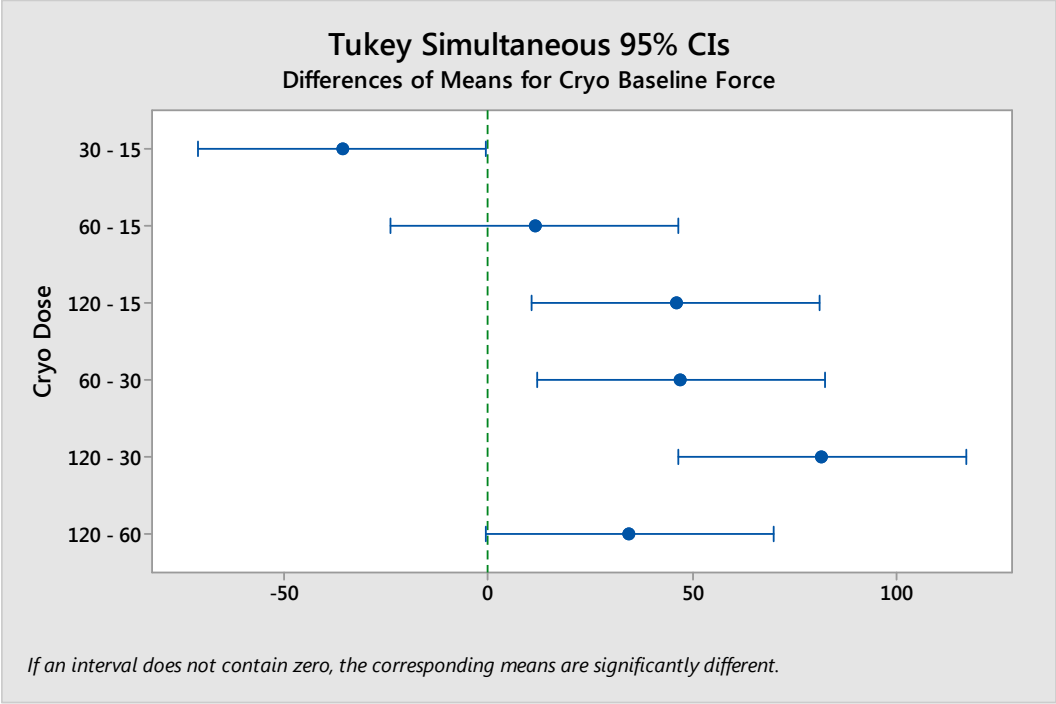

Figure 190: Statistical analysis for swine esophagus CRA baseline force

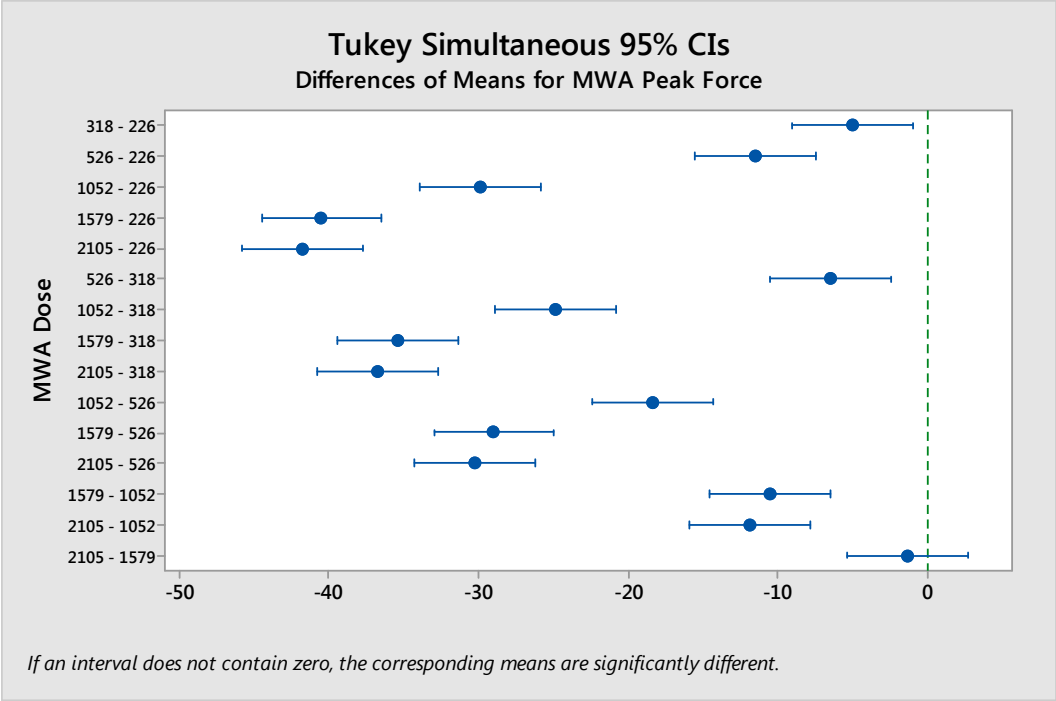

Figure 191: Statistical analysis for swine esophagus MWA peak force

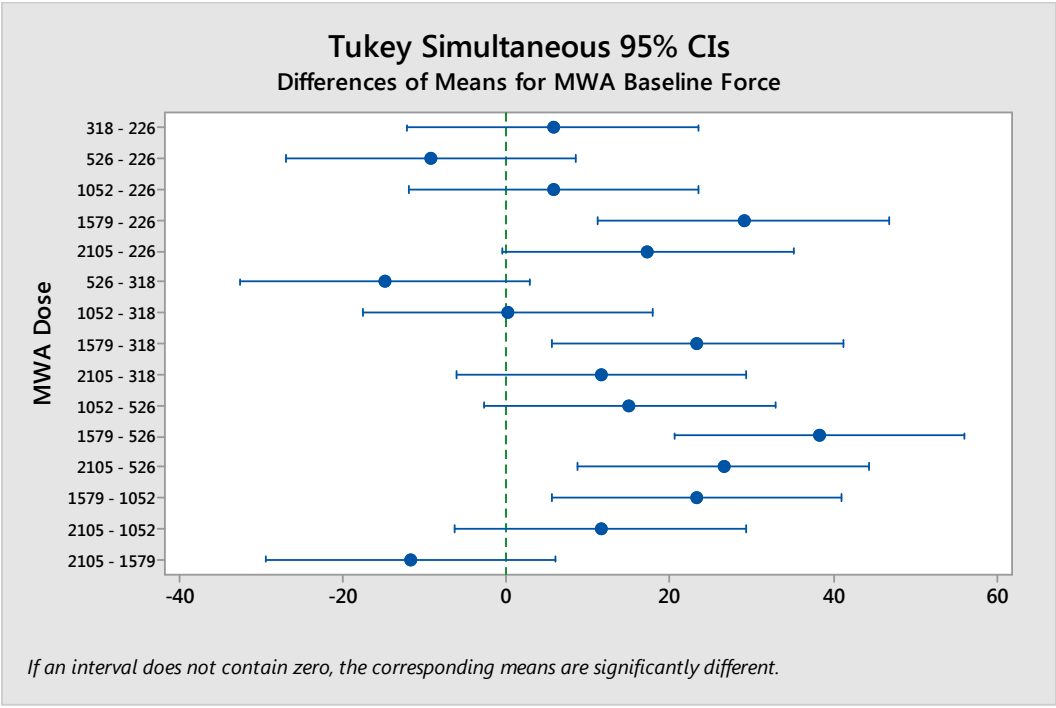

Figure 192: Statistical analysis for swine esophagus MWA baseline force

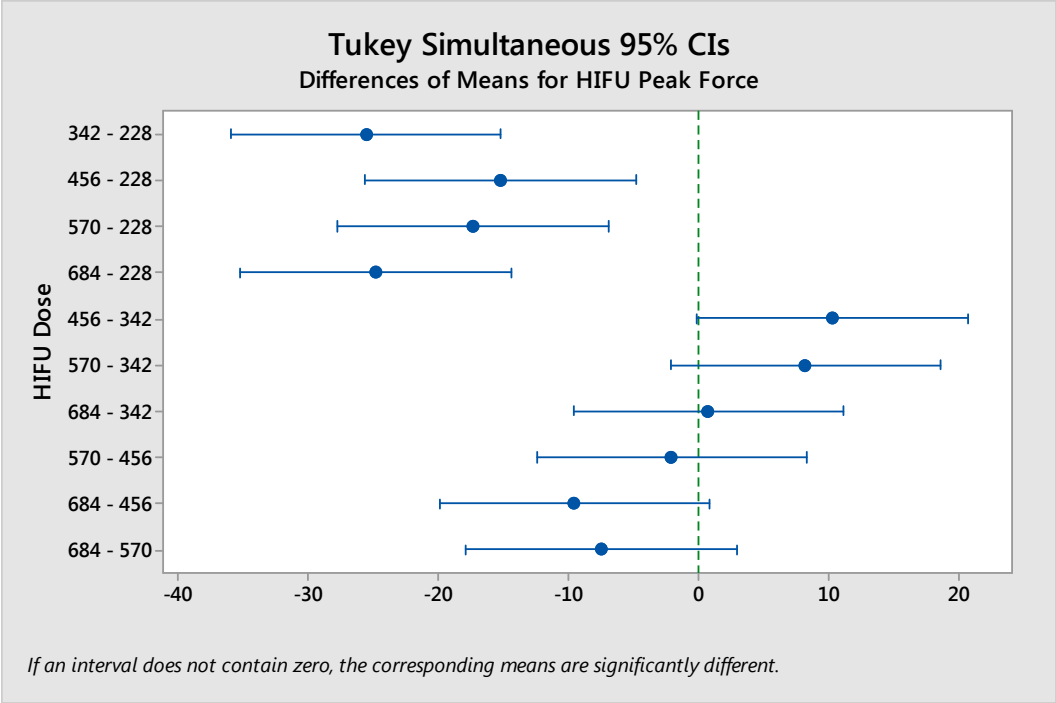

Figure 193: Statistical analysis for swine esophagus HIFU peak force

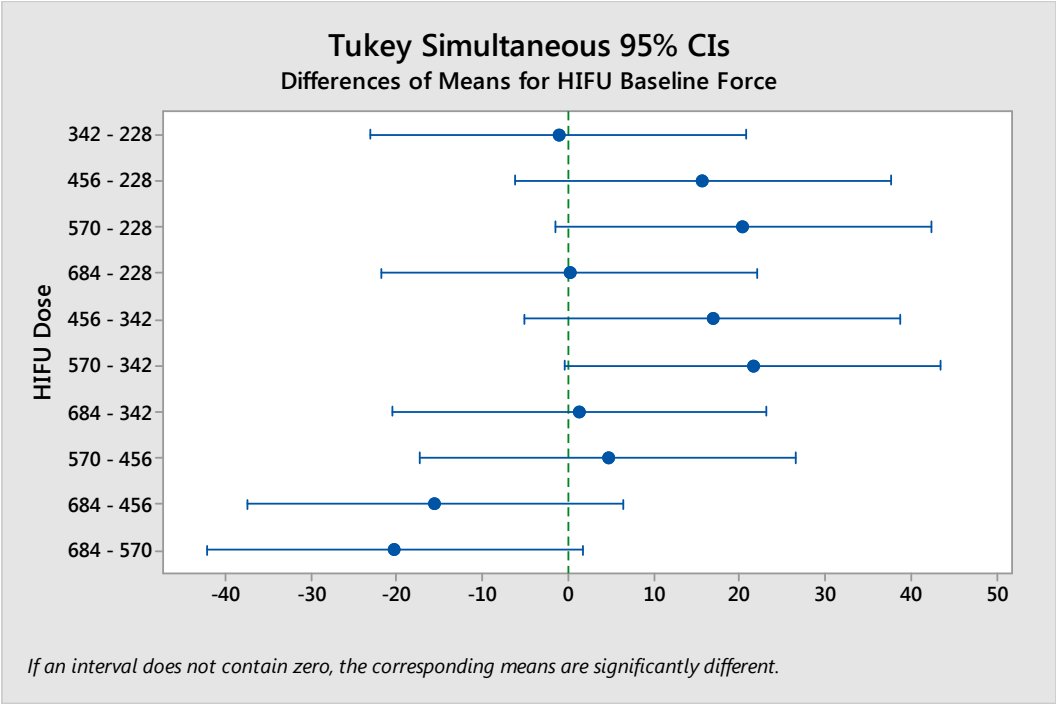

Figure 194: Statistical analysis for swine esophagus HIFU baseline force

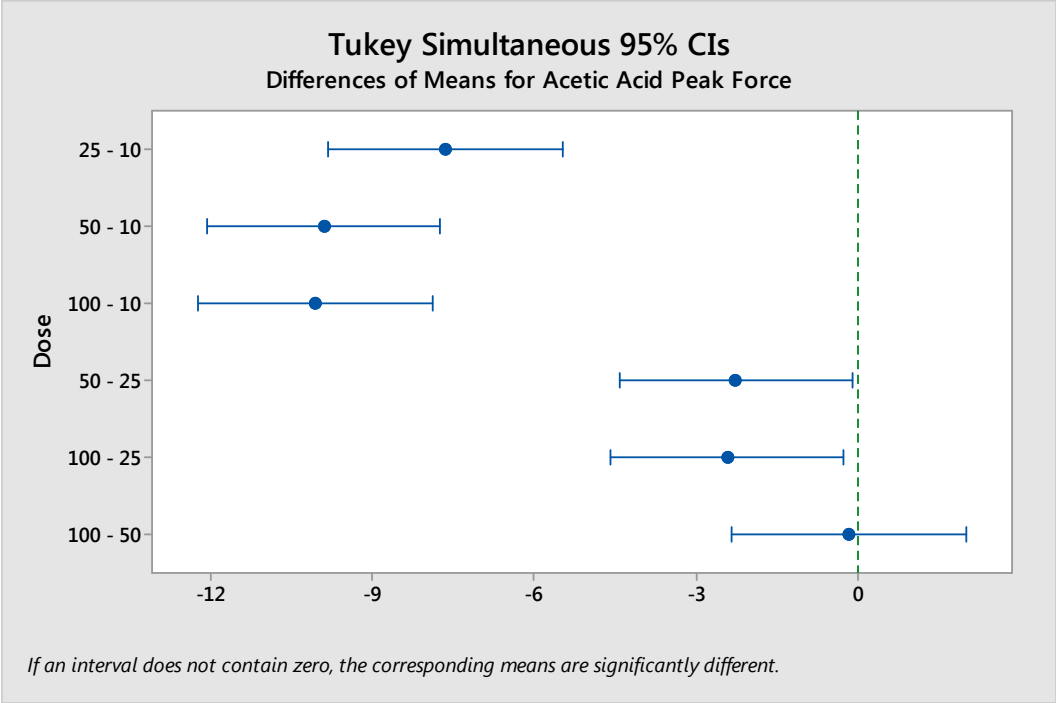

Figure 195: Statistical analysis for swine esophagus acetic acid peak force

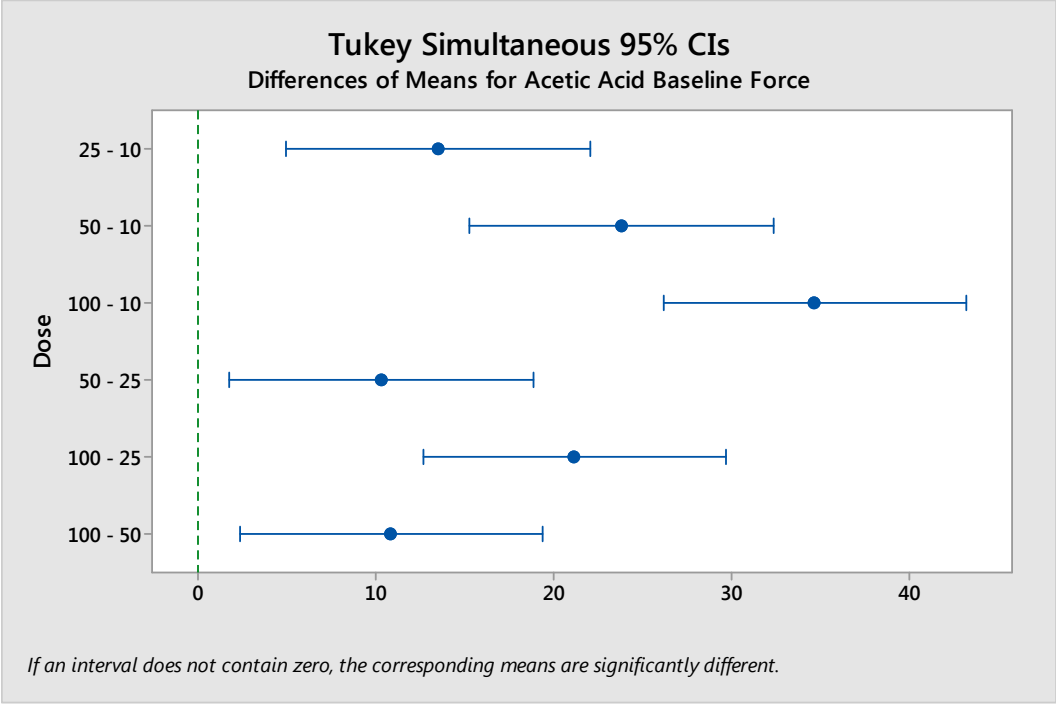

Figure 196: Statistical analysis for swine esophagus acetic acid baseline force

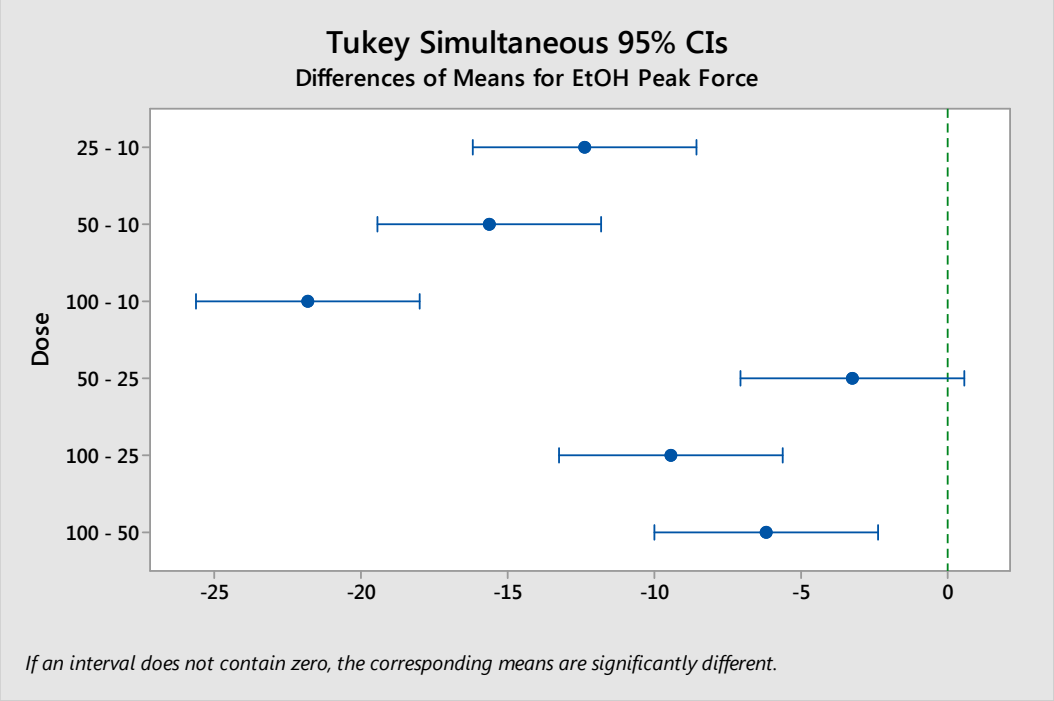

Figure 197: Statistical analysis for swine esophagus ethanol peak force

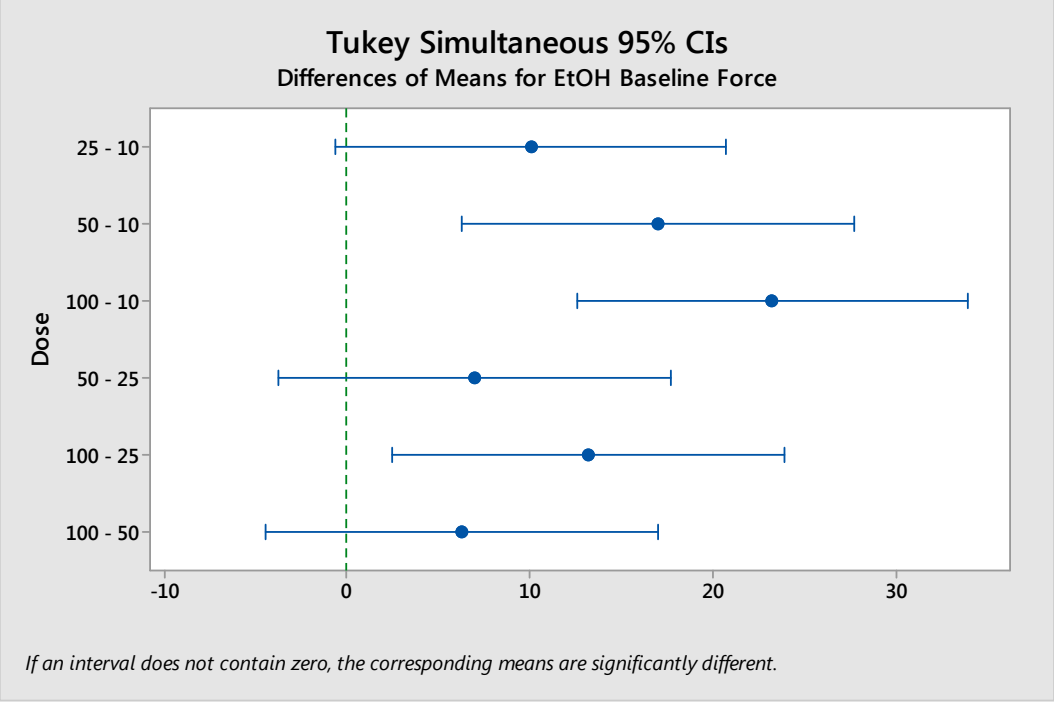

Figure 198: Statistical analysis for swine esophagus ethanol baseline force

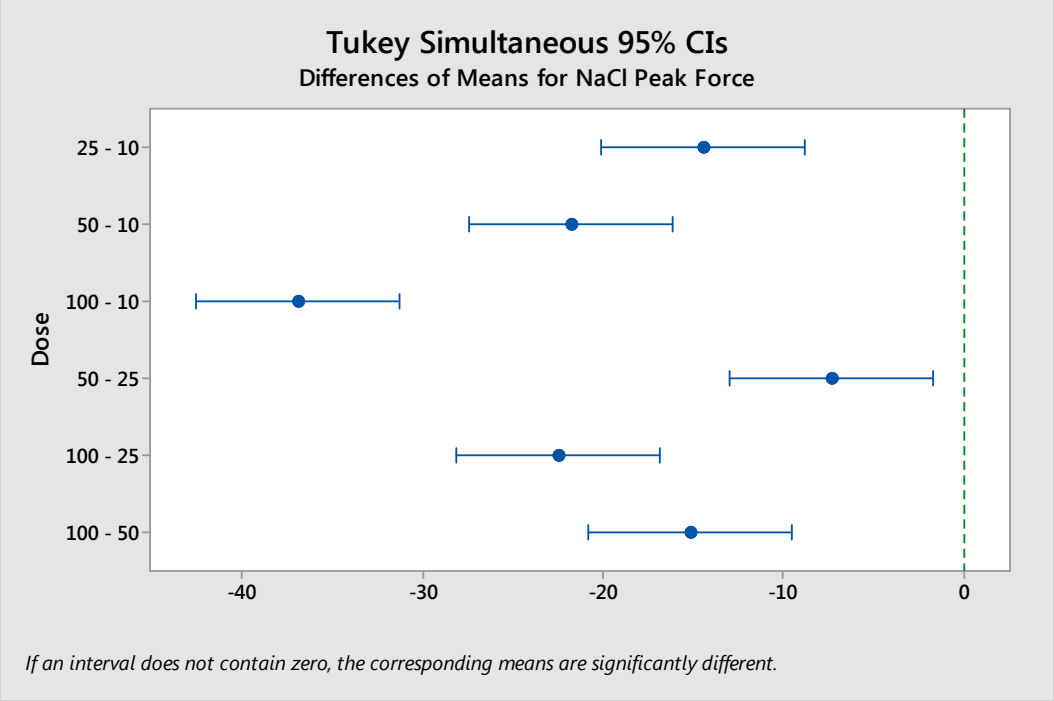

Figure 199: Statistical analysis for swine esophagus hypertonic sodium chloride peak force

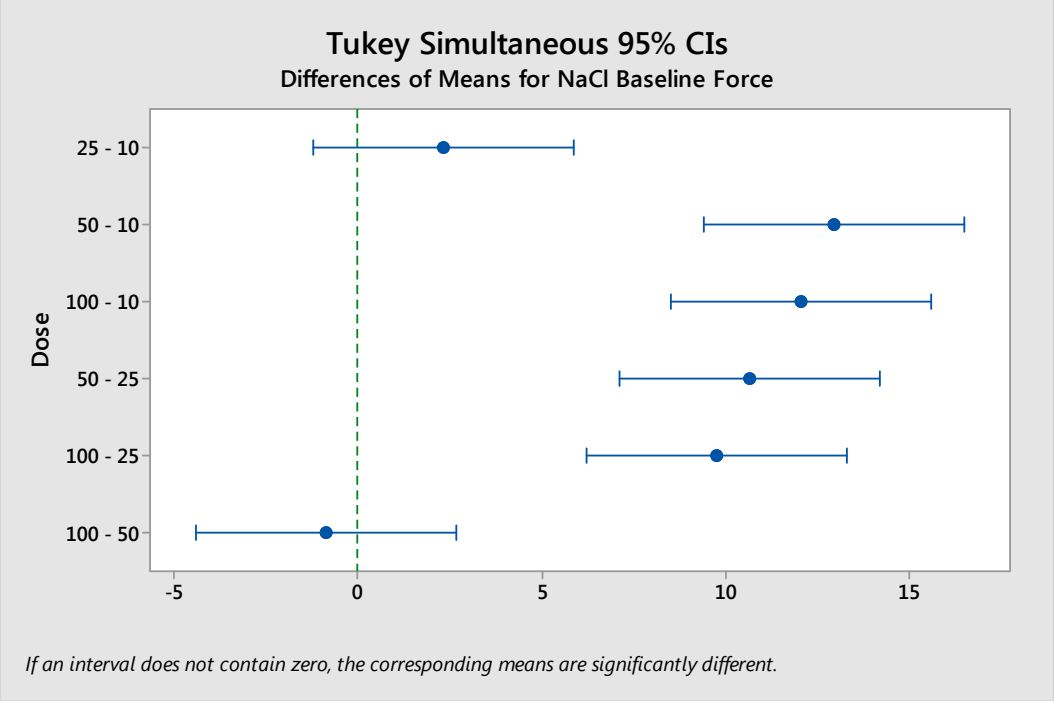

Figure 200: Statistical analysis for swine esophagus hypertonic sodium chloride baseline force

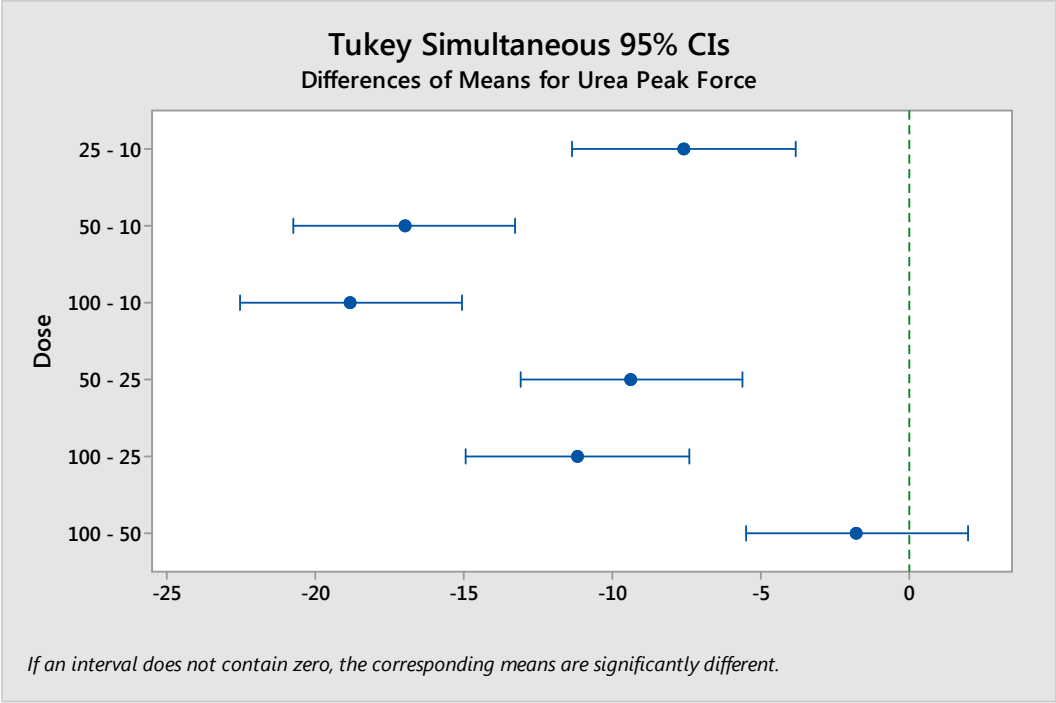

Figure 201: Statistical analysis for swine esophagus urea peak force

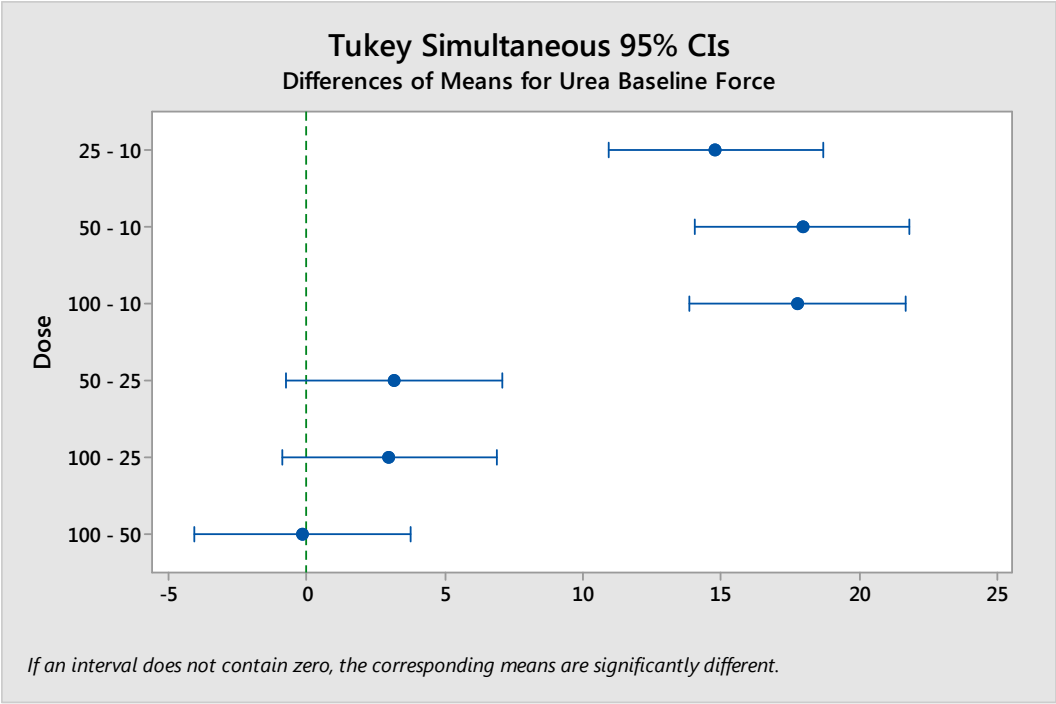

Figure 202: Statistical analysis for swine esophagus urea baseline force

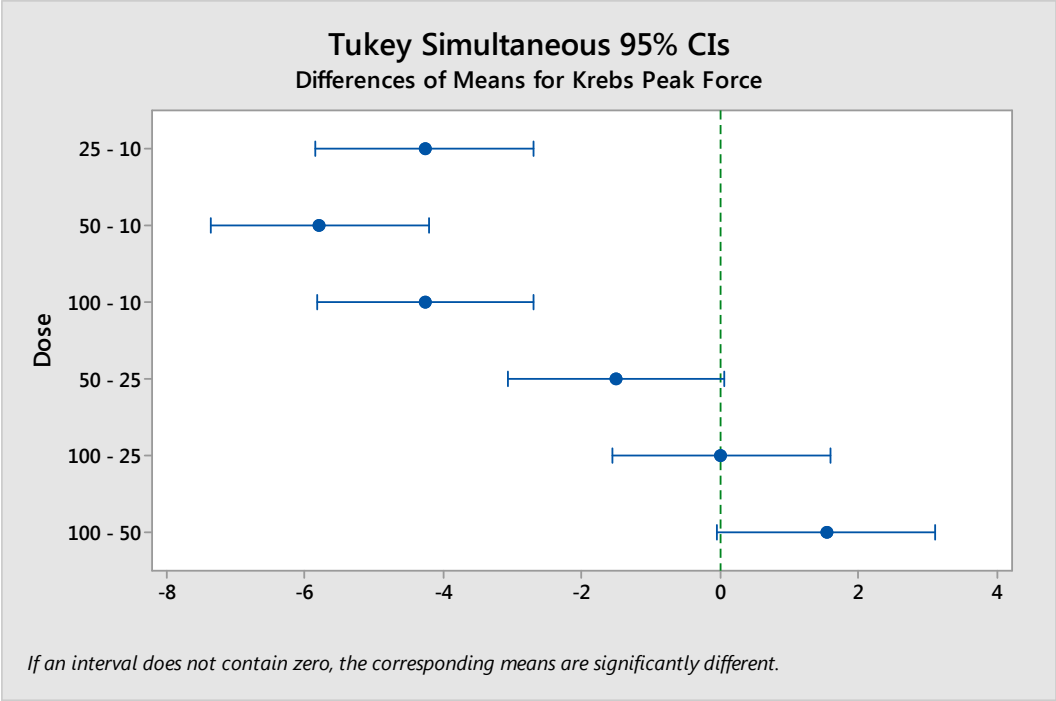

Figure 203: Statistical analysis for swine esophagus Krebs injection peak force

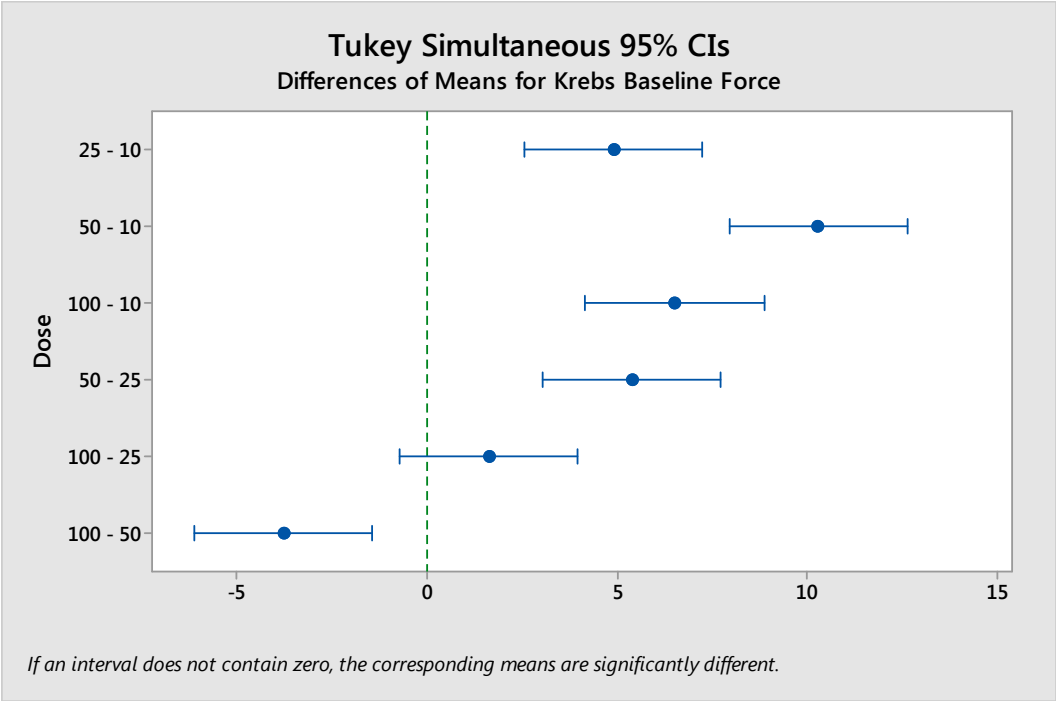

Figure 204: Statistical analysis for swine esophagus Krebs injection baseline force

Appendix 5: Calculation of Tissue Ablated Area in Response to Ablative Modalities

Ashish Singal, Jennifer Chmura, Charles L. Soule, Paul A. Iaizzo

Preface

This article will be submitted to the Journal of Medical Devices (2015).

Introduction

Both thermal and chemical ablative treatments result in tissue necrosis. Although numerous methods exist to assess the amount of tissue necrosis, we performed triphenyltetrazolium chloride (TTC) staining of muscle bundles to calculate the amount of ablated area for a subset of thermal and chemical ablation modalities. ImageJ (freeware image processing and analysis software) was used for analysis.

Methods

Muscle bundles of swine trabeculae and diaphragmatic tissue were ablated as described previously and left in the tissue baths for at least three hours to study post-ablation effects on muscle physiology and recovery. Following completion of the physiological protocol, the muscle bundles were

pictured before performing TTC staining. An example of muscle bundles that were cryoablated is shown in Figure 205. Cryoablations were performed towards the center of the muscle bundle and necrosed/ablated tissue can be seen in each sample. In order to assess tissue viability, small subsets of muscle bundles were stained with 1% TTC in Trizma buffer (7.4 pH) at 37 °C for 2 hours post completion of the physiological assessment protocol. As shown in Figure 206, each muscle bundle was completely soaked in individual tubular compartments containing TTC solution and then immersed in a water bath maintained at constant temperature. TTC works by using a dehydrogenase enzyme that converts tetrazolium salt to a formazan pigment within viable tissue (red formazan derivative). Thus, cells with preserved enzymatic activity undergo a cytochemical color change to red-maroon. Whereas, cells that lack the enzymatic activity (dead and necrotic) are unable to metabolize the tetrazolium salt, do not stain, and turn pale or white. This stain has been validated and widely used previously for identification of infarct regions in variety of models [1].

Figure 207 shows the muscle bundles after 2 hours of TTC staining. The distinct color change demarcates the healthy and ablated region of the muscle bundles. The sutures on both ends of the muscle bundle were cut and thin slices of the left over cylindrical muscle bundle were prepared using a #11 surgical blade. Slices were made as thin as possible along the entire length of the muscle bundle with approximately 3 mm inter-slice distance. Each slice was placed sequentially

from top to bottom on gauze with the cross-sectional surface visible (Figure 208). Slices were then photographed with a camera, which were then used for analysis using the ImageJ software. Figure 209 and Figure 210 are examples of swine diaphragm muscle bundles injected with Krebs-buffer solution. As expected, no visible necrotic area is visible upon TTC staining. These muscle bundles (Krebs injection) were used as controls.

Data Analysis

The cross-sectional images were analyzed using ImageJ software to calculate the ablated area as shown in Figure 211. Two measurements were made for each cross-sectional surface of every sample: (1) the total circumferential surface area and, (2) the necrotic tissue area. The surface area was calculated by selecting the circumferential surface of the muscle bundle using the “Freehand selections” tool in ImageJ, thus measuring the area within that selection. The necrotic area on the muscle bundle cross-sectional surface was identified by the distinct pale-white color. TTC staining distinguished viable tissue as red while necrotic tissue is pale-white. Only areas of the distinctive pale-white color were considered necrotic, whereas red colored tissue was considered viable which was not affected by the ablative energy. The necrotic tissue area was measured by selecting the regions of pale-white and thus, measuring the area within that selected region. If an area was questionably part of a lesion, it was included regardless, therefore, results more accurately include

the area in between the healthy-ablated tissue zone. The resulting surface areas and necrotic tissue areas for all the sections within a tissue bundle were added. The percent ablated area was calculated by taking the percent ratio of the area of necrotic tissue to that of the viable tissue. Data are shown as mean ± standard deviation.

Results

Figure 212 displays the percent of tissue ablated for all tissue samples with each ablation modality at various doses. The control Krebs-injections showed no necrosis at any dose, suggesting that the necrosis seen in the ablated tissue samples is indeed a result of injury from ablations. For every ablative modality, the percent ablated area was dose dependent. In other words, a larger necrotic area was observed at higher ablation doses. A consistent increase in percent ablated area was observed with increasing ablation dose, except at 25 µl dose of sodium chloride. Acetic acid ablations displayed the greatest percentage of ablated tissue area, followed by cryoablation, and then ethanol and urea. Ablations with hypertonic sodium chloride showed the least necrotic area as compared to all the ablative modalities.

In another observation, the extent of necrosis caused by ablations also depended on the tissue type. Figure 213 displays the percent of ablated tissue for diaphragm and trabeculae tissue types for two chemical ablative agents (acetic acid and ethanol). For each ablative agent, and at each dose, a larger

ablated area was observed for trabeculae muscle bundles as compared to the diaphragm muscle bundles. This difference was more profound with acetic acid than ethanol. At a dose of acetic acid above 40 μL, the trabeculae muscle bundle were observed to be 100% ablated, while the diaphragmatic muscle bundles were 66% to 76% ablated.

Conclusions

These results are from preliminary studies. We were able to detect changes in tissue morphology (color) as a result of TTC stating the tissue samples following ablation. Although we have not tried reduced incubation times, we believe 2 hours is sufficient time for the TTC biochemical reaction to exhibit a distinct color change in tissue samples. We found that ImageJ, freeware downloadable software is a good tool for image analysis and processing of these images.

As described here, the authors believe that understanding and interpretation of these results could be of high value to interventional radiologists and physicians performing ablation procedures.

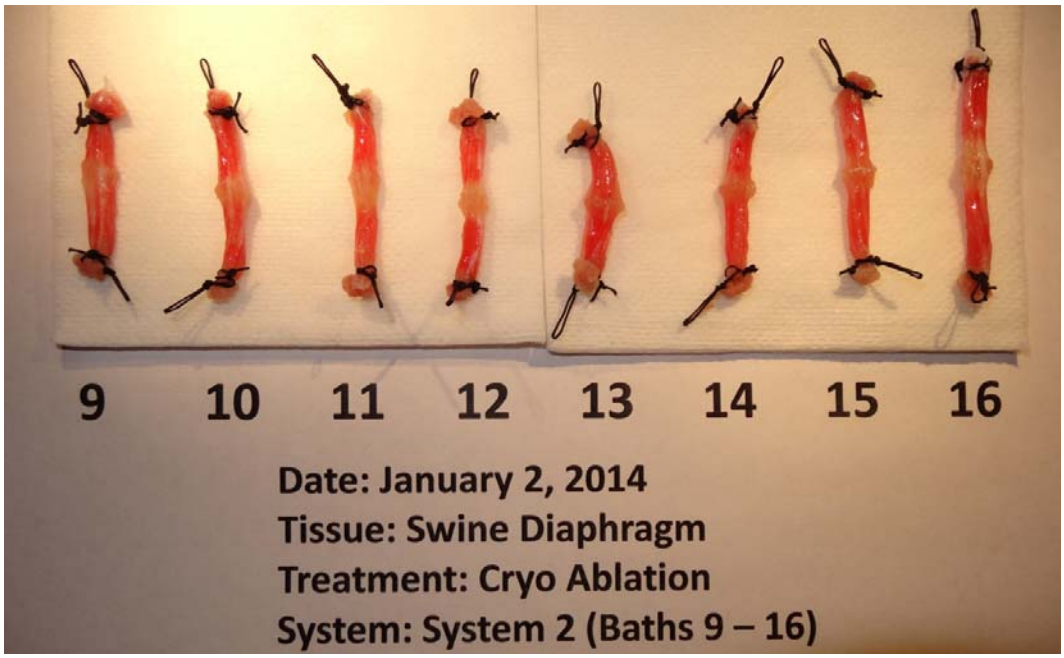

Figure 205: Cryoablated swine diaphragm muscle bundles post completion of physiological assessment protocol

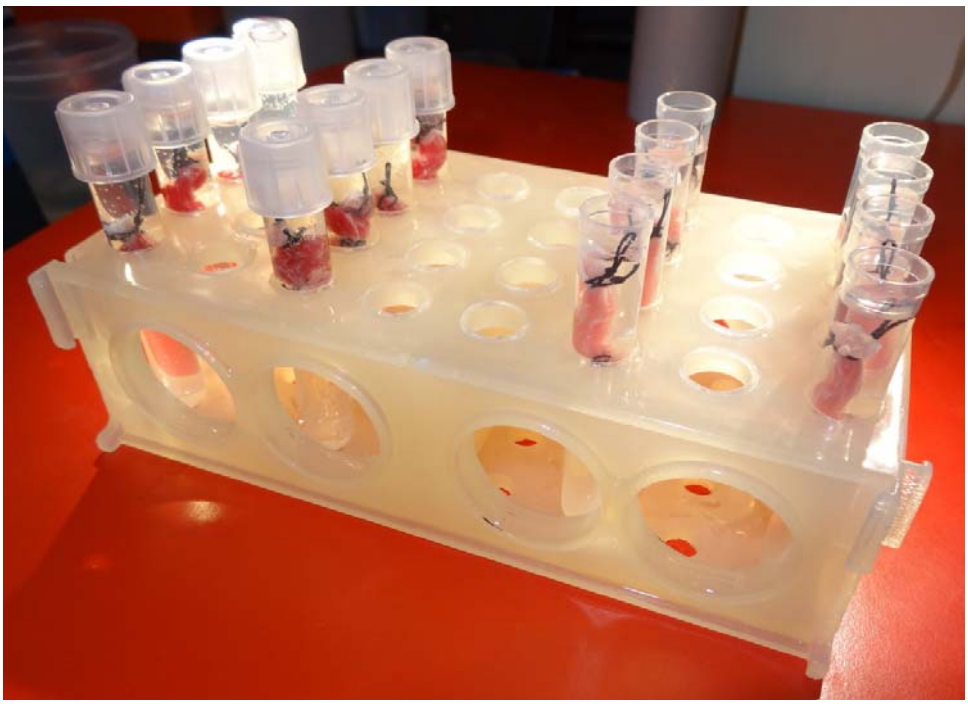

Figure 206: TTC staining of muscle bundles

Each muscle bundle is immersed in individual tubular compartments containing TTC staining solution. Samples were stained for 2 hours at 37 ° C

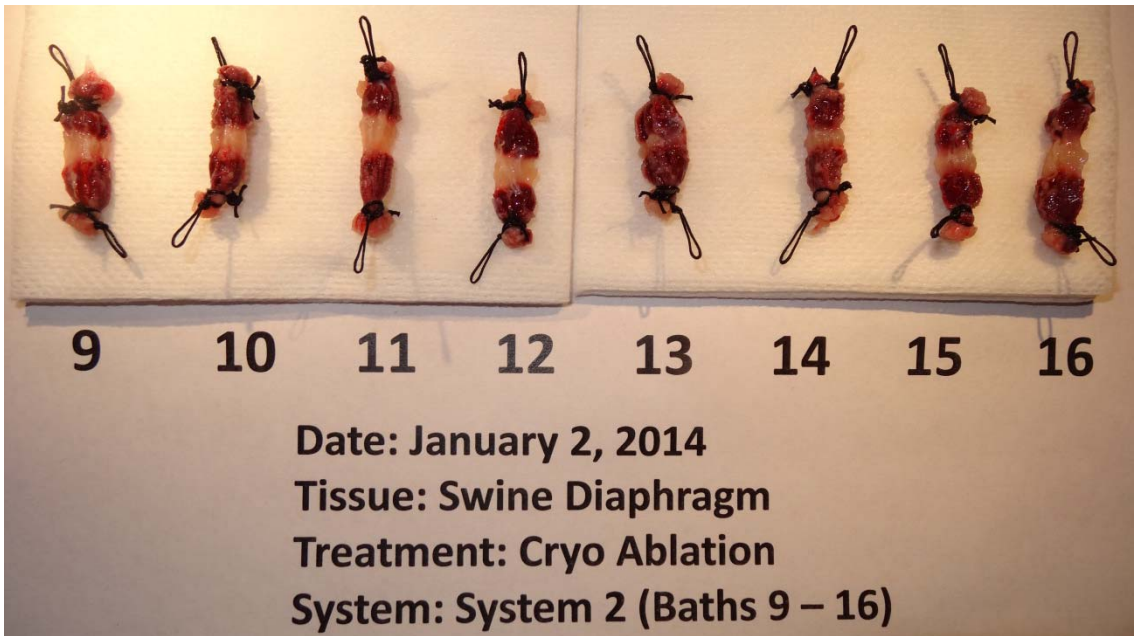

Figure 207: Cryoablated swine diaphragm muscle bundles after 2 hours of TTC staining

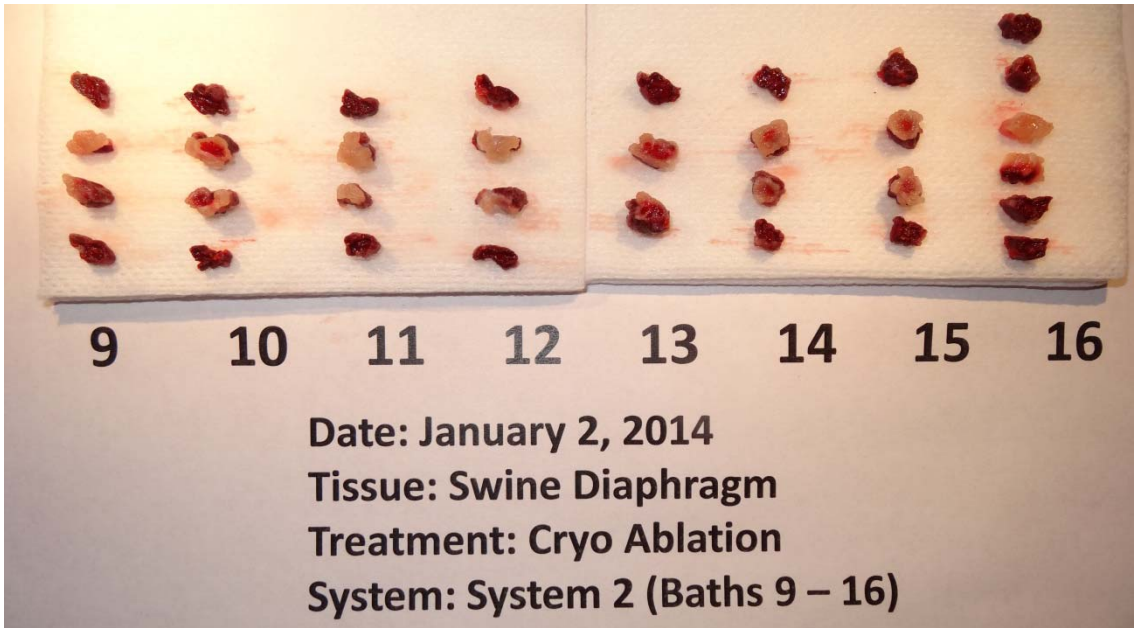

Figure 208: Cross-sectional slices of swine diaphragm

A surgical blade (#11) was used to cut thin cross-sectional slices of each muscle bundle post TTC staining. The dark-red (viable tissue) and pale-white (necrotic tissue) affected by cryoablation can be visualized in each sample. These cross-sectional slices were used in ImageJ software to calculate percent ablated area.

Figure 209: Control (Krebs-buffer injected) swine diaphragm muscle bundles after 2 hours of TTC staining

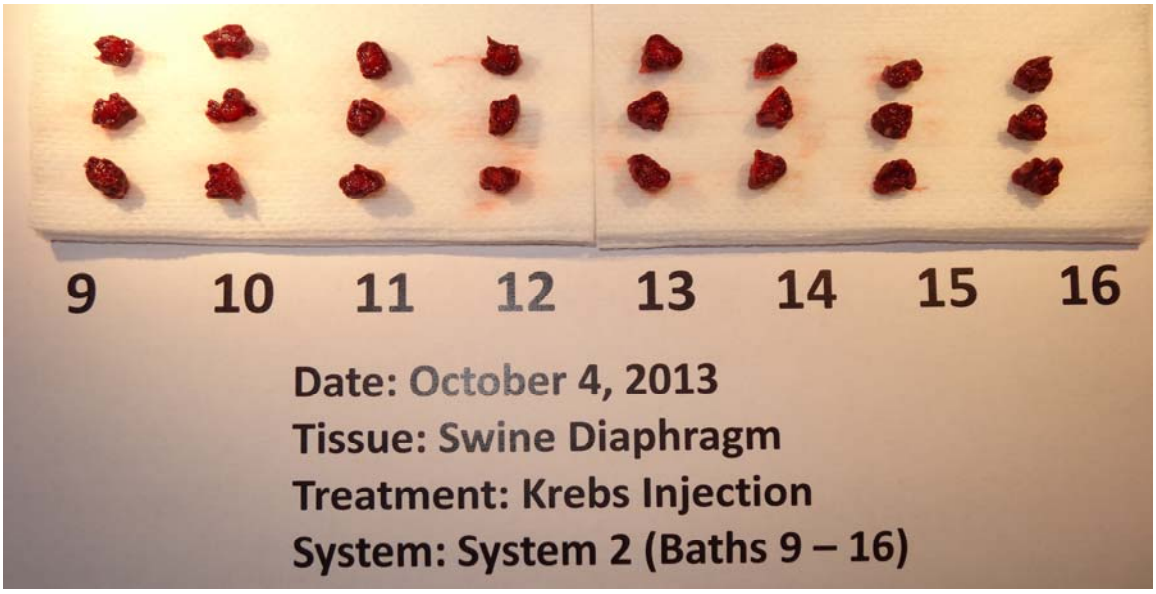

Figure 210: Cross-sectional slices of Krebs-buffer injected swine diaphragm muscle bundles

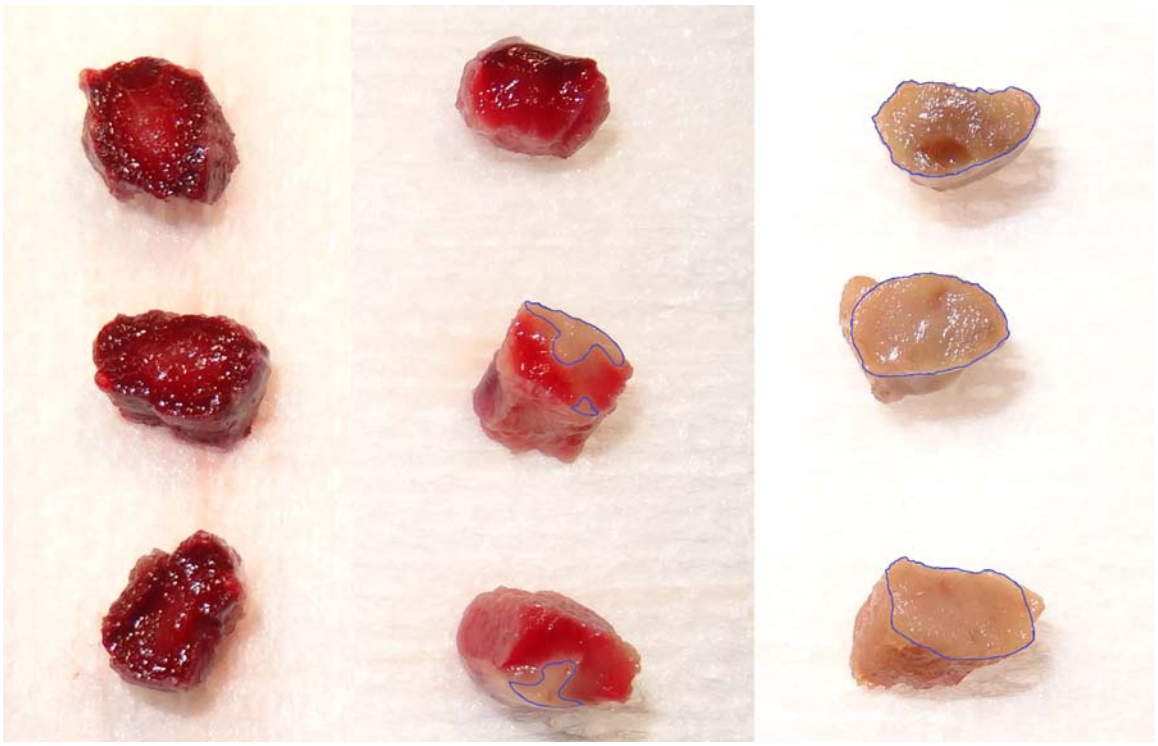

Figure 211: Ablated area determination using ImageJ software tool

The leftmost muscle bundles are swine diaphragm muscle bundles injected with Krebs-buffer solution (controls). In center and right column are swine trabeculae muscle bundles injected with 50 µL of ethanol and 50 µL of acetic acid, respectively. The ablated regions are marked in each sample.

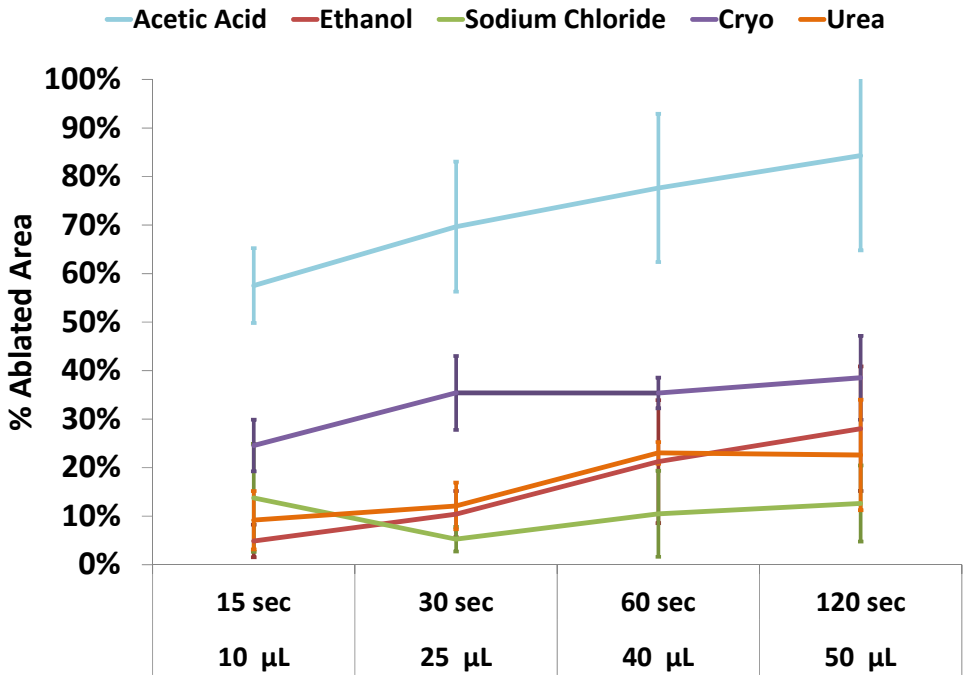

Figure 212: Dose effects of chemical and thermal ablative modalities on swine trabeculae and diaphragmatic muscle bundles on calculation of percent ablated area

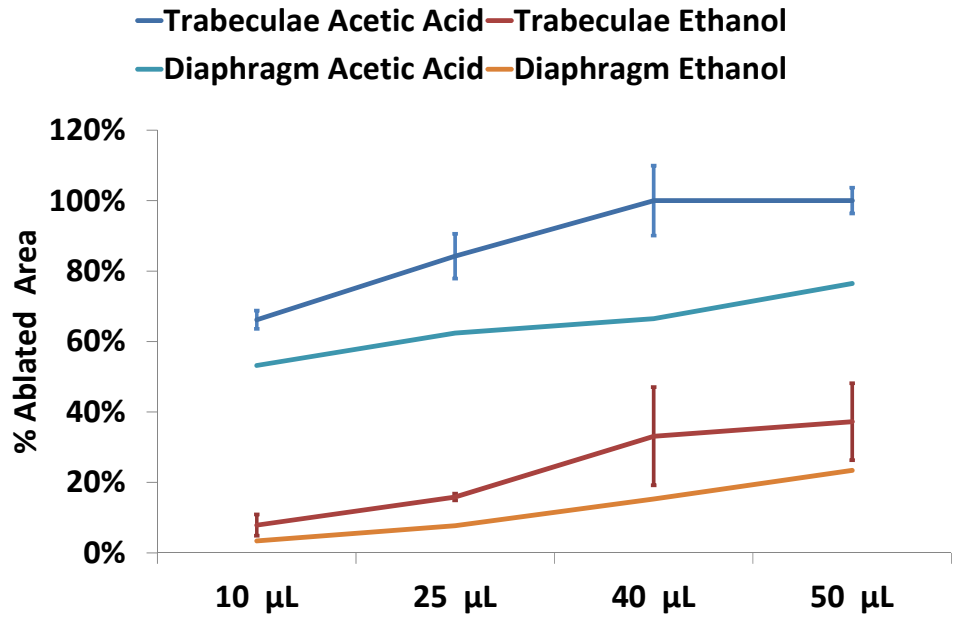

Figure 213: Dose effects on percent ablated area of swine trabeculae and diaphragmatic muscle bundles in response to ablations with acetic acid and ethanol

References

1. Fishbein MC, Meerbaum S, Rit J, Lando U, Kanmatsuse K, Mercier JC, Corday E, Ganz W. Early phase acute myocardial infarct size quantification: validation of the triphenyl tetrazolium chloride tissue enzyme staining technique. Am Heart J. 1981 May;101(5):593-600.

Appendix 6: Assessment of Biomechanical Properties of Swine and Human Non-Contractile Tissues

Ashish Singal, Charles L. Soule, Paul A. Iaizzo

Preface

Our plan is to submit this article in Journal of Medical Devices (2015).

Introduction

Scientific advances in the field of biomedical engineering are fueling the demand of new and improved medical devices and biomaterials. As new medical devices and biomaterials are developed, scientists and engineers face the enduring task of testing these devices for reliability and quality. However, one of the most desired characteristic of any prostheses is its ability to mimic, as close as possible, to the native tissue in both form and function. In order to test these devices, plethora of standardized tests are used, one of them is the uniaxial pull test that allows assessment of the biomechanical properties of the biomaterial. Tensile testing is an important method for the mechanical characterization of soft tissue.

Moreover, results from tensile testing of biomaterials must not only be compared to some standards, but also match as closely as possible to the native

tissues. Hence, testing of native tissue is as important as testing of new biomaterials so that standards can be established and universal benchmarks can be recognized.

The testing of native tissues has a lot of potential. It allows medical scientists and engineers to understand the basic and translational properties of tissues, test the performance, compatibility and quality of new biomaterials. More importantly, these test results can help in assessing how the biomaterials compare to the native tissues. The tests are performed in vitro in controlled conditions without putting the patients at risk. This testing allows for the evaluation of critical and complex issues in a controlled and repeatable manner without putting the patients at risk.

In this investigation, we sought to assess the biomechanical properties of native swine and human tissues by performing uniaxial pull tests. We hope that these results will be useful for understanding tissue properties, comparing tissue types, comparing species differences, and aid in design and development of newer biomaterials.

Methods

These studies were approved by the University of Minnesota Institutional Animal Care and Use Committee. Fresh tissue biopsies were obtained from healthy castrated male Yorkshire-cross swine (n=85, mean weight of approximately 70 kg) which were euthanized as part of another unrelated

protocol. Whenever possible, fresh human tissue biopsies (n=24) were obtained through research collaboration with LifeSource (St. Paul, MN, USA). Experimental samples included swine and human aorta, trachea, pericardium, lungs, and rectus abdominus muscle.

The native biopsies were pinned in an oxygenated, temperature controlled dissection dish, and muscle bundles were prepared as described in detail in methods Chapter 2. Tissue samples were prepared, as much as possible, in a dog bone shape [1], and superglue was used at either ends of the suture to impart added strength at the suture-tissue interface. Uniaxial pulls were performed to calculate the following biomechanical parameters: (1) avulsion forces, (2) elastic modulus, (3) avulsion strain, (4) total strain, (5) avulsion energy, and (6) total energy.

Results

Table 29 shows the biomechanical properties of both swine and human tissue samples. A total of 296 tissue sample were prepared from 5 different swine tissues and a total of 66 tissue samples were prepared from 4 different human tissues. In both species, the avulsion forces and elastic moduli for pericardium were the highest, followed by trachea, aorta, and then lungs. Interspecies differences were observed for all tissue types. In general, mechanical properties for swine tissue samples were consistently higher than human tissue samples. For example, avulsion force of swine pericardium was

20% higher than human, and avulsion force of swine aorta was 34% higher than human as shown in Figure 214. On the contrary, the avulsion force of human trachea was 58% higher than swine, and avulsion force of human lungs were 73% higher than swine. Rectus abdominus is a skeletal muscle whose avulsion forces compared well with some of the other skeletal muscles that we have measured (eg: diaphragm, with avulsion force of 0.17 N/mm^2).

Conclusions

We have developed methodologies that can be used to quantify the biomechanical properties of various tissues. These results can not only be used to understand tissue properties, but also aid in medical device design (eg: new biomaterials). Although only uniaxial tests were performed, these results can be expanded to biaxial testing which may allow for additional information in multiple axes.

These results can be beneficial in design and development of artificial heart valves made from pericardial tissue, segments of trachea in case of tracheal cancer, aortic stents in case of aortic aneurysms, and artificial lung segments in case of lung cancer.

References

1. Kemper AR, Santago AC, Stitzel JD, Sparks JL, Duma SM. Biomechanical response of human liver in tensile loading. Ann Adv Automot Med. 2010;54:15-26.

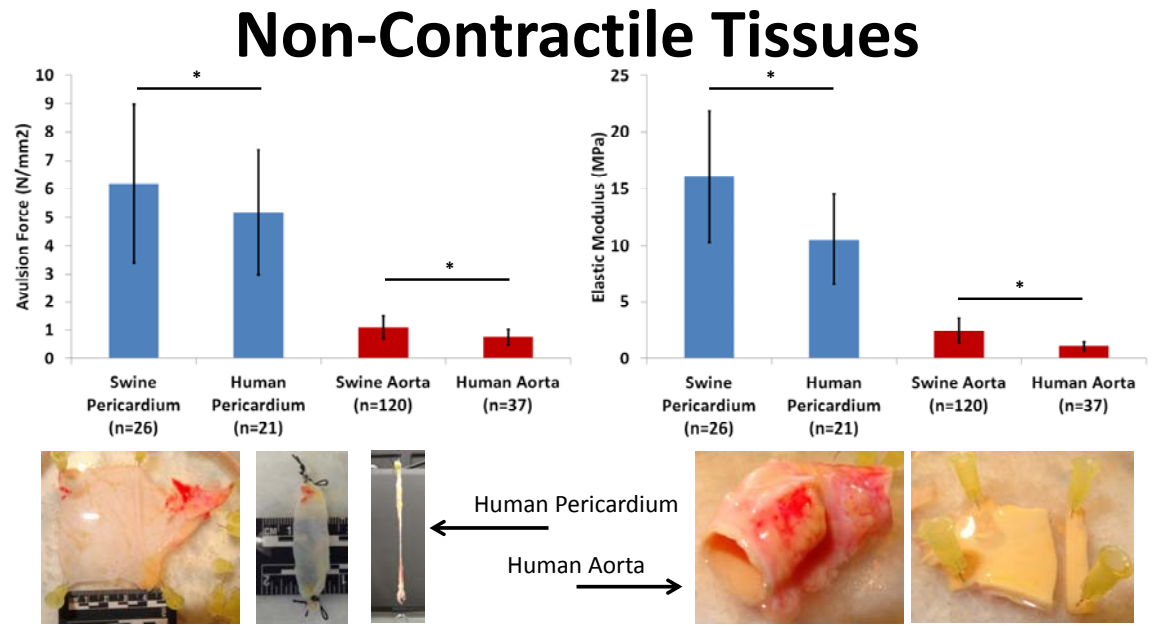

Figure 214: Inter-species comparison of biomechanical properties of non-contractile tissues

Comparison of avulsion force and elastic modulus of swine and human pericardium and aorta tissue bundles. The mechanical properties for swine tissue samples were consistently higher than human tissue samples.

	Initial Cross-sectional Area (mm^2)	Initial Volume (mm^3)	Avulsion Force (N/mm^2)	Elastic Modulus (N/mm^2)	Avulsion Strain ($\Delta l/L$)	Total Strain ($\Delta l/L$)	Avulsion Energy (mJ/mm^3)	Total Energy (mJ/mm^3)
Swine								
Pericardium (n=26)	1.94±0.39	93.63±38.30	6.19±2.79	16.07±5.81	0.68±0.25	0.88±0.25	1414.00±1094.20	1733.40±1207.50
Aorta (n=120)	6.98±2.87	172.80±105.18	1.02±0.29	2.43±1.14	1.02±0.29	1.22±0.41	230.41±127.64	304.96±182.87
Lungs (n=33)	20.45±14.95	372.44±332.88	0.11±0.05	0.22±0.14	1.03±0.39	1.81±0.67	25.94±15.28	47.58±23.15
Rectus Abdominus (n=74)	14.21±12.43	380.27±292.43	0.13±0.07	0.32±0.17	0.82±0.31	1.12±0.44	23.51±13.90	35.50±28.09
Trachea (n=43)	7.91±4.98	226.62±218.53	1.78±0.89	4.65±2.60	0.68±0.37	0.88±0.52	322.51±207.73	409.46±261.06
Human								
Pericardium (n=21)	3.70±1.24	124.88±57.85	5.18±2.19	10.55±3.97	0.76±0.34	1.07±0.44	1225.90±827.27	1545.50±998.67
Aorta (n=37)	13.59±3.84	297.33±136.21	0.76±0.28	1.00±0.40	1.44±0.35	1.76±0.48	245.91±117.05	337.67±173.64
Lungs (n=5)	18.38±6.00	526.62±187.97	0.19±0.08	0.49±0.19	0.78±0.16	1.15±0.42	38.96±20.75	50.78±28.01
Trachea (n=3)	4.33±0.00	31.34±0.00	2.82±1.93	2.35±0.21	1.74±1.08	2.10±1.14	1649.50±1972.20	2154.50±2536.60

Table 29: Mean ± SD dimensional characteristics and biomechanical parameters of swine and human non-contractile tissue bundles

Appendix 7: Conus Arteriosus as an Alternate Pacing Site

Ashish Singal, Noora Hussain, Robert Marcaccini,
Anthony J Weinhaus, Paul A Iaizzo

Published technical brief in the Journal of Medical Devices, Volume 7, Issue 3, 030902 (Jul 03, 2013)

Background

Since pacing for bradycardia began in the 1960s, physicians and medical device companies have focused on improving the software, hardware and longevity of implantable device, without paying substantial attention to the optimal pacing site within the right ventricle (RV). Historically, apical pacing within the RV was chosen as it was easily accessible, the lead placements were relatively stable and/or rates of dislodgement/infections were low. However, more recent studies have suggested potential deleterious effects of long-term RV apical pacing: i.e., some degree of induced heart failure with associated decreased hemodynamic [1] or ventricular function [2]. Both short-term [3] and long-term [4] studies on humans have confirmed these suggested adverse effects, more specifically including, abnormal ventricular activation times, right and left ventricular dysfunctions, which have been linked to genesis of heart failure. These observations have fuelled growing interest to perform alternate site pacing, but to do so without the risks for dislodgements. In other words, one

hopes to pace the heart in a more physiological manner exploiting the natural conduction system of the heart. As such, alternative pacing methods have been proposed which include: 1) Right Ventricular Outflow Tract (RVOT) pacing; 2) Direct His Bundle Pacing (DHBP); and 3) Bi-Ventricular Pacing (BVP) pacing.

The RV can be divided into a posteroinferior inlet portion (sinus) that contains the tricuspid valve apparatus, an apical heavily trabeculated region (together known as the RV inflow tract, RVIT), and an anterosuperior outflow tract (infundibulum) that extends to the pulmonary valve. Conus arteriosus (infundibulum) has been loosely defined in the literature, often as a conical extension of the right ventricle in the heart, from which the pulmonary artery originates; it is also called the arterial cone. It has been interchangeably called infundibulum having a glabrous, or smooth walls [5]. In medical literature, the word infundibulum is a generic word describing a funnel or funnel-shaped structure or passage. Wilcox defines outlet of the right ventricle as a complete muscular cone or the subpulmonary infundibulum, which extends from the ventricular base as a muscular sleeve and supports the leaflets of the pulmonary valve having parietal, septal and atrioventricular components.

A number of studies have focused on the hemodynamic benefits associated with pacing from the RVOT [6], which have resulted in RVOT as one of the most investigated alternate pacing sites [7]. Nevertheless, in general, the specific anatomy and features of the RVOT is poorly defined in the pacing literature. More specifically, the RVOT term is loosely used to describe a variety

of pacing sites all the way from supra RV apical region to the summit of the conus arteriosus just inferior to the pulmonary valve. Therefore, to better correlate the relationship between alternate pacing sites and improved cardiac function, an understanding of cardiac anatomy is essential.

In this investigation, we examined the region of RVOT in a large sample of human hearts, in particular, the conus arteriosus to develop an understanding of the anatomy and morphology of this anatomical landmark (Figure 215). We suggest that selective walls of conus arteriosus may be potential pacing sites which not only allow utilization of the natural conduction system of the heart to minimize ventricular dyssynchrony, but may also allow better lead fixation techniques due to presence of trabeculation (i.e. minimize dislodgements).

Methods

Visual examinations/evaluations of conus arteriosus from 139 formalin-fixed adult human cadaver heart specimens, of both sexes were performed. The walls of conus arteriosus (or infundibulum) in each heart were classified into four regions: the anterior, posterior, medial and lateral wall. Walls were visually examined and categorized as having a smooth morphology if the underlying tissue was smooth and trabeculated if the underlying tissue had a significantly coarse/rough appearance (i.e., due to the presence of trabeculae). All observations were obtained by more than one investigator for added verification. Figure 216 shows all 4 defined walls of the conus arteriosus and provided are

examples of either trabeculated or smooth wall morphologies. The border and demarcation between walls was determined by orienting the heart in anatomically correct position and referring to standard anatomical definitions.

Results

All four walls of conus arteriosus were visualized in all 139 formalin-fixed adult human cadaver heart specimens. In 35.7% (45/126) hearts, the anterior wall was observed to elicit significant trabeculations. Similarly, in 48.9% (64/131) hearts, the medial wall was trabeculated; in 1.4% (2/139) hearts, the posterior wall was trabeculated, and in 36.8% (50/136) hearts, the lateral wall was trabeculated. In the following number of hearts/cases: (anterior = 13; medial = 8; posterior = 0; lateral = 3) visual interpretation could not be made, because the wall was either dissected out or not present in the specimen.

In approximately 30.2% (42/139) hearts, all 4 walls were smooth (Figure 217). In 0.7% (1/139) heart, all 4 walls were trabeculated. In approximately 9.4% (13/139) hearts, all three walls, i.e. anterior, medial and lateral walls were trabeculated. Results are summarized in Figure 218.

Interpretation

We have described the region of conus arteriosus and shown that it may not always have smooth wall morphology as shown in medical literature. Conus arteriosus is an important alternate pacing site for the electrophysiologic evaluation of hemodynamic function. This is consistent with previous reports that

pacing in RVOT has both acute and chronic benefits in permanent cardiac pacing. RVA pacing is associated with LV dyssynchrony resulting in decrease in global indexes of contractility and relaxation. In contrast, pacing from the RVOT preserves cardiac performance and generates a normal, physiological activation pattern. Therefore, RVOT serves to be a potential pacing site which not only allows utilization of the natural conduction system of the heart to minimize ventricular dyssynchrony, but may also allow easy lead fixation due to presence of trabeculations. This may have important clinical significance in future of cardiac pacing, that is, understanding efficacy of alternate pacing sites, development of different types of pacing leads, tools such as catheters, stylets, and lead placement/implantation techniques.

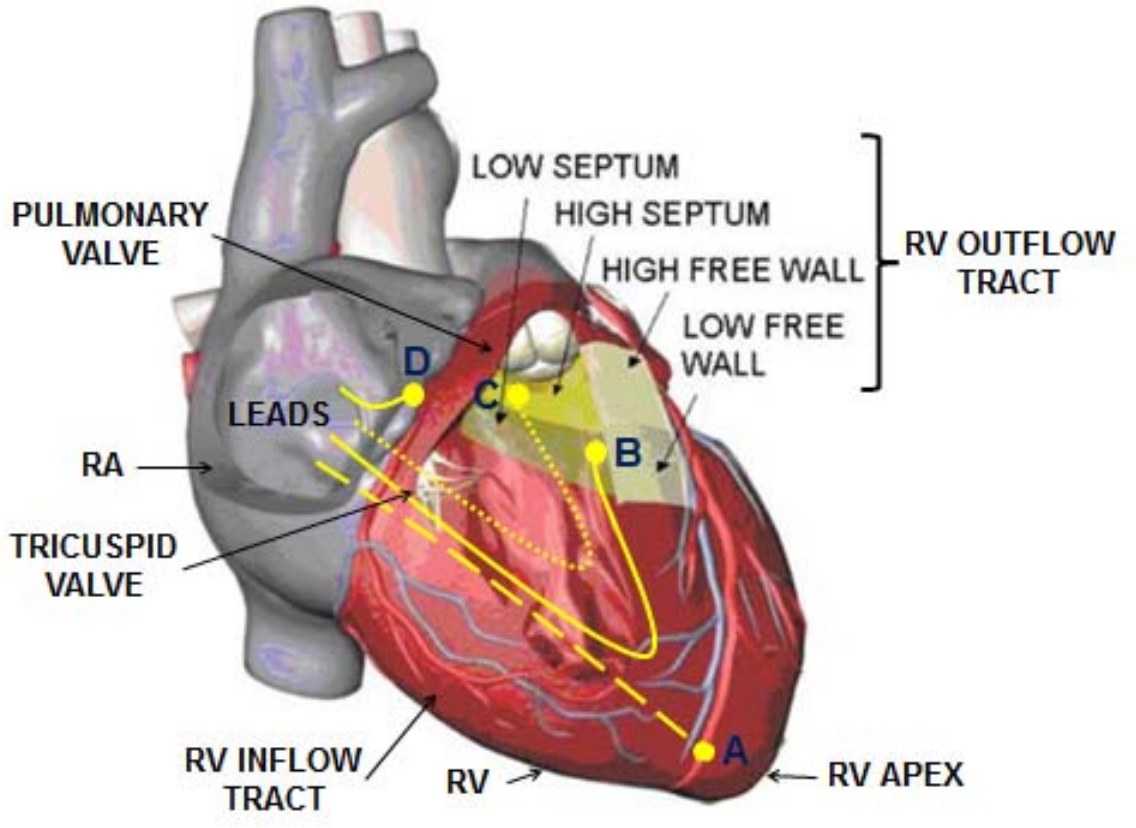

Figure 215: Illustration of different pacing sites in the RV

A: RV apical pacing site; B: RVOT low septal pacing site; C: RVOT high septal pacing site; D: Direct His Bundle pacing site on the membranous septum in the atrial aspect of tricuspid valve annulus. In this investigation, visual examination of presence of trabeculations in the septal and free wall region of RVOT was performed [8].

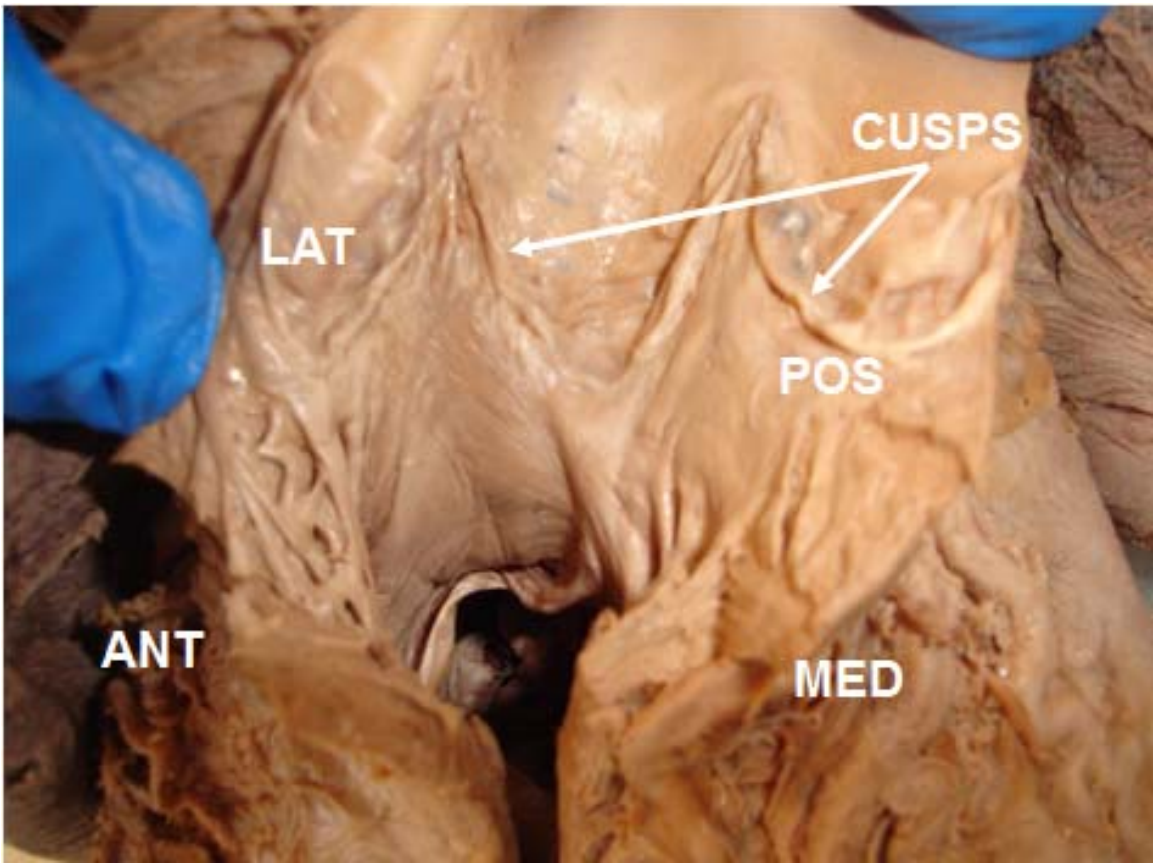

Figure 216: A look into a cadaver RVOT through the pulmonary valve

A top-down view of the pulmonary artery looking down into the RVOT through the pulmonary valve. The Anterior (Ant), Medial (Med), Posterior (Pos) and Lateral (Lat) walls of conus arteriosus are shown. In this specimen, trabeculations can be seen in the anterior and medial walls, and smoothness can be seen in the posterior and lateral walls. Also shown are the cusps of the pulmonary valve.

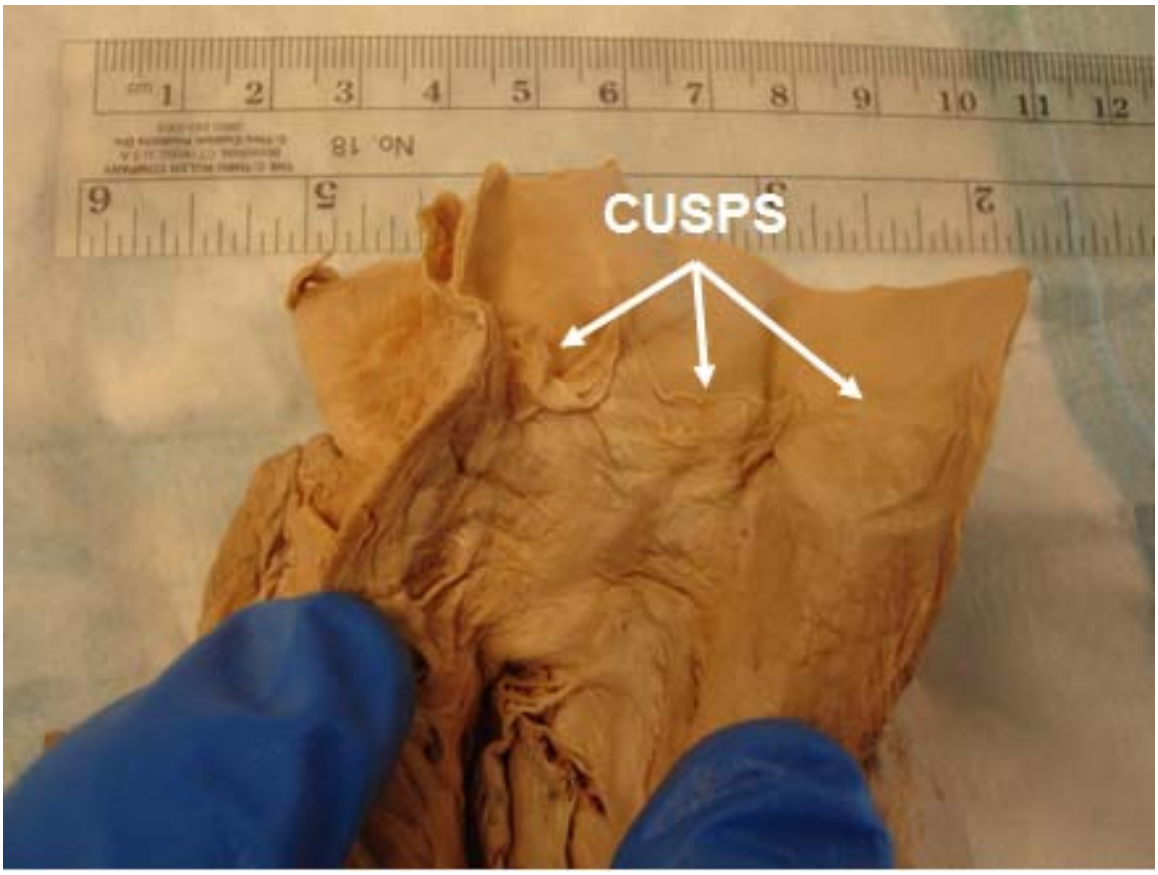

Figure 217: Longitudinal section of RVOT showing smooth morphology

Longitudinal section of RVOT (conus arteriosus) reflected after incision in the anterior wall, showing smooth morphology of all 4 walls of the conus. Also shown are the cusps of the pulmonary valve.

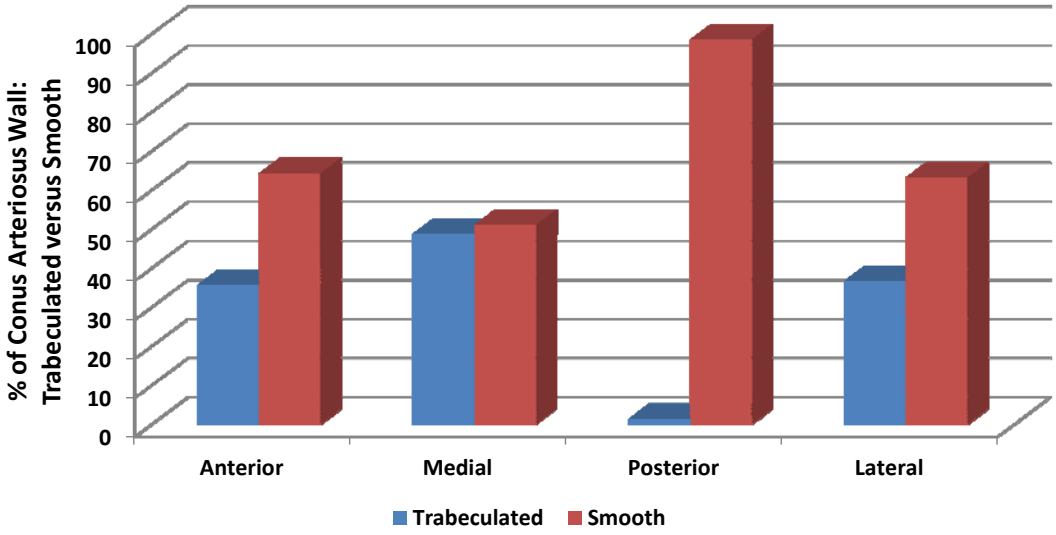

Figure 218: Percent trabeculations in RVOT (conus arteriosus) region

Percent trabeculation and smoothness observed in all four walls of conus arteriosus in 139 formalin-fixed adult human cadaver hearts.

References

1. Cock CC, Giudici MC, Twisk JW. 2003. Comparison of the haemodynamic effects of right ventricular outflow-tract pacing with right ventricular apex pacing: a quantitative review. Europace; 5:275-8.
2. Deshmukh P, Casavant DA, Romanyshyn M, Anderson K. 2000. Permanent, direct His-bundle pacing: a novel approach to cardiac pacing in patients with normal His-Purkinje activation. Circulation; 101:869-77.
3. Karpawich P, Mital S. 1997. Comparative left ventricular function following atrial, septal, and apical single chamber heart pacing in the young. Pacing Clin Electrophysiol; 20:1983-1988.
4. Tse HF, Lau CK. 1997. Long term effects of right ventricular pacing on myocardial perfusion and function. J Am Coll Cardiol; 29:744-749.
5. Agur AMR, Dalley AF. 12th Edition. Grant's, Atlas of Anatomy. Lippincott Williams & Wilkins, New York, p 57.
6. Benchimol A, Liggett MS. 1966. Cardiac hemodynamics during stimulation of the right atrium, right ventricle, and left ventricle in normal and abnormal hearts. Circulation; 33:933-44.
7. Hillock RJ, Stevenson IH, Mond HG. 2007. The right ventricular outflow tract: a comparative study of septal, anterior wall, and free wall pacing. Pacing Clin Electrophysiol; 30:942-7.
8. Vlay SC. 2006. Right ventricular outflow tract pacing: practical and beneficial. A 9-year experience of 460 consecutive implants. Pacing Clin Electrophysiol; Oct;29(10):1055-62.